Table of Content

Fluid Mechanics

The 5th International Conference on Engineering Mechanics and Automation (ICEMA 5)
Hanoi, October 11÷12, 2019

Nearshore wave current calculating in Thien Cam beach - Ha Tinh province

Dang Song Ha[a], Dinh Van Manh[b,c]

[a] *Institute of Mechanics, 264 Doican Str. riversong2104@gmail.com*
[b] *Institute of Mechanics, 264 Doican Str. dvmanh@imech.vast.vn*
[c] *Graduate University of Science and Technology, VAST, 18 Hoangquocviet Str.*

Abstract

Coastal areas of Ha Tinh province have a complex flow regime, influenced by many factors such as tide, wind, wave... In some previous researches, the authors calculated and simulated the typical wave regimes of the study area with a high degree of confidence. This research inherits the results from previous researches and focuses on the calculation of the nearshore current generated by wave radiation stresses.

Keywords: Nearshore wave current, wave induced current, Thien Cam beach

1. Introductions

Wave current is a type of ocean flow that greatly affects to coastal hydrodynamic processes. This is a relatively complex form of ocean currents, formed by a combination of random factors such as waves, tides, sea bottom and shoreline topographies. The most known of these is the RIP current, the form of the split current that can be dangerous to human life.

The area selected for research is Thien Cam beach, Ha Tinh province. According to the actual record, RIP currents in this area does not appear as often and fixed as in some beaches in Nha Trang or Da Nang cities, so its appearance is unexpected, difficult to predict and causing serious consequences. With the purpose of understanding the cause and the mechanism of RIP current in Thien Cam beach, this research will simulate and analyse the wave induced current of the research area.

The model used in the simulations was developed by a team of the Institute of Mechanics. The processes include: wave propagation, reflection, bottom dissipation and breaking waves. These processes often predominate in nearshore areas. The calculation plans are based on the characteristic wave statistics from the wave data series collected in research area.

2. Processes and formulations

The process of calculating the propagation of waves from offshore to nearshore based on the energy balance equation(Mase,2001). In order to improve the prediction ability of the model in surf zone, Pham Thanh Nam (Nam, P.T., 2009) and his colleagues improved the calculation of energy dissipation due to wave breaking by the method of Dally. Then, the equilibrium equation of the model can be written as follows:

$$\frac{\partial(\nu_x S)}{\partial x}+\frac{\partial(\nu_y S)}{\partial y}+\frac{\partial(\nu_\theta S)}{\partial \theta}=\frac{\kappa}{2\omega}\left\{(CC_g\cos^2\theta S_y)_y-\frac{1}{2}CC_g\cos^2\theta S_{yy}\right\}-\frac{K}{h}C_g(S-S_{stab}) \quad (1)$$

where h is the water depth, K is the decomposition coefficient, S_{stab} is the stable wave energy density determined by the stable wave height H_{stab} (=Γh), with Γ is the coefficient of stability.

Suppose S and S_{stab} are quadratic functions of wave height and wave stability. Then, equation (1) is rewritten in the following form:

$$\frac{\partial(\nu_x S)}{\partial x}+\frac{\partial(\nu_y S)}{\partial y}+\frac{\partial(\nu_\theta S)}{\partial \theta}=\frac{\kappa}{2\omega}\left\{(CC_g\cos^2\theta S_y)_y-\frac{1}{2}CC_g\cos^2\theta S_{yy}\right\}-\frac{K}{h}C_gS\left\{1-\left(\frac{\Gamma h}{H_s}\right)^2\right\} \quad (2)$$

The decomposition and stability factor are defined as a functions of the sea bed slope, wave height and wave length as follows:

$$\Gamma=0.45+\beta, K=\frac{0.9}{8}\left(1+\frac{\beta}{\sqrt{H_0/L_0}}\right) \quad (3)$$

where β is the sea floor slope, H_0 and L_0 are wave height and wave length.

The nearshore and the inside breaking wave zone, wave propagation were calculated using the MSWave module, based on the Second order time dependent mild slope equation (Ching-PiaoTsai, 2014).

$$\frac{\partial\eta}{\partial t}+\nabla.\left[\left(\frac{c^2}{g}+\eta\right)\vec{U}\right]=0, \quad (4)$$

$$n\frac{\partial\vec{U}}{\partial t}+g\nabla\eta+\frac{1}{2}\left(1-3\frac{k^2c^4}{g^2}\right)\nabla(\vec{U}.\vec{U})=\frac{1}{c^2}\nabla\left[\frac{c^2(1-n)}{k^2}\left(\nabla.\frac{\partial\vec{U}}{\partial t}\right)\right] \quad (5)$$

where:
∇: the horizontal vector operator;
$\vec{U}$: the horizontal velocity identical to mean flow velocity in shallow water condition;
η: the water surface elevation;
t: the time;
g: the acceleration due to gravity.

The process of calculating the wave induce current is performed in the WST19 module. This module was developed and perfected by a team of the Institute of Mechanics. The basic equations for this module are Continuity equation(6) and Momentum eaquation(7,8) (Mengguo LI, 2003):

$$\frac{\partial[(h+\zeta)u]}{\partial x}+\frac{\partial[(h+\zeta)v]}{\partial y}=0 \quad (6)$$

$$u\frac{\partial u}{\partial x}+v\frac{\partial u}{\partial x}=-g\frac{\partial\zeta}{\partial x}+T_x+P_x+M_x-F_x \quad (7)$$

$$u\frac{\partial v}{\partial y}+v\frac{\partial v}{\partial y}=-g\frac{\partial\zeta}{\partial y}+T_y+P_y+M_y-F_y \quad (8)$$

where x and y are the coordinates in the Cartesian coordinate system; u and v are depth averaged nearshore current velocity components; g is acceleration due to gravity; h is still water depth; ζ is the water surface displacement; T_x,T_y are components of acting force on unit mass water body caused by radiation stress in x and y directions respectively; P_x, P_y are components of acting force on unit mass water body caused by rollers in breaking wave in x and y directions respectively; M_x, M_y are components of acting force on unit mass water body caused by eddy viscosity; F_x, F_y are are components of acting force on unit mass water body caused by bottom friction.

The radiation stresses can be define by:

$$S_{xx}=E[(2n-1/2)-n\sin^2\theta]-\frac{\rho M_{Wx}^2}{h+\zeta} \quad (9)$$

$$S_{yy}=E[(2n-1/2)+n\sin^2\theta]-\frac{\rho M_{Wx}M_{Wy}}{h+\zeta} \quad (10)$$

$$S_{xy}=S_{yx}=En\sin\theta\cos\theta-\frac{\rho M_{Wy}^2}{h+\zeta} \quad (11)$$

where n= C_g/C; C_g is wave group velocity; C is wave celerity; θ is wave direction; ρ is water density; $E=\rho gH^2/8$; H is wave height; M_{Wx}, M_{Wy} are water discharges representing the onshore mass flux.

The stresses due to rollers in breaking waves can be define by:

$$R_{xx}=2E_r\cos^2\theta \quad (12)$$

$$R_{yy}=2E_r\sin^2\theta \quad (13)$$

$$R_{xy}=R_{yx}=E_r\sin2\theta \quad (14)$$

In wich, E_r is the roller energy per unit area.

3. Data collection

3.1. Bathymetry data

a. Measurement data: Actual measurements for the Thien Cam - Ha Tinh area are directly measured by a depth measuring system combined with GPS for very detailed topographic results with resolution up to 2m with a beach topography and 10m with sea bed topography. In addition, topographic data related to the calculation area has been collected from many other sources such as digitized data from the Naval map, data from neighboring surveys.

b. GEBCO_08 data: The General Bathymetric Chart of the Oceans (GEBCO). GEBCO_08 data grid is a global bathymetry mesh data set. The mesh size is about 30 seconds longitude – latitude (about 900m) , created by combining the depth points measured by ships with depth data determined from satellite image data.

c. SRTM_4.1 data: Shuttle Radar Topography Mission (SRTM). It has a high resolution (about 25m), has almost global coverage (from 56 °S to 60 °N), and it is free data.

Figure 1. Bathymetry scatter points

3.2. Wave data

Measurement data by AWAC: Field survey data are recorded by AWAC instrument located offshore to measure offshore wave data.

Wave data from SWAN model. SWAN model can calculate wave fields from wind fields. Input wind data for this model can be downloaded for free at NOAA's website. Offshore wave data was recalculated using SWAN model to provide wave data in case absence of data.

Nearshore wave data: Nearshore wave data at some observation locations were recorded and analyzed by Wave Monitoring method by Camera.

3.3. Tidal data

Tidal data in the calculations are referenced and extracted from adjacent international tidal stations with high reliability. In this research, the authors compared the obeserver tidal data with the tidal data collected from Hon Nieu – An Nam IHO international tidal station. The comparison results show a very high level of similarity between the tidal of the calculated area and the tidal at Hon Nieu tide station. Thus, in calculations for the research area we can refer directly to tidal data at Hon Nieu international tidal station.

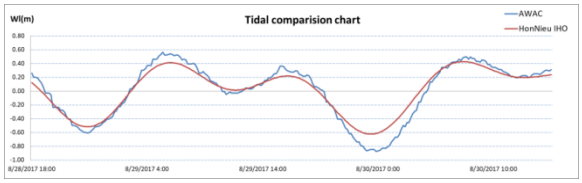

Figure 2. Tidal comparison chart

4. Model setting

4.1. Domain setting

With the task of calculating the wave induce currents for the research area, the calculation model was setup for the Thien Cam area including 3 domains:

Deep water domain: Mesh size is140x170 grid cells with 200x200m grid step covering the entire region from 24m deep water to the shore.

Nearshore domain: Mesh size is 270x520 grid cells with 5x5m grid step.

Detailed mesh for shallow water near the shore is created for each offshore wave directions. The grid step is 2x2m.

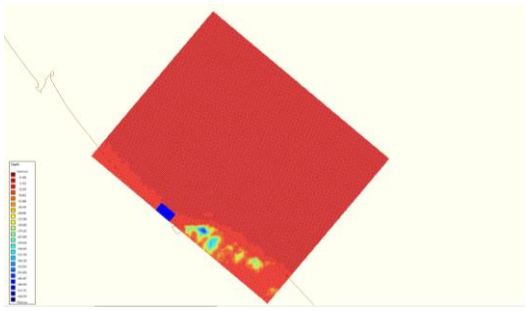

Figure 3. Domain for the calculation model

4.2. Model calibration and verification

As stated in some previous researches, the model has been calibrated and verified for good results. Typical wave fields also was calculated for the research area.(Ha.D.S et. al, 2019).

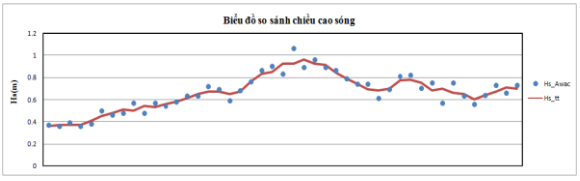

Figure 4. Wave height comparison chart (offshore)

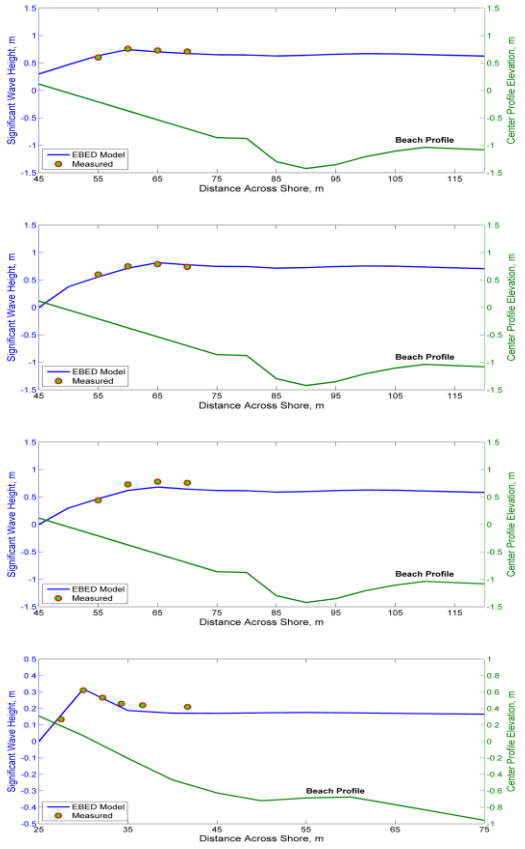

Figure 5. Wave height comparison charts (nearshore)

5. Simulations for wave induced current

5.1. Simulation plans

Re-analyzed wave data for this parth is calculate results of SWAN model for location with coordinates are 106.375^{0}E and 18.373^{0}N, off the shore of Ha Tinh sea. The collected data is hourly data from 2005 to 2018. Base on the series of re-analyzed wave data, the calculation plans will be built on the basis of analyzing this wave sequence and selecting the options that effect to the research area. Because of the rotation angle of the shoreline, we only focus to the directions of the incoming waves in the range from N direction to E-SE direction.

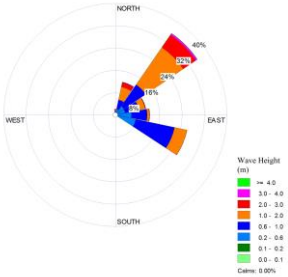

Figure 6. Wave rose for the research area in 6 main directions

Wave parameters at the open boundary are determined by Roelvink formula (2012):

$$H_{s,rep} = \left(\frac{\sum_i p_i H_{s,i}^{2.5}}{\sum_i p_i}\right)^{1/2.5} \quad (15)$$

where: p_i is the frequency of wave, $H_{s,i}$ is the wave height in the i direction.

Wave boundary conditions for the nearshore domain are outputs of the offshore wave calculations(Ha.D.S et. al, 2019). The results are showed in the table:

Table 1. The Calculation options

Plans	Dir.	Nearshore wave parameters		
		Hs(**m**)	Tp(**s**)	θ(**deg.**)
1	N	0.83	4.7	11.6
2	N-NE	1.32	5.31	27.8
3	NE	1.36	5.71	42.8
4	E-NE	0.72	4.49	61.8
5	E	0.53	4.56	77.0
6	E-SE	0.48	4.2	86.0

5.2. Simulation results

Nearshore wave parameters of the calculation options are applied for the open boundary of the

detailed domain. Wave propagations and wave stress are calculated by mild slope equation. Wave – current interaction process are computed in hydodynamic module and outputs of the model give us detailed 2D current fields of the research area. Some results are shown in the following figures:

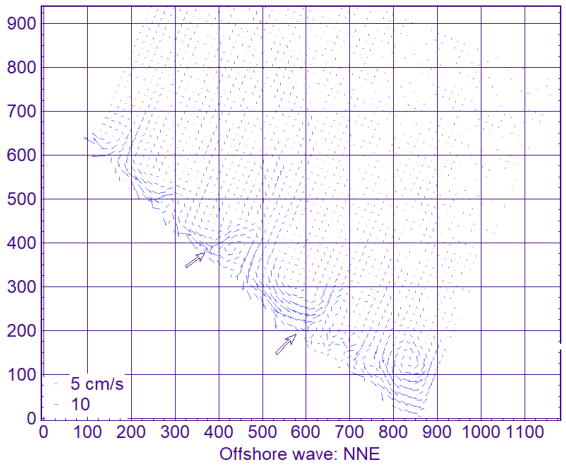

Figure 7. Current field (N-NE wave direction)

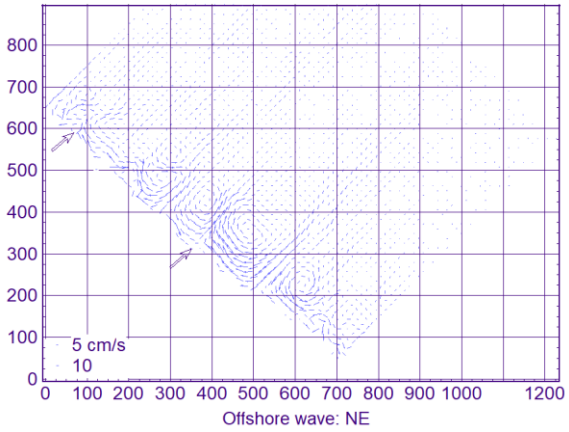

Figure 8. Current field (NE wave direction)

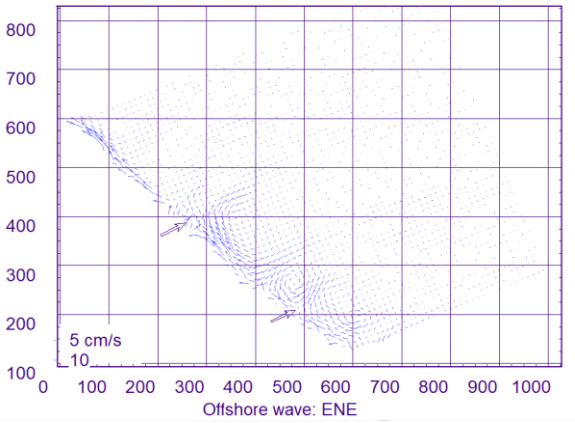

Figure 9. Current field (E-NE wave direction)

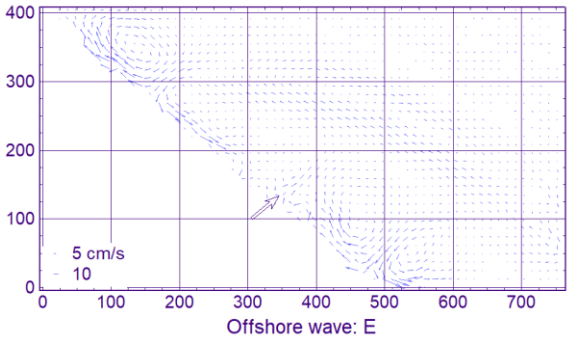

Figure 10. Current field (E wave direction)

The simulation results of wave induced current show that:

- There is a phenomenon of RIP current in the research area.

- With the calculated plans, RIP currents appears clearly in the N-NE, NE, E-NE and E wave directions. In other wave directions, it is not appear or not very clear.

- RIP currents in the research area happen in some locations where the headland protrudes into the sea or the shoreline is not aligned (*see the arrow position in the figures*), like the fixed RIP type.

- Also according to the simulation results, the RIP current speed is not very strong, but it depends on the wave direction, wave height and the bathymetry. The impact of these factors will be considered in more detail when taking into account the influence of tides in the next research of the authors.

6. Conclusions

This research collected and analyzed a lot of topographic and wave data of the research area.

The offshore wave regime of Hatinh was evaluated.

This research has developed and perfected the wave and current calculation modules for good test results.

A system of numerical models has been setup in order to calculate in detail the wave induced current for Thien Cam beach. Under some wave conditions, the RIP current in this area would be

occurred, such as N-NE, NE, E-NE and E wave directions.

In order to have a more detail wave field and RIP current characteristics in Thien Cam beach, it necessary to get more detailed topographic of the research area.

Acknowledgments

The authors acknowledge supports for this research through grants of VAST.NĐP.01/16-17.

References

Ching-PiaoTsai et. al, (2014). *Second-Order Time-Dependent Mild-Slope Equation for Wave Transformation.* Mathematical Problems in Engineering Volume 2014, 15 pages.

Ha, D. S. et. al, (2019). *Applying testing method of observing near-shore wave by Camera.* Vietnam national mechanical conference.

Ha, D. S. et. al, (2019). *Application of M-EBED model to research nearshore wave field in Thien Cam - Ha Tinh.* Vietnam national mechanical conference.

Mase, H., (2001). *Multi-directional random wave transformation model based on energy balance equation.* Coastal Engineering Journal 43(4),pp. 317-337.

Mengguo LI, (2003). *Numerical simulation of wave induced nearshore current.*International Conference on Estuaries and Coasts November 9-11, 2003, Hangzhou, China.

Nam, P.T., Larson, M., Hanson, H., Hoan, L.X., (2009). *A numerical model of nearshore waves, currents, and sediment transport.* Coastal Engineering 56,pp. 1084-1096.

The 5th International Conference on Engineering Mechanics and Automation (ICEMA 5)
Hanoi, October 11÷12, 2019

Design and simulation of a vertical axis wind turbine for using on navigational buoys

Dang The Ba[a], Do Huy Diep[a], Pham Hai Yen[b] and Nguyen Van Duc[a]

[a]*Faculty of Mechanics and Automation Engineering ,VNU University of Engineering and Technology, VNU*
[b]*Faculty of Electrical Engineering - Mechatronics, Phuong Dong University*
Email : badt@vnu.edu.vn

Abstract:

At present, wind turbine is mainly designed in two forms: vertical and horizontal axis turbines. However, they cannot be installed on navigational buoys because of disadvantages such as difficulty in balancing and easily damaging when colliding with external objects. A vertical axis wind turbine for navigation buoys has been developed. The report presents the structure development, simulation and design of a vertical axis wind turbines suitable for navigation buoys. This device can also be developed appropriately located in many location in the city to provide electricity to households or offices in a simple, portable and still safe way.

Key words: Wind energy, Vertical wind turbine, CFD.

1. Introduction

The horizontal axis turbines have the advantage of high conversion efficiency and large capacity. It is suitable for open areas and strong winds. However, in areas where space is limited or the operating conditions of horizontal wind turbines are not sufficient, vertical axis turbines should be selected, for example in urban areas. However, the current vertical turbine is still designed with unprotected wings, so it is still not safe to install in low places, likely to collide with vehicles, people or animals.

The published researches generally centered on the hydrodynamic simulation of turbine blades and the logic setting of the controller; CFD technology has been widely applied in turbine design. Hirsch (1990) [1] applied CFD in blade simulation. Bardina et al. (1997) [2] commented that the SST k-ω turbulence model derived by the Menter (1994) [3] was suitable for predicting the flows with separation under adverse pressure gradients. Since the 2000s, much attention has been paid to achieving higher efficiency for wind turbines. Eftichios et al. (2006) [4] applied the Perturb and Observe Algorithm to track the maximum power of the turbine system by the controller. Adam et al. (2007) [5] set Fuzzy Logic in the controller to obtain maximum power. Qing'an et al. (2015) [6] tested the effect of blade number on aerodynamic forces of a straight-bladed VAWT, and it was clarified that the power coefficient decreases with the increase of numbers of blades. Kosasih, and Hudin (2016) [7] improved the performance of the turbine system by detecting turbulence intensity. Yin et al. (2016) [8] analyzed the system design, basic dynamic characteristics, thermal losses and management aspects; hydro-viscous transmission was applied to enhance the overall efficiency. Natapol and Thananchai (2016) [9] presented a wind booster to enhance

performance of the VAWT at both low and high wind speeds. In Jian et al. (2016) [10], an airfoil family was specified by a coupled approach. This airfoil family achieved higher efficiency than traditional NACA 0015 by 15.5%. Besides, it was verified that the thickness-chord ratio had the biggest effect on the blade efficiency. Abdolrahim et al. (2017) [11] simulated a VAWT by 2D unsteady Reynolds-averaged Navier-Stokes. It was verified the 3D tip effects are negligible as the aspect ratio of the turbine is high. Ghulam, and Uzma (2017) [12] applied magnetic levitation method to the axial flux permanent magnet generator of a VAWT for increasing the efficiency. Under the inspiration of migrating geese flying in a V or I formation to save energy, Baoshou et al. (2017) [13] presented a novel wake energy reuse method to optimize the Savonius-type VAWT. Qing'an et al. (2017) [14] investigated the effect of rotor aspect ratio and solidity on a straight-bladed VAWT by 3D Panel Method. It was concluded the peak of power coefficient increases with the increase of the ratio of the blade span length and diameter at the fixed solidity. In this report, a structural model of vertical axis wind tower was built, the wind tower has the function of changing the horizontal wind direction to vertical wind direction, then the rotor structure will be used as the horizontal axis wind turbine, but mounted on the vertical axis of the wind tower. CFD simulation tool will be used to simulate airflow through the tower, thereby calculating and determining the effective structure for wind flow conversion..

2. Structure of wind tower on buoy

Navigational buoys are mainly made of steel, wood or composite. The specific structure of a buoy can be different, but it is usually in the form like Fig.1. The buoy must ensure some specific requirements such as: stable floating on the water, on the buoy must be attached with indicator symbols (marker) in accordance with Vietnamese and world regulations.

The purpose of navigational buoys is to set up tools and operate on water; be anchored or tied in a certain position to guide sea-going people and related organizations and individuals to orient and determine the position of ships and boats; Navigational buoys may use visible signs or use the AIS (Automatic Indentification System) to inform informationn. Signal range is the maximum distance from the observer to the signal that the observer perceives that signal to orient or determine his position; The meaning of the sign is shown on the signboard as prescribed in the regulations of QCVN 20:2010/BGTVT [20]; signal buoys have two main parts: buoys and markers on it. In many cases, buoys have additional lights so they can signal at night. Shape, color, brightness are also specified in QCVN 20:2010/BGTVT.

Fig. 1. Navigational buoy

With the purpose of using wind energy to supply lights and equipment on the buoy, a wind tower is designed to change the direction of the wind into the turbine from horizontal to vertical. The rotor structure and the conversion mechanism are still the same as the horizontal axis turbine, but the vertical axis is installed. This structure is simple, both taking advantage of the horizontal axis turbine but ensuring balance and protecting the rotor from being exposed to the outside, safe during operation.

This structure is suitable for assembly on signal buoys as well as other buoys that require power. Moreover, this structure can also enlarge in size and combine with other energy sources such as

the solar and waves to form a renewable energy station at sea for socio-economic purposes on the sea and islands.

The structure of signal buoys with wind energy tower is depicted in Fig.2a. The structure of renewable energy stations including wind, solar and wave is described as Fig.2b. To determine the structure of high efficiency and accordingly, simulation and calculations for airflow through the wind tower will be performed. The tool will be ANSYS FLUENT software.

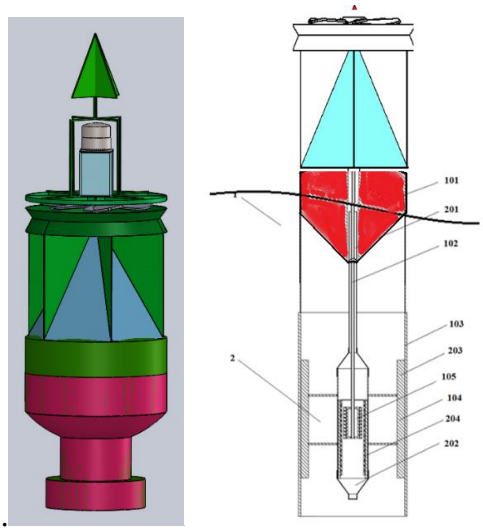

a) b)

Fig.2. a)Buoy with wind tower and b) Renewable energy station on the sea.

3. Numerical modelling

3.1 Mathematical model

The aerodynamics of the present study case is investigated by using the commercial CFD software, ANSYS FLUENT. The SST (Shear-Stress Transport) k-ω turbulence model of the second-order upwind scheme with the SIMPLE algorithm method is applied to solve the Reynolds-averaged Navier Stokes (RANS) equations. ANSYS Fluent solves the RANS equations by finite element discretization. The SST k-ω model introduced by Menter (1992) [15] is applied in this paper. The SST k-ω model has been strongly recommended by Menter (1992) [16]. The SIMPLE algorithm derived by Patankar & Spalding (1972) [17] was used to solve the incompressible flow. The main idea of this scheme is to update the pressure and velocities by corrected terms.

3.2 The governing equations

For this problem and from Yuwei et al. (2012) [18] mentioned that the flow in wind tower is still essentially incompressible with Mach numbers did not exceed 0.25; thus, it was reasonable to consider the flow as incompressible in this paper. With the assumptions of incompressible and turbulent-steady flow, mass and momentum conservation equations can be written respectively as below:

$$\frac{\partial \overline{u}_j}{\partial x_j} = 0 \tag{1}$$

$$\rho \frac{\partial \overline{u}_i}{\partial t} + \rho \overline{u}_j \frac{\partial (\overline{u}_i)}{\partial x_j} = -\frac{\partial P}{\partial x_i} + \frac{\partial}{\partial x_j}\left(\mu \frac{\partial (\overline{u}_i)}{\partial x_j} \right) + \frac{\partial R_{ij}}{\partial x_i} \tag{2}$$

where $\overline{u}_j$ is the average velocity along the x_j direction, ρ is the fluid density, P is average pressure, R_{ij} is the Reyonlds stress.

$$R_{ij} = -\rho \overline{u_i' u_j'} \tag{3}$$

3.3 The applied turbulent model

The two equations of SST k-ω model are as followings [15].

Turbulence Kinetic:

$$\frac{\partial \rho k}{\partial t} + \frac{\partial (\rho k \overline{u}_i)}{\partial x_i} = \frac{\partial}{\partial x_j}\left(\Gamma_k \frac{\partial k}{\partial x_j} \right) + G_k - Y_k + S_k \tag{4}$$

Specific Dissipation Rate:

$$\frac{\partial \rho \omega}{\partial t} + \frac{\partial (\rho \omega \overline{u}_i)}{\partial x_i} = \frac{\partial}{\partial x_j}\left(\Gamma_\omega \frac{\partial \omega}{\partial x_j} \right) + G_\omega - Y_\omega + S_\omega + D_\omega \tag{5}$$

Here G_k is the turbulence kinetic energy caused by the mean velocity gradients, G_ω the generation of ω, Γ_k and Γ_ω the effective diffusivity of k and ω, Y_k and Y_ω the dissipation of k and ω due to turbulence, S_k and S_ω source terms, and D_ω the cross-diffusion term.

3.4 SIMPLE algorithm method

The SIMPLE algorithm is often used to solve the incompressible flow. The main ideal of this scheme is to update the pressure and velocities by corrected terms. In this scheme, the momentum equation is replaced by following discrete form.

$$a_n u_n^{'} = \sum_{nb} (a_{nb} u_{nb}^{'}) + A_n (P_P^{'} - P_N^{'}) \quad (6)$$

where a_{nb} is the coefficient of the convective and diffusive terms summed by the nearby grid points. $A_n(P_P - P_N)$ presents the pressure force on the control volume. The corrections in velocity from the nearby grid points are assumed to be ignorable.

$$\sum_{nb} (a_{nb} u_{nb}^{'}) = 0 \quad (7)$$

The corrected terms in velocities can be reformed.

$$\begin{aligned} u_n^{'} &= d_n (P_P^{'} - P_N^{'}) = \frac{A_n}{a_n} (P_P^{'} - P_N^{'}) \\ v_e^{'} &= d_e (P_P^{'} - P_E^{'}) = \frac{A_e}{a_e} (P_P^{'} - P_E^{'}) \\ \mathrm{w}_u^{'} &= d_u (P_P^{'} - P_U^{'}) = \frac{A_u}{a_u} (P_P^{'} - P_U^{'}) \end{aligned} \quad (8)$$

The corrected term in pressure can be calculated by following.

$$aP^{'} = \sum a_{nb} P_{np}^{'} \quad (9)$$

Thus, the updated pressure and velocities are as below.

$$\begin{aligned} P &= P^{*} + P^{'} \\ u &= u^{*} + d_n (\Delta P^{'}) \\ v &= v^{*} + d_e (\Delta P^{'}) \\ \mathrm{w} &= \mathrm{w}^{*} + d_u (\Delta P^{'}) \end{aligned} \quad (10)$$

3.5 Meshing arrangement

A wind tower for VAWT with 8 sections for redirecting the wind from horizon to vertical as shown in Fig.3 is a started case study in this paper. The diameter of wind tower is 1.0m, and the hight is 1.5m. The 3D CFD simulation is carried out in this paper. The computing doain was the 7x5x5.7m along X. Y, Z direction respectively as shows in Fig.4. The applied meshes including 319176 active nodes and 1727420 active elements are shown in Fig.5. Fig.5 shows the meshes on the wind tower surface intensive. The mesh size increases from the tower wall toward the downstream, upstream and computing domain walls directions.

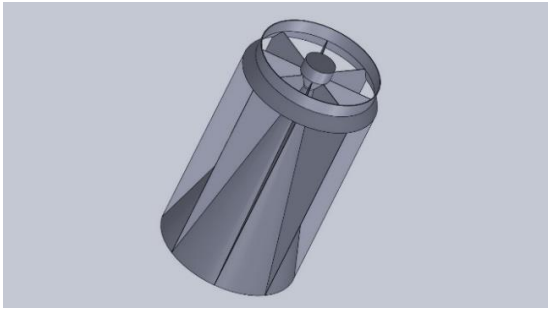

Fig3. The outline of the discussed wind tower for wind turbine

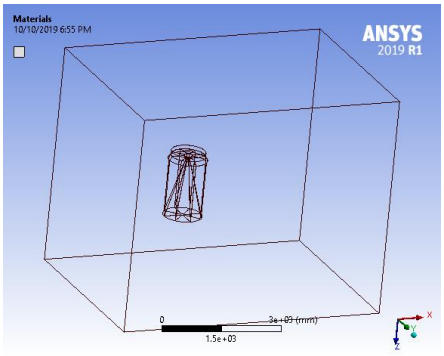

Fig.4. The computing domains and applied boundary conditions

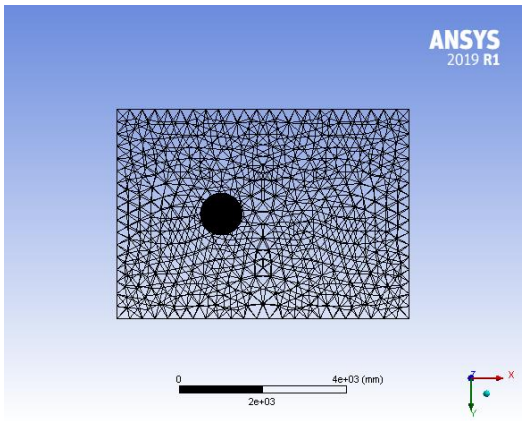

Fig.5. The arranged meshes

The boundary conditions for the present simulation are indicated in Fig.4. On the outer-domain inlet, a steady uniform velocity, V, is imposed and the outer-domain outlet is set as a pressure outlet. The outer-domain walls are considered as stationary with no slip.

4. Results and discussions

In case of inlet wind speed of 10m/s, the tower is divided into 8 sections, the guide plates are straight with an angle of 75^o, the steady state solution is received after about 30 iterations. The convergence is achieved with residual 10^{-4} for the velocity components, 10^{-3} for k and ω, the specific values are shown in Table 1. The convergence process is shown in Fig.6.

The results of the wind speed distribution in the plane across the position of the turbine blades are shown in Fig.7. The distribution of the velocity, streamline and pressure in the vertical plane across the center line of the wind tower are shown in Fig.8 and 9.

From these results, it can be seen that the wind in the wind tower at the position of the turbine blades has been converted to vertical wind, the largest wind speed velocity in the wind tower is greater than the initial wind speed value, reach 15m/s.

Table 1. Residuals after 30 iteration.

Ite.	Variables					
	u	v	w	p	k	ω
30	$4.36e^{-2}$	$4.42e^{-4}$	$2.16e^{-4}$	$2.41e^{-4}$	$9.42e^{-3}$	$1.14e^{-3}$

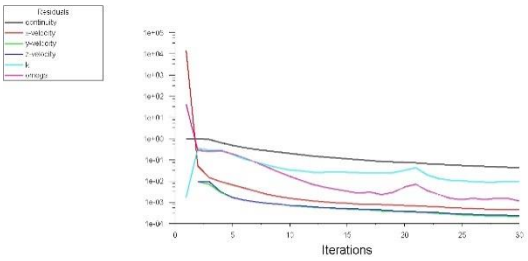

Fig.6. Residuals vs. itertions

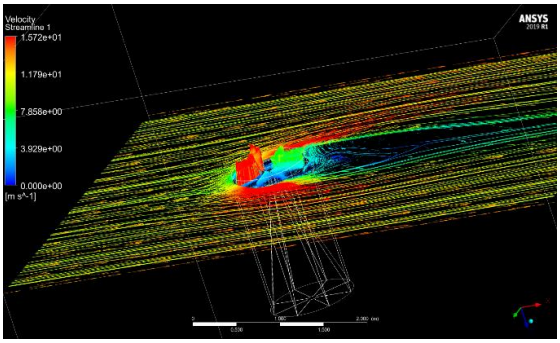

Fig. 8. Vector field in plane across the position of the turbine blades

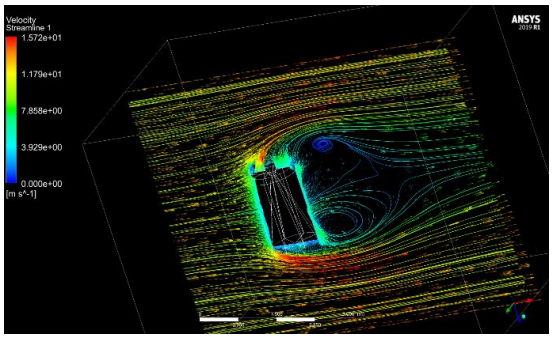

Fig 9. Vector field and streamline in plane across the center line of the wind tower

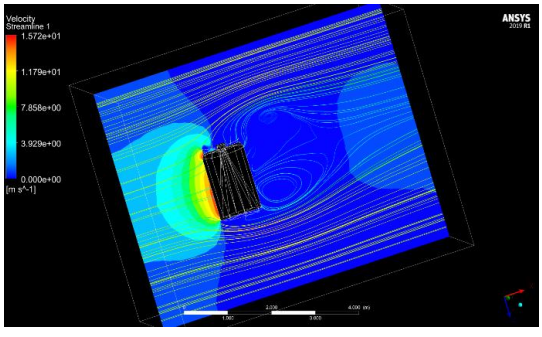

Fig. 10. Pressure in plane across the center line of the wind tower

To determine the effective configuration, different structures of the wind tower were

designed and surveyed. Two cases of design changes have been investigated, which are:

In case study 1, the tower are divided into 8 zones, but the structure of each zone is different. These structures are described as in Fig.10, in which the directional plates can be planed or curved, with large slopes (3 layer) or small slopes (1 layer). The results are shown in Tab.2. The results show that changing the directional plate curvature can make better turnaround performance (average velocity in the turbine area is higher). However, reducing the slope of the air deflector by dividing it into three layers makes the performance decrease.

In case study 2, the wind tower have a different number of sectors but only one layer, the calculation results are as shown in Tab.2. From this result, we can see that the wind tower divided into 6 sectors have better average performance.

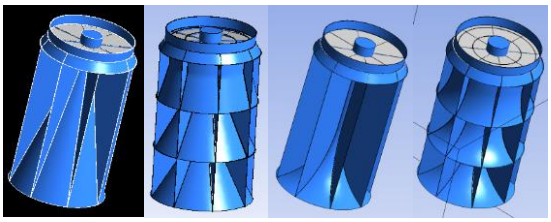

Fig.10. Changes in tower structure

Tab.2. Performance of wind tower structures.

No.	Design	Ave. w speed
1	8 linear sectos 1 layer	4.02
2	8 linear sectos 3 layer	2.70
3	8 curved sectos 1 layer	4.16
4	8 curved sectos 3 layer	3.00
5	6 curved sectos 1 layer	5.18
6	12 curved sectos 1 layer	3.28

Conclusions

The main purpose of this paper was to develop a structure to set up the vertical axis wind turbines for suppling electricity to navigational buoys. Several points can be concluded, as follows:

1. A wind tower can be used to direct wind to axial axes, ensuring a balanced work when mounted on buoys; Wind tower structure has the function of protecting the rotor from external collision. Wind tower structure allows easier integration of other renewable energy converters at sea such as waves and solar.

2. Ansys Fluent tool was used to simulate and evaluate the efficiency of wind tower in converting wind from horizontal to vertical.

3. The simulation calculations show that the conversion efficiency is higher when the tower has one layė, the directional plates have curved surfaces and the tower is divided into 6 sectors (case 5).

3. The proposed method of achieving an optimal structure is still in the developmental stage. The Renewable power station in coporated wind, solar and wave conversion are suggested for future study.

References

[1] Hirsch Charles. (1990) Numerical Computation of Internal and External Flows. Wiley.

[2] Bardina, J. E., Huang, P. G., & Coakley, T. J. (1997) Turbulence Modeling Validation, Testing, and Development. NASA Technical Memorandum No. 110446.

[3] Menter, F. R. (1994) Two-Equation Eddy-Viscosity Turbulence Models for Engineering Applications. AIAA J., Vol. 32, No. 8: 1598–1605.

[4] Eftichios Koutroulis, & Kostas kalaitzakis (2006) Design of a Maximum Power Tracking System for Wind-Energy-Conversion Applications. IEEE Transactions on Industrial Electronics, Vol. 53, No. 2: 486-494.

[5] Adam Mirecki, Xavier Roboam, & Frederic Richardiau (2007) Architecture Complexity and Energy Efficiency of Small Wind Turbines. IEEE Transactions on Industria l Electronics, Vol. 54, No. 1.

[6] Qing'an Li, Takao Maeda, Yasunari Kamada, Junsuke Murata, Kazuma Furukawa, & Masayuki Yamamoto (2015) Effect of number of blades on aerodynamic forces on a straight-

bladed Vertical Axis Wind Turbine. Energy, Vol. 90, Part 1: 784–795.

[7] Kosasih, B., & Hudin, H. S. (2016) Influence of Inflow Turbulence Intensity on The Performance of Bare And Diffuser-Augmented Micro Wind Turbine Model. Renewable Energy, Vol. 87, Part 1: 154–167.

[8] Yin, X. X., Lin, Y. G., Li, W., & Gu, H. G. (2016) Hydro-viscous Transmission Based Maximum Power Extraction Control For Continuously Variable Speed Wind Turbine With Enhanced Efficiency. Renewable Energy, Vol. 87, Part 1: 646–655.

[9] Natapol Korprasertsak, & Thananchai Leephakpreeda. (2016) Analysis and optimal design of wind boosters for Vertical Axis Wind Turbines at low wind speed. Journal of Wind Engineering and Industrial Aerodynamics, Vol. 159, pp. 9–18. [

10] Jian Chen, Liu Chen, Hongtao Xu, Hongxing Yang, Changwen Ye, & Di Liu (2016). Performance Improvement of a Vertical Axis Wind Turbine by Comprehensive Assessment of an Airfoil Family. Energy, Vol. 114: 318–331.

[11] Abdolrahim Rezaeiha, Ivo Kalkman, & Bert Blocken (2017) CFD Simulation of a Vertical Axis Wind Turbine Operating at a Moderate Tip Speed Ratio: Guidelines For Minimum Domain Size And Azimuthal Increment. Renewable Energy, Vol. 107: 373–385.

[12] Ghulam Ahmad, & Uzma Amin (2017) Design, Construction And Study of Small Scale Vertical Axis Wind Turbine Based on a Magnetically Levitated Axial Flux Permanent Magnet Generator. Renewable Energy, Vol. 101: 286–292.

[13] Baoshou Zhang, Baowei Song, Zhaoyong Mao, & Wenlong Tian (2017) A Novel Wake Energy Reuse Method to Optimize The Layout For Savonius-Type Vertical Axis Wind Turbines. Energy, Vol. 121: 341–355.

[14] Qing'an Li, Takao Maeda, Yasunari Kamada, Kento Shimizu, Tatsuhiko Ogasawara, Alisa Nakai, & Takuji Kasuya (2017) Effect of Rotor Aspect Ratio And Solidity on a Straight-Bladed Vertical Axis Wind Turbine in Three-Dimensional Analysis by The Panel Method. Energy, Vol. 121: 1–9.

[15] Menter F. R. (1992) Performance of Popular Turbulence Model For Attached And Separated Adverse Pressure Gradient Flows. AIAA journal, Vol. 30, No. 8: 2066-2072.

[16] Menter F. R. (1992) Improved Two-Equation K-Omega Turbulence Models For Aerodynamic Flows. NASA TM 103975.

[17] Patankar S. V., & Spalding, D.B. (1972) A Calculation Procedure For Heat, Mass And Momentum Transfer in Three-Dimensional Parabolic Flows. Int. J. of Heat and Mass Transfer, Vol. 15, issue 10, October 1972: 1787-1806.

[18] Yuwei Li, Kwang-Jun Paik, Tao Xing, & Pablo M. Carrica (2012) Dynamic Overset CFD Simulations of Wind Turbine Aerodynamics. Renewable Energy, Vol. 37, issue 1: 285-298.

[19] Steffen Wußow, Lars Sitzki, & Thomas Hahm (2001) 3D-Simulation of The Wake of a Wind Turbine. DEWI Magazine Nr. 18.

[20] Bộ giao thông vận tải Việt Nam, 2014. Quy chuẩn việt nam

The 5th International Conference on Engineering Mechanics and Automation (ICEMA 5)
Hanoi, October 11÷12, 2019

Design of Linear Generator with Halbach Dual Magnet Structure According to Wave Energy Converter for Navigational Buoys

Do Huy Diep [a], Dang The Ba [b*] and Nguyen Van Duc [c]

[a] *Faculty of Mechanics and Automation Engineering ,VNU University of Engineering and Technology, email : diepdh@vnu.edu.vn*
[b] *Faculty of Mechanics and Automation Engineering ,VNU University of Engineering and Technology, email : badt@vnu.edu.vn*
[c] *Faculty of Mechanics and Automation Engineering ,VNU University of Engineering and Technology, email : nvduc@vnu.edu.vn*

Abstract:

Operating equipments on river and sea require power but the supply conditions are usually difficult. With the characteristics of continuous operation, the navigational buoys need a stable and active power supply. The report presents the results of constructing structural design, operational modeling and simulation models to calculate the operation of wave energy converter for supplying power to navigational buoys. Simulation calculations were performed to test the device model and performance. The magnetic field in the linear generator is modeled according to the conventional magnet arrangement and the dual Halbach structure, thereby showing the advantage of the Halbach dual magnet array. The program was used to calculate and determine the construction parameters for actual design, manufacturing and testing of equipment in the next study.

Key Words: Navigational buoys, wave energy, electrical linear generator, dual Halbach array.

1. Introduction

With the special feature of the waterway transport is water activities, the energy for equiments and devices also has certain characteristics such as: the ability to supply electricity from traditional sources is high and unstable; easily cause bad effects on the environment ... but there are more renewable energy sources such as the sun, wind and waves. Therefore, the researchs and developments use renewable energy sources to provide energy for waterway transportation activities is very useful and necessary[1].

In waterway transport activities, there are systems of navigational buoys and station systems requiring energy but they must be located or built in locations far from the city, uninhabited. Therefore, the demand of a supply electricity with characteristics of stable, low cost, environmentally friendly are important and nescesssary [8].

In this report, studies analyzing the structural characteristics, operations of the navigational buoys as well as the characteristics of the renewable energy source at working environments. From these analyzes, the modified buoy structure will be built in such a way as to ensure that the standard function is operative, while ensuring the exploitation of renewable energy sources could provides the needed power of the buoys. Models for calculating the capacity and operation of

equipment will be developed and implemented. The investigation of magnetic field of the permanent magnet sequence in a linear generator using simulation software shows that the generator power can be improved using the Halbach dual-magnet structure. The calculations on the model will be used to determine the construction parameters and serve the design calculations. A sample navigational buoy using renewable energy will be developed and proposed to be manufactured for testing.

II. Navigational buoys

Navigational buoys are mainly made of steel, wood and composite materials. The structure of the buoy may not be the same and is usually seen as Figures 1a and 1b, but they must comply with some regulations and ensure its functioning.

The main regulations and functions include: navigational buoys set up and operate on water, anchored or tied at specific position to guide water users, related organizations and individuals; localize the direction and location of ships and boats; Buoys can use visible marks or use the AIS system to inform information. Signal range is the maximum distance from the observer to the signal that the observer perceives that signal to orient or determine his position; the effect of signals is shown on the signs according to the regulations of QCVN 20: 2010 /BGTVT. Navigational buoys have two main parts: buoys and marks; in many cases the marks used are indicator lights; shape, color, brightness are also specified in QCVN 20: 2010 / BGTVT.[10]

a) steel bouy *b) composite bouy*

Figure 1. Navigational buoys

A common buoy has the specifications: diameter 1.3 m, total height 4.0 m, weight about 500 kg.

The lamps are usually mounted on the top of buoys emitting light according to convention to notify necessary signals to the subjects participating in traffic. The light is usually attached to the controller and uses electricity from an battery. The structure of the light is usually in the form and structure as shown in Figure 2. Today, the commonly used lights are super bright LEDs, using 12V battery power.

Therefore, in order to design navigational buoys using renewable energy to supply electricity for lights and controllers, it must firstly comply with the construction standards of the buoys and secondly the mounting parts must not change or interfere with the navigational buoy's function.

Some design directions for buoys are as follows: Choose a standard float that is being produced and widely used in Vietnam Waterway Department. Shapes and major functional structures will be maintained as specified. Other necessary components may be changed to install equipment to convert renewable energy sources to provide power to equipment on the signal buoy to ensure the signaling role of buoys.

The analysis of the selection of renewable energy sources intend to be used will be described in the next section as well as the functional structure diagram of the components.

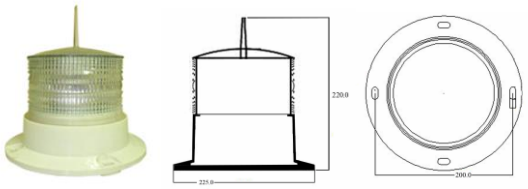

Figure 2. Structure of light

III. Structure and operation principle of navigational buoy using wave energy

On the basis of reference types of buoys, the POLYETHYLENE GBP-1800 prototype is used

The schematic structure of the navigational buoy when installing 2 parts is as shown in Figure 3. Additional components include the wave energy converter and the solar converter.

The solar converter has been much developed and looks like the one shown in Figure 4. The wave energy converter has been developed by the team of researchers, but will be recalculated in terms of dimensions and specific construction suitable for the power of the signal lights.

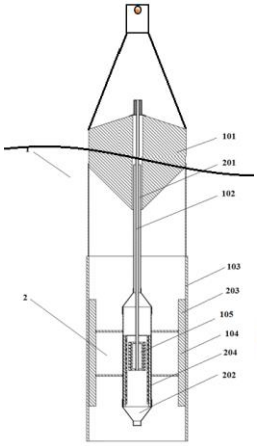

Figure 3. Structure of navigational buoys with WEC2

Figure 4. Structure of a solar light

Controller will be installed inside of lamp holder. The circuit in the controller will consist of 2 parts, one is a battery charger circuit and the other is a light control circuit. The lamp control part is made separately according to signal requirements. The battery charging circuit from two separate energy sources of solar and waves is built to collect electricity from two sources and fully charge the battery, ensuring electricity is always maintained.

Thus with this modified bouy structure, the battery is always charged alternately from the wave energy or solar power source, the two complementary sources make the power source always adequate, ensuring the operation of the buoy in a continuous manner.

IV. Calculate the design of the wave energy conversion

A simulation model for the operation of a wave energy converter, has been formulated like equations (4.1) to (4.8).

First floating buoy, connected to the core of the generator, small size (radius <0.2 wavelength), the equation of motion of the vertical component has the form [2,3]:

$$m_{d1}\ddot{s}_d(t) = -R_d\dot{s}_d(t) - S_d s_d(t) + F_{d,e}(t) + R_{b,d}\dot{s}_b(t) + F_u(t) \quad (1)$$

Where m_b is the mass of the buoy, $\ddot{s}_b(t)$ is the vertical shift accerlaration of the buoy, $F_{e,b}(t)$ is the vertical excitation force of the incident wave, $F_{r,b}(t)$ is the vertical force due to scatter waves, $F_{b,b}(t)$ is the total hydrostatic thrust on the buoy, $F_{b,v}(t)$ is the viscous drag, $F_{b,f}(t)$ is the total friction force of the devices attached to the buoy, $F_{b,u}(t)$ is the external force due to the energy collecting device connected to the buoy. In this study, the transmission mechanism is a linear generator, so the coupling force is the electromagnetic force in the generator and will be included in the generator model part [6].

In the case of buoys having a cylindrical structure, the diameter of $2r$, the length excluding the bottom $2l_b$, in which the submerged part under the water without waves is l_b, the total weight of the buoy and the cage is m_b, the bottom is structured as tip of pyramid, cross section of buoy is S_{wb}. The expression for the forces can be written as follows [2,3,7]:

The vertical excitation force of the incident wave, $F_{e,b}(t)$:

$$F_{e,b}(t) = \exp(-kl_b)\kappa_{b33}\rho g S_{wb}\eta_a \cos(\omega t) \quad (2)$$

The vertical force due to scatter waves, $F_{r,b}(t)$:

$$F_{r,b} = -m_{b33}\ddot{s}_b(t) - R_{b33}\dot{s}_b(t) \quad (3)$$

The hydrostatic thrust on the buoy, $F_{b,b}(t)$:

$$F_{b,b}(t) = -S_{b,b}s_b(t) \quad (4)$$

Friction forces act on the buoy through the mechanical mechanisms attached to the buoy, $F_{b,f}(t)$ in the structure as Figure 3 including 2 components, the first component is the friction of the disc in the cage, the second component is between the coil frame and the generator housing. The expression for the forces can be written as:

$$F_{b,f}(t) = -(R_{f,db} + R_{f,g})(\dot{s}_b(t) - \dot{s}_d(t)) \quad (5)$$

The resistance of water to the bouy is twofold. One on the bouy and one on the cage, writing is as follows:

$$F_{b,drag}(t) = -0.5\rho(C_T A_T + C_b A_b)\,|\,\dot{s}_b(t)\,|\,\dot{s}_b(t) \quad (6)$$

In the above expressions, the enclosed mass of buoys, $m_{b33} = (2\pi/3)r_b^3\rho\mu_{b33}$; μ_{b33} is dimensionless coefficient depends on wave number, radiu of buoy, length of buoy and the depth of water; Coefficient of drag resistance, $R_{b33} = \exp(-2kl_b)\omega\rho(2\pi/3)r_b^3\varepsilon_{b33}$; ε_{b33} is a Havelock dimensionless drag coefficient depending on the wave number and the bouy radius; κ_{33} is the dimensionless excitation coefficient of the incident wave; Lifting coefficient, $S_b = \pi\rho g r^2$, $R_{b,f}$ is the mechanical friction drag coefficient of the moving mechanism attached to the bouy, $R_{b,v}$ is the viscous drag coefficient on the float cage, A_T is the cross area of buoy[11].

b) Movement of bouy containing generator shell - second bouy

The equation for the motion of the second buoy is similar to the equation for the first buoy, with the index symbol below the letter *d*. The forces acting on the second buoy also include the same expressions as for the first buoy but with the parameters of the second buoy, and can be written in the form [4-7]:

$$m_{d1}\ddot{s}_d(t) = -R_d\dot{s}_d(t) - S_d s_d(t) + F_{d,e}(t) + R_{b,d}\dot{s}_b(t) + F_u(t) \quad (7)$$

where $m_{d1} = m_d + m_{d33}$ is the total weight of the second buoy and the generator attached volume due to motion of the second buoy, $R_d = R_{d33} + R_{d,v} + R_{b,d}$ is the sum of the drag coefficient on the second buoy containing the generator; $R_{b,d} = R_{f,bd} + R_{f,g}$ is the total drag generated by the first and second bouy linkage and the coil movement relative to the magnet core.

***c)* Magnetic fields of linear generator**

Relative motion of the coil (connected to the first bouy) compared to the magnets (attached to the case and attached to the second bouy), calculated by the motion of the two bouys,[5]

$$y(t) = s_b(t) - s_p(t) \quad (8)$$

Electric current is generated when the moving coil through the flux lines between the pairs of magnets. Schematic diagram of the generator is described as figure 5

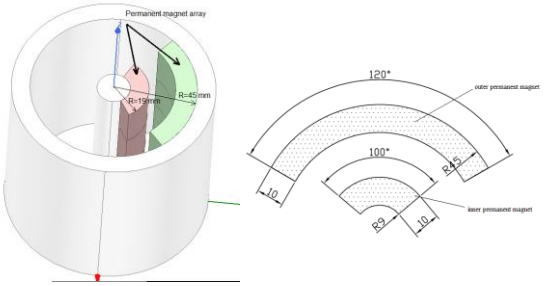

3D model of linear generator *Magnets parameters*

Figure 5. Model of linear generator

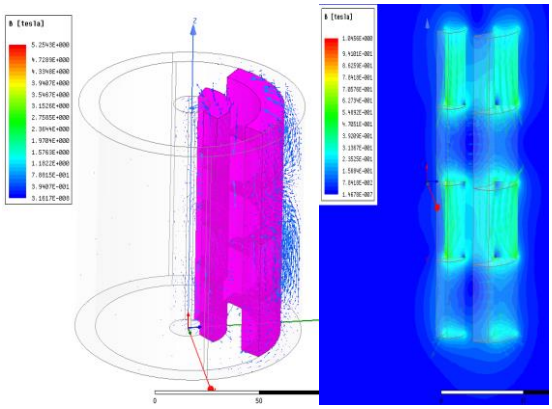

Figure 5a. 3D simulation of magnetic field

Figure 5b. Cross section of magnetic field inside linear generator

Due to the axial symmetry, we will investigate the 2D magnetic field in the plan along generator and across to center of a magnetic slot. For analysis magnetic flux field in generator with the arranging of magnet array, two case studies are simulated. In the first case, permanent magnets with size of length 25mm and width 10mm are arranged regularly with space 7mm. In the second uses double Halbach arrays magnets as shown in Fig.7.

Based on PM arrangement, magnetic field distribution in the generator is formulated with Laplace's and Poisson's equations. Numerical computation from finite element method is utilized to analyze and observe flux variation in air gap of generator**.**

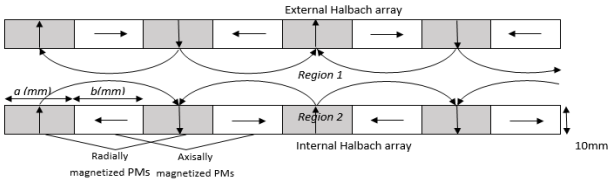

Figure 7 Polarization pattern and geometry of dual Halbach array

In formulation of the magnetic field, the generator space under study is divided into two regions bases on magnetic characteristics. The air gap or coil space that has permeability of 1.0 is denoted as Region 1. The permanent magnet volume filled with rare-earth magnetic material is denoted as Region 2. The magnetic field property of Region 1 and 2 is characterized by the relationship between magnetic field intensity, H (in A/m) and flux density, B (in Tesla) as:

$$\vec{B}_1 = \mu_0 \vec{H}_1, \qquad (9)$$

$$\vec{B}_2 = \mu_0 \mu_r \vec{H}_2 + \mu_0 \vec{M} \qquad (10)$$

Where $\mu 0$ is the permeability of free space with a value of 4π x 10^{-7} H/m, μ_r is the relative permeability of permanent magnets, $\mathbf{M} = \mathbf{B}_{rem}/\mu_0$ is the residual magnetization vector in A/m, and B_{rem} is the remanence.

The governing equations of magnetic field, i.e. Laplace's and Poisson's equations, are significant for the solution of magnetic field. The Gauss's law for magnetisms is state that

$$\nabla \cdot \vec{B}_i = 0 \quad \textit{where } i = 1,2. \qquad (11)$$

Thus, we can have a magnetic vector potential, $\mathbf{A}_i$, so that

$$\vec{B}_i = \nabla \times \vec{A}_i \qquad (12)$$

Therefore the equation can be written as

$$\nabla \times \vec{B}_i = -\nabla^2 \vec{A}_i \qquad (13)$$

In region 1, the combination of Maxwell's equation and Eq. 9 gives

$$\nabla \times \vec{B}_1 = \nabla \times \mu_0 \vec{H}_1 = \mu_0 \vec{J} \qquad (14)$$

Substituting Eq. 13 into 14 yields

$\nabla^2 \vec{A}_1 = -\mu_0 \vec{J}$ where $\mathbf{J}$(A/m^2) is current density in the field. In permanent magnet $\mathbf{J}$=0, therefore the Laplace's equation for Region 1 is obtained as

$$\nabla^2 \vec{A}_1 = 0 \qquad (15)$$

For Region 2, the combination of Maxwell's equation and Eq. 10 gives

$$\nabla \times \vec{B}_2 = \mu_0 \mu_r \vec{J} + \mu_0 \nabla \times \vec{M} \qquad (16)$$

Similarly, Eq. 13 and Eq. 15 yield the Poisson equation for Region 2

$$\nabla^2 \vec{A}_2 = -\mu_0 \nabla \times \vec{M} \qquad (17)$$

In next part, computational simulations will be conducted in accordance to FEM method and Ansys Maxwell tool to solve Maxwell equations to draw conclusion about magnetic field as well as magnetic flux density.

Relative permeability	1.0997785406
Magnetic coercivity	-890000 (A/m2)
Bulk conductivity	625000 (Siemens/m)
remanenceBr	1.23 (Tesla)

V. Simulation results of the magnetic field inside generator using dual Halbach array

The numerical simulation results show of the magnetic field flux in the generator as shown in the figure, the magnetic field lines clearly show the energy density is markedly improved compared to the previous configuration..

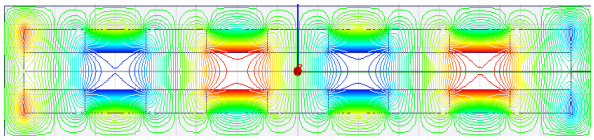

Figure 8. Flux lines of dual Halbach array

The magnetic flux consists of two components: parallel magnetic flux and magnetic flux perpendicular to the oscillation direction of mechanical waves. The parallel magnetic flux component is parallel to the direction of the movement of the mechanical wave which does not produce electricity when moving, so there is only necessary to examine the magnetic flux

component perpendicular to the direction of motion caused by the waves . Simulating the magnetic flux density B perpendicular to the direction of motion of the mechanical wave inside the generator results in the figure

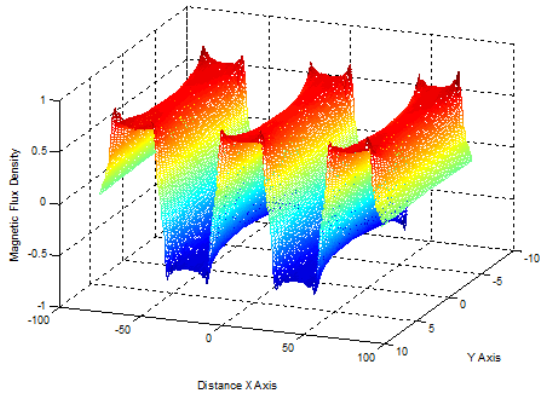

Figure 9. Perpendicular to excited displacement magnetic flux in generator

Comparing the perpendicular magnetic flux density of the generator in 2 cases shows that the maximum magnetic flux density value increases significantly (more than 10%) compared to the case when not using the dual Halbach array structure.

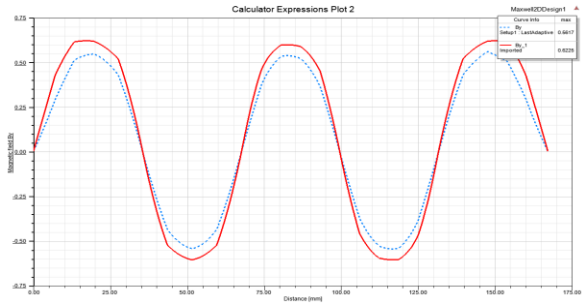

Figure 10. Magnetic flux in the center of linear generator in 2 cases.

As results above, the flux density is periodically symmetry respect to the central axis along the Ox direction. Thus the magnetic flux field distribution along the Ox axis can be described by the equation

$$\varphi_x(y)=\varphi\sin(\frac{2\pi}{\lambda}x) \qquad (18)$$

Where φ is the maximum average flux intensity value from the face of the inside magnets to the outside magnet, λ is the magnetic wavelength of the magnet configuration. The magnetic flux distribution field can then be expressed as the sum of sine and cosine functions that have a period equal to a multiple of the magnet frequency ω.

$$\varphi_x(y)=\varphi\sin(\frac{2\pi}{\lambda}x)=\sum\{A_n\sin(n\omega x)+B_n\cos(n\omega x)\} \qquad (19)$$

To analyze the characteristics of the generator and calculate the electromotive force generated in the coils, the wave oscillation is assumed to have a periodic form represented by the equation.:

$$x(t)=d\sin(\omega_m t) \qquad (20)$$

where d is the amplitude of wave, ω_m is the angular frequency of buoys collected based on the action of water waves. When the moving coils in a linear generator cross the magnetic field lines, it will produce inductive electricity according to Faraday's law.:

$$\xi=\frac{d\Phi}{dt} \text{ where } \Phi=\int_0^t N\varphi_y(x)x'(t)\,dt$$

N is the number of copper wires that move across the magnetic field line.

When the coil is connected to an external circuit consist of resistance R and inductance L. According to the law KVL, derive the equation for the electric current intensity of the source circuit generated by a coil of a generator of the form:

$$L\frac{dI_L(t)}{dt}=-\left(\frac{R_L+R_i}{L}\right)R_L I_L(t)+\frac{R_L e(t)}{L} \qquad (21)$$

In the Eq. 21, L (henry) is the inductance of the coil, expressed as $L = \mu_o.\ \mu.N^2.S/l_{ống}$

with S is the coil area, μ_o is the permeability of the air, μ is the core magnetic permeability, N is the number of turns, $l_{ống}$ is the length of wire tube.

Power consumption on the external load is calculated by the expression $P = I_L^2 R_L$

The electromagnetic force acting on the coil is calculated as $F_u = Nl\varphi_x I_L$

The results of energy calculation by the wave energy converter are shown in the figure

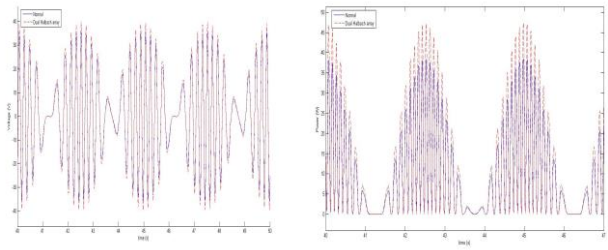

Voltage on load *Power on load*

Figure 11. Simulation results of the current supplied of 40W generator in 2 cases.

According to the simulation result, the power on external circuit can be improved significantly compared to the case without Halbach array structure.

V. Conclusion

This report studied the renewable energy sources intend to supply power to equipments on the sea. Through study, it was determined that the demand for electricity supply for navigational buoys on the river and sea.

Selected a common navigational buoy of the Inland Waterways Administration to research and install solar and wave energy conversion devices as electricity sources. The power from the wave and solar energy will be charged into the 12V battery as currently used.

Simulation models have been built and programmed to calculate. Calculations were made to test the model and operation of the device.

Ansys program has been used for simulated the magnetic flux field in the generator. The simulation result show that the power of generator can be improved significantly when using dual Halbach array.

The test design and manufacturing will continue to be carried out so that actual testing can be implemented.

References

[1] A. Clement, P. McCullen, A. Falcao, A. Fiorentino, F. Gardner, K. Hammarlund, G. Lemonis, T. Lewis, K. Nielsen, S. Petroncini, P. Schild M.-T. Pontes, B.-O. Sjostrom, H. C. Sorensen, and T. Thorpe. 2002. *Wave energy in europe: current status and perspectives*. Renewable and Sustainable Energy Reviews, 6:405–431

[2] A. F. de O. Falcão (2007), *Modelling and control of oscillating-body wave energy converters with hydraulic power take-off and gas accumulator*, Ocean Engineering, vol. 34, pp. 2021-2032.

[3] A. Weinstein, G. Fredrikson, M. J. Parks and K. Nielsen (2004), *AquaBuoy, the offshore wave energy converter numerical modelling and optimization*, in Proceedings of the MTTS/IEEE Techno-Ocean ’04 Conference, Kobe, Japan, vol. 4, pp. 1854-1859.

[4] Dang The Ba, Nguyen Dong Anh, Phung Van Ngoc (2015), *Numerical simulation and experimental analysis for a linear trigonal double-face permanent magnet generator used in direct driven wave energy conversion*, Procedia Chemistry, 14, 130 – 137.

[5] Dang The Ba (2013), *Numerical Simulation of a Wave Energy Converter Using Linear Generator*, Vietnam Journal of Mechanics, Vol.35, No.2, P.103-111

[6] J. Falnes (2002), *Ocean Waves and Oscillating Systems.* Cambridge University Press

[7] J. Falnes (1999), *Wave-energy conversion through relative motion between two single-mode oscillating bodies*, Journal of Offshore Mechanics and Arctic Engineering, vol. 121, pp. 32-38

[8] Hữu Nhật và cộng sự (2002). *Nghiên cứu sử dụng năng lượng sóng biển làm nguồn chiếu sáng phao tín hiệu hoạt động ngoài khơi biển Việt Nam*. Báo cáo tổng kết đề tài cấp Bộ Giao thông Vận tải, Viện Công nghệ Giao thông Vận tải, Hà Nội

[9] O. Danielsson and M. Leijon (2007). *Flux distribution in linear permanent-magnet synchronous machines including longitudinal end effects*. IEEE Transaction on Magnetics, 43(7):3197–3201

[10] QCVN 20: 2010 / BGTVT

[11] U. A. Korde (2003), *Systems of reactively loaded coupled oscillating bodies in wave energy conversion*, Applied Ocean Research, vol. 25, pp. 79-91.

The 5th International Conference on Engineering Mechanics and Automation (ICEMA 5)
Hanoi, October 11÷12, 2019

A Comparative Study of Different Cavitation and Turbulent Models of Cavitating Flow Using OpenFOAM

Duong Ngoc Hai[a,b] and Nguyen Quang Thai[c]

[a] *Graduate University of Science and Technology, VAST, Hanoi, Vietnam, Hanoi City, Vietnam*
[b] *University of Engineering and Technology, VNU, Hanoi City, Vietnam*
dnhai@vast.vn
[c] *Institute of Mechanics, VAST, Hanoi, Vietnam*
nqthai@imech.vast.vn

Abstract

While an object moving within a fluid, due to evaporation of the fluid at ambient temperature if the relative speed between the object and fluid is large enough, the natural vapour cavities can appear around the object's surface. The mixture flow of such fluids and cavities are called as the natural cavitating flows or cavitating flows. The mass transfer rate of liquid to vapour phase is modelled often by various cavitation models. Some examples of the cavitation model are the model of Kunz, Schnerr-Sauer, Merkel, Singhal, etc. This paper presents some comparative results of numerical simulation of cavitating flow around a moving object in water with different cavitation models such as the Kunz, and Schnerr-Sauer models with two possible turbulent models: LES (Large-Eddy Simulation) and RAS (Reynolds-Averaged Simulation) to evaluate the effect of the turbulent model to the numerical simulation of each cavitation model. The paper results might be helpful for investigation on cavitation phenomena by using the numerical modelling software.

Key Words: cavitation model, turbulent model, OpenFOAM

1. Introduction

While an object moving within a fluid, due to evaporation of the fluid at ambient temperature if the relative speed between the object and fluid is large enough, the natural vapour cavities can appear around the object's surface. The appearance of the vapour cavity in the flow is due to the drop of local pressure to the saturation pressure of the fluid at ambient temperature. The mixture flow of such fluids and cavities are called as the natural cavitating flows or cavitating flows (Franc et al., 2006). This flow is usually found around the underwater operating vehicle, such as propeller, submarine, hydrofoil, and etc. When the vapour cavity has enough size to cover the vehicle body, the drag force of liquid flow may significantly reduce. And the vapour cavity is called is supercavity or partial cavity according the cavity length which sufficient enough or not to cover vehicle body. The main characteristic of cavitating flow as soon as cavity and surper/partial cavity has been investigated both of theoretical and experimental studies for many years ago (Rouse et al., 1948), (Plesset, 1957), (Garabedian, 1956), (Brennen, 1969) and (May, 1975). The main dimension parameter on the cavitating flow is the cavitation number σ in the equation (1) in (Rouse et al., 1948) below:

$$\sigma = \frac{p_\infty - p_c}{0.5\rho U_\infty^2}, \qquad (1)$$

where, p_∞ is the pressure at the infinity inflow; p_c is pressure inside the cavity domain, ρ is the liquid density, U_∞ is the flow speed at the infinity inflow. In the vapour cavity, p_c is usually approximated to the

vapour saturation pressure p_v in many studies (Franc et al., 2006).

To studies further on cavitating flow, besides the experimental approach, numerical simulation is another main approach. In the numerical studies on cavitating flow, the mass transfer rate between the liquid and vapour fluid is model by the cavitating models, such as, Singhal' model in (Singhal et al., 2002), Kunz model in (Kunz et al., 2000), Schnerr-Sauer model in (Schnerr et al., 2001), Zwart model in (Zwart et al., 2004) and etc. To performance the numerical studies, these cavitation models have complied into many Computational Fluid Dynamics (CFD) software, such as ANSYS Fluent, CFX, OpenFOAM, etc. The OpenFOAM (Open Source Field Operation and Manipulation) is the very effective CFD software with the highlighted advantage that all source code documents are provided for everyone to modify or develop the simulation program become suitable to a special problem (Jasak, 2009). For the cavitating flow, OpenFOAM has many available two-phase and multiphase flow solves. One of them is *interPhaseChangeFoam* solver with the Kunz, Sauer and Merkel models are compiled. These models provide many option model for user to simulate the cavitating flow (Greenshields, 2015). However, which is the suitable model for a special problem may be the common question before the problem is modelled. For this issue, the previous researches show that with each pair of cavitation model and turbulent model, the behaviours of cavitating flow around body object may appear different in (Pendar et al., 2016), (Roohi et al.,2016) and (Nguyễn Tất Thắng, 2017 and 2018). Therefore, the accuracy of numerical simulation results of the pair of the cavitation and turbulent models can be different. So, to provide the recommendations for the cavitating flow numerical studies using OpenFOAM. The paper presents some comparative results of numerical simulation of cavitating flow around a moving object in water with pairs of different cavitation models such as the Kunz and Schnerr-Sauer models and two possible turbulent method: LES (Large-Eddy Simulation) and RAS (Reynolds-Averaged Simulation) to evaluate the effect of each pair of the turbulent and the cavitation model. For each method, the one equation model and the *k-ω* SST model have been used respectively. The numerical simulation for cavitating flow around the hemisphere head body at σ = 0.2 is performed to evaluate the accuracy of each pair cavitation model – turbulent model. The paper results might be helpful for investigation on cavitation phenomena by using the numerical modelling software

2. Numerical method

2.1. Governing equations

Three-dimensional incompressible Navier–Stokes equations for a homogeneous mixture flow are given by equation (2) and (3) (Nigmatulin, 1990) below:

$$\partial_t \rho + \nabla.(\rho \mathbf{u}) = 0, \quad (2)$$

$$\partial_t(\rho \mathbf{u}) + \nabla.(\rho \mathbf{u} \otimes \mathbf{u}) = -\nabla p + \nabla.\mathbf{s}, \quad (3)$$

where, $\mathbf{s}$ is the viscous stress tensor, defined by $s=2\mu \boldsymbol{D}$ with $\boldsymbol{D}=0.5[\nabla \mathbf{u} + (\nabla \mathbf{u})^T]$; mixture density ρ and mixture viscosity μ are computed from liquid volume fraction γ as the equations (4) and (5) below:

$$\rho = \rho_l \gamma + (1-\gamma)\rho_k, \quad (4)$$

$$\mu = \mu_l \gamma + (1-\gamma)\mu_k. \quad (5)$$

The interface between the vapour and liquid phases can be modelled by a compressive volume of fluid (VOF) method. Consider a control volume, liquid volume fraction γ is defined by the equation (6) below:

$$\gamma = \frac{liquid\ volume}{liquid\ volume + liquid\ volume}, \quad (6)$$

where, $\gamma \in [0,1]$ and the value of γ respective with the position of calculating domain as follows: $\gamma = 1$ for liquid phase; $\gamma = 0$ for vapour phase and $0 < \gamma < 1$ for interface with a mixture of liquid and vapour phases.

The vapour volume fraction equation with a source term for the rate of mass transfer $\dot{m}$ between liquid and vapour phases due cavitation is write as equation (7) below:

$$\partial_t \gamma + \nabla.(\gamma \mathrm{u}) = \dot{m}/\rho. \quad (7)$$

OpenFOAM uses a compressive velocity $\mathbf{u_c}$ instead of $\mathbf{u}$ equation (7) to track the interface between the vapour and liquid phases as equation (8) below:

$$\partial_t \gamma + \nabla.(\gamma \mathrm{u}) + \nabla.[\gamma(1-\gamma)\mathrm{u}_c] = \dot{m}/\rho, \quad (8)$$

where, $\mathbf{u_c}$ is defined by $\mathbf{u_c} = min\left[C_\gamma |U|, max(U)\right]\frac{\nabla \gamma}{|\nabla \gamma|}$ with $C\gamma$ is a constant, which $C\gamma$=0 respective no compression, $C\gamma$=1 respective a conservative compression and if $C\gamma$>1 respective high compression in (Rusche, 2002).

2.2. Cavitation modelling

The mass transfer rate $\dot{m}$ is calculated by the cavitation models. Two available cavitation models in OpenFOAM: Kunz and Schnerr-Sauer models are used in this study. In the Kunz model, $\dot{m}$ is calculated from equations (9) and (10) below with two empirical constants C_v=1000 and C_c=1000 in OpenFOAM (Kunz et al., 2000).

$$\dot{m}^- = \left(\frac{C_v}{0.5 U_\infty^2 t_\infty}\right)\gamma \frac{\rho_v}{\rho_l} \min[0, p - p_v], \text{ (vaporization)} \quad (9)$$

$$\dot{m}^+ = \left(\frac{C_c}{t_\infty \rho_l}\right)\gamma^2 (1-\gamma) p_v \quad \text{(condensation)}, \quad (10)$$

where the characteristic time $t_\infty = D_c/U_\infty$ with characteristic size D_c of object body (diameter for disk or sphere).

The Sauer model is constructed from the Rayleigh – Plesset equation (Schnerr et al., 2001). The mass transfer use the mass transfer rate in the Sauer model is determined by the equation (11) below:

$$\dot{m} = \rho_v \rho_l (1-\gamma_v)\gamma_v \frac{3}{\mathrm{R}_b}\sqrt{\frac{2}{3}\frac{|p-p_v|}{\rho_l}} \quad (11)$$

In equation (11), R_b is supposed to be equal for all the bubbles. The equation (12) bellow discusses the relation of R_b and an initial number of bubbles n_0.

$$\mathrm{R}_b = \left(\frac{3}{4\pi n_0}\frac{\gamma_v}{1-\gamma_v}\right)^{1/3} \quad (12)$$

In OpenFOAM solvers, R_b and n_0 are constants this study, the value of n_0 =1.6 x10^{13} and R_b = 2x10^{-6} m.

2.3. Turbulence modelling

In this study, the turbulence flow is modelling by Large Eddy Simulation (LES) method and Reynolds Average Simulation (RAS) method. In the LES approach, the smaller subgrid eddies are modelled. Any variable, i.e., f, is separated into grid-scale and subgrid-scale components, i.e., where $f = G * f$ is the grid-scale component, $G = G(x, \Delta)$ is the filter function, and also $\Delta = \Delta(x)$ is the filter width in (Ghosal, 1996). The filtered Navier–Stokes equations are written as equations (13) and (14) below:

$$\frac{\partial(\rho u_j)}{\partial t} + \frac{\partial(\rho u_j u_j)}{\partial x_j} = \frac{\partial p}{\partial x_j} + \frac{\partial}{\partial x_j}\left(\mu\frac{\partial u_i}{\partial x_j}\right) - \frac{\partial \tau_{\mathrm{ij}}}{\partial x_j}, \quad (13)$$

$$\frac{\partial p}{\partial t} + \frac{\partial u_j}{\partial x_j} = 0, \quad (14)$$

where the sub-grid scale stress tensor $\tau_{ij} = \frac{2}{3}\rho k l - 2\mu_k S_{ij}$; $S_{ij} = \frac{1}{2}\left(\frac{\partial u_i}{\partial x_j} + \frac{\partial u_j}{\partial x_i}\right)$ with S_{ij} is the rate-of-strain tensor for the resolved scale and the subgrid-scale turbulent viscosity μ_k is then computed by $\mu_k = c_k \rho \Delta\sqrt{k}$. To obtain turbulence kinetic energy k, the one equation eddy viscosity model subgrid-scale is used. Following equation (15) is solved with $\varepsilon = c_\varepsilon k^{3/2}/\Delta$.

$$\partial_t(\rho k) + \nabla.(\rho k u) = -\tau_{\mathrm{ij}}.S_{\mathrm{ij}} + \nabla.(\mu_k \nabla k) + \rho\varepsilon \quad (15)$$

With constants c_ε=1.048 and c_k = 0.094 in OpenFOAM respectively.

The RAS method, the *k-ω* shear stress transport (SST) turbulence model is used in this study. The *k-ω* SST model in OpenFOAM is based on the Menter's model (Menter et al., 2003). In this study, the complete formulation of the SST model is given with the limited number of modification highlighted.

$$\frac{\partial(\rho k)}{\partial t} + \frac{\partial(\rho U_i k)}{\partial x_i} = \widetilde{P_k} - \beta^* \rho k \omega + \frac{\partial}{\partial x_i}\left[(\mu + \sigma_k U_t)\frac{\partial k}{\partial x_i}\right] \quad (16)$$

$$\frac{\partial(\rho\omega)}{\partial t} + \frac{\partial(\rho U_i \omega)}{\partial x_i} = \alpha\rho S^2 - \beta\rho\omega^2 + \frac{\partial}{\partial x_i}\left[(\mu + \sigma_\omega U_t)\frac{\partial \omega}{\partial x_i}\right] + 2(1-F_1)\rho\sigma_{\omega 2}\frac{1}{\omega}\frac{\partial k}{\partial x_i}\frac{\partial \omega}{\partial x_i} \quad (17)$$

Where the blending function F_1 is defined by:

$$F_1 = tanh\left\{\left\{min\left[max\left(\frac{\sqrt{k}}{\beta^*\omega y}, \frac{500v}{y^2\omega}\right), \frac{4\rho\sigma_{\omega 2}k}{CD_{k\omega}y^2}\right]\right\}^4\right\} \quad (18)$$

With $CD_{k\omega}$=max$\left(2\rho\sigma_{\omega 2}\frac{1}{\omega}\frac{\partial k}{\partial x_i}\frac{\partial \omega}{\partial x_i}, 10^{-10}\right)$ and y is the distance to the nearest wall. F_1 is equal to zero away from the surface (*k-ε* model), and switches over to one inside the boundary layer (*k-ω* model). The turbulent eddy viscosity is defined as follows:

$$v_t = \frac{a_1 k}{\max(a_1\omega, SF_2)} \quad (19)$$

Where S is the invariant measure of the strain rate and F_2 is a second blending function defined by:

$$F_2 = tanh\left[\left[max\left(\frac{\sqrt{k}}{\beta^*\omega y}, \frac{500v}{y^2\omega}\right)\right]^2\right] \quad (20)$$

A production limiter is used in the SST model to prevent the build-up of the turbulence in the stagnation regions:

$$P_k = \mu_t \frac{\partial U_i}{\partial x_j}\left(\frac{\partial U_i}{\partial x_j} + \frac{\partial U_j}{\partial x_i}\right) \quad (21)$$

$$\rightarrow \widetilde{P_k} = min(P_k, 10 \cdot \beta^* \rho k \omega)$$

All constants are computed by a blend from the corresponding constants of the *k-ε* and the *k-ω* model via $\alpha = \alpha_1 F + \alpha_2 (1-F)$ etc. The constants for this model are β =0.09, α_1=5/9, β_1=3/40, σ_{k1}=0.85, $\sigma_{\omega 1}$=0.5, α_2=0.44, β_2=0.0828, σ_{k2}=1, $\sigma_{\omega 2}$=0.856.

2.4. Simulation set-up

The computation domain and boundary information are shown in Figure 1 below.

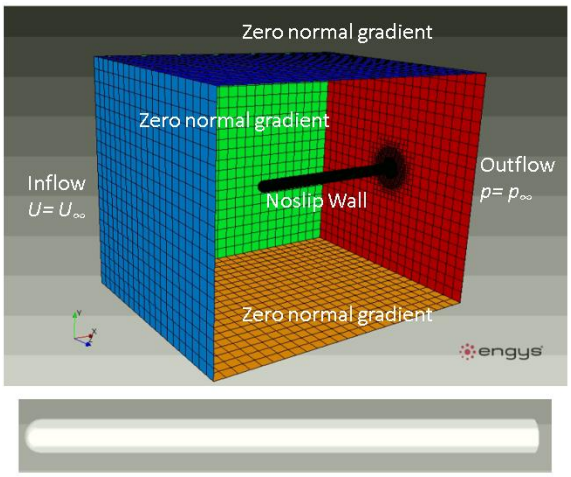

Figure 1. Computation domain.

The *interPhaseChangeFoam* solver working with the PIMPLE algorithm as shown in Figure 2 below.

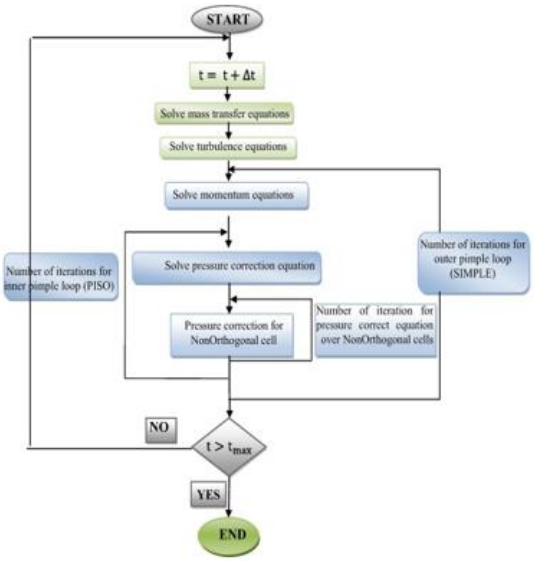

Figure 2. Flowchart of the PIMPLE solution procedure [Roohi et al., 2016]

The HELYX-OS v2.4 has been used to build the polyhedral grid for the simulation. Figure 3 shows the simulation grid around the body wall and outlet.

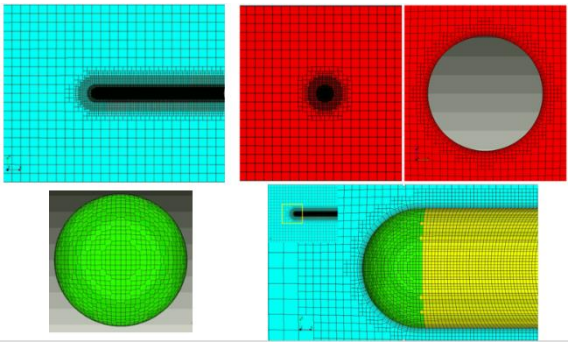

Figure 3. Grid around body wall

2.5. Grid dependence study

The effect of grid size is evaluated by comparing shown in Figure 4. The coarse grid has 2073508 elements. The medium grid has 608416 elements. The fine grid has 1800908 elements. As comparing shown in Figure 4, the numerical result is almost the same between the medium and fine grid. So, this study uses the medium grid for simulation cases.

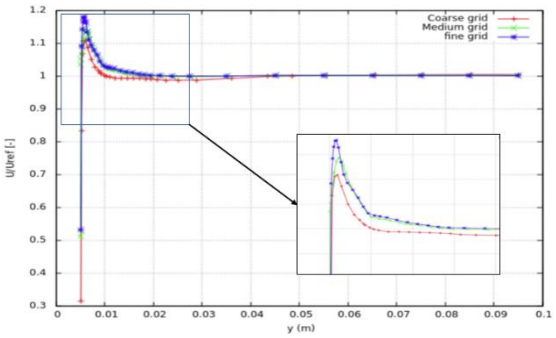

Figure 4. Effect of grid size

3. Results

To evaluate the accuracy of each pair of cavitation model and turbulent model, the comparing of cavity size and pressure coefficient distribution on body wall are performed. The experimental data in (Rouse et al, 1948) has been used to compare with the numerical results.

3.1. The cavity's size

Figure 5 below shows the compare the cavity size by each case to the experimental data. The cavity size of RAS-Sauer pair is well suitable to the experimental data. And the LES-Kunz case has been largest different to the experimental data.

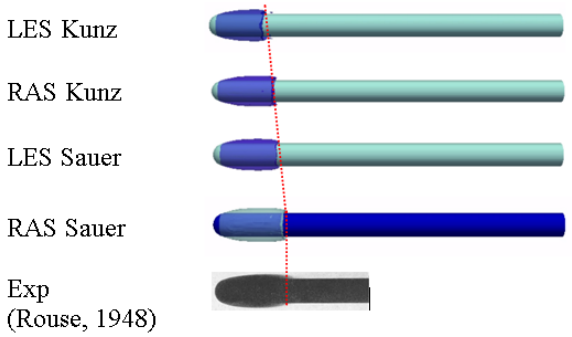

Figure 5. Comparing of cavity size between the numerical results and experimental data

3.2. Pressure coefficient distribution on the body wall

Figure 6 below shows the comparison of pressure coefficient distribution C_p on the body wall of each pair of cavitation model and turbulent model.

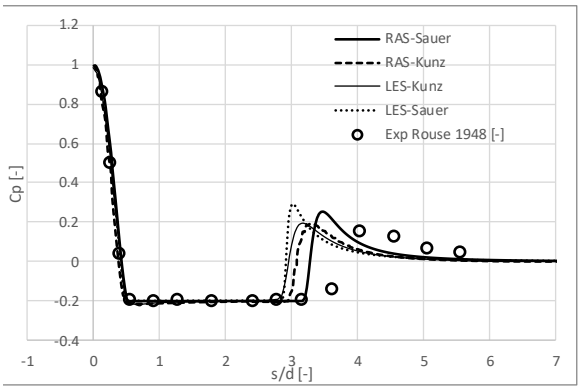

Figure 6. Comparing numerical cases and experimental data on C_p distribution

The C_p distribution from RAS-Sauer is the best suitable. LES-Sauer case is the largest difference from the experimental data.

4. Conclusions

The cavitating flow at $\sigma=0.2$ has been conducted with the *interPhaseChangeFoam* solver with Kunz and Sauers cavitation models

LES-One equation model and RAS-$k\omega$ SST model have complied with the *interPhaseChangeFoam* solve to simulation the turbulent cavitating flow around the hemisphere head body.

The accurate of each pair of the cavitation model and turbulent model have been compared with the published experimental data by the cavity size and pressure coefficient distribution on the body wall. Results of the study show that the pair of RAS-Sauer has the best accuracy with the experimental data on both of cavity size and C_p distribution.

Therefore, we recommend RAS-Sauer pair for the cavitating flow, especially the cavitating flow around the hemisphere head body case at $\sigma=0.2$ as this study.

Acknowledgements

This work was supported by the IMECH scientific research project (whose the project manager is the third author, M.Sc. Nguyen Quang Thai) of the fiscal year 2019.

References

Franc, J. P., and Michel J. M. (2006). *Fundamentals of Cavitation*. Springer.

Rouse, H., and McNown, J. S., (1948). *Cavitation and Pressure Distribution, Head Forms at Zero Angle of Yaw*, Iowa Institute of Hydraulic Research, Iowa City.

Plesset, M. S. (1957). Physical effects in cavitation and boiling. *Proc. 1st Symp. on Naval Hydrodynamics*.

Garabedian, P.R. (1956). Calculation of Axially Symmetric Cavities and Jets, *Pacific Journal of Mathematics*, 6(4), pp. 611-684.

Brennen, C. A. (1969). Numerical solution of axisymmetric cavity flows. *Journal of Fluid Mechanics*, 37(4), pp. 671-688.

May, A. (1975). *Water Entry and the Cavity-Running Behavior of Missiles*, Naval Surface Weapons Center, White Oak Laboratory.

Singhal, A.K., Athavale, M.M., Li, H. and Jiang, Y., (2002). Mathematical basis and validation of the full cavitation model. *Journal of fluids engineering*, 124(3), pp.617-624.

Kunz, R.F., Boger D.A., Stinebring D.R., Chyczewski T.S., Lindau J.W., Gibeling H.J., Sankaran V. and Govindan T.R. (2000). A preconditioned Navier–Stokes method for two-phase flows with application to cavitation prediction. *Computers & Fluids* 29(8), pp.849-875.

Schnerr, G.H., Sauer, J., (2001). Physical and numerical modeling of unsteady cavitation dynamics. In: *Proceedings of 4th International Conference on Multiphase Flow*. New Orleans, USA

Zwart, P.J., Gerber, A.G. and Belamri, T., (2004). A two-phase flow model for predicting cavitation dynamics. *In Fifth international conference on multiphase flow*, Yokohama, Japan (Vol. 152).

Jasak, H., (2009). OpenFOAM: open source CFD in research and industry. *International Journal of Naval Architecture and Ocean Engineering*, 1(2), pp.89-94.

Greenshields, C.J., (2015). *Openfoam user guide*. OpenFOAM Foundation Ltd, version, 3(1), p.e2888.

Pendar, M.R. and Roohi, E., (2016). Investigation of cavitation around 3D hemispherical head-form body and conical cavitators using different turbulence and cavitation models. *Ocean Engineering*, 112, pp.287-306.

Roohi, E., Pendar, M.R. and Rahimi, A., (2016). Simulation of three-dimensional cavitation behind a disk using various turbulence and mass transfer models. *Applied Mathematical Modelling*, 40(1), pp.542-564.

Nguyễn Tất Thắng, Dương Ngọc Hải, Nguyễn Quang Thái, and Trương Thị Phượng. (2017). Experimental measurements of the cavitating flow after horizontal water entry. *Fluid Dyn. Res*., 49(5), 055508.

Nguyễn Tất Thắng, Dương Ngọc Hải, Nguyễn Quang Thái and Kikura, H. (2018). CFD simulations of the natural cavitating flow around high-speed submerged bodies. *In: Lecture Notes in Mechanical Engineering*, Vol. Part 3, Springer, pp. 851-873.

Nigmatulin, R.I. (1990), *Dynamics of Multiphase Media. Part 1, 2*, New York: Hemisphere Publishcation.

Rusche, H. (2002), *Computational Fluid Dynamics of Dispersed Two-Phase Flows at High Phase Fractions*. Ph.D. thesis, Imperial College, University of London.

Ghosal, S., (1996). An analysis of numerical errors in large-eddy simulations of turbulence. *Journal of Computational Physics*, 125(1), pp.187-206.

Menter, F.R., Kuntz, M. and Langtry, R., (2003). Ten years of industrial experience with the SST turbulence model. *Turbulence, heat and mass transfer*, 4(1), pp.625-632.

Nigmatulin, R.I., Khabeev, N.S. and Hai, Z.N., (1988). Waves in liquids with vapour bubbles. *Journal of fluid mechanics*, 186, pp.85-117.

The 5th International Conference on Engineering Mechanics and Automation (ICEMA 5)
Hanoi, October 11÷12, 2019

Lagrangian Vortex Particle Method for Complex Flow Simulation

Duong Viet Dung[a], Lavi Rizki Zuhal[b] and Hari Muhammad[c]

[a] *VNU-University of Engineering and Technology, 144 Xuan Thuy, Cau Giay, Vietnam, duongdv@vnu.edu.vn*
[b] *Institut teknologi Bandung, Bandung, Indonesia, lavirz@ae.itb.ac.id*
[c] *Institut teknologi Bandung, Bandung, Indonesia, hari@ftmd.ac.id*

Abstract

In order to solve complicated simulation problem for complex deforming objects under complicated motions found in aerospace, aerodynamic, meteorology, biology engineering, this paper presents Lagrangian vortex method based on Brinkman penalization. The Brinkman penalization acts as an external force, which is implicitly enforced into Navier-Stokes equation in the velocity-vorticity form. The advantage of the method is the capability to remove the pressure factor which causes errors in other numerical methods due to the complexity of shape of the object. Furthermore, the method is able to model the complex geometry, complex motions as well as 3D deformation of the object. In particular, the Navier-stokes equation can be solved in a classical strategy: applying Bio-Savart law formula is to deal with the convection process; employing fast multipole method to accelerate the velocity computation. The convergence is verified in several simulation applications such as air flow over low aspect ratio wing, rotation wings, influent of wind gust on high-raised building, and fish swimming.

Key Words: brinkman penalization, vortex particle method, complex flow applications

1. Introduction

Flow problems around complexs deformable bodies have attracted a lot of interest within this decade in Rasmusen (2008), Li et al (2012), Mattia et al (2011), Eric (2004). Predicting the fluid-structure interaction responses also plays an important role in order to avoid potential aero-elastic and hydro-elastic instability issues, or to enhance performance by adapting the structural configuration. However, conducting experiments to study the flow over deformable bodies are difficult, see Eric (2004). In addition, a distinguishing feature of deformable bodies in real fluids is the generation of vorticity and the shedding of vortices into the wake, which is difficult to predict using analytical approach.

Due to current development of high performance computers, these problems can be overcome using numerical methods known as computational fluid dynamics (CFD). In CFD, there are two main approaches: grid-based and meshless methods. As suggested by the name, in the more traditional grid-based methods, the Navier-Stokes equation is solved using discretized grid. However, simulation of flow over deformable body is very difficult, if not impossible, using the grid-based CFD. In particular, the difficulty is due to requirement to generate grid at every time step because of the

continuous change in the geometry of deformable body.

On the other hand, meshless methods, such as smoothed particle hydrodynamics (SPH) in Kajtar and Monaghan (2012) and vortex element methods in Barba (2004), Cottet and Poncet (2004), have benefited from their inherent adaptivity. Specifically, the meshless or Lagrangian methods use Lagrangian grid points, which follow the movement of the flows. Therefore, such methods can handle irregular and complex geometries without any complication.

As far as complex vortical flow is concerned, vortex element method is the suitable solver to resolve the vorticity region correctly with high resolution in Kamemoto (2004). In addition, another advantage of the method is that it can be easily implemented in parallel computation in order to allow long time simulation.

Accordingly, the fully meshfree version of the vortex element method (VEM) is developed in this research in order to simulate the complex 3D flow problems. Fast Multipole Method (FMM) is employed to accelerate the computation of the developed VEM. A novel Brinkman penalization boundary condition is introduced to model the complex deformable geometries under its motions (translation and rotation). Finally, the performance of the developed method is investigated by performing benchmark bounded flow simulations ranging from aerospace engineering to biological engineering and wind engineering.

1.1. Vortex particle method

The vortex methods are based on the momentum equation and the continuity equation for incompressible flow which are written in vector form as follows:

$$\frac{\partial \underline{u}}{\partial t} + (\underline{u}.\nabla)\underline{u} = -\frac{1}{\rho}\nabla p + \nu\nabla^2\underline{u} \tag{1}$$

$$\nabla.\underline{u} = 0 \tag{2}$$

Taking the *Curl* of both equations (1) and (2) it follows:

$$\frac{\partial \underline{\omega}}{\partial t} + (\underline{u}.\nabla)\underline{\omega} = (\underline{\omega}.\nabla)\underline{u} + \nu\nabla^2\underline{\omega} \tag{3}$$

$$\nabla^2 p = -\rho\nabla.(\underline{u}\nabla\underline{u}) \tag{4}$$

where $\underline{u}$ is velocity vector, p the pressure, and ρ the density. The vorticity $\underline{\omega}$ is defined as

$$\underline{\omega} = \nabla \times \underline{u} \tag{5}$$

The pressure p can be independently calculated by the Poisson equation (4) once needed. Lagrangian expression for the vorticity transport expressed in Eq. (3) is then given by

$$\frac{d\underline{\omega}}{dt} = (\underline{\omega}.\nabla)\underline{u} + \nu\nabla^2\underline{\omega} \tag{6}$$

When a two-dimensional flow is dealt with, the first stretching term of the right hand side in Eq. (6) disappears and so the two-dimensional vorticity transport equation is simply reduced as diffusion equation:

$$\frac{d\underline{\omega}}{dt} = \nu\nabla^2\underline{\omega} \tag{7}$$

In order to solve this equation numerically there is a need to approve by means of a viscous splitting algorithm. The algorithm includes two steps. The first step, the so-called convection, is to track particle elements containing the certain vortices with their own local convective velocity by Biot-Savart formulation

$$\underline{u}(\underline{x},t) = \frac{1}{4\pi}\int \frac{\underline{\omega}(\underline{x}',t)\times(\underline{x}-\underline{x}')}{|\underline{x}-\underline{x}'|^3}\, d\underline{x}' \tag{8}$$

where $\underline{x}$ is vector of position. The term inside integral in (8) is integrated over all particles in the computational domain. The Biot-Savart formulation is N-body problem that involves $O(N^2)$ evaluations. The calculation that involves $O(N^2)$ evaluations is called 'direct computation'. It makes this method not practical because of high memory requirement.

1.2. Fast multipole method

In order to overcome the N-body problem mentioned above, the Fast Multipole Method (FMM) is employed in this work to accelerate the velocity computation in Greengard and Rokhlin (1978). The method reduces significantly the velocity computation time due to the fact that interactions among particles are

not computed directly. In more details, the FMM, first, constructs the data of particles by tree structure of box in which particles are laid on. Second, the direct interactions of box's centers are evaluated by using multipole expansions of all these centers. Finally, the interaction of all direct particle pairs is translated from these centers to their own particles. Therefore, it reduces amount of computation process to the order of $O(N)$. Reducing amount of computation process affects computational speed that is major problem in analyzing FSI.

1.3. Brinkman penalization

The penalization method enforces the no-slip boundary condition on the surface of a body in an incompressible flow by introducing a source term localized around the surface of the body. This source term is added into the momentum equation. The velocity of the flow $\underline{u}$ is modified by the penalization term as

$$\frac{\partial \underline{u}}{\partial t} = \lambda\chi(\underline{u}_s - \underline{u}) \qquad (9)$$

where $\underline{u}_s$ denotes the velocity of the body and $\underline{u}$ denotes the velocity field of the flow. The penalization parameter λ has unit (s^{-1}), called reciprocal quantity of the penalization term, and is equivalent to a porosity of the body. The characteristic function χ is defined in Rasmusen (2008).

Hence, the velocity field is corrected with the penalization term which can be evaluated independently. Using an Euler time integration scheme for Equation (31), the correction can be evaluated implicitly as

$$\underline{u}^{n+1} = \frac{\underline{u}^n + \lambda\Delta t\chi\underline{u}_s}{1+\lambda\Delta t\chi} \qquad (10)$$

The penalization term can be expressed in the vorticity formulation

$$\frac{\partial \underline{\omega}}{\partial t} = \nabla\times[\lambda\chi(\underline{u}_s - \underline{u})] \qquad (11)$$

This vorticity form of the penalization can be implemented by an explicit evaluation

$$\underline{\omega}^{n+1} = \underline{\omega}^n + \nabla\times[\chi(\underline{u}_s - \underline{u})] \qquad (12)$$

where the penalization parameter λ is chosen to be $\lambda = \frac{1}{\Delta t}$.

2. Results and discussions

2.1. Flow over transverse spinning sphere

The impulsively started flow around a spinning sphere at Re = DU_∞/ν = 300 and a spin rate $WD/2U_\infty$ = 0.5 are considered, where D is the sphere diameter, U_∞ is freestream velocity and W is the angular velocity of the sphere.

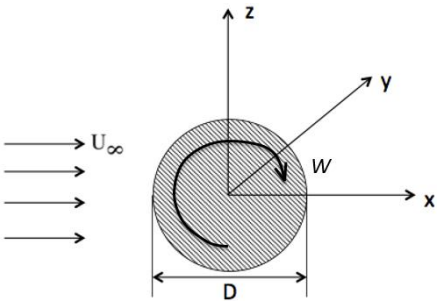

Figure 1. Configuration and coordinate system for flow over a spinning sphere.

The free-stream velocity is in the direction of $\mathbf{e}_x$. Two configurations are studied, one per direction of the angular velocity vector: $\mathbf{e}_x$ and $\mathbf{e}_y$. Both the free-stream and the rotation are impulsively started at t = 0. In this case, $W = \mathbf{e}_y$. In particular, the wall thus moves in the direction of the freestream for $z > 0$ and against it for $z < 0$.

Figure 2 shows the magnitude of the skin friction for several instants during a shedding cycle. The figure shows clearly the reattachment point of the present results (depicted on the left-hand side) which are in a good agreement with the reference results in Chatelain (2005) (depicted on the right-hand side). We obtain averaged values of C_D and C_L and compare

(2)

those reference results in Chatelain (2005) and Kim and Choi (2002).

Table 1. Drag and lift coefficients of flow over a transversely spinning sphere at Re = 300.

	C_D	C_L
Present	0.89	0.51
Kim and Choi (2002)	0.74	0.45
Chatelain (2005)	0.81	0.42

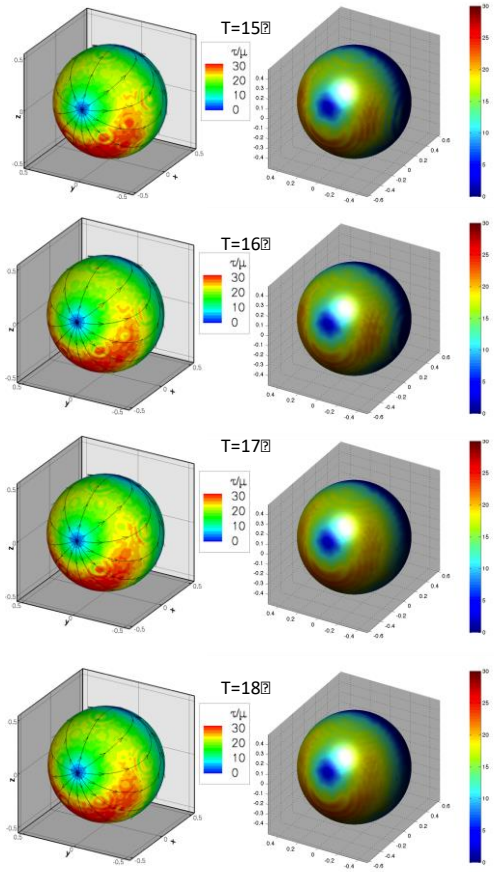

Figure 2. Spinning sphere at Re = 300, transverse rotation, transverse shear magnitude; Left: reference results in Chatelain (2005), right: present results.

The Table 1 expresses averaged values of drag and lift coefficients in period of simulation time T = 4 in which the drag coefficient approaches steady state. The present result demonstrates the higher difference of average value of drag with references. Hence, it is possible to conclude that a slightly different flow state are reached compared to references. In general, it is fair to conclude that the current algorithm works accurately compared to reference.

2.2. Flow over low aspect ratio wing

For a low aspect ratio wing application in aerospace engineering as used in the present study, flow separation behavior is more complex than on a conventional airplane. This section will focus on the flow separation and its interaction with wingtip vortices at 10^0 angle of attack. To obtain a better understanding of the flow separation phenomena, the vortex structure visualization is employed. The vortex patterns in the wake of the wing, are presented in Figure 2 which clearly demonstrates the complex 3D flows on the upper surface such as hairpin structure, helical structure, and wing-tip structure.

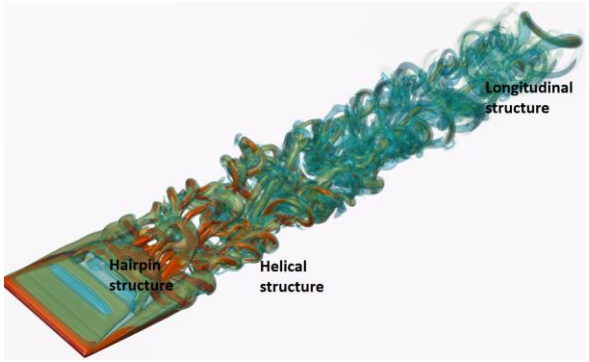

Figure 2. Complex flow structures developed within the wake region of the low aspect ratio wing at 10^0 angle of attack.

As clearly shown in the figure, the wingtip vortex occupies a large proportion on the wing suction sides. The wingtip vortex and its interaction with boundary layer separation may induce strong 3D structures which do not exist on the 2D airfoils. These structures are very crucial to determine the drag coefficient, which is one of the important aerodynamic parameters for unmanned aerial vehicle designs.

2.3. Flow over a rotating wing

For a rotating wing application in aerospace engineering as used in the present simulation, the rotating wings were considered as two rectangular plate with 8% thickness at 10^0 angle of attack. The rotating rate is set to be 0.5. The complex flow structures generated by the

rotating wings are clearly captures including wingtip structures and helical structures. The wingtip structures are generated with the hairpin shapes producing dynamic drag acting on the tip of the wings. The helical structures are more stable compared to hairpin structures. That is because the tip velocities, which two structures are generated, are different from tip to root of the wings.

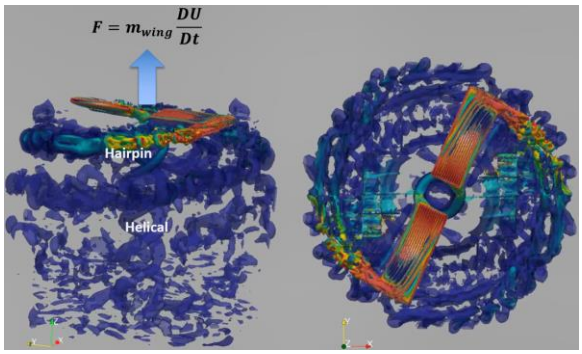

Figure 3. Complex flow structures developed within the wake region of the rotating wing platforms at 10^0 angle of attack.

2.4. Anguilliform swimming

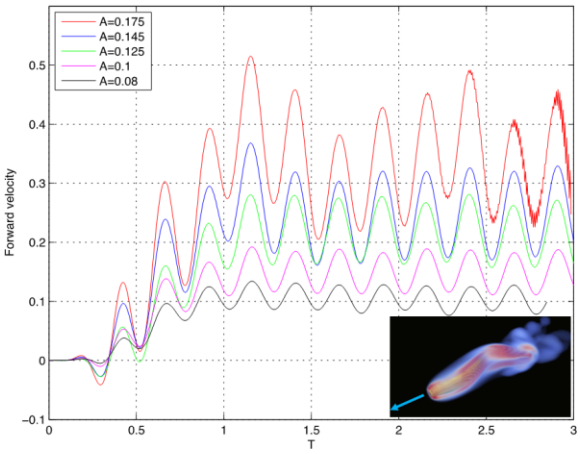

Figure 4. Time history of forward swimming velicities at different deforming amplitudes.

To extend the application of present computational algorithm for fluid-structure interaction in biological engineering, the simulation is started by setting the immersed anguiliform fish demonstrated in Figure 2, and let the fish freely deform during the computation to obtain the vorticity field. The anguilliform is allowed translations only in $z = 0$ plane and rotations are restricted to those around the z-axis.

The fluid structure interaction is used to enforce the brinkman penalization boundary condition for vortex particle method to calculate the flow field. The time step for the simulation was set to be $\Delta t = 0.005$. The length of the anguilliform, L, is set to be 1. The amplitude of the deformation A is set from 0.08 to 0.175 while the frequency, $f = \frac{1}{T}$, is set to be a constant value, 2. A Reynolds number of this flow can be defined as $Re = 2\pi fAL/\nu = 400$. This simulation is a fluid-structure interaction because the feedback from the fluid is considered to change the translational ($\dot{\mathbf{x}}_{cm}$) and angular ($\dot{\boldsymbol{\theta}}$) velocities of the anguilliform.

As shown in Figure 4, the time history of forward velocity of the anguilliform for slow deformation (A=0.125), approaches the periodicity stage from $t/T = 1$ while for the fast deformation it reaches to the periodicity stage from $t/T = 1.25$ (A=0.175). However, the magnitude of forward velocity in slow deformation case at the periodic stage is smaller than that in fast deformation case. Hence, it is fair to conclude that the current results are convergent.

2.5. Wind load on high-rised building region

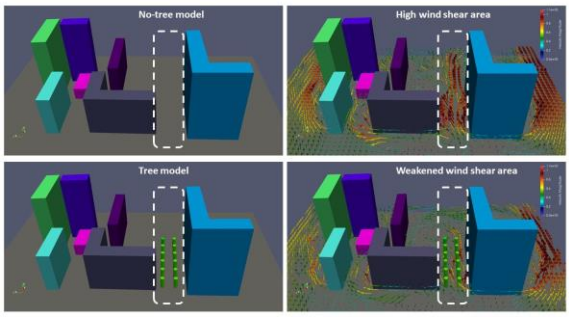

Figure 5. Effect of planting trees on the wind load reduction on the high-rised building region. High wind shear region will be 80% removed by the tree planting.

For wind engineering applications, wind gust is very important and needs to be evaluated for the estimation of the environmental disaster on the

high-rised building region. Otherwise, the current method is possible to enable the capability for complex geometry (high-rised building region), turbulent flow to investigate the wind load dynamics and sensitivities on the complex geographic region.

The simulation of such kind of turbulent flow is demonstrated in Figure 5 with respect to the effect of trees allocated within building area using the current method. As shown by the figure, the allocation of two rows of planting trees reduces the high wind shear acting on the main road between two high rised buildings.

3. Conclusions

The current work presents a construction of Brinkman penalization coupled with the vortex method algorithm for dealing with complex moving and deforming geometries in viscous flow simulation. An algorithm for a vortex method combined with the Brinkman penalization was briefly described and validated from near field to far field bounded flow simulations. For the validation of the code, simulation of three-dimensional incompressible flow around transverse spinning sphere at three 300 Reynolds numbers is performed. This study highlights the comparison of the wake characteristics between the current results and references listed in literature. The Brinkman penalization method is validated to be converged. The extension of the current vortex method algorithm is also performed to be highly applicable ranging from aerospace engineering (complex wake structures on low aspect ratio wing and a rotating wing) to biological (anguilliform swimming) and environmental engineering (wind load on high-rised building region).

References

Barba L.A. (2004). *Vortex Method for Computing High-Reynolds Number Flows: Increased Accuracy with a Fully Mesh-less Formulation*. PhD dissertation, Department of Aeronautical Engineering, California Institute of Technology, California.

Chatelain, P. (2005). *Contributions to the three-dimensional vortex element method and spinning bluff body flows*. PhD thesis, California Institute of Technology.

Cottet G.-H. and Poncet P. (2004). Advances in direct numerical simulations of 3D wall-bounded flows by vortex-in-cell methods, *Journal of Computational Physics*, 193, pp.136–158.

Eric D.T. (2004). The hydrodynamics of eel swimming II. Effect of swimming speed. *Journal of Experimental Biology*, 207, pp.3265-3279.

Kajtar J. B., Monaghan P.P. (2012). On the swimming of fish like bodies near free and fixed boundaries. *European Journal of Mechanics - B/Fluids*, 33, pp.1-13.

Kamemoto K. (2004). On Contribution of Advanced Vortex Element Methods Toward Virtual Reality of Unsteady Vortical Flows in the New Generation of CFD. *Brazilian Congress of Thermal Sciences and Engineering*, 26, pp.368-378.

Kim, D. & Choi, H. (2002). Laminar flow past a sphere rotating in the streamwise direction. *Journal of Fluid Mechanics*, 461, pp. 365–386.

L. Greengard, V. Rokhlin (1987). A fast algorithm for particle simulations. *J. Computational Physics*, 73, pp. 325-348.

Li G., Müller U.K., van Leeuwen J.L., Liu H (2012). Body dynamics and hydrodynamics of swimming fish larvae: a computational study. *Journal of Experimental Biology*, 215, pp.4015-4033.

Mattia G., Chatelain P., Rees W. M., Koumoutsakos P. (2011). Simulations of single and multiple swimmers with non-divergence free deforming geometries. *Journal of Computational Physics*, 230, pp.7093–7114.

Ramussen T.R (2008). *A penalization Interface Method for 3D Particle Vortex Methods*. Master Thesis, Mechanical Engineering, Technical University of Denmark.

The 5th International Conference on Engineering Mechanics and Automation (ICEMA 5)
Hanoi, October 11÷12, 2019

Numerical Analysis of Cavity Pressure According to Ventilated Condition of Supercavitating Underwater Vehicle

Dong-Hyun Kim[a], Warn-Gyu Park[b*],

[a] *School of Mechanical Engineering, Pusan National University, Busan, Korea, dhyunkim@pusan.ac.kr*
[b] *School of Mechanical Engineering, Pusan National University, Busan, Korea, wgpark@pusan.ac.kr*

Abstract

The shape, size, and orientation of the cavity are important factors in the case of supercaviting underwater vehicle. In order to overcome experimental limitations for this study, we performed computational analysis approach through the study. In this study, we developed multiphase flow analysis code using a homogeneous mixture model for the 3D Navier-Stokes equation. The experimental results and the computational analysis results of the cavity tunnels were compared and verified. As a result of this comparison process, it showed fairly good agreement under various condition. Computational analysis was carried out on the change of cavity shape and cavity number according to injection flow rate by artificial injection.

Key Words: Cavitation, Artificial supercavitation, Air entrainmentcoefficient, Gravitational effect

1. Main instructions

Cavity refers to one of the vaporization phenomena due to local pressure drop, and in the general mechanical engineering category, there is a negative perception of problems such as corrosion and noise of the machine resulting from the process of creating and destroying cavities. Recently, however, researches have been conducted to apply these cavitations in various ways. One of them, the field of underwater vehicles, is actively researching super-cavity-high speed underwater vehicles using cavitation.

In the super-cavity underwater vehicle using the cavitation, the entire body is covered by the cavity except for the part of the head, which causes the overall drag to decrease drastically due to the difference in water and density. his drag reduction leads to an increase in speed, which achieves ultrafast conditions. Although foreign countries have already conducted a considerable amount of research and actual size experiments, some groundbreaking results have been published, but most of them are not publicly related to the military sector. In the results published overseas, partial & super cavitation studies using preconditioning and dual time stepping methods were performed using the Homogeneous mixture model (Kunz et al. , 2000). However, Kunz's model did not consider the compressibility effect, and recently a computational analysis using the fully compressible model considering both compressibility and temperature change was performed (Linau et al., 2003; Kunz and Merkle, 2003; Owis and Nayfeh, 2003). Fundamental research has been actively conducted in the last few years. A partial cavity flow analysis around an underwater vehicle was performed using a three-dimensional Navier-Stokes equation-based

computational analysis program (Kim et al., 2013). A multiphase flow computational analysis of the injection cavity considering the compressibility effect was also performed (Ha et al., 2016). Recently, several cavity tunneling experiments have been carried out (Ahn et al., 2016, Paik, 2016). However, there are not many examples of the development of computational analysis program that can be directly compared with the super cavity experiment. In addition, there are still not enough direct comparisons with the super-cavity computational analysis based on the three-dimensional Navier-Stokes equation that takes into account the viscous effects.

In this paper, we compared and verified the results of a multi-phase flow analysis program based on the three-dimensional Navier-Stokes equation developed in-house for cavity experiment. Experimental results and verification were performed through analysis of injection cavity under different injection volume conditions. On the basis of this, computational analysis on the change of cavity shape according to various angles of attack.

2. Governing equations

In this study, we identified the dimensionless variables that are needed for the related studies of the cavity shape around the underwater vehicle. In order to confirm the characteristics of the cavity according to the change of the dimensionless variable and to confirm it, the computational analysis using the multiphase flow analysis program was performed. The program solves each continuous equation separately for multiphase based on the three-dimensional Navier-Stokes equation. In the case of the momentum equation, a homogeneous mixture model using a mixture equation is used.

$$\frac{\partial \alpha_l}{\partial t}+\left(\frac{\alpha_l}{\beta^2}\right)\frac{\partial p}{\partial \tau}+\frac{\partial \alpha_l}{\partial \tau}+\frac{\partial \alpha_l}{\alpha x_j}(\alpha u_j)=\left(\dot{m}^{+}+\dot{m}^{-}\right)\left(\frac{1}{\rho_l}\right) \quad (1)$$

$$\frac{\partial \alpha_v}{\partial t}+\left(\frac{\alpha_v}{\beta^2}\right)\frac{\partial p}{\partial \tau}+\frac{\partial \alpha}{\alpha x_j}+\frac{\partial \alpha_v}{\alpha x_j}(\alpha_v u_j)=\left(\dot{m}^{+}+\dot{m}^{-}\right)\left(\frac{1}{\rho_v}\right) \quad (2)$$

$$\frac{\partial \alpha_{ng}}{\partial t}+\left(\frac{\alpha_{ng}}{\beta^2}\right)\frac{\partial p}{\partial \tau}+\frac{\partial \alpha}{\alpha x_j}+\frac{\partial \alpha_{ng}}{\alpha x_j}(\alpha_{ng} u_j)=0 \quad (3)$$

$$\frac{\partial}{\partial t}(\rho_m u_i)+\frac{\partial}{\partial \tau}(\rho_m u_i)+\frac{\partial}{\partial x_j}(\rho_m u_i u_j) \quad (4)$$
$$=-\frac{\partial p}{\partial x_i}+\frac{\partial}{\partial x_j}\left[(\mu_m+\mu_{m,t})\left(\frac{\partial u_i}{\partial x_j}+\frac{\partial u_j}{\partial x_i}\right)\right]+\rho_m g_i$$

Where subscript v is the gas phase, l is the liquid phase, and ng is the non-condensing gas.

3. Computational Analysis Results

3.1. Verification of Injection cavity

Fig. 1 and Fig. 2 show the change of cavity shape according to the change of Cq value due to the change of injection volume of injection cavity when Fn between experiment and analysis is 10.8. In the same Cq value, Fn is increased to 14.4 (Paik,2018). When Fn is 10.8, it can be seen that the area of the cavity covering the body increases as the injection coefficient increases, and the experimental and computational results are in good agreement. This agreement shows that the maximum diameter of the cavity is not changed by the shielding effect when Fn is increased to 14.4 while maintaining Cq at 0.20. But as the effect of gravity decreases, it can also be seen that the cavity tail remains more horizontal.

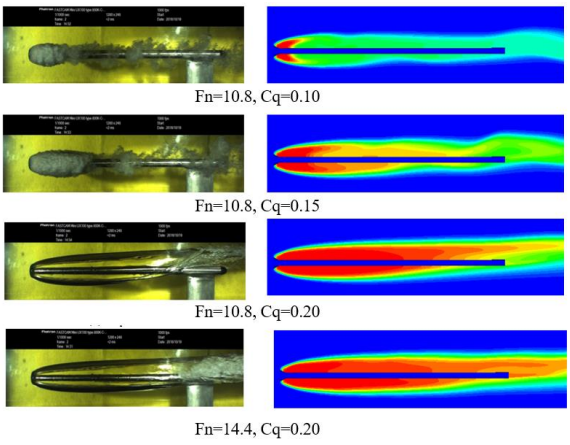

Figure 1. Cavity formation at various ventilated rate coefficient (Fn=10.8, 14.4, Cq=0.10, 0.15, 0.20)

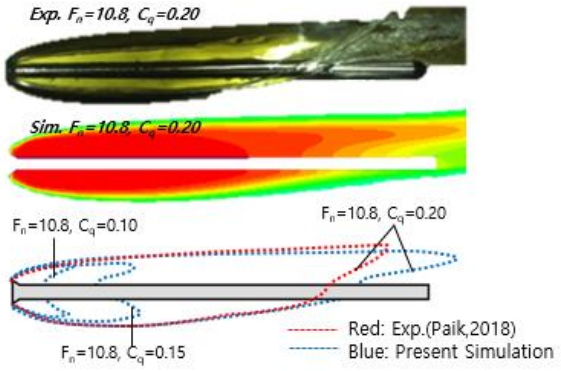

Figure 2. Cavity formation at various ventilated rate coefficient (Fn=10.8 Cq=0.10, 0.15, 0.20)

The size of the cavity covering the body can be seen that the maximum diameter and the length to the rear increases as the injection amount Cq increases. Fig. 2 is the dotted line representing the cavity boundary that can be clearly distinguished between the experiment and the computational analysis when Fn = 10.8. When Fn = 10.8 and Cq = 0.20, the cavity shape and size comparisons of the analysis and experiment show that the initial development of the cavity and the size and point of occurrence of the maximum diameter are in good agreement. The cavity asymmetry / elevation effect due to the tail buoyancy phenomenon is also shown well, but some differences occur in the rear part shape. This is because, in the case of the experiment, the flow of the front of the strut is influenced by the strut supporting the body. Therefore, it was confirmed that the difference occurred at the rear of the cavity as much as the part interrupted by the strut.

3.2. Cavity change with angle of attack

Factors that determine the maximum diameter and length of the cavity are Fn at ambient speed and Cq and σ_C at injection rate. In addition, there are angles of attack of the cavitator that can have a very large impact in real environments. In this study, we studied how the shape of cavity changes when the cavator has angle of attack. Fig. 3 shows the cavity shape change according to the angle of attack of the cavitator in the injection cavity computational analysis with the injection characteristic of Cq = 0.15. When the angle of attack (AoA) is 0 °, the cavity asymmetry due to the rise of the cavity tail due to the gravity / buoyancy effect occurs as shown in Fig.2. If the angle of attack is 10 degrees, the cavity generated from the cavitator is generated below the body, thereby canceling the asymmetry of the cavity trailing edge caused by buoyancy. This phenomenon, when the angle of attack is 15 °, the cavity shape becomes more prominent, it can be seen that the cavity covers more area under the body. Fig. 4 shows the maximum diameters of the upper and lower surfaces of the cavity according to the angle of attack. As the cavitator has the angle of attack in the downward direction, the cavity size of the lower surface gradually increases as the angle of attack increases. In the case of the upper surface, as the angle of attack increases, if the angle of attack is 15 °, it can be confirmed numerically. Fig. 5 shows the distance to the maximum diameter of the cavity and the point where the cavity is maintained. For the distance that the maximum diameter of the cavity occurs, it can be seen that a small increase as the angle of attack increases. In contrast, when the angle of attack is 0 °, the length of the upper cavity is longer than the length of the lower cavity, but it is reversed as the angle of attack increases. Being able to predict the length of the cavity according to the angle of attack is important information in maintaining super cavity.

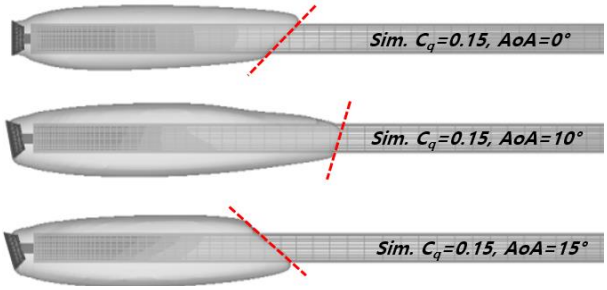

Figure 3. Cavity formation at differnt cavitator AoA (Cq=0.15, AoA=0, 10, 15°).

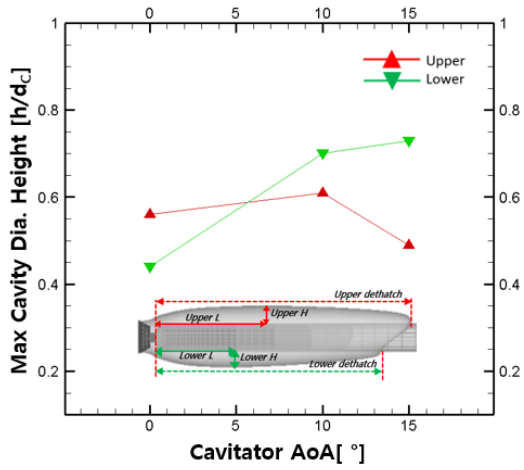

Figure 4. Comparison of Max. Cavity Dia. for various AoA.

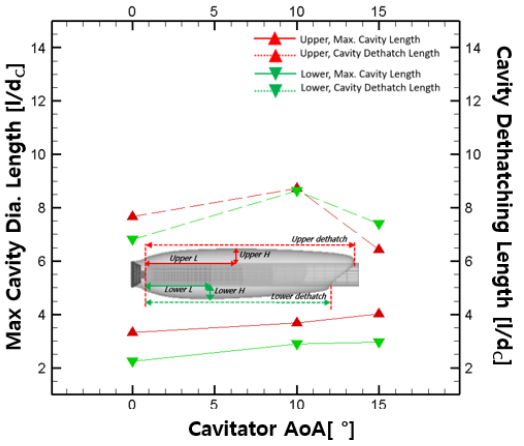

Figure 5. Comparison of length for max. Cavity dia. and dethatch for various AoA.

Acknowledgements

This work was supported by the National Research Foundation of Korea(NRF) grant funded by the Korea government(MSIT) (No. 2018R1A2B6008864)

References

B.G. Paik(2018), *Fundamental Studies for Ventilated Supercavitation Experiments in New High-speed Cavitation Tunnel*, Journal of the Society of Naval Architects of Korea, Vol. 55, No. 4, pp. 330-340

C.T. Ha, W.G.Park(2016). *Evaluation of a New Scaling Term in Preconditioning Schemes for Computations of Compressible Cavitating and Ventilated Flows*. Ocean Engineering, Vol. 126, pp. 432-466.

Kawakami, R. Arndt(2011). *Investigation of the Behavior of Ventilated Supercavities*. Journal of Fluids Engineering, Vol. 133, 091305-1.

D.H.Kim, W.G.Park, C.M.Jung(2013). *Numerical simulation of cavitating flow past axisymmetric body.* International J. of Naval Architecture and Ocean Engineering, Vol.4, No.3, pp. 256~266.

W.GPark, C.T.Ha, C.K.Merkle(2006). *Multiphase flow analysis of cylinder using a new cavitation model*. 7th International Symposium on Cavitation, CAV2009, Paper No.99

The 5th International Conference on Engineering Mechanics and Automation (ICEMA 5)
Hanoi, October 11÷12, 2019

Experimental and Numerical Study of Hot Water Cavitation on a NACA0015 Hydrofoil

Anh Dinh Le[a], Okajima Junnosuke[b] and Iga Yuka[b]

[a] VNU - University of Engineering and Technology; 144 Xuanthuy, Caugiay, Hanoi – Email: anh.ld@vnu.edu.vn
[b] Institute of Fluids Science; Tohoku University; 2-1-1Katahira, Sendai, Miyagi, Japan – Email: j.okajima@tohoku.ac.jp and iga@cfs.ifs.tohoku.ac.jp

Abstract

In this paper, the thermodynamic effect on water cavitation at high temperature was studied. The cavitation on a NACA0015 hydrofoil was experimented in high-temperature and high-pressure water tunnel. The temperature depression inside the cavity was measured using a highly accurate thermistor probe. According to the results, the temperature depression was increased when the free-stream temperature of water increased. The temperature drop of 0.33°C was measured in the water at 90°C. The numerical simulation was then performed using homogeneous model coupled with a simplified thermodynamic model. As the results, the satisfactory prediction of cavity volume and temperature drop were reproduced in present model compare with experimental data.

Key Words: Cavitation, Thermodynamic Effect, Computational Fluid Dynamics, NACA0015

1. Introduction

Cavitation is the formation of vapor phase inner liquid phase when the local pressure decreases to its saturated vapor pressure due to the flow acceleration. Cavitation is the major concern in hydraulic machinery due to the increase in noise, vibration, performance degradation and erosion. When cavitation occurs, the heat supplied from surrounding liquid is needed for vaporization, hence the liquid temperature is decreased and cavitation is suppressed. Hence, the system performance can be improved. Therefore, the thermodynamic effects can significantly suppress the cavity volume. A number of cavitation experiments have been conducted with water at room temperature which is far from the liquid critical temperature, so that the thermodynamics effect is usually neglected (Petkovsek and Dulaz, 2013). However, when the fluid temperature is close to the critical temperature, its effect becomes importance and cannot ignore. For example, in cryogenic liquids (LN_2, LH_2, etc.) (see Hord, 1973), or hot water, which are the working fluids in industrial application (Petkovsek and Dulaz, 2013).

Up to date, the studies on the thermodynamic effect are extremely limited owing to the difficulty on measurement technique and the limitation of measurement device. Most of studies were paid attention on the consequence rather than its mechanism.

In this study, the thermodynamic effect on cavitation in hot water up to 90°C is studied by both experimental and numerical approach. At first, the experimental of cavitating flow is conducted for NACA0015 hydrofoil as a cavitator. The degree of thermodynamic effect is investigated by measuring the temperature difference between the cavity and freestream using the highly accurate thermistor probe. Then, the numerical study is performed using the homogeneous model coupled with a simplified thermodynamic model to reproduce the temperature flow field. The numerical result is quantified by

comparing with the measured temperature depression and visualized cavity aspect.

2. Experimental Method

2.1 Experimental Setup and Measurement Method

The cavitation experiment in hot water was conducted in high temperature and high-pressure water tunnel in Tohoku University. In this tunnel, the pressure can rise up to 0.5 MPa, and the temperature can heat up to 140°C using an electric heater with accuracy of 0.1°C. The test section is a rectangular channel with 30mm height x 20mm width in cross section and 330mm long. An observation window, made of glass, was installed to front wall of test section enables visualization of cavitation

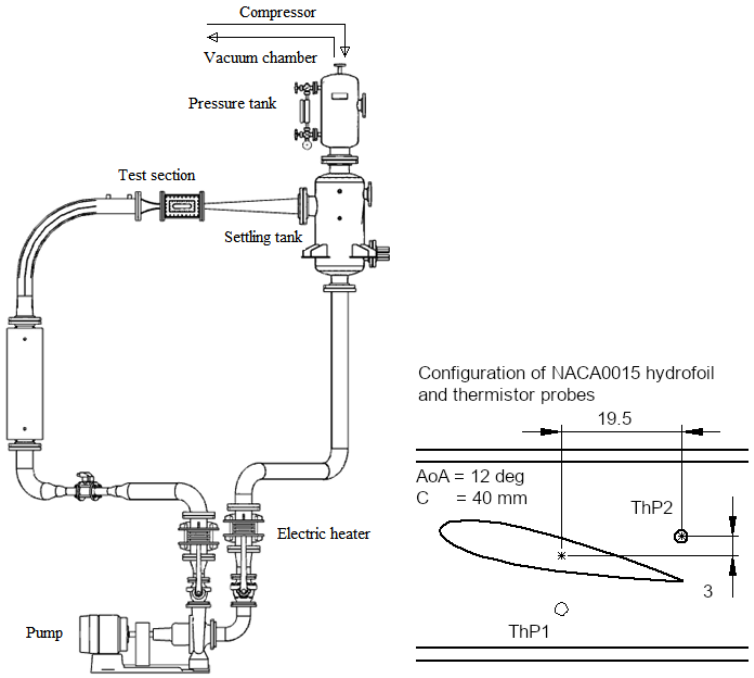

Fig. 1. Configuration of high-temperature and high-pressure water tunnel (left) and measurement approach on NACA0015 hydrofoil (right)

appearance. The tank pressure was controlled using compressor and vacuum pump; the flow rate was adjusted by controlling the pump rotation speed. The overview of tunnel configuration is shown in left of Fig.1. The pressure at upstream and downstream of the test object was measured using KYOWA DPM-911B pressure transducer.

The NACA0015 hydrofoil with the chord length of 40mm and 20mm span width, which is similar to previous our work by Yamaguchi et al. (2014), was used with angle of attack of 12 degrees. Two thermistor probes (Nikkiso-Thermo Co., Ltd.), which has highly accurate with a large change in electric resistance versus temperature, were inserted to mid span of channel to measure the freestream temperature T_0 (ThP1) and cavity temperature T_c (ThP2), with help of stainless steel tube of 2mm in diameter and 0.5mm in thickness. The thermistor's head was fixed at 2mm away the tube. The ThP1 was placed 10mm below the center of channel and was upstream bended to avoid the cavitation occurs at the thermistor head. The ThP2 was placed 3mm above the channel center and 19.5mm downstream from the center of hydrofoil as shown on the right of Fig.1. These thermistor probes were calibrated using quartz thermometer. The resistance of thermistor probe was measured using Tektronix DMM4040 digital multimeter, with the uncertain less than 0.01°C. The instantaneous freestream and cavity temperature data were recorded every 2 seconds, and the measured temperature was averaged in 30 seconds. The Fast Photon high-speed CCD camera was used to visualize the cavity aspect.

2.2 Experimental Conditions

In the experiment, the freestream temperature was heated from room temperature up to 90ºC. The flow velocity was set as 8m/s. The water was degassed to the condition of saturated rate of dissolved oxygen of about 30%, which was measured using the HACH LDO HQ30d. The constant cavitation number σ of 1.6 was set in this study. Two different flow temperatures were experimented and measured simultaneously. The details of experimental conditions are shown in Table 1.

Table 1. Experimental conditions

AoA = 12 deg., σ = *1.6*	
***U_0* (m/s)**	***Temperature T_0* (ºC)**
8	60
	90

The calculation domain corresponding to experimental test-section is shown in Fig.2. A C-type orthogonal boundary fitted grid (253 x 70) was made, with the y^* was in range from 40 to 261. The inlet was located at three chord length from the leading edge of hydrofoil; the outlet was located at five chord length from the trailing edge. At the inlet, the uniform velocity, temperature, void fraction, and turbulent quantities (Chen et al., 2016) were adopted. The static pressure was specified at the outlet boundary. No-slip and adiabatic condition were applied at the top/bottom wall and hydrofoil. Chen's (2016) model is used to model the eddy viscosity versus water freestream temperature. The numerical results were compared with the experimental data based on the visualized image and measured temperature depression.

5. Results and Discussion

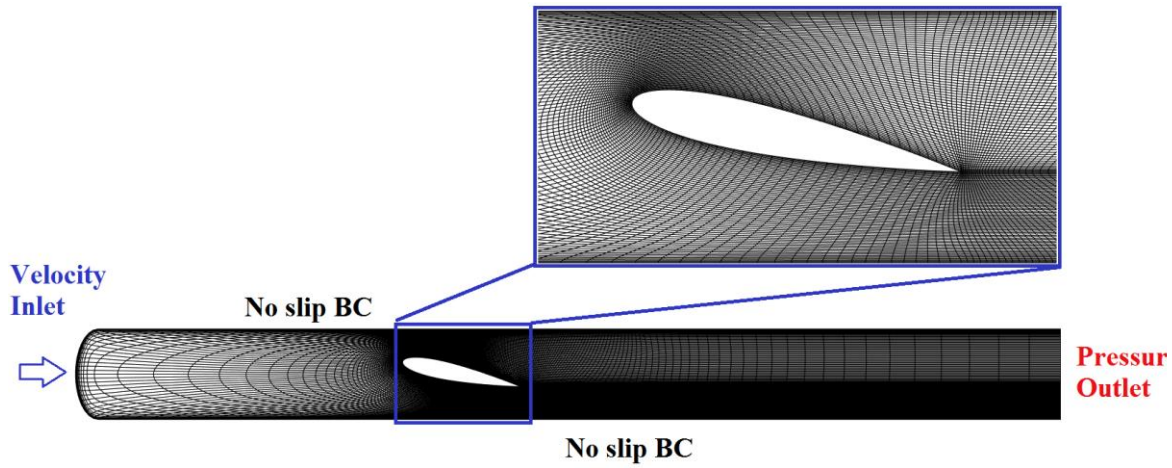

Fig. 2. Calculation domain and C-Grid type over NACA0015 hydrofoil

3. Numerical Method

In this study, the homogeneous model, which has been previously derived (Iga et al., 2003 and 2004), is choose for modeling the compressible gas-liquid two-phase flow medium. A simplified thermodynamic model with the modification of heat input by condensation is used to account the thermodynamic effect when cavitation occurs. The detail of governing equation and the simplified thermodynamic model can be referred in our previous paper (Anh et al., 2019a and 2019b). Our lab cavitation model is employed for modeling the phase change rate by cavitation, with C_e = 1000 and C_c =1, respectively (Ochiai et al., 2010). The saturated pressure $p_v(T)$ was estimated by Sugawara equation (Ochiai et al., 2010).

Figure 3 shows the instantaneous image of the appearance of cavity with freestream temperature of T_0 = 60ºC and T_0 = 90ºC on the flow condition of σ = 1.6, U_0 = 8m/s. The supercavitation occurred and the second thermistor probe (ThP2) was fully immersed inside cavity, therefore the temperature inside the cavity can be measured in this condition. Here, although the cavitation appeared on the supporting pipe of ThP1, the appearance place was far away the head of thermistor probe, the effect of cavitation on its measurement data is therefore negligible. Besides, the effect of cavity volume appeared behind the supporting tube of ThP1 on the flow field was ignored since the ThP2 was fully immersed inside the cavity in supercavitation condition.

Figure 4 shows a quantitatively comparison of the temperature depression (T_0 – T_c) in present numerical simulation, present measured result, and the previous measured data by Yamaguchi et al. [3] versus freestream temperature. The present measured temperature depression roughly agreed with Yamaguchi's data at 60°C. According to results, the temperature depression became bigger when the freestream temperature increased. The temperature drop was measured about 0.32°C at freestream temperature of $T_0 \approx 90$°C.

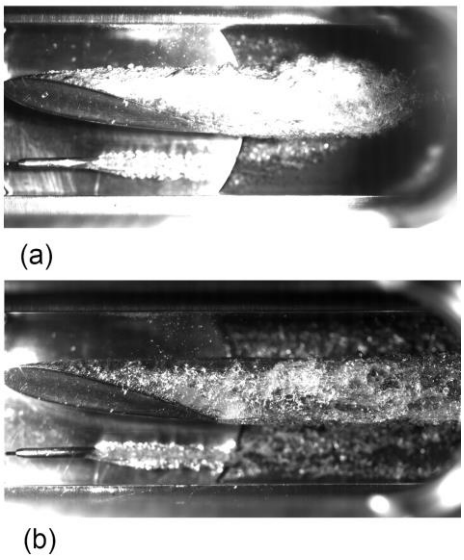

Fig. 3. Visualization of cavity aspect at T_0 = 60°C (a) and T_0 = 90°C (b)

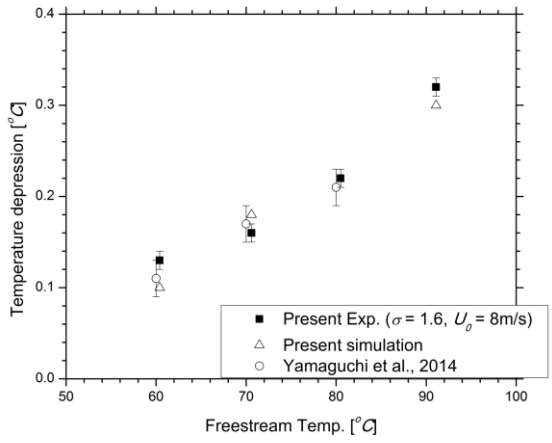

Fig. 4. Comparison of temperature depression between present simulation, present measurement, and Yamaguchi measurement data.

As the result, the satisfaction prediction of temperature depression with measured data was reproduced in numerical calculation for both runs at T_0 = 60°C, and T_0 = 90°C. The numerical tendency of temperature depression agreed with experimental data.

Figure 5 shows the comparison of numerical result and experimental data at T_0 = 60°C – (left) and T_0 = 90°C – (right), respectively. The orders in figure are instantaneous image of cavity in experiment (a), instantaneous void fraction distribution (b), and temperature distribution in simulation (c). The cavity aspect and length compared good with experimental visualization. The minimum temperature appeared at the region behind hydrofoil trailing edge, where the vapor void fraction is high. This is consistent with the measurement result of temperature distribution for unsteady cavitation by Petkovsek (2013).

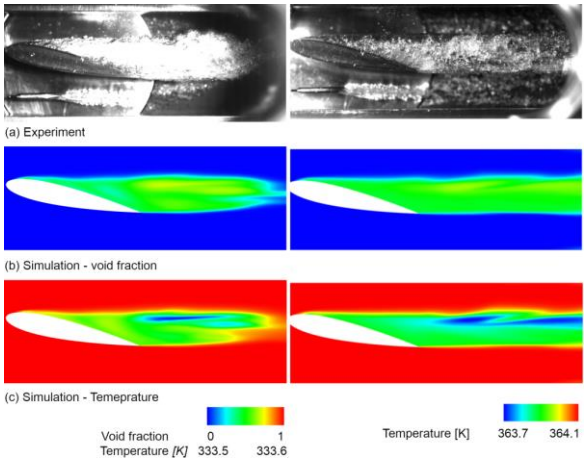

Fig. 5. Comparison of instantaneous image of cavity aspect in experiment (a), vapor void fraction in simulation (b), and temperature distribution in simulation (c) at T_0 = 60°C (left) and T_0 = 90°C (right)

6. Conclusions

In this study, the thermodynamic effect of cavitation in water at temperature up to 90°C was investigated. The cavitating flow experiment through NACA0015 hydrofoil was conducted. The degree of thermal effect was investigated by measuring the temperature drop inside the cavity with highly accurate thermistor probe. The numerical simulation was performed base on the experimental data by coupling the homogeneous model with a simplified

thermodynamic model. The main results are summarized as follows:

1. The temperature depression inside the cavity was increased with the increase of water temperature.

2. The suppression effect does not appear in water cavitation at temperature up to 90^{o}C. In that, the longer cavity length was visualized when freestream temperature increased.

3. The satisfactory prediction of temperature depression with measured data was reliable produced in numerical simulation. The numerical void fraction aspect and length corresponded well with visualization data.

References

Anh, D. L., Okajima, J., and Iga, Y., 2018. Modification of Energy Equation for Homogeneous Cavitation Simulation with Thermodynamic Effect, *ASME J. Fluids Eng.,* 141, 081102-1-12.

Anh, D. L., Okajima, J., and Iga, Y., 2019. Numerical Simulation Study of Cavitation in Liquefied Hydrogen, *Cryogenics* 101.

Chen, T., Huang, B., Wang, G., and Zhao, X., 2016, "Numerical Study of Cavitating Flows in a Wide Range of Water Temperature with Special Emphasis on Two Typical Cavitation Dynamics," *International Journal of Heat and Mass Transfer*, 101, pp. 886-900.

Hord, J., 1973, "Cavitation in Liquid Cryogens II – Hydrofoil," *NASA CR-2156*.

Iga, Y., Nohmi, M., Goto, A., Shin, B. R., Ikohagi, T., 2003, "Numerical Study of Sheet Cavitation Breakoff Phenomenon on a Cascade Hydrofoil," *ASME J. Fluids Eng.,* Vol. 125, pp. 643-651.

Iga, Y., Nohmi, M., Goto, A., Ikohagi, T., 2004, "Numerical Analysis of Cavitation Instabilities Arising in the Three-Blade Cascade," *ASME J. Fluids Eng.*, Vol. 126, pp. 419-429.

Ochiai, N., Iga, I., Nohmi, M., Ikohagi, T., 2010, "Numerical Prediction of Cavitation Erosion Intensity in Cavitating Flows around a Clark Y 11.7% Hydrofoil," *Journal of Fluid Science and Technology*, Vol. 5, No 3.

Petkovsek, M., and Dulaz, M., 2013, "IR Measurements of the Thermodynamic Effects in Cavitating Flow," *International Journal of Heat and Fluid Flow*, 44, pp. 756-763.

Yamaguchi, Y., and Iga, Y., 2014, "Thermodynamics Effects on Cavitation in High Temperature Water," *ASME-FEDSM 2014-21433*.

The 5th International Conference on Engineering Mechanics and Automation (ICEMA 5)
Hanoi, October 11÷12, 2019

Some of water replenishment plans for the inner river system in Hanoi

Nguyen Chinh Kien[a], Dinh Van Manh[a,b], Nguyen Thi Hang[a]

[a] *Institute of Mechanics, Vietnam Academy of Science and Technology, 264 Doi Can, Ba Dinh, Hanoi – Email: nckien@imech.vast.vn*
[b] *VNU University of Technology, 144 Xuan Thuy, Hanoi*

Abstract

The inner river system in Hanoi includes Nhue River, To Lich River, Kim Nguu River, Lu River and Set River. Today, they are channels for rainwater and the city's sewage, not be real rivers because they have small slope and cross section, backfilled, with much mud and garbage and therefore, their flow discharge is small. The high pollution of water caused by the amount of waste water from unprocessed trade villages, domestic waste water (above 8 million people), and industrial waste water are discharged directly into the rivers.

In this report, IMECH1D software is used to research and test some of water replenishment plans to clean water, to improve the aquatic environment of the rivers and to ensure the supply of irrigation water for production.

Key Words: Hanoi, river, pollution, water replenishment, Imech 1D.

1. Numerical Modelling

1.1. 1D equations

Hydraulic equations:

$$B\frac{\partial H}{\partial t}+\frac{\partial Q}{\partial x}=q \quad (1)$$

$$\frac{\partial Q}{\partial t}+\frac{\partial}{\partial x}\left[\beta\frac{Q^2}{A}\right]+gA+\left[\frac{\partial H}{\partial x}+S_f\right]=0 \quad (2)$$

where, x and t denote space and time; A is the area of wet cross-section; B - the width of cross-section; H - water level; Q - discharge; β – is momentum correction factor ($\beta \approx 1$); q is additional (or loss) discharge per unit length; S_f - friction slope (defined by the formula: $S_f = g|Q|Q/C^2R$ with R – hydraulic radius) and C – Chezy coefficient.

Advection - Dispersion equation:

$$\frac{\partial A_t S}{\partial t}+\frac{\partial QS}{\partial x}=\frac{\partial}{\partial x}\left(A_t D\frac{\partial S}{\partial x}\right)+G(S) \quad (3)$$

where S is pollutant concentration; D – diffusion coefficient; $G(S)$ – additional source.

Mass balance equation:

$$F_D(DO)=k_2(DO_s-DO)-k_3.BOD \quad (4)$$

$$F_D(BOD)=-k_3.BOD \quad (5)$$

where k_2 - dissolved oxygen coefficient of the water; k_3 - decomposition coefficient of BOD.

Numerical solving techniques

The finite difference method is used to solve numerically. The Preissman 4-points finite difference scheme is applied for 1D hydraulic

equations (1) and (2), the up-wind scheme for the mass conservation equation (3).

1.2. Research area

The research area consists of Tich Bui river, a part of Day river, To Lich river, Lu river, Set river, Kim Nguu river and Nhue river, limited by Phu Ly station at downstream. The river system consists of 7 rivers and 3 channels with 178 cross sections and 12 junctions.

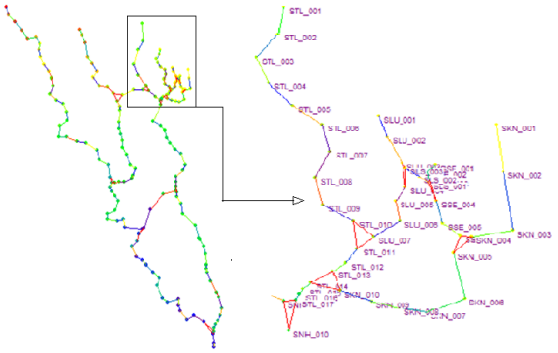

Fig 1: Cross section system of research area.

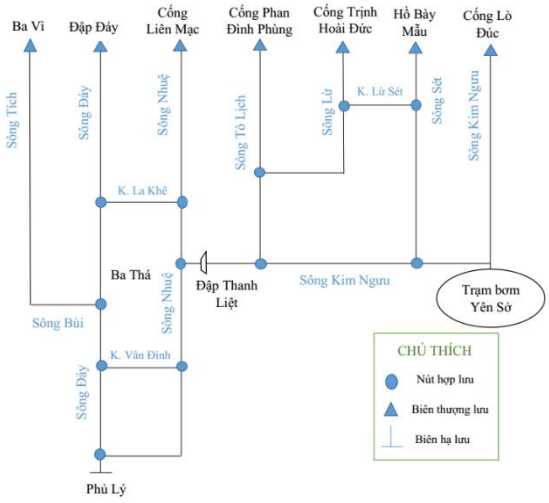

Fig 2: Hydraulic scheme of research area.

Upstream boundary: Dong Mo on Tich river, Day dam on Day river, Lien Mac gate on Nhue river, Phan Dinh Phung gate on To Lich river, Trinh Hoai Duc gate on Lu river, Ba Trieu gate on Set river and Lo Duc gate on Kim Nguu river.

Downstream boundary: Phu Ly station on Day river.

2. Calibration and verification numerical model

2.1. Hydraulic

By using 2014 data for calibration, it is impossible to get the observed data on all cross section, the model parameters are calibrated by using the observed data at some locations only: Ba Tha on Day river, Ha Dong, Dong Quan, Nhat Tuu, Luong Co on Nhue river, ... To evaluate the accuracy between calculated results (Cal.) and the Observed data (Obs.), index Nash-Sutcliffe Efficiency (NSE) is used.

On the basis of the calibration parameters, several calculations using the measured data in 2016 and 2019 are carried out.

Table 1: Calculation times.

Year	Season	Start	End
2014	Rainy	25/8/2014	15/9/2014
2016	Rainy	27/7/2016	11/8/2016
2019	Dry	4/01/2019	15/3/2019

a) Calibration

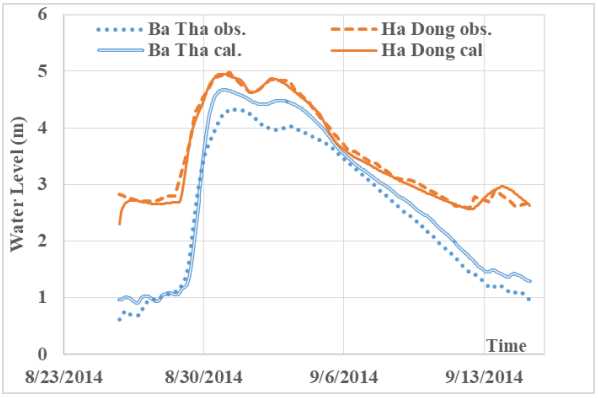

Fig 3: Calculated and measured water levels at Ba Tha station and Ha Dong station in 2014

Table 2: NSE index at some stations in 2014.

Station	Ba Tha	Ha Dong	Dong Quan	Nhat Tuu	Luong Co
NSE	0.95	0.96	0.91	0.87	0.86

The Nash–Sutcliffe efficiency index hit a good accuracy (NSE > 0.85).

b) Verification

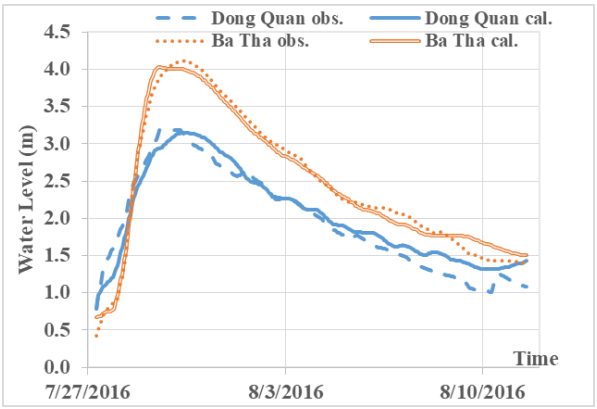

Fig 4: Calculated and measured water levels at Ba Tha station and Dong Quan station in 2016

Table 3: NSE index at some stations in 2016

Station	Ba Tha	Ha Dong	Dong Quan	Nhat Tuu	Luong Co
NSE	0.89	0.88	0.86	0.85	0.85

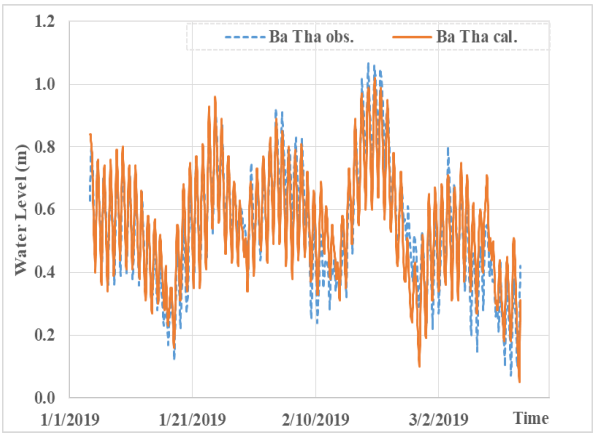

Fig 5: Calculated and measured water levels at Ba Tha station in 2019

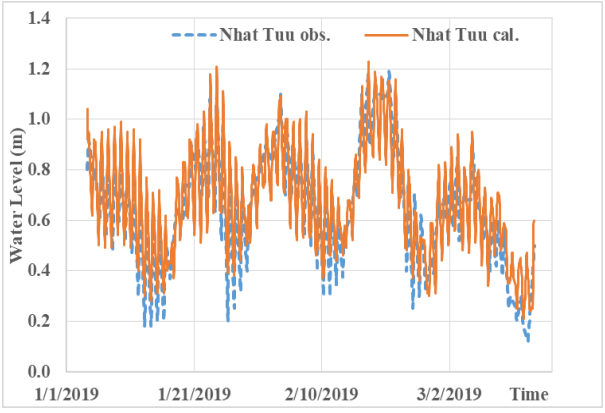

Fig 6: Calculated and measured water levels at Nhat Tuu station in 2019

Table 4: NSE index at some stations in 2019

Station	Ba Tha	Nhat Tuu	Luong Co
NSE	0.81	0.78	0.79

The comparisons between calculated and measured water levels in Figs 4 to 6 and table of NSE index hit a good accuracy, the numerical model are verified and ready to apply to simulate hydrodynamic in the area.

2.2. Water quality

It is estimated that the total amount of wastewater discharged into the Hanoi river system is approximately 850,000 m^3/day.

Due to limited measured water quality data, the average DO and BOD_5 values should only be used in some locations on the Nhue River such as Lien Mac, Phuc La, Cau To and Cu Da to calibration and verification.

a) Calibration

Same with hydraulics, 2014 data is used for calibration. The average Cals. and Obs. data are drawn on one graph with B1, B2 level, which are regulated in "National standard of water surface quality QCVN 08:2008/BTNMT", to accuracy water quality.

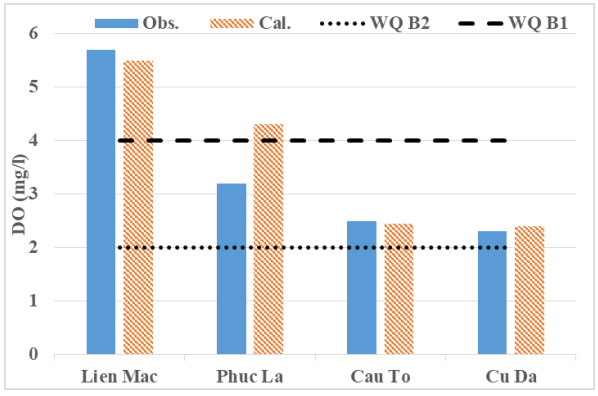

Fig 7: Calculated and measured DO values at some stations on Nhue river in 2014

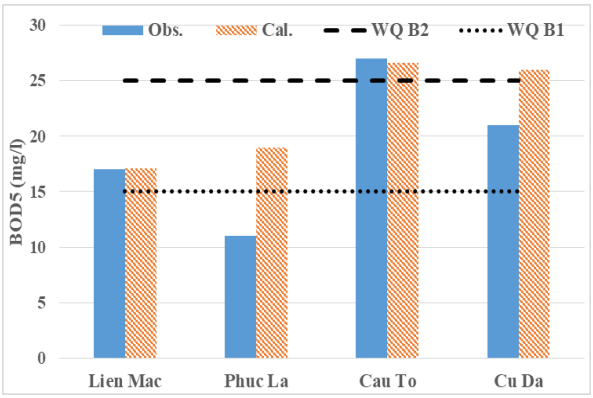

Fig 8: Calculated and measured BOD_5 values at some stations on Nhue river in 2014

Results show that calculated DO values are the same as measured values, and BOD_5 values are acceptable.

b) Verification

Several calculations using the measured data in 2016 and 2019 are carried out.

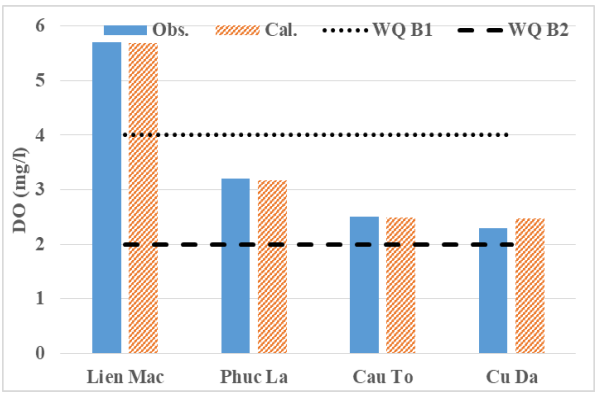

Fig 9: Calculated and measured DO values at some stations on Nhue river in 2016

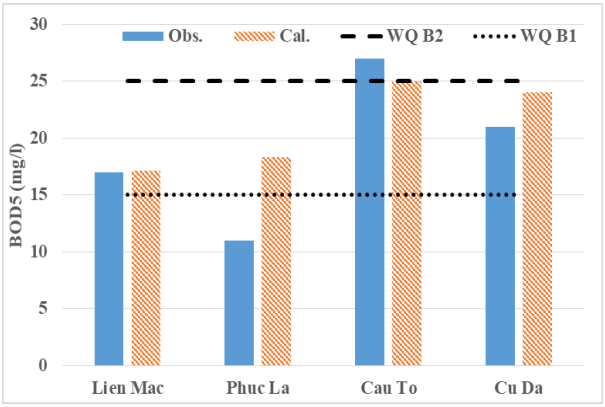

Fig 10: Calculated and measured BOD_5 values at some stations on Nhue river in 2016

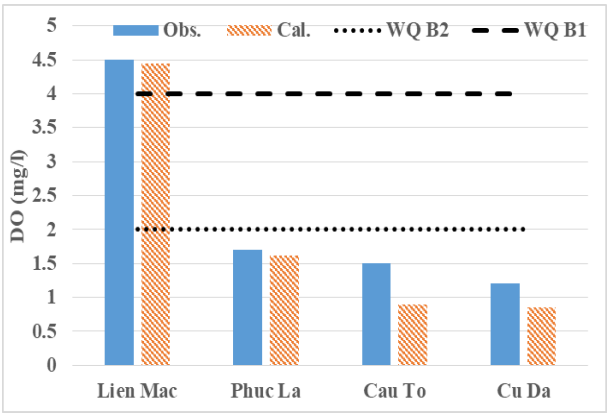

Fig 11: Calculated and measured BOD_5 values at some stations on Nhue river in 2019

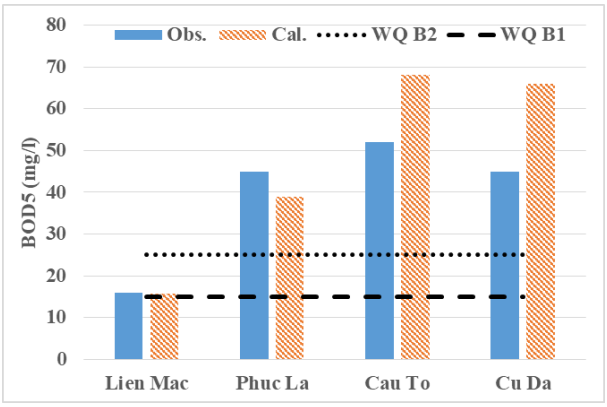

Fig 12: Calculated and measured BOD_5 values at some stations on Nhue river in 2019

The comparisons show that calculated water quality values in rainy season in 2016 are verified rather well because using the calibration parameters of same season in 2014. These parameters are used for dry season in 2019, DO values are good, but BOD_5 values are differences with measured values, explained by the sampling at the measurement points and distribution of waste sources between model and reality. However, overall, all calculated data are consistent in both values and trends with measured data, and ready to apply to simulate hydrodynamic and water quality in the area.

3. Calculation scenarios

In recent years, rivers in Hanoi are gradually becoming polluted, directly affecting the quality of agricultural products, food, environmental landscape, and people's health. Therefore, it is

required to treat pollution, restore river flows and improve the environment, proposed by scientists and managers.

Two calculation scenarios are carried out:

- Scenario 1: Take water from West Lake into the To Lich river with a discharge Q=1.8m^3/s (proposed by Hanoi Sewerage And Drainage Limited Company: Take water from the Red River into West Lake with 156,000 m^3/day, equivalent to 1.8m^3/s for washing West Lake, after that transferring all water flow to To Lich river).
- Scenario 2: Take water from the Red River through Lien Mac gate with a discharge Q=30m^3/s into Nhue river to improve the flow.

3.1. Scenario 1

a) Hydraulic

The comparison water level along the To Lich river between before and after taking water from West lake is shown in Fig 13.

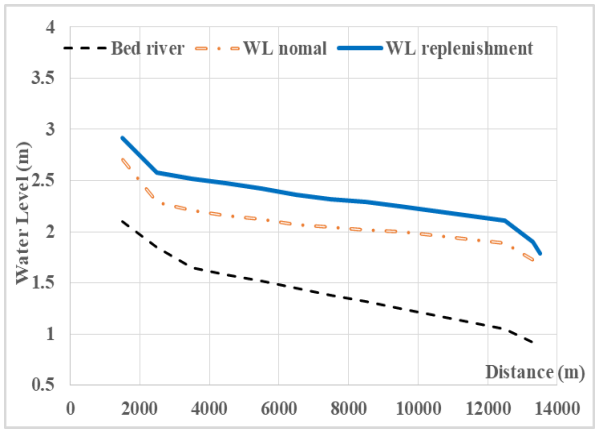

Fig 13: Water level along the To Lich river before and after taking water from West Lake.

After reaching a steady state, water level along the To Lich river increased significantly. The difference in water level is from 20 - 30 cm. The water level difference decreases further downstream.

The velocity also increases significantly. At the cross section STL_001, velocity of flow increased from 0.2 m/s to 0.4 m/s; at the cross section STL_008 (km8.5 from upstream), velocity of flow increased from 0.09 m/s to 0.18 m/s.

b) Water quality

Calculated values are compared with "National standard of water surface quality QCVN 08:2008/BTNMT" to assess pollution levels before and after taking water.

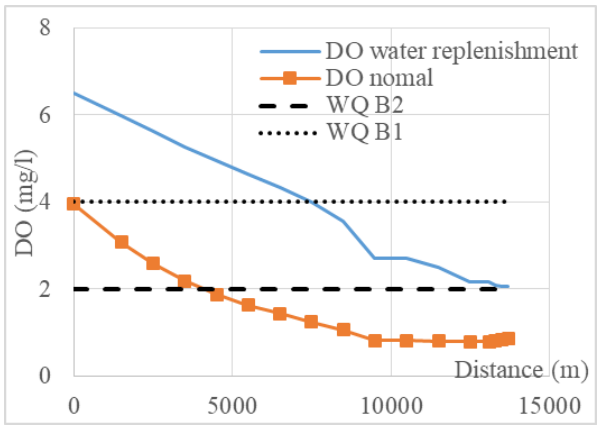

Fig 14: DO values along the To Lich river in scenario 1.

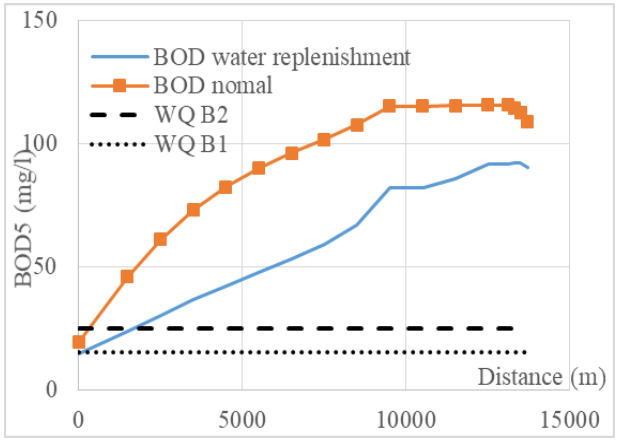

Fig 15: BOD_5 values along the To Lich river in scenario 1

In Fig. 14, DO values increased significantly. From Phan Dinh Phung gate (upstream) to km8, DO values still above the B1 level, and forward to B2 level at Thanh Liet gate.

With BOD_5 values always bigger than B2 level from 1 to 5 times, taking water is no significant effect. BOD_5 values above B1 level because clean water from West Lake, however, quickly forward to B2 level at km2 in Fig. 16.

By scenario 1, taking water contributes to unfreeze the river flow, reduces the BOD_5 values and increases the DO values. But, with only a

discharge Q = 1.8m^3/s into the upstream river, it has no significant effect, the majority of values are still above B2 level.

3.2. Scenario 2

a) Hydraulic

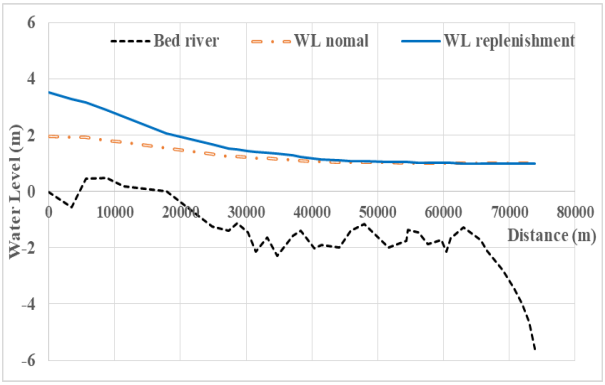

Fig 16: Water level along the Nhue river before and after taking water from Red river.

With a discharge Q=30m^3/s into Nhue river, water level increased significantly. Maximum difference of water level up to 2m at the upstream of the river. Water level at downstream also increased after long time to steady state, sample at wards of Phu Xuyen district, water level increased by 0.8m more than the average of the dry season.

After 60h from the beginning taking water, wards in Thanh Tri, Thanh Oai, Thuong Tin district can take water to canal in field. After 100h, Phu Tuc, Hoang Long, Quang Trung, Son Ha wards in Phu Xuyen district also can start taking water for agricultural production.

b) Water quality

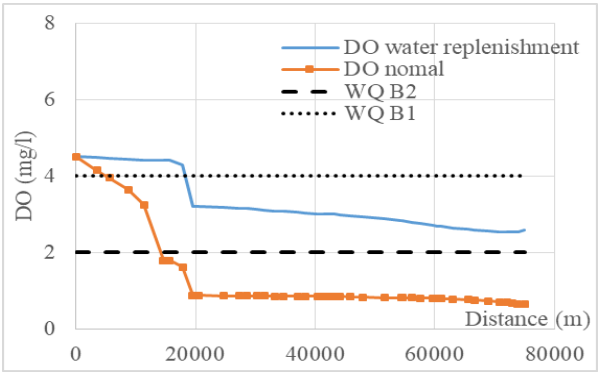

Fig 17: DO values along the Nhue river in scenario 2

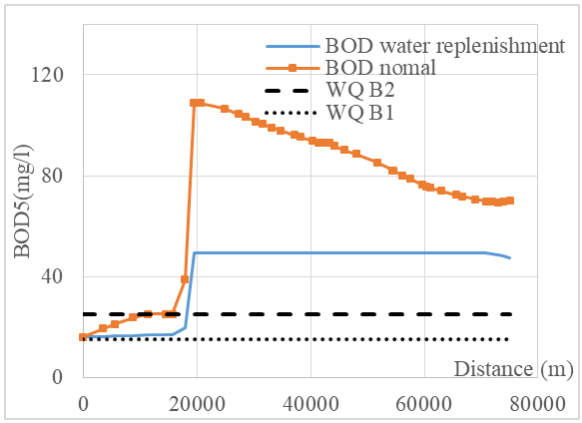

Fig 18: BOD_5 values along the Nhue river in scenario 2

Along the Nhue river, in dry season, DO values are relatively small, BOD_5 values are high. With a discharge Q=30m^3/s into upstream of Nhue river, DO values increased significantly, from 0.5mg/l to above 2.5 mg/l (fig. 17), BOD_5 values decreases significantly and keeping at level ~ 40mg/l from Cau To to downstream of Nhue river.

4. Conclusion

The 1D numerical model for calculating hydrodynamics and water quality has been established for river system in Hanoi. Model is calibrated and verified with the measured data in 2014, 2016 and 2019.

Two calculation scenarios are carried out, their results are shown that: although effective in changing hydraulic and water quality, it is not much, especially on To Lich river. Therefore, it is necessary to study other water replenishment plans as well as combine with other solutions: filter water with probiotics, collect and filter water by factory at downstream, limit discharge directly into the rivers, …

References

Hue Huu Nguyen and Thanh Huu Nguyen (2018), *Study on creation of water sources supplying the inner river system in Hanoi city with continuous flow for cleaning the aquatic environment*, MATEC Web of Conferences.

Institute of water resources planning (2007), *Water resources planning in the Nhue river system in 2007*, Report.

Ministry of Natural Resources and Environment (2012), *Report on the status of the national environment in 2012*, HaNoi.

Nguyen Chinh Kien, Dinh Van Manh and Hoang Van Lai (2014), *Evaluation of salinity intrusion in the Southwest coastal zone of Vietnam*, ICEMA3, HaNoi.

Nguyen Thi Nhu Quyen (2012), *Study status of the water environment for planning wastewater treatment system on the To Lich river - The section from Hoang Quoc Viet to Nga Tu So*, Master thesis.

Lương Duy Hanh et al. (2016), Assessing the surface water quality related to odor problem of some rivers in Ha Noi inner city, *Viet Nam university Ha Noi Journal of Science: Earth and Environmental Sciences*, volume 32, 1S, pp. 147-155.

Vu Thi Phuong Thao (2014), Assessing water quality of Nhue river from headwaters to Cau Chiec, *Journal of Marine Science and Technology*, volume 14, 3, pp. 280-288.

Website: https://vanban.hanoi.gov.vn

The 5th International Conference on Engineering Mechanics and Automation (ICEMA 5)
Hanoi, October 11÷12, 2019

Application of Capacitance-Resistance Model for Predicting Performace of Oil Wells in a Waterflood Reservoir

Nguyen The Duc[a], Phan Ngoc Trung[b], Nguyen Van Tuan[c], Dang The Ba[d], Le Trung Dung[d], Nguyen Quang Thai[e], Nguyen Van Tung[e], Nguyen Hong Phan[e]

[a] *Vietnam Petroleum Institute*
[b] *Vietnam Oil and Gas Group*
[c] *Thainguyen University of Technology*
[d] *University of Engineering and Technology, Vietnam National University*
[e] *Institute of Mechanics, Vietnam Academy of Science and Technology*

Abstract

Numerical reservoir simulation is a valuable tool for the design, evaluation and operation of oil wells in hydrocarbon fields. However, such grid-based reservoir models are complex, time consuming to build, yet uncertain and ussualy developed based on limited information. Generally, production predictions by reservoir simulation models doesn't provide reliable results in case of there is a lot of uncertainty about model inputs and parameters, for example in the case of the fractured basement reservoir popular in Vietnam. In these cases, the use of alternative models based on the field's production history data to reliably quantify inter-well connectivity and support well control decisions is preferred.

The Capacitance-Resistance Model (CRM), one type of data-driven models, has proved to be effective for making well production optimisation decisions in waterflooded reservoirs. The research presented here has developed a production prediction tool for oil wells using a CRM model. Developed tools are applied to predicting performace of oil wells in a large waterflood reservoir in Vietnam. Application results show that predition results of CRM models are in good agreement with measurements.

Key Words: Numerical Simulation, Capacitance-Resistance Model, Waterflood Reservoir

1. Introduction

The main goal of any reservoir management strategy is to increase the value of the reservoir asset by producing oil in an economically efficient manner. During primary production, producers are placed in locations that should maximize oil production while minimizing the cost of well construction. Secondary production usually involves a water flood, where decisions of where to place the injectors and how much water to inject must also balance costs of injection and well construction vs. the expected value of the additional oil produced. Whether the engineer is able to achieve the goal of increased reservoir performance depends mainly on the ability to accurately model past reservoir behavior and to use this model to forecast future behavior.

Currently engineers typically use numerical simulations to inform management decisions for

these reservoirs. These models divide the reservoir into many grid blocks and impose discretized material balance equations to account for the fluid flow into and out of each cell. A geologic model is required to define the physical properties of the reservoir, such as rock permeability, porosity, and compressibility. Fluid properties of both the oil and water phases at reservoir pressures must also be properly defined a priori. One disadvantage of using numerical simulations is that they can becomputationally intensive, some simulations requiring hours of computation time. Also, because the geologic model must be specified before simulation and future prediction, significant research and testing must be conducted to find values for the geologic properties that lead to an acceptable history match of past production data. History matching in this manner can take months to find an acceptable numerical model.

The disadvantages of numerical simulation models indicate the need for alternative types of modeling for production prediction work in many cases. The most widely used alternative model today is the capacitance-resistance model (CRM). The CRM Model is one type of data-driven models. The study of CRM model has been done by many authors, e.g. Albertoni and Lake (2003), Gentil (2005), Yousef et al. (2006), Sayarpour (2008) and Liang et al. (2007). In these studies, CRhas proved to be effective for making well production optimisation decisions in waterflooded reservoirs.The research presented here has developed a production prediction tool for oil wells using a CRM model. Developed tools are applied to predicting performace of oil wells in a large waterflood reservoir in Vietnam. Application results show that predition results of CRM models are in good agreement with measurements.

2. Description of prediction model

2.1. Capacitance-Resistance Model Background

The capacitance-resistance model (CRM) is an input-output model that characterizes a reservoir using only data available at the wells. It represents a significant departure from traditional reservoir models that require estimation of reservoir properties in each grid block. In the CRM, the input signal (injection rates) is converted to an output signal (total production rates) in a similar manner as electronic potential is converted to voltage or current in a resistor-capacitor (RC) circuit (Thompson, 2006), hence the name capacitance-resistance model.

The model requires estimation of two types of model parameters – connectivities (or gains) and time constants. Simple linear models comprised of gains and time constants are frequently used in process control. The gains represent connections between wells and measure the effects of permeability and porosity of the reservoir as well as fluid properties. The time constants allow for attenuation of the injection signal and reflect the effects of reservoir compressibility, pore volume, and the productivity index of a producing well.

Model parameters are calculated via multivariate nonlinear regression onto historic injection and production rate data. A priori estimation of physical reservoir properties is not required. However, history matching of the model to historic data provides valuable information about the reservoir. The CRM has some different forms, depending on the control volume selected. Two forms of CRM are studied in this presented research: CRMT (Representing the entire field as a single control volume) and CRMP (Multiple control volumes for the drainage volume around each production well).

2.2. CRM Model with Single Tank Representation of the Reservoir (CRMT)

In the CRMT representation, the control volume for the governing continuity equations is the drainage volume of the entire reservoir. Summing the rates of the all the production wells into a single pseudo-producer and the rates of all the injection wells into a single pseudo-injector allows the representation of the reservoir as a single tank with one inlet rate and one outlet rate. This construction is presented schematically in Figure 1.

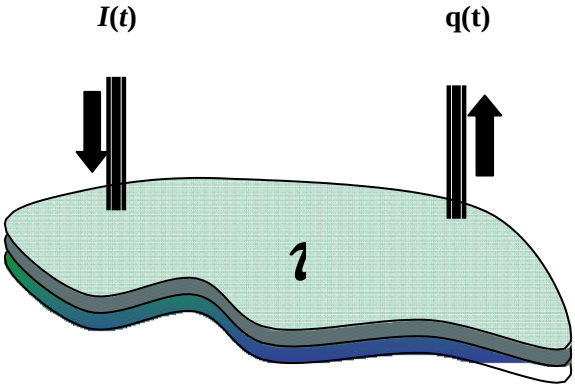

Figure 1. Schematic representation of a reservoir with one injector and one producer used by the CRMT

A material balance or continuity equation mathematically accounts for the total fluid entering into, exiting from and accumulating in a given control volume. The continuity equation governing a reservoir with one injector and one producer is given in Sayarpour (2008) as

$$C_t V_p \frac{d\bar{p}(t)}{dt} = I(t) - q(t) \quad (1)$$

where c_t is the total compressibility of the reservoir [1/pressure] , V_p is the pore volume of the reservoir [volume], $\bar{p}(t)$ is the average pressure in the reservoir at time *t* [pressure], *I(t)* is the injection rate of the pseudo-injector at time *t* [volume/time], *q(t)* is the total fluid production rate of the pseudo-producer at time *t* [volume/time]

The total fluid production rate *q(t)* can also be defined in terms of the productivity index, J, (Walsh and Lake, 2003)

$$q(t) = J(\bar{p}(t) - p_{wf}(t)) \quad (2)$$

where $p_{wf}(t)$ is the bottom-hole pressure (BHP) of the pseudo-production well at time *t* [pressure].

Substituting (2) into (1) to eliminate the average reservoir pressure, $\bar{p}$, gives the following continuity equation in terms of total fluid production rate

$$q(t) = I(t) - \frac{c_t V_p}{J}\frac{dp(t)}{dt} - c_t V_p \frac{dp_{wf}(t)}{dt} \quad (3)$$

Assuming that part of the total field injection may either be lost from the reservoir (not contributing to total fluid production) or be supplemented by injection outside of the control volume (as an aquifer may drive production), one may modify the total injection rate *I* by the factor *f*, which leads to the effective injection rate, *fI*(*t*), in the material balance

$$q(t) = fI(t) - \frac{c_t V_p}{J}\frac{dq(t)}{dt} - c_t V_p \frac{dp_{wf}(t)}{dt} \quad (4)$$

The physical meaning of the gain *f* is the fraction of injection *I* that contributes to total fluid production in the reservoir. Further, the time constant for the control volume, , is defined as

$$\tau = \frac{c_t V_p}{J} \quad (5)$$

This leads to the continuity equation

$$q(t) = fI(t) - \tau\frac{dp(t)}{dt} - J\tau\frac{dp_{wf}(t)}{dt} \quad (6)$$

Integrating (6) over a discrete time interval ⊿t and assuming that injection rates are constant over the interval and bottom-hole pressures vary linearly gives the following analytical solution for the total field production rate in time period *k*

$$q_k = q_{(k-1)}e^{-\Delta t/\tau} + (1 - e^{-\Delta t/\tau})(fI_k - J\tau\frac{p_{wf}^{(k)} - p_{wf}^{(k-1)}}{\Delta t}) \quad (7)$$

The construction of the CRM as a single tank leads to a model with three parameters: a gain, *f*, a time constant, τ , and the productivity index, *J*. These parameters reflect the average effect of properties of the entire reservoir. If bottom-hole pressure data are unavailable (as is sometimes the case), *pwf* is assumed to be constant over the history of the reservoir, giving a simpler equation for total field production rate

$$q_k = q_{(k-1)} e^{-\Delta t/\tau} + (1 - e^{-\Delta t/\tau}) f I_k \quad (8)$$

Sayarpour (2008) showed that these equations (7 and 8) satisfy superposition in time, i.e. that one can substitute the value of the previous period's production (q( ) k-1) with the equation for that time period to arrive at an equation that is only dependent on the initial production rate and the injection rates for each time period.

Model parameters (the gain and time constant) are estimated using nonlinear regression. This involves the formulation of a nonlinear program (NLP) with the following objective function:

$$\min z = \sum_{k=1}^{n_t} (\sum_{j=1}^{n_p} q_{jk}^{obs} - q_k)^2 \quad (9)$$

where q_{jk}^{obs} is the total observed production rate of producer j at time step k, q_k is the calculated total production rate of the field at time step k as defined by either (7) or (8), n_p is the total number of producers, n_t is the total number of historic time periods.

The gain and time constant are simply constrained to be positive. A gain less than one means that part of the total field injection is lost in the reservoir or does not contribute to total field production. Calculating a gain greater than one indicates additional support for total field production, either from an aquifer or from injection outside the field.

The CRMT is used as a quick and simple method to characterize the behavior of the reservoir as a whole. There are only two parameters and the values found by solving the NLP above can be used as initial values for the subsequent, more complicated CRM's. While this simple reservoir description has been shown to be quite accurate (Sayarpour, 2008), typical hydrocarbon reservoirs benefit from a more complex treatment.

2.3. CRM Model with Producer-Based Representation of the Reservoir (CRMP)

Constructing the control volume as the drainage volume around a given producer leads to the schematic representation in Figure 2. Liang et al. (2006) characterizes the time-dependent effects of injection wells on production wells using connectivities (or gains) and time constants for each input-output pair using the following continuity equation for the total (oil and water) production rate of a given production well:

$$q_j(t) = \sum_{i=1}^{n_i} f_{ij} I_i(t) - \tau_j \frac{dq_j(t)}{dt} - J_j \tau_j \frac{dp_{wf}^{(j)}(t)}{dt} \quad (10)$$

where $q_j(t)$ is the total production rate (oil plus water) of producer j at time t [volume/time], $I_i(t)$ is the injection rate of injector i at time t [volume/time], f_{ij} is the connectivity (gain) between injector i and producer j [dimensionless], τ_j is the time constant associated with the drainage volume around producer j [time], J_j is the productivity index associated with producer j [volume/(time pressure)], n_i is the total number of injectors

Physically, the gain f_{ij} represents the steady-state fraction of water injected in injector i that contributes to production of both oil and water in producer j.

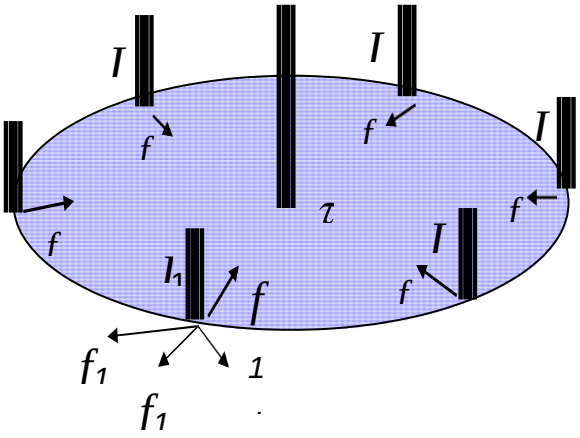

Figure 2. Schematic representation of a drainage volume around a single producer used in the CRMP.

Following Sayarpour (2008) and integrating (10) over a discrete time period, Δt , over which the injection rates of all injectors are assumed constant, and the producer

bottom-hole pressure is assumed to vary linearly, and assuming a known initial production rate for all producers, $q_{j(k-1)}$, gives the following analytical solution for the production rate in time period *k*:

$$q_{ij} = q_{j(k-1)} e^{-\Delta t/\tau_j} + (1 - e^{-\Delta t/\tau_j})\left(\sum_{i=1}^{n_j} f_{ij} I_{ik} - J_j \tau_j \frac{p_{wf}^{(jk)} - p_{wf}^{(j(k-1))}}{\Delta t}\right) \quad (11)$$

This shows that the current total production rate of producer *j* is a weighted average of the previous production rate and the combined effect of the current rate of arrival of water at that producer from all injectors and the bottom-hole pressure change at the well. The weights are the exponential terms, both positive and summing to one.

In the absence of bottom-hole pressure data, *pwf* is assumed to be constant and that term of the model disappears giving the more simple equation

$$q_{ij} = q_{j(k-1)} e^{-\Delta t/\tau_j} + \left(1 - e^{-\Delta t/\tau_j}\right)\sum_{i=1}^{n_j} f_{ij} I_{ik} \quad (12)$$

As with the CRMT, these equations (11 and 12) satisfy superposition in time (Sayarpour, 2008).

The CRMP still exploits the fact that detailed data regarding the state of the reservoir fluid is available only at the wells, since there are no measurements of subsurface variables. The number of parameters, though greater than with the CRMT, is drastically reduced compared to a traditional reservoir simulator, although there are tens of thousands of gains in a field with hundreds of producers and injectors. The fraction of water injected in a given well that will flow to a given production well is modeled as a gain between the two wells. Similarly, the time constant for the producer depends on the compressibility of the fluid and corresponds to the time it takes for the production rate to reach 63% of its ultimate response to a change in injection rate (as in process control step testing). The model can be fitted for a selected time horizon to actual field data or using model predictions from a traditional reservoir simulator.

Model parameters (the gains and time constants) are again estimated using multivariable nonlinear regression. The required objective function is slightly different than that used for the CRMT:

$$\min z = \sum_{k=1}^{n_t} \sum_{j=1}^{n_p} (q_{jk}^{obs} - q_{jk})^2 \quad (13)$$

where q_{jk} is the calculated total production rate of producer *j* at time step *k* as defined by either (11) or (12). This objective function is constrained by (11) or (12) as well as the following additional constraints:

$$\sum_{j=1}^{n_p} f_{ij} < 1 \text{ for all } i \quad (14)$$

$$f_{ij}, \tau_j \geq 0 \text{ for all } i \text{ and } j \quad (15)$$

The constraint (14) represents a material balance on the injected fluid allowing for a loss of water injected within the control volume when the sum of gains is less than one. Since the gains in (14) are summed over the producer index *j*, the application of this constraint requires solving for the model parameters for all producers at the same time.

3. Application to a Real Field in Vietnam

3.1. Production data and CRM models

Basement formation of Bach Ho field has produced commercially since 1988. Base on the welltests results of production wells (2, 401, 401, 417) which were the first exploration, appraisal, and production wells, initial reservoir pressure was 417 atm at 3650 mTVDss. In the first production stage, reservoir drive mechanisms were rock or compaction drive and solution gas without water drive and water injection supply, after several years of production reservoir pressure decreased significantly to 280 atm. Pressure maintenance by water injection was initiated in 1993 when a number of production wells were converted to

injection wells and connected with the water injection system.

To test the accuracy of CEM model's prediction, the daily measurement data of the Bach Ho field was collected. Data was collected over a period of more than 15 years. These daily measurements of injector water rate and producer liquid rate are used to contruct and test the CRMT and CRMP models. Data of the first twelve (12) years are used for constructing models. The remain data (of the last three years) are used for testing models.

3.2. Results and Discussions

In the first step of application, the CRMT model is constructed from the measurement data of total injection water rate and the total production liquid rate of the whole field over the first 12 years.

Figure 3 shows the comparison between the calculation results of the CRMT model and the measurement data used in constructing the model. The comparison between the calculation results of the CRMT model and the measurement data used in testing are presented in Figure 4. The figures show a good agreement between calculations and measurement.

Another way to evaluate the agreement is to calculate the correlation coefficient. The correlation coefficient is a statistical measure that calculates the strength of the relationship between the relative movements of two variables. The correlation coeficient in this case is equal to 0.981 for constructing data and equal to 0.812 for testing data.

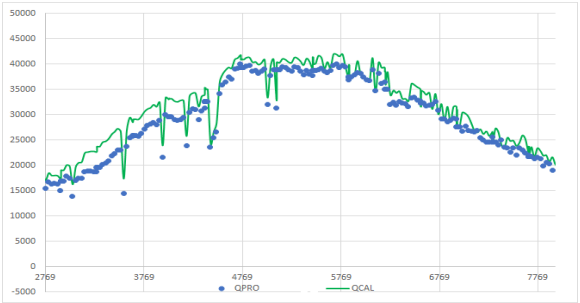

Figure 3. Comparison between the calculation results of the CRMT model and the measurement data used in constructing the model.

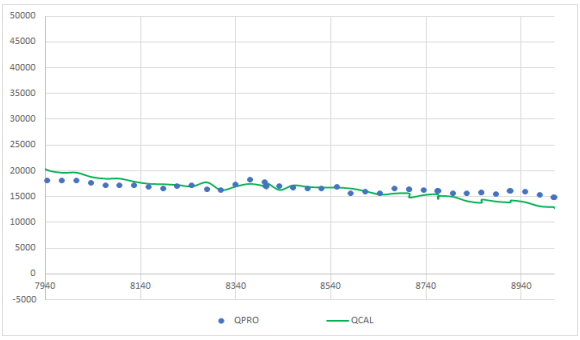

Figure 4. Comparison between the calculation results of the CRMT model and the measurement data used in testing the model.

In the second step of application, the CRMP model is constructed from the measurement data of injectors' water rates and the producers' liquid rates over the first 12 years. Due to the large number of producers, only the results of the two wells with the longest production periods are presented here.

Figure 5 shows the comparison between the calculation results of the CRMP model and the measurement data used in constructing the model for well P1. The comparison between the calculation results of the CRMT model and the measurement data used in testing for well P1 are presented in Figure 6. The figures also show a good agreement between calculations and measurement. The correlation coeficient in this case is equal to 0.920 for constructing data and equal to 0.706 for testing data.

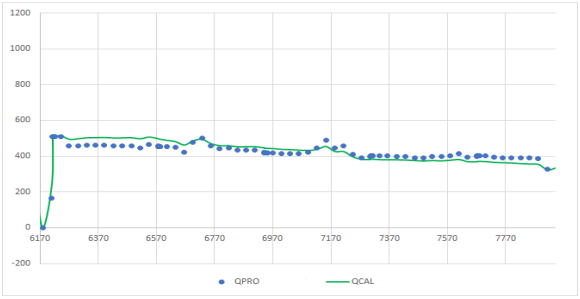

Figure 5. Comparison between the calculation results of the CRMP model and the measurement data of well P1 used in constructing the model.

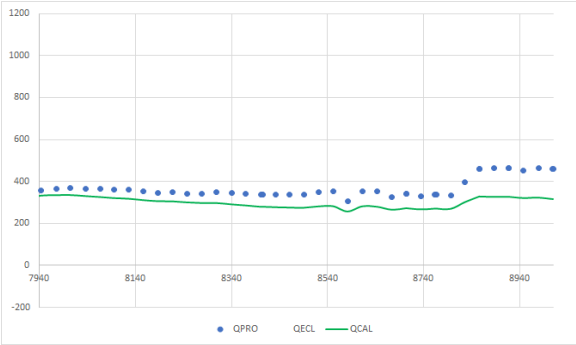

Figure 6. Comparison between the calculation results of the CRMP model and the measurement data of well P1 used in testing the model.

For another well, Figure 7 shows the comparison between the calculation results of the CRMP model and the measurement data used in constructing the model for well P2. The comparison between the calculation results of the CRMT model and the measurement data used in testing for well P2 are presented in Figure 8. The figures also show a good agreement between calculations and measurement. The correlation coeficient in this case is equal to 0.855 for constructing data and equal to 0.909 for testing data.

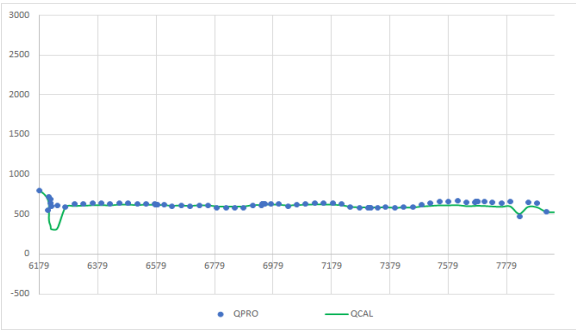

Figure 7. Comparison between the calculation results of the CRMP model and the measurement data of well P2 used in constructing the model.

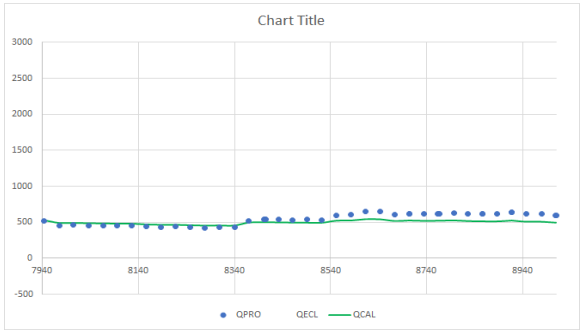

Figure 8. Comparison between the calculation results of the CRMP model and the measurement data of well P2 used in testing the model.

4. Conclusion

The research presented here has developed production prediction tools for oil wells using a CRMT and CRMP models. Developed tools are applied to predicting performace of oil wells in a large waterflood reservoir in Vietnam. Application results show that predition results of CRM models are in quite good agreement with measurements. These reasonable prediction results have been obtained with a short computation time. The results show the applicability of the CRM model to reservoir management in real time.

Acknowledgement

This research was partially supported by a research program of the Vietnamese Ministry of Industry and Trade. The research project name is “Study of production prediction and water injection optimization for the mature oil and gas fields using combination of some artificial intelligence algorithms”

References

Albertoni, A. and Lake, L. W. (2003). Inferring Connectivity Only From Well-Rate Fluctuations in Waterfloods. *SPE Reservoir Evaluation and Engineering Journal*, 6 (1): pp. 6-16.

Gentil, P. H. (2005). *The Use of Multilinear Regression Models in Patterned Waterfloods: Physical Meaning of the Regression Coefficients*. M.S. Thesis, The University of Texas at Austin, Austin, Texas.

Liang, X., Weber, D.B., Edgar, T.F., Lake, L.W., Sayarpour, M. and Yousef, A.A. (2007). Optimization of Oil Production Based on a Capacitance Model of Production and Injection Rates. *Paper SPE 107713, presented at the 2007 SPE Hydrocarbon Economics and Evaluation Symposium, Dallas, TX, 1-3 April*.

Sayarpour, M. (2008). *Development and Application of Capacitance-Resistive Models in Water/CO2 Floods*, Ph.D. Dissertation. The University of Texas at Austin, Austin, Texas.

Thompson, M. (2006). Intuitive Analog Circuit Design. *Elsevier e-Book*, Ch. 2, p. 16.

Yousef, A.A., Gentil, P.H., Jensen, J.L. and Lake, L.W. (2006). A Capacitance Model to Infer Interwell Connectivity from Production and Injection Rate Fluctuations. *SPEREE*, 9 (5): pp. 630-646.

The 5th International Conference on Engineering Mechanics and Automation (ICEMA 5)
Hanoi, October 11÷12, 2019

Influence of the water velocity on a remotely operated vehicle motion

Nguyen The Luc[a], Nguyen Van Tung[b], Tran Thu Ha[c], Nguyen Thai Dung[d]

[a] *Le Quy Don Technical University, 236 Hoang Quoc Viet, Hanoi, Nguyenthelucnavy@gmail.com*
[b] *Institute of Mechanics – 264 Doi Can, VAST 18 Hoang Quoc Viet, Hanoi, Tungnv92@gmail.com*
[c] *Institute of Mechanics – 264 Doi Can, VAST 18 Hoang Quoc Viet, Hanoi, ttha@imech.vast.vn*
[d] *Le Quy Don Technical University, 236 Hoang Quoc Viet, Hanoi, thaidung1966@gmail.com*

Abstract

On the imperfect water entry, a remotely operated vehicle (ROV) moves in the forward direction. The ROV motion makes turbulence in water flow. The water velocity and pressure fields make reaction to ROV motion. In this paper, the coupling simulation model is a combination of two-sub models: In the first sub-model, the motion of ROV considering the water velocity is calculated. The equation system of this sub-model is solved by Runge-Kutta method; In the second sub-model, the water flow and pressure fields under the ROV motion are simulated by CFD model. Using this couple model the effect of water velocity on the motion of ROV is studied.

Key Words: underwater vehicle, water velocity, hydrodynamic motion, water flow, coupling model

1. Introduction

The exploration of oceanic resources and protection of marine environment are important for humankind to develop sustainably. To help people discover and explore the ocean, study of remotely operated vehicles is developed.

In this paper we will study ROV motion made by controlled propeller forces from two thrusters with the effect of operating water velocity and turbulence flow. The ROV is consisted of 4 parts: a main body, two lights, two thrusters and two balance blocks. The main body's shape is considered as an elongated spheroid with major diameter L and minor diameter D (see figure 1). The mathematic model of ROV running with a velocity less than 10 m/s under water is the combination of two equation sub-systems.

1. The first equation sub-system expresses ROV motion. This sub-system is solved by Runge-Kutta method. In order to simplify the challenges of calculating progress, some assumptions can be applied in this model:

- ROV is deeply submerged in a homogeneous, unbound fluid. The effect of surface waves, walls and bottom can be ignored;

- ROV is rigid with the constant mass;

- ROV has 2 symmetric planes: port-starboard plane, fore-aft plane;

- The linear and angular couple terms in damping are neglected;

- The damping terms with orders greater than second are neglected;

2. The second equation sub-system describes the state of water flow under reaction of the ROV motion. In the viscous flow model, the Navier-Stockes equation is solved. The equations are solved to describe the turbulence term in Navier-

Stockes equation. This equation system is solved by CFD model. The getting result set is the pressure fluctuation and velocity fields of fluid.

In this paper, two of those equation sub-systems are connected by influences of water and ROV velocities in the motion equation and the boundary condition.

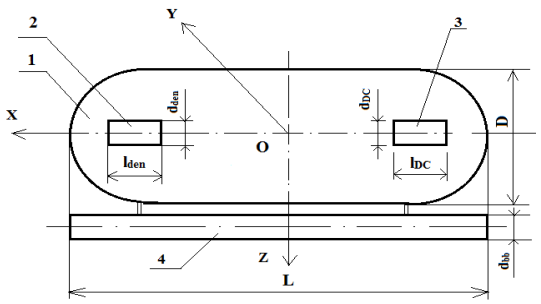

Figure 1. ROV model

1. Main body; 2. Light; 3. Thruster; 4. Balance block

- L, D are the length and diameter of the ROV respectively;

- l_{den}, d_{den} are the length and diameter of two lights respectively;

- l_{DC}, d_{DC} are the length and diameter of two thrusters respectively;

- L, d_{bb} are the length and diameter of two balance blocks respectively;

2. Theoretical formulation

The mathematical model is the combination of the following two sub-models:

- Mathematical sub-model calculating the ROV motion: the ROV velocities are solved by this model considering the water velocity in the dynamic equation.

- The sub-model simulating flow velocity and pressure field: the water flow velocity and pressure field are solved by this model applying the ROV velocities at the ROV gravity center.

2.1. Mathematical sub-model calculated the ROV motion

To describe the ROV motion, a body-fixed coordinate system shown in figure 2 is chosen. (X_0,Y_0, Z_0) is the inertial reference frame with the origin at O_0 and (X, Y, Z) is the non-inertial reference frame with the origin O at the body center of gravity.

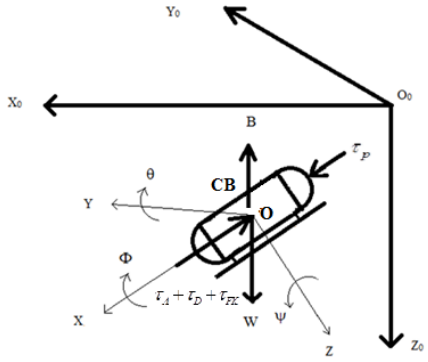

Figure 2. Earth-fixed and body-fixed reference frame

Denote $\eta_1 = [x, y, z]^T, \eta_2 = [\phi, \theta, \psi]^T$ the position and orientation of the ROV with respect to the inertial or earth-fixed reference frame;

$\tau_1 = [X, Y, Z]^T, \tau_2 = [K, M, N]^T$ the total forces and moments acting on the ROV with respect to the body-fixed reference frame. The ROV velocity in the body-fixed frame is $V = [v_1, v_2] = [u, v, w, p, q, r]^T$

with $v_1 = [u, v, w]^T$, $v_2 = [p, q, r]^T$ are the translational and rotational velocities of the ROV with respect to the body-fixed reference frame. The description can be seen in figure 2 for a diagram of the body coordinate system.

The following coordinate transform relates translational velocities between body-fixed and inertia or earth coordinate (Fossen, 2011) and (Khang, 2007)

$$\begin{bmatrix} \dot{x} \\ \dot{y} \\ \dot{z} \end{bmatrix} = J_1(\eta_2) \begin{bmatrix} u \\ v \\ w \end{bmatrix} \quad (1)$$

with $J_1(\eta_2) = \begin{bmatrix} c\psi c\theta & -s\psi c\phi + c\psi s\theta s\phi & s\psi s\phi + c\psi s\theta c\phi \\ s\psi c\theta & -c\psi c\phi + s\psi s\theta s\phi & -c\psi s\phi + s\psi s\theta c\phi \\ s\theta & c\theta s\phi & c\theta c\phi \end{bmatrix}$

Where: $s = \sin, c = \cos$

Note that $J_1(\eta_2)$ is orthogonal $(J_1(\eta_2))^{-1} = (J_1(\eta_2))^T$

The second coordinate transform relates rotational velocities between body-fixed and earth fixed coordinates:

$$\begin{bmatrix} \dot{\phi} \\ \dot{\theta} \\ \dot{\psi} \end{bmatrix} = J_2(\eta_2) \begin{bmatrix} p \\ q \\ r \end{bmatrix} \quad (2)$$

where: $J_2(\eta_2)=\begin{bmatrix}1 & \sin\phi\tan\theta & \cos\phi\tan\theta\\ 0 & \cos\phi & -\sin\phi\\ 0 & \sin\phi/\cos\theta & \cos\phi\cos\theta\end{bmatrix}$

The velocity of the body relative to the water current, which expressed in the body reference frame, is defined as $V_r=\left[V_{r_1},V_{r_2}\right]^T=V-V_{water}$

where: $V_{r_1}=\left[u_r,v_r,w_r\right]^T, V_{r_2}=\left[p_r,q_r,r_r\right]^T$ and

$$V_{water}=\left[u_l,v_l,w_l,0,0,0\right]^T \qquad (3)$$

The mathematic model is used to describe the motion of the ROV (Khalid Isa, M.R. Arshad, Syafizal Ishak, 2014). The motion of ROV in both phases is written by the following equations:

$$M_{RB}\dot{V}+C_{RB}(V)V=\tau \qquad (4)$$

where: M_{RB} is the generalized mass matrix of the ROV. M_{RB} is given by:

$$M_{RB}=\begin{bmatrix}m & 0 & 0 & 0 & mz_G & -my_G\\ 0 & m & 0 & -mz_G & 0 & mx_G\\ 0 & 0 & m & my_G & -mx_G & 0\\ 0 & -mz_G & my_G & I_{xx} & I_{xy} & I_{xz}\\ mz_G & 0 & -mx_G & I_{yx} & I_{yy} & I_{yz}\\ -my_G & mx_G & 0 & I_{zx} & I_{zy} & I_{zz}\end{bmatrix}$$

Where:

m is the body mass in the air, $I_{xx},I_{yy},I_{zz},I_{xy},I_{yx},I_{yz},I_{zy},I_{xz},I_{zx}$ are the terms represented the initial tensors with respect to center of gravity. As the products of inertial I_{xy},I_{xz},I_{yz} are small compared to the moments of inertia I_{xx},I_{yy},I_{zz}, we assume that they are zero, in effect assuming that the body has two axial planes of symmetry. x_b,y_b,z_b represent the buoyancy center of the ROV comparing with the origin coordinate, x_G,y_G,z_G represent the center of gravity of the ROV. C_{RB} is the Coriolis and central force matrix (Khalid Isa, M.R. Arshad, Syafizal Ishak, 2014):

$$C_{RB}(V)=\begin{bmatrix}0 & -mr & mq & m(y_Gq+z_Gr) & -mx_Gq & -mx_Gr\\ mr & 0 & -mp & -my_Gp & m(z_Gr+x_Gp) & -my_Gr\\ -mq & mp & 0 & -mz_Gp & -mz_Gq & m(x_Gp+y_Gq)\\ -m(y_Gq+z_Gr) & my_Gp & mz_Gp & 0 & I_{zx}p+I_{zy}q+I_{zz}r & -I_{yx}p-I_{yy}q-I_{zy}r\\ mx_Gu & -m(z_Gr+x_Gp) & mz_Gq & -I_{zx}p-I_{zy}q-I_{zz}r & 0 & I_{xx}p+I_{xy}q+I_{xz}r\\ mx_Gr & my_Gr & -m(x_Gp+y_Gq) & I_{yx}p+I_{yy}q+I_{yz}r & -I_{xx}p-I_{xy}q-I_{xz}r & 0\end{bmatrix}$$

τ is the total forces and moments acting on the ROV.

$$\tau=\left[\tau_1,\tau_2\right]^T=\tau_{HS}+\tau_A+\tau_D+\tau_{FK}+\tau_p \qquad (5)$$

where τ_{HS} is the sum of the restoring forces and moments; τ_D is the damping forces and moments, τ_A is the added mass forces and moments, τ_{FK} the Froude-Kriloff forces, τ_p is the thruster force from propellers.

τ_{HS} is given by (Xiao Liang, Yongjie Pang, Lei Wan and Bo Wang, 2008):

$$\tau_{HS}=\begin{bmatrix}-(W-B)\sin\theta\\ (W-B)\cos\theta\sin\phi\\ (W-B)\cos\theta\cos\phi\\ (y_GW-y_BB)\cos\theta\cos\phi-(z_GW-z_BB)\cos\theta\sin\phi\\ -(z_GW-z_BB)\sin\theta-(x_GW-x_BB)\cos\theta\cos\phi\\ (x_GW-x_BB)\cos\theta\sin\phi-(y_GW-y_BB)\sin\theta\end{bmatrix} \qquad (6)$$

here: $W=m.g$, $B=\nabla\rho g$; g is the gravitational acceleration; ∇ is the ROV volume; m is the body mass; ρ is the water density; x_b,y_b,z_b and x_G,y_G,z_G are the center of buoyancy and the center of gravity with respect to origin coordinate respectively;

The added mass forces are obtained due to the inertia of the surrounding fluid, which depends on the acceleration of the body with respect to water. Generally, the formulation of the added mass forces is similar to the formulation of the rigid-body system inertia matrix M_{RB} and the Coriolis-centripetal matrix $C_{RB}(V)$. Hence the added mass forces can be expressed as: (Khalid Isa, M.R. Arshad, Syafizal Ishak, 2014)

$$\tau_A = -\left(M_A.\dot{V}_r + C_A\left(V_r\right).V_r\right) \qquad (7)$$

With M_A and $C_A\left(V_r\right)$ are the added mass and Coriolis-like matrix induced by M_A respectively. Because ROV has 2 symmetric planes: port-starboard plane, fore-aft plane and the center of origin is placing in at the center of mass then the added mass matrix M_A is (Fossen, 2011, p. 172):

$$M_A = -\begin{bmatrix} X_{\dot{u}} & 0 & 0 & 0 & X_{\dot{q}} & 0 \\ 0 & Y_{\dot{v}} & 0 & Y_{\dot{p}} & 0 & 0 \\ 0 & 0 & Z_{\dot{w}} & 0 & 0 & 0 \\ 0 & K_{\dot{v}} & 0 & K_{\dot{p}} & 0 & 0 \\ M_{\dot{u}} & 0 & 0 & 0 & M_{\dot{q}} & 0 \\ 0 & 0 & 0 & 0 & 0 & N_{\dot{r}} \end{bmatrix} \qquad (8)$$

or

$$M_A = \begin{bmatrix} m_{11} & 0 & 0 & 0 & m_{15} & 0 \\ 0 & m_{22} & 0 & m_{24} & 0 & 0 \\ 0 & 0 & m_{33} & 0 & 0 & 0 \\ 0 & m_{42} & 0 & m_{44} & 0 & 0 \\ m_{51} & 0 & 0 & 0 & m_{55} & 0 \\ 0 & 0 & 0 & 0 & 0 & m_{66} \end{bmatrix} \qquad (9)$$

where m_{ij} terms are the ROV added mass and $m_{ij} = m_{ji}$. According to Thor.I.Fossen (Fossen, 2011), the off-diagonal elements of a positive inertia matrix is much smaller than the diagonal counterparts. Therefore, the off-diagonal elements in the matrix M_A can be neglected.

The values m_{ij} of the ROV described by the figure 1 can be calculated by using empirical 3D data (D.Blevins, 2003), (N.Newman, 1977) and the strip theory (Ole A. Eidsvik; Ingrid Schjølberg, 19-24 June 2016).

$C_A\left(V_r\right)$ is a Coriolis-like matrix induced by $C_{RB}\left(V\right)$ written as follows (Fossen, 2011, p. 121):

$$C_A\left(V_r\right) = \begin{bmatrix} 0 & 0 & 0 & 0 & Z_{\dot{w}}w_r & -Y_{\dot{v}}v_r \\ 0 & 0 & 0 & -Z_{\dot{w}}w_r & 0 & X_{\dot{u}}u_r \\ 0 & 0 & 0 & Y_{\dot{v}}v_r & -X_{\dot{u}}u_r & 0 \\ 0 & Z_{\dot{w}}w_r & -Y_{\dot{v}}v_r & 0 & N_r r_r & -M_{\dot{q}}q_r \\ -Z_{\dot{w}}w_r & 0 & X_{\dot{u}}u_r & -N_r r_r & 0 & K_{\dot{p}}p_r \\ Y_{\dot{v}}v_r & -X_{\dot{u}}u_r & 0 & M_{\dot{q}}q_r & -K_{\dot{p}}p_r & 0 \end{bmatrix} \qquad (10)$$

The viscous damping force τ_D is given by:

$$\tau_D = D\left(V_r\right)V_r \qquad (11)$$

Here, the damping matrix $D\left(V_r\right)$ is written (Nguyen The Luc, Tran Thu Ha, Nguyen Thai Dung, Nguyen Van Tung, 2019), (Sia Chuan, Tang, 1999):

$$D\left(V_r\right) = \begin{bmatrix} X_{u|u|}\cdot|u_r| & 0 & 0 & 0 & 0 & 0 \\ 0 & Y_{v|v|}\cdot|v_r| & 0 & 0 & 0 & 0 \\ 0 & 0 & Z_{w|w|}\cdot|w_r| & 0 & 0 & 0 \\ 0 & K_{v|v|}\cdot|v_r| & 0 & K_{p|p|}\cdot|p_r| & 0 & 0 \\ M_{u|u|}\cdot|u_r| & 0 & 0 & 0 & M_{q|q|}\cdot|q_r| & 0 \\ 0 & 0 & 0 & 0 & 0 & N_{r|r|}\cdot|r_r| \end{bmatrix} \qquad (12)$$

Where $X_{u|u|}, Y_{v|v|}, Z_{w|w|}, K_{p|p|} M_{q|q|}, N_{r|r|}...$ are the quadratic damping coefficients and they can be calculated by using the formula (Prestero, 2001, p. 25), (Sia Chuan, Tang, 1999, p. 78) as follows:

$$X_{u|u|} = -\frac{1}{2}\rho c_d A_{fx},\ Y_{v|v|} = -\frac{1}{2}\rho c_{dc} A_{fy},\ Z_{w|w|} = -\frac{1}{2}\rho c_{dc} A_{fz} \qquad (13)$$

where ρ is the density of the surrounding fluid, A_{fx}, A_{fy}, A_{fz} is the ROV frontal area along OX, OY, OZ; c_d is the axial drag coefficient of the ROV and c_{dc} is the crossflow drag coefficient of the ROV. According to Hoerner (Hoerner, 1965), the crossflow drag coefficient of a cylinder $c_{dc} = 1.1$.

$K_{p|p|}, M_{q|q|}, N_{r|r|}$ are the damping moment coefficients of the ROV and can be calculated by using the strip theory (Sia Chuan, Tang, 1999, pp. 78-80).

$K_{p|p|}$ is caused by two lights, two thrusters and two balance blocks. It can be calculated by using the formula as follows:

$$K_{p|p|} = \sum_i K^i_{p|p|} = -\frac{1}{2}\sum_i \rho\left(\int_{a+b_i}^{a+b_i+c_i} c_{dc} l_i y^2 |y| dy\right) \quad (14)$$

where: i is the number of parts, a is the radius of the main body, b_i is the length of the connection bar between the main body and the part i, c_i is the diameter of the part i, l_i the length of the part i.

$$M_{q|q|} = N_{r|r|} = -\frac{1}{2}\rho c_{dc}\int_{x_t}^{x_N} 2x^3 R(x)dx \quad (15)$$

where $R(x)$ is the body radius as a function of axial position.

The Froude-Kriloff forces appear due to the inertia matrix of the displaced fluid. These forces are defined as (Khalid Isa, M.R. Arshad, Syafizal Ishak, 2014), (N.Newman, 1977):

$$\tau_{FK} = M_{FK}\dot{V}_{water} \quad (16)$$

Where: M_{FK} is the Froude-Kriloff mass of the ROV.

Based on the study of Khalid Isa, (Khalid Isa, M.R. Arshad, Syafizal Ishak, 2014), to simplify the calculation process, M_{FK} can be equal to the mass of the ROV:

$$M_{FK} = M_{RB} \quad (17)$$

The vector of the thruster force from propellers τ_p can be calculated as follows:

$$\tau_p = \begin{bmatrix} X_p & Y_p & Z_p & K_p & M_p & N_p \end{bmatrix}^T \quad (18)$$

Using the equations (5), (6), (7), (11)-(18) the equation (4) can be rewritten as follows:

$$[M_{RB} + M_A]\dot{V}_r = -C_{RB}(V)V - C_A(V_r)V_r + \tau_D + \tau_{HS} + \tau_p \quad (19)$$

or

$$\dot{V} = \dot{V}_{water} + B^{-1}\left[-C_{RB}(V)V - C_A(V_r)V_r + \tau_D + \tau_{HS} + \tau_p\right] \quad (20)$$

Where:

$$B = M_{RB} + M_A \quad (21)$$

Denote V_0 be the initial state vector of the ROV velocity vector V:

$$V_0 = (u_0, v_0, w_0, p_0, q_0, r_0)^T$$

The equations (20) with the initial condition $V(0) = V_0$ can be rewritten as follows:

$$\begin{cases} \dfrac{\partial V}{\partial t} = \dot{V}_{water} + B^{-1}A(V, V_r) \\ V(0) = V_0 \end{cases} \quad (22)$$

where:

$$A(V, V_r) = \left[-C_{RB}(V)V - C_A(V_r)V_r + \tau_D + \tau_{HS} + \tau_p\right]$$

To solve the equation (22), the Runge-Kutta method is used.

2.2. Mathematical sub-model simulated water flow under reaction of the ROV motion.

The water flow and pressure field, where the ROV is running, are described by the following equations (Faber, 1995):

The continuity equation of fluid is written in the form:

$$\nabla U_l = 0 \quad (23)$$

with $U_l = (u_1, u_2, u_3)$

The momentum equation:

$$\frac{\partial(\rho u_i)}{\partial t} + \frac{\partial(\rho u_j)}{\partial x_j} = \rho F_i - \frac{\partial P}{\partial x_i} + \frac{\partial \tau_{ij}}{\partial x_j} \quad (24)$$

with: F_i *(i=1,2,3)* are the components of a given, externally applied force (e.g. gravity)

$$\tau_{ij} = (\mu_l + \mu_{lt})\left(\frac{\partial u_i}{\partial x_j} + \frac{\partial u_j}{\partial x_i}\right), \mu_{lt} = \frac{\rho_l C_\mu k^2}{\varepsilon}$$ (Jones M.P, Launder B.E, 1972)

The $k-\varepsilon$ model is represented in the following equations:

$$\begin{cases} \dfrac{\partial(\rho k)}{\partial t} + \dfrac{\partial(\rho k u_j)}{\partial x_j} = \dfrac{\partial}{\partial x_j}\left(\dfrac{\mu_{lt}}{\sigma_k}\dfrac{\partial k}{\partial x_j}\right) \\ \qquad\qquad + P - \rho\varepsilon \\ \dfrac{\partial(\rho \varepsilon)}{\partial t} + \dfrac{\partial(\rho \varepsilon u_j)}{\partial x_j} = \dfrac{\partial}{\partial x_j}\left(\dfrac{\mu_{lt}}{\sigma_\varepsilon}\dfrac{\partial \varepsilon}{\partial x_j}\right) \\ \qquad\qquad + (C_{1\varepsilon}P - C_{2\varepsilon}\rho\varepsilon)\dfrac{\varepsilon}{k} \end{cases} \quad (25)$$

$C_{1\varepsilon}$, $C_{2\varepsilon}$, C_μ, σ_k, σ_ε are the constant parameters (Jones M.P, Launder B.E, 1972).

The flow condition on the ROV boundary and initial flow condition are:

$$U_l \vec{n} = -\dot{\eta}_1 \vec{n} \quad (26)$$

$$U_l(0) = \left(u_1(0), u_2(0), u_3(0)\right) \quad (27)$$

The water flow model is described by the equations (23)-(27). To solve these equations the mathematical sub-model CFD is used.

3. Coupling model of two sub-models by UDF subroutine

The schema of coupling model of the ROV motion and water flow is shown in figure 3 (Ernst Arndt Reinecke, Stephan Kelm, Wilfried Jahn, Christian Jakel, Hans-Josef Allelein , 2012). The Outside Program (OP), which calculates the ROV's state $V = (u, v, w, p, q, r)^T$, is executed at certain steps in CFD program flow. Getting the input values from OP, CFD is executed to find out flow velocity, pressure, density. Using these results as well as the input data OP calculates a new ROV state at the next step. Data handling between OP and CFD is performed by means of the CFD Memory Management System (MMS) (Tran Thu Ha, Nguyen Duc Thuyen, Nguyen Thai Dung, Duong Ngoc Hai, 2016). The OP execution is fully controlled by CFD. All variable fields are stored in MMS and read out as an initialization for OP in the next step.

The coupling model of the ROV motion and water flow is performed using the following user routines:

- Junction box routine named by *Outcomputer.F*, which calculates the ROV state $V = (u, v, w, p, q, r)^T$ of equation (20) and $\dot{\eta}_1$, $\dot{\eta}_2$ by the equations (1) and (2), is executed at certain steps in CFD program flow.

- User CEL Function (Tran Thu Ha, Nguyen Duc Thuyen, Nguyen Thai Dung, Duong Ngoc Hai, 2016) named by *Readmms.F* giving back data of U_l, p, ρ and V_{water} to CFD reading, is executed if data is requested.

- Junction Box Routine (Tran Thu Ha, Nguyen Duc Thuyen, Nguyen Thai Dung, Duong Ngoc Hai, 2016) named by *Initialization* writes the values of U_l, p, ρ and V_{water} to MMS.

Simulation process by CFD is executed based on the diagram presented in the figure 3. The locations, where User CEL Functionsor User Junction Box Routineare called, are listed by this simulation diagram (Ernst Arndt Reinecke, Stephan Kelm, Wilfried Jahn, Christian Jakel, Hans-Josef Allelein , 2012).

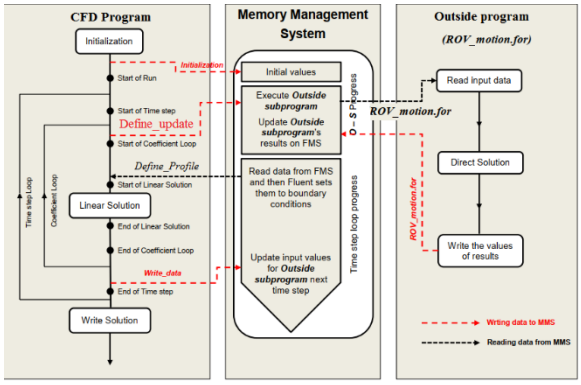

Figure 3. Data management for a coupled Outside Program and CFD Program

Algorithm to solve the couple model problem

The coupling process of two sub-models can be described by the following steps:

1) At Start of Run: The subroutine *Initialization* is called first time, which initializes data of ROV state $V = (u, v, w, p, q, r)^T$, water velocity in ROV frame V_{water}. The input parameters such as length, diameter, mass … are saved to the MMS by this subroutine. This information is the data input of the OP programming.

2) At Start of Time Step: OP is called once. The input values are provided by previous time step or from subroutine *Initialization* if it is the first time step.

3) Then OP is running to find out the ROV state vector $V = (u, v, w, p, q, r)^T$ of equation (20) and then $\dot{\eta}_1, \dot{\eta}_2$ in inertial frame by the equations (1)-(2). This process is shown by the black dashed line in the right side of figure 3.

4) After simulating, OP writes back the getting state results $V = (u, v, w, p, q, r)^T$ and $\dot{\eta}_1, \dot{\eta}_2$ as the

body's data to MMS. This process is shown by the red dashed line in the right side of figure 3.

5) While the CFD 'coefficient loops' are performed, the subroutine *Readmms.F* is called some times (the number of calls is depending on the number of time steps per Run (Tran Thu Ha, Nguyen Duc Thuyen, Nguyen Thai Dung, Duong Ngoc Hai, 2016) to get ROV data and $\dot{\eta}_1, \dot{\eta}_2$ from MMS. This data is the input for CFD.

6) The CFD solves the equations (23)-(27) to find out the flow values U_l, P.
7) Calculate water velocity V_{water} in Body-fixed reference frame by the formula (3)

8) The results (U_l, P) and then V_{water} are written to MMS by the subroutine *Initialization.* These results also are the data input for OP at next step. This process is shown by the third redline in the left side of figure 3.

9) Come back to step 2.

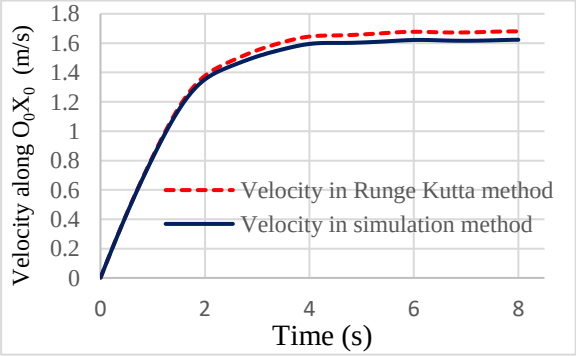

Figure 4. Velocity along O_0X_0 of ROV in two methods

4. Simulation method

Let the ROV with m=42.5kg, L=0.8m, D=0.25m, Ixx=0.81 kgm^2; Iyy=2.73 kgm^2; Izz=2.62 kgm^2; Ixy=Iyz=Izx=0; l_{den}=0.11m, d_{den}=0.06m, l_{DC}=0.102m, d_{DC}=0.097m, d_{bb}=0.086m run with the initial conditions: u_0=0m/s, v_0=0, w_0=0, p_0=0, q_0=0, r_0=0, x_0=0, y_0=0, z_0=1m, ϕ_0=0, θ_0=0, ψ_0=0, $\tau_p = 40N$

We will consider the following methods:

- The first method: Without the flow velocity V_{water}, the equation (16) is solved by Runge-Kutta method in the time period T=20s.

- The second method: By the algorithm presented in the section 4 the equation system (20), (23)-(27) is solved in the time period T=8s. In every 0.002 second step, the interaction between ROV's motion and flow motion is expressed by the exchange of the ROV velocities, water velocity U_l getting by the CFD sub-model and the formula (3) V_{water}.

The velocities V along the O_0X_0 direction of two methods are presented in the figure 4. The vector of the velocity field in 4.000 simulation steps is presented in the figure 5.

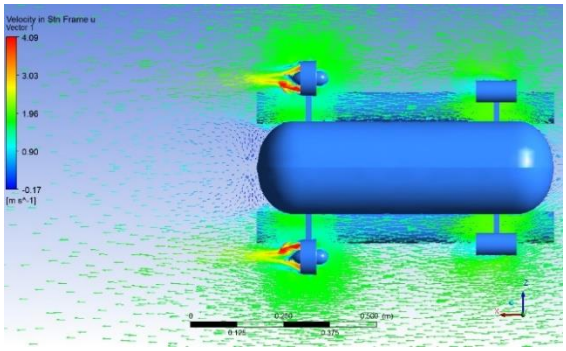

Figure 5. Velocity field of the water flow

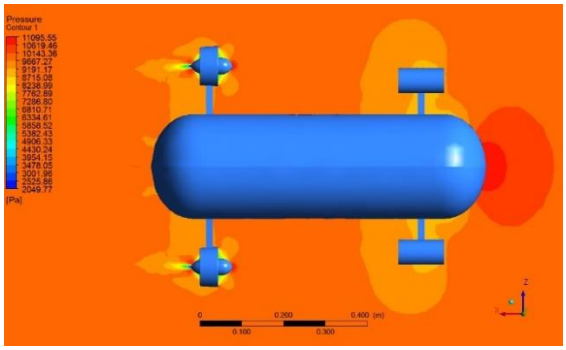

Figure 6. Pressure field of the water flow

5. Conclusions

1) In the couple model the exchanging interaction between the ROV motion and fluid flow is considered. In every time step, this interaction is expressed as follows:

- First, the equation (22) solving the ROV velocity in body-fixed frame shows that the ROV motion is affected by the flow velocity V_{water} in body-fixed frame.

- Second, the formula (26) shows that the flow velocities U_l is influenced by the ROV's velocity $\dot{\eta}_1$ in the inertial frame.

2) In figure 4 we can see that under the interaction between the ROV motion and water flow, the ROV velocity along O_0X_0 simulated by the coupling model is lower than the other one calculated by the Runge-Kutta method for the first sub-model. The difference between two velocities is about 3.7%.

3) Figure 5 shows the velocity field of water flow surrounding the ROV. The turbulent flows are appeared mainly behind two propellers and slightly behind the bottom of the ROV. This result is coincided with the water velocity field in reality when the ROV runs under water.

4) The figure 6 shows that, the pressure field of the water flow surrounding the ROV changes and depends on the structure of the ROV. The pressure of the water flow is maximum at the top of the ROV. It is appropriate to a pressure field made by the ROV in reality.

Acknowledgements

The authors gratefully acknowledge the financial support from the NVCC03.03/20-20 funds.

References

D.Blevins, R. (2003). *Applied Fluid Dynamics Handbook.* Florida: Krieger Publishing Company.

Ernst Arndt Reinecke, Stephan Kelm, Wilfried Jahn, Christian Jakel, Hans-Josef Allelein . (2012). Simulation of the efficiency of hydrogen recombiners as safety devices. *International Journal of Hydrogen energy , 38*(8), 117-214.

Faber, T. (1995). *Fluid Dynamics for Physicists.* New York: Cambridge University Press.

Fossen, T. I. (2011). *Handbook of Marine craft Hydrodynamics and Motion Control.* Trondheim: A John Wiley & Sons.

Hoerner, S. F. (1965). Fluid Dynamic Drag.

Jones M.P, Launder B.E. (1972). The prediction of laminarization with a Two-Equation Model of Turbulence. *International Journal of Heat and Mass Transfer, 15*, 301-304.

Khalid Isa, M.R. Arshad, Syafizal Ishak. (2014). A hybrid-driven underwater glider model, hydrodynamic estimation, and an analysis of the motion control. *Ocean Engineering, 81*, 111-129.

Khang, G. N. (2007). *Động lực học hệ nhiều vật.* Hà Nội: Nhà xuất bản Khoa học và Kỹ thuật.

N.Newman, J. (1977). *Marine Hydrodynamics.* The MIT Press.

Nguyen The Luc, Tran Thu Ha, Nguyen Thai Dung, Nguyen Van Tung. (2019). Calculating a suitable hydrodynamic drag coefficient for a complex-shaped underwater vehicle. *National Mechanics Conference 2019* (pp. 1-8). Hanoi: Institude of Mechanics.

Ole A. Eidsvik; Ingrid Schjølberg. (19-24 June 2016). Determination of hydrodynamic parameters for Remotely Operated Vehicles. *Proceedings of the ASME 2016 35th International Conference on Ocean, Offshore and Arctic Engineering*, (pp. 1-10). Busan.

Prestero, T. (2001). *Verification of a Six-Degree of Freedom Simulation Model for the REMUS Autonomous Underwater Vehicle.* California: Cambridge, Massachusetts.

Sia Chuan, Tang. (1999). *Modeling and SImulation of the Autonomous Underwater Vehicle, Autolycus.* Massachusetts: Massachusetts Institute of Technology.

Tran Thu Ha, Nguyen Duc Thuyen, Nguyen Thai Dung, Duong Ngoc Hai. (2016). Super cavity model with the coupling reaction of splender body motion and water flow. *Vietnam Journal of Mechanics*, 1-13.

Xiao Liang, Yongjie Pang, Lei Wan and Bo Wang. (2008). Dynamic Modelling and Motion Control for Underwater Vehicles with Fins. In *Underwater Vehicles* (p. 582). Vienna: InTech.

The 5th International Conference on Engineering Mechanics and Automation (ICEMA 5)
Hanoi, October 11÷12, 2019

Modeling and simulation of free surface and water entry of bodies

Van-Tu Nguyen, Thanh-Hoang Phan and Warn-Gyu Park

School of Mechanical Engineering, Pusan National University, Busan, Korea

Abstract

The present work is dedicated to modeling and application of numerical approaches for simulation of free surface and water entry of bodies. A preliminary evaluation of numerical models for simulation of complex, free surface, and water impact problems was performed. The dual-time, pseudo-compressibility method is adopted in order to solve the Navier–Stokes equations by using a high-order compact differencing scheme in a vector form. By implementing the combination of the equations and special treatments for the interfaces between phases, e.g., the VOF interface tracking method or interface sharpening method in a generalized curvilinear coordinate system, the proposed model is capable of predicting complex, arbitrary, free surface, and water impact flows in hydraulic and hydrodynamic fields that occur in geometrically complex domains. Several sets of example computations concerning important physical characteristics of complex free surface and water impact flows of structures and the use of Chimera grids and 6DOF motions model confirm that the numerical methods are promising for extensive applications to accurate and efficient simulations of both simple and full 3D free surface, water impact flows in practical problems.

Key Words: Multiphase, Volume of fluid, Sharp interface, Interface treatment, Free surface, Water impact

1. Introduction

Numerical simulation of the hydrodynamics of free-surface and water impact flows have received growing research attention in solving many problems in environmental, naval, and ocean engineering, such as in the evaluation of potential risks of the rupture of levees, dams, and reservoirs; interaction of extreme waves with floating structures, moving ships, and green water on decks; problems in harbors and coastal areas. The main challenges of the existing numerical methods in terms of fluid model, accurate interface position description, tracking of moving interfaces, coupling with structures, and implementation of boundary conditions when solving such highly nonlinear interface discontinuity problems include the highly violent motions of the interface, such as unsteady fragmentation, turbulence, discontinuities, splashing, wave breaking, and mixing or entrapment of one fluid within another, and the determination of the dynamic pressure loads by water impact. These challenges have motivated researchers to develop novel, efficient, and accurate numerical models for high-resolution two-dimensional and three-dimensional (3D) flow simulations for application to many hydraulic and hydrodynamic problems in engineering.

This work provides an assessment of solution methods against the challenges, especially the full three-dimensional behavior of free surface and the dynamic pressure loads by water impact.

Two popular methods consisting of the volume of fluid (VOF) interface tracking method and VOF interface sharpening method together with a simple three-equation two-phase model are considered and evaluated for simulation of this flow. The VOF approach is a good tool for numerical simulations of free surface flows. In the VOF methods, each phase is represented by a scalar field, which is the fraction of the cell occupied by liquid. The value of this field is unity in the liquid phase and zero in the gas phase, whereas the values are intermediate at the interface. The scalar field is advected passively with the flow velocities and satisfies the advection equation. In typical VOF interface tracking methods, there are two main steps: interface reconstruction and computing fluxes over the faces of the control volume using a geometrical tool to solve the advection equation(Nguyen, Vu et al. 2014, Nguyen and Park 2016). This approach yields a good approximation of the interface shape, prevents artificial diffusion, and ensures reasonable conservation of mass.

In VOF interface sharpening methods, the interface is captured implicitly based on a VOF discretization scheme with a special interface treatment to reduce the numerical diffusion and maintain the interface sharpness. Thus, the position of the interface can be determined without the complex geometrical reconstruction required in the interface-reconstruction approach. The advantages of these methods are the simplicity of implementation on arbitrary three-dimensional meshes, high computational efficiency, and applicability in modeling complex interface structure flows (Nguyen and Park 2017, Nguyen, Thang et al. 2018).

For the isothermal compressible flow model, the standard explicit solver for compressible flows is applied to solve the simple three-equation two-phase model. The Tait EOS was used to model the pressure, which is a function of density only, and hence, the energy equations were omitted.

The water entry of a hemisphere is computed to examine the accuracy and efficiency of the method. Comparisons of the results between these three numerical methods are presented. The numerical simulations of ricochet behavior of a water entry cylinder also show flow scenarios of the problems.

2. Physical Formulation

2.1. Numerical models for incompressible flows

The governing equations for incompressible flows consist of the mixture continuity, mixture momentum, and phasic volume fraction equations. The volume fraction of one of the fluids is used to indicate the composition of the phase components in a volume element in the domain. The mixture is assumed to be in thermodynamic and mechanical equilibrium so that the pressure, *p*, and velocity components, *u*, *v*, and *w* of the phases are uniform amongst all species.

$$\nabla.\mathbf{u} = 0 \tag{1}$$

$$\frac{\partial}{\partial t}\left(\rho_{\mathrm{m}}\mathbf{u}\right)+\nabla.\left(\rho_{\mathrm{m}}\mathbf{u}\otimes\mathbf{u}\right)=-\nabla p+ \nabla.\left[\mu_{\mathrm{m,t}}\left(\nabla\mathbf{u}+\nabla\mathbf{u}^{T}\right)\right]+\mathbf{F}_{b}, \tag{2}$$

$$\frac{\partial\alpha^{s}}{\partial t}+\nabla.\left(\alpha^{s}\mathbf{u}\right)=0 \tag{3}$$

where t is the physical time, p is the pressure, $\mathbf{u}$ is the flow velocity, $\mathbf{F}_b$ includes gravitational and surface tension forces, and α^s is the volume fraction of the s^{th} phasic component that satisfies the constraints, $0 \le \alpha^s \le 1$ and $\sum_{s=1}^{N}\alpha^s = 1$.

The governing equations lack a time derivative in the continuity equation, therefore, standard time-marching compressible flow solvers used extensively in the aerospace industry cannot be applied incompressible flows. The dual time-preconditioning/artificial compressibility algorithms can allow the standard time marching finite-volume Riemann schemes to be used and the incompressible flow model can be solved in a compact vector forms.

The equations can be solved based on a dual-time pseudo-compressibility method. In which the pseudo time derivative terms with a preconditioning parameter are added to the governing equations and the time variation of the incompressible flow is treated as a compressible flow to couple the velocity and pressure fields at each time iteration. The artificial compressibility (or pseudo-compressibility) method was originally introduced by Chorin for computing steady-state incompressible flows (Chorin 1997). The unsteady NS system of equations of motion for the incompressible flows is written as (Nguyen and Park 2017):

$$\left(\frac{1}{\beta\rho_{\mathrm{m}}}\right)\frac{\partial p}{\partial\tau}+\frac{\partial u_j}{\partial x_j}=0, \tag{4}$$

$$\frac{\partial}{\partial t}\left(\rho_{\mathrm{m}}u_i\right)+\frac{\partial}{\partial\tau}\left(\rho_{\mathrm{m}}u_i\right)+\frac{\partial}{\partial x_j}\left(\rho_{\mathrm{m}}u_iu_j\right)= -\frac{\partial p}{\partial x_i}+\frac{\partial}{\partial x_j}\left[\mu_{\mathrm{m,t}}\left(\frac{\partial u_i}{\partial x_j}+\frac{\partial u_j}{\partial x_i}\right)\right]+\rho_{\mathrm{m}}g_i, \tag{5}$$

where β is the preconditioning compressibility parameter, p is the pressure, t is the physical time, τ is the pseudo time, u is the flow velocity.

An alternative method is a pseudo-compressibility method based on the basic principle of the classical methods; however, pseudo-time derivative terms are constructed by replacing true density by pseudo-density and pressure is calculated as a given function (referred to as the pseudo-law of state) of pseudo-density. The unsteady NS system of equations for the incompressible flows can be expressed as follows (Nguyen and Park 2016):

$$\frac{\partial\tilde{\rho}}{\partial\tau}+\frac{\partial\rho u_j}{\partial x_j}=0, \tag{6}$$

$$\frac{\partial\tilde{\rho}u_i}{\partial\tau}+\frac{\partial\rho u_i}{\partial t}+\frac{\partial\rho u_iu_j}{\partial x_j}= -\frac{\partial p}{\partial x_i}+\frac{\partial}{\partial x_j}\left[\mu\left(\frac{\partial u_i}{\partial x_j}+\frac{\partial u_j}{\partial x_j}\right)\right]+\rho g_i, \tag{7}$$

where t is physical time, τ is pseudo-time, u is flow velocity, and p is pressure.

The pseudo-time derivatives use pseudo-density $\tilde{\rho}$, which is introduced in Eqs. (6) and (7), and the pressure field is calculated based on an additional pseudo-state equation (Nguyen, Vu et al. 2014),

$$p=\rho U_0^2\ln\left(\frac{\tilde{\rho}}{\rho_\infty}\right)+p_\infty, \tag{8}$$

where the parameters are set in accordance with $U_0=U_\infty$ or $U_0=\sqrt{u^2+v^2+w^2}$, in which u, v, and w are the local values of the respective velocities obtained at a previous iteration step in pseudo-time.

2.2. Interface treatment

To proceed with the numerical procedure, the advection equation is solved using a known velocity field to update the density and viscosity fields in the next time step. Alternatively, the advection equation is written as

$$\frac{\partial\alpha}{\partial t}+\frac{\partial\alpha u_j}{\partial x_j}=\alpha\frac{\partial u_j}{\partial x_j}. \tag{9}$$

The equation can be discretized based on the standard conservative finite-difference in the x direction as

$$\alpha^{n+1}=\alpha^n-\frac{\Delta t}{\Delta x}\left[F_{i+1/2}-F_{i-1/2}\right]+\alpha\frac{\Delta t}{\Delta x}\left[u_{i+1/2}-u_{i-1/2}\right]. \tag{10}$$

In this work, two types of special treatments for the interface between two phases are implemented to keep the interface sharp.

The first is a VOF/PLIC method in which a geometrical tool is employed to calculate convection fluxes. Using the method, the advection equation can be solved accurately to determine the volume fractions of the liquid and gas phases. The method comprises two steps, i.e., interface reconstruction and interface propagation. The reconstruction technique is a geometrical tool used to determine the orientation of an interface by approximating the unit normal

vector, **n,** to the interface using a PLIC algorithm (Youngs 1982, Gueyffier, Li et al. 1999, Nguyen and Park 2016). The normal vector, **n,** and volume fraction, α , in each cell are used to calculate the VOF fluxes across the faces of each computational cell in the propagation step. Here, the Lagrangian approach is used in the computational space, and an operator split advection algorithm based on the fluxes is used for the advection of the volume fractions at the next physical time step.

The second technique is an interface-sharpening technique (IST)(Nguyen and Park 2017, Nguyen, Thang et al. 2018). The regular discretization methods may smear the interface and introduce artificial mixing of two fluids because of numerical diffusion errors. To solve this problem, an interface-sharpening technique is implemented as post-processing for the volume-fraction field after each time step. This process is independent of the discretization scheme of the VOF equation. The interface-sharpening equation can be written as follows:

$$\frac{\partial \alpha}{\partial \tau} = -\nabla.\left(\tilde{f}(\alpha)\mathbf{n} - D(\nabla \alpha.\mathbf{n})\mathbf{n}\right), \tag{11}$$

where $\tilde{f}(\alpha) = \alpha(1-\alpha)$, is used to maintain the resolution of contact discontinuities in regions where $0 < \alpha < 1$, and the local interface normal vector was introduced into the interface-sharpening equation to lead the compression acting in the normal direction of the interface. The low viscosity $\nabla \alpha$ enables a reduction in the diffusion error at the interface, D is a stopping criterion for defining the desired interface thickness and is defined as $D = \frac{1}{2}V^{1/3}$, and V is the volume of a cell.

2.3. Isothermal compressible flow model

In this section, a Eulerian diffuse interface model for simulation of free surface flows is presented. The model is a simplified two-phase model from the Baer–Nunziato model for free surface flows (Dumbser 2011). In which the Baer–Nunziato model so-called "the full seven-equation two-fluid model" is reduced to a three-equation model. The simplifying assumption is that the density of gas phase is much smaller than the one of the liquid phase and the pressure of gas phase can be considered to remain constant at atmospheric conditions everywhere and for all time. Therefore, only equations of liquid phase are active and the dynamics of air phase is omitted. In addition, the Tait equation of state is used to model the pressure, in which the pressure is only a function of density and hence the energy equations are not dropped. By this simplification, the governing equations are solved only in regions of water and interface, hence the computational cost is significantly reduced. The governing equations are written as

$$\frac{\partial \alpha\rho}{\partial t} + \frac{\partial \alpha\rho u_j}{\partial x_j} = 0, \tag{12}$$

$$\frac{\partial}{\partial t}(\alpha\rho u_i) + \frac{\partial}{\partial x_j}\left(\alpha\left(\rho u_i u_j + pI\right)\right) = \frac{\partial}{\partial x_j}\left[\mu\left(\frac{\partial u_i}{\partial x_j} + \frac{\partial u_j}{\partial x_i}\right)\right] + \alpha\rho g_i, \tag{13}$$

$$\frac{\partial \alpha}{\partial t} + u_j \frac{\partial \alpha}{\partial x_j} = 0, \tag{14}$$

where p is the pressure, t is the physical time, u is the flow velocity, ρ is the liquid density, α is the volume fraction of the i^{th} phasic component.

The assumption of isothemal flow is applied and the Tait equation of state is used to model the pressure as:

$$p = p(\rho) = B\left[\left(\frac{\rho}{\rho_0}\right)^{\gamma} - 1\right] + p_0 \tag{15}$$

and the speed of sound *c* is defined as usual:

$$c^2 = \frac{\partial p}{\partial \rho} = \frac{B\gamma\rho^{\gamma-1}}{\rho_0{}^{\gamma}}, \tag{16}$$

where B is the bulk modulus of fluid, that can be calculated as

$$B = \frac{\rho_0 |U_{ref}|^2}{\gamma M^2} \tag{17}$$

where U_{ref} is the characteristic reference velocity.

The governing equations can be expressed in the generalized curvilinear coordinates and discretized in a general structured grid (Nguyen and Park 2015, Nguyen, Vu et al. 2016, Nguyen, Thang et al. 2018). Accordingly, the solver based on the characteristic information of the governing equations is used to compute convective flux derivatives. Hence, the flux Jacobian matrix is divided into two sub-vectors that are associated with non-negative and non-positive eigenvalues. The convective flux vector is discretized using a cell-centered finite volume procedure. For the extrapolated Riemann variables a MUSCL procedure with a third-order accuracy (Nguyen and Park 2016) and compressional limiter called "supperbee" is employed to obtain a sharp interface.

3. Result and discussion

3.1. Water impact of a hemisphere

The numerical methods was assessed by computing a water entry of a hemisphere. The hemisphere enters the water at the entry velocity of 4.0 *m/s* and has a diameter and mass of 0.3 *m* and 11.5 *kg*, respectively. The water entry of a freefalling hemisphere was simulated using the VOF interface tracking model (Nguyen and Park 2016) and the VOF interface sharpening model (Nguyen and Park 2017), and the predicted results were compared with the experimental data (De Backer, Vantorre et al. 2009). In this study, the problem was computed on four different grids using the SETTM model. The computational domain for this case consisted of two blocks as shown in Fig. 1. For a coarse grid, the first block contained the base region with the dimensions of 100×50×40; the second block had the dimensions of 25×75×40. The medium, fine, and very fine grids had the dimensions of (200×100×40 and 50×150×40), (300×150×40 and 75×200×40), and (400×200×40 and 100×250×40), respectively. Fig. 2 shows the predicted visualizations of the water entry of the hemisphere at 0.016 *s* on the four grids. Owing to the water impact, a large free-surface deformation was generated, and jets running out along the hemisphere boundaries appeared. It can be observed that the simulation on the coarse grid failed in capturing the thin jets, whereas the other computations on the finer grids show better resolution, especially in the simulation on the very fine grid.

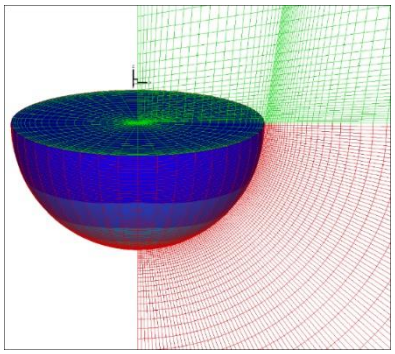

Fig. 1 Curvilinear body-fitted grid for simulation of water entry of a hemisphere

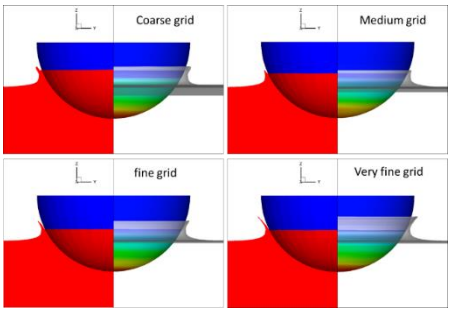

Fig. 2 Visualizations of water entry of a hemisphere including the predicted pressure, deformation of free surface, and pressure distribution on the body at t = 0.016 s using four different grid sizes

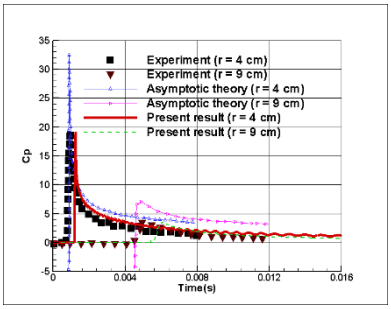

Fig. 3 Comparison of impact pressures on the surface of a hemisphere during water entry

Fig. 3 shows the predicted, theoretical, and experimental data of temporal pressure distribution coefficients at positions on the surface of the hemisphere where the horizontal distances from the symmetric axis are *r* = 4.0 *cm*

cm and r = 9.0 *cm*. Good consistency is observed between the predicted and experimental data, where the theoretical solutions show a remarkable overestimation. Fig. 4 shows that the peak of the predicted pressure distribution coefficients at the position r = 4.0 *cm* using the four grids converges to the experimental data. The peak values of pressure at both positions that are often of interest to material designers are reasonably captured by the numerical method, and the predicted pressure at r = 4.0 *cm* has an error of 34.2% on the coarse grid, 15.7% on the medium grid, 7.8% on the fine grid, and 0.3% on the very fine grid. The discrepancies are similar in the simulation on the medium grid using the VOF interface tracking model and the VOF interface sharpening model with errors of 16.6% and 15.2%, respectively.

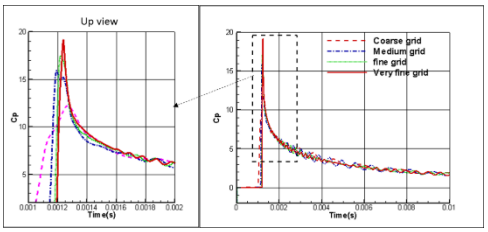

Fig. 4 Impact pressure on the surface of a hemisphere during water entry simulation using four different grid sizes

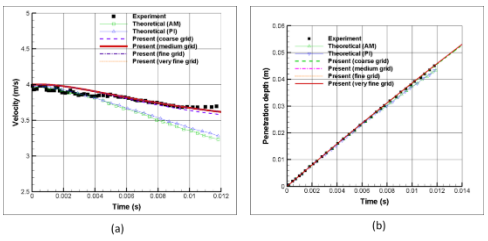

Fig. 5 Water entry of a hemisphere: (a) velocity of the hemisphere and (b) vertical penetration depth of the hemisphere

The velocity and vertical penetration depth of the hemisphere were also predicted and compared with the experimental data as shown in Fig. 5. The simulations confirm the ability of the present method in determining the impact loads generated by the interaction of the free surface and structure, and the impact flows of water entry bodies.

3.3 Ricochet of a circular cylinder off the water surface

The ricochet of a body off water is the rebound of a water entry body off the water and it is an important phenomenon in engineering. When the solid body enters the water at a certain angle and velocity, the dynamic and kinematic behaviors of the ricochet body is of interest. The interest in the ricochet and its effects have been initially on naval application. Recently, the phenomenon becomes an increasing interest in the application in different areas such as the navigation technology for the water landing of airplanes so-called ditching problem, aircraft, missiles, and big boats. For the further understanding of the ricochet behavior of objects, the whole process with the variation of translational and angular velocities and accelerations as well as the trajectory of a neutrally buoyant cylinder on the water have been numerically studied. The cylinder has a diameter of 25.4 *mm* and a solid-water density ratio of 1.0. The cylinder enters the water at an initial velocity of 10.0 *m/s* and entry angle of 10^o which is defined as the angle between the water surface and the velocity vector of the center of mass of the cylinder as illustrated in Fig. 6 (a). As the cylinder enters the water, the dynamics of the cylinder are governed by the combined actions of the water impact and the various external forces and moments. The flow is dominated by the unsteadiness of arbitrary translational and rotational motions of the bodies. The initial entry angle is quite small, therefore the cylinder moves within a large domain and it requires many grid points or elements. Additionally, in cases of high-speed bodies, the bodies may move out of the fixed domain, leading to unreliable simulation later (Moxnes, Frøyland et al. 2016, Farouk, Bassindowah et al. 2019). However, thank to the moving overlapping grid modeling strategy (Nguyen, Vu et al. 2016), in which the grid system will move based on the positions and orientation of the body, the solution domain only requires a small domain with a length of 20D and a height of 10D and the overlapping grids with a total size of 180,200 grid points. The grid is clustered in the vicinity of the cylinder and is initially set up as shown in Fig. 6 (b). In case the strategy is not used, the total size of Cartesian grids would be about 5,300,000 at the same resolution level.

The numerical simulations can provide visualizations of the fluid patterns in both the air and the water regions. Fig. 7 shows the sequence snapshots in the simulation of the ricochet of the cylinder, including a free-surface profile, vertical velocity distribution and pressure distribution around the cylinder. Owing to the hit of the cylinder on the water surface at the small angle, a large free surface deformation was generated and a front long jet running out along the front surface boundaries of the cylinder appeared during the rebound process of the cylinder. At t = 4.195 *ms*, the front jet has run up to the top of the cylinder and continued developing to a long jet until the cylinder lately rebounds off the water surface at t = 32.080 ms. The vertical velocity distribution in Fig. 7 (b) shows that the jet grows rapidly and then gradually decelerate due to the gravity effect. The pressure gradient due to the water impact gradually decreases and the pressure distribution tends to return a hydrostatic distribution as the ricochet occurs (Fig. 7 (c)).

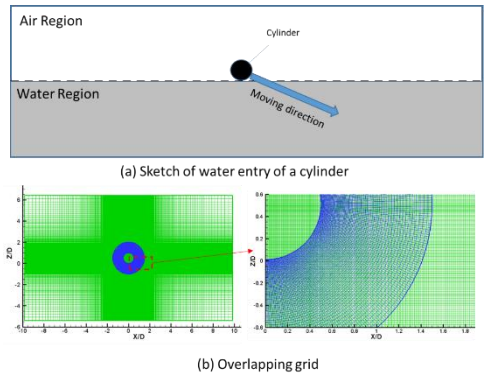

Fig. 6 The solution domain and magnifications showing refined and overlapping grid in the vicinity of the solid

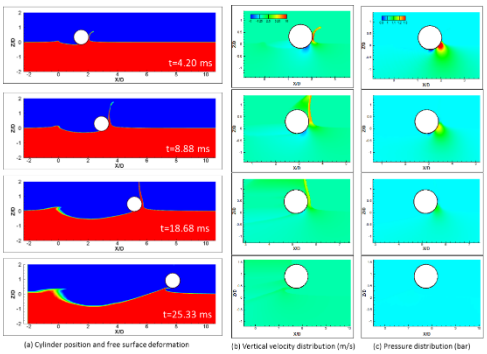

Fig.7 Ricochet of a water entry cylinder at an initial entry angle of 10 (deg) and entry velocity of 10 m/s. The simultaneous snapshots at times of 4.195 ms, 8.880 ms, 25.332 ms, and 32.080 ms.

3. Conclusion

The physical formulations of numerical methods including the VOF interface sharpening model, the VOF interface tracking model, and the isothermal compressible flow model are presented. An assessment of the accuracy and efficiency of three numerical methods for free surface water impact flows and the numerical results show good validation and high accuracy. The numerical simulations of ricochet behavior of a water entry cylinder are presented. The results provide clearly physical pictures of the problems.

Acknowledgment

This work was supported by the National Research Foundation of Korea (NRF) grant funded by the Korea government (MSIT) (no. 2018R1A2B6008864), and by the Nuclear Safety Research Program through the Korea Foundation of Nuclear Safety (KOFONS), with financial resource granted by the Nuclear Safety and Security Commission (NSSC), Republic of Korea (no. 1305011).

References

Chorin, A. J. (1997). "A Numerical Method for Solving Incompressible Viscous Flow Problems." Journal of Computational Physics **135**(2): 118-125.

De Backer, G., M. Vantorre, C. Beels, J. De Pré, S. Victor, J. De Rouck, C. Blommaert and W. Van Paepegem (2009). "Experimental investigation of water impact on axisymmetric bodies." Applied Ocean Research **31**(3): 143-156.

Dumbser, M. (2011). "A simple two-phase method for the simulation of complex free surface flows." Computer Methods in Applied Mechanics and Engineering **200**(9): 1204-1219.

Farouk, B., H. Bassindowah and S. Segletes (2019). "Impact and ricochet of a high-speed rigid projectile from an air-water interface." 2019 **13**(2).

Gueyffier, D., J. Li, A. Nadim, R. Scardovelli and S. Zaleski (1999). "Volume-of-Fluid Interface Tracking with Smoothed Surface Stress Methods for Three-Dimensional Flows." Journal of Computational Physics **152**(2): 423-456.

Moxnes, J. F., Ø. Frøyland, S. Skriudalen, A. K. Prytz, J. A. Teland, E. Friis and G. Ødegårdstuen (2016). "On the study of ricochet and penetration in sand, water and gelatin by spheres, 7.62 mm APM2, and 25 mm projectiles." Defence Technology **12**(2): 159-170.

Nguyen, V.-T. and W.-G. Park (2015). "A free surface flow solver for complex three-dimensional water impact problems based on the VOF method." International Journal for Numerical Methods in Fluids **82**: 3–34.

Nguyen, V.-T. and W.-G. Park (2016). "A free surface flow solver for complex three-dimensional water impact problems based on the VOF method." International Journal for Numerical Methods in Fluids **82**(1): 3-34.

Nguyen, V.-T. and W.-G. Park (2017). "A volume-of-fluid (VOF) interface-sharpening method for two-phase incompressible flows." Computers & Fluids **152**: 104-119.

Nguyen, V.-T., V.-D. Thang and W.-G. Park (2018). "A novel sharp interface capturing method for two- and three-phase incompressible flows." Computers & Fluids.

Nguyen, V.-T., D.-T. Vu, W.-G. Park and C.-M. Jung (2016). "Navier–Stokes solver for water entry bodies with moving Chimera grid method in 6DOF motions." Computers & Fluids **140**: 19-38.

Nguyen, V.-T., D.-T. Vu, W.-G. Park and Y.-R. Jung (2014). "Numerical analysis of water impact forces using a dual-time pseudo-compressibility method and volume-of-fluid interface tracking algorithm." Computers & Fluids **103**: 18-33.

Youngs, D. L. (1982). "Time dependent multi material flow with large fluid distortion." Num. Methods for Fluid Dynamics, N.Y: 273-285.

The 5th International Conference on Engineering Mechanics and Automation (ICEMA-5)
Hanoi, October 11÷12, 2019

Some characteristics of seawater level rises in the coastal zone from Quang Ninh to Quang Binh

Pham Tri Thuc[a], Dinh Van Manh[b, d], Nguyen Ba Thuy[c]

[a] *Naval Academy; 30 Tran Phu-Nhatrang-Vietnam. Email: pthucacademy@yahoo.com.vn*
[b] *Institute of Mechanics; 264 Doi Can-Ba Dinh-Hanoi-Vietnam. Email: dinhvanmanh@gmail.com*
[c] *National Center for Hydro; 62 Nguyen Chi Thanh-Hanoi-Vietnam. Email: thuybanguyen@gmail.com*
[d] *Graduate University of Science and Technology, VAST; 18 Hoang Quoc Viet-Cau Giay-Hanoi-Vietnam*

Abstract

The abnormal seawater level rises phenomenon along the Vietnam coast has been of interest to scientists for a long time, especially the studies on monsoon and storm surges. The achieved results of the recent projects on storm surges such as the basic characteristics of storm surge height, the annual exceedance probability curves of seawater level (including tide and storm surges) along the coast of Vietnam are applied for warning and forecasting natural disasters, designing and upgrading the sea dike system and constructions of the coastal zones. However, it is need to understand in more detail about this dangerous phenomenon, especially when the seawater level rises not only during storm landed but also several hours or more after landed time.

In this paper, on the basis of statistical calculations of the hourly measured seawater level data at some tide stations from Quang Ninh to Quang Binh in the 1960-2017 period, some more storm surge characteristics are revealed. The historical seawater level data showed that the abnormal seawater level rises (greater than 0.5m) could occur at the coast sites rather far from the landed storm point in several hours after the landed time. It is means storm can cause flood not only surrounding the landed point but also in the coastal zones out of direct affection of storm.

Keywords: *storm surges, Hon Dau tide station, Hon Ngu tide station, Son Tra tide station, statistical analysis*

1. Introduction

Storm surge is one of dangerous natural disasters occurred frequently in the coastal zones. The high rise of seawater level combined with high wave can cause flooding, beach erosion, sea dike and construction damages ... It is especially dangerous when storm hits the land during the high tide. In history, there were many storms with strong winds, heavy rains, high waves and high rises water to inundate coastal areas on a large scale, causing many human and property losses for example Katrina typhoon attacked in New Orleans-USA in 8/2005, Nargis typhoon hits in Myanmar in 5/2008. Ketsana typhoon (9/2009) hit the coast of Quang Nam-Da Nang (Vietnam) causing surges over 1.1 m at Son Tra, combined with the flood of 3.2 m high in Hoi An, causing in 30 deaths and 170.000 people to evacuate**.**

Typically storm surges occur just before or after its landing time (i.e. about 1 to 2 hours arounding the landfall time of the storm).

However, sometimes there are high seawater level rises occurring several hours later the typhoon landfall time and existing for many hours. In the history, Sooyoul Kim et al. (2014) pointed out the Songda typhoon (with the lowest pressure at the center of 925 mb and maximum wind speed of 46.3 m/s), landed on the Japanese coastal on 08/9/2004, made high surges for many hours before and after the landfall time, caused greatly affecting and suffering in localities The measured data (see Figure 1b) pointed out that, along the coastal of Tottori (Japan), high after-storm surge occurred after from 15 to 18 hours, (Sooyoul Kim et al., 2014).

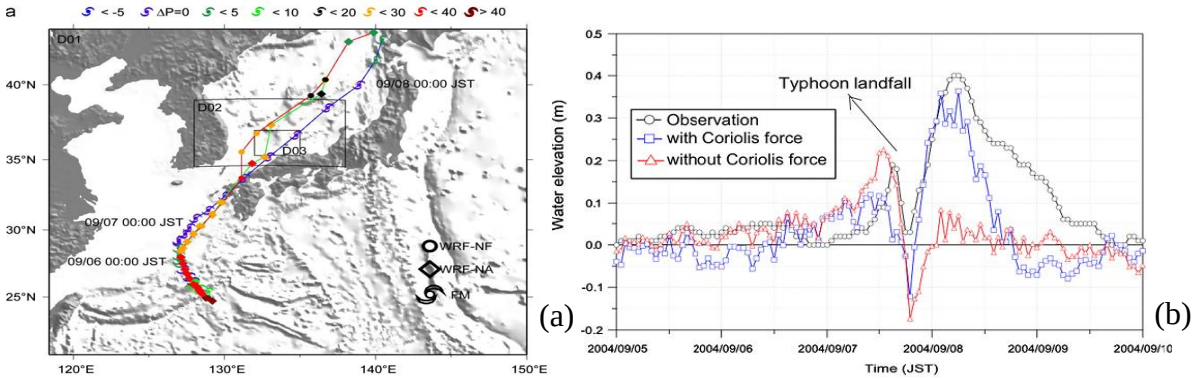

Figure 1. (a) -The track of Songda typhoon (9/2004) and (b) -Fluctuating water levels at Tottori-Japanese coastal, 05-10/09/2004, (Sooyoul Kim et al., 2014).

The coastal area from Quang Ninh to Quang Binh are frequently affected by natural disasters including typhoon and storm surges. The topography of the shoreline is constantly divided with many estuaries, with many islands located beyond the sea. This has a great influence on hydrodynamics in general and storm surges in particular. Statistically, there were 37.8% of the storms occurred the East Vietnam sea to be landed on the coastal area from Quang Ninh to Quang Binh. Normally typhoons occur from June to October. Because the study area is an open sea with shallow and relaxed terrain, the coast is composed mainly of sand without embankments storms hitting this area are often strong, so storm surges are quite large. On the basis of the hourly water level measured data at some tide gauge stations in the period from 1960 to 2017, it is shown that there are 101 typhoon caused high storm surges in this area, such as typhoon Niki (8/1996) causing a 1.6 m at Hon Dau station; typhoon Becky (8/1990) causing a 1.7m at Hon Ngu station, (see Figure 2a, b).

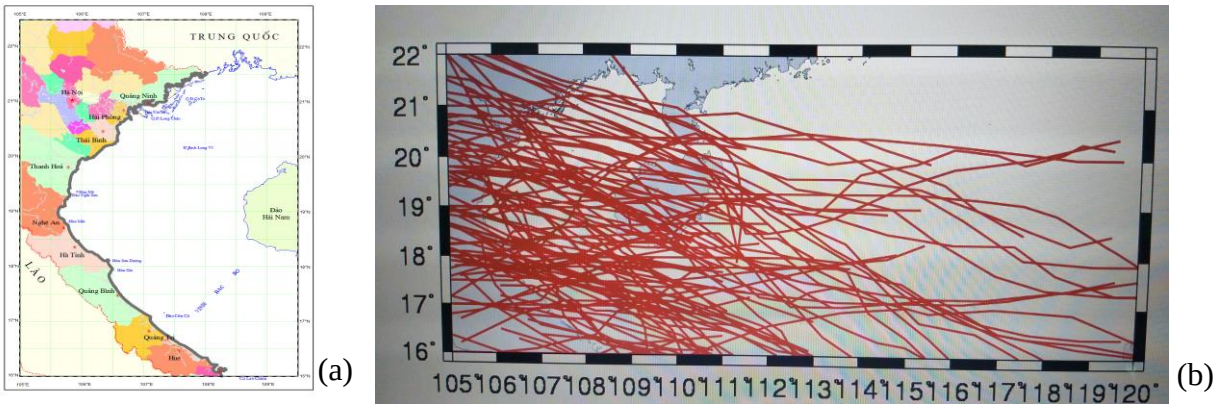

Figure 2. (a)-Research area and (b)- tracks of the selected storms that cause surges ≥ 0.5m in the period 1960-2017 from Quang Ninh to Quang Binh.

2. Data and methodology

2.1. Data collection

Storm data (including time, the location of the storm center, the direction storm's movement, air pressure depression at storm center, maximum wind speed, radius of max wind speed) from 1960 to 2017 are collected from the US besttrack (http://www.weather.uniys.com) and Japanese JMA site (http://www.jma.go.jp/en/typh).

Hourly measured water level data at Hon Dau, Hon Ngu and Son Tra stations are collected from the Center of the Oceanography, (see Table 1).

Table 1. Locations and time of hourly measured seawater level data

Station name	Longitude [degree]	Latitude [degree]	Year of observation
Hon Dau	106º48.00'	20º40.00'	1960-2017
Hon Ngu	105º46.00'	18º48.00'	1961-2017
Son Tra	108º13.00'	16º06.00'	1982-2017

2.2. Separating seawater level rises from measured data

The seawater level data measured at the coastal hydrographic stations are essentially a combination of two components: astronomical tides (ξ_t) and seawater level rises (ξ_{nd}). With the purpose of investigating separately the characteristics of seawater level rises, it is necessary to separate the seawater level rises component from the total seawater level value. Furthermore, the pure seawater level rises values are also used to calibrate and validate numerical models, to evaluate the role of seawater level rises in the individual storm case. At locations having suitable data series of measured seawater levels, the tidal harmonic constants can be calculated by the least square method, detailed in (Pham Van Huan et al., 2009), (Dinh Van Manh et al., 2014), then the astronomical tide level at any moment is easily specified (Pham Tri Thuc et al., 2018). Therefore, seawater level rises value at the any moment (t) will be determined by the following formula:

$$\xi_{nd}(t) = \xi_d(t) - \xi_t(t) \quad (1)$$

where, $\xi_d(t)$ is the measured seawater level at time (t), $\xi_t(t)$ is the astronomical tidal at time (t), $\xi_{nd}(t)$ is the seawater level rises.

A program (called by DBtrieu) to get the seawater rise from the hourly measured seawater level data or to predict the tide levels at a location was written in Fortran 90 language with the following flow chart, (see Figure 3). This program is developed on the basis of the tide harmonic constants by Ng. V. Moi., 2002 in Institute of Mechanics.

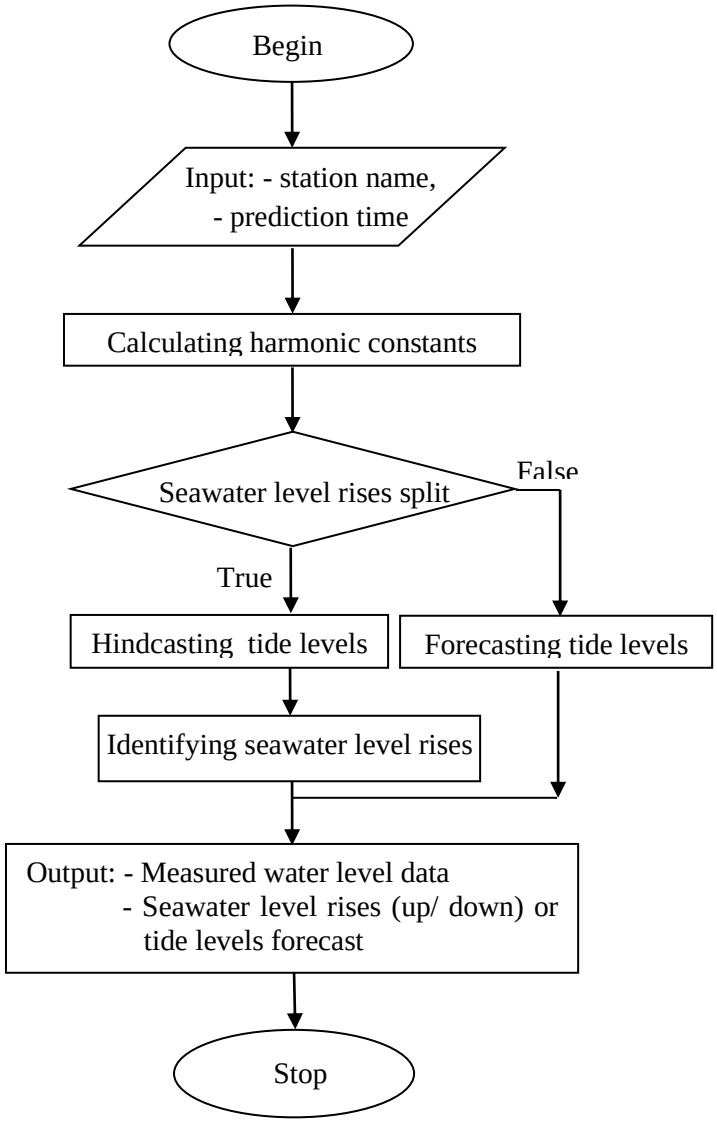

Figure 3. Flow chart of BDtrieu program

2.3. Identifying the landfall time of storms

It is defined that the landfall time of a storm is the time, the storm center is moved across the coast and landed on the main land. Therefore, the landfall times of storms actived and landed in the study area in the 1960-2017 period are identified by the moment when the storm track met the shoreline. Because the storm tracks are built up by locations of storm centers at the standard observation times only (at 1^h, 7^h, 13^h, 19^h), so the landfall times are by the linear interpolation method.

3. Results and discussion

3.1. Occurrence of seawater level rises in Quang Ninh-Quang Binh coastal zone from 1960 to 2017

From 1960 to 2017, on the basis of the hourly observed seawater levels at the Hon Dau, Hon Ngu and Son Tra stations, there were 371 times of seawater level rises greater than 0.5m occurred (from now on the seawater level rises greater than 0.5m will be called by significant seawater rise). In which, at Hon Dau station, there were 101 times (occupied 27.2%), at Hon Ngu 236 times (63.6%) and at Son Tra 34 times (9.2%). The occurrence frequencies of significant seawater rise with different magnitude ranges at Hon Dau, Hon Ngu and Son Tra stations are shown in Table 2 and Figure 4. In the investigated period, occurrence times of significant seawater rise with the magnitude greater than 0.5m at Hon Ngu station are much more than that at Hon Dau and Son Tra, however, the occurrence times with the values greater than 1.5m are the same, no time at Son Tra station.

Table 2. Occurrence frequency of significant seawater rise in magnitude range at Hon Dau, Hon Ngu and Son Tra stations in the 1960-2017 period

Station name	0.5 - 1.0 **m**		1.0 - 1.5 **m**		≥ 1.5 **m**	
	occurrence times	Percent **[%]**	occurrence times	Percent **[%]**	occurrence times	Percent **[%]**
Hon Dau	77	76.2	21	20.8	3	3.0
Hon Ngu	221	93.6	12	5.1	3	1.3
Son Tra	31	91.2	03	8.8	0	0.0

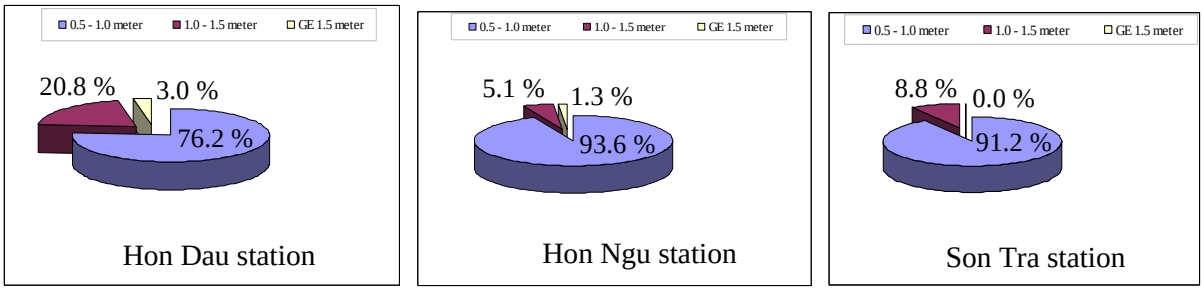

Figure 4. Occurrence frequency of significant seawater rise at Hon Dau, Hon Ngu and Son Tra stations

In combination of seawater levels and weather data, it is shown that the water rises in the study coastal areas are caused by storm (or tropical depression), then caused by monsoon or monsoon combined with circulation after the storm activity, seismic… In statistics, from 1960 to 2017 at Hon Dau, Hon Ngu and Son Tra stations, had a total of 154 times of significant seawater rise related to storm's activity (41.5%), the remain rises unrelated to storm or tropical depression activity are 217 times of significant seawater rise (58.5%). At Hon Dau station, there were 64 times of significant seawater rise due to storm (63.4%) and the remaining 37 times of significant seawater rise (36.6%) were due to monsoon or unknown causes. At Hon Ngu station, the significant seawater rise due to storm were 65 times (27.5%), the remaining 171 times due to other causes (72.5%). At Son Tra station, the significant seawater rise due to storm were 25 times (73.5%), the remaining 9 times due to

other causes (26.5%) as shown in Table 3 and Figure 5.

Table 3. Original causes relative to surges at Hon Dau, Hon Ngu and Son Tra stations

Original cause	Hon Dau station		Hon Ngu station		Son Tra station	
	occurrence times	Percent **[%]**	occurrence times	Percent **[%]**	occurrence times	Percent **[%]**
storm	64	63.4	65	27.5	25	73.5
monsoon and others	37	36.6	171	72.5	9	26.5

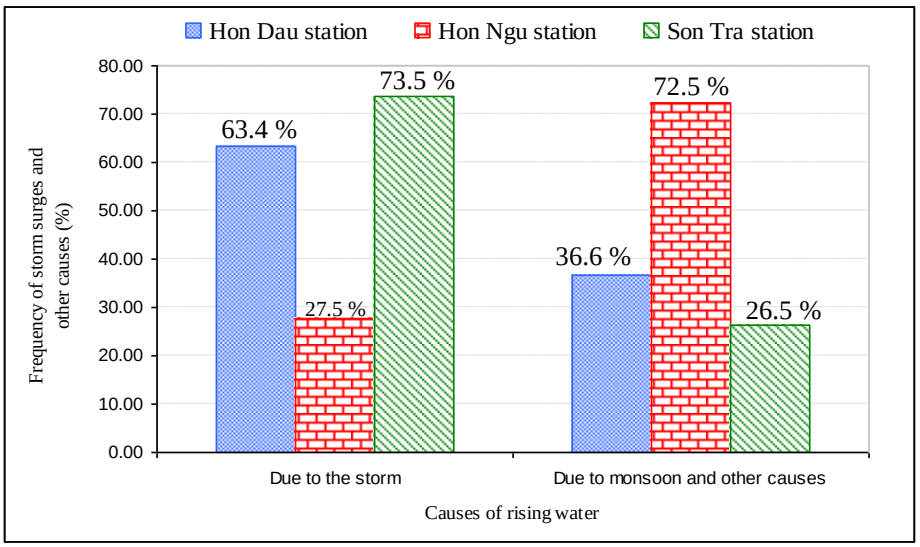

Figure 5. Frequency of original causes relative to surges at the Hon Dau, Hon Ngu and Son Tra stations in the 1960-2017 period

Significant seawater rise occur at the same time with high tides will flood the whole area. Statistics show that from 1960 to 2017, in the North coastal area, there were 73 times of significant seawater rise appear during high tide, equivalent to 19.7%; 136 times appear during medium tide, equivalent to 36.7% and 162 times appear during low tide, equivalent to 43.7%. In which, at Hon Dau station, the significant seawater rise occur during high tide are 18.8%; during medium tide are 30.7% and during low tide are 50.5%. At Hon Ngu station, the significant seawater rise occur during high tide are 18.2%; during medium tide are 40.7% and during low tide are 41.1%. At Son Tra station, the significant seawater rise occur during high tide are 32.3%; during medium tide are 26.5% and during low tide are 41.2% as shown in Table 4.

Table 4. The occurrence frequency of significant seawater rise during high tide or low tide at Hon Dau, Hon Ngu and Son Tra stations in the 1960-2017 period

Station name	High tide		Medium tide		Low tide	
	occurrence times	Percent **[%]**	occurrence times	Percent **[%]**	occurrence times	Percent **[%]**
Hon Dau	19	18.8	31	30.7	51	50.5
Hon Ngu	43	18.2	96	40.7	97	41.1
Son Tra	11	32.3	9	26.5	14	41.2

In almost cases, the significant seawater rise occurred immediately, 1 or 2 hours earlier or later the storm landfall time. However, in rarely cases (depending on movement directions relative to the coast, storm tracks, or due to the circulation after the typhoon combined with the monsoon), the significant seawater rise could occur several hours later the landfall time. In the 1960-2017 period, in the coastal area from Quang Ninh to Quang Binh there were 16 storms caused significant seawater rise later than 4 hours since their landfall time, especially, 20 hours later by storm Willie-96 at Hon Ngu station, as shown in Table 5. It is noted that in these cases, the landfall locations of storms were in the north or in a long distance to observation point.

Table 5. Significant seawater rise occurred after the storm landfall time in the 1960-2017

Storm name	Landfall location	Landfall time	Max value of seawater rise **[m]**	Occurred moment **[hour]**	Lasting Time **[hour]**	Occurred location
CHARLOTTE-62	Thanh Hoa	17^h 22/09/1962	0.77	4	4	Hon Ngu
N^0 03-62	Thua Thien Hue	09^h 27/09/1962	0.61	8	8	Hon Ngu
FAYE-63	Nam Dinh	05^h 09/09/1963	0.85	4	6	Hon Dau
WINNIE-64	Quang Ninh	04^h 03/07/1964	1.11	4	13	Hon Dau
			0.71	8	4	Hon Ngu
CLARA -64	Ha Tinh	07^h 08/10/1964	0.66	7	6	Hon Dau
NADINE-65	Nghe An	16^h 18/08/1965	1.12	7	11	Hon Ngu
HARRIET-71	Ninh Binh	22^h 07/07/1971	0.61	12	4	Hon Ngu
VERA-83	Quang Ninh	06^h 18/07/1983	1.16	4	10	Hon Dau
N^0 01-83	Thanh Hoa	23^h 03/10/1983	0.69	6	7	Hon Ngu
WAYNE-86	Thai Binh	01^h 06/09/1986	0.63	8	4	Hon Dau
ANGELA-89	Quang Binh	17^h 10/10/1989	0.62	11	7	Hon Dau
ZEKE-91	Quang Ninh	03^h 14/07/1991	1.03	4	9	Hon Dau
			0.61	7	5	Hon Ngu
FRANKIE-96	Nam Dinh	04^h 24/07/1996	0.79	5	6	Hon Ngu
WILLIE-96	Nghe An	00^h 22/09/1996	0.75	20	3	Hon Ngu
KAEMI-00	Da Nang	15^h 22/08/2000	1.58	5	7	Hon Ngu
KALMAEGI-14	Quang Ninh	22^h 16/09/2014	0.98	4	14	Hon Dau
			0.64	7	5	Hon Ngu

On the other hand, some storms could cause a significant seawater rise much earlier than the time of landfall. In the history data, there were 26 surges occurred several hours before the storm landfall time as shown in Table 6.

Table 6. Significant seawater rise occurred before the storm landfall time in the 1960-2017 period

Storm name	Landfall location	Landfall time	Max value of seawater rise **[m]**	Occurred moment **[hour]**	Lasting Time **[hour]**	Occurred location
BESS-68	Thua Thien Hue	22^h 05/09/1968	0.73	9	4	Hon Ngu
N^0 03-70	Ha Tinh	07^h 19/08/1970	0.72	6	4	Hon Ngu
HARRIET-71	Ninh Binh	22^h 07/07/1971	0.65	10	5	Hon Ngu
NANCY-82	Thanh Hoa	13^h 18/10/1982	0.71	16	15	Son Tra
N^0 01-83	Thanh Hoa	23^h 03/10/1983	0.89	4	18	Hon Ngu
LEX-83	Quang Binh	11^h 26/10/1983	0.75	1	25	Son Tra

Storm name	Landfall location	Landfall time	Max value of seawater rise **[m]**	Occurred moment **[hour]**	Lasting Time **[hour]**	Occurred location
CECIL-85	Thua Thien Hue	04h 16/10/1985	0.76	5	6	Son Tra
BETTY-87	Thanh Hoa	15h 16/08/1987	0.71	12	11	Son Tra
CARY-87	Nghe An	20h 22/08/1987	0.53	10	3	Son Tra
			0.75	12	11	Hon Dau
IRVING-89	Thanh Hoa	06h 24/07/1989	0.96	3	24	Hon Ngu
			0.54	27	7	Son Tra
BRAIN-89	Nghe An	16h 03/10/1989	0.62	10	5	Son Tra
ANGELA-89	Quang Binh	17h 10/10/1989	0.75	10	6	Hon Dau
			0.71	7	20	Son Tra
DAN-89	Ha Tinh	20h 13/10/1989	0.69	6	17	Son Tra
N0 06-90	Thua Thien Hue	01h 19/09/1990	0.99	5	22	Son Tra
EVE-99	Quang Binh	08h 20/10/1999	0.63	9	18	Son Tra
KAEMI-00	Da Nang	15h 22/08/2000	1.07	1	6	Hon Ngu
			0.64	1	12	Son Tra
VICENTE-05	Ha Tinh	15h 18/09/2005	0.54	8	5	Son Tra
KAITAK-05	Ha Tinh	13h 02/11/2005	0.75	17	15	Son Tra
NALGAE-11	Ha Tinh	19h 05/10/2011	0.59	23	17	Son Tra
WUTIP-13	Ha Tinh	16h 30/09/2013	0.63	6	6	Son Tra
VAMCO-15	Quang Nam	20h 14/09/2015	0.68	6	4	Son Tra
DOKSURI-17	Ha Tinh	11h 15/09/2017	0.54	8	5	Son Tra

3.2. Significant seawater rise appears before and after the storm landfall time

According to the statistics in table 5, there are 3 storms causing surges at both Hon Dau and Hon Ngu stations. There storm surges occur from 4 to 8 hours after the landfall, the duration of significant seawater rise from 4 to 14 hours, magnitude of from 0.6 to 1.1m. These storms landed in Quang Ninh caused high storm surges of over 1.0m, the long existence time from 9 to 14 hours occur at Hon Dau station several hours after the landed time. Later (about 3, 4 hours) the lower surges occurred in Hon Ngu station as shown in Table 5 and Figure 6a,b.

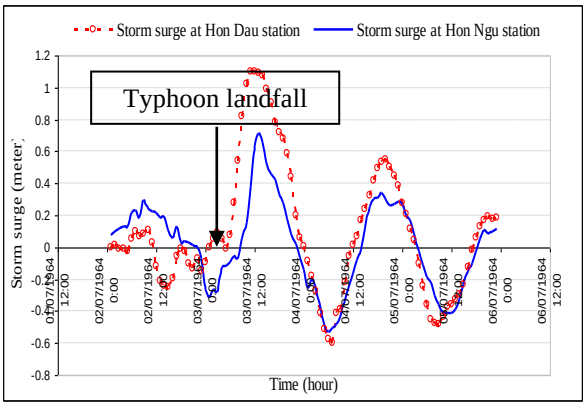

(a)

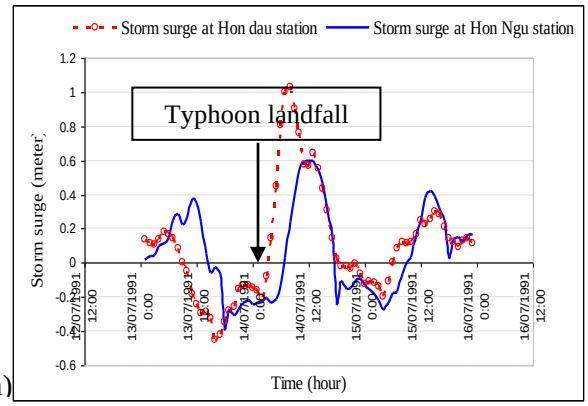

(b)

Figure 6. The occurred time and magnitude of storm surges due to: (a)-Typhoon Winnie-64 hit on Quang Ninh and (b)-Typhoon Zeke-91 hit on Quang Ninh at Hon Dau and Hon Ngu stations

The after storm surge in typhoon Kalmaegi-14 hit on Quang Ninh, at low tide and did not cause flooding at that time. However, 6 hours later, the circulation due to the storm combined with the South-West monsoon caused the surge up to 1.0m, in about 12 hours; this storm surges

combined with high tide and high waves had caused severe flooding in the coastal area of Do Son-Hai Phong as shown in Figure 7a. Typhoon Nadine-65 hit on Nghe An coastal at the high tide time and caused a high and long surge in Hon Ngu station as shown in Figure 7b.

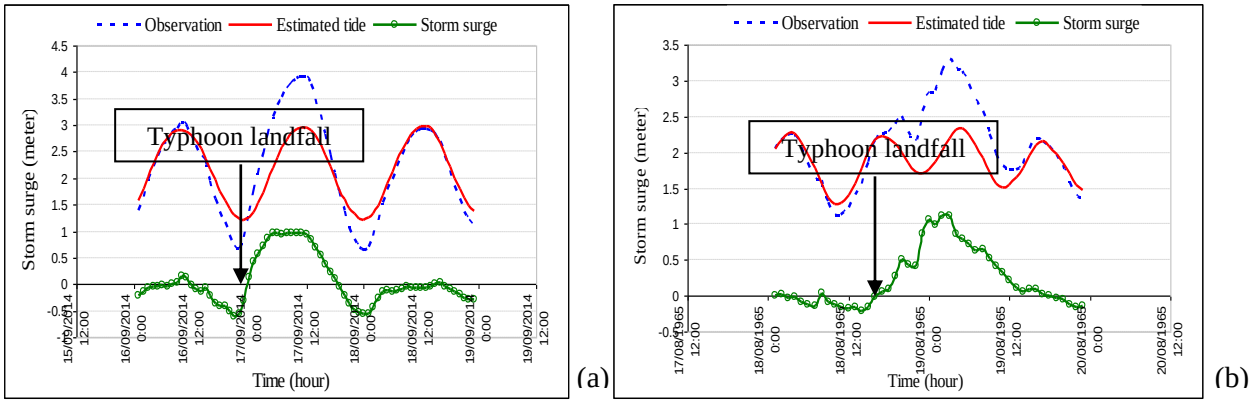

Figure 7. After-storm surges: (a)-at the Hon Dau station due to typhoon Kalmaegi-14 hit on Quang Ninh and (b)-at the Hon Ngu station due to typhoon Nadine-65 hit on Nghe An

Typhoon Bess-68 hit on Thua Thien Hue, caused the significant seawater rise at 9 hours before the landfall time and lasting for 4 hours. Typhoon Cecil-85 hit on Thua Thien Hue, caused the significant seawater rise at 5 hours before the landfall time and lasting for 6 hours as shown in Figure 8a,b.

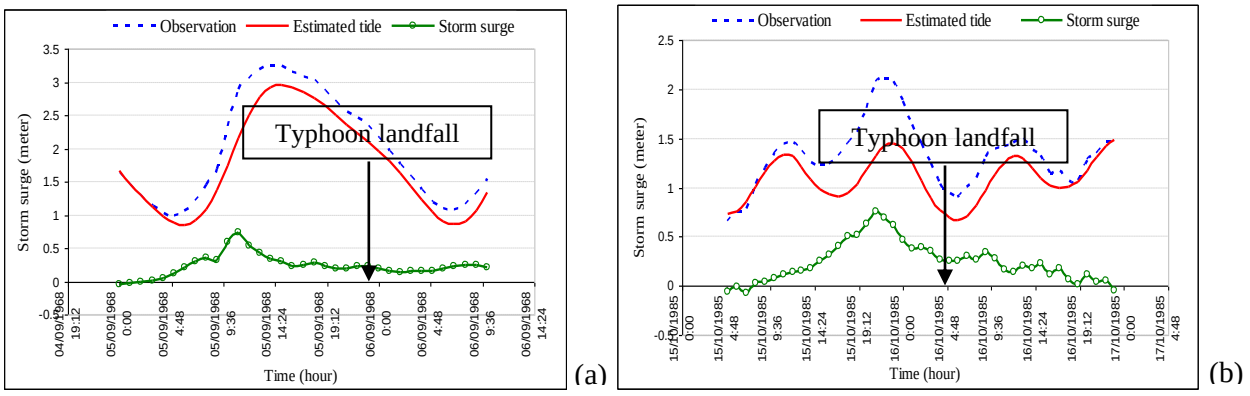

Figure 8. Before-storm surge: (a)-at the Hon Dau station due to typhoon Bess-68 hit on Thua Thien Hue and (b)-at the Son Tra station due to typhoon Cecil-85 hit on Thua Thien Hue

3.3. Significant seawater rise appears during high tide or low tide

Historically, many storms causing significant seawater rise at the high tide had left very serious consequences. Such as typhoon Kalmaegi-14 hit on Quang Ninh, the surge combined with high tide (see Figure 7a) and high waves have caused severe flooding in the coastal area of Do Son-Hai Phong. Typhoon Washi-05 hit on Nam Dinh, causing storm surge of 1.2m in the high tide (see Figure 9a), so in the coastal area of Hai Phong, the total water level of 4.2m measured. Typhoon Warren-81 hit on Ninh Binh, also caused storm surge of 1.2m, but at the low tide (see Figure 9b), the total water level in Hai Phong was only 2.5m.

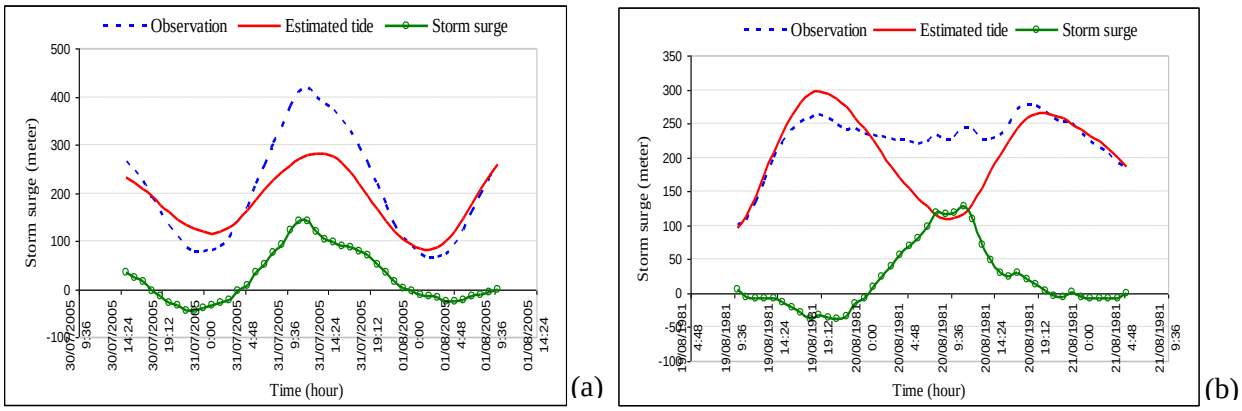

Figure 9. (a)- The significant seawater rise at the Hon Dau station due to typhoon Washi-05 hit on Nam Dinh and (b)-at the Hon Dau station due to typhoon Warren-81 hit on Ninh Binh

3.4. Non-storm significant seawater rise

The statistical results show that, a apart from significant seawater rise by typhoon, there are many causes of other reason, such as the significant seawater rise occurred on 01-03/01/1965 at Hon Dau station or significant seawater rise ocurred on 17-19/02/2000 at Hon Ngu station as shown in Table 7 and Figure 10a,b (but not any evidence of typhoon or tropical depression revealed).

Table 7. Non-storms significant seawater rise at Hon Dau and Hon Ngu stations

Time	Hon Dau station		Hon Ngu station	
	Max value of seawater level rises **[m]**	Occurred moment **[hour]**	Max value of seawater level rises **[m]**	Occurred moment **[hour]**
07^h - 13^h 01/01/1965	0.864	7		
08^h - 13^h 02/01/1965	0.987	6		
11^h - 13^h 03/01/1965	0.908	3		
11^h - 16^h 17/02/2000			0.579	6
12^h - 17^h 18/02/2000			0.646	6
13^h - 19^h 19/02/2000			0.701	7

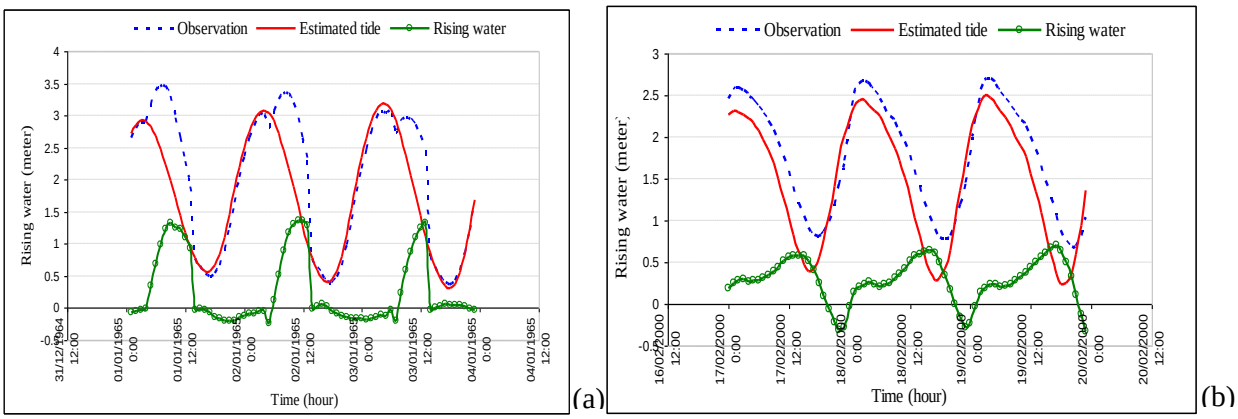

Figure 10. Non-storms significant seawater rise: (a)-at the Hon Dau station on 01-03/01/1965 and (b)-at the Hon Ngu on 17-19/02/2000

4. Conclusions

1. A program to get seawater level rises from the observed water level data was written in Fortran 90 language. Statistics result for data in the 1960-2017 period, from Quang Ninh to Quang Binh show that, there were a total of 371 times of significant seawater rise; including 154 times related to the activity of typhoon or tropical depressions (occupied 41.5%); the remaining 217 times due to monsoon and other causes (occupied 58.5%).

2. At Hon Dau station, in 57 years there were 101 times of significant seawater rise. The average annual are 1.8 times/year. In which 76.2% of significant seawater rise from 0.5 to 1.0m; from 1.0 to 1.5m is 20.8%; greater than 1.5m is 3.0%.

3. At Hon Ngu station, in 56 years there were 236 times of significant seawater rise. The average annual are 4.2 times/year. In which 93.6% of significant seawater rise from 0.5 to 1.0m; from 1.0 to 1.5m is 5.1%; greater than 1.5m is 1.3%.

4. At Son Tra station, in 35 years there were 34 times of significant seawater rise. The average annual are 1.0 time/year. In which 91.2% of significant seawater rise from 0.5 to 1.0m; from 1.0 to 1.5m is 8.8%; without of significant seawater rise over 1.5m.

5. The most times of significant seawater rise at Hon Ngu; meanwhile, the significant seawater rise over 1.5m at Hon Dau station is the most.

References

Pham Van Huan and Hoang Trung Thanh (2009). *Detailed diagram of tidal conditioning analysis*. Science magazine Hanoi National Universty. Vol 25, Nº 1S, pp. 66-75.

Dinh Van Manh and Do Ngoc Quynh et al (2014). *Calculating sea level elevation for design of coastal construction in Vietnam*. Science and Technology publishing house, Ha Noi.

Nguyen Van Moi (2002). *Tide harmonic analysis by the least square method and its applications for Vietnam sea area.* Master thesis on fluid mechanics. Institute of Mechanics.

Pham Tri Thuc and Dinh Van Manh et al (2018). *Typical storm surge due to the Northern coastal region.* Collection of National mechanical engineering conferences, Nº21, pp. 762-772.

Sooyoul Kim and Yoshiharu Matsumi et al (2014). *Storm surges along the Tottori coasts following a typhoon*. Ocean Engineering, Vol 91, pp. 133-145.

Website http://www.weather.uniys.com

Website http://www.jma.go.jp/en/typh

The 5th International Conference on Engineering Mechanics and Automation (ICEMA 5)
Hanoi, October 11÷12, 2019

Dynamic Investigations of Two-Body Mechanical System an Airship Towed by a Vessel with Automatic Control of Tension Force and Altitude Stabilization

Tran Duy Duyen[a,*], Nguyen Duc Cuong[b]

[a] *Air Defence-Air Force Academy, duyduyen85@gmail.com*
[b] *Vietnam Aerospace Association, cuongnd45@gmail.com*

Abstract

The air transportation system using lighter-than-air vehicle (airship) towed by a vessel allows a significant increase in the rate of payload on the airship. The airship is equipped with four or more control rotors (quadrotor/multirotor) to stabilize the flight altitude, to improve the stability of the airship when affected by the wind, at the same time the rotors ensures vertical take-off and landing. This transportation system promises to create a highly efficient, safe and environmental friendly flight vehicle, especially when it is used to carry sightseeing tourists [1]. The paper [3] presented the dynamic model of the two-body mechanical system "an airship towed by a vessel" in windy conditions and confirmed the feasibility of the automatic controller to maintain the tension of the towing rope to avoid jerk phenomenon leading to structural damage. However, the article [3] has not considered the automatic altitude stabilization and the "pendulum" model including the payload and quadrotor hung below the balloon. This paper develops the aforementioned dynamic model when the flight altitude is stabilized and a "pendulum" model is considered. The model is a simplified three-body system. The investigations results on this computerized model allow us to make useful recommendations for designing new scheme of the airship.

Key Words: dynamics and control, an airship towed by a vessel, airship with sightseeing tourists.

1. Introduction

The air transportation system using lighter-than-air vehicle (airship) towed by a vessel that allows a significant increase in the rate of payload on the airship. The airship is equipped with four or more control rotors (quadrotor/multirotor) to provide the flight altitude stability of the airship, to ensure altitude stability in cruise flight, at the same time the rotors ensure vertical take-off and landing. This transportation system promises to create a highly efficient, safe and environmentally friendly flight vehicle, especially when it is used to carry sightseeing tourists [1]. Figure 1.1 depicts the major components of the airship of new scheme.

The paper [2] has presented the a dynamics model of “an airship towed by a vessel” with the impact of wind of different directions and has shown that it is necessary to have a controller that automatically maintains the tension of the towing rope to avoid "jerk" phenomenon leading to structural damage.

The paper [3] has presented the a dynamics model of “an airship towed by a vessel” with the

automatic control of the winch to maintain tension which allows to determine the main requirements for the control system: The inertia of the actuator should not to be too large and the system must have warning when the towing rope length approaches the limits L_{cpmax} and L_{cpmin}. Investigations on the above mentionned model also show that although there is an automatic tension-maintaining device, there is still a need of an elastic element to reduce the requirements for fast reaction of the actuator.

Figure 1.1. The airship for tourism of new scheme: The sphere with light gas (helium gas) (1) pulled by a vessel (2) via the smart winch and towing system (3). a quadrotor / multirotor (4) is hung under the sphere and is connected with passenger compartment (5), a safety toroidal airbag (6) is connected at the bottom .

This paper presents the a dynamics model of an airship towed by a vessel with the automatic control of the winch to maintain tension and altitude stabilization. The dynamic model of mechanical system is considered closer to reality: the sphere with light gas and hung quadrotor/mulltirotor (MR) connected to the payload . The model is a simplified three-body mechanical model: a vessel pulls a sphere with a "pendulum" . After presenting a dynamic model with two automatic control systems (tension and altitude stabilization), the paper presents some investigation results to determine the validity of the results and proposes useful recommendations for designing of the airship of new scheme.

2. Content

2.1. A Dynamic model of the mechanical system

The paper [2] has presented the a dynamics model of an airship towed by a vessel with the impact of wind from different directions and some calculation assumptions such as: considering vessel and airship are two mass points that are linked together by a rope with elastic element,the vertical movement of the system is not considered, the longitudinal axis of airship always is in the direction of the airspeed vector (angle of sliding β_a=0).

The paper [3] investigates a dynamics model of an airship towed by a vessel with automatic tension control is developed on the basis of the paper [2]. The only difference is that this model has a winch control system to maintain the tension of the rope within a certain range (figure 2.1), This system is modeled as an inertia element with a time constant of T_{qt} in order to simulate latency due to the inertia of the winch.

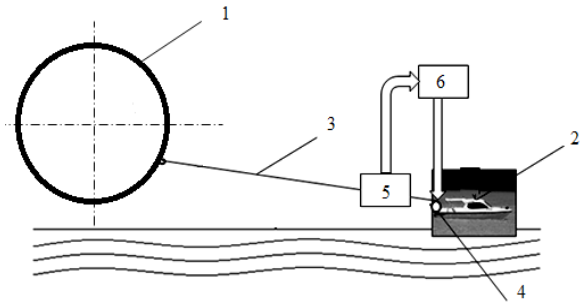

Figure 2.1. Diagram of an airship towed by a vessel with automatic tension control, where : 1 – sphere; 2 – vessel; 3 – rope; 4 – winch; 5 – tension sensor ; 6 - The microcontroller creating a command that fits the tension measurement sensor signal.

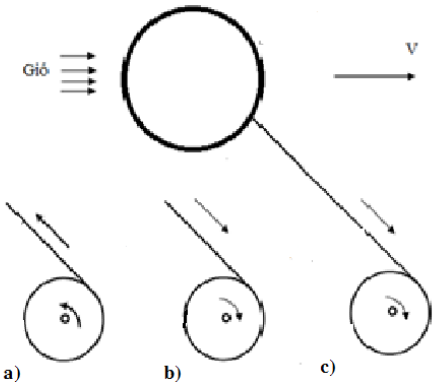

Figure 2.2. The winch changes the natural length to maintain the tension of the rope, a) taking off, b) landing and c) when the wind is downward

The physical essence of the winch control system that maintains the desired tension (T_{mm}) of the

rope is to maintain the desired elongation (ΔL_{mm}) corresponding to the given tension T_{mm}. This is done by changing the length of the rope by releasing the rope if the tension of the rope $T>T_{mm}$ or towing the rope if $T < T_{mm}$ (figure 2.2). However, the winch has an inertia and is modeled in the form of an inertia element with a time constant (T_{qt}) to simulate that the actual natural length of the rope (L_{0tt}) is not the desired one. The difference between desired natural length (L_{0mm}) and L_{0tt} (difference L_{0tt}- L_{0mm}) increase or decrease compared to the desired elongation (ΔL_{mm}) to increase or decrease the desired tensile force. Therefore, the process of maintaining tension of the rope is greatly influenced by the inertia of the winch (via parameter T_{qt}). In addition, the stiffness parameter k of the rope significantly affects the process of maintaining tension.

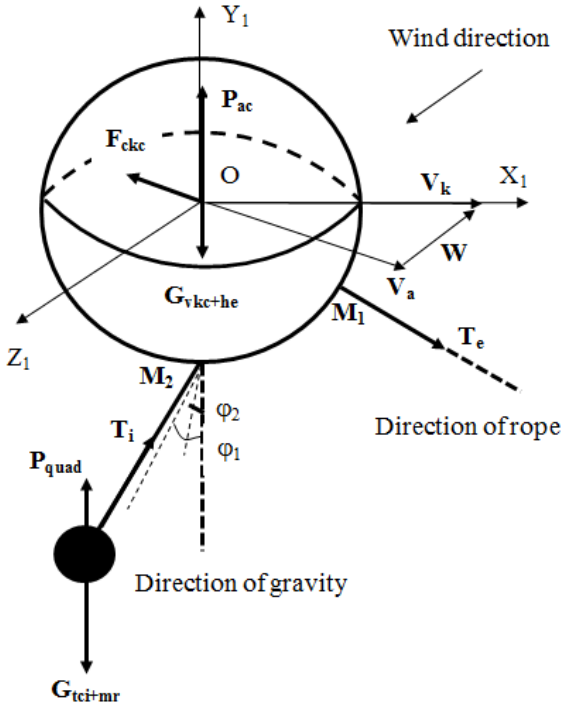

Figure 2.3. Diagram of the forces acting on the sphere, the pendulum, and some parameters.

This mechanical system is characterized by a stable attitude of the sphere and a "pendulum" around the nadir direction because the weight of the payload and MR is quite large compared to the weight of the sphere and the buoyancy force is always vertical (similar to the stability of a ship with ballast loading at the bottom of the ship, or as a tumbler). Moreover, because the external torques acting on the sphere are relatively small (due to the forces having the directions passing through the center of symmetry of the sphere, or oscillating near the center of symmetry), the rotation of the sphere around the center of symmetry is slow enough. We can assume that the sphere moves together with the pendulum as as one whole body, thus deducing the acceleration of motion of the whole body is the same of the hanging point M_2 (fig. 2.3). On that basis, the approximate established angles of the "pendulum" is compared with the nadir direction φ_1 (deviation in longitudinal plane X_1OY_1) and φ_2 (deviation in cross plane Z_1OY_1) corresponding to the acceleration of the hanging point M_2. It is more correct to consider the whole movement process of the "pendulum", however, because the airship itself serves the sightseeing and automatically maintains tension, it will move smoothly and accelerations of the hanging point M_2 are rather small than the acceleration of gravity, with the weight of "pendulum" (thousands of N) so the angles $|\varphi_1|$ and $|\varphi_2|$ can be considered small and is set immediately corresponding to the value of the hanging point acceleration. The controlling force of MR is assumed to act always in the vertical direction (not considering the inclination of MR to control the trajectory).

With the above mentionned assumptions, we have the system of equations of the simplified three-body mechanical system in the trajectory reference system as follows:

– For the vessel:

$$\begin{cases} m_{cn}\left(\frac{dV_{kcn}}{dt}\right) = P + T_{xcn} - F_{xcn} \\ -m_{cn}V_{kcn}\left(\frac{d\Psi_{cn}}{dt}\right) = T_{zcn} + F_{zcn} \\ \frac{dX_{cn}}{dt} = V_{kcn}\cos\Psi_{cn} \\ \frac{dZ_{cn}}{dt} = -V_{kcn}\sin\Psi_{cn} \end{cases} \quad (2.1)$$

– For the sphere:

$$\begin{cases} m_{kc}\left(\frac{dV_{kkc}}{dt}\right) = T_{xkc} - F_{xkc} \\ +\left(P_{quad} + P_{ac} - G_{kc}\right)\sin\theta_{kc} \\ m_{kc}V_{kkc}\left(\frac{d\theta_{kc}}{dt}\right) = T_{ykc} + F_{ykc} \\ +\left(P_{quad} + P_{ac} - G_{kc}\right)\cos\theta_{kc} \\ -m_{kc}V_{kkc}\left(\frac{d\Psi_{kc}}{dt}\right)\cos\theta_{kc} = T_{zkc} + F_{zkc} \\ J_z\left(\frac{d\omega_z}{dt}\right) = \sum M_z \\ \frac{dX_{kc}}{dt} = V_{kkc}\cos\theta_{kc}\cos\Psi_{kc} \\ \frac{dY_{kc}}{dt} = V_{kkc}\sin\theta_{kc} \\ \frac{dZ_{kc}}{dt} = -V_{kkc}\cos\theta_{kc}\sin\Psi_{kc} \\ \frac{d\vartheta_{kc}}{dt} = \omega_z \end{cases} \quad (2.2)$$

– For the pendulum:

$$\begin{cases} \varphi_1 \approx \frac{-a_x}{g+a_y} \\ \varphi_2 \approx \frac{-a_z}{g+a_y} \end{cases} \quad (2.3)$$

Mechanical movement parameters meanings for details in the paper [2]. In addition, the deflection angles φ_1, φ_2 are calculated approximately according to the formula (2.3), in which: $a_x = \frac{dV_{kkc}}{dt}$ is tangential acceleration; $a_z = V_{kkc}\left(\frac{d\Psi_{kc}}{dt}\right)\cos\theta_{kc}$ is the normal acceleration in the z direction and $a_y \approx \frac{P_{quad}+P_{ac}-G_{kc}}{m_{kc}}$ is the normal acceleration in the y direction of the pendulum in the trajectory reference system. Particularly for the "sphere-pendulum" block, there is an additional rule to control altitude by MR:

$$P_{quad} = k_H(Y_{kc} - h_{bb}) + k_\theta\theta_{kc} \quad (2.4)$$

In which: h_{bb} is the desired flight cruising altitude, Y_{kc} is the altitude of the center of the sphere, k_H and k_θ are the control coefficients according to the altitude error and the trajectory angle θ_{kc} error.

The algorithm to maintain tension of the rope is presented in the article [3].

2.2. Simulation results and discussion

Input data:

– Input data of vessel:

Mass m_{cn}=2000[kg]; Drag coefficient: C_{xcn}=0.3; Cross-sectional area: S_1=2[m^2].

– Input data of sphere:

Diameter D=9[m]; Mass of the sphere envelope: m_{vkc}=145[kg]; Moment of inertia around the z-axis: J_z=3000[kgm^2]; Drag coefficient: C_{xkc}=0.3;

– Other metrics:

Mass of payload: m_{tci}=200[kg]; Mass of MR: m_{mr}=15[kg]; Density of air: ρ_{kk}=1.225[kg/m^3]; Density of water ρ_n=1000[kg/m^3]; Density of helium gas: ρ_{He}=0.17[kg/m^3]; Gravitational acceleration g=9.81[m/s^2]; Rope stiffness k=180[N/m]; flight altitude : h_{bb}=200[m]; The original natural length of the rope L_0=500[m]; Rated speed of vessel v_{dm}=7[m/s]; The desired tension: T_{mm}=625[N]; x_{M1}=4.12[m], y_{M1}= -1.8 [m], z_{M1}=0[m]; x_{M2}=0[m], y_{M2}=-4.5[m], z_{M2}=0[m]; k_H=-150 N/m; k_θ=-50 N/deg; Maximum MR control force: $P_{quadmax}$=400[N].

Methods, simulation tools:

Using numerical method with Rute-Kuta algorithm to solve the system of differential equations of motion of the system by Matlab software on computer based on the codes presented in the [2].

The time step dt for numerical solution is selected dt=step=0.004 to achieve high accuracy.

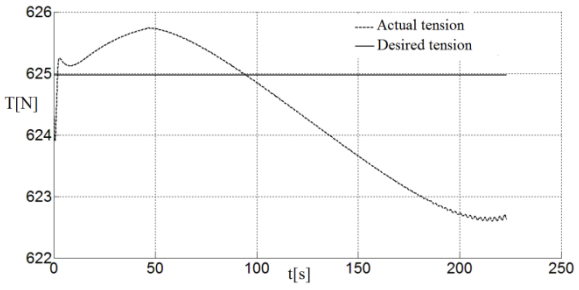

Figure 2.3. T=f(t) corresponds to T_{qt}=0.01s, East wind W=5m/s, F_n=-0.005m_{cn}g

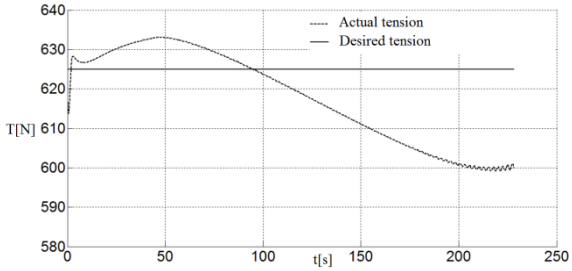

Figure 2.4. T=f(t) corresponds to T_{qt}=0.05s, east wind W=5m/s, F_n=-0.005m_{cn}g

Simulation results and comments:

– *Verification of the software:*

It's impossible to verify the software quantitatively except for organizing an expensive natural experiment, so we must to limit ourselves by some qualitative tests on computer. Figure 2.3 and Figure 2.4 are the graph of tensile force of the vessel-sphere with T_{qt}=0.01s, T_{qt}=0.05s in the same calculation condition. When T_{qt}=0.01s, the ability to track the desired tension is better than T_{qt}=0.05s. This qualitative result is entirely reasonable.

Figure 2.5 and Figure 2.6 are graphs of sphere flight altitude vs time corresponding to T_{qt}=0.01s, T_{qt}=0.05s. The results show that the altitude of the sphere in these two cases is basically unchanged and the ability to track the desired flight altitude is quite satisfactory (maximum deviation is less than 1m). This qualitative result is entirely appropriate because the MR control force is not operating at full capacity (in the simulation software, when the MR control force reaches its maximum value, the author stops the program).

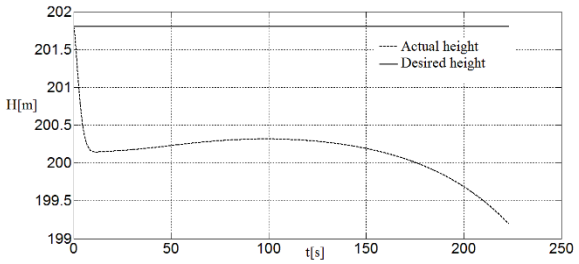

Figure 2.5. H=f(t) corresponds to T_{qt}=0.01s, East wind W=5m/s, F_n=-0.005m_{cn}g

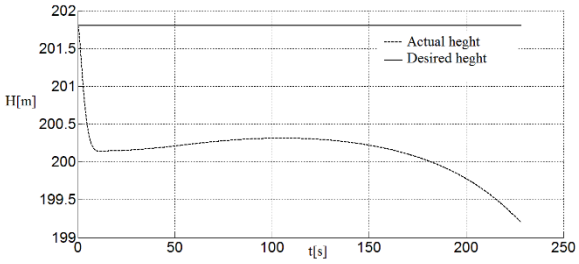

Figure 2.6. H=f(t) corresponds to T_{qt}=0.05s, East wind W=5m/s, F_n=-0.005m_{cn}g

Figure 2.7 and Figure 2.8, the path of vessel and the path of sphere vs the time corresponding to the East wind (the wind from the East) and the West wind W = 5m / s, the calculation conditions are the same.

The results showed that the sphere was "drifted" to the West when there was a East wind and "drifted" to the East when the West wind acting. The simulation results are perfectly reasonable.

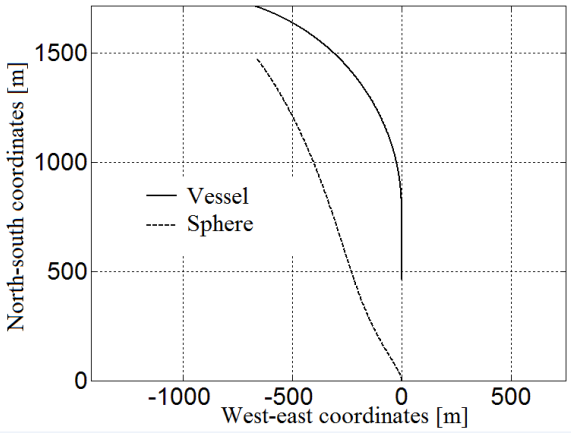

Figure 2.7. Orbit of vessel and Orbit of center of sphere corresponds to T_{qt}=0.01s, East wind W=5m/s, F_n=-0.005m_{cn}g

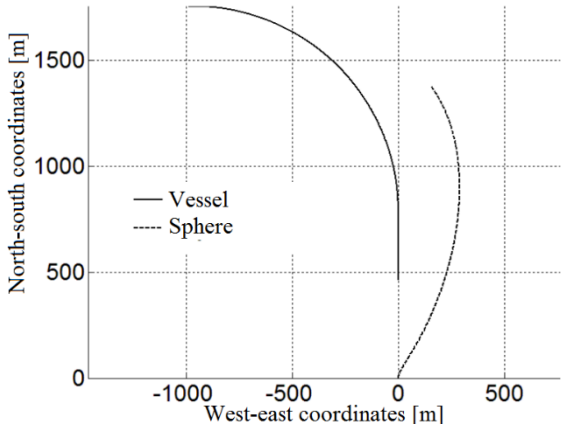

Figure 2.8. The path of vessel and the path of sphere corresponds to T_{qt}=0.01s, West wind W=5m/s, F_n=-0.005m_{cn}g

Through some of the above conclusions, it is possible that the modeling and calculation software can be trusted.

– *Some investigation results and comments*:

Comment 1:

Figures 2.9 to 2.17 are graphs showing the length of the vessel-sphere draw, the angle of the rope against the horizontal plane and the MR control

force is time dependent in the case of downwinds, normal force effect on different vessel (round vessel with different radius).

When there is a strong downwind W=5m/s or when the vessel turns with a small radius (the normal force F_n=-0.02m_{cn}g corresponding to R=250 m, the reduced length of the rope (Figure 2.9, Figure 2.12) will cause the angle between the direction of the rope and the horizontal plane to increase (Figure 2.10, Figure 2.13), resulting in an increase in the pull-down component force T_y, forcing the MR control force to increase the lift (Figure 2.11, Figure 2.14). However, when P=$P_{quadmax}$=400N, no further increase is available, the altitude will decrease to 0, it's quite dangerous. If the turning radius wider than R = 1000m corresponding to F_n=-0,005m_{cn}g, this phenomenon does not occur. (Figure 2.15, Figure 2.16, Figure 2.17). ***Thus, it is necessary to limit the minimum length of the rope from the condition of maximum MR control force $P_{quadmax}$.***

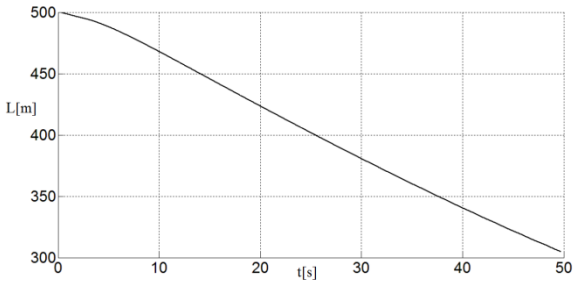

Figure 2.9. L=f(t) corresponds to T_{qt}=0.01s, downwind W=5m/s, F_n=-0.005m_{cn}g

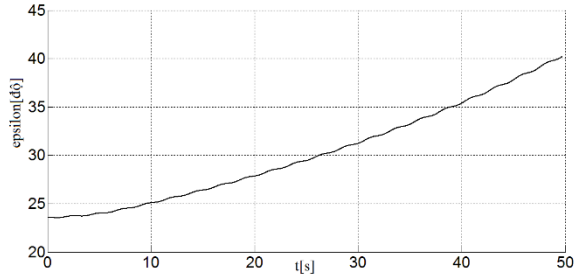

Figure 2.10. ε_y=f(t) corresponds to T_{qt}=0.01s, downwind W=5m/s, F_n=-0.005m_{cn}g

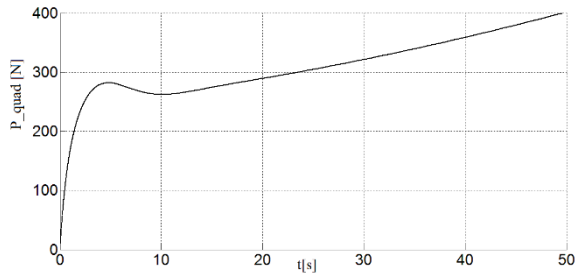

Figure 2.11. P_{quad}=f(t) corresponds to T_{qt}=0.01s, downwind W=5m/s, F_n=-0.005m_{cn}g

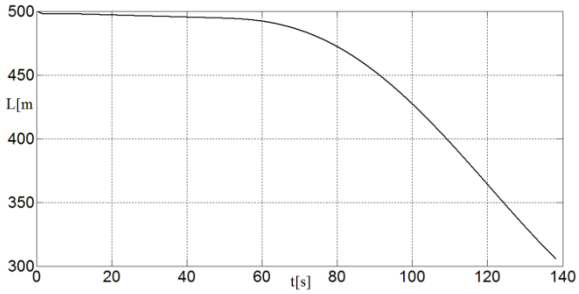

Hình 2.12. L=f(t) corresponds to T_{qt}=0.01s, wind W=0 m/s, F_n=-0.02m_{cn}g

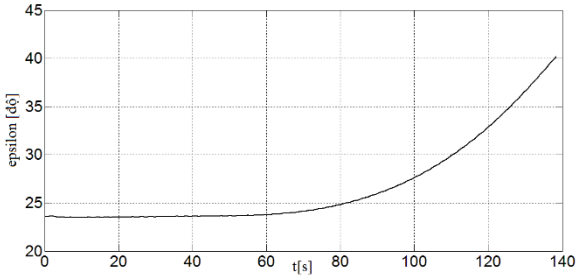

Figure 2.13. ε_y=f(t) corresponds to T_{qt}=0.01s, wind W=0m/s, F_n=-0.02m_{cn}g

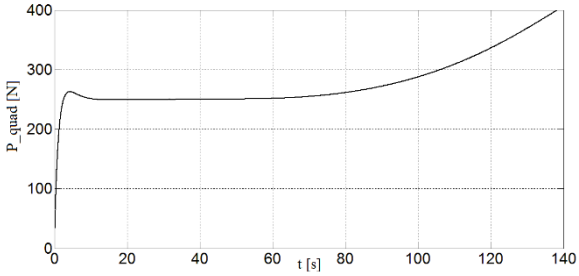

Figure 2.14. P_{quad}=f(t) corresponds to T_{qt}=0.01s, wind W=0m/s, F_n=-0.02m_{cn}g

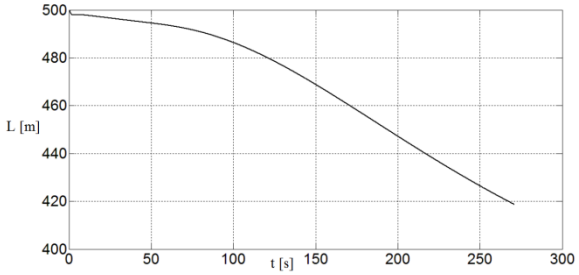

Figure 2.15. L=f(t) corresponds to T_{qt}=0.01s, wind W=0 m/s, F_n=-0.005m_{cn}g

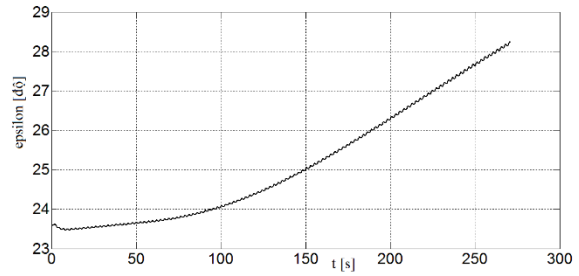

Figure 2.16. ε_y=f(t) corresponds to T_{qt}=0.01s, wind W=0m/s, F_n=-0.005m_{cn}g

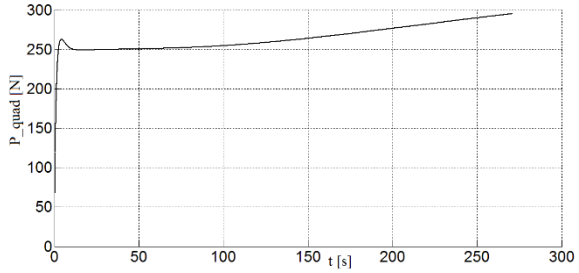

Figure 2.17. P_{quad}=f(t) corresponds to T_{qt}=0.01s, wind W=0m/s, F_n=-0.005m_{cn}g

Comment 2:

Figure 2.18 is a graph showing the length of the rope in the case of strong backwind W=5m/s.

When flying against the quite strong wind , the winch must always release the rope, making the length of the rope greatly extended (up to thousands of meters). At this time, if the vessel goes straight, the vessel driver only needs to reduce the throttle, but if the vessel runs around, depending on the relative movement of the vessel and the sphere, the vessel driver is to increase the throttle (see the case shown on the - figure 2.7: East wind W=5m/s and F_n=-0,005m_2g). ***Therefore, there is a need to display the trajectories of the sphere and vessel on an electronic map to assist the vessel driver.***

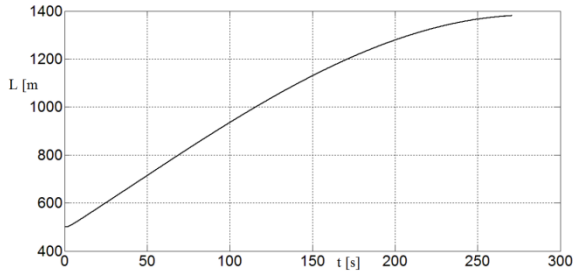

Figure 2.18. L=f(t) corresponds to T_{qt}=0.01s, reverse wind W=5m/s, F_n=-0.005m_{cn}g

3. Conclusion

The article has built a model of mechanical dynamics of a flying airship with automatic systems that maintains tension and stabilizes flight altitude, taking consideration of the "pendulum" model of payload and quadrotor / multirotor hung under the sphere. The computerized investigation results allow us to make useful recommendations for designing of the airship of new scheme.

Acknowledgments: The article is conducted in the frameworks of the R&D project of the Vietnam Union of Science and Technology Associations, the project is chaired by Vietnam Aerospace Association.

References

[1]. Mô tả sáng chế (2018), "*Hệ thống điều khiển trên không tốc độ chậm có điều khiển*," Công báo Sở hữu công nghiệp, Cục Sở hữu trí tuệ Việt Nam.

[2]. Nguyễn Đức Cương, Trần Duy Duyên, Phạm Văn Hiệp (Số 61-6-2019). *Mô hình động lực học cơ hệ ca nô kéo khí cầu bay có điều khiển*. Tạp chí KH &CN Quân sự,, Viện KHCNQS.

[3]. Nguyen Duc Cuong, Tran Duy Duyen, Mai Duy Phương (No 64, May 2019). *A dynamic model of two body mechanical system "an aiship towed by a vessel" with automatic tension control*. J. of Military Science and Technology, Hanoi.

[4]. Nguyễn Đức Cương (2002), "*Mô hình hóa chuyển động của khí cụ bay tự động*," NXB Quân đội nhân dân.

[5]. Nguyễn Văn Khang (2012), "*Cơ học kỹ thuật*", NXB giáo dục Việt nam.

Solid Mechanics

The 5th International Conference on Engineering Mechanics and Automation (ICEMA 5)
Hanoi, October 11÷12, 2019

Axisymmetric Plastic Flow of Polymers near Very Rough Walls

S. Alexandrov[a], Dinh Van Manh[b] and Nguyen Dinh Kien[b]

[a] *Institute for Problems in Mechanics, RAS, 101-1 Prospect Vernadskogo, 119526 Moscow, Russia*
[b] *Institute of Mechanics, VAST, 18 Hoang Quoc Viet, Hanoi, Vietnam*

Abstract

The main objective of the present paper is to study, by means of a problem permitting a semi-analytic solution, the qualitative behavior of solution for a model that is used for describing deformation of incompressible polymers near frictional interfaces. It is assumed that the regime of sticking occurs at the friction interfaces. The constitutive equations of the model are a pressure-dependent yield criterion and a flow rule. Such features of the solutions as non-existence and singularity are emphasized.

Key Words: Rough wall, Friction, Singularity, Plasticity

1. Introduction

Experimental studies demonstrate that skin layers are often generated in the vicinity of frictional interfaces in injecting molding of polymers. A review of such experimental results is provided in Pantani et al. (2005). It is known from the theory of plasticity for metals that the equivalent strain rate approaches infinity near maximum friction surfaces, Alexandrov and Richmond (2001), Alexandrov and Jeng (2013), Alexandrov and Mustafa (2013). This feature of solution behavior is used to describe the generation of fine grain layers in metal forming processes, Goldstein and Alexandrov (2015). It is of interest to extend this approach to processing of polymers. To this end, it is necessary to understand whether or not the behavior of solutions for models that are used for polymers is similar to that found in Alexandrov and Richmond (2001), Alexandrov and Jeng (2013), and Alexandrov and Mustafa (2013). In the present paper, the yield criterion for polyethylene proposed in Spitzig and Richmond (1979) is adopted. This yield criterion is pressure dependent. However, the volume change of polyethylene is similar to that observed in metals, Spitzig and Richmond (1979). Therefore, it is reasonable to assume that the equation of incompressibility is satisfied.

In order to study the behavior of solutions near frictional interfaces, it is not necessary to solve a boundary value problem of practical significance. It is more important to study an exact solution (i.e. the solution that exactly satisfies all the equations and boundary conditions). An ideal plane strain boundary value problem consists of a deformation comprising the simultaneous shearing and expansion (or contraction) of a hollow cylinder, Alexandrov and Harris (2006), Alexandrov and Mishuris (2009), Lyamina and Date (2016). An axisymmetric analogue to this problem is a deformation comprising the simultaneous shearing and expansion (or contraction) of a material between two conical surfaces. This boundary value problem is solved in the present paper.

2. Constitutive equations

The linear and quadratic stress invariants, I_1 and I_2, may be defined as

$$I_1 = \sigma_1 + \sigma_2 + \sigma_3, \quad I_2 = \sqrt{\frac{3}{2}\left(\tau_1^2 + \tau_2^2 + \tau_3^2\right)} \qquad (1)$$

where σ_1, σ_2 and σ_3 are the principal stresses. Moreover, $\tau_1 = \sigma_1 - I_1/3$, $\tau_2 = \sigma_2 - I_1/3$ and $\tau_3 = \sigma_2 - I_1/3$. The yield criterion for polyethylene proposed in Spitzig and Richmond (1979) is

$$I_2 + c_1 I_1 = c \qquad (2)$$

where c and c_1 are material constants. This material is practically incompressible, see Spitzig and Richmond (1979). Therefore, the plastic potential function of Mises is adopted in the present paper. In this case the flow rule results in

$$\xi_1 = \lambda\tau_1, \ \xi_2 = \lambda\tau_2, \xi_3 = \lambda\tau_3 \qquad (3)$$

where ξ_1, ξ_2 and ξ_3 are the principal strain rates and λ is a non-negative multiplier. It follows from (3) that

$$\xi_1 + \xi_2 + \xi_3 = 0 \qquad (4)$$

3. Statement of the problem

Consider a conical layer of plastic material between two conical surfaces of total angles $2\theta_1$ and $2\theta_2$. It is convenient to introduce a spherical coordinate system (r, θ, ϕ) with the axis $\theta = 0$ with the axis of symmetry of the conical surfaces (Fig. 1). The plastic material occupies the domain $0 \le r \le \infty$, $\theta_1 \le \theta \le \theta_2$ and $0 \le \phi \le 2\pi$. Let u_r, u_θ and u_ϕ be the velocity components referred to this coordinate system. The rate of increasing of the angle θ_1 will be denoted by ω_1. Then,

$$u_\theta = \omega_1 r \qquad (5)$$

for $\theta = \theta_1$. The conical surfaces are friction surfaces. It is assumed that the regime of sticking occurs at these surfaces. The internal conical surface is fixed against rotation.

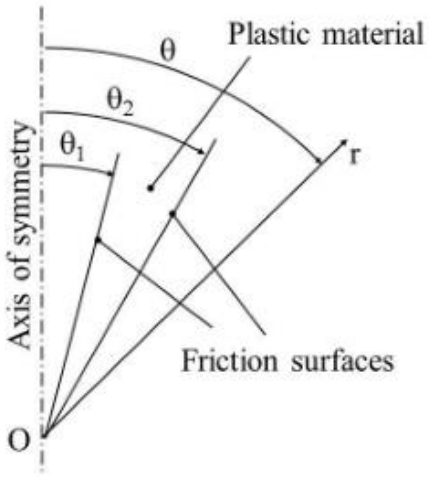

Figure1. Deformation of plastic material between conical surfaces.

Therefore,

$$u_\phi = 0 \qquad (6)$$

for $\theta = \theta_1$. The external conical surface rotates with an angular velocity ω_2. Therefore,

$$u_\theta = r\omega_2 \sin\theta_2 \qquad (7)$$

for $\theta = \theta_2$. Let $\xi_{rr}, \xi_{\theta\theta}, \xi_{\phi\phi}, \xi_{r\theta}, \xi_{r\phi}$, and $\xi_{\theta\phi}$ be the components of the strain rate tensor referred to the spherical coordinate system. It is possible to assume with no loss of generality that $\omega_2 > 0$. Then,

$$\xi_{\theta\phi} > 0 \qquad (8)$$

Let $\sigma_{rr}, \sigma_{\theta\theta}, \sigma_{\phi\phi}, \sigma_{r\theta}, \sigma_{r\phi}$ and $\sigma_{\theta\phi}$ be the components of the stress tensor referred to the spherical coordinate system. The boundary conditions formulated show that the solution is independent of ϕ. Then, the equilibrium equations are

$$\begin{aligned}
&\frac{\partial\sigma_{rr}}{\partial r} + \frac{\partial\sigma_{r\theta}}{r\partial\theta} + \frac{2\sigma_{rr} - \sigma_{\theta\theta} - \sigma_{\phi\phi} + \sigma_{r\theta}\cot\theta}{r} = 0,\\
&\frac{\partial\sigma_{r\theta}}{\partial r} + \frac{\partial\sigma_{\theta\theta}}{r\partial\theta} + \frac{\left(\sigma_{\theta\theta} - \sigma_{\phi\phi}\right)\cot\theta + 3\sigma_{r\theta}}{r} = 0,\\
&\frac{\partial\sigma_{r\phi}}{\partial r} + \frac{\partial\sigma_{\theta\phi}}{r\partial\theta} + \frac{2\sigma_{\theta\phi}\cot\theta + 3\sigma_{r\phi}}{r} = 0.
\end{aligned} \qquad (9)$$

The strain rate components are expressed in terms of the velocity components as

$$\begin{aligned}
&\xi_{rr}=\frac{\partial u_r}{\partial r},\ \xi_{\theta\theta}=\frac{1}{r}\left(\frac{\partial u_\theta}{\partial\theta}+u_r\right),\\
&\xi_{\phi\phi}=\frac{1}{r\sin\theta}\left(u_r\sin\theta+u_\theta\cos\theta\right),\\
&\xi_{\theta\phi}=\frac{1}{2r\sin\theta}\left(\sin\theta\frac{\partial u_\theta}{\partial\theta}-u_\phi\cos\theta\right),\\
&\xi_{r\theta}=\frac{1}{2}\left(\frac{\partial u_\theta}{\partial r}-\frac{u_\theta}{r}+\frac{\partial u_r}{r\partial\theta}\right).
\end{aligned}\tag{10}$$

4. General solution

It is reasonable to seek the general velocity of the form

$$u_r=0,\ u_\theta=rW_\theta(\theta),\ u_\phi=rW_\phi(\theta)\tag{11}$$

where $W_\theta(\theta)$ and $W_\phi(\theta)$ are arbitrary function of θ. Substituting (11) into (10) yields

$$\begin{aligned}
&\xi_{rr}=0,\ \xi_{\theta\theta}=\frac{dW_\theta}{d\theta},\ \xi_{\theta\theta}=W_\theta\cot\theta,\\
&\xi_{\theta\phi}=\frac{\sin\theta}{2}\frac{d}{d\theta}\left(\frac{W_\phi}{\sin\theta}\right),\\
&\xi_{r\phi}=0,\ \xi_{r\theta}=0.
\end{aligned}\tag{12}$$

Therefore, one of the principal strain rate (and stress) directions coincides with the $r-$ direction. It is possible to assume with no loss of generality that $\sigma_{rr}\equiv\sigma_3$ and $\xi_{rr}=\xi_3$. Then, the principal stresses σ_1 and σ_2 are in the (θ,ϕ) plane. Let φ be the inclination of the principal stress direction corresponding to the stress σ_1 to the $\theta-$direction. It follows from the transformation equations for stress components that

$$\begin{aligned}
&\tau_{\theta\theta}=-\frac{\tau_3}{2}+\frac{(\tau_1-\tau_2)\cos2\varphi}{2},\\
&\tau_{\phi\phi}=-\frac{\tau_3}{2}-\frac{(\tau_1-\tau_2)\cos2\varphi}{2},\\
&\sigma_{\theta\phi}=\frac{(\tau_1-\tau_2)\sin2\varphi}{2}.
\end{aligned}\tag{13}$$

It has been taken into account here that $\tau_1+\tau_2+\tau_3\equiv0$. Also, $\tau_{\theta\theta}=\sigma_{\theta\theta}-\sigma$ and $\tau_{\phi\phi}=\sigma_{\phi\phi}-\sigma$ where σ is the hydrostatic stress. It follows from (3) and (12) that $\tau_3=0$. Then, $\tau_1+\tau_2=0$ and equation (13) becomes

$$\begin{aligned}
&\tau_{\theta\theta}=\tau_1\cos2\varphi,\ \tau_{\phi\phi}=-\tau_1\cos2\varphi,\\
&\sigma_{\theta\phi}=\tau_1\sin2\varphi.
\end{aligned}\tag{14}$$

Since the model is coaxial, it is evident from (12) that $\sigma_{r\phi}=\sigma_{r\theta}=0$. Substituting these equations and (14) into (9) yields

$$\begin{aligned}
&\frac{\partial\sigma}{\partial r}=0,\\
&\frac{\partial\sigma}{\partial\theta}+\frac{\partial(\tau_1\cos2\varphi)}{\partial\theta}+2\tau_1\cos2\varphi\cot\phi=0,\\
&\frac{\partial\sigma_{\theta\phi}}{\partial\theta}+2\sigma_{\theta\phi}\cot\theta=0.
\end{aligned}\tag{15}$$

The third equation can be immediately integrated to give

$$\sigma_{\theta\phi}=\frac{cp}{\sin^2\theta}\tag{16}$$

where p is a constant of integration. It is seen from (8) that $\sigma_{\theta\phi}>0$ and, therefore, $p>0$. The first equation in (15) shows that σ is independent of r. Then, the second equation becomes

$$\frac{d\sigma}{d\theta}+\frac{d(\tau_1\cos2\varphi)}{d\theta}+2\tau_1\cos2\varphi\cot\theta=0\tag{17}$$

It has been assumed that both τ_1 and φ are independent of r. It is seen from (1) that $I_1=3\sigma$. It is possible to assume with no loss of generality that $\tau_1>0$. This inequality together with the inequality $\sigma_{\theta\phi}>0$ and (14) shows that

$$0<\varphi<\pi/2\tag{18}$$

Since $\tau_3=0$, it follows from (1) that $I_2=\sqrt{3}\tau_1$. Then, equation (2) becomes

$$\sqrt{3}\tau_1+3c_1\sigma=c\tag{19}$$

It follows from (14), (16) and (19) that

$$\tau_1 = \frac{cp}{\sin 2\varphi \sin^2\theta},$$
$$\sigma = \frac{c}{3c_1} - \frac{cp}{\sqrt{3}c_1 - \sin 2\varphi \sin^2\theta}. \quad (20)$$

Equations (17) and (20) combine to give

$$\frac{d\varphi}{d\theta} = \frac{\cot\theta \sin 2\varphi}{\sqrt{3}c_1 - \cos 2\varphi}. \quad (21)$$

Integrating results in to give

$$C_2 \sin\theta = \frac{\tan^n \varphi}{\sqrt{\sin 2\varphi}} \quad (22)$$

where C_2 is a constant of integration and $n = \sqrt{3}c_1 / 2$. The incompressibility equation (4) can be rewritten as $\xi_{rr} + \xi_{\theta\theta} + \xi_{\theta\theta} = 0$. Using (12) transforms this equation to $dW_\theta / d\theta + W_\theta \cot\theta = 0$. This equation can be immediately integrated to give

$$W_\theta = \frac{W_0}{\sin\theta} \quad (23)$$

where W_0 is a constant of integration. It follows from (5), (11) and (23) that $W_0 = \omega_1 \sin\theta_1$. Then, equation (23) becomes

$$W_\theta = \frac{\omega_1 \sin\theta_1}{\sin\theta}. \quad (24)$$

A consequence of equation (3) is $\xi_{\theta\theta} = \lambda\tau_{\theta\theta}$ and $\xi_{\theta\phi} = \lambda\sigma_{\theta\phi}$. Eliminating λ in these equations yields $\xi_{\theta\theta}\sigma_{\theta\phi} = \xi_{\theta\phi}\tau_{\theta\theta}$. Using (12), (14) and (24) leads to

$$\frac{d}{d\theta}\left(\frac{W_\phi}{\sin\theta}\right) = -\frac{2\omega_1 \sin\theta_1 \tan 2\varphi \cos\theta}{\sin^3\theta}. \quad (25)$$

It is seen from (6) and (11) that $W_\phi = 0$ at $\theta = \theta_1$. The solution of equation (25) satisfying this boundary condition can be written as leads to

$$W_\phi = -2\omega_1 \sin\theta_1 \sin\theta \int_{\theta_1}^{\theta} \frac{\tan 2\varphi \cos\theta}{\sin^3\beta} d\beta. \quad (26)$$

It is understood here that φ is a function β found from (22). It follows from (7) and (11) that $W_\phi = \omega_2 \sin\theta_2$ at $\theta = \theta_2$. This boundary condition and (26) combine to give

$$\omega_2 = -2\omega_1 \sin\theta_1 \int_{\theta_1}^{\theta_2} \frac{\tan 2\varphi \cos\theta}{\sin^3\theta} d\theta. \quad (27)$$

5. Analysis of the solution

The denominator on the right hand side of (21) vanishes at

$$\varphi = \varphi_c = \frac{1}{2}\arccos\left(\sqrt{3}c_1\right). \quad (28)$$

It is seen from (26) that $\omega_1 > 0$ if $\tan 2\varphi < 0$ in the range $\theta_1 \le \theta \le \theta_2$ and $\omega_1 < 0$ if $\tan 2\varphi > 0$ in the range $\theta_1 \le \theta \le \theta_2$. These two cases should be treated separately. Firstly, assume that $\omega_1 > 0$. Then, taking into account (18) it is possible to find that the value of φ varies in the range $\pi/4 \le \varphi \le \pi/2$. It is evident that φ_c does not belong to this range. Therefore, the denominator on the right hand side of (21) never vanishes, $d\varphi / d\theta > 0$ in the range $\theta_1 \le \theta \le \theta_2$ and φ may attain the value of $\pi/4$ at $\theta = \theta_1$. In this case, it follows from (27) that $\omega_2 \to \infty$ at $\theta \to \theta_1$. Therefore, the solution at sticking always exists independently of other conditions.

Assume that $\omega_1 < 0$. Then, taking into account (18) it is possible to find that the value of φ varies in the range $0 \le \varphi \le \pi/4$. The value of φ_c belongs to this range. Moreover, it is seen from (22) that θ considered as a function of φ attains a minimum at $\varphi = \varphi_c$. Therefore, $\varphi = \varphi_c$ at $\theta = \theta_1$. Using this conditions it is possible to find C_2 involved in (22) and this equation becomes

$$\sin\theta = \frac{\tan^n \varphi}{\sqrt{\sin 2\varphi}} \frac{\sqrt{\sin 2\varphi_c}\sin\theta_1}{\tan^n \varphi_c}. \quad (29)$$

Using this equation the integral in (27) can be evaluated giving a maximum possible value of ω_2. No solution at sticking exists at lager values

of ω_2. Consider the behavior of the strain rate component $\xi_{\theta\phi}$ when $\varphi = \varphi_c$ at $\theta = \theta_1$. It follows from (12) and (21) that

$$\xi_{\theta\varphi} = \frac{\sin\theta}{2}\frac{d}{d\theta}\left(\frac{W_\phi}{\sin\theta}\right) = \frac{\sin\theta\cot\theta\sin 2\varphi}{2\left(\sqrt{3}c_1 - \cos 2\varphi\right)}\frac{d}{d\varphi}\left(\frac{W_\phi}{\sin\theta}\right). \quad (30)$$

It is seen from this equation and (28) that $\left|\xi_{\theta\phi}\right| \to \infty$ as $\theta \to \theta_1$. This feature of the solution predicts the existence of a layer of intensive deformation in the vicinity of this friction surface. This deformation may be responsible for the generation of skin layers [1].

6. Conclusions

Using the boundary value problem permitting a semi-analytic solution the qualitative behavior of the solution in the vicinity of the friction interface for the yield criterion proposed in [6] has been studied. From this work, the following conclusions can be drawn.

1. In the case of $\omega_1 > 0$ (Fig. 1), the solution satisfying the regime of sticking at the inner conical surface exists independently of the other boundary conditions.
2. In the case of $\omega_1 < 0$ (Fig. 1), the solution satisfying the regime of sticking does not exist if the value of ω_2 is large enough.
3. In the case of $\omega_1 < 0$ (Fig. 1), the solution is singular, $\left|\xi_{\theta\phi}\right| \to \infty$ as $\theta \to \theta_1$, at the transition from the regime of sticking to the regime of sliding at the surface $\theta = \theta_1$.
4. The singularity in the velocity field may describe the generation of skin layers.

Acknowledgment

The authors acknowledge financial support of this research through grants RFBR-17-51-540003 (Russia) and VAST.HTQT.NGA.07/17-18 (Vietnam).

References

Alexandrov, S. and O. Richmond, (2001). Singular plastic flow fields near surfaces of maximum friction stress. *International Journal of Non-Linear Mechanics*, 36, pp. 1-11.

Alexandrov, S. and Y.-R. Jeng (2013). Singular rigid/plastic solutions in anisotropic plasticity under plane strain conditions. *Continuum Mechanics and Thermodynamics*, 25, pp. 685–689.

Alexandrov, S. and Y. Mustafa, (2013). Singular solutions in viscoplasticity under plane strain conditions. *Meccanica*, 48, pp. 2203-2208.

Alexandrov, S. and D. Harris, (2006). Comparison of solution behaviour for three models of pressure-dependent plasticity: A simple analytical example. *International journal of mechanical sciences*. 48, pp. 750-762.

Alexandrov, S. and G. Mishuris, (2009). Qualitative behaviour of viscoplastic solutions in the vicinity of maximum-friction surfaces. Journal of Engineering Mathematics . 65, pp. 143-156.

Goldstein, R.V. and S.E. Alexandrov, (2015). An approach to prediction of microstructure formation near friction surfaces at large plastic strains. Physical Mesomechanics. 18, pp. 223-227.

Lyamina, E.A. and Date, P.P. (2016). Planar plastic flow of polymers near very rough walls. Structural Engineering and Mechanics . 58, pp. 707–718.

Pantani, R., I. Coccorullo, V. Speranza, and G. Titomanlio, (2005). Modeling of morphology evolution in the injection molding process of thermoplastic polymers. *Progress in Polymer Science*. 30, pp. 1185-1222.

W.A. Spitzig, W.A. and O. Richmond, (1979). Effect of hydrostatic pressure on the deformation behavior of polyethylene and polycarbonate in tension and in compression. *Polymer Engineering and Science*. 19, pp. 1129-1139 (1979).

The 5th International Conference on Engineering Mechanics and Automation (ICEMA 5)
Hanoi, October 11÷12, 2019

Experimental research on dynamic response of beams with anisotropic restraints

Do Xuan Quy[a], Ta Thi Hien [b], Luong Xuan Binh[c], Hoang Van Tuan[d] and Le Thanh Tam[e]

[a] *The University of Transport and Communications, Ha noi, Viet Nam. Email: quysbvl@utc.edu.vn*
[b] *The University of Transport and Communications, Ha noi, Viet Nam. Email: hiengt79@utc.edu.vn*
[c] *The University of Transport and Communications, Ha noi, Viet Nam. Email: lxbinh0201@utc.edu.vn*
[d] *The University of Transport and Communications, Ha noi, Viet Nam. Email: hoangtuan0406@utc.edu.vn*
[e] *The University of Transport and Communications, Ha noi, Viet Nam. Email: lethanhtam8689@utc.edu.vn*

Abstract

Structures with anisotropic restraints are quite commonly used in civil engineering, for instance, beams or plates resting on elastic foundations, tunnel shells and wire structures. A dominant feature of these structures is that the reaction force of the restraint is changed depending on the value and direction of the displacement at the restraint point. In the presence of anisotropic restraints, the analytical model of the structure is changed according to the value of the applying loads. Therefore the dynamic characteristics, the natural frequency of the structure, is not a constant in comparison to conventional structures without isotropic restraints. This paper presents some experimental results on the dynamic response of the beam with anisotropic restraints.

Key Words: Anisotropic restraints, beams, dynamic response, experimental research, nonlinear restraints.

1. Instruction

For many years, studies on dynamic responses of structures with anisotropic restraints have been conducted. In Dai (2014), analyzed the dynamic behavior of non-ballast rail structure with the model of single and two degrees of freedom in which the rubber sole, sleeper cushion and rail cushion were treated as a series of single springs attached in parallel to viscous damper. In Celep et al. (2011), investigated the static and dynamic behavior of a completely free elastic beam resting on a two-parameter tensionless Pasternak foundation, in which model symmetrical beam was assumed to be subjected to a uniformly distributed load and concentrated load at its middle. In Lin and Adams (1987), proposed solution for an infinitely long elastic beam resting under moving loads as well as beam was rested on a tensionless elastic foundation. This action results in the creation of lift-off regions between the beam and the foundation that impact on the character of the response. In Diego et al. (2017), carried out the numerical FEM analysis of the dynamic response of a simply-supported Euler-Bernoulli elastic beam resting on a spatially homogeneous nonlinear cubic elastic Winkler foundation subjected to a concentrated moving load. In Jorge et al. (2014), presented a study on the dynamic response of simple beams on an elastic foundation, subjected to moving loads.

The response of the system was studied for three types of mechanical behavior of the foundation: linear elastic (classic Winkler model), nonlinear elastic and bilinear elastic. Force-displacement relation of a nonlinear elastic foundation was introduced as polynomial function which has degree of 3. In Rodrigues et al. (2018), introduced a study on the dynamic response of beams on elastic foundations, subjected to a uniformly moving oscillator. Numerical dynamic analysis of beams on nonlinear elastic foundations under harmonic moving load also impremented and reported in study of Froio et al. (2016). In the study of Abdelghany et al. (2015), dynamic response of non-uniform Euler–Bernoulli beam was studied which was subjected to moving load. The beam is rested on a nonlinear viscoelastic foundation. Akour (2010), investigated a simply supported nonlinear beam resting on linear elastic foundation and subjected to harmonic loading. The equation is analyzed numerically using Runk-Kutta technique.

However, these previous studies virtually emphasized on the model of restraint as linear behavior. Although nonlinear responses of restraints are presented, the assumed function is polynomial one with a degree of 3 to describe nonlinear terms. Such works in relation to anisotropic restraints, on the other hand, are rare proposed. In parallel research with this present study, Quy et al. (2018), reported that the natural frequency of beam with anisotropic restraints is not a unique constant. Instead of that, the frequency values vary in a wide range depending mostly on the amplitude of vibration.

This paper aims at presenting the results from an experiment to validate the finding point regarding varying-frequency that was reported in the previous analytical work of authors in Quy et al. (2018). Experimental results have shown that the frequency of the structure with anisotropic restraints is a domain. It is not a particular value compared with conventional structures where the frequency is uniquely identified.

2. Anisotropic restraints

Restraints, in general, can be literally described as a series or group of each single restraint (unilateral direction). In this study, the concept of anisotropic restraints is considered as a single restraint.

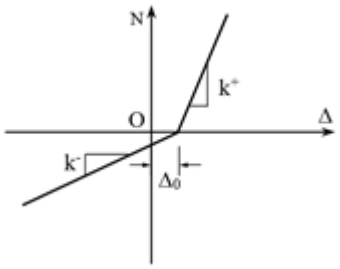

Figure 1. Scheme of an anisotropic restraint

Anisotropic restraint is a restraint in which the reaction force of the restraint is changed according to the value and direction of the displacement at the restraint point. Mechanical behavior of single anisotropic restraint proposed in this study is depicted in Figure 1. According to proposed scheme, the force-displacement relation are obtained as shown in Eq. (1).

$$N = \frac{k^+ + k^-}{2}(\Delta - \Delta_0) + \frac{k^+ - k^-}{2}\left|\Delta - \Delta_0\right| \qquad (1)$$

where

N is reaction force;

Δ is displacement at anisotropic restraint;

Δ_0 is initial displacement;

k^+ and k^- are positive and negative stiffness of anisotropic restraint.

3. Experiment

3.1. Experimental scheme

a) Actual model

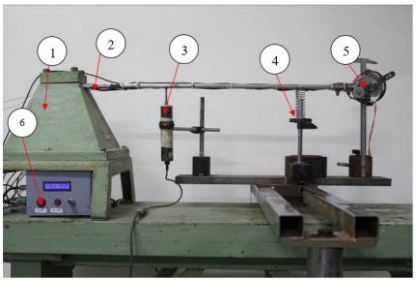

Figure 2. Experimental mode (picture by author)

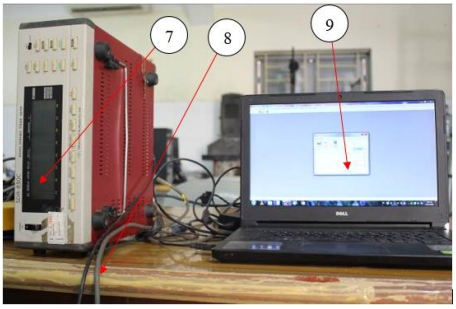

Figure 3. Vibration measurement equipment (SDA 830C)

in which

1. Machine pedestal
2. Beam
3. Displacement sensor
4. Elastic spring
5. Electrical motor
6. Adapter to change motor speed
7. Vibration measurement equipment (SDA 830C)
8. Signal cables
9. Laptop.

Figure 2 shows the mode of the beam with a single anisotropic restraint using in the experiment. Steel beam has following properties: length l = 0.778 **m**; rectangular cross section b = 0.03965 **m**, h = 0.0083 **m**. Sensor is placed at a distance of 0.23 meters from fixed end of beam to capture vibration of beam. Elastic spring with stiffness k is also placed at a distance of 0.59 meter from the fixed end of beam. A motor with the weight of Q and the eccentric mass of m is attached to the beam at free end. Excitation forces are generated from the motor through eccentric mass. When beam vibrates downward, displacements of beam at spring location pose compression in the spring, creating reaction force in the spring. When beam vibrates upward, there is no contact between beam and spring (lift-off), hence spring does not work (completely ineffective). Figure 3 illustrates the actual vibration measurement instrument (SDA 830C) to measure vibration of the beam.

b) Measurement of beam parameters, spring stiffness and weight of motor

Plastic ruler, calipers and electronic scales are used to measure initial parameters of beam and spring. These dimensions and parameters are depicted in Figure 4. In which, beam length l = 77.8 c**m**, width of cross section b = 3.965 **cm**, height of cross section h = 0.83 **cm**, motor weight Q = 0.013871 **kN**, eccentric mass in motor m = 13.15 g, eccentric lever arm r = 4.5 **cm**, spring stiffness k = 0.030943951 **kN/cm**

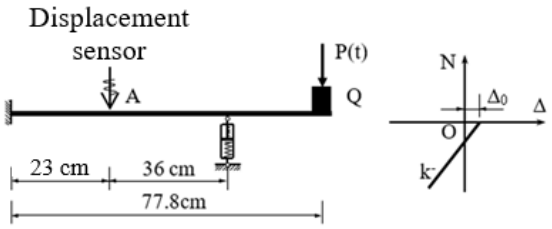

Figure 4. Experimental scheme

3.2. Dynamic response of beam with anisotropic restraint under excitation loads (excitation frequency f = 7 Hz)

Fine element model of beam are utilized, dividing beam into 3 fundamental elements with mechanical and geometrical properties as: Young modulus $E = 2.10^{11}$ **N/m²**, moment of inertia of cross section $J_x = 1.88928.10^{-9}$ **m⁴**, area of cross section A = 0.000329095 **m²**, anisotropic stiffness of spring (negative stiffness $k^- = 3094.395$ **N/m** and positive stiffness $k^+ = 0$), initial displacement of beam at spring Δ_0 = -0.004911 **m** (caused by self-weight of beam and weight of motor). It is assumed that dynamic model of beam herein is a single degree of freedom. The mass of the system includes mass of motor and equivalent mass of beam which is normalized to the end of beam by multiple to 33/140. Other assumption is that the structure here is undamped. All these input parameters are

prepared in txt file as shown in Figure 5. The total running time in the program (ANISOL) is 5 seconds with time interval of 0.0001 seconds. Vibration of beam, at the cross section located at 0.23 meter from the fixed end, are drawn and depicted in Figure 6. The results observed from experiment and numerical analysis can be described as: In the first few periods of vibration, vibration amplitude, period and natural frequency obtained from experiment agree well with those results from numerical analysis (using ANISOL). After a certain period, the error between experiment and numerical analysis (using ANISOL) increases. The reason for this increasing error caused by the assumption that beam is modeled as undamped system, intrinsic damping of cable is neglected. Equivalent mass of beam which is normalized to the end of the beam is also considered as an element of being erroneous.

```
PHANTU
3
2E+11  1.88928E-09   0.000329095   1   0   0   0   2   0.23   0   0
2E+11  1.88928E-09   0.000329095   2   0.23   0   0   3   0.59   0   0
2E+11  1.88928E-09   0.000329095   3   0.59   0   0   4   0.778   0   0
LIENKET
2
1   1E+30   1E+30   0   1E+30   1E+30   0   1E+30   1E+30   0
3   0   0   0   0   3094.3951   -0.004911   0   0   0
TAITRONG
1
2   -18.33993125   3   0.188   0
```

Figure 5. Input parameters of beam and load imported into program ANISOL

Numerical results from ANSOL shown that the vibration period and natural frequency of the beam do not change during vibration whereas vibration amplitudes obtained from experiment decreases. The reduction of response amplitude as well as natural frequency of beam caused by the effect of environment damping coefficient on vibration of the system. Results are presented in Figure 6 and Figure 7 corresponding to time and frequency domain. It is clear from the Figure 7 that the results from experiment coincide well with those from numerical analysis using ANISOL, error within 2.222 %

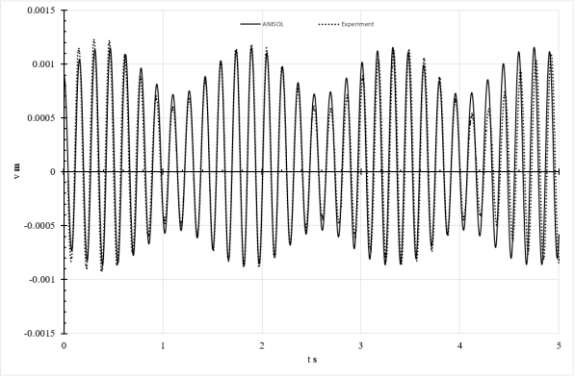

Figure 6. Experiment and numerical results (using ANISOL) presented in time domain

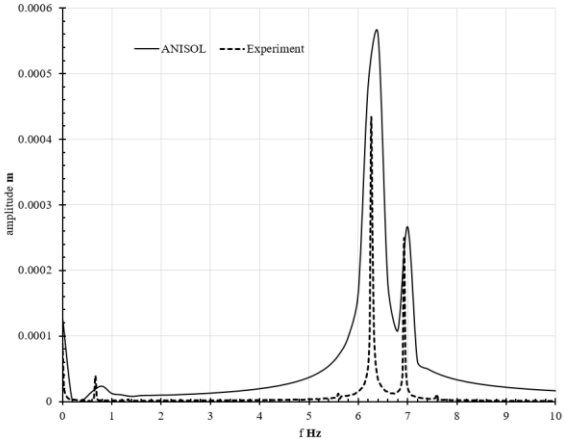

Figure 7. Experiment (EX) and numerical results (using ANISOL) presented in frequency domain.

Table 1. Natural frequency between experiment and numerical analysis

	Natural frequency **Hz**	
	f_1	f_2
Experiment	6.261	6.927
ANISOL	6.4	7
Error (%)	2.222	1.046

Through results presented in Table 1, the analytical model, algorithms as well as analytical solution for vibration of beam with anisotropic restraint are verified.

3.3. Free vibration of beam with anisotropic restraint in the presence of environmental damping.

In the presence of environmental damping existing in experiment room, the experiment was

conducted, and the results are shown in Figure 8, Figure 9 and Table 2.

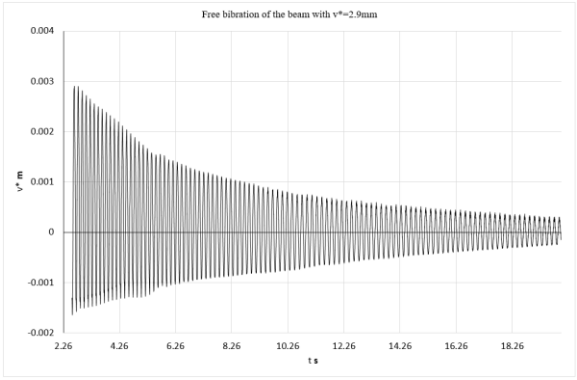

Figure 8. Vibration of beam in the presence of environmental damping, presented in time domain

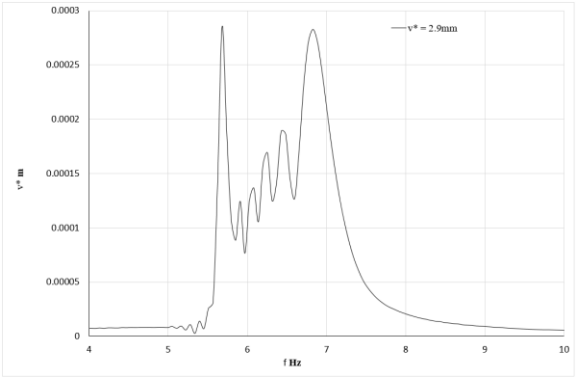

Figure 9. Vibration of beam in the presence of environmental damping, presented in frequency domain

Table 2. Natural frequency of beam in the presence of environmental damping

Frequency	f1 **Hz**	f2 **Hz**	f3 **Hz**)	f4 **Hz**
	5.24	5.37	5.5	5.69
f5 **Hz**	f6 **Hz**	f7 **Hz**	f8 **Hz**	f9 **Hz**
6	6.13	6.32	6.51	6.89

During vibration of beam, nine frequency modes of vibration were observed.

The results found in the experiment reinforce the conclusions reported in Quy et al (2018) that the frequency of the free vibration of the beam with anisotropic restraints is a domain. It is not a particular value compared with conventional structures where the frequency is uniquely identified. The specific natural frequency depends on the value of response amplitude at that identified time.

4. Conclusions

The experimental model of the beam with an anisotropic restraint is proposed in this study. The experiment was conducted in experimental room. The brief conclusions obtained through this work are as follows:

- Theory, algorithms and computing program for analyzing the dynamic response of the beam with an anisotropic restraint are validated. The error between experimental and analytical results is not significant, so that the feasibility of the proposed solution is confirmed.

- The results found in the experiment reinforce the conclusions reported in Quy et al (2018) that the frequency of the free vibration of the beam with anisotropic restraints is a domain. It is not a particular value compared with conventional structures where the frequency is uniquely identified. The specific natural frequency depends on the value of response amplitude at that identified time. The mechanical sense for this phenomenon is that: Since the frequency domain relies virtually on vibration amplitude, the occurrence of resonance of the beam structure with anisotropic restraints under excitation forces is rarely seen, or only instantaneous resonance can be found.

Acknowledgement

Authors acknowledge University of Transport and Communication for providing financial support.

References

Dai, N. X. (2014). Analyzed the dynamic behavior of non-ballast rail structure with the model of single and two degrees of. *Journal of science and technology* (2), pp. 10-18 (in vietnamses).

Celep, Z., K. Güler, and F. Demir (2011). Response of a completely free beam on a tensionless Pasternak foundation subjected to dynamic load. *Structural Engineering and Mechanics*, 37(1), pp. 61-77.

Lin, L. and G.G. Adams (1987). Beam on Tensionless Elastic Foundation. *Journal of Engineering Mechanics* (113), pp 542-553.

Diego, F., E. Rizzi, M.F.S. Fernado and P. d. C Antonio (2017). Critical velocities of a beam on nonlinear elastic foundation under harmonic moving load. *Procedia Engineering*(199), pp. 2585-2590.

Jorge, P.C., M. F. S. Fernado and P. d. C Antonio (2014). Finite element dynamic analysis of beams on non-uniform nonlinear viscoelastic foundations under moving loads. *Proceedings of the 9th International Conference on Structural Dynamics, EURODYN 2014*, Portugal.

Rodrigues, C. V. et al (2018). Finite element dynamic analysis of beams on nonlinear elastic foundations under a moving oscillator. *European Journal of Mechanics - A/Solids*. 68, pp. 9-24.

Froio, D., R. Moioli and E. Rizzi (2016). Numerical dynamic analysis of beams on nonlinear elastic foundation under harmonic moving load. *ECCOMAS Congress 2016, VII European Congress on ComputationalMethods in Applied Sciences and Engineering, Greece*.

Abdelghany, S. M. et al (2015). Dynamic response of non-uniform beam subjected to moving load and resting on non-linear viscoelastic foundation. *Beni-Suef University Journal of Basic and Applied Sciences*. 4(3), pp. 192-199.

Akour, S. N. (2010). Dynamics of Nonlinear Beam on Elastic Foundation. *Proceedings of the World Congress on Engineering 2010*, London, U.K.

Quy, D. X., L. X. Binh, H. V. Quan and L. T. Tam (2018). Reseach on dynamic response of bars with anisotropic restraints. *The 14th national conference on solid mechanics*, pp.556-561 (in vietnamses).

Binh L. X., D. X. Quy and N. X. Luu (2007). Analysis of struture with anisotropic restraints by finite element method. *The 8th* national conference on mechanics, pp. 57-68 (in vietnamses).

The 5th International Conference on Engineering Mechanics and Automation (ICEMA 5)
Hanoi, October 11÷12, 2019

Free vibration of simply supported panel by using higher-order shear plate theory

Quang Van Duong[a], Doan Ngoc Tran[a]

[a] *Le Quy Don Technical University, 236 Hoang Quoc Viet Street, Hanoi, Vietnam*

Abstract

This paper analyzed the free vibration of a simply supported panel based on the high-order shear deformation theory account for the transverse normal stress effect. The governing equations of motion for the panel were established using Hamilton's principle. The natural frequencies were evaluated by Navier solution. Free vibration of 2D isotropic panels analyses were performed for various models to study the influences of the higher order terms in the shear deformation theories. The numerical results show that the high-order polynomials model can provide the different level of accuracy.

Key Words: free vibration, simply supported panel, the high-order shear deformation theory.

1. Introduction

There are various plate theories describing the behaviour of plate type structures. The classical plate theory (CPT) (Kirchhoff, 1850) model is based on the Kirchhoff-Love hypothesis that the straight lines remain straight and perpendicular to the middle plane after deformation. These assumptions imply the vanishing of the shear and normal strains, and consequently, neglecting the shear and normal deformation effects. The CPT is the simplest model which suitable only for thin plates where the shear and normal deformation effects are inconsiderable.

The other well-known plate theory is Mindlin plate theory or the first-order shear deformation plate theory (FSDT) (Mindlin, 1951). In that theory the distribution of the transverse shear strain with respect to the thickness coordinate is assumed to be constant (constant shear angle theory). Since this theory assumes for constant transverse shear strain along the thickness of the plate, shear correction factor is suggested firstly by Mindlin for homogeneous isotropic plates in order to match the response predicted by this two-dimensional theory with that of three dimensional elasticity theory.

Donnell's approach (Donnell, 1976) is to make correction to the classical plate deflections. Donnell assumed uniform distribution of shear force across the thickness of the plate, and, to rectify the effects of the assumption, introduces a numerical factor, which needs to be adjusted.

Levinson's formulation (Levinson, 1980) is based on displacement approach and his theory does not require shear correction factor. The governing equations for the motion of a plate obtained by Levinson's approach are similar those obtained by Mindlin's theory, provided that the shear coefficient value associated with the Mindlin's theory is taken as 5/6.

However, the shear correction factor is difficult to determine since it depends not only on geometric parameters but also on the loading

and boundary conditions [5,6] (Reddy, 1997) (Huu-Tai Thai, 2015).

To avoid the use of the shear correction factor, higher-order shear deformation theories (HSDTs) were introduced. The HSDT can be developed by expanding the displacement components in power series of the thickness coordinate. In principle, the theories developed by this mean can be made as accurate as desired by including a sufficient number of terms in the series. Among the HSDTs, the third-order shear deformation theory (TSDT) of Reddy (1984) is the most widely used one due to the simplicity and accuracy.

Thai and Kim (2013) developed a new shear deformation theory for bending and free vibration analysis of functionally graded (FG) plates.

The thickness stretching effect is ignored in the most of shear deformation theories by assuming the transverse displacement as constant. This assumption is inaccurate especially for thick plates. To overcome this problem, some quasi 3D theories presented in the literature.

Matsunaga (2008) analyzed the natural frequencies and buckling stresses of FG plates by taking into account the effects of transverse shear and normal deformations and rotatory inertia. Neves et al. (2012) presented a higher order shear deformation theory which account for through the thickness deformations for the bending and free vibration analysis of plates. Zenkour (2013) derived a refined trigonometric higher-order plate theory which the effects of transverse shear strains as well as the transverse normal strain are taken into account for bending analysis of plates. Thai and Choi (2014) improved a refined pate theory to account for the effect of thickness stretching in plates. Belabed et al. (2014) presented an efficient and simple higher order shear and normal deformation theory for FG plates.

In that period, other lines in the expansion of the plates theory are being developed, in which transverse deformations are consistently taken into account with local equations of equilibrium and uniformity of materials. One of those is called the "energy-consistent" theory (Vasiliev & Morozov, 2013), (Vasiliev & Lur'e, 1990).

The displcement model which satisfy "energy-consistent" theory was used in Firsanov & Doan (2011), Firsanov & Doan (2015), Quang et al., 2017) and Doan et al. (2018) to study thin walled structures. Results showed that the stress in nearly boundary area in these studies was much difference when compared with to that one based on other plate theory. In away from boundary aera, the stress approximate when compared to those based on other plate theory.

In this study, free vibration analysis of 2D isotropic panels based on the various higher order shear deformation theories account for the transverse normal stress effect which satisfy "energy-consistent" theory. Governing equations are derived from the Hamilton's principle. Navier solution is used to solve the partical differential equations for simply supported panels. The objective of the present study is to capture the influence of the higher order terms in the shear deformation theories on free vibration of 2D isotropic panels.

2. Fundamental formulations

Considering the 2D panels, having uniform length *a*, thickness *h* shown Fig.1. On the higher order shear deformation palte theory including the effect of transverse normal stress, the displacement field of the panels can be described as:

$$u\left(x,y,z\right)=\sum_{i=0}^{k}U_i\left(x,t\right)\frac{z^i}{i!},$$
$$w\left(x,y,z\right)=\sum_{i=0}^{q}W_i\left(x,t\right)\frac{z^i}{i!}. \quad (1)$$

Where, *u*, *w* are displacements in the *x*, *z* directions, respectively. U_0 are the in-plane tangential displacements and W_0 is the transverse displacement of a point on the panel's middle surface. U_1 are the rotations of the normals to the panel's middle surface (*z*=0) along '*Y*' axes. $U_i, W_i\left(i=3..\mathrm{n}\right)$ are the higher order terms in the Taylor's series expansion and represent the higher order

transverse cross-sectional deformation modes. The various models with their nomenclatures formulated in the present study based on higher order theories are given in Table 1.

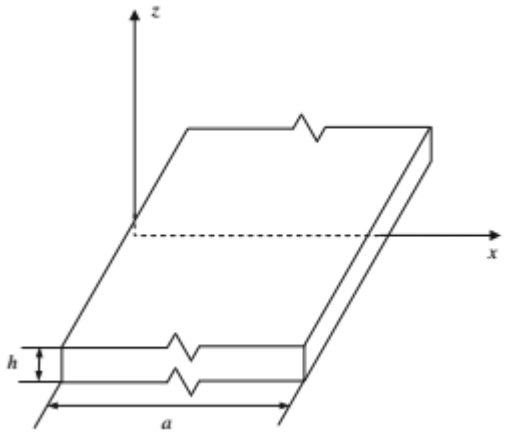

Figure 1. Geometry and coordinates of the 2D isotropic panel.

The general linear strain–displacement relations at a point within a plate are:

$$\varepsilon_{xx} = \frac{\partial u}{\partial x};$$
$$\gamma_{xz} = \frac{\partial u}{\partial z} + \frac{\partial w}{\partial x}, \quad (2)$$
$$\varepsilon_{zz} = \frac{\partial w}{\partial z}.$$

where ε_{xx}, ε_{zz} are the normal strains in x, z direction and γ_{xz} is the shear strain.

The stress-strain relations for an 2D isotropic material panel are expressed as:

$$\sigma_{xx} = \varepsilon_{xx}C_{11} + \varepsilon_{zz}C_{13},$$
$$\sigma_{zz} = \varepsilon_{xx}C_{31} + \varepsilon_{zz}C_{33}, \quad (3)$$
$$\tau_{xz} = \gamma_{xz}C_{55}.$$

where: σ_{xx}, σ_{zz}, τ_{xz} are stress; C_{ij} is the stiffness coefficients of the panels.

In which:

$$C_{11} = C_{33} = \frac{E(1-\mu)}{(1-2\mu)(1+\mu)},$$
$$C_{13} = C_{31} = \frac{E\mu}{(1-2\mu)(1+\mu)},$$
$$C_{55} = \frac{2E}{(1+\mu)}. \quad (4)$$

where: E, μ are the elastic module and the Poisson's ratio.

Table 1. List of displacement models based on higher order shear deformation theories.

Model	Displacement field as defined in Eq. (1)
HOSTU3W2	$u = U_0 + zU_1 + \frac{z^2}{2}U_2$ $w = W_0 + zW_1$
HOSTU4W2	$u = U_0 + zU_1 + \frac{z^2}{2}U_2 + \frac{z^3}{6}U_3$ $w = W_0 + zW_1$
HOSTU3W3	$u = U_0 + zU_1 + \frac{z^2}{2}U_2$ $w = W_0 + zW_1 + \frac{z^2}{2}W_2$
HOSTU4W3	$u = U_0 + zU_1 + \frac{z^2}{2}U_2 + \frac{z^3}{6}U_3$ $w = W_0 + zW_1 + \frac{z^2}{2}W_2$

The equation of the motion of the panels is also formulated by Hamilton's principle:

$$\int_{t_1}^{t_2} (\delta K - \delta U)\, dt = 0 \quad (5)$$

where the virtual kinetic energy δK, the virtual strain energy δU are given by:

$$\delta K = \int_{\Omega_0} \int_{-\frac{h}{2}}^{\frac{h}{2}} \left(\rho \ddot{u}\delta u + \rho \ddot{w}\delta w\right) dz dx \quad (6)$$

$$\delta U = \int_{\Omega_0} \int_{-\frac{h}{2}}^{\frac{h}{2}} \left(\sigma_{xx} \delta \varepsilon_{xx} + \tau_{xz} \delta \gamma_{xz} + \sigma_{zz} \delta \varepsilon_{zz} \right) dz dx \tag{7}$$

where Ω_0 is the plate area, ρ is the plate desnity, and dot denotes the derivative with respect to time.

For a typical HOSTU4W3 the equations of motion is represented as:

$$\delta u_0 : \frac{\partial N}{\partial x} = I_0 \ddot{U}_0 + I_1 \ddot{U}_1 + \frac{I_2}{2} \ddot{U}_2 + \frac{I_3}{6} \ddot{U}_3,$$

$$\delta u_1 : \frac{\partial M^{(1)}}{\partial x} - Q = I_1 \ddot{U}_0 + I_2 \ddot{U}_1 + \frac{I_3}{2} \ddot{U}_2 + \frac{I_4}{6} \ddot{U}_3,$$

$$\delta u_2 : \frac{\partial M^{(2)}}{\partial x} - P^{(1)} = \frac{I_2}{2} \ddot{U}_0 + \frac{I_3}{2} \ddot{U}_1 + \frac{I_4}{4} \ddot{U}_2 + \frac{I_5}{12} \ddot{U}_3,$$

$$\delta u_3 : \frac{\partial M^{(3)}}{\partial x} - P^{(2)} = \frac{I_3}{6} \ddot{U}_0 + \frac{I_4}{6} \ddot{U}_1 + \frac{I_5}{12} \ddot{U}_2 + \frac{I_6}{36} \ddot{U}_3,$$

$$\delta w_0 : \frac{\partial Q}{\partial x} = I_0 \ddot{W}_0 + I_1 \ddot{W}_1 + \frac{I_2}{2} \ddot{W}_2,$$

$$\delta w_1 : \frac{\partial P^{(1)}}{\partial x} - R = I_1 \ddot{W}_0 + I_2 \ddot{W}_1 + \frac{I_3}{2} \ddot{W}_2,$$

$$\delta w_2 : \frac{\partial P^{(2)}}{\partial x} - S = \frac{I_2}{2} \ddot{W}_0 + \frac{I_3}{2} \ddot{W}_1 + \frac{I_4}{4} \ddot{W}_2. \tag{8}$$

where: the force resultans operator and the mass moments of inertia of Eqs. (8) are calculated by:

$$N = \int_{-\frac{h}{2}}^{\frac{h}{2}} \sigma_{xx} dz, \; Q = \int_{-\frac{h}{2}}^{\frac{h}{2}} \tau_{xz} dz,$$

$$R = \int_{-\frac{h}{2}}^{\frac{h}{2}} \sigma_{zz} dz, \; S = \int_{-\frac{h}{2}}^{\frac{h}{2}} \sigma_{zz} z dz,$$

$$M^{(j)} = \int_{-\frac{h}{2}}^{\frac{h}{2}} \sigma_{xx} \frac{(z)^j}{j!} dz \; (j = 1,2,3),$$

$$P^{(k)} = \int_{-\frac{h}{2}}^{\frac{h}{2}} \tau_{xz} \frac{(z)^k}{k!} dz \; (k = 1,2).$$

$$I_i = \int_{-\frac{h}{2}}^{\frac{h}{2}} \rho (z)^i dz \; (i = 0,1,2,...6) \tag{9}$$

3. Solution technique

Among all the analytical methods available the Navier solution technique is very simple and easy to use when the plate is of rectangular geometry with simply supported edge conditions.

The boundary conditions for the 2D simply supported panels using a typical model HOSTU4W3 are:

At edges $x = 0$ and $x = a$:

$$w_0 = 0; \; w_1 = 0; \; N_0 = 0;$$

$$N_1 = 0; \; N_2 = 0; \; N_3 = 0.$$

The generalized displacement field for HOSTU4W3 to satisfy the above boundary conditions is expanded in double Fourier series as:

$$U_0 = \sum_{i=1}^{m} u_{0i} \cos\left(m\pi\xi\right) e^{\Omega t},$$

$$U_1 = \sum_{i=1}^{m} u_{1i} \cos\left(m\pi\xi\right) e^{\Omega t},$$

$$U_2 = \sum_{i=1}^{m} u_{2i} \cos\left(m\pi\xi\right) e^{\Omega t},$$

$$U_3 = \sum_{i=1}^{m} u_{3i} \cos\left(m\pi\xi\right) e^{\Omega t}, \qquad (10)$$

$$\mathrm{W}_0 = \sum_{i=1}^{m} \mathrm{w}_{0i} \sin\left(m\pi\xi\right) e^{\Omega t},$$

$$\mathrm{W}_1 = \sum_{i=1}^{m} \mathrm{w}_{1i} \sin\left(m\pi\xi\right) e^{\Omega t},$$

$$\mathrm{W}_2 = \sum_{i=1}^{m} \mathrm{w}_{2i} \sin\left(m\pi\xi\right) e^{\Omega t}.$$

where: $\xi = \dfrac{x}{a}$

Using the above generalized displacement field and following the standard steps described in previous section, we obtain the following eigenvalue problem for any fixed values of m:

$$\left(\left[K\right]_{7\times7} - \omega_m^2 \left[M\right]_{7\times7}\right) \begin{pmatrix} u_{0m} \\ u_{1m} \\ u_{2m} \\ u_{3m} \\ w_{0m} \\ w_{1m} \\ w_{2m} \end{pmatrix}_{1\times7} = 0 \qquad (11)$$

Here, [K] is the coefficient matrix using displacement HOSTU4W3, [M] is the mass matrix using HOSTU4W3. ω_m is the circular natural frequency of vibration of the system associated with *m*th mode in *x*-direction. $u_{0m}, u_{1m}, u_{2m}, u_{3m}, w_{0m}, w_{1m}, w_{2m}$ are seven unknown coefficients. The above eigenvalue problem can be solved for the various eigenvalues and associated eigenvectors. To obtain non-trivial solution, we must set $\left|\left[K\right] - \omega_m^2 \left[M\right]\right| = 0$ The real positive roots of Eq. (11) yield the circular natural frequency ω_m corresponding to vibration modes *m*th. The lowest eigenvalue gives the square of the fundamental natural frequency of vibration of 2D panels.

4. Results and disscusions

Free vibration analysis of 2D simply supported isotropic panel is analyzed by using the various displacement models as presented in Table 1.

The geometrical sizes and material properties are as follows: a=1 m, h=0.02 m, E=210 Gpa, υ=0.3, ρ=7,860 kg.m^{-3}, $G = E/\left[2\left(1+\upsilon\right)\right]$.

The non-dimensional frequencies $\bar{\omega}_m$ are presented in Table 2 along with the results by Li (2014) based on CPT and FSDT. Figure 2 shows the comparison value of results based on various displacement models. It can be seen that the present results are in agreement with the results of Li.

In addition, results showed that the non-dimensional frequencies in studies which based on higher-order shear deformation including the effect of transverse normal stress was different when compared with to that one based on other plate theory.

As can be seen, the natural non-dimensional frequencies decreased with increasing the value of the order of formulated displacement for the same mode. The influence of higher order term in displacement model on natural frequencies for the high modes is larger than ones for the low modes.

Comparisons value of non-dimensional frequencies according to HOSTU3W2 with HOSTU4W2, HOSTU3W3 with HOSTU4W3, the frequencies decrease slightly with the rising of order in *u*-displacement term.

Table 2. Comparison of non-dimensional natural frequencies $\bar{\omega}_m = \omega_m a^2/h\sqrt{12\rho\left(1-\upsilon^2\right)/E}$ of simply supported isotropic panels

Model	$\bar{\omega}_m$				
	Mode 1	Mode 2	Mode 3	Mode 4	Mode 5
CPT (Li, 2014)	48.67	187.51	421.89	750.03	1171.92
FSDT (Li, 2014)	46.85	187.06	419.66	743.05	1155.00
HOSTU3W2	46.08	182.99	412.77	730.89	1136.22
HOSTU4W2	46.07	183.78	411.72	727.61	1128.36
HOSTU3W3	41.63	166.27	373.18	661.13	1028.40
HOSTU4W3	41.63	166.23	372.96	660.42	1026.72

Comparisons value of non-dimensional frequencies according to HOSTU3W2 with HOSTU3W3, HOSTU4W2 with HOSTU4W3, the frequencies drop sharply with the rising of order in *w*-displacement term.

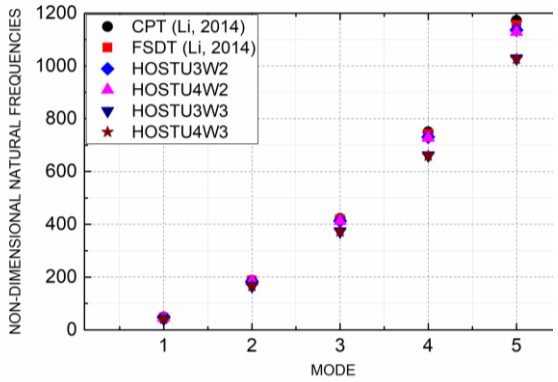

Figure 2. Non-dimensional frequencies of the 2D isotropic panel.

5. Conclusions

In this study, various displacement models were presented for free vibration analysis of isotropic panels. The present method was based on the higher order shear deformation theory accounted for the effect of transverse shear stress and transverse normal stress. The governing equations was obtained by Hamilton principle. The Navier solution technique employing double Fourier series was used to solve the partical differential equations. The numerical results of each displacement model were compared with the results of other studies and also with the other displacement model under similar edge conditions and material. The results obtained by the present study are summarized as follows:

- The effect of transverse normal stress on free vibration behavior are just as important as the effect of transverse shear stress and must be taken into account in numerical.
- The natural non-dimensional frequencies are proportional with the order of formulated displacement. The influence of higher order term on natural frequencies for the high modes is larger than ones for the low modes.
- The effect of order in u-displacement term to value of the natural non-dimensional frequencies is less than one of w-displacement term.

References

Belabed, Z., Houari, M., Tounsi, A., Mahmoud, S., & Beg, O. (2014). An ef ficient and simple higher order shear and normal deformation theory for functionally graded material (FGM) plates. *Composite Part B* (60), pp.274-83.

Doan, T. N., Firsanov, V., & Quang, D. V. (2018). Supersonic flutter analysis of two dimensional composite laminated panels based on non-classical plate theory. *Technical*

Science, Izvestia Tulskovo Universiteta(16), pp.299-309.

Donnell, L. (1976). *Beams, Plates and Shells.* New York: McGraw-Hill Book Company.

Feng-Ming Li, Zhi.-Guang Song (2014). Aeroelastic flutter analysis for 2D Kirchhoff and Mindlin panel with diffirent boundary conditions in supersonic airflow. *Acta Mech*.

Firsanov, V.V., Doan, T.N. (2011). Energy-consistent theory of cylindrical shells. *Journal of Machinery Manufacture and Reliability*(6), pp.543-548.

Firsanov, V.V., Doan, T.N. (2015). Investigation of the statics and free vibrations of cylindrical shells on the basis of a nonclassical theory. *Composites: Mechanics, Computations, Applications: An International Journal, II*, pp.135-166.

Huu-Tai Thai, S.-E. K. (2015). A review of theories for the modeling and analysis of functionally graded plates and shells. *Composite Structures*.

Jha, D., Kant, T., & Singh, R. (2012). Higher order shear and normal deformation theory for natural frequency of functionally graded rectangular plates. *Nuclear Engineering and Design*(250), pp.8–13.

Kirchhoff, V. (1850). Uber das gleichgewicht und die bewegung einer elastischen scheibe. *Journal Fur Die Reine und Angewandte Mathematik*, pp.31-38.

Levinson, M. (1980). An accurate, simple theory of the statics and dynamics of elastic plates. *Mechanics Research Communications*, pp.343–350.

Matsunaga, H. (2008). Free vibration and stability of functionally graded plates according to a 2-D higher-order deformation theory. *Composite Structure* (82), pp.499-512.

Mindlin, R. (1951). Influence of rotatory inertia and shear on flexural motions of isotropic elastic plates. *Journal of Applied Mechanics*, pp.31-38.

Neves, A. F. (2012). A quasi-3D hyperbolic shear deformation theory for the static and free vibration analysis of functionally graded plates. *Compos Struct*(94), 1814-25.

Quang, D. V., Doan, T. N., & Thanh, D. N. (2017). Flutter of panel based on higher order shear deformation plates theory. *The tenth National Conference on Mechanics*, pp.902-909. Ha Noi.

Reddy, J. (1984). A simple higher-order theory for laminated composite plates. *Journal of Applied Mechanics*(51), pp.745-752.

Reddy, J. (1997). *Mechanics of laminated composite plates, theory and analysis.* New York: CRC Press.

Thai, H. C. (2014). Improved refined plate theory accounting for effect of thickness stretching in functionally graded plates. *Composite Part B*(56), pp.705-16.

Thai, H. K. (2013). A simple higher-order shear deformation theory for bending and free vibration analysis of functionally graded plates. *Composite Structure* (96), pp.165-73.

Vasiliev, V.V., Lur'e, S. (1990). On Refinement of Depressed Shells Theory. *Izv. Akad. Nauk. Mekh. Tverd. Tela*(6), pp.139–146.

Vasiliev, V.V, Morozov, E. (2013). *Advanced Mechanics of Composite Materials and Structural Elements.* Elsevier.

Zenkour, A. (2013). A simple four-unknown refined theory for bending analysis of functionally graded plates. *Appl Math Model* (37(20-21)), pp.9041-51.

Appendix

The equations of motion HOSTU3W3 model:

$$\delta u_0 : \frac{\partial N}{\partial x} = I_0\ddot{U}_0 + I_1\ddot{U}_1 + \frac{I_2}{2}\ddot{U}_2,$$

$$\delta u_1 : \frac{\partial M^{(1)}}{\partial x} - Q = I_1\ddot{U}_0 + I_2\ddot{U}_1 + \frac{I_3}{2}\ddot{U}_2,$$

$$\delta u_2 : \frac{\partial M^{(2)}}{\partial x} - P^{(1)} = \frac{I_2}{2}\ddot{U}_0 + \frac{I_3}{2}\ddot{U}_1 + \frac{I_4}{4}\ddot{U}_2,$$

$$\delta w_0 : \frac{\partial Q}{\partial x} = I_0\ddot{W}_0 + I_1\ddot{W}_1 + \frac{I_2}{2}\ddot{W}_2,$$

$$\delta w_1 : \frac{\partial P^{(1)}}{\partial x} - R = I_1 \ddot{W}_0 + I_2 \ddot{W}_1 + \frac{I_3}{2} \ddot{W}_2,$$

$$\delta w_2 : \frac{\partial P^{(2)}}{\partial x} - S = \frac{I_2}{2} \ddot{W}_0 + \frac{I_3}{2} \ddot{W}_1 + \frac{I_4}{4} \ddot{W}_2. \quad \text{(A.1)}$$

The force resultans operator and the mass moments of inertia of Eqs. (A.1):

$$N = \int_{-\frac{h}{2}}^{\frac{h}{2}} \sigma_{xx} dz, \; Q = \int_{-\frac{h}{2}}^{\frac{h}{2}} \tau_{xz} dz,$$

$$R = \int_{-\frac{h}{2}}^{\frac{h}{2}} \sigma_{zz} dz, \; S = \int_{-\frac{h}{2}}^{\frac{h}{2}} \sigma_{zz} z dz,$$

$$M^{(j)} = \int_{-\frac{h}{2}}^{\frac{h}{2}} \sigma_{xx} \frac{(z)^j}{j!} dz \; (j = 1,2),$$

$$P^{(k)} = \int_{-\frac{h}{2}}^{\frac{h}{2}} \tau_{xz} \frac{(z)^k}{k!} dz \; (k = 1,2).$$

$$I_i = \int_{-\frac{h}{2}}^{\frac{h}{2}} \rho (z)^i dz \; (i = 0,1,2,...4) \quad \text{(A.2)}$$

The equations of motion HOSTU4W2 model:

$$\delta u_0 : \frac{\partial N}{\partial x} = I_0 \ddot{U}_0 + I_1 \ddot{U}_1 + \frac{I_2}{2} \ddot{U}_2 + \frac{I_3}{6} \ddot{U}_3,$$

$$\delta u_1 : \frac{\partial M^{(1)}}{\partial x} - Q = I_1 \ddot{U}_0 + I_2 \ddot{U}_1 + \frac{I_3}{2} \ddot{U}_2 + \frac{I_4}{6} \ddot{U}_3,$$

$$\delta u_2 : \frac{\partial M^{(2)}}{\partial x} - P^{(1)} = \frac{I_2}{2} \ddot{U}_0 + \frac{I_3}{2} \ddot{U}_1 + \frac{I_4}{4} \ddot{U}_2 + \frac{I_5}{12} \ddot{U}_3,$$

$$\delta u_3 : \frac{\partial M^{(3)}}{\partial x} - P^{(2)} = \frac{I_3}{6} \ddot{U}_0 + \frac{I_4}{6} \ddot{U}_1 + \frac{I_5}{12} \ddot{U}_2 + \frac{I_6}{36} \ddot{U}_3,$$

$$\delta w_0 : \frac{\partial Q}{\partial x} = I_0 \ddot{W}_0 + I_1 \ddot{W}_1,$$

$$\delta w_1 : \frac{\partial P}{\partial x} - R = I_1 \ddot{W}_0 + I_2 \ddot{W}_1, \quad \text{(A.3)}$$

The force resultans operator and the mass moments of inertia of Eqs. (A.3):

$$N = \int_{-\frac{h}{2}}^{\frac{h}{2}} \sigma_{xx} dz, \; Q = \int_{-\frac{h}{2}}^{\frac{h}{2}} \tau_{xz} dz,$$

$$R = \int_{-\frac{h}{2}}^{\frac{h}{2}} \sigma_{zz} dz, P = \int_{-\frac{h}{2}}^{\frac{h}{2}} \tau_{xz} \frac{z}{k!} dz,$$

$$M^{(j)} = \int_{-\frac{h}{2}}^{\frac{h}{2}} \sigma_{xx} \frac{(z)^j}{j!} dz \; (j = 1,2,3),$$

$$I_i = \int_{-\frac{h}{2}}^{\frac{h}{2}} \rho (z)^i dz \; (i = 0,1,2,...6) \quad \text{(A.4)}$$

The equations of motion HOSTU3W2 model:

$$\delta u_0 : \frac{\partial N}{\partial x} = I_0 \ddot{U}_0 + I_1 \ddot{U}_1 + \frac{I_2}{2} \ddot{U}_2,$$

$$\delta u_1 : \frac{\partial M^{(1)}}{\partial x} - Q = I_1 \ddot{U}_0 + I_2 \ddot{U}_1 + \frac{I_3}{2} \ddot{U}_2,$$

$$\delta u_2 : \frac{\partial M^{(2)}}{\partial x} - P^{(1)} = \frac{I_2}{2} \ddot{U}_0 + \frac{I_3}{2} \ddot{U}_1 + \frac{I_4}{4} \ddot{U}_2,$$

$$\delta w_0 : \frac{\partial Q}{\partial x} = I_0 \ddot{W}_0 + I_1 \ddot{W}_1,$$

$$\delta w_1 : \frac{\partial P}{\partial x} - R = I_1 \ddot{W}_0 + I_2 \ddot{W}_1, \quad \text{(A.5)}$$

The force resultans operator and the mass moments of inertia of Eqs. (A.5):

$$N = \int_{-\frac{h}{2}}^{\frac{h}{2}} \sigma_{xx} dz, \; Q = \int_{-\frac{h}{2}}^{\frac{h}{2}} \tau_{xz} dz,$$

$$R = \int_{-\frac{h}{2}}^{\frac{h}{2}} \sigma_{zz} dz, P = \int_{-\frac{h}{2}}^{\frac{h}{2}} \tau_{xz} \frac{z}{k!} dz,$$

$$M^{(j)} = \int_{-\frac{h}{2}}^{\frac{h}{2}} \sigma_{xx} \frac{(z)^j}{j!} dz \; (j = 1,2),$$

$$I_i = \int_{-\frac{h}{2}}^{\frac{h}{2}} \rho (z)^i dz \; (i = 0,1,2,3,4) \quad \text{(A.6)}$$

The 5th International Conference on Engineering Mechanics and Automation (ICEMA-5)
Hanoi, October 11÷12, 2019

Numerical and experimental study on seismic behavior of shallow foundations

Huynh Van Quan[a], Nguyen Xuan Huy[b], Nguyen Trung Kien[b] and Tran Thu Hang[c]

[a] *Faculty of Civil Engineering, University of Transport and Communications, Campus in Ho Chi Minh City, Viet Nam.*
[b] *Research and Application centre for technology in Civil Engineering (RACE), University of Transport and Communications, Hanoi, Viet Nam.*
[c] *Faculty of Civil Engineering, University of Transport and Communications, Hanoi, Viet Nam*

Abstract

This paper presents a 3D macro-element simulates the soil-shallow foundation system with the coupling of irreversible elastoplastic soil behavior (material non-linearity) and the possible foundation uplift (geometric non-linearity) under spatial seismic loading. A model with five degrees-of-freedom (DOF) for 3D macro-element solved by a suitable Newmark time integration scheme. The proposed macro-element is subsequently validated using shaking table tests on shallow foundations at University of Transport and Communications, Vietnam. The comparison between the experimental and simulation results shows the performance of the proposed model.

Key Words: Macro-element, material and geometric non-linearity, seismic loading, shaking table.

1. Introduction

In the structural design, soil–foundation interaction (SFI) is an important phenomenon that has to be taken into account. However, simulating SFI often necessitates the use of complex models for the soil and the foundation, leading to a great number of DOF and thus to significant computational costs. This is the reason why various simplified modelling strategies have recently been developed. The macro-element consists in modelling the soil-foundation system as a unique non-linear macro-element with a limited number of DOF. This approach helps reproducing the non-linear behavior of the foundations considering material and geometric non-linearities. The macro-element reduces the size of the problem significantly while preserving the essential features of the dynamic response of the system.

The term "macro-element" was initially introduced by Nova and Montrasio (1991) in their study of the settlements of shallow foundations on sand. Montrasio and Nova (1997) completed an elastic-plastic macro-element formulations for strip and circular footings under quasi-static monotonic loading. Based on the Nova and Montrasio's model, Paolucci (1997) proposed a numerical tool permitting the study of the response of simple structures subject to seismic loading and taking into account the coupling between the non-linear response of the SFI and the response of the superstructure. Cremer et al. (2002) developed the first application of the macro-element for purely cohesive soils with no resistance to tensile stresses. This macro-element can be used not only for static loading but also for dynamic (seismic) loading, considering the plasticity of the soil and the uplift of the foundation. Macro-

element models for seismic SFI problems are also available in the literature, such as those proposed by Cremer et al. (2001), Chatzigogos et al. (2009), Grange et al. (2008, 2009), Figini et al. (2012) and di Prisco et al. (2011). For shallow foundations, [6,7,8] used the macro element of quasi-static monotonic loading to analyse the structures under seismic loading. In Paolucci (1997) and Paolucci et al. (2008), the superstructure was represented by a single-degree-of-freedom mass and the macro-element only took into account the plasticity of the soil or the uplift of the foundation. In Figini et al. (2012), authors completed these model when considering the uplift-plasticity coupling, but not be suitable for earthquake loads because they changed in time and fully recovered once the seismic loadings eccentricity come back.

Inspired by these last works, the present paper proposes a 3D macro-element with the material-geometric coupling for seismic analysis of shallow foundation. It consists of 5 DOF macro-element based on the models of Paolucci et al. (1997, 2008) with the differential equations of system's motion. After the description of the 3D macro-element, comparisons of results with laboratory tests are shown the good performance of the proposed approach.

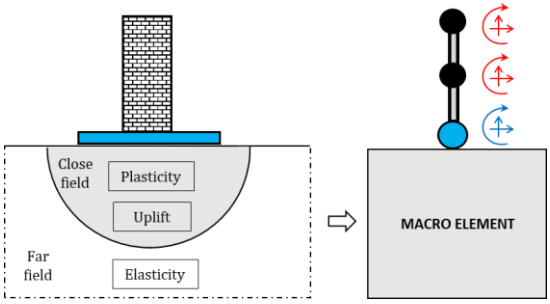

Figure 1. Macro element concept: decomposition in close field and far field

2. Description of the proposed macro-element

2.1. The general structure

The structure of a macro-element model will follow the scheme presented in Figure 1. Two fields are divided in the soil domain, the close field where all material and geometric non-linearities are lumped and the far field describes the area where the response of the system remains linear. The far field works linearly and the near field works non-linearly with constitutive relationship. The entire soil-foundation system is replaced by a single element located at the base of the superstructure (Figure 1).

A 5 DOF model (x, y and z translations, plus rocking around x, y axes) is formulated describing the resultant force-displacement behavior of the footing centre (Figure 2, in $x-z$ plane). In this formulation, the footing is considered as a rigid body. The single macro-element restrained by the system of equivalent springs and dashpots to describe the non-linear interactions between soil and foundation (Figure 2). Two types of nonlinearities of a macro-element: the material type due to non-linear soil or interface behavior and the geometric type due to rocking and uplift of the footing accompanied by the creation of a detachment area at the soil-footing interface. These two distinct mechanisms are coupled (material-geometric coupling).

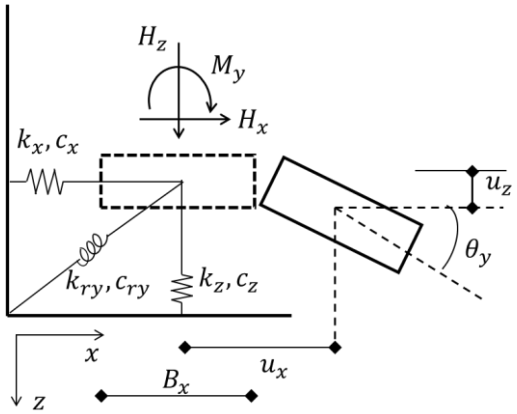

Figure. 2. Macro element modelling of a soil-shallow foundation system: foundation static impedances in $x-z$ plane

2.2. The variables of forces and displacements

The entire soil-footing system is lumped in a single point at the footing centre, a macro-element model has terms of generalized forces and displacement variables (Figure 3).

The vector $\boldsymbol{F}$ of the generalized force variables is defined as:

$$\boldsymbol{F} = [H_x \quad H_y \quad M_x \quad M_y \quad H_z]^T \tag{1}$$

whereas the vector $\boldsymbol{u}$ of generalized displacement variables is defined as:

$$\boldsymbol{u} = [u_x \quad u_y \quad \theta_x \quad \theta_y \quad u_z]^T \tag{2}$$

In the previous equations, H_x, H_y are the reduced horizontal forces; H_z is the reduced vertical force; M_x, M_y are the reduced moments applied to the foundation; whereas u_x, u_y are the reduced horizontal displacements; u_z is the reduced vertical displacement; θ_x, θ_y are the reduced rotations (Figure 3).

It is worth noting that because the soil-foundation system is lumped in a single point, the corresponding stiffness matrix in the elastic case can be considered diagonal, and it is written as follows:

$$\boldsymbol{K}^{F0} = \begin{bmatrix} k_{0x} & 0 & 0 & 0 & 0 \\ 0 & k_{0y} & 0 & 0 & 0 \\ 0 & 0 & k_{rx} & 0 & 0 \\ 0 & 0 & 0 & k_{ry} & 0 \\ 0 & 0 & 0 & 0 & k_z \end{bmatrix} \tag{3}$$

The terms on the diagonal represent the foundation static impedances ($k_{0x,y}$, k_z and $k_{rx,y}$ are the stiffness of the equivalent elastic springs to the horizontal direction, vertical direction and rotation, respectively) changed over time during the earthquake process, which can be determined from Gazetas's formulas (Gazetas, 1991).

2.3. The yield function and flow rule

Owing to the good agreement with the Paolucci's experimental results for shallow strip footings on dry sand under seismic loading conditions. This paper calls again the yield function and flow rule which Paolucci employed in 3D.

The yield function $f(F)$:

$$f(F) = h_x^2 + h_y^2 + m_x^2 + m_y^2 - v^2(1-v)^{2\xi} \tag{4}$$

where $h_x = H_x/(\mu N_{max})$, $h_y = H_y/(\mu N_{max})$, $v = H_z/N_{max}$, $m_x = M_x/(\psi B_x N_{max})$, $m_y = M_y/(\psi B_y N_{max})$; N_{max} is the ultimate bearing capacity under vertical central load. For the yield function parameters, selected $\psi = 0.43$, that is an intermediate value in the range between 0.35 and 0.5 for which the best agreement with observations was obtained; $\mu = tan\varphi$, φ is the soil friction angle; $\xi = 0.95$, in agreement with the value suggested by Nova and Montrasio (1991).

As for the calculation of inelastic displacements and rotations, this paper adopted the non-associative plastic flow rule from Paolucci (2008) in 3D:

$$g(F) = \lambda^2\left(h_x^2 + h_y^2\right) + \chi^2\left(m_x^2 + m_y^2\right) + v^2 \tag{5}$$

The optimum parameters $\lambda = 4$ and $\chi = 6$ were selected.

2.4. The stiffness matrix

Before appearing material-geometric coupling, the elastic stiffness matrix of a macro-elements is defined in equation (3). During the strongly nonlinear phase of the seismic excitation reveals that the instantaneous foundation–soil contact area changes over time successive cycles of foundation rotations. This is explained by irrecoverable downward movement of soil beneath the foundation induced by severe foundation rotations during successive seismic loading, resulting in a reduction of the effective foundation width (B') along the considered direction that can be expressed as follows:

$$B' = B(1-\delta) \tag{6}$$

where B is the actual width of the footing and δ can be interpreted as a degradation parameter defined in the range $0 \le \delta \le 1$. Initially, the value of δ is set to zero, and the value of δ is updated throughout the seismic excitation due to accumulation of inelastic foundation tilting. Although the footing has a square shape, reduction in the footing–soil contact in transverse direction results in a rectangular contact area. Substituting equation (6) into the approximate static stiffness formulas for a rectangular footing, and supposing that the square-shaped foundation base is in full contact with the soil prior to the seismic excitation, the reduced stiffness factors in the considered plane for each vibration mode are obtained as:

$$k'_0 = k_0[0.74(1-\delta)^{0.35} + 0.09 + 0.17(1-\delta)] \tag{7}$$

$$k'_r = k_r[(1-0.2\delta)(1-\delta)^2] \tag{8}$$

$$k'_v = k_v[0.66(1-\delta)^{0.25} + 0.34(1-\delta)] \tag{9}$$

where k'_0, k'_r and k'_v are the modified stiffnesses in terms of δ; k_0, k_r, k_v are the equivalent elastic spring coefficients of the soil-foundation system defined in the previous section for each considered plane. It will be shown in the following that stiffness degradation is essential to explain some important details of the foundation response during the most severe seismic loading condition. For this purpose, we have selected the following simple degradation function:

$$\delta(\theta^p) = \frac{\delta_1}{1+\frac{1}{\delta_2 \theta^p}} \quad (10)$$

where δ_1 =0.75 and δ_2 =5000/rad are model parameters related to the ultimate δ value and to the degradation speed, respectively, while is θ the cumulated plastic foundation rotation at a specified instant of time, calculated as:

$$\theta^p = \sum_n |\Delta\theta_n - \Delta M_n / k'_r| \quad (11)$$

In equation (11), n and M_n are the increments of foundation rotation and overturning moment, respectively, calculated at the nth time step. When, the 3D elastic stiffness matrix obtained as equation (12).

The soil behavior is assumed to be linear visco-elastic until the failure surface in equation (4) is reached. When the failure surface is reached, only the radiation contribution should be retained. So, plastic flow occurs when $f(\boldsymbol{F}) \geq 0$ and $df(\boldsymbol{F}) = 0$, the elastic stiffness matrix of macro-elements will be reduced a differential value $d\boldsymbol{K}^F$ for initial value in equation (3). This is calculated as a function of the elastic stiffness matrix $\boldsymbol{K}^{F0}$ and the derivatives of the yield and plastic potential functions.

$$\boldsymbol{K}^{F\prime} = \begin{bmatrix} k'_{0x} & 0 & 0 & 0 & 0 \\ 0 & k'_{0y} & 0 & 0 & 0 \\ 0 & 0 & k'_{rx} & 0 & 0 \\ 0 & 0 & 0 & k'_{ry} & 0 \\ 0 & 0 & 0 & 0 & k'_{z} \end{bmatrix} \quad (12)$$

$$d\boldsymbol{K}^F = \boldsymbol{K}^{F0}\left(\frac{\partial g}{\partial \boldsymbol{F}}\right)\left(\frac{\partial f}{\partial \boldsymbol{F}}\right)^T \boldsymbol{K}^{F0}\left[\left(\frac{\partial f}{\partial \boldsymbol{F}}\right)^T \boldsymbol{K}^{F0}\left(\frac{\partial g}{\partial \boldsymbol{F}}\right)\right]^{-1} \quad (13)$$

Thus, the elastoplastic stiffness matrix of the proposed macro-element in step of nth is determined by the formula:

$$\boldsymbol{K}^F = \boldsymbol{K}^{F\prime} - d\boldsymbol{K}^F \quad (14)$$

When geometric is coupled with material plasticity, the elastic stiffness matrix given by equation (3) is then calculated based on the effective base width B' given in equation (14).

3. Evaluating the proposed macro-element model

3.1. Setting up and solving the dynamic equilibrium equations of macro-element

In this application, we used the simplified model with five DOFs shallow foundation (horizontal, lateral and vertical motion, plus rocking around its center directions of mass) in Figure 2. The differential equations of motion are presented in equation (15).

$$\boldsymbol{M}\ddot{x} + \boldsymbol{C}\dot{x} + \boldsymbol{F} = \boldsymbol{P} \quad (15)$$

Where

$$\boldsymbol{x} = \begin{bmatrix} \boldsymbol{x_0} & \boldsymbol{y_0} & \phi_{\mathbf{x}} & \phi_{\mathbf{y}} & \mathbf{z} \end{bmatrix}^{\boldsymbol{T}} \quad (16)$$

$$\boldsymbol{P} = [-m_0\ddot{x}_g \quad -m_0\ddot{y}_g \quad 0 \quad 0 \quad -m_0\ddot{z}_g]^T \quad (17)$$

$$\boldsymbol{F}^F = [H_x \quad H_y \quad M_x \quad M_y \quad V]^T \quad (18)$$

$$\boldsymbol{M} = \begin{bmatrix} m_0 & 0 & 0 & 0 & 0 \\ 0 & m_0 & 0 & 0 & 0 \\ 0 & 0 & J_x & 0 & 0 \\ 0 & 0 & 0 & J_y & 0 \\ 0 & 0 & 0 & 0 & m_1 + m_0 \end{bmatrix} \quad (19)$$

$$C = \begin{bmatrix} c_{0x} & 0 & 0 & 0 & 0 \\ 0 & c_{0y} & 0 & 0 & 0 \\ 0 & 0 & c_{rx} & 0 & 0 \\ 0 & 0 & 0 & c_{ry} & 0 \\ 0 & 0 & 0 & 0 & c_v \end{bmatrix} \quad (20)$$

$\boldsymbol{x}$, vector of the displacements of the basement; $\boldsymbol{P}$, vector of base excitations; $\boldsymbol{F}$, vector of soil reactions. x_0, y_0, horizontal displacements of the basement; ϕ_x, ϕ_y rocking motion of the basement; x_v, vertical displacements, respectively. $\ddot{x}_g$, $\ddot{y}_g$, $\ddot{z}_g$, horizontal and vertical base excitations, respectively. m_0, J

mass of the foundation and sum of the centroid moments of inertia of the foundation, respectively. c_0, c_r, c_v equivalent dashpot coefficients of the soil-foundation system corresponding to the translational, rocking and vertical modes of vibration, respectively.

The Newmark time integration scheme was used for solving the motion equations equation (15). Denoting by the subscript n the quantities calculated at time $t = n\Delta t$, the motion form of Newmark time integration scheme of Equation (15) can be rewritten as equation (21).

$$\left[\frac{\boldsymbol{M}}{\beta(\Delta t)^2}+\frac{\boldsymbol{C}\gamma}{\beta\Delta t}\right]\boldsymbol{x}_{n+1}+\boldsymbol{F}_{n+1}(\boldsymbol{x}_{n+1})=\boldsymbol{p}_{n+1}+\boldsymbol{M}\left[\frac{1-2\beta}{2\beta}\ddot{\boldsymbol{x}}_n+\frac{\dot{\boldsymbol{x}}_n\Delta t+\boldsymbol{x}_n}{\beta(\Delta t)^2}\right]+\boldsymbol{C}\left[\left(\frac{\gamma}{2\beta}-1\right)\ddot{\boldsymbol{x}}_n\Delta t+\left(\frac{\gamma}{\beta}-1\right)\dot{\boldsymbol{x}}_n+\frac{\gamma}{\beta\Delta t}\boldsymbol{x}_n\right] \quad (21)$$

Where Δt is the time step, $\beta = 0.25$ and $\boldsymbol{\gamma} = 0.5$ are the Newmark integration parameters.

3.2. Validation

In order to validate the capability of the present numerical strategy, the proposed macro- element is implemented in Matlab by using the motion equation form of Newmark time integration scheme, equation (21). The present method validated by seismic laboratory shaking table tests at University of Transport and Communications.

The seismic behavior of a shallow foundation placed on the dense sand medium is simulated. This shallow foundation is a square-shape of 0.25×0.25m in plan and 0.1m high. The dense sand medium in 0.667m layer thickness from the shallow foundation bottom to the bed sand box (Figure 3). The input acceleration time history for Tolmezzo earthquake was used for horizontal loading with 2.42 m/s^2 peak ground acceleration, figure 4.

The calculated horizontal acceleration of footing center is compared with the experimental results with other peak ground accelerations in Figure 5, Figure 6, Figure 7 and Figure 8, which shows that a relatively satisfactory agreement.

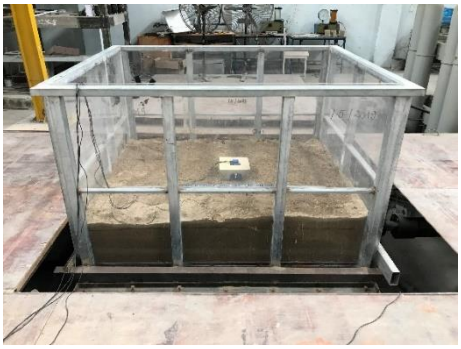

Figure 3. The experimental set-up

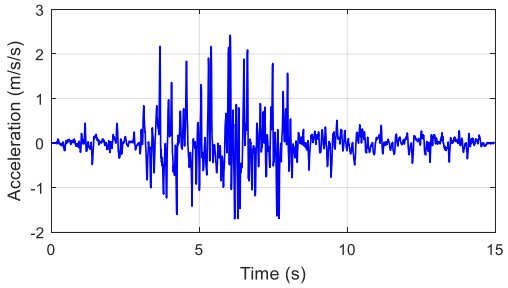

Figure 4. Tolmezzo earthquake with 2.42 m/s^2 peak ground acceleration

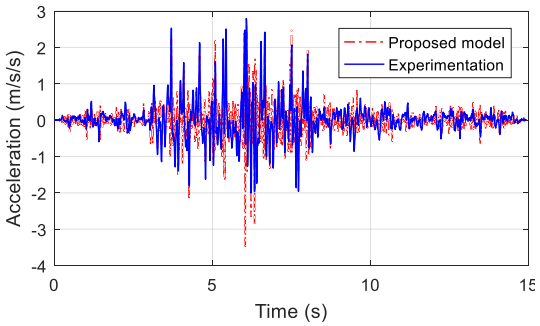

Figure 5. Horizontal acceleration of footing center time history with 2.42 m/s^2 peak ground acceleration

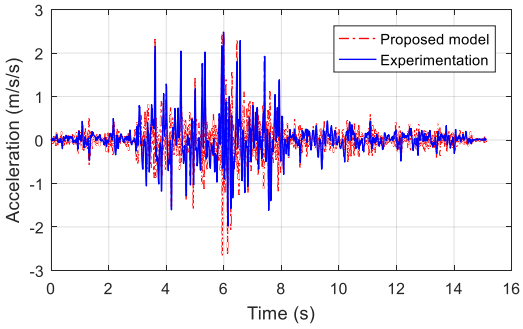

Figure 6. Horizontal acceleration of footing center time history with 2.155 m/s^2 peak ground acceleration

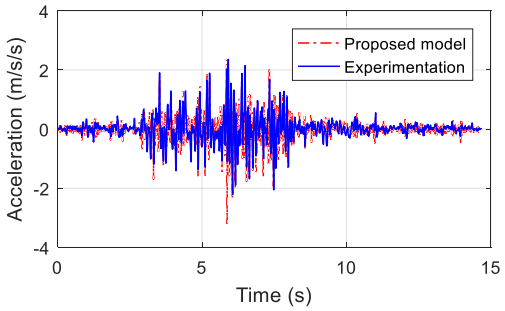

Figure 7. Horizontal acceleration of footing center time history with 2.045 m/s^2 peak ground acceleration

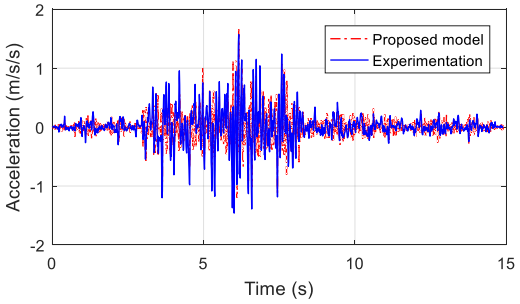

Figure 8. Horizontal acceleration of footing center time history with 1.460 m/s^2 peak ground acceleration

4. Conclusions

In this paper, a new macro-element for modelling the behavior of soil-shallow foundation interaction under seismic loading have been presented. The proposed macro-element considered simultaneously the material and geometric non-linearities response of foundation. It includes of 5 DOF macro-element with the differential equations of system's motion. Comparisons of numerical result obtained from the macro-element and the experimental result are shown that this model is suited to simulate the couple of material and geometric behaviors of shallow foundation under seismic loading. Based on the results obtained it seems now possible to use this approach to investigate numerically the behavior of a wider variety of configurations.

In the future, possible improvements of the proposed macro-element are necessary, especially concerning superstructures. This approach is straightforward and will be presented in next publication.

References

Nova, R. and Montrasio, L. (1991) "Settlements of shallow foundations on sand," *Geotechnique* 41(2), 243-256.

Montrasio, L. and Nova, R. (1997) "Settlements of shallow foundations on sand: Geometrical effects," *Geotechnique* 47(1), 49-60.

Paolucci, R. (1997) "Simplified Evaluation of Earthquake-Induced Permanent Displacements of Shallow Foundations," *Journal of Earthquake Engineering* 01(03), 563-579.

Cremer, C., Pecker A. and Davenne, L. (2002) "Modelling of nonlinear dynamic behavior of a shallow strip foundation with macro-element," *Journal of Earthquake Engineering* 06(02), 175-211.

Cremer, C., Pecker, A. and Davenne, L. (2001) "Cyclic macro-element for soil-structure interaction: material and geometrical non-linearities," *Int. J. Numer. Anal. Meth. Geomech* 25(13), 1257-1284.

Chatzigogos, C. T., Pecker, A. and Salencon J., (2009) "Macroelement modeling of shallow foundations," *Soil Dynamics and Earthquake Engineering* 29(5), 765–781.

Grange, S., Kotronis, P. and Mazars, J. (2008) "A macro-element for a circular foundation to simulate 3D soil–structure interaction," *Int. J. Numer. Anal. Meth. Geomech* 32(10), 1205–1227.

Grange, S., Kotronis, P. and Mazars, J. (2009) A macro-element to simulate dynamic Soil-Structure Interaction," *Engineering Structures* 31(12), 3034–3046.

Figini, R., Paolucci R. and Chatzigogos, C. T. (2012) "A macro-element model for non-linear soil–shallow foundation–structure interaction under seismic loads: theoretical development and experimental validation on large scale tests," *Earthquake engineering and structural dynamics* 41(3), 475-493.

Priscon, C. and Pisano, F. (2011) "Seismic response of rigid shallow footings," *European Journal of Environmental and Civil Engineering* 15(1), 185-221.

Paolucci, R., Shirato, M. and Tolga Yilmaz, M. (2008) "Seismic behavior of shallow foundations: Shaking table experiments vs numerical modelling," *Earthquake engineering and structural dynamics* 37(4), 577-595.

Gazetas, G. (1991) "Chapter15. Foundation Vibrations," in *Foundation Engineering Handbook*,

ed. H. Y. Fang (2nd Editions, Springer, MA), pp. 553-593.

Chopra, A. K. (1995) Dynamics of structures (Prentice Hall, California, USA).

The 5th International Conference on Engineering Mechanics and Automation (ICEMA 5)
Hanoi, October 11÷12, 2019

Dynamic behavior of a bidirectional functionally graded sandwich beam underof a moving load based on a high-order shear deformation theory

Le Thi Ha

University of Transport and Communications, Lang Thuong, Dong Da, Hanoi

*Email: lethiha@utc.edu.vn

Abstract

This paper studies dynamic behavior of a bidirectional functionally graded sandwich (BFGSW) beam under a moving by using a high-order deformation beam theory. The beam is composed of unidirectional functionally graded core, an isotropic bottom layer and a bidirectional functionally graded top layer. Equations of motion in the context of finite element analysis are derived from energy expressions, and solved by the direct integration Newmark method. The accuracy of the derived formulation is confirmed by comparing the obtained results with the published data. The effects of material and loading parameters on the dynamic behavior of the beam are examined and discussed.

Key Words: BFGSW beam, high-order shear deformation theory, moving load, dynamic behavior, finite element analysis

1. Introduction

Functionally graded materials (FGMs), a new generation of composite materials, were initiated

by Japanesescientists in Sendai in the mid-1984s [1]. FGMs are produced by varying volume fraction of constituent materials in one ormore desired spatial directions. Functionally graded materials (FGMs), are increasingly used as structural elements in modern industries such as aerospace structures, turbine blades and rocket engine components. Many researches on vibration behavior of FGM sandwich beam structures have been reported in the literature, the papers that are most relevant to the present work are briefly discussed below.

Such as, Vo and his co-authors [2] adopted a refined shear deformation theory in studying the free vibration and buckling of FG sandwich beams. Vo et al. [3] presented a finite element model for the free vibration and buckling analyses of FG sandwich beams.The investigations cited above, however, are related to FG beams with material properties varying in one spatial direction only. There are practical circumstances, in which the unidirectional FGMs may not be so appropriate to resist multi-directional variations of thermal and mechanical loadings. Therefore, it is of great importance to develop FGMs with effective material properties varying in two or three directions to withstand severe general loadings. Vibration analysis of structures made of bi-dimensional FGMs has been carried out by several authors recently. Studies on the static and dynamic behavior of beams formed from two-directional functionally graded materials (2-D FGMs) have been

recently reported by several researchers. In this line of works, Şimşek [4,5] considered the material properties being varied in both the thickness and length directions by an exponent function in the forced vibration and buckling analyses of 2-D FGM Timoshenko beams. The author showed that the vibration and bucking behavior of the 2-D FGM beams is significantly influenced by the material distribution. Based on an analytical method, Wang et al. [6] investigated the free vibration of FGM beams with the material properties vary through the thickness by an exponential function and along the length by a power-law distribution. The numerical investigations by the authors show that the variation of material properties has a strong influence on the natural frequencies, and there is a critical frequency at which the natural frequencies have an abrupt jump when they across the critical frequency. Based on a finite element procedure, Nguyen et al. [7] studied the forced vibration of 2-D FGM Timoshenko beams excited by a moving load. The material properties in [7] were assumed to vary in both the thickness and longitudinal directions by a power-law function. Recently, Shafiei et al.[8] studied the vibration behavior of 2-D FG nano and microbeams formed from two types of porous FGMs. The generalized differential quadrature method has been employed by the authors to solve the governing equations of motion. Nguyen et al. [9] studied an efficient and free of shear locking finite element model is developed and employed to study free vibration of tapered bidirectional functionally graded material (BFGM) beams. The beam material is assumed to be formed from four distinct constituent materials whose volume fraction continuously varies along the longitudinal and thickness directions by power-law functions. The finite element formulation based on the first-order shear deformation theory is derived by using hierarchical functions.

In this paper, the vibration of power-law bi-dimensional FG sandwich beams excited by a moving concentrated load is studied. The beam material is assumed to be formed from two distinct constituent materials whose volume fractions vary in both the thickness and longitudinal directions by powerlaw functions. In this regard, a finite element formulation is developed and used in combination with the Newmark method in solving the equations of motion of the problem considered herein. A parametric study is carried out to highlight the effect of material distribution and the speed of the moving load on the vibration characteristics of the beams. The influence of the aspect ratio of the dynamic behavior of the beams is also examined and discussed.

2. Sandwich beam underof a moving load

Figure 1 shows a bi-dimensional FG sandwich beam with length of L subjected to a concentrated load F, moving from left to right with a constant speed v. In the Figure, a Cartesian coordinate system (x, z) is introduced such that the x-axis is on the mid-plane, and the z-axis is perpendicular to the mid-plane, and it is directed upward. The beam cross section is assumed to be rectangular with width b and height h.

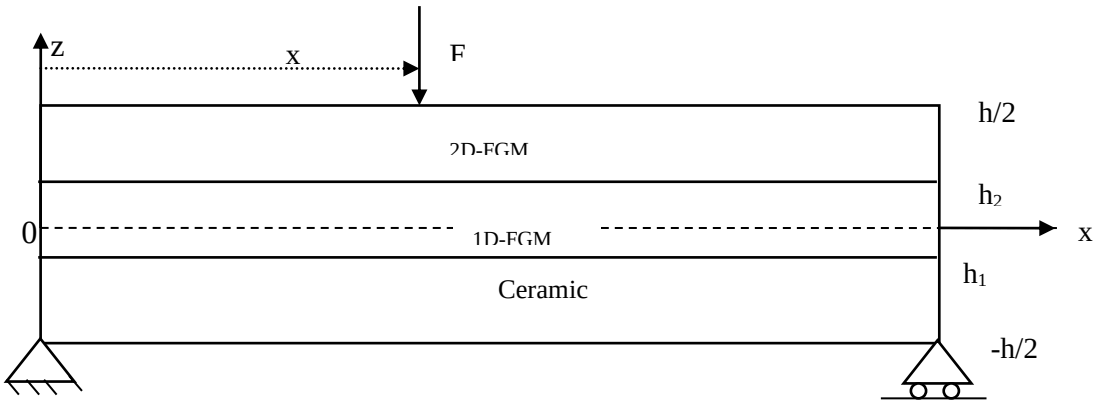

Fig 1. Sandwich beam under a moving load

The beam material is assumed to be formed from ceramic and metal whose volume fraction varies in both the thickness and longitudinal directions [10] as follows:

$$\begin{cases} V_c^3(x,z)=1 & z\in\left[-\dfrac{h}{2};h_1\right] \\ V_c^2(x,z)=\left(\dfrac{z-h_2}{h_1-h_2}\right)^n & z\in\left[h_1;h_2\right] \\ V_c^1(x,z)=\left(1-\dfrac{x}{2L}\right)^m\left(\dfrac{2.(z-h_2)}{h-2.h_2}\right)^n & z\in\left[h_2;\dfrac{h}{2}\right] \end{cases} \tag{2.1}$$

where *n* and *m* are the grading indexes, which dictate the variation of the constituent materials in the thickness and longitudinal directions, respectively. $V_c^k(x,z)$ is the volume fraction function of ceramic material of the k-th layer. The effective material properties *(P)* (such as Young's modulus and mass density, etc.) for the beam are evaluated by the Voigt model as

$$P^k(x,z)=(P_c-P_m)V_c^k(x,z)+P_m \tag{2.2}$$

where *P*c, *P*m denote the properties of ceramic, metal, respectively, P^k denote the effective material properties of the k-th layer. Based on the third-order shear deformation theory [11], the axial and transverse displacements at any point of the beam, u(x, z, t) and w(x, z, t), respectively, are given

$$\begin{cases} u(x,z,t)=u_0+z(\gamma_0-w_{0,x})-\alpha z^3\gamma_0 \\ w(x,z,t)=w_0 \end{cases} \tag{2.3}$$

where *t* is the time variable and $\alpha = 4/3\ h^2$; $u_0(x, t)$ and $w_0(x, t)$ are, respectively, the axial and transverse displacements of the point on the *x*-axis, γ_0 is the transverse shear rotation. The axial strain and shear strain resulted from Eq. (2.3) are of the forms

$$\begin{aligned} \varepsilon_{xx}&=u_{0,x}+z\left(\gamma_{0,x}-w_{0,xx}\right)-\alpha z^3\gamma_{0,x} \\ \gamma_{xz}&=\gamma_0-3\alpha z^2\gamma_0 \end{aligned} \tag{2.4}$$

Based on the assumption of Hooke's law, the constitutive relation for sandwich beam with the 2-D FGM is as follows

$$\begin{aligned} \sigma_{xx}&=E(x,z).\varepsilon_{xx}=E(x,z)[u_{0,x}+z(\gamma_{0,x}-w_{0,xx})-\alpha z^3\gamma_{0,x}] \\ \tau_{xz}&=G(x,z)\gamma_{xz}=\frac{E(x,z)}{2(1+\upsilon)}\left[\gamma_0-3\alpha z^2\gamma_0\right] \end{aligned} \tag{2.5}$$

Where $E(x,z)$ and $G(x,z)$ are, respectively, the elastic modulus and shear modulus, which are functions of both the coordinates *x*, *z*, σ_{xx} and τ_{xz} are the axial stress and shear stress, espectively. The elastic strain energy resulted from beam deformation:

$$U=\frac{1}{2}\int_0^L\begin{bmatrix} A_{11}u_{0,x}^2+2A_{12}u_{0,x}(\gamma_{0,x}-w_{0,xx}) \\ +A_{22}(\gamma_{0,x}-w_{0,xx})^2-2A_{34}\alpha u_{0,x}\gamma_{0,x} \\ -2\alpha A_{44}\gamma_{0,x}(\gamma_{0,x}-w_{0,xx}) \\ +\alpha^2A_{66}\gamma_{0,x}^2+B_{44}\gamma_0^2 \end{bmatrix}dx \tag{2.6}$$

In Eqs. (2.6), A_{11}, A_{12}, A_{22}, A_{34}, A_{44}, A_{66} and B_{44} are the beam rigidities, defined as:

$$\begin{aligned} &(A_{11},A_{12},A_{22},A_{34},A_{44},A_{66})(x,z) \\ &=\int_A E^k(x,z)(1,z,z^2,z^3,z^4,z^6)dA \\ &B_{44}(x,z)=\int_A G^k(x,z)(1-6\alpha z^2+9\alpha^2z^4)dA \end{aligned} \tag{2.7}$$

where $E^k(x,z)$, $G^k(x,z)$ are, respectively, the elastic modulus and shear modulus of the *k*-th layer. The kinetic energy (T) of the beam are then given by

$$T=\frac{1}{2}\int_0^L\begin{bmatrix} I_{11}(\dot{u}_0^2+\dot{w}_0^2)+I_{22}(\dot{\gamma}_0-\dot{w}_{0,x})^2+\alpha^2I_{66}\dot{\gamma}_0^2 \\ +2I_{12}\dot{u}_0(\dot{\gamma}_0-\dot{w}_{0,x})-2\alpha I_{34}\dot{u}_0\dot{\gamma}_0 \\ -2\alpha I_{44}\dot{\gamma}_0(\dot{\gamma}_0-\dot{w}_{o,x}) \end{bmatrix}dx \tag{2.8}$$

In Eqs. (2.8), I_{11}, I_{12}, I_{22}, I_{34}, I_{44}, I_{66} are the mass moments, defined as

$$\begin{aligned} &(I_{11},I_{12},I_{22},I_{34},I_{44},I_{66})(x,z) \\ &=\int_A\rho^k(x,z)(1,z,z^2,z^3,z^4,z^6)dA \end{aligned} \tag{2.9}$$

where, $\rho^k(x,z)$ is the mass density of the *k*-th layer. The potential of the moving load *(V)* is simply given by

$$V = -Fw(x)\delta(x - vt_i) \tag{2.10}$$

where $\delta(.)$ is the Dirac delta function, and *x* is the abscissa, measured from the left end of the beam. Using the finite element method, the beam is assumed to be divided into a number of two-node beam elements of length *l*. The vector of nodal displacements *(***d***)* for the element considering the transverse shear rotation γ_0 as an independent variable contains eight components as

$$d = \left\{u_i, w_i, w_{i,x}, \gamma_i, u_j, w_j, w_{j,x}, \gamma_j\right\}^T \tag{2.11}$$

Where $u_i, w_i, w_{i,x}, \gamma_i, u_j, w_j, w_{j,x}, \gamma_j$ are the values of u_0, w_0, $w_{0,x}$ and γ_0 at the node *i* and at the node *j*. In Eq. (2.11), and hereafter, a superscript '*T*' is used to denote the transpose of a vector or a matrix**.**

The axial displacement, transverse displacement and transverse shear deformation are interpolated from the nodal values according to

$u_0 = Nu.\mathbf{d}$, $w_0 = Nw.\mathbf{d}$, $\gamma_0 = N\gamma.\mathbf{d}$ (2.12)

where *Nu*, *Nw* and *Nγ* denote the matrices of shape functions for u_0, w_0 and γ_0, respectively. In the present work, linear shape functions are used for the axial displacement and the shear rotation, using the above interpolation schemes, one can write the strain energy of the beam defined by Eqs. (2.6) as

$$U = \frac{1}{2}\sum^{ne} \mathbf{d}^T \mathbf{k} \mathbf{d} \tag{2.13}$$

where *ne* is the total number of the elements, and **k** is the element stiffness matrix with the following form

$\mathbf{k} = \mathbf{k}_{11} + \mathbf{k}_{12} + \mathbf{k}_{22} + \mathbf{k}_{34} + \mathbf{k}_{44} + \mathbf{k}_{66} + \mathbf{k}_s$ (2.14)

with

$$\mathbf{k}_{11} = \int_0^l N_{u,x}^T A_{11} N_{u,x} dx;$$

$$\mathbf{k}_{12} = 2\int_0^l N_{u,x}^T A_{12} (N_{\gamma,x} - N_{w,xx}) dx;$$

$$\mathbf{k}_{22} = \int_0^l (N_{\gamma,x} - N_{w,xx})^T A_{22} (N_{\gamma,x} - N_{w,xx}) dx;$$

$$\mathbf{k}_{34} = -2\alpha\int_0^l N_{u,x}^T A_{34} N_{\gamma,x} dx;$$

$$\mathbf{k}_{44} = -2\alpha\int_0^l N_{\gamma,x}^T A_{44} (N_{\gamma,x} - N_{w,xx}) dx;$$

$$\mathbf{k}_{66} = \alpha^2\int_0^l N_{\gamma,x}^T A_{66} N_{\gamma,x} dx;$$

$$\mathbf{k}_s = \int_0^l N_\gamma^T B_{44} N_\gamma dx \tag{2.15}$$

Similarly, the kinetic energy in Eq. (2.8) can be rewritten as

$$T = \frac{1}{2}\sum^{ne}\left(\frac{\partial \mathbf{d}}{\partial t}\right)^T \mathbf{m}\left(\frac{\partial \mathbf{d}}{\partial t}\right) \tag{2.16}$$

where

$\mathbf{m} = \mathbf{m}_{11} + \mathbf{m}_{12} + \mathbf{m}_{22} + \mathbf{m}_{34} + \mathbf{m}_{44} + \mathbf{m}_{66}$ (2.17)

is the element consistent mass matrix, in which

$$\mathbf{m}_{11} = \int_0^l \left(N_u^T + N_w^T\right)\mathbf{m}_{11}\left(N_u + N_w\right) dx;$$

$$\mathbf{m}_{12} = 2\int_0^l N_u \mathbf{m}_{12}\left(N_\gamma - N_{w,x}\right) dx;$$

$$\mathbf{m}_{22} = \int_0^l \left(N_\gamma - N_{w,x}\right)^T \mathbf{m}_{22}\left(N_y - N_{w,x}\right) dx;$$

$$\mathbf{m}_{34} = -2\alpha\int_0^l N_u^T \mathbf{m}_{34} N_\gamma dx;$$

$$\mathbf{m}_{44} = -2\alpha\int_0^l N_{\gamma,x}^T\, \mathbf{m}_{44}\left(N_y - N_{w,x}\right) dx;$$

$$\mathbf{m}_{66} = \alpha^2\int_0^l N_\gamma^T \mathbf{m}_{66} N_\gamma dx; \tag{2.18}$$

Are the element mass matrices stemming fromaxial, transverse translations, axial translation–sectional rotationcoupling, and cross-sectional rotation, respectively. Having the

element stiffness and mass matrices derived, the equations of motionfor the free vibration analysis in the context of finite element analysis can be written inthe form

$$\mathbf{M}\left(\frac{\partial^2 \mathbf{D}}{\partial^2 t}\right)+\mathbf{KD}=\mathbf{F}^{ex} \tag{2.19}$$

where **D, M**, and **K** are the structural nodal displacement vector, mass and stiffness matrices, obtained by assembling the element displacement vector **d**, mass matrix **m**, and stiffness matrix **k** over the total elements, respectively. In Eqs. (2.19), $\mathbf{F}^{ex}$ is the structural nodal load vector.

3. Numerical results

Numerical investigations are carried out in this Section to study the effects of the material distribution (or the power-law indexes) and the moving load speed on vibration of the bi-dimensional FG sandwich beam. To this end, a simply supported FG sandwich beam formed from steel (Fe), alumina (Al2O3) with the material properties (steel(Fe), Em= 210 Gpa, ρm = 7800 kg/m3,ν = 0.23, alumina(Al2O3), Ec = 390 Gpa, ρc = 3960 kg/m3, ν=0.3). The validation of the derived formulation is necessary to confirm before computing the vibration characteristics of the beam. Since there is no data on the vibration of bi-dimensional FG sandwich beams with the power-law variations of the material properties as considered in the present paper, the fundamental frequency and dynamic response of one-dimensional FG beam obtained in the present work are compared with the data available in the literature.

In Table 1, the fundamental frequency parameter (μ) of the one-dimensional transverse FG beam composed of alumina and steel of the present work is compared with that obtained by an analytical method inref.[12]. In Table 2, the maximum dynamic magnification factor and the corresponding speed of the simply supported FG beam made of steel and alumina are compared to the result obtained by¸Simsek and Kocatürk in Ref. [12] The fundamental frequency parameter (μ) in Table 1is defined according to Simsekand Kocatürk in Ref. [12] as

$$\mu=\sqrt{\frac{\omega_1 L^2}{h}}\sqrt{\frac{\rho_m bh}{E_m bh^3/12}} \tag{3.1}$$

where ω_1 is the fundamental frequency, and the dynamic magnification factor (f_D) in Table 2 is defined as follows**:**

$$f_D=\max\left(\frac{w_0(L/2,t)}{w_{st}}\right) \tag{3.2}$$

where $w_{st}= F L^3/48EmI$ is the static deflection of a full metal beam under the load F acting at mid-span. The frequency and dynamic magnification factor in the above two tables are obtained by setting m to zero and using the geometric and material data of the corresponding references. A very good agreement between the results of the present work with those of the references is noted from Tables 1 and 2.

Table 1. Comparison of fundamental frequency parameter μ for FG beam (h1 = - 0.5h, h2 = 0.5h, m = 0)

	E_c/E_m	n=0.2	n=3	n=10
Ref [12]	0.25	2.4606	2.8623	3.0084
Pre	0.25	2.4576	2.8592	3.0044
Ref [12]	2	3.6301	3.3500	3.2725
Pre	2	3.6244	3.3447	3.2669

Table 2. Comparison of maximum dynamic magnification factor, f_D, and corresponding speed of moving load (h1= - 0.5h, h2 = 0.5h, m = 0)

n	f_D- ref. [12]	f_D- present	v(m/s) - ref. [12]	v(m/s)- present
0.2	1.0344	1.0403	222	221
0.5	1.1444	1.1505	198	197
1	1.2503	1.2570	179	178
2	1.3376	1.3452	164	163

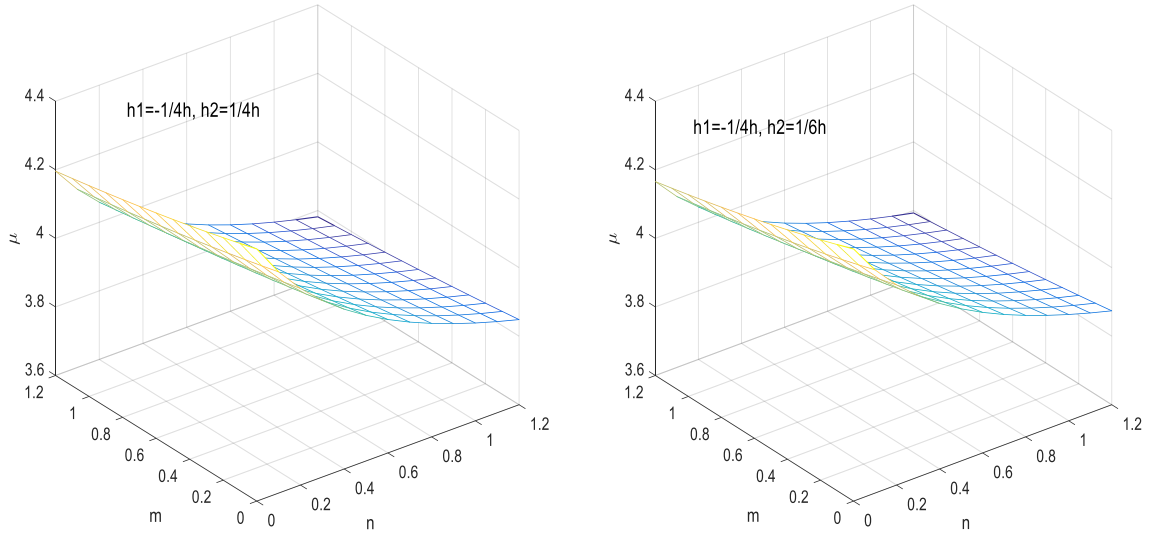

Fig 2.Fundamental frequency parameter of FG sandwich beamwith indexes *n* and *m*

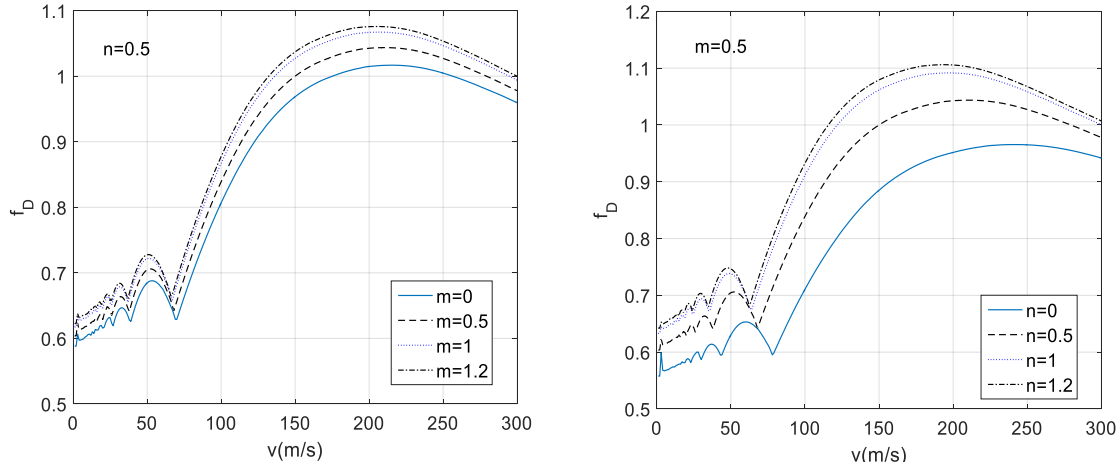

Fig. 3. Relation between dynamic magnification factor and moving load speed with different indexes(h_1 = -*h*/4, h_2 = *h*/4, L/h = 20)

Fig. 2 shows the variation of the first frequency parameter with the grading indexes. The frequency parameters in the figure are defined by (3.1) for two values of the h_1, h_2. As seen from Fig.2, the frequency parameter is decreased by the increase in the grading index n and the increase in the index *m*. The dependence of the frequencies on the grading indexes can be explained by the change in the percentage of the constituent materials with the *n* and *m*. As known from the beam vibration theory, the frequencies are proportional to the stiffness (that is, Young's modulus), and they are inversely proportional to the mass of the beam. The Fig.2 shows an decrease in the fundamental frequency by the decrease h_2/h ratio.

In Fig. 3, the relation between the dynamic magnification factor f_D and the moving load

speed v is illustrated for various values of the indexes n and m, and the result is depicted in Fig. 3 for $h_1 = -h/4$, $h_2 = h/4$ and $L/h = 20$. The dynamic magnification factor in the Figureis defined according to Eq. (3.2), in which w_{st} is the static deflection of the pure metal beam. As seen from the Figure, the relation between f_D and v of the bi-dimensional FG sandwich beam is similar to that of an isotropic beam under a moving load, that is, the factor f_D both increases and decreases, and it then monotonously increasesto a maximum value when increasing the moving load speed [13]. The repeated increase and decrease of the factor f_D for lower values of the moving load speed in Fig. 3, as mentioned above, is associated with the oscillations ofthe sandwich beam under the load with the lower moving load speed to the critical speed ratios. The effect of the grading index n on the factor f_D is similar to that of the index m. The dynamic magnification factor steadily increases as the index m increases, and it increases by the increase in the index n. The effect of the two grading indexes on the factor f_D can be explained by the dependence of the rigidities on these indexes. As mentioned above, the sandwich beam associated with a higher index m ontains more ceramic and metal, and thus, its rigidities are higher.

4. Conclusion

The vibration of bi-dimensional FG sandwich beams excited by a moving concentrated load has been investigated in the present work. The material properties are assumed to vary in both the thickness and longitudinal directions by the power-law functions. Based on the third-order shear deformation theory, the governing equations of motion are derived and they are solved by a finite element formulation in combination with the Newmark method. The accuracy of the derived formulation was validated by comparing the numerical result obtained in the present paper with the data available in the literature. A parametric study has been carried out to highlight the influence of the material distribution, the moving load speed, and the aspect ratio on the vibration characteristics. A parametric study has been carried out to highlight the influence of the material distribution, the moving load speed, and the aspect ratio on the vibration characteristics.

References

Koizumi, M.: FGM activities in Japan. *Compos. Part B Eng*. **28**, 1–4 (1997)

Vo, T.P., H.T.Thai, T.K.Nguyen, A.Maheri, and J. Lee.Finite lement model for vibration and buckling of functionally graded sandwich beams based on a refined shear deformation theory. *Engineering Structures*, 64 (2014), pp. 12-22.

Vo, T.P., H.T. Thai, T.K. Nguyen, A. Maheri, F. Inam, and J. Lee. A quasi-3D theory forvibration and buckling of functionally graded sandwich beams. *Composite Structures*, 119 (2015), pp. 1-12.

Şimşek M. - Bi-directional Functionally Graded Materials (BDFGMs) for free and forcedvibration of Timoshenko Beams with various boundary conditions, *Composite Structures*133 (2015) 968-978.

Şimşek M. - Buckling of Timoshenko beams composed of two-dimensional functionally graded material (2D-FGM) having different boundary conditions,*Composite Structures* 149 (2016) 304–314.

Wang Z., Wang X., Xu G., Cheng S., and Zeng T. - Free vibration of two- directional functionally graded beams. *Composite Structures***135** (2016) 191–198.

Nguyen D.K., Nguyen Q.H., Tran T.T., and Bui V.T. - Vibration of bi-dimensional functionally graded Timoshenko beams excited by a moving load, *Acta Mechanica***228** (2017)141-155.

Shafiei N., Mirjavadi S. S., Afshari B. M., Rabby S., and Kazem M. - Vibration of twodimensional imperfect functionally graded (2D-FG) porous nano-/micro-beams, *Computer Methods in Applied Mechanics and Engineering***322** (2017) 615-632.

Nguyen D.K., Tran T.T.-Free vibration of tapered BFGM beams using an efficient shear deformable finite element model, *Steel and Composite Structures*, Vol. 29, No. 3(2018)363-377.

Karamanlı. Bending behaviour of two directional functionally graded sandwich beams by using a quasi-3d shear deformation theory. Composite Structures 174 (2017), pp 70–86.

G.shi and K. Y. Lam. Finite element formulation vibration analysis of composite beams based on higher-order beam theory,*Journal of Sound and Vibration* (1999), 219, pp. 696-610.

Şimşek, M., and T. Kocatürk. Free and forced vibration of a functionally graded beam subjected to a concentrated moving harmonic load, *Composite Structures* 90(2009), pp. 465–473

Olsson, M.: On the fundamental moving load problem. J. Sound Vib. **145**, 229–307 (1991)

The 5th International Conference on Engineering Mechanics and Automation (ICEMA 5)
Hanoi, October 11÷12, 2019

Exact receptance function of continuous beams carrying concentrated masses

Khoa Viet Nguyen[a], Thao Thi Bich Dao[a], Mai Van Cao[a], Quang Van Nguyen[a]

[a]Institute of Mechanics, Vietnam Academy of Science and Technology
18 Hoang Quoc Viet, Cau Giay, Hanoi, Vietnam
[a]Email: nvkhoa@imech.vast.vn

Abstract

This paper establishes the exact receptance function of beams carrying concentrated masses with general boundary conditions. In this paper, the derivation of exact receptance and numerical simulations are provided. The influence of the concentrated masses on the receptance is investigated. The numerical simulations show that a peak in the receptance decreases when there is a mass located close to that peak position.

Key Words: Receptance, frequency response function, concentrated mass.

1. Introduction

The receptance function has been applied widely in mechanical systems and dynamic structures. The receptance method was first introduced by Bishop and Johnson (1960). This method has been applied wildly in mechanical system and structural dynamics. Milne (1989) presented a general solution of the receptance function of uniform beams. The receptance function developed in this paper can be applied for all combinations of beam end conditions. Lin and Lim (1997) presented the derivation of the receptance sensitivity with respect to mass modification and stiffness modification from the limited vibration test data. Mottershead (1998) studied the measured zeros form frequency response functions and its application to model assessment and updating. Gurgoze (2000) focused on the receptance matrices of viscously damped systems subject to several constraint equations. The frequency response matrix of the constrained system was obtained from the frequency response matrix of the unconstrained system and the coefficient vectors of the constraint equations. Gurgozeg and Erol (2002) established the frequency response function of a damped cantilever simply supported beam carrying a tip mass. In this paper, the frequency response function was derived by using a formula established for the receptance matrix of discrete linear systems subjected to linear constraint equations, in which the simple support was considered as a linear constraint imposed on generalized co-ordinates. Karakas and Gurgoze (2003) established a formulation of the receptance matrix of non-proportionally damped dynamic systems in which the

receptance matrix was obtained directly. Muscolino and Santoro (2014) presented the explicit frequency response functions of discretized structures with uncertain parameters. Burlon et al. (2016) presented an exact frequency response function of axially loaded beams with viscoelastic dampers. The method relies on the theory of generalized functions to handle the discontinuities of the response variables, within a standard 1D formulation of the equation of motion. Burlon et al. (2016) proposed and exact frequency response of two-node coupled bending-torsional beam element with attachments.

In the literature, the exact form of frequency response function of continuous beam carrying concentrated masses with general boundary conditions has not been established yet. Also, the influence of the mass configuration on the receptance at resonant frequencies has not been investigated yet. The aim of the present paper is to derive a general exact solution for the receptance function of beams with general boundary conditions carrying an arbitrary number of concentrated masses. The derived formulas of receptance functions can be applied easily to investigate the dynamic response of beam at an arbitrary point to a harmonic force acted at any point along the beam. The influence of concentrated masses on the receptance of a particular clamped-clamped beam carrying concentrated masses is investigated.

2. Theoretical background

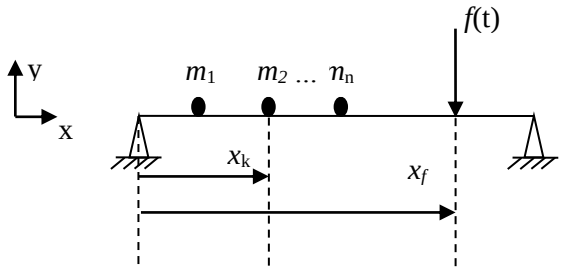

Fig. 1. A beam with concentrated masses

Let us consider the Euler-Bernoulli beam carrying concentrated masses subjected to a force as shown in Fig. 1. The governing equation of bending vibration of the beam can be extended as follows (Laura (1974)):

$$EIy'''' + \left[m + \sum_{k=1}^{n} m_k \delta\left(x - x_k\right) \right] \ddot{y} = \delta\left(x - x_f\right) f\left(t\right) \tag{1}$$

where E is the Young's modulus, I is the moment of inertia of the cross sectional area of the beam, μ is the mass density per unit length, m_k is the k^{th} concentrated mass located at x_k, $y(x, t)$ is the bending deflection of the beam at location x and time t, $f(t)$ is the force acting at position x_f, $\delta\left(x - x_f\right)$ is the Dirac delta function.

Eq. (1) can be rewritten in the form:

$$EIy'''' + m\ddot{y} = \delta\left(x - x_f\right) f\left(t\right) - \sum_{k=1}^{n} m_k \delta\left(x - x_k\right) \ddot{y} \tag{2}$$

Eq. (2) can be considered as the equation of forced vibration of a beam without concentrated masses which is acted by the inertia forces of n concentrated masses and the external force $f(t)$. The solution of Eq. (2) can be found in the form:

$$y\left(x,t\right) = \sum_{i=1}^{\infty} \phi_i\left(x\right) q_i\left(t\right) \tag{3}$$

where ϕ_i is i^{th} mode shape of the beam without any concentrated masses and q_i is the i^{th} generalized coordinate.

Substituting (3) into (2) leads to:

$$\begin{aligned} &EI \sum_{i=1}^{\infty} \phi_i''''\left(x\right) q_i\left(t\right) + \mu \sum_{i=1}^{\infty} \phi_i\left(x\right) \ddot{q}_i\left(t\right) \\ &= -\sum_{k=1}^{n} \delta\left(x - x_k\right) m_k \sum_{i=1}^{\infty} \phi_i\left(x\right) \ddot{q}_i\left(t\right) + \delta\left(x - x_f\right) f\left(t\right) \end{aligned} \tag{4}$$

Multiplying Eq. (4) by $\phi_j(x)$ and integrating from 0 to L and considering the definition of the Dirac delta function, one obtains:

$$\begin{aligned} &\int_0^L EI \sum_{i=1}^{\infty} \phi_i''''\left(x\right) \phi_j\left(x\right) q_i\left(t\right) dx \\ &+ \int_0^L \mu \sum_{i=1}^{\infty} \phi_i\left(x\right) \phi_j\left(x\right) \ddot{q}_i\left(t\right) dx \end{aligned} \tag{5}$$

$$= -\int_0^L \sum_{k=1}^{n} m_k \sum_{i=1}^{\infty} \phi_i(x)\phi_j(x)\ddot{q}_i(t) + \phi_j(x_f) f(t)$$

From the orthogonality of the normal mode shapes of the beam without concentrated masses, one has:

$$\int_0^L \phi_i(x) EI \phi_i''''(x) q_j(t) dx = 0 \quad if\ i \neq j \tag{6}$$

$$\int_0^L \phi_i(x) \mu \phi_j(t) dx = 0 \quad if\ i \neq j \tag{7}$$

Integrating the first equation in Eq. (6) twice by parts, yields:

$$\begin{aligned} &\phi_i(x) EI\, \phi_j'''(x)\Big|_0^L - \phi_i'(x) EI\, \phi_j''(x)\Big|_0^L \\ &+\int_0^L \phi_i''(x) EI \phi_j''(x) = 0 \quad if\ i \neq j \end{aligned} \tag{8}$$

It is noted that, for general boundary conditions the first two terms in Eq. (8) will be zero:

$$\begin{cases} \phi_i(x) EI\, \phi_j'''(x)\Big|_0^L = 0 & \forall i, j \\ \phi_i'(x) EI\, \phi_j''(x)\Big|_0^L = 0 & \forall i, j \end{cases} \tag{9}$$

Therefore, from Eqs. (8)-(9) we have:

$$\int_0^L \phi_i''(x) EI \phi_j''(x) dx = \begin{cases} 0 & ,i \neq j \\ \int_0^L \phi_i''^2(x) EI dx & ,i = j \end{cases} \tag{10}$$

Applying Eqs. (6)-(10), Eq. (5) can be rewritten as:

$$\begin{aligned} &\left[\int_0^L \mu \phi_i^2(x) dx + \sum_{k=1}^{n} m_k \phi_i^2(x_k)\right] \ddot{q}_i(t) \\ &+\left[EI \int_0^L \phi_i''^2(x) dx\right] q_i(t) = \phi_j(x_f) f(t) \end{aligned} \tag{11}$$

Eq. (11) can be expressed in matrix form as follows:

$$\mathbf{M}\ddot{\mathbf{q}}(t) + \mathbf{K}\mathbf{q}(t) = \mathbf{\Phi}(x_f) f(t) \tag{12}$$

where:

$$\mathbf{M} = \begin{bmatrix} M_1 & M_{12} & \dots & M_{1N} \\ M_{21} & M_2 & \dots & M_{2N} \\ \dots & \dots & \ddots & \dots \\ M_{N1} & M_{N2} & \dots & M_N \end{bmatrix} \tag{13}$$

$$M_i = \int_0^L \mu \phi_i^2 dx + \sum_{k=1}^{n} m_k \phi_i^2(x_k), i = 1,\dots,N$$

$$M_{ij} = \sum_{k=1}^{n} m_k \phi_i(x_k) \phi_j(x_k), i, j = 1,\dots,N$$

$$\mathbf{K} = EI \begin{bmatrix} \int_0^L \phi_1''^2 dx & 0 & \dots & 0 \\ 0 & \int_0^L \phi_2''^2 dx & \dots & 0 \\ \dots & & & \dots \\ 0 & 0 & \dots & \int_0^L \phi_N''^2 dx \end{bmatrix} \tag{14}$$

$$\begin{aligned} \mathbf{\Phi}(x) &= \left[\phi_1(x),\dots,\phi_N(x)\right]^T \\ \ddot{\mathbf{q}}(t) &= \left[\ddot{q}_1(t),\dots,\ddot{q}_N(t)\right]^T \\ \mathbf{q}(t) &= \left[q_1(t),\dots,q_N(t)\right]^T \end{aligned} \tag{15}$$

If the force is zero, Eq (12) becomes:

$$\mathbf{M}\ddot{\mathbf{q}}(t) + \mathbf{K}\mathbf{q}(t) = \mathbf{0} \tag{16}$$

Eq. (16) is the free vibration equation of the beam-masses system. The natural frequency Ω of beam carrying concentrated masses can be derived by solving the eigenvalue problem associated with Eq. (16), that is:

$$\mathbf{det}\left[\mathbf{K} - \Omega^2 \mathbf{M}\right] = 0 \tag{17}$$

If the force is harmonic $f(t) = \bar{f} e^{i\omega t}$ then the solution of Eq. (12) can be found in the form:

$$\mathbf{q}(t) = \bar{\mathbf{q}} e^{i\omega t} \tag{18}$$

Substituting Eq. (18) into Eq. (12) yields:

$$\left(\mathbf{K} - \omega^2 \mathbf{M}\right) \bar{\mathbf{q}} = \mathbf{\Phi}(x_f) \bar{f} \tag{19}$$

Dividing Eq. (19) by $\left(\mathbf{K} - \omega^2 \mathbf{M}\right) \bar{f}$ and left multiplying with $\mathbf{\Phi}^T(x)$, the receptance at x due to the force at x_f is obtained:

$$\alpha\left(x,x_f,\omega\right)=\frac{\mathbf{\Phi}^T\left(x\right)\bar{\mathbf{q}}}{\bar{f}}=\mathbf{\Phi}^T\left(x\right)\frac{\mathbf{\Phi}\left(x_f\right)}{\mathbf{K}-\omega^2\mathbf{M}} \quad (20)$$

In this paper the exact receptance of beams carrying concentrated masses with general boundary conditions will be presented.

2.1. Simply supported beam

For the simply supported beam we have:

$$\begin{cases}\phi_i\left(x\right)=\sin\dfrac{i\pi x}{L}\\ \phi_i''\left(x\right)=-\dfrac{i^2\pi^2}{L^2}\sin\left(\dfrac{i\pi x}{L}\right)\\ \int_0^L\mu\phi_i^2\left(x\right)dx=\dfrac{\mu L}{2}\\ \int_0^L\left[\phi_i''\left(x\right)\right]^2dx=\dfrac{\left(i\pi\right)^4}{2L^3}\end{cases} \quad (21)$$

with conditions boundary is:

$$\begin{cases}\phi\left(0\right)=0,\ \phi''\left(0\right)=0\\ \phi\left(L\right)=0,\ \phi''\left(L\right)=0\end{cases}$$

Applying Eq. (21) the matrices **M** and **K** can be expressed as follows:

$$\mathbf{M}=\begin{bmatrix}\dfrac{\mu L}{2}+\beta_{11} & \beta_{12} & \ldots & \beta_{1N}\\ \beta_{21} & \dfrac{\mu L}{2}+\beta_{22} & \ldots & \beta_{2N}\\ \ldots & \ldots & \ddots & \ldots\\ \beta_{N1} & \beta_{N2} & \ldots & \dfrac{\mu L}{2}+\beta_{NN}\end{bmatrix} \quad (22)$$

$$\mathbf{K}=\frac{EI\pi^4}{2L^3}\begin{bmatrix}1 & 0 & \ldots & 0\\ 0 & 2^4 & \ldots & 0\\ \ldots & & & \ldots\\ 0 & \ldots & & N^4\end{bmatrix} \quad (23)$$

where

$$\beta_{ij}=\sum_{k=1}^{n}m_k\left[\sin\left(\frac{i\pi x_k}{L}\right)\sin\left(\frac{j\pi x_k}{L}\right)\right] \quad (24)$$

Substituting Eqs. (21)-(24) into Eq. (20) the exact formula of the receptance of the simply supported beam carrying concentrated masses will be determined.

3. Numerical simulation

3.1. Reliability of the theory

In order to check the reliability of the formulas derived in this work, frequency parameters $\alpha_i L$ of a cantilever beam carrying a mass at the free end are calculated from Eq. (15) using the first ten modes and compared to Laura (1974).

Four lowest frequency parameters of the cantilever beam with a concentrated mass $\bar{m}_1$ =0.6 attached at the free end obtained by two methods are listed in Table 1. As can be seen from this table, the first four frequency parameters of the present work are in excellent agreement with Laura (1974).

Table 1. Frequency parameter of the cantilever beam

Frequency parameter	Ref. [13]	Present paper	Error (%)
$\alpha_1 L$	1.37566854	1.37567572	0.000005
$\alpha_2 L$	4.08665324	4.08694366	0.000071
$\alpha_3 L$	7.17252465	7.17449760	0.000275
$\alpha_4 L$	10.28498044	10.29123907	0.000608

3.2. Influence of location of the concentrated masses on the receptance

In this paper, numerical simulations of a simply supported beam with two masses is presented. Parameters of the steel beam are: Mass density ρ=7800 kg/m^3; modulus of elasticity E=2.0x10^{11} N/m^2; L=1 m; b=0.02 m; h=0.01 m. Two equal concentrated masses of 0.6 kg are attached on the beam in nine scenarios as listed in Table 2. The receptance matrices are calculated at 50 points spaced equally on the beam while the force moves along these points.

Table 2. Nine scenarios of attached masses

Scenario	ω	Position of m_1	Position of m_2
1	$\omega=\omega_1$	0.25L	-
2	$\omega=\omega_1$	0.75 L	-

3	$\omega = \omega_2$	0.25 L	-
4	$\omega = \omega_2$	0.75 L	-
5	$\omega = \omega_3$	0.17 L	-
6	$\omega = \omega_3$	0.5 L	-
7	$\omega = \omega_3$	0.83 L	-
8	$\omega = \omega_3$	0.17 L	0.5 L
9	$\omega = \omega_3$	0.17 L	0.83 L

The receptance of the simply supported beam without a mass is calculated first. Fig. 1 presents the receptance of the beam without a concentrated mass when the forcing frequencies equal to the the first, second and third natural frequencies of the beam-mass system, respectively. As can be seen from Fig. 1a when the forcing frequency is equal to the first natural frequency, the receptance is maximum at the middle of the beam which corresponds to the position where the amplitude of the first mode is maximum. As can be observed from Fig. 1b, when the forcing frequency is equal to the second natural frequency, the receptance is maximum at the positions of about 0.25L and 0.75L from the left end of the beam. Meanwhile, the receptance is smallest at the middle of beam. Fig. 1c presents the receptance matrix of the beam when the forcing frequency is equal to the third natural frequency. The receptance is maximum at the positions of about L/6, 0.5L and 5L/6. The receptance is minimum at the positions of about L/3 and 2L/3. It is noted that, the positions of maxima and minima of the receptance obtained at a natural frequency coincide with these of the corresponding mode shape. Therefore, similar to the mode shape, we call the maxima in the receptance "peaks of receptance" and the minima in the receptance "nodes of receptance".

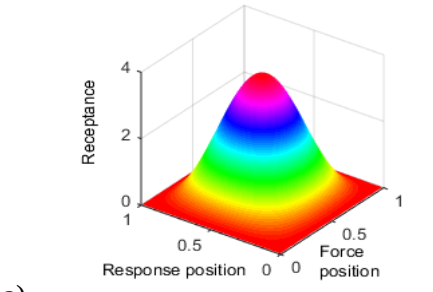

a)

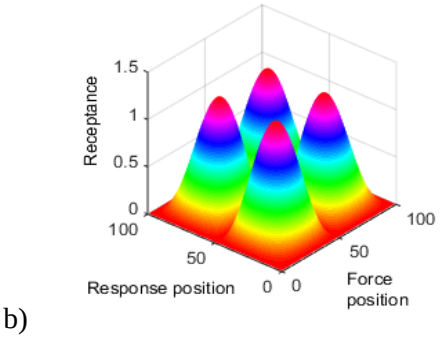

b)

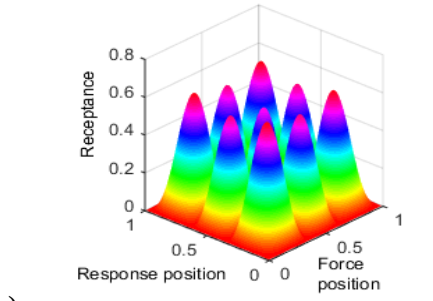

c)

Fig. 1 Receptance of beam without a masse: a) $\omega=\omega_1$; b) $\omega=\omega_2$; c) $\omega=\omega_3$

When there is a concentrated mass, the receptance matrix of the beam is changed. Fig. 2 presents the recetance matrices when the forcing frequency is equal to the first natural frequency of the beam-mass system. As can be seen from this figure, when the mass is located 0.25L and 0.75L the position of the peak in receptance "moves" to the left and the right ends of beam, respectively. However, when the mass is located at the middle of the beam, the shape of the receptance is unchanged. The change of the peak position in the receptance is depicted clearer in Fig. 3 when the force is fixed at position 0.5L. As can be observed from this figure, the peak of the receptance moves to the positions of 0.4L and 0.6L when the mass is

located at 0.25L and 0.75L, respectively. The receptance seems to be "pulled" toward the mass position.

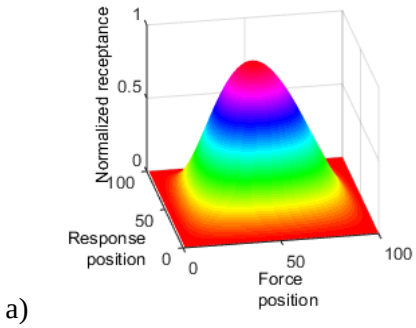

a)

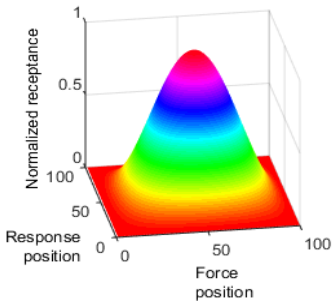

b)

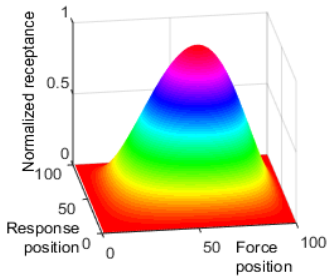

c)

Fig. 2. Receptance matrices at $\omega=\omega_1$ with mass attached at: a) 0.25L; b) 0.5L; c) 0.75L

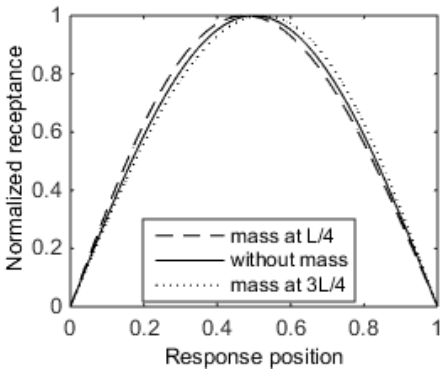

Fig. 3. Receptance of beam with force position is at $L/2$; $\omega=\omega_1$

Fig. 4 presents the receptance of beam carrying a concentrated mass at different positions when the forcing frequency is equal to the second natural frequency. As shown in Fig. 4a, when the mass is located at 0.25L, the peaks corresponding to either the response position of 0.25L or the force position of 0.25L decrease significantly. When the mass is located the middle of the beam, the receptance shape is unchanged as shown in Fig. 4b. When the mass is located at 0.75L, the peaks corresponding to the either response position of 0.75L or the force position of 0.75L decrease significantly as shown in Fig. 4c. These results show that when the mass is attached at a peak of the receptance matrix, the peaks corresponding to either the response position or force position which is close to the mass position will decrease. Meanwhile, the shape of receptance is unchanged when the mass is attached at the nodal point of the receptance. The change in receptance can be observed in more detail as presented in Fig. 5 when the force is fixed at the position 0.25L. As can be seen from this figure, the peak of the receptance at the position of the attached mass decreases. In addition, the peak of the receptance moves slightly toward the mass position.

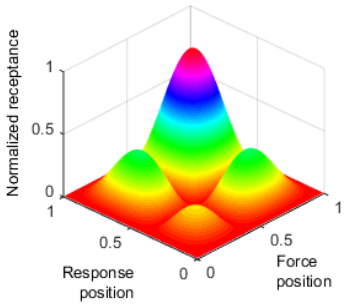

a)

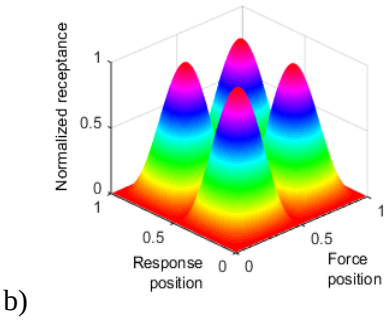

b)

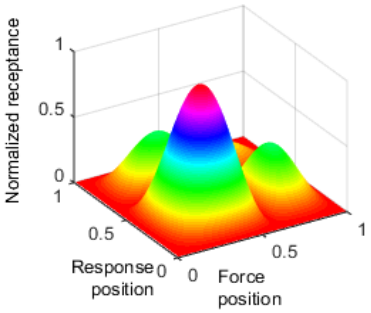

c)

Fig. 4. Receptance of beam at $\omega=\omega_2$ with the mass attached at: a) 0.25L; b) 0.5L; c) 0.75L

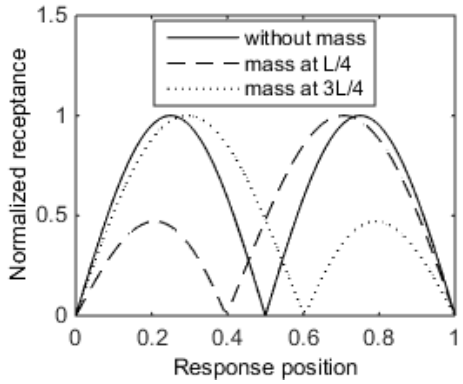

Fig. 5. Measured receptance with the force acting at 0.25L, $\omega=\omega_2$

Fig. 6 illustrates the receptance when the forcing frequency is equal to the third natural frequency. As can be observed from this figure, the peaks at the positions of the attached masses decrease. When a mass is attached at the position of L/6, five peaks corresponding to either the response position of L/6 or the force position of L/6 decrease significantly as depicted in Fig. 6a. When the mass is located at the middle of the beam, five peaks corresponding to either the response position of 0.5L or the force position of 0.5L decrease as shown in Fig. 6b. As shown in Fig. 6c, when the mass is located at 5L/6 the result is similar to the case when the mass is located at L/6 since these two attached positions are symmetric on the beam. When two masses are located at the positions of L/6 and 0.5L, the peaks corresponding to either the response positions of L/6 and 0.5L or the force positions of L/6 and 0.5L decrease as demonstrated in Fig. 6d. When two masses are located at the positions of L/6 and 5L/6, the peaks corresponding to either the response positions of L/6 and 5L/6 or force positions of L/6 and 5L/6 decrease as presented in Fig. 6e.

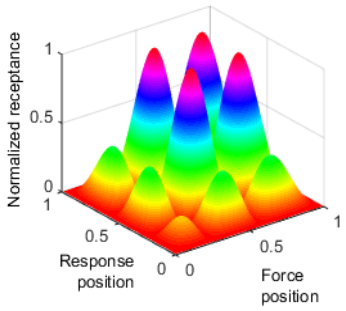

a)

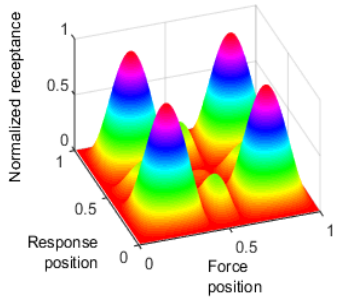

b)

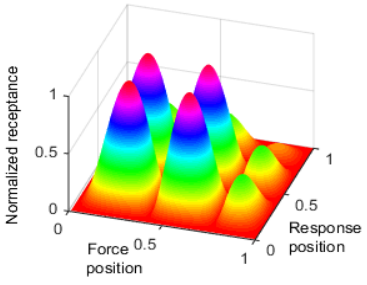

c)

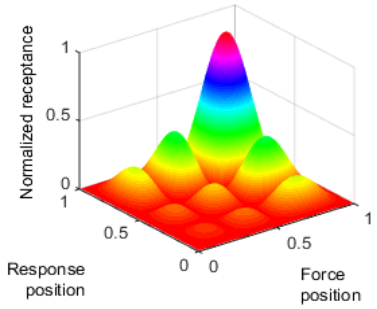

d)

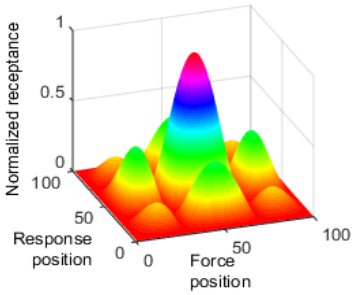

e)

Fig 6. Receptance of beam at $\omega=\omega_2$: Mass is attached at: a) $L/6$; b) $0.5L$; c) $5L/6$; two masses are attached: d) at $L/6$ and $0.5L$; e) at $L/6$ and $5L/6$

The change in receptance can be seen in more detail when the force is fixed at position $0.2L$ as depicted in Fig. 7. A conclusion can be drawn from this figure that when there is a mass attached at a peak, this peak will decrease significantly. When there is one mass attached the peaks of the receptance move toward the mass positions. When there are two masses attached symmetrically on the beam at the positions of $0.2L$ and $0.8L$, the peak at $0.2L$ moves to the left end, while the peak at $0.8L$ moves to the right end. When there are two masses attached at $0.2L$ and $0.5L$, the receptance is "pulled" to the left end. In this case, the receptance tends to "move" toward the heavier side of the beam.

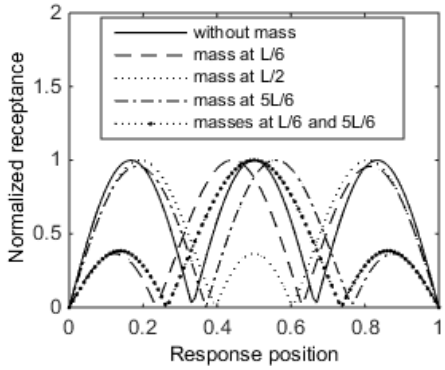

Figure 7. Normalized receptance when the force is fixed at $0.2L$, $\omega=\omega_3$

4. Conclusion

In this paper, the exact receptance function of beam carrying concentrated masses is presented. The formulas of receptance function derived in this paper can be applied for investigating the response of the beam under a harmonic excitation. The influence of the concentrated mass on the receptance of beam is also investigated.

When the excitation frequency is equal to a natural frequency, the maximum and minimum positions of the receptance are the same with these of the corresponding mode shape. When there is a concentrated mass the shape of receptance is changed. When the mass position is close to a peak in the receptance, this peak will decrease significantly. When the mass is located at the nodes of receptance, the receptance is not influenced. The influence of the masses on the receptance matrix can be used to control the vibration amplitude at some specific positions at given forcing frequencies.

The experiment has been carried out at the first three natural frequencies of the beam carrying concentrated masses. The experimental and simulation results are in very good agreement which justifies the proposed method.

Acknowledgements

This research is funded by Vietnam National Foundation for Science and Technology Development (NAFOSTED) under grant number 107.02-2017.300.

References

Andrea Burlon, Giuseppe Failla, Felice Arena, Exact frequency response analysis of axially loaded beams with viscoelastic dampers. *International Journal of Mechanical Sciences* 115-116 (2016) 370–384.

G. Muscolino, R. Santoro, A. Sofi, *Explicit frequency response functions of discretized structures with uncertain parameters*, Computers and Structures 133 (2014) 64–78.

A. Karakas, M. Gurgoze, A novel formulation of the receptance matrix of non-proportionally damped dynamic systems. *Journal of Sound and Vibration* 264 (2003) 733–740.

M. Gurgoze and H. Erol, On the frequency response function of a damped cantilever simply supported in-span and carrying a tip mass. *Journal of Sound and Vibration* (2002) 255(3), 489-500.

[6] M. Gurgoze, Receptance matrices of viscously damped systems subject to several constraint equations, *Journal of Sound and Vibration* (2000) 230(5), 1185-1190.

J.E. Mottershead, *On the zeros of structural frequency response functions and their sensitivities*, Mechanical Systems and Signal Processing 12 (1998) 591–597.

R.M. Lin, M.K. Lim, Derivation of structural design sensitivities from vibration test data, *Journal of Sound and Vibration* 201 (1997) 613–631.

H.K. Milne, The receptance functions of uniform beams. *Journal of Soundand Vibration* (1989) 131(3), 353-365.

Laura PAA, Pombo JL, Susemihl EA. A note on the vibrations of a clamped-free beam with a mass at the free end, *Journal of Sound and Vibration* (1974) 37(2), 161-168.

R.E.D. Bishop, D.C. Johnson, *The Mechanics of Vibration*, Cambridge University Press, Cambridge, 19.

The 5th International Conference on Engineering Mechanics and Automation (ICEMA 5)
Hanoi, October 11÷12, 2019

Exact receptance function of AFG beam carrying concentrated masses

Khoa Viet Nguyen[a], Thao Thi Bich Dao[a], Mai Van Cao[a]

[a]Institute of Mechanics, Vietnam Academy of Science and Technology
18 Hoang Quoc Viet, Cau Giay, Hanoi, Vietnam
[a]Email: nvkhoa@imech.vast.vn

Abstract

This paper presents the receptance of axially functional graded beam carrying concentrated masses based on the exact formulas of the receptance functions of beams. The general form of receptance function of the axially functional graded (AFG) beams is derived by applying the exact mode shapes developed in this work. Based on the derived receptance functions the receptance matrix of the AFG beams are presented. The influences of the concentrated masses and the varying of the material properties on the receptance of the beams are investigated. The numerical calculations show that when there are concentrated masses, the receptance matrices are changed. Especially, when masses are attached peak positions of the receptance matrices, these peaks will decrease significantly.

Key Words: Receptance, frequency response function, concentrated mass.

1. Introduction

The receptance function is very important in vibration problems such as control design, system identification or damage detection since it interrelates the harmonic excitation and the response of a structure in the frequency domain. This method has been applied wildly in mechanical system and structural dynamics. The topic of vibration of beams carrying concentrated masses has been studied extensively over the years. Laura et al. (1974) was concerned with the free vibrations of a clamped-free beam with a mass at the free end. Wu and Lin (1990) proposed the analytical and numerical combined method to study the free vibration of a uniform beam with point masses. Posiadala (1997) presented the solutions of free vibrations of Timoshenko beams with attachments by using the Lagrange multiplier formalism. Wu and Chou (1999) proposed a combination method using numerical technique and conventional methods to solve the eigenvalues and the corresponding eigenvectors. Wu and Hsu (2007) analysed the free vibration of simply supported beams carrying multiple point masses and spring-mass systems with mass of each helical spring considered. Not only the vibration of uniform beams has been concerned, the vibration of AFG beams has attracted many researchers for decades, such as Shahba et al. (2011) or Rossit et al. (2017).

The aim of this paper is to present the general exact form of the receptance function of the AFG beam carrying an arbitrary number of concentrated masses. AFG beam is a special kind of nonhomogeneous functionally gradient material structure, whose material properties vary continuously along the axial direction of the beam by a given distribution form. The exact receptance functions of the AFG beam is

established from the exact form of mode shape developed in this work. The derived formula of receptance functions can be applied easily to investigate the dynamic response of beam at an arbitrary point to a harmonic force acted at any point along the beam. The influences of the concentrated masses and the varying of material properties on the receptance of beams are investigated.

2. Theoretical background

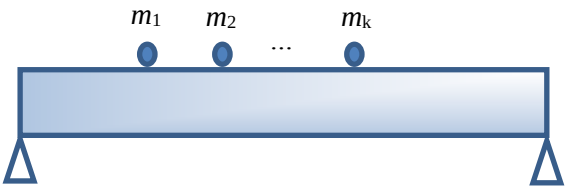

Fig. 1. A beam with concentrated masses

Let us consider the Euler-Bernoulli beam carrying concentrated masses subjected to a force as shown in Fig. 1. The governing equation of bending vibration of the beam can be presented as follows (Laura (1974)):

$$\left[EI(x)y''\right]'' + \left[\mu(x) + \sum_{k=1}^{n} m_k \delta(x - x_{mk})\right]\ddot{y} = \delta(x - x_f) f(t) \quad (1)$$

where E is the Young's modulus, I is the moment of inertia of the cross sectional area of the beam, μ is the mass density, m_k is the k^{th} concentrated mass located at x_{mk}, $y(x, t)$ is the bending deflection of the beam at location x and time t, $f(t)$ is the force acting at position x_f, $\delta(x - x_f)$ is the Dirac delta function.

Introducing the non-dimensional coordinate $\xi = \frac{x}{L}$ and after some transformations Eq. (1) can be expressed in matrix form as follows:

$$\mathbf{M}\ddot{\mathbf{q}}(t) + \mathbf{K}\mathbf{q}(t) = \mathbf{\Phi}(\xi_f) f(t) \quad (2)$$

where:

$$\mathbf{M} = L^4 \begin{bmatrix} A_1 & B_{12} & \dots & B_{1N} \\ B_{21} & A_2 & \dots & B_{2N} \\ \dots & & \ddots & \dots \\ B_{N1} & B_{N2} & \dots & A_N \end{bmatrix} \quad (3)$$

$$A_i = \int_0^1 \frac{\mu}{L^4} \phi_i^2 d\xi + \sum_{k=1}^{n} m_k \phi_i^2(\xi_{mk}), i = 1,...,N$$

$$B_{ij} = \sum_{k=1}^{n} m_k \phi_i(\xi_{mk}) \phi_j(\xi_{mk}), i, j = 1,...,N$$

$$\mathbf{K} = L^4 \begin{bmatrix} K_1 & 0 & \dots & 0 \\ 0 & K_2 & \dots & 0 \\ \dots & \dots & \ddots & \dots \\ 0 & 0 & \dots & K_N \end{bmatrix} \quad (4)$$

$$K_i = \int_0^1 EI \phi_i''^2 d\xi, i = 1,...,N$$

$$\mathbf{\Phi}(\xi) = \left[\phi_1(\xi),...,\phi_N(\xi)\right]^T \quad (5)$$

$$\ddot{\mathbf{q}}(t) = \left[\ddot{q}_1(t),...,\ddot{q}_N(t)\right]^T$$

$$\mathbf{q}(t) = \left[q_1(t),...,q_N(t)\right]^T$$

If the force is harmonic $f(t) = \bar{f}e^{i\omega t}$ then the solution of Eq. (2) can be found in the form:

$$\mathbf{q}(t) = \bar{\mathbf{q}}e^{i\omega t} \quad (6)$$

Substituting Eq. (6) into Eq. (2), the receptance at ξ due to the force at ξ_f is obtained:

$$\boldsymbol{\alpha}(\xi, \xi_f, \omega) = \frac{\mathbf{\Phi}^T(\xi)\bar{\mathbf{q}}}{\bar{f}} = \mathbf{\Phi}^T(\xi) \frac{\mathbf{\Phi}(\xi_f)}{\mathbf{K} - \omega^2 \mathbf{M}} \quad (7)$$

In order to derive formula (8), the mode shape ϕ of the beam without attached masses needs to be determined. Any mode shape ϕ is determined by solving the eigenvalue problem:

$$\left[EI(\xi)\phi_i''(\xi)\right]'' - L^4\omega^2\mu(\xi)\phi_i(\xi) = 0 \quad (8)$$

Assume that the elasticity modulus $E(x)$ and the mass density $\mu(x)$ of the AFG Euler-Bernoulli beam is varied as follows (Wu (2007)):

$$E(x) = E_0\left[1-\alpha_1\xi^n\right]$$
$$\mu(x) = \mu_0\left[1-\alpha_2\xi^n\right] \quad (9)$$

Where E_0 and μ_0 are Young's modulus and mass density at ξ=0, respectively; $0<\alpha<1$. In most of the previous work in order to derive the analytical solution of Eq. (9) by applying Adomian decomposition method (Wu (1999)), the ratio n=1 is often considered for the simplicity reason. In this work, we will develop a more general solution for the AFG beam by considering the ratio n as an arbitrary integer.

Substituting Eq. (9) into Eq. (8), yields:

$$\phi_i'''' - \frac{2n\alpha_1 X^{n-1}}{1-(\beta X)^n}\phi_i''' - \frac{n(n-1)\alpha_1 X^{n-2}}{1-(\beta X)^n}\phi_i'' + \lambda^2\frac{1-\alpha_2 X^n}{1-(\beta X)^n}\phi_i = 0 \quad (10)$$

where $\beta = \sqrt[n]{\alpha_1}$, $\lambda^2 = \dfrac{\omega^2 A\rho_0 L^4}{E_0 I}$

Solved Eq. (10) by Adomian decomposition method in which ϕ is decomposed into the infinite sum of convergent series:

$$\phi_i(\xi) = \sum_{k=0}^{\infty} C_k\xi^k \quad (11)$$

Introducing linear operators where $\ell = \dfrac{d^4}{d\xi^4}$ and $\ell^{-1} = \int_0^\xi\int_0^\xi\int_0^\xi\int_0^\xi(...)d\xi d\xi d\xi d\xi$, we have:

$$\ell^{-1}\ell(\phi_i) = \ell^{-1}\left(\phi_i''''\right) = \phi_i - C_0 - C_1\xi - C_2\xi^2 - C_3\xi^3 \quad (12)$$

Substituting Eq. (12) into Eq. (10) yields:

$$\phi_i = \sum_{k=0}^{3} C_k\xi^k + \ell^{-1}\left\{\frac{2n\alpha_1\xi^{n-1}\phi_i'''}{\left[1-(\beta\xi)^n\right]} + \frac{n(n-1)\alpha_1\xi^{n-2}\phi_i''}{\left[1-(\beta\xi)^n\right]} + \frac{\lambda^2\phi_i}{1-(\beta\xi)^n} - \frac{\lambda^2\alpha_2\xi^n\phi_i}{1-(\beta\xi)^n}\right\} \quad (13)$$

Since $\beta\xi$<1, using the power series:

$$\frac{1}{1-(\beta\xi)^n} = \sum_{m=0}^{\infty}\left(\beta^n\xi^n\right)^m$$

Applying Cauchy product, one has:

$$\sum_{m=0}^{\infty}\left(\beta^n\xi^n\right)^m\sum_{k=0}^{\infty}C_k\xi^k = \sum_{k=0}^{\infty}\xi^k\sum_{i=0}^{m}\beta^{(m-i)n}C_{in+p} \quad (14)$$

where $m = /\!/\frac{k}{n}/\!/$ is the largest integer that is less than or equal to $\frac{k}{n}$, p is the remainder of $\frac{k}{n}$.

Substituting Eq. (14) into Eq. (12) and integrating, yields:

$$\phi_i = \sum_{k=0}^{3}C_k\xi^k + \sum_{k=0}^{\infty}\xi^{k+n+3}X_2 + \sum_{k=0}^{\infty}\xi^{k+n+2}X_3 + \sum_{k=0}^{\infty}\xi^{k+4}X_4 - \sum_{k=0}^{\infty}\xi^{k+n+4}X_5 \quad (15)$$

$$X_2 = \frac{2n\alpha_1\sum_{i=0}^{m}\beta^{in}(i+1)(i+2)(i+3)C_{k-in+3}}{\prod_{j=n}^{n+3}(k+j)}$$

$$X_3 = \frac{n(n-1)\alpha_1\sum_{i=0}^{m}\beta^{in}(i+1)(i+2)C_{k-in+2}}{\prod_{j=n-1}^{n+2}(k+j)}$$

$$X_4 = \frac{\lambda^2\sum_{i=0}^{m}\beta^{(m-i)n}C_{in+p}}{\prod_{j=1}^{4}(k+j)};\ X_5 = \frac{\lambda^2\alpha_2\sum_{i=0}^{m}\beta^{(m-i)n}C_{in+p}}{\prod_{j=n+1}^{n+4}(k+j)}$$

The coefficients C_k where k<4 can be determined from the boundary conditions. Let us consider a cantilever beam, the boundary conditions can be expressed as:

$$\phi(0) = 0,\ \phi'(0) = 0 \quad (16)$$

$$\phi(1) = 0,\ \phi'(1) = 0 \quad (17)$$

From Eqs. (16) and (17) we have:

$$C_0 = 0,\ C_1 \neq 0,\ C_2 = 0,\ C_3 \neq 0 \quad (18)$$

For $k\geq 4$ the coefficients C_k can be calculated from the recurrent relations depending on the value of n as follows:

$$C_k = s_1 + s_2 + s_3 + s_4 \tag{19}$$

$$s_1 = \frac{2n\alpha_1 \sum_{i=0}^{m_1} \beta^{(m_1-i)n}(i+1)(i+2)(i+3)C_{in+p_1+3}}{(k-3)(k-2)(k-1)k}$$

$$s_2 = \frac{n(n-1)\alpha_1 \sum_{i=0}^{m_2} \beta^{(m_2-i)n}(i+1)(i+2)C_{in+p_2+2}}{(k-3)(k-2)(k-1)k}$$

$$s_3 = \frac{\lambda^2 \sum_{i=0}^{m} \beta^{(m_3-i)n} C_{in+p_3}}{(k-3)(k-2)(k-1)k}$$

$$s_4 = -\frac{\lambda^2 \alpha_2 \sum_{i=0}^{m} \beta^{(m_4-i)n} C_{in+p_4}}{(k-3)(k-2)(k-1)k}$$

where $m_1 = /\!/\frac{k-n-3}{n}/\!/$, $m_2 = /\!/\frac{k-n-2}{n}/\!/$, $m_3 = /\!/\frac{k-4}{n}/\!/$, $m_4 = /\!/\frac{k-n-4}{n}/\!/$; p_1, p_2, p_3, p_4 are the remainders of $\frac{k-n-3}{n}$, $\frac{k-n-2}{n}$, $\frac{k-4}{n}$, $\frac{k-n-4}{n}$, respectively.

Therefore, ϕ_i in Eq. (15) can be expressed as a linear function of C_1 and C_3. Since coefficients C_k is determined from the recurrent equation (19), the coefficients C_k are the functions of C_1, C_3 and λ, thus ϕ_i is also function of C_1, C_3 and λ.

By substituting Eq. (12) into Eq. (17), we have: $\sum_{k=0}^{\infty} C_k = 0 \Leftrightarrow f_{11}(\lambda)C_1 + f_{12}(\lambda)C_3 = 0$ (20)

$$\sum_{k=0}^{\infty}(k+1)C_{k+1} = 0 \Leftrightarrow f_{21}(\lambda)C_1 + f_{22}(\lambda)C_3 = 0 \tag{21}$$

In order to have non-trivial C_1 and C_3 of Eqs. (19) and (20), the following condition must be satisfied:

$$f_{11}(\lambda) f_{22}(\lambda) - f_{12}(\lambda) f_{21}(\lambda) = 0 \tag{22}$$

Solving Eq. (21), the dimensionless frequency λ_i is determined. Substituting the solution λ_i into Eqs. (19), C3 can be calculated as:

$$C_3 = -\frac{f_{11}(\lambda)}{f_{12}(\lambda)} C_1 \tag{23}$$

The n^{th} mode shape ϕ_n corresponding to λ_n is calculated from Eq. (15). Once the mode shape ϕ_i is determined, the following relations is derived:

$$\phi^2{}_i(\xi) = \sum_{k=0}^{\infty} C_k \xi^k \sum_{k=0}^{\infty} C_k \xi^k = \sum_{k=0}^{\infty} \xi^k \sum_{i=0}^{k} C_{k-i} C_i \tag{23}$$

$$\begin{aligned}\phi_i''^2(\xi) &= \sum_{k=0}^{\infty} C_k \xi^k (k+1)(k+2) \times \\ &\times \sum_{k=0}^{\infty} C_k \xi^k (k+1)(k+2) \\ &= \sum_{k=0}^{\infty} \xi^k \sum_{i=0}^{k} P^*\end{aligned} \tag{24}$$

$$P^* = C_{k-i+2} C_{i+2} (i+1)(i+2)(k-i+1)(k-i+2)$$

$$\begin{aligned}\int_0^1 \mu \phi_i^2 d\xi &= \int_0^1 \mu_0 (1-\alpha_2 \xi^n) \sum_{k=0}^{\infty} \xi^k \sum_{i=0}^{k} C_{k-i} C_i d\xi \\ &= \sum_{k=1}^{\infty} \frac{\mu_0 \left[(k+1)(1-\alpha_2) + n + 1\right]}{(k+1)(k+n+1)} \sum_{i=0}^{k} C_{k-i} C_i\end{aligned} \tag{25}$$

$$\begin{aligned}\int_0^1 IE \phi_i''^2 d\xi &= \int_0^1 IE_0 (1-\alpha_1 \xi^n) \sum_{k=0}^{\infty} \xi^k \sum_{i=0}^{k} P^* d\xi \\ &= \sum_{k=1}^{\infty} \frac{IE_0 \left[(k+1)(1-\alpha_1) + n + 1\right]}{(k+1)(k+n+1)} \sum_{i=0}^{k} P^*\end{aligned} \tag{26}$$

Plugging Eqs. (23)-(26) into Eqs. (3) and (4), matrices **M** and **K** will be obtained, thus the receptance formula (7) is determined.

3. Numerical simulation

In this paper, numerical simulations of a simply supported beam with two masses is presented. AFG beam consist of two constituent materials of steel and alumina (ALO3). Parameters of AFG beam are: Mass density ρ_s = 7800 kg/m^3; E_s = 210 GPa; ρ_{al} = 3960 kg/m^3; E_{al} = 390 GPa; L = 1 m; b = 0.02 m; h = 0.01 m. Two equal concentrated masses of 0.6 kg are attached on the beam in nine scenarios as listed in Table 1. The receptance matrices are calculated at 50 points spaced equally on the beam while the force moves along these points.

Table 1. Nine scenarios of attached masses

Scenario	ω	Position of m_1	Position of m_2
1	$\omega=\omega_1$	0.25L	-
2	$\omega=\omega_1$	0.75L	-
3	$\omega=\omega_2$	0.25L	-
4	$\omega=\omega_2$	0.75L	-
5	$\omega=\omega_3$	0.17L	-
6	$\omega=\omega_3$	0.5L	-
7	$\omega=\omega_3$	0.73L	-
8	$\omega=\omega_3$	0.17L	0.5L
9	$\omega=\omega_3$	0.17L	0.83L

Fig. 2 presents the receptance of the AFG beam with n=2 without concentrated masses at three frequencies close to the first three natural frequencies. One can observe clearly from this figure that, the positions of maxima and minima of the receptance obtained at a natural frequency coincide with the positions of maxima and minima of the corresponding mode shape. The amplitude on the left side which is the heavier side of the AFG beam, decreases in comparison with that of the uniform beam. The nodes and the peaks of the receptance move toward the right end in comparison with the uniform beam as can be seen from Fig. 2. It is recalled that when the Yong's modulus and the mass density increase the vibration amplitude decreases. Therefore, the decrease in vibration amplitude on the right side of beam where the Young's modulus decreases and the mass density increases suggests that, in the case of alumina-steel beam, the mass density has greater effect on the vibration amplitude than that of the Young's modulus.

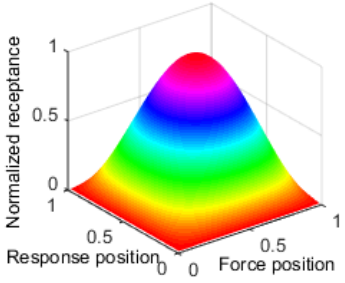

a)

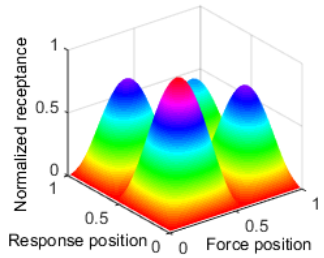

b)

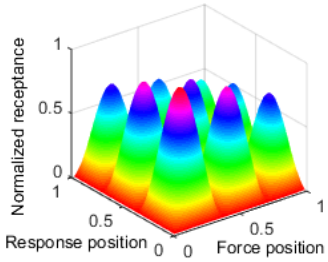

c)

Fig. 2. Receptance matrices of AFG beam without attached masses:

a) $\omega=\omega_1$; b) $\omega=\omega_2$; c) $\omega=\omega_3$

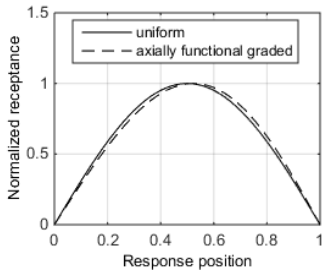

a)

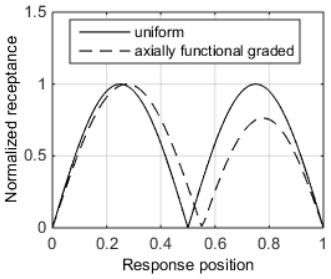

b)

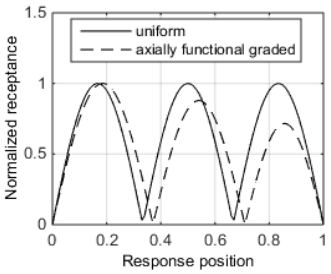

c)

Fig. 3. Receptance curves of beams without attached masses: a) $\omega=\omega_1$; b) $\omega=\omega_2$; c) $\omega=\omega_3$.

When there is a concentrated mass, the receptance matrix of the beam is changed. Fig. 4 present the 3D and 2D graphs of the recetance of beams carrying masses when the forcing frequency is equal to the first natural frequency of the beam-mass system. The influence of the masses on the receptance matrices is very small so that it cannot be observed from 3D graph in Fig. 4a. However, the influence of the masses on the receptance can be inspected visually as presented in Fig. 4b when the receptance curves are extracted while the force is fixed at 0.5L. When there is an attached mass at L/4 or 3L/4 the peak of receptance moves to the left and the right ends of beam, respectively. This means that the receptance is "pulled" toward the mass position. However, when the mass is located at the middle of the beam, the shape of the receptance is unchanged. It is concluded that, the influence of the mass on the receptance of the uniform beam and the axially functional graded beam are similar when the forcing frequency is equal to the first natural frequency of the beam-mass system.

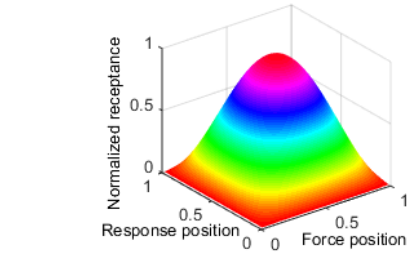

a)

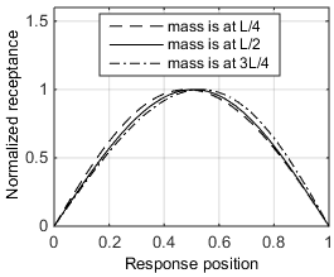

b)

Fig. 4. Receptance with one attached mass at L/4, $\omega=\omega_1$: a) 3D; b) 2D

Fig. 5 depicts the receptance of beam carrying a concentrated mass at different positions when the forcing frequency is equal to the second natural frequency. As can be observed from Fig. 5a, when the mass is located at L/4, the peaks corresponding to either the response position or the force position of L/4 are reduced significantly, whereas the peak at the mass position is most reduced. Similarly, when the mass is located at 3L/4, the peak corresponding to the position of 3L/4 decrease significantly as shown in Fig. 5b. Meanwhile, the simulation showed that the shape of receptance is unchanged when the mass is attached at the nodes of the receptance. The differences between the receptances of the uniform and the axially functional graded beam can be observed in 2D graph as presented in Fig. 6 when receptance curves are extracted while the force is fixed at L/4. When the mass is located at the heavy side of the beam, the peak at the mass position of the axially functional graded beam decreases more significant than that of the uniform beam. In contrast, when the mass is attached in the light side of the beam, the peak at the mass position of the AFG beam decreases less significant than that of the uniform beam.

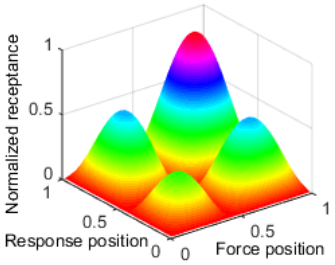

a)

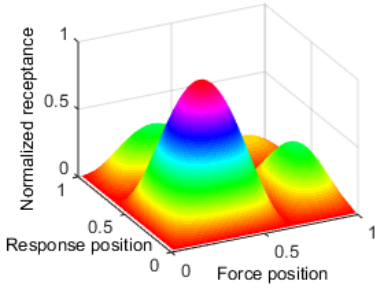

b)

Fig. 5. Receptance matrices of beam with one attached mass, $\omega=\omega_2$. a) L/4; b) 3L/4

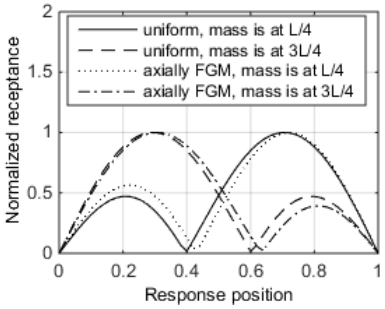

Fig. 6. Receptance curves of beams with one attached mass, $\omega=\omega_2$

Fig. 7 illustrates the receptance of AFG beam when the forcing frequency is equal to the third natural frequency. When a mass is attached at positions of $L/6$, $L/2$ and $5L/6$ respective, five peaks corresponding to positions of $L/6$, $L/2$ and $5L/6$ decrease significantly whereas the peak at the mass position is most reduced. When two masses are located at the positions of $L/6$ and $3L/6$, the peaks corresponding to these positions decrease as demonstrated in Fig. 7c. When two masses are located at the positions of $L/6$ and $5L/6$, the peaks corresponding to these positions decrease as presented in Fig. 7d.

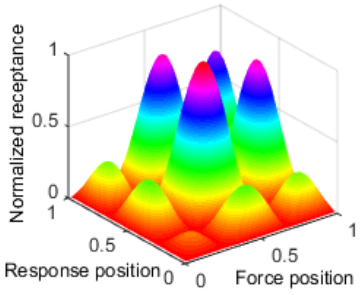

a)

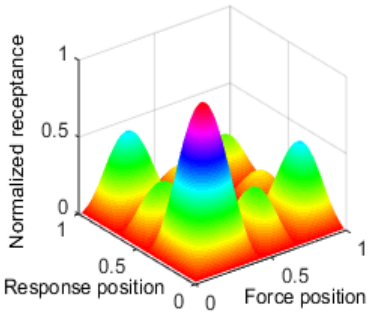

b)

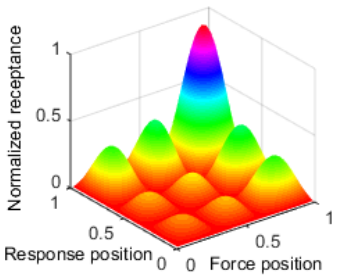

c)

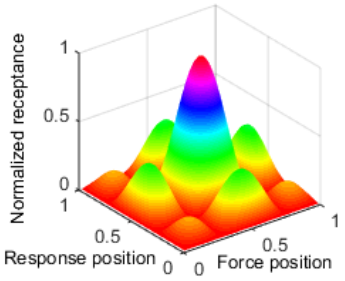

d)

Fig 7. Receptance matrices of beams, $\omega=\omega_3$, mass is at: a) $L/6$; b) $L/2$; c) $L/6$ and $L/2$; e) $L/6$ and $5L/6$

The change in receptance can be seen in more detail when the force is fixed at the position of $L/2$ as depicted in Fig. 9. One can observe clearly from this figure that when there are masses attached at peaks of the receptances, these peaks will decrease significantly. It is noted that, when one mass is attached at the middle of the beam not only the peak at $L/2$ decreases significantly, but also the peak at $5L/6$ decreases, or in other words both peaks in the heavier side of the beam decrease. Another conclusion can be drawn from this figure is that in all the scenarios of attached masses the receptances of the AFG beam tend to "move" toward the heavier side of the beam.

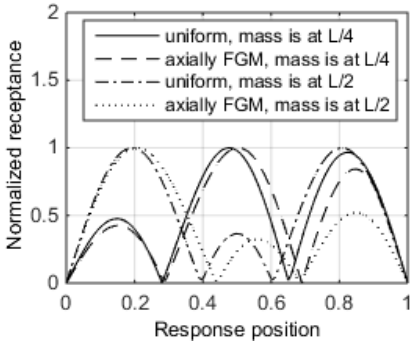

a)

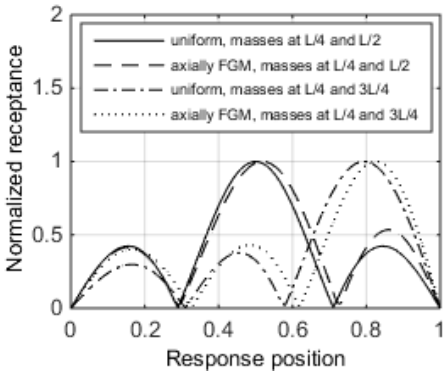

b)

Figure 8. Receptance curves of beams, $\omega=\omega_3$: a) Uniform beam; b) AFG beam.

4. Conclusion

In this paper, the exact receptance functions of the AFG beam carrying concentrated masses are presented. The derived receptance functions can be applied easily to investigate the dynamic response of beam at an arbitrary point to a harmonic force acted at any point with any forcing frequency. The influence of the concentrated masses and the varying of material properties on the receptances of beam are also investigated.

When the excitation frequency is equal to natural frequencies, the maxima and minima positions of the receptances are the same with the maxima and minima positions of the corresponding mode shape. In the case of the alumina-steel material, the influence of the mass on the receptance is greater than that of the Young's modulus. Due to the varying properties of material, the peaks in the receptance of the AFG beam in the heavier side is smaller than that of the uniform beam. The receptances of the AFG beam tend to move to the heavier side of the beam.

When there are concentrated masses the shape of receptances are changed. When the masses are attached at peaks of the receptance, these peaks will decrease significantly. When the masses are located at the nodes of receptances, the receptances are not influenced. The influence of the masses on the receptance matrix can be used to control the vibration amplitude at some specific positions at given forcing frequencies.

Acknowledgements

This research is funded by Vietnam National Foundation for Science and Technology Development (NAFOSTED) under grant number 107.02-2017.300.

References

Rossit CA, Bambill DV, Gilardi GJ. Free vibration of AFG cantilever tapered beams carrying attached masses. *Structural Engineering Mechanics* 2017; 61(5), 685-691.

Banerjee JR. *Free vibration of beams carrying spring-mass systems*: A dynamic stiffness approach, Computers and Structures 104–105 (2012) 21–26.

Shahba A, Attarnejad R, Marvi MT, Hajilar S. *Free vibration and stability analysis of axially functionally graded tapered Timoshenko beams with classical and non-classical boundary conditions*. Composites: Part B 42 (2011), 801–808.

Wu JS, Hsu TF. Free vibration analyses of simply supported beams carrying multiple point masses and spring-mass systems with mass of each helical spring considered, International Journal of Mechanical Sciences 49 (2007) 834–852.

Cha PD. Eigenvalues of a linear elastica carrying lumped masses, springs and viscous dampers, *Journal of Sound and Vibration* 257 (2002) 798–808.

Chang TP, Chang FI, Liu MF. On the eigenvalues of a viscously damped simple beam carrying point masses and springs, *Journal of Sound and Vibration* 240 (2001) 769–778.

Gurgoze M. Alternative formulations of the characteristic equation of a Bernoulli–Euler beam to which several viscously damped spring–mass systems are attached in-span, *Journal of Sound and Vibration* 223 (1999) 666–677.

Wu JS, Chou HM. A new approach for determining the natural frequencies and mode shapes of a uniform beam carrying any number of spring masses, *Journal of Sound and Vibration* 220 (1999) 451–468.

Posiadala B. Free vibrations of uniform Timoshenko beams with attachments, *Journal of Sound and Vibration* 204 (1997) 359–369.

Wu JS, Lin TL. Free vibration analysis of a uniform cantilever beam with point masses by an analytical- and numerical-combined method, *Journal of Sound and Vibration* 136 (1990) 201–213.

Laura PAA, Pombo JL, Susemihl EA. A note on the vibrations of a clamped-free beam with a mass at the free end, *Journal of Sound and Vibration* (1974) 37(2), 161-168.

The 5th International Conference on Engineering Mechanics and Automation (ICEMA 5)
Hanoi, October 11÷12, 2019

Crack detection of beams using receptance function and wavelet transform

Khoa Viet Nguyen [a], Mai Van Cao [a] and Thao Thi Bich Dao [a]

[a] *Institute of Mechanics, Vietnam Academy of Science and Technology*
18 Hoang Quoc Viet, Cau Giay, Hanoi, Vietnam
nvkhoa@imech.vast.vn or nguyenvietkhoa_vc@yahoo.com

Abstract

This paper presents the combination method using exact receptance function and wavelet transform for crack detection of beams. The influence of the crack on the receptance is investigated by applying wavelet transform. The results show that when there are cracks the wavelet coefficients of receptance is influenced significantly at crack positions. This is useful for the detection of cracks. In this paper, the derivation of exact receptance of beam with general boundary conditions is presented and the numerical simulations are provided.

Keywords: Receptance, frequency response function, crack, crack detection, wavelet transform

1. Introduction

The receptance method which was first introduced by Bishop and Johnson [14] has been applied wildly in mechanical system and structural dynamics. Yang [11] presented the exact receptances of non-proportionally damped dynamic systems. Based on a decomposition of the damping matrix, an iteration procedure is developed which does not require matrix inversion. Lin and Lim [10] developed a new and effective method to derive the structural design sensitivities which include the receptance sensitivity with respect to mass modification and stiffness modification from the limited vibration test data. Mottershead [9] investigated the measured zeros form frequency response functions and its application to model assessment and updating. Gurgoze [6] was concerned with receptance matrices of viscously damped systems subject to several constraint equations. The frequency response matrix of the constrained system was established in terms of the frequency response matrix of the unconstrained system and the coefficient vectors of the constraint equations. Recently, Muscolino and Santoro [1] presented the explicit frequency response function of beams with cracks of uncertain depths in order to evaluate the main statistics as well as the upper and lower bounds of the response.

As is known, early crack detection is very important in engineering structures and this issue has attracted many researchers in the last three decades. Since the cracks may have significant influence on the dynamic characteristics of structures such as natural frequencies and mode shape etc., these dynamic characteristics have been investigated and applied wildly for crack detection of structures. Chondros and Dimarogonas [13], Lee and Chung [7] studied the change in natural

frequencies of beams caused by a crack. Hu and Liang [12] presented an integrated method using the knowledge of changes in natural frequencies for crack detection. Kessissoglou [5] investigated the relationship between natural frequency of a cracked beam to the depth and location of the crack. The results in these papers showed that the natural frequency of the cracked beam decreases as the crack depth increases. Caddemi and Calio [2, 4] presented the exact closed-form solution for the mode shapes of the Euler-Bernoulli beam with multiple open cracks. The author of this paper [3] applied the wavelet transform to investigate the change in the response of beam subjected to moving load at the crack positions.

In this paper, the effect of the crack on the receptance of cracked beams is investigated by using wavelet transform to show that the receptance has significant changes at crack positions. These results can be useful for crack detection. The derivation of the exact receptance function and the wavelet transform of the receptance is presented and the numerical simulations are provided in this paper.

2. The receptance function of a cracked beam

2.1. Cracked beam

The exact closed form of the mode shape of a beam with n cracks is adopted from [4] as follows:

$$\begin{aligned}\phi_k(\xi) = C_1 \Bigg\{ & \frac{1}{2\alpha_k}\sum_{i=1}^{n}\lambda_i\mu_i \\ & \times\left[\sin\alpha_k(\xi-\xi_{oi})+\sinh\alpha_k(\xi-\xi_{0i})\right] \\ & \times U(\xi-\xi_{oi})+\sin\alpha_k\xi\Bigg\} \\ + \Bigg\{ & \frac{1}{2\alpha_k}\sum_{i=1}^{n}\lambda_i\zeta_i \\ & \times\left[\sin\alpha_k(\xi-\xi_{oi})+\sinh\alpha_k(\xi-\xi_{oi})\right] \\ & \times U(\xi-\xi_{oi})+\sinh\alpha_k\xi\Bigg\}\end{aligned} \tag{1}$$

where α_k is the dimensionless frequency parameter $\alpha_k^4 = \dfrac{\omega_k^2 mL^4}{EI}$; ξ_{0i} is the position of the i^{th} crack, where $0<\xi_{01}<\xi_{02}<\ldots<\xi_{0n}<1$; U is Heaviside function; μ, ν, ζ, η, λ are given by [4].

$$C_1 = -\frac{\dfrac{1}{2\alpha_k}\sum_{i=1}^{n}\lambda_i\zeta_i\left[\sin\alpha_k(1-\xi_{0i})+\sinh\alpha_k(1-\xi_{0i})\right]+\sinh\alpha_k}{\dfrac{1}{2\alpha_k}\sum_{i=1}^{n}\lambda_i\mu_i\left[\sin\alpha_k(1-\xi_{0i})+\sinh\alpha_k(1-\xi_{0i})\right]+\sin\alpha_k} \tag{2}$$

In order to derive the exact formulas of receptance as presented in Eqs. (8), the integral of the square of the mode shape need to be calculated.

For simplicity, the operator $S(\alpha_k,\xi)=\sin\alpha_k(\xi-\xi_{oi})+\sinh\alpha_k(\xi-\xi_{oi})$ is presented.

Applying the property of Heaviside function, we have:

$$\begin{aligned}\int_0^1 f(\xi)U(\xi-\xi_{0i})d\xi &= \int_{\xi_{0i}}^1 f(\xi)d\xi \\ &= F(1)-F(\xi_{0i})\end{aligned} \tag{3}$$

where F is the antiderivative function of f.

It is noted that:

$$U(\xi-\xi_{0i})U(\xi-\xi_{0i}) = \begin{cases} U(\xi-\xi_{0i}), & \text{if } i\geq j \\ U(\xi-\xi_{0j}), & \text{if } i<j \end{cases} \tag{4}$$

From Eq. (3) and Eq. (4) we have:

$$\begin{aligned}&\int_0^1 f(\xi)U(\xi-\xi_{0i})U(\xi-\xi_{0j})d\xi \\ &= \begin{cases} \int_0^1 f(\xi)U(\xi-\xi_{0i})d\xi, & \text{if } i\geq j \\ \int_0^1 f(\xi)U(\xi-\xi_{0j})d\xi, & \text{if } i<j \end{cases} \\ &= \begin{cases} \mathrm{F}(1)-\mathrm{F}(\xi_{0i}), & \text{if } i\geq j \\ \mathrm{F}(1)-\mathrm{F}(\xi_{0j}), & \text{if } i<j \end{cases}\end{aligned} \tag{5}$$

Eq. (5) can be rewritten in the form:

$$\begin{aligned}&\int_0^1 f(\xi)U(\xi-\xi_{0i})U(\xi-\xi_{0j})d\xi \\ &= F(1)-F(\xi_{0i})U(\xi_{0i}-\xi_{0j}) \\ &\quad -F(\xi_{0j})U(\xi_{oj}-\xi_{0i})+F(\xi_{0i})\delta_{ij}\end{aligned} \tag{6}$$

where δ_{ij} is the Kronecker delta.

Analytical calculations show that the term $F(\xi_{0i})\delta_{ij}$ in Eq. (6) vanishes. From Eqs. (1) to (6), the following equation is obtained:

$$\begin{aligned}
\int_0^1 \phi_k^2(\xi)d\xi = &\frac{1}{8\alpha_k^2}\sum_{i=1}^{n}\sum_{j=1}^{n}\lambda_i\lambda_j A_1 \\
&\times\Big\{\cos\alpha_k(\xi_{0i}-\xi_{0j}) - \cosh\alpha_k(\xi_{0i}-\xi_{0j}) \\
&+\frac{1}{\alpha_k}\sin\alpha_k(1-\xi_{0i})\cosh\alpha_k(1-\xi_{0j}) \\
&-\frac{1}{\alpha_k}\cos\alpha_k(1-\xi_{0i})\sinh\alpha_k(1-\xi_{0j}) \\
&+\frac{1}{\alpha_k}\sin\alpha_k(1-\xi_{0j})\cosh\alpha_k(1-\xi_{0i}) \\
&-\frac{1}{\alpha_k}\cos\alpha_k(1-\xi_{0j})\sinh\alpha_k(1-\xi_{0i}) \\
&+\frac{1}{\alpha_k}\cosh\alpha_k(1-\xi_{0j})\sinh\alpha_k(1-\xi_{0i}) \\
&-\frac{1}{2\alpha_k}\sin(2-\xi_{0i}-\xi_{0j}) \\
&-\Big[\xi_{0i}\cos\alpha_k(\xi_{0i}-\xi_{0j})+\frac{1}{2\alpha_k}\sin\alpha_k(\xi_{0i}-\xi_{0j}) \\
&\quad-\xi_{0i}\cosh\alpha_k(\xi_{0i}-\xi_{0j}) \\
&\quad-\frac{1}{\alpha_k}\sinh\alpha_k(\xi_{0i}-\xi_{0j})\Big]\times U(\xi_{0i}-\xi_{0j}) \\
&-\Big[\xi_{0i}\cos\alpha_k(\xi_{0i}-\xi_{0j})+\frac{1}{2\alpha_k}\sin\alpha_k(\xi_{0i}-\xi_{0j}) \\
&\quad-\xi_{0i}\cosh\alpha_k(\xi_{0i}-\xi_{0j})\Big]\times U(\xi_{0i}-\xi_{0j}) \\
&+\frac{1}{2\alpha_k}\sum_{i=1}^{n}\lambda_i A_2 \\
&\times\Big[(1-\xi_{0i})\cos\alpha_k\xi_{0i}-\frac{1}{2\alpha_k}\sin\alpha_k(2-\xi_{0i}) \\
&-\frac{1}{2\alpha_k}\sin\alpha_k\xi_{0i}+\frac{1}{\alpha_k}\sin\alpha_k\cosh\alpha_k(1-\xi_{0i}) \\
&-\frac{1}{\alpha_k}\cos\alpha_k\sinh\alpha_k(1-\xi_{0i})\Big] \\
&+\frac{1}{2\alpha_k}\sum_{i=1}^{n}\lambda_i A_3 \\
&\times\Big[(\xi_{0i}-1)\cosh\alpha_k\xi_{0i}+\frac{1}{2\alpha_k}\sinh\alpha_k(2-\xi_{0i}) \\
&+\frac{1}{2\alpha_k}\sinh\alpha_k\xi_{0i}+\frac{1}{\alpha_k}\sin\alpha_k(1-\xi_{0i})\cosh\alpha_k \\
&-\frac{1}{\alpha_k}\cos\alpha_k(1-\xi_{0i})\sinh\alpha_k\Big] \\
&+\frac{1}{2}\left(C_1^2-1\right)-\frac{C_1^2}{4\alpha_k}\sin 2\alpha_k+\frac{1}{4\alpha_k}\sinh 2\alpha_k \\
&+\frac{C_1}{\alpha_k}\sin\alpha_k\cosh\alpha_k-\frac{C_1}{\alpha_k}\cos\alpha_k\sinh\alpha_k
\end{aligned} \tag{7}$$

where:

$$\begin{aligned}
A_1 &= C_1^2\mu_i\mu_j+\zeta_i\zeta_j+2C_1\mu_i\zeta_j \\
A_2 &= C_1^2\mu_i+C_1\zeta_i;\ A_3=\zeta_i+C_1\mu_i
\end{aligned} \tag{8}$$

Substituting Eqs. (3) to (7) the exact receptance of the simply supported beam will be obtained.

2.2. Wavelet transform

The continuous wavelet transform is defined as follows (Daubechies [1992]):

$$W(a,b)=\frac{1}{\sqrt{a}}\int_{-\infty}^{\infty} f(t)\psi^*\left(\frac{t-b}{a}\right)dt \tag{9}$$

Where a is a real number called scale or dilation, b is a real number called position, $W(a,b)$ are wavelet coefficients at scale a and position b, $f(t)$ is input signal, $\psi\left(\frac{t-b}{a}\right)$ is wavelet function and $\psi^*\left(\frac{t-b}{a}\right)$ is complex conjugate of $\psi\left(\frac{t-b}{a}\right)$. In order to simplify the expression of the wavelet transform, denote $\psi_{a,b}(t)=\frac{1}{\sqrt{a}}\psi^*\left(\frac{t-b}{a}\right)$, the wavelet transform (9) can be written:

$$W(a,b)=\int_{-\infty}^{+\infty} f(t)\psi_{a,b}dt \tag{10}$$

3. Numerical simulation and discussions

Numerical simulations of a simply supported beam with two cracks is presented in this section. Parameters of the beam are: Mass density ρ=7800 kg/m3; modulus of elasticity E=2.0x1011 N/m2; L=1 m; b=0.02 m; h=0.01 m. Two cracks with the same depths are made at arbitrary positions of 0.42*L* and 0.76*L* from the left end of the beam. Five levels of the crack depth ranging from 0% to 20% have been applied. These five cases are numbered in Table 1. The receptance and the wavelet transform of the receptance matrices are calculated at 100 points spaced equally on the beam while the force moves along these points.

Table 1. Five cases with cracks of varying depths

Case	Crack depth (**%**)
1	0
2	10
3	20
4	30

3.1. Receptance of beam

In this section, the receptance matrices of the beam with different forcing frequencies ranging from the first natural frequency to the third natural frequency are investigated. The first two natural frequencies of the intact beam are listed in Table 2.

Table 2. Three natural frequencies of the intact beam

Mode	Natural frequency (**Rad/s**)
1	293
2	1171

Fig. 1 presents the 3D graphs of normalized receptance matrices at three forcing frequencies close to the first three natural frequencies of the intact beam. As can be seen from Fig. 1a, for every position of force, when the forcing frequency is 293.1 Rad/s which is close to the first natural frequency, the receptance is zero at the ends of the beam and then increases and reaches the maximum when the response point moves from the ends to the middle of beam. When the forcing frequency is 1171.1 Rad/s which is close to the second natural frequency, the receptance matrix is minimum at the middle of the beam and becomes maximum at positions *L*/4 and 3*L*/4 as depicted in Fig. 1b. In order to show these receptance matrices in more details, the receptance along the beam when the force acts at a fixed point is extracted from these receptance matrices. When the force position is fixed, in order to obtain the response of beam at the first three natural frequencies, the force position should not be the same with the nodes in the first three mode shapes. For this reason, the force position is selected at 0.42*L*. Fig. 2 illustrates the 2D graphs of receptance when the force acts at 0.42*L*. As can be seen from this figure, the receptance curves are smooth except the minimum position. The positions of maxima and minima of these receptance graphs coincide with the positions of nodes of the corresponding mode shapes. These results imply that the responses along the beam can be predicted by using the receptance matrices or the mode shapes when the forcing frequency is close to natural frequencies.

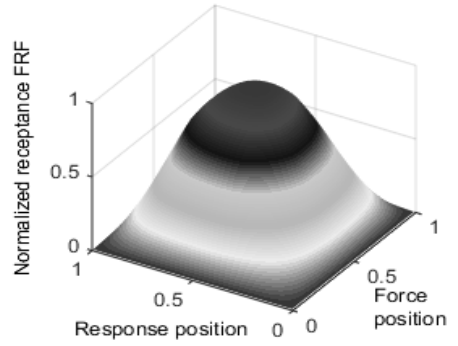

a) $\omega \approx \omega_1$

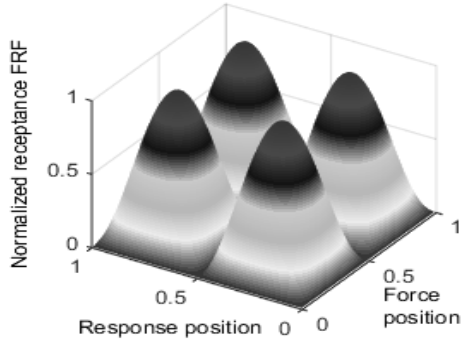

b) $\omega \approx \omega_2$

Fig. 1. Receptance matrices of the intact beam

Fig. 2 illustrates the 2D graphs of receptance when the force acts at 0.42L. As can be seen

from this figure, the receptance curves are smooth except the minimum position. The positions of maxima and minima of these receptance graphs coincide with the positions of nodes of the corresponding mode shapes. These results imply that the responses along the beam can be predicted by using the receptance matrices or the mode shapes when the forcing frequency is close to natural frequencies.

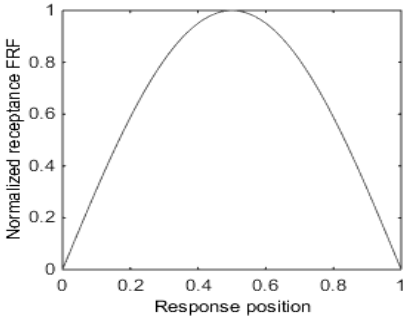

a) $\omega \approx \omega_1$

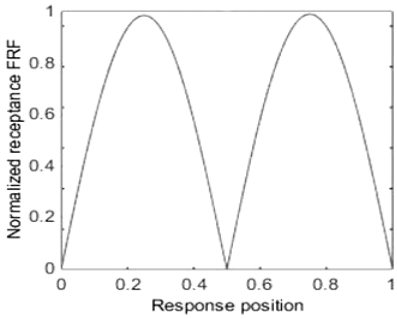

b) $\omega \approx \omega_2$

Fig. 2. Receptance of the intact beam, $\hat{x}$=0.42L

However, when the forcing frequency is in between two natural frequencies, the responses along the beam are more complicated. For example, as presented in Fig. 3a when the forcing frequency is 700 Rad/s, between the first and the second frequencies, the receptance matrix has two main peaks in the middle area of beam and two small peaks close to the ends. The shape of this receptance matrix suggests that it is a hybrid shape between the shapes of receptance matrices of mode 1 and mode 2 where the two main peaks correspond to mode 1 and two other peaks correspond to mode 2. This means that in this case mode 1 and mode 2 are excited and mode 1 is dominant. In another example, when the forcing frequency is 2100 Rad/s, between the second and the third natural frequencies, the receptance matrix has six main peaks and two other small peaks as can be observed from Fig. 3b. In this case modes 2 are excited. These results show that, for an arbitrary forcing frequency the distribution of response amplitude along the beam may be complicated but it can be predicted in advance at any position.

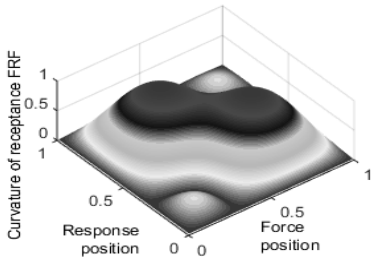

a)ω=840 Rad/s

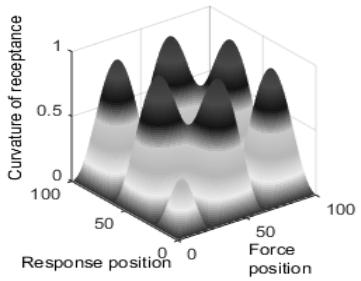

b) ω=1903 Rad/s

Fig. 3. Receptance matrices of the intact beam

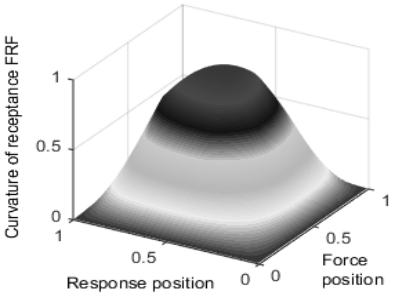

a) Receptance matrix

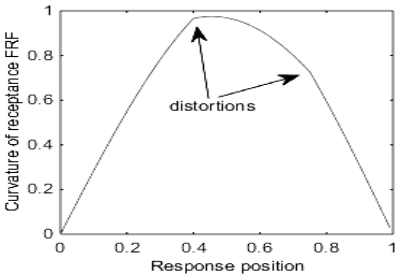

b) Receptance with $\hat{x}$=0.42L

Fig. 4. Receptance of the cracked beam, crack depth=50%, $\omega=\omega_1$

As presented in Fig. 2, the receptance of the intact beam are smooth except the nodal points of mode shapes. When there are cracks the mode shapes will have sharp changes at the crack positions leading to the changes in the receptance at the crack positions as mentioned in Section 2.2. In this paper, simulation results show that the changes in the receptance are small when the crack depth is small and they only become significant when the crack depth is large. Fig. 4 depicts the distortions of the receptance matrix at the first natural frequency when the crack depth is up to 50% of the beam height. As can be seen from this figure, the receptance matrix is distorted at the crack positions. As can be observed from Fig. 4b the distorted positions coincide with the crack positions at 0.42L and 0.76L.

Although the receptance matrices have small changes at the crack positions when the crack depth is small, the the wavelet transform of the receptance matrices might have significant changes at the crack positions. In order to study the influence of the small crack on the response, the the wavelet transform of the receptance matrices of the cracked beam are established and investigated in the following section.

3.2. Wavelet transform of receptance

In this section, the wavelet of receptance of the cracked beam with the crack depth ranging from 10% to 50% are investigated. Fig. 5 presents the graphs of wavelet of receptance of the cracked beam with different levels of the crack depth when the forcing frequencies is equal to the first natural frequency. As can be seen from this figure, there are sharp peaks in the wavelet transform of receptance at 0.42L and 0.76L which are the same with the crack positions. It is noted that for each level of the crack depth, when the crack position is closer to the maxima of the receptance, the height of sharp peak is greater. Meanwhile, when the crack position is far from the maxima of the receptance, the height of sharp peak is smaller.

Fig. 5 presents the wavelet transform of the receptance when the forcing frequencies is equal to the second natural frequency. As can be observed from this figure, the two peaks are located clearly at the position of 0.42L and 0.76*L* which coincide with the locations of the cracks. Furthermore, the peak closer to the maximum of the receptance is greater than the peak closure to the minimum of the receptance. Simulations showed that when a crack is located at the minimum position of the receptance, the peak in the wavelet transform of the receptance caused by the crack coincide the peak caused by the minimum of the receptance. Thus, the peak located at the minimum of the receptance cannot be detected. For this reason, the receptance of obtained when the forcing excitation is equal to the first mode is suitable for crack detection while the higher frequencies are not recommended.

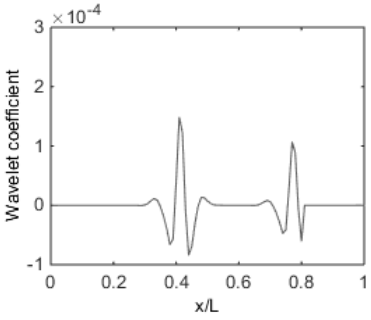

a) Crack depth=10%

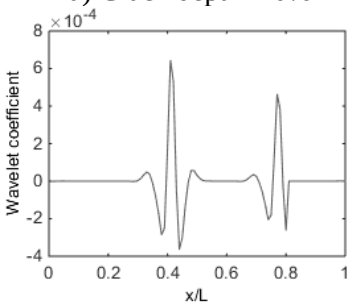

a) Crack depth=30%

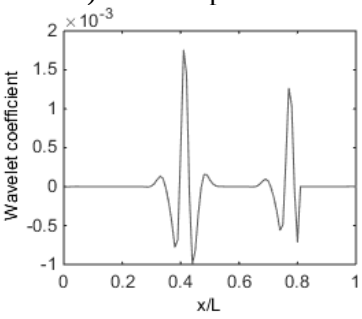

c) Crack depth=50%

Fig. 5. The wavelet transform of the receptances of the cracked beam, $\hat{x}$=0.42L, $\omega=\omega_1$

These results mean that, the sharp peaks in the wavelet transform of the receptance can be used

for crack detection. In order to detect the cracks, only one the wavelet transform of the receptance measured along the beam when the force acts at a fixed point is needed. The sharp peaks in this measured the wavelet transform of the receptance indicate the existence of cracks, the positions of these sharp peaks point out the positions of cracks, and the heights of sharp peaks correspond to the crack severities. In addition, the numerical simulations show that in order to have better results for crack detection purpose, the force and the response should be applied at maximum positions of the the wavelet transform of the receptance matrices. When the crack is located at the minimum position of the the wavelet transform of the receptance, the crack cannot be detected. Clearly, only the the wavelet transform of the receptance corresponding to the first mode shape can be used for detecting arbitrary cracks on the beam since the first mode shape do not have any node.

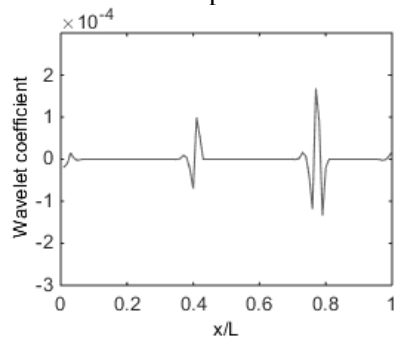

a) Crack depth=10%

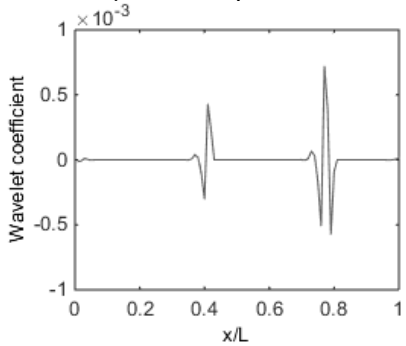

b) Crack depth=30%

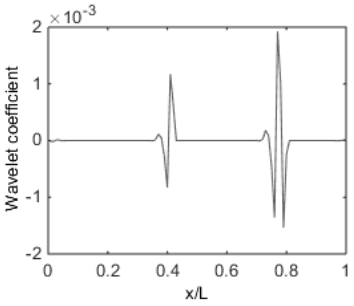

c) Crack depth=50%

Fig. 6. The wavelet transform of the receptances of the cracked beam, $\hat{x}$=0.42L, $\omega=\omega_2$

3.3. Influence of the noise

In order to simulate the noisy measurements, white noise is added to the receptance obtained at the first frequency of the beam having two cracks at 0.42L and 0.76*L* with depths of 50%. The white noise vector is obtained as following formula:

$$\text{noise} = \sqrt{\frac{\sigma^2}{\exp\left(\frac{SNR*\ln(10)}{10}\right)}} * \text{R} \qquad (11)$$

Where σ^2 is the variance of the the wavelet transform of the receptance, *SNR* is the desired signal to noise ratio and **R** is a standard normal distribution vector with zero mean value and unit standard deviation. The noisy the wavelet transform of the receptance is the sum of the simulated the wavelet transform of the receptance and the noise vector presented in Eq. (11).

Fig. 7 presents the wavelet transform of noisy receptance at the first frequency with the *SNR* of 70, 40 and 30. For a *NSR* of 70, the plot is very similar to noise free case (Fig. 7a). When the noise level *SNR* is of 40, the two peaks at the crack positions can still be detected clearly as can be observed from Fig. 7b. However, when the *SNR* equal to 30, the peaks at crack positions cannot be detected clearly as presented in Fig. 7c. These results suggest that, the proposed method can be applied efficiently to detect crack depth from noisy measurements, but it cannot be applied for very high levels of noise.

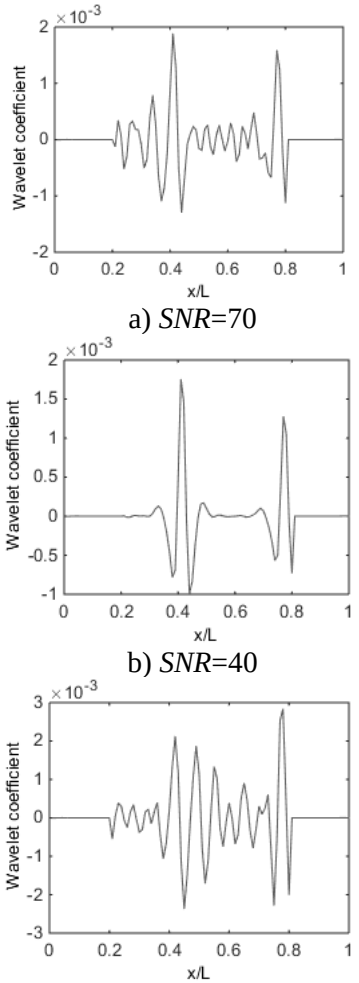

a) *SNR*=70

b) *SNR*=40

c) *SNR*=30

Fig. 7. The wavelet transform of the receptances at the first natural frequency, crack depth=50%, $\hat{x}=0.42L$.

4. Conclusions

In this paper, exact formulas of the receptance of a cracked simply supported beam is presented. The advantage of the exact receptance function is that the frequency response at any point of a cracked beam can be easily predicted while the present receptance matrix methods can only predict the response at specific points.

When there are cracks, the receptance of beam will be changed at the crack positions. However, this change can only be seen visually when the crack depth is large. In order to inspect the small changes caused by cracks in the receptance, the wavelet transform is applied. When there are cracks, the wavelet transform of the receptance curve has significant peaks at the locations of cracks. The sharp peaks in the the wavelet transform of the receptances can be detected clearly when the crack depth is as small as 10% of the beam height.

The influence of the measurement noise is also investigated. It is concluded that the proposed method can be applied for the polluted measurements with the *SNR* of 30%.

Acknowledgements

This research is funded by Vietnam National Foundation for Science and Technology Development (NAFOSTED) under grant number 107.02-2017.300.

References

[1] G. Muscolinoa, R.Santoro, Explicit frequency response function of beams with crack of uncertain depth, *Procedia Engineering* 199 (2017) 1128–1133.

[2] S. Caddemi, I. Caliò, Exact reconstruction of multiple concentrated damages on beams, *Acta Mechanica*, 225(11), 3137-3156, 2014.

[3] K.V. Nguyen, Mode shapes analysis of a cracked beam and its application for crack detection, *Journal of Sound and Vibration* (2014), 333, 848–872.

[4] S. Caddemi and I. Calio, Exact closed-form solution for the vibration modes of the Euler–Bernoulli beam with multiple open cracks, *Journal of Sound and Vibration* 327 (2009), 473-489.

[5] D.Y. Zheng and N.J. Kessissoglou, Free vibration analysis of a cracked beam by finite element method, *Journal of Sound and Vibration* 273 (2004), 457–475.

[6] M. Gurgoze, Receptance matrices of viscously damped systems subject to several constraint equations, *Journal of Sound and Vibration* (2000) 230(5), 1185-1190.

[7] Y. Lee and M. Chung, A study on crack detection using eigenfrequency test data, *Computers and Structures* 77 (2000), 327-342.

[8] M.M. Abdel Wahab, Damage detection in bridges using modal curvature: application to a real damage scenario, *Journal of Sound and Vibration* 226(2) (1999), 217-235

[9] J.E. Mottershead, On the zeros of structural frequency response functions and their sensitivities,

Mechanical Systems and Signal Processing 12 (1998) 591–597.

[10] R.M. Lin, M.K. Lim, Derivation of structural design sensitivities from vibration test data, *Journal of Sound and Vibration* 201 (1997) 613–631.

[11] B. Yang, Exact receptances of nonproportionally damped systems, *Transactions of American Society of Mechanical Engineers Journal of Vibration and Acoustics* 115 (1993) 47–52.

[12] J. Hu, R.Y. Liang, An integrated approach to detection of cracks using vibration characteristics, *Journal of the Franklin Institute* 330 (5) (1993) 841–853.

[13] T.G. Chondros and A.D. Dimarogonas, Identification of cracks in welded joints of complex structures. *Journal of Sound and Vibration* 1980, 69: 531–538.

[14] R.E.D. Bishop, D.C. Johnson, *The Mechanics of Vibration*, Cambridge University Press, Cambridge, 1960.

The 5th International Conference on Engineering Mechanics and Automation (ICEMA 5)
Hanoi, October 11÷12, 2019

Exact receptance curvature function of continuous cracked beams and its application for crack detection

Khoa Viet Nguyen [a], Mai Van Cao [a] and Thao Thi Bich Dao [a]

[a] *Institute of Mechanics, Vietnam Academy of Science and Technology*
18 Hoang Quoc Viet, Cau Giay, Hanoi, Vietnam
nvkhoa@imech.vast.vn or nguyenvietkhoa_vc@yahoo.com

Abstract

The receptance function is very important which interrelates the harmonic excitation and the response of a structure in the frequency domain. This paper presents the exact receptance curvature function of continuous cracked beams. In this work, the "receptance curvature" is defined as the second derivative of the receptance. The influence of the crack on the receptance curvature is investigated. The results show that when there are cracks the receptance curvature is influenced significantly at crack positions. This might be useful for the detection of cracks. In this paper, the derivation of exact receptance of beam with general boundary conditions is presented and the numerical simulations are provided.

Key Words: Receptance, curvature of receptance, frequency response function, crack, crack detection.

1. Introduction

As is known the receptance method that interrelates the harmonic excitation and the response of a structure in the frequency domain was first introduced by Bishop and Johnson [15]. Mottershead [11] studied the measured zeros form frequency response functions and its application to model assessment and updating. Gurgoze [10] investigated receptance matrices of viscously damped systems subject to several constraint equations. The frequency response matrix of the constrained system was established in terms of the frequency response matrix of the unconstrained system and the coefficient vectors of the constraint equations. Karakas and Gurgoze [9] developed a formulation of the receptance matrix of non-proportionally damped dynamic systems. The receptance matrix was obtained directly without using the iterations as presented in [1].

Early crack detection is extremely important in mechanical systems and engineering structures and this issue has attracted many researchers in the last three decades. Since the cracks may influence significantly on the dynamic characteristics of structures such as natural frequencies and mode shapes, etc. These dynamic characteristics have been investigated and applied wildly for crack detection of structures. Muscolino and Santoro [1] presented the explicit frequency response functions of discretized structures with uncertain parameters. Thalapil and Maiti [2] investigated the change in natural frequencies caused by longitudinal cracks for crack detection. While the change in natural frequencies can be applied for detection of the existence of cracks, the change in mode

shape can be used to detect the location of cracks in structures since the cracks influence the mode shape locally. Albertelli et al. [5] proposed a method using receptance coupling substructure method to improve chatter free cutting conditions prediction. Ruotolo and Surace [12], VakilBaghmisheh et al. [8], applied genetic algorithms for crack detection of structures using natural frequencies. Some authors presented methods to calculate and apply the mode shape of cracked structures for crack detection purposes. Very early works by Pandey et al. Gudmundson [14] studied the influence of cracks on the natural frequencies of slender structures using a flexibility matrix approach. The results showed that the sharp changes in mode shapes at the crack positions can be applied for detecting small cracks.

In this work, the formula of "receptance curvature" defined as the second derivative of the receptance with respect to the coordinate of beam is presented. The effect of the crack on the receptance curvature of cracked beams is investigated to show that the receptance curvature has significant changes at crack positions. These results might be useful for crack detection. The derivation of the exact receptance function and receptance curvature is presented and the numerical simulations are provided in this paper.

2. Derivation of the receptance function of a cracked beam

2.1. Intact beam

In this work, the undamped Euler-Bernoulli beam is considered. The forced vibration equation of undamped beam can be written as:

$$\frac{\partial^2}{\partial x^2} EI \frac{\partial^2 v(x,t)}{\partial x^2} + m(x)\frac{\partial^2 v(x,t)}{\partial t^2} = P(x,t) \quad (1)$$

Introducing a non-dimensional coordinate $\xi = \frac{x}{L}$, Eq. (1) becomes:

$$\frac{\partial^2}{\partial \xi^2} EI(\xi) \frac{\partial^2 v(\xi,t)}{\partial \xi^2} + L^4 m(\xi)\frac{\partial^2 v(\xi,t)}{\partial t^2} = L^4 P(\xi,t) \quad (2)$$

The solution of Eq. (1) can be found in the form:

$$v(\xi,t) = \sum_{k=1}^{\infty} \phi_k(\xi) Y_k(t) \quad (3)$$

Where $\phi_k(x)$ is the k^{th} mode shape of the beam, $Y_k(t)$ is the time-dependent amplitude, which is referred to as generalized coordinate. Substituting Eq. (3) into Eq. (2), yields:

$$\sum_{k=1}^{\infty} \frac{d^2}{d\xi^2}\left[EI(\xi)\frac{d^2\phi_k(\xi)}{d\xi^2}\right] Y_k(t) + \sum_{k=1}^{\infty} L^4 m(\xi)\phi_k(\xi)\ddot{Y}_k(t) = L^4 P(\xi,t) \quad (4)$$

The orthogonality conditions of beam can be expressed as:

$$\int_0^1 m(\xi)\phi_k(\xi)\phi_n(\xi)d\xi = 0 \;\; if\; k \neq n$$
$$\int_0^1 \phi_n(\xi)\frac{d^2}{d\xi^2}\left[EI(\xi)\frac{d^2\phi_k(\xi)}{d\xi^2}\right] d\xi = 0 \;\; if\; k \neq n \quad (5)$$

Applying this orthogonality conditions Eq. (5) becomes:

$$L^4 \ddot{Y}_n(t)\int_0^1 m(\xi)\phi_n{}^2(\xi)d\xi + Y_n(t)\int_0^1 \phi_n(\xi)\frac{d^2}{d\xi^2}\left(EI(\xi)\frac{d^2\phi_n(\xi)}{d\xi^2}\right) d\xi = L^4\int_0^L \phi_n(\xi)P(\xi,t)d\xi \quad (6)$$

If the force is harmonic $P = \hat{P}\sin\omega t$ exciting at the point $\xi = \hat{\xi}$, then $Y_n(t) = \bar{Y}_n \sin\omega t$, and from (6) we have:

$$\left(\omega_n^2 - \omega^2\right)\bar{Y}_n(t)\int_0^1 m(\xi)\phi_n^2(\xi)d\xi = \phi_n\left(\hat{\xi}\right)\hat{P} \quad (7)$$

Therefore, the receptance at ξ due to the force at $\hat{\xi}$ can be obtained as:

$$\alpha_{\xi\hat{\xi}}(\omega) = \sum_{n=1}^{\infty} \frac{1}{\omega_n^2 - \omega^2}\frac{\phi_n(\xi)\phi_n\left(\hat{\xi}\right)}{\int_0^1 m(\xi)\phi_n^2(\xi)d\xi} \quad (8)$$

2.2. Cracked beam

When there is a crack, the mode shapes of the beam will have sharp change at the crack position as reported in previous works, e.g. [3],

[4]. Therefore, the receptance might be changed at the crack position since the receptance is calculated from mode shapes as presented in Eq. (8). Although in general the change in mode shapes caused by the crack at the crack position is small when the crack depth is small, the curvature of the mode shape at the crack position can be significant since the mode shape is changed sharply at the crack position. In this paper, we define the "receptance curvature" as the second derivative of the receptance function with respect to ξ variable as follows:

$$\frac{\partial^2 \alpha_{\xi\hat{\xi}}(\omega)}{\partial \xi^2} = \sum_{n=1}^{\infty} \frac{1}{\omega_n^{\,2} - \omega^2} \frac{\phi_n\left(\hat{\xi}\right)}{\int_0^1 m(\xi)\phi_n^{\,2}(\xi)\,d\xi} \frac{d^2\phi_n(\xi)}{d\xi^2} \tag{9}$$

From Eq. (9), the receptance curvature of a cracked beam is expected to have significant change at the crack position in comparison with the receptance since the receptance curvature is proportional to the curvature of the mode shape.

In this work, we consider the elementary case with $m(x)$ set equal to constant m, Eq. (9) becomes:

$$\frac{\partial^2 \alpha_{\xi\hat{\xi}}(\omega)}{\partial \xi^2} = \sum_{n=1}^{\infty} \frac{1}{\omega_n^{\,2} - \omega^2} \frac{\phi_n\left(\hat{\xi}\right)}{m\int_0^1 \phi_n^{\,2}(\xi)\,d\xi} \frac{d^2\phi_n(\xi)}{d\xi^2} \tag{10}$$

The exact closed form of the mode shape of a beam with n cracks is adopted from [6] as follows:

$$\begin{aligned}
\phi_k(\xi) = C_1 &\left\{ \frac{1}{2\alpha_k} \sum_{i=1}^{n} \lambda_i \mu_i \right. \\
&\times \left[\sin\alpha_k\left(\xi - \xi_{oi}\right) + \sinh\alpha_k\left(\xi - \xi_{0i}\right) \right] \\
&\left. \times U\left(\xi - \xi_{oi}\right) + \sin\alpha_k\xi \right\} \\
+C_2 &\left\{ \frac{1}{2\alpha_k} \sum_{i=1}^{n} \lambda_i \nu_i \right. \\
&\times \left[\sin\alpha_k\left(\xi - \xi_{oi}\right) + \sinh\alpha_k\left(\xi - \xi_{oi}\right) \right] \\
&\left. \times U\left(\xi - \xi_{oi}\right) + \cos\alpha_k\xi \right\} \\
+C_3 &\left\{ \frac{1}{2\alpha_k} \sum_{i=1}^{n} \lambda_i \zeta_i \right. \\
&\times \left[\sin\alpha_k\left(\xi - \xi_{oi}\right) + \sinh\alpha_k\left(\xi - \xi_{oi}\right) \right] \\
&\left. \times U\left(\xi - \xi_{oi}\right) + \sinh\alpha_k\xi \right\} \\
+C_4 &\left\{ \frac{1}{2\alpha_k} \sum_{i=1}^{n} \lambda_i \eta_i \right. \\
&\times \left[\sin\alpha_k\left(\xi - \xi_{oi}\right) + \sinh\alpha_k\left(\xi - \xi_{oi}\right) \right] \\
&\left. \times U\left(\xi - \xi_{oi}\right) + \cosh\alpha_k\xi \right\}
\end{aligned} \tag{11}$$

Where C_1, C_2, C_3, C_4 are calculated from boundary conditions; α_k is the dimensionless frequency parameter $\alpha_k^4 = \dfrac{\omega_k^2 m L^4}{EI}$; ξ_{0i} is the position of the i^{th} crack, where $0 < \xi_{01} < \xi_{02} < \ldots < \xi_{0n} < 1$; U is Heaviside function; μ, ν, ζ, η, λ are given by [6].

In order to derive the exact formulas of receptance and curvature receptance as presented in Eqs. (8) and (10), the second derivative of the mode shape and the integral of the square of the mode shape need to be calculated.

For simplicity, the operator $S\left(\alpha_k, \xi\right) = \sin\alpha_k\left(\xi - \xi_{oi}\right) + \sinh\alpha_k\left(\xi - \xi_{oi}\right)$ is presented.

Applying the property of Heaviside function, we have:

$$\begin{aligned}
\int_0^1 f(\xi) U\left(\xi - \xi_{0i}\right) d\xi &= \int_{\xi_{0i}}^1 f(\xi)\,d\xi \\
&= F(1) - F\left(\xi_{0i}\right)
\end{aligned} \tag{14}$$

where F is the antiderivative function of f.

It is noted that:

$$U\left(\xi - \xi_{0i}\right) U\left(\xi - \xi_{0i}\right) = \begin{cases} U\left(\xi - \xi_{0i}\right), & \text{if } i \geq j \\ U\left(\xi - \xi_{0j}\right), & \text{if } i < j \end{cases} \tag{15}$$

From Eq. (14) and Eq. (15), we have:

$$\begin{aligned}
&\int_0^1 f(\xi) U\left(\xi - \xi_{0i}\right) U\left(\xi - \xi_{0j}\right) d\xi \\
&= \begin{cases} \int_0^1 f(\xi) U\left(\xi - \xi_{0i}\right) d\xi, & \text{if } i \geq j \\ \int_0^1 f(\xi) U\left(\xi - \xi_{0j}\right) d\xi, & \text{if } i < j \end{cases} \\
&= \begin{cases} \mathrm{F}(1) - \mathrm{F}\left(\xi_{0i}\right), & \text{if } i \geq j \\ \mathrm{F}(1) - \mathrm{F}\left(\xi_{0j}\right), & \text{if } i < j \end{cases}
\end{aligned} \tag{16}$$

Eq. (16) can be rewritten in the form:

$$\begin{aligned}&\int_0^1 f(\xi)U(\xi-\xi_{0i})U(\xi-\xi_{0j})d\xi\\&=F(1)-F(\xi_{0i})U(\xi_{0i}-\xi_{0j})\\&\quad -F(\xi_{0j})U(\xi_{oj}-\xi_{0i})+F(\xi_{0i})\delta_{ij}\end{aligned}\tag{17}$$

where δ_{ij} is the Kronecker delta.

Analytical calculations show that the term $F(\xi_{0i})\delta_{ij}$ in Eq. (17) vanishes. From Eqs. (14) to (17), the following equation is obtained (18). Substituting Eqs. (14) to (17) into Eqs. (8) and (10) the exact receptance and curvature receptance of the simply supported beam will be obtained.

$$\begin{aligned}&\int_0^1 \phi_k^2(\xi)d\xi=\\&\frac{1}{8\alpha_k^2}\sum_{i=1}^{n}\sum_{j=1}^{n}\lambda_i\lambda_j A_1\times\\&\times\Big\{\cos\alpha_k(\xi_{0i}-\xi_{0j})\\&\quad-\frac{1}{2\alpha_k}\sin(2-\xi_{0i}-\xi_{0j})-\cosh\alpha_k(\xi_{0i}-\xi_{0j})\\&\quad+\frac{1}{\alpha_k}\sin\alpha_k(1-\xi_{0i})\cosh\alpha_k(1-\xi_{0j})\\&\quad-\frac{1}{\alpha_k}\cos\alpha_k(1-\xi_{0i})\sinh\alpha_k(1-\xi_{0j})\\&\quad+\frac{1}{\alpha_k}\sin\alpha_k(1-\xi_{0j})\cosh\alpha_k(1-\xi_{0i})\\&\quad-\frac{1}{\alpha_k}\cos\alpha_k(1-\xi_{0j})\sinh\alpha_k(1-\xi_{0i})\\&\quad+\frac{1}{\alpha_k}\cosh\alpha_k(1-\xi_{0j})\sinh\alpha_k(1-\xi_{0i})\\&\quad-\Big[\xi_{0i}\cos\alpha_k(\xi_{0i}-\xi_{0j})+\frac{1}{2\alpha_k}\sin\alpha_k(\xi_{0i}-\xi_{0j})\\&\qquad-\xi_{0i}\cosh\alpha_k(\xi_{0i}-\xi_{0j})\\&\qquad-\frac{1}{\alpha_k}\sinh\alpha_k(\xi_{0i}-\xi_{0j})\Big]U(\xi_{0i}-\xi_{0j})\\&\quad-\Big[\xi_{0j}\cos\alpha_k(\xi_{0j}-\xi_{0i})+\frac{1}{2\alpha_k}\sin\alpha_k(\xi_{0j}-\xi_{0i})\\&\qquad-\xi_{0j}\cosh\alpha_k(\xi_{0j}-\xi_{0i})\Big]U(\xi_{0j}-\xi_{0i})\Big\}\\&+\frac{1}{2\alpha_k}\sum_{i=1}^{n}\lambda_i A_2\\&\times\Big[(1-\xi_{0i})\cos\alpha_k\xi_{0i}-\frac{1}{2\alpha_k}\sin\alpha_k(2-\xi_{0i})\\&\quad-\frac{1}{2\alpha_k}\sin\alpha_k\xi_{0i}+\frac{1}{\alpha_k}\sin\alpha_k\cosh\alpha_k(1-\xi_{0i})\\&\quad-\frac{1}{\alpha_k}\cos\alpha_k\sinh\alpha_k(1-\xi_{0i})\Big]\\&+\frac{1}{2}(C_1^2-1)-\frac{C_1^2}{4\alpha_k}\sin 2\alpha_k+\frac{1}{4\alpha_k}\sinh 2\alpha_k\\&+\frac{C_1}{\alpha_k}\sin\alpha_k\cosh\alpha_k-\frac{C_1}{\alpha_k}\cos\alpha_k\sinh\alpha_k\end{aligned}\tag{18}$$

3. Numerical simulation and discussions

Numerical simulations of a simply supported beam with two cracks is presented in this section. Parameters of the beam are: Mass density ρ=7800 kg/m^3; modulus of elasticity E=2.0x10^{11} N/m^2; L=1 m; b=0.02 m; h=0.01 m.

Table 1. Four cases with cracks of varying depths

Case	Crack depth (**%**)
1	0
2	10
3	20
4	30

Two cracks with the same depths are made at arbitrary positions of 0.42L and 0.76L from the left end of the beam. Five levels of the crack depth ranging from 0% to 30% have been applied. These five cases are numbered in Table 1. The receptance and receptance curvature matrices are calculated at 100 points spaced equally on the beam while the force moves along these points.

3.1. Receptance curvature of the cracked beam

In this section, the receptance curvature matrices of the cracked beam with the crack depth ranging from 10% to 30% are investigated. Figs.

1, 3, 5 present the graphs of normalized receptance curvature matrices of the cracked beam with different levels of the crack depth when the forcing frequencies are 293.1 Rad/s, 1171.1 Rad/s which are close to the first, the second natural frequencies, respectively. As can be seen from these figures, there are sharp peaks in the receptance curvature matrices at crack positions. In order to determine exactly the sharp peak positions in the receptance curvature matrices, the receptance curvatures along the beam with the force acting at a fixed position are extracted from the receptance curvature matrices. The positions of these sharp peaks can be observed clearly as shown in Figs. 2, 4, 6 when the force acts at a fixed position of 0.42L. As can be observed from these figures, the positions of the sharp peaks are at 0.42L and 0.76L, which are the same with the crack positions. It is noted from Figs. 1-6 that for each level of the crack depth, when the crack position is closer to the maxima of the receptance curvature matrices, the heights of sharp peaks are greater. Meanwhile, when the crack position is far from the maxima of the receptance curvature, the heights of sharp peask in receptance curvature are smaller.

These results mean that, the sharp peaks in receptance curvature can be used for crack detection. In order to detect the cracks, only one receptance curvature measured along the beam when the force acts at a fixed point is needed. The sharp peaks in this measured receptance curvature indicate the existence of cracks, the positions of these sharp peaks point out the positions of cracks, and the heights of sharp peaks correspond to the crack severities. In addition, the numerical simulations show that in order to have better results for crack detection purpose, the force and the response should be applied at maximum positions of the receptance curvature matrices. When the crack is located at the minimum position of the receptance curvature, the crack cannot be detected. Clearly, only the receptance curvature corresponding to the first mode shape can be used for detecting arbitrary cracks on the beam since the first mode shape do not have any node.

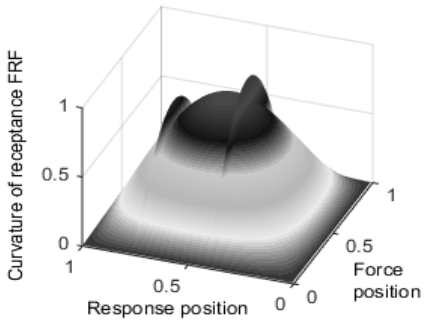

a) $\omega \approx \omega_1$

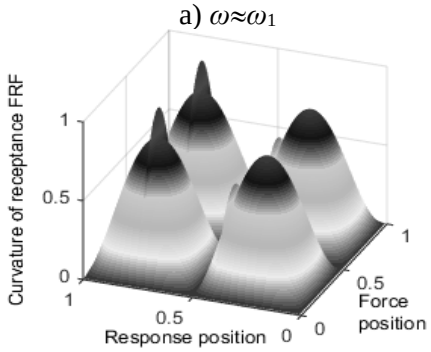

b) $\omega \approx \omega_2$

Fig. 1. Receptance curvature matrices of the cracked beam, crack depth=10%

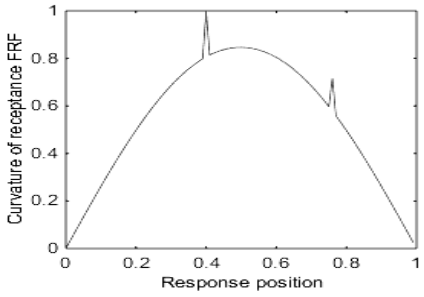

a) $\omega \approx \omega_1$

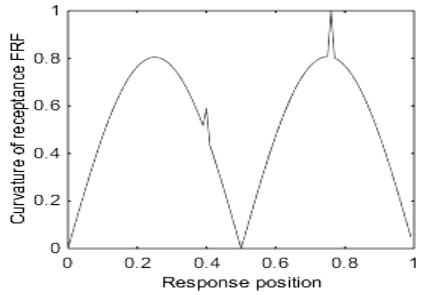

b) $\omega \approx \omega_2$;

Fig. 2. Receptance curvatures of the cracked beam, crack depth=10%, $\hat{x}$ =0.42L

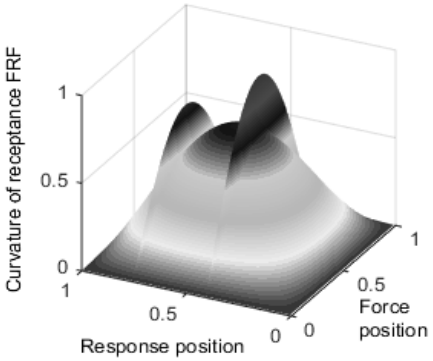

a) $\omega \approx \omega_1$

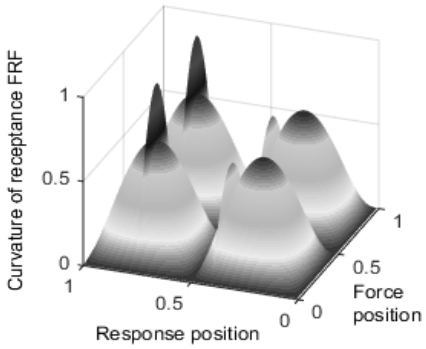

b) $\omega \approx \omega_2$

Fig.3. Receptance curvature matrices of the cracked beam, crack depth=20%

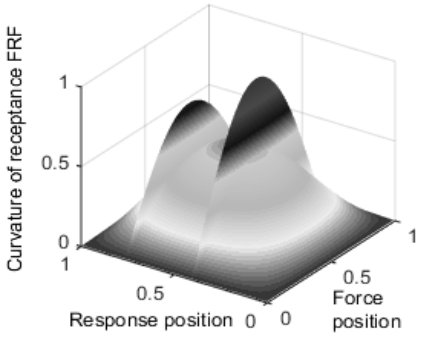

a) $\omega \approx \omega_1$

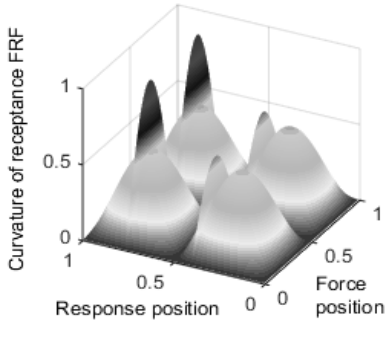

b) $\omega \approx \omega_2$

Fig. 5. Receptance curvature matrices of the cracked beam, crack depth=30%

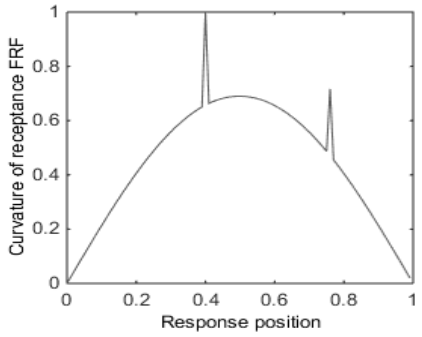

a) $\omega \approx \omega_1$

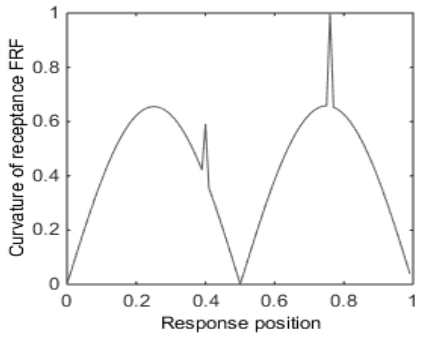

b) $\omega \approx \omega_2$

Fig. 4. Receptance curvatures of the cracked beam, crack depth=20%, $\hat{x}=0.42L$

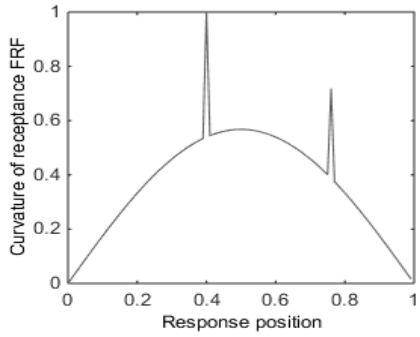

a) $\omega \approx \omega_1$

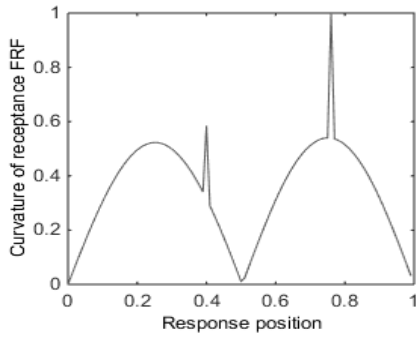

b) $\omega \approx \omega_2$

Fig. 6. Receptance curvatures of the cracked beam, crack depth=30%, $\hat{x}=0.42L$

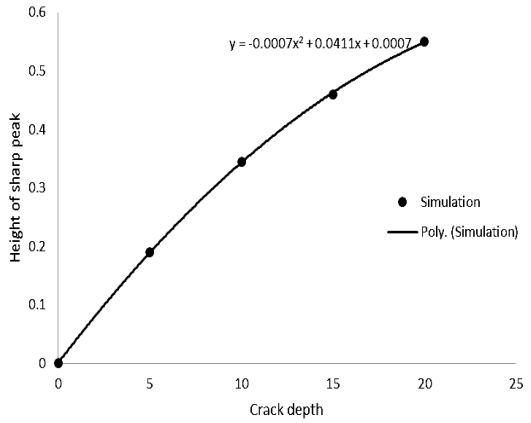

Fig. 7. Intensity factor versus crack depth

When the crack depth increases from 10% to 30% the height of sharp peaks in receptance curvature increase as demonstrated in Figs 2, 4, 6. Therefore, the height of sharp peaks can be considered as an intensity factor, which relates the change in receptance curvature to the crack depth. From these figures, establishing a graph of the first sharp peak height of the receptance curvature corresponding to the first natural frequency versus crack depth, a relationship between the height of sharp peak and crack depth is obtained as shown in Fig. 7. It can be seen that this relationship is a second-degree polynomial function. This relationship can be used for the estimation of crack depth.

3.2. Influence of the noise

In order to simulate the noisy measurements, white noise is added to the receptance curvature obtained at the first frequency of the beam having two cracks at 0.42*L* and 0.76*L* with depths of 30%. The white noise vector is obtained as following formula [7]:

$$\mathbf{noise} = \sqrt{\frac{\sigma^2}{\exp\left(\frac{SNR * \ln(10)}{10}\right)}} * \mathbf{R} \quad (19)$$

Where σ^2 is the variance of the receptance curvature, *SNR* is the desired signal to noise ratio and **R** is a standard normal distribution vector with zero mean value and unit standard deviation. The noisy receptance curvature is the sum of the simulated receptance curvature and the noise vector presented in Eq. (19).

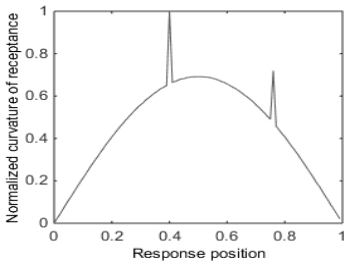

a) *SNR*=50

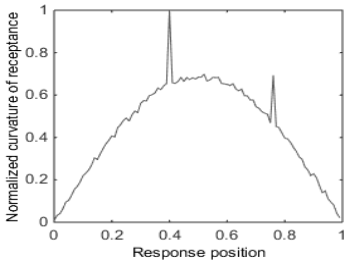

b) *SNR*=30

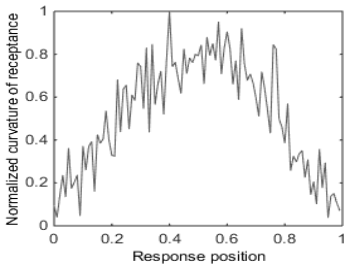

b) *SNR*=10

Fig. 8. Receptance curvatures at the first natural frequenct, crack depth=30%, $\hat{x}$=0.42*L*.

Fig. 8 presents the noisy receptance curvature at the first frequency with the *SNR* of 50, 30 and 10. For a *NSR* of 50, the plot is very similar to noise free case (Fig. 7a). When the noise level *SNR* is of 30, the two peaks at the crack positions can still be detected clearly as can be observed from Fig. 7b. However, when the *SNR* equal to 10, the peaks at crack positions cannot be detected as presented in Fig. 7c. These results suggest that, the proposed method can be applied efficiently to detect cracks in noisy measurements, but it cannot be applied for very high levels of noise.

4. Conclusions

In this paper, exact formulas of the receptance curvature function of a cracked beam is presented. When there are cracks, the receptance curvature of beams will be changed significantly

at the crack positions. The relationship between the height of sharp peak and the crack depth is the second-degree polynomial function and this relationship can be used for the estimation of crack depth. Once the receptance curvature along the beam excited by a force at fixed point and frequency is measured, the sharp peaks in the receptance curvature is the indicator of the existence of cracks and the positions of the sharp peaks show the positions of the cracks. The crack depth can be estimated from the relationship between the height of the sharp peak and the crack depth. The cracks can be detected by the proposed method in the pollutted measurements, but it cannot be detected from the signals polutted with very high levels of noise.

Acknowledgements

This research is funded by Vietnam National Foundation for Science and Technology Development (NAFOSTED) under grant number 107.02-2017.300.

References

[1] G. Muscolino, R. Santoro, A. Sofi, Explicit frequency response functions of discretized structures with uncertain parameters, *Computers and Structures* 133 (2014) 64–78.

[2] J. Thalapil, S.K. , Detection of longitudinal cracks in long and short beams using changes in natural frequencies, *International Journal of Mechanical Sciences* 83 (2014) 38–47.

[3] S. Caddemi, I. Caliò, Exact reconstruction of multiple concentrated damages on beams, *Acta Mechanica*, 225(11), 3137-3156, 2014.

[4] K.V. Nguyen, Mode shapes analysis of a cracked beam and its application for crack detection, *Journal of Sound and Vibration* (2014), 333, 848–872.

[5] P. Albertelli, M. Goletti, M. Monno, A new receptance coupling substructure analysis methodology to improve chatter free cutting conditions prediction. International *Journal of Machine Tools & Manufacture* 72 (2013) 16–24.

[6] S. Caddemi and I. Calio, Exact closed-form solution for the vibration modes of the Euler–Bernoulli beam with multiple open cracks, *Journal of Sound and Vibration* 327 (2009), 473-489.

[7]. R. F. Hoskins. Delta function. Second edition 2009 by Horwood Publishing Limited.

[8] M. Vakil-Baghmisheh, M. Peimani, M. Sadeghi, M. Ettefagh, Crack detection in beam-like structures using genetic algorithms, *Applied Soft Computing* 8 (2008), 1150-1160.

[9] A. Karakas, M. Gurgoze, A novel formulation of the receptance matrix of non-proportionally damped dynamic systems. Journal of Sound and Vibration 264 (2003) 733–740.

[5-10] M. Gurgoze, Receptance matrices of viscously damped systems subject to several constraint equations, Journal of Sound and Vibration (2000) 230(5), 1185-1190.

[11] J.E. Mottershead, On the zeros of structural frequency response functions and their sensitivities, Mechanical Systems and Signal Processing 12 (1998) 591–597.

[12] R. Ruotolo, C. Surace, Damage assessment of multiple cracked beams: numerical results and experimental validation, *Journal of Sound and Vibration* 206 (4) (1997) 567–588.

[13] A.K. Pandey M. Biswas, and M.M. Samman, Damage detection from changes in curvature mode shapes, *Journal of Sound and Vibration* 145(2) (1991), 321-332.

[14] P. Gudmundson, The dynamic behaviour of slender structures with cross-sectional cracks, *Journal of the Mechanics and Physics of Solids* 31 (1983); 329-45.

[15] R.E.D. Bishop, D.C. Johnson, *The Mechanics of Vibration*, Cambridge University Press, Cambridge, 1960.

The 5th International Conference on Engineering Mechanics and Automation (ICEMA 5)
Hanoi, October 11÷12, 2019

Cracking analysis of reinforced concrete bridge deck subjected to overload vehicle

Nguyen Duc Hieu[a], Tran The Truyen[b], Bui Thanh Tung[b] and Doan Bao Quoc[b]

[a] *University of Transport and Communications Campus in Ho Chi Minh City, Vietnam.*
[b] *University of Transport and Communications, Hanoi, Vietnam.*

Abstract

The cracking prediction of cracking remains a main concern regarding the behavior of reinforced concrete elements. The effects of a crack on the durability of a structure are a major concern as long as the predictivity improvement for the cracking analysis is required. Not only the crack pattern but also the crack features such as spacing, openings, rugosity and tortuosity have to be addressed at a structural scale. The purpose of this study is to propose a combining the use of concrete fracture mechanics and reinforced concrete theory to analysis the pre and post-cracking of reinforced concrete bridge deck subjected to overload vehicle.

Key Words: concrete, reinforced concrete, bridge deck, crack, overloaded vehicles.

1. Instructions

Reinforced Concrete Bridge Desk (RCBD) is the structure which is supported by main girders to make the way for vehicles on bridges, cover under structures and distribute load from live load on main girder. Cracks in RCBD may effect to operation capacity, durability and artistry of constructions. Crack can derive from different causes in which over-load vehicles running over bridges is one. Under effects of over-load vehicles, new cracks can be formed and propagated along with propagation of existing cracks. In operation process of bridges, condition of over-load vehicles over these bridges is still occuring at a certain degree which could cause cracks in RCBD. This condition is relatively popular on the main roads connecting between different areas such as industry zones, ports and national roads [10].

Calculation and control methods for restriction of cracking development in bridge desk in

current specifications which are through distances between reinforcements or axial stress in reinforcements have yet sufficiently approached to destructively mechanical theory or fracture mechanics. Apart from this, to simplify calculation models, relative slab strip model is applied which bridge desks are modeled to beams subjected by concentrated loads from wheel axel. In this research, the calculation model of bridge desk is according to spatial model and load model of wheels is according to distributed load. Formation mechanism of cracks is according to theory of Willam and Warnke (1975) which is applied in a lot of recent studies. Effect parameters of crack in bridge desk are studied related to formation, distribution and propagation of cracks under over-load vehicles.

ANSYS Mechanical APDL 2019R1 is used to model bridge desk of this research. This specialized software for structure analysis with reliable results.

2. Elementary theory

2.1. The criterion for failure of concrete

The concrete material model predicts the failure of brittle materials. Both cracking and crushing failure modes are accounted for.

The criterion for failure of concrete due to a multiaxial stress state can be expressed in the form Willam and Warnke (1975):

$$\frac{F}{f_c} - S \geq 0 \quad (1)$$

where:

F = a function of the principal stress state (σ_{xp}, σ_{yp}, σ_{zp})

S = failure surface expressed in terms of principal stresses and five input parameters f_t, f_c, f_{cb}, f_1, f_2

f_c = uniaxial crushing strength

(σ_{xp}, σ_{yp}, σ_{zp}) = principal stresses in principal directions

If (1) is satisfied, the material will crack or crush.

A total of five input strength parameters (each of which can be temperature dependent) are needed to define the failure surface as well as an ambient hydrostatic stress state.

Table 1. Concrete Material Table

Label	*Description*
f_t	Ultimate uniaxial tensile strength
f_c	Ultimate uniaxial compressive strength
f_{cb}	Ultimate biaxial compressive strength
σ_{ah}	Ambient hydrostatic stress state
f_1	Ultimate compressive strength for a state of biaxial compression superimposed on hydrostatic stress state σ_{ah}
f_2	Ultimate compressive strength for a state of uniaxial compression superimposed on hydrostatic stress state σ_{ah}

Considering stress situations with a low hydrostatic stress component, the failure surface can be specified with a minimum of two constants, f_t and f_c. The other three constants default to Willam and Warnke (1975):

$$f_{cb} = 1{,}2f_c;\ f_1 = 1{,}45f_c;\ f_2 = 1{,}725f_c \quad (2)$$

However, these default values are valid only for stress states where this condition is satisfied:

$$\left|\sigma_h\right| \leq \sqrt{3}f_c \quad (3)$$

where:

$$\sigma_h = \frac{1}{3}\left(\sigma_{xp} + \sigma_{yp} + \sigma_{zp}\right) \quad (4)$$

All five failure parameters should be specified when a large hydrostatic stress component is expected.

When the crushing capability is suppressed with f_c = -1.0, the material cracks whenever a principal stress component exceeds f_t.

Both the function F and the failure surface S are expressed in terms of principal stresses denoted as σ_1, σ_2, and σ_3 where:

$$\sigma_1 = \max\left(\sigma_{xp}, \sigma_{yp}, \sigma_{zp}\right) \quad (5)$$

$$\sigma_3 = \min\left(\sigma_{xp}, \sigma_{yp}, \sigma_{zp}\right) \quad (6)$$

$$\sigma_1 \geq \sigma_2 \geq \sigma_3$$

The failure of concrete is categorized into four domains:

1. $0 \geq \sigma_1 \geq \sigma_2 \geq \sigma_3$
2. $\sigma_1 \geq 0 \geq \sigma_2 \geq \sigma_3$
3. $\sigma_1 \geq \sigma_2 \geq 0 \geq \sigma_3$
4. $\sigma_1 \geq \sigma_2 \geq \sigma_3 \geq 0$

2.2. Finite Element Model of Steel Reinforcement

There are three techniques that exist to model steel reinforcement in finite element models for reinforced concrete: the discrete model, the embedded model, and the smeared model. In the

work presented in this paper, discrete model technique is used for modelling the reinforcement. The reinforcement in the discrete model (Fig. 1) uses bar or beam elements that are connected to concrete mesh nodes. Therefore, the concrete and the reinforcement mesh share the same nodes and concrete occupies the same regions occupied by the reinforcement [1].

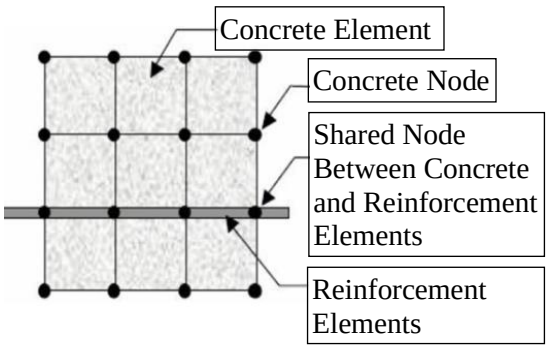

Figure 1. Discrete Models for Reinforcement.

2.3. Calculation model of RCBD.

Reinforced Concrete Bridge Deck which is modeled is slab on two stiff boundary sides as follows Figure 1.

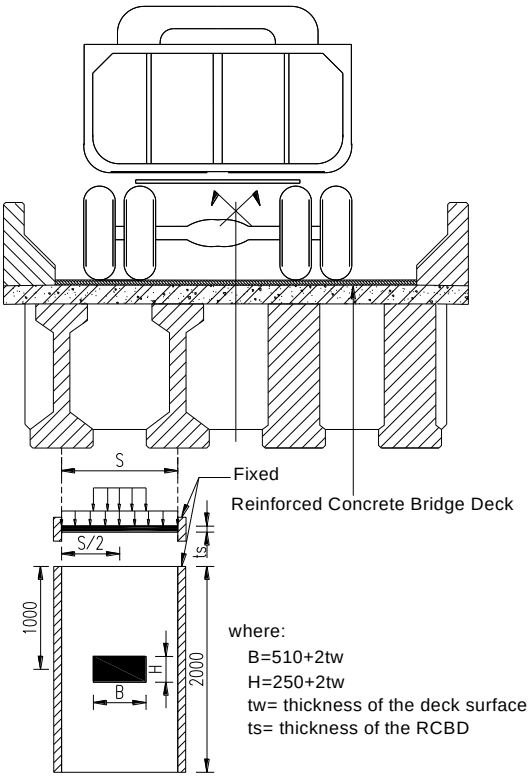

Figure 2. Calculated layout of deck slab

The span of slab is equal to space between two adjacent girders. This space is from 0.95m to 2.5m which is popular in bridges in Viet Nam. Loads subjected on slab include self-weight, surface load, wheel axel load of over-load vehicles.

Basic RCBD model built has parameters as follows:

- The width of slab according to the longitudinal direction of bridge is 2000mm.
- Space between adjacent main girders is S = 1750mm.
- The depth of slab is t_s = 180mm.
- Concrete strength of slab is f'_c = 27MPa as follows in Table 1.
- Yield strength of reinforcements arranged in slab is f_y = 420MPa as follows Table 2.
- Reinforcement Arrangement: Reinforcements are laid to two network layers is upper and under layers. In each network, 13mm diameter reinforcements are arranged with distance of 150mm in transverse direction 10mm diameter reinforcements are arranged with distance of 200mm in longitudinal direction.
- Wheel axel load is 253.75kN. This is axel load of over-load vehicle exceeding 175% in comparison with one of standard design truck which is 145kN [5]. Wheel axel load is equally distributed on tire contact area with desk bridge which dimensions are BxH. The distributed load is increased with a factor of dynamic load allowance being 1+IM = 1.33 [5] before divide for value of tire contact area. The most unfavorable position is when wheel is put on the middle of slab as follows Figure 2. 3. Analysis of reinforced concrete bridge deck using ANSYS

3.1. Types of Elements

Steel Reinforcement: A Link180 element is used to model steel reinforcement. This element is a 3D spar element and it has two nodes with three degrees of freedom – translations in the nodal x, y, and z directions. This element is also capable of plastic deformation. This element is shown in Fig. 3.

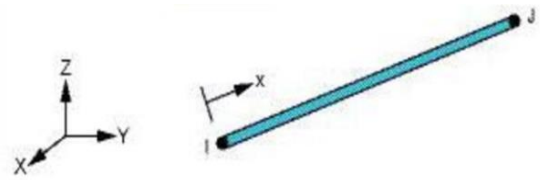

Figure 3. LINK180 Geometre

Concrete: The Solid65 element is used to model the concrete. This element has eight nodes with three degrees of freedom at each node – translations in the nodal x, y, and z directions. This element is capable of plastic deformation, cracking in three orthogonal directions, and crushing. A schematic of the element is shown in Fig. 4.

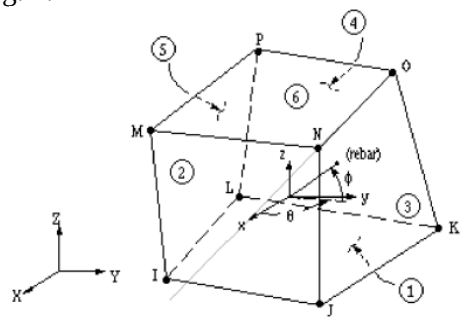

Figure 4. SOLID65 3-D Geometre

3.2. Material properties

To investigate behavior of RCBD in dependence on physio-mechanical property of concrete, RCBD would be modeled with two grades of concrete being f'_c = 37MPa and f'_c = 27MPa. Physio-mechanical properties of concrete are showed in Table 2.

Table 2. Material properties for concrete (Solid65) in FEM models [3]

Element Type	*Concrete*	*f'c = 27* ***MPa***
Solid65	Open Shear Transfer Coefficients	0.3
	Close Shear Transfer Coefficients	0.7
	Uniaxial Tensile Cracking Stress	3.22
	Uniaxial Crushing Stress	27
	Biaxial Crushing Stress	0
	Hydrostatic Pressure	0
	Hydro Biaxial Crushing Stress	0
	Hydro Uniaxial Crushing Stress	0
	Tensile Crack Factor	0

Table 3. Material properties for steel (Link180) in FEM models [3]

Element Type	*description*		
Link180	Linear Isotropic		
	Ex	200000 **MPa**	
	PRXY	0.3	
		Yield strength, **MPa**	Mod Tang, **MPa**
	Bilinear D13	420	20000
	Bilinear D10	420	20000

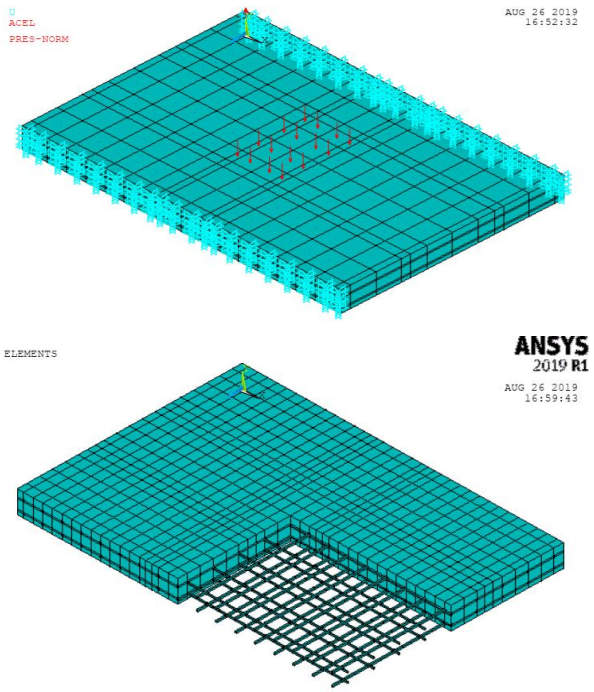

Figure 5. Basic RCBD model in ANSYS software.

4. Analysis result of basic RCBD model in ANSYS software.

4.1. Analysis result of basic RCBD model.

Calculation result of Von-Mises stress in reinforcements:

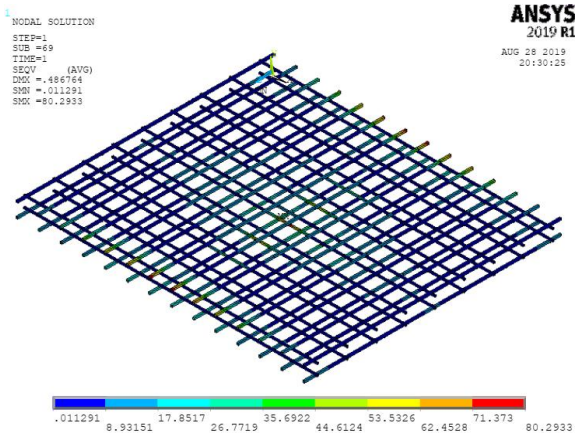

Figure 6. Von-mises stress in reinforcements of basic RCBD model.

Comment: The greatest Von-Mises stress in reinforcements is 80.29Mpa which is much less than yield strength of steel, f_y = 420Mpa.

Deflection of slab:

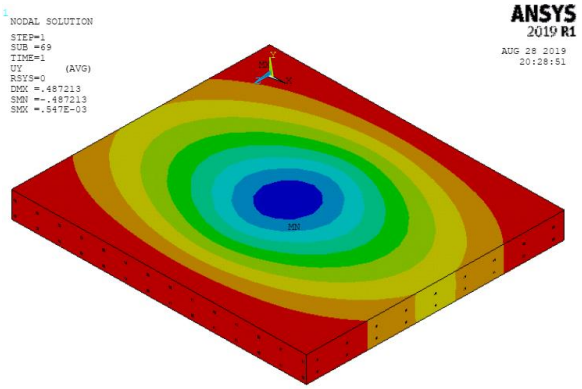

Figure 7. Deflection of basic RCBD model.

Comment: Maximum deflection of slab is 0.49mm which is much less than allowable deflection S/800 = 2.19mm.

Analysis result of crack in slab:

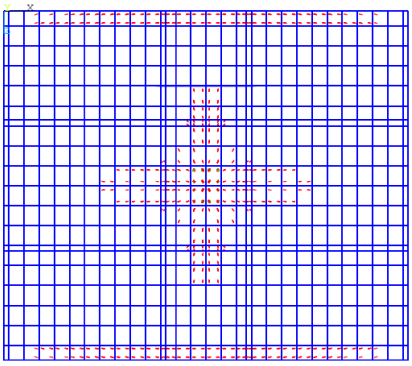

a. Cracking distribution on underside of slab

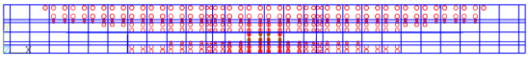

b. Craking distribution in slab according to longitudinal direction of bridge.

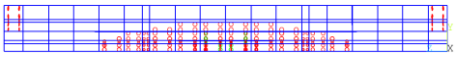

c. Craking distribution in slab according to tranverse direction of bridge

Figure 8. Cracking distribution in slab of basic RCBD model.

Comment:

- In the middle of slab: In area under immediately position subjected load of wheel, fracture is complicated according to different directions, the depth of cracks is developed from underside of slab to nearly upper reinforcement network. Transverse long cracks form in a narrow strip while longitudinal cracks form in a large strip and lengthen according to longitudinal direction of bridge. Diagonal cracks is short. Cracking density and the maximum depth of cracks are in the middle area of slab and decreasing tendency according to distant direction of this area.
- In stiff boundary side of slab: Longitudinal cracks seem to be lengthened according to the length of slab. Cracking strip is narrow in this area. The development of cracking depth is from upper-side of slab to the middle of slab cross section.

5. Investigation of parameters to effect of cracks in RCBD.

Each investigated RCBD model in comparison with basic RCBD model, only one parameter is changed to compare the effect of changing this parameter in the same load condition.

5.1. Investigation of material parameter.

Basic RCBD model is formed with concrete strength f'_c = 27MPa. Comparison models of RCBD are modeled with kinds of concrete strength, namely 21MPa, 35MPa, 40MPa and 50MPa.

Analysis result of crack in slab:

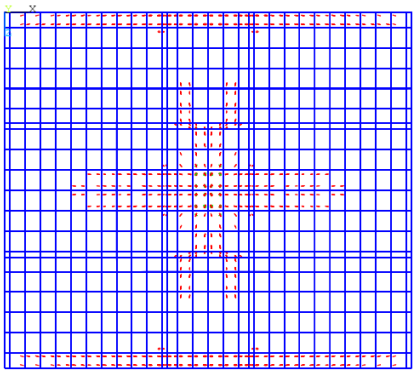

a. Case of f'_c = 21MPa

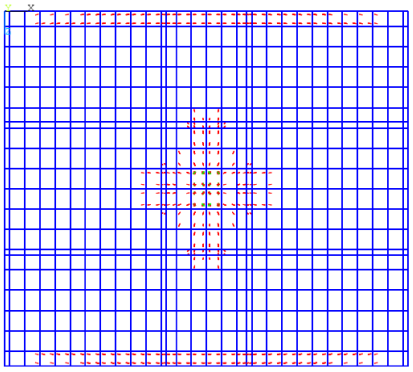

b. Case of f'_c = 35MPa

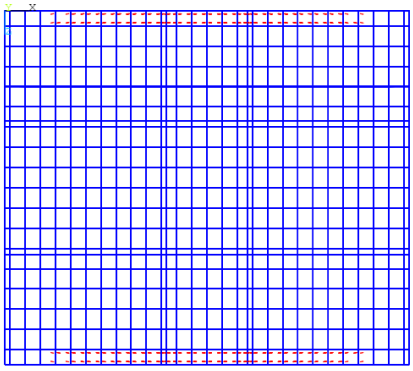

c. Case of f'_c = 40MPa

Figure 9. Investigation of the concrete strength effect to cracking behavior in RCBD.

Comment: Increase of concrete strength is correlative to reduction of cracking area. In case of f'_c = 50Mpa, cracks have yet appeared in slab. On the contrary, in case of f'_c = 21Mpa, cracking area is large and cracks are dense along with direction changes.

5.2. Investigation of the depth parameter of slab.

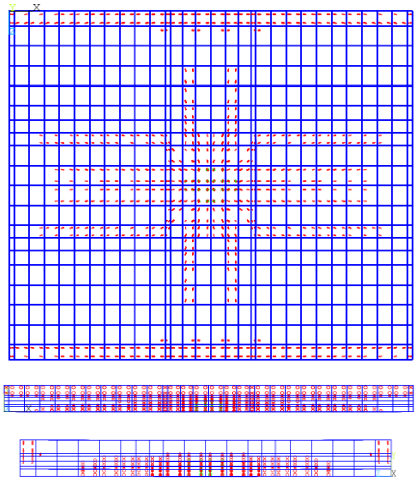

a. Case of t_s = 150mm

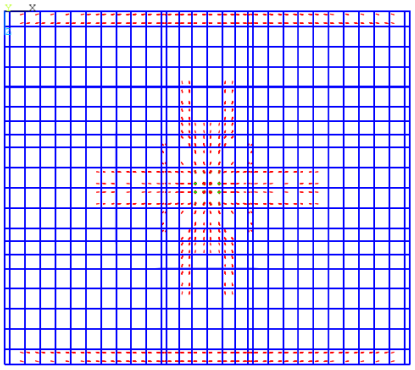

b. Case of t_s = 175mm

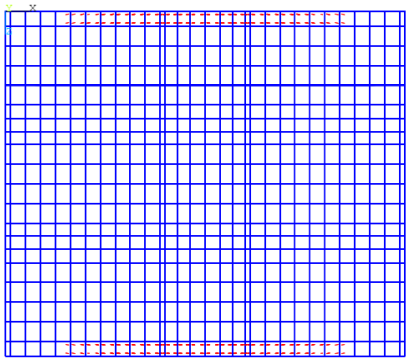

c. Case of t_s = 200mm

Figure 10. Investigation of the slab depth effect to cracking behavior in RCBD.

Comment: Increase of the slab depth is correlative to reduction of cracking area. RCBD with the depth t_s = 220mm has not cracked yet. On the contrary, in RCBD with the depth t_s = 150mm, cracking area is large along with appearance of diagonal cracks. Outside area subjected load, there are appearance of deeply longitudinal and transverse cracks.

5.3. Investigation of the space parameter between main girders.

Space between main girders in basic RCBD model is S = 1.75m. Cracking analysis also is implemented on cases of spaces between main girders, namely 0.95m, 1.25m, 2.1m and 2.5m.

Cracking analysis results:

- In the case of space between main girders is 0.95m: Cracks have yet appeared in RCBD.
- In the case of space between main girders is 1.25m: Cracks according to longitudinal direction of bridge have appeared as follows in Figure 11.a.
- In the case of space between main girders is 2.5 m: Longitudinal cracks are distributed in a large strip and lengthened according to the length of slab. The depth of cracks is from upper side to upper network reinforcement.

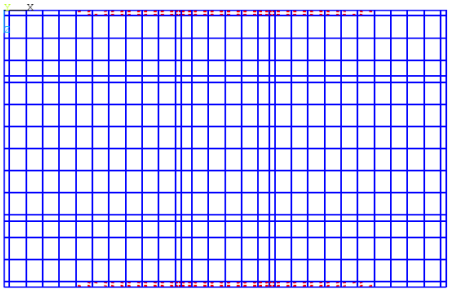

a. Case of S = 1250mm

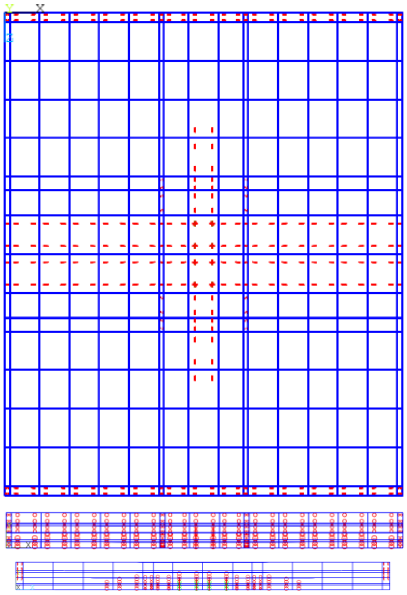

b. Case of S = 2500mm

Figure 11. Investigation of the space effect of main girders to cracking behavior of RCBD.

6. Proposal of anti-cracking for RCBD.

The investigation results of effect parameters to formation of cracks in RCBD showed that to reduce formation of cracks, it is necessary to increase concrete strength, the depth of bridge desk and decrease space between main girders. However, construction cost would be high when use high strength concrete for bridge desk, quantity of construction material and dead load would go up with increase of the slab depth, the number of main girders would increase when decrease space between main girders. In current

designs, the depth slab t_s is usually from 175mm to 250mm, concrete strength f'_c is commonly from 25MPa to 35MPa, the space between main girders is from 0.9m to 2.5m. Therefore the alternative on technical and economic aspects is t_s = 220mm, f'_c = 35Mpa, space between main girders S = 2.5m.

Cracking analysis results of the alternative of RCBD showed that cracks have yet appeared in RCBD when RCBD is subjected by load from wheel axels, cracks only appeared in stiff boundary areas as showed in Figure 12.

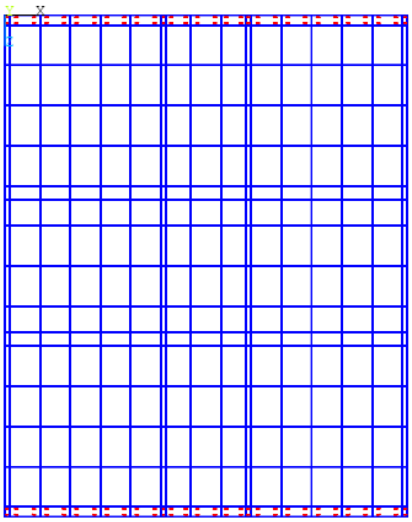

Figure 12. Cracking analysis result of the RCBD alternative.

The case of space between main girders is less than, the depth slab and concrete strength could be reduced. However, decrease of the depth slab would affect to anti-cracking effect dramatically.

7. Conclusion

RCBD is cracked under influence of over-load vehicles, cracking behavior depends on lots of factors. When the depth slab is slender, space between main girders is large and concrete strength is low then lengthened cracks appear and the depth of cracks develop from sides of slab to deeply inside slab. At old bridges, RCBD was designed to be slender, thus they should be considered to strengthen for anti-cracking ability.

References.

[1] Dawari, V. B., & Vesmawala, G. R. (2014). Application of nonlinear concrete model for finite element analysis of reinforced concrete beams. *International Journal of Scientific & Engineering Research*, 5(9).

[2] Dahmani, L., Khennane, A., & Kaci, S. (2010). Crack identification in reinforced concrete beams using ANSYS software. *Strength of materials*, 42(2), 232-240.

[3] Halahla, A. (2019). Identification of Crack in Reinforced Concrete Beam Subjected to Static Load Using Non-linear Finite Element Analysis. *Civil Engineering Journal*, 5(7), 1631-1646.

[4] Lemaitre, J. (Ed.). (2001). *Handbook of Materials Behavior Models, Three-Volume Set: Nonlinear Models and Properties*. Elsevier.

[5] Ministry of Science and Technology (2017), *Bridge Specfication*, TCVN 11823:2017.

[6] Recho, N. (2012). *Fracture mechanics and crack growth*. John Wiley & Sons.

[7] Saxena, A. (1998). *Nonlinear fracture mechanics for engineers*. CRC press.

[8] Shah, S. P., Swartz, S. E., & Ouyang, C. (1995). *Fracture mechanics of concrete: applications of fracture mechanics to concrete, rock and other quasi-brittle materials.* John Wiley & Sons.

[9] Shi, Z. (2009). *Crack analysis in structural concrete: theory and applications*. Butterworth-Heinemann.

[10] Tran Duc Thuan (2016), Study on the effect of the number of axles and axle load on the behavior of pre-stressed concrete girder on simple bridges. *Master thesis*, UTC.

[11] Willam, K. J. (1975). Constitutive model for the triaxial behaviour of concrete. *Proc. Intl. Assoc. Bridge Structl. Engrs*, 19, 1-30.

[12] Wolanski, A. J. (2004). *Flexural behavior of reinforced and prestressed concrete beams using finite element analysis* (Doctoral dissertation).

The 5th International Conference on Engineering Mechanics and Automation (ICEMA 5)
Hanoi, October 11÷12, 2019

Nonlinear dynamic response of auxetic honeycomb cylindrical panels reinforced by orthogonal stiffeners

Pham Hong Cong[a], Pham Dinh Nguyen[b], Tran Hoan Huy[c], Nguyen Dinh Duc[d]

[a]Centre for Informatics and Computing (CIC), Vietnam Academy of Science and Technology, 18 Hoang Quoc Viet - Cau Giay – Hanoi – Vietnam, phcong@cic.vast.vn
[b]Advanced Materials and Structures Laboratory, VNU-Hanoi - University of Engineering and Technology (UET), 144 – Xuan Thuy – Cau Giay – Hanoi – Vietnam, phamdinhnguyenk58@gmail.com
[c]Advanced Materials and Structures Laboratory, VNU-Hanoi - University of Engineering and Technology (UET), 144 – Xuan Thuy – Cau Giay – Hanoi – Vietnam, hoanhuy01997@gmail.com
[d]Advanced Materials and Structures Laboratory, VNU-Hanoi - University of Engineering and Technology (UET), 144 – Xuan Thuy – Cau Giay – Hanoi – Vietnam, ducnd@vnu.edu.vn

Abstract

In this paper, we study the nonlinear dynamic response of auxetic (negative Poisson's ratio) honeycomb cylindrical panels reinforced by orthogonal stiffeners resting on elastic foundations and subjected to blast load. This study considers a three – layer cylindrical panel in which the core layer is the auxetic material with negative Poisson's ratio, and the external layers are reinforced by a system of orthogonal stiffeners. Based on the analytical solution, Reddy's first order shear deformation theory with the geometrical nonlinear in von Karman and Airy stress functions method, Galerkin method and the fourth-order Runge-Kutta method, our explicit expressions of fundamental frequency and dynamic response can be determined. Numerical results are provided to explore the effects of geometrical parameters, material properties, elastic foundations, eccentrically stiffeners, mechanical and blast loads on the nonlinear dynamic response of auxetic honeycomb cylindrical panels reinforced by orthogonal stiffeners.

Key Words: Auxetic honeycomb cylindrical panels; Stiffeners; Reddy's first order shear deformation theory.

1. Introduction

The safety condition of buildings and infrastructures are topics of great concern recently as the extreme static and dynamic loads occured due to the increasing number of terrorist attacks, accidental explosions, ...One of the technical solutions to handle the problem is the introduction of materials with abnormal characteristics, e.g., negative Poisson's ratio, negative compressibility, or negative normal stress (Huang et al. 2016). As a most studied branch of mechanical metamaterials, auxetic materials exhibit counter-intuitive deformation behaviour during deforming period. To be more specific, under uniaxial compression (tension), conventional materials expand (contract) in the directions orthogonal to the applied load. In contrast, auxetic materials contract (expand) in the transverse direction, as shown in Figure 1.

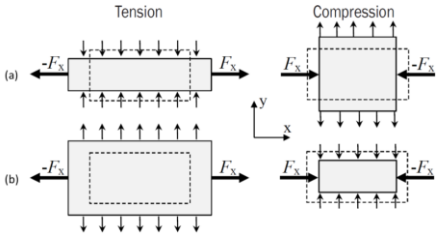

Figure 1. Behaviours in tensile and compressive load: (a) non-auxetic material; (b) auxetic material.

In recent years, the dynamic response problems of auxetic plates and shells have paid attention to research. In (Duc and Cong, 2018; Cong et al., 2019; Cong et al., 2018; Duc et al., 2017a; Duc et al., 2017b), the authors investigated the dynamic response of auxetic sandwich plates and shells without stiffeners by the analytical approach. The finite element method and Ritz method applied to study the vibration of the auxetic sandwich plates in (Zhu et al., 2018; Di and Mao, 2016). From the above-mentioned overview, research on nonlinear dynamic response of auxetic honeycomb cylindrical panels reinforced by orthogonal stiffeners using analytical approach has not been studied.

In this paper, we use the analytical solution to study nonlinear dynamic response of auxetic honeycomb cylindrical panels reinforced by orthogonal stiffeners. And from this basis we show the efects of some parameters on fundamental frequency and dynamic response.

2. Auxetic honeycomb cylindrical panels reinforced by orthogonal stiffeners

2.1. Model of auxetic honeycomb cylindrical panels

In this paper, consider the model of auxetic honeycomb cylindrical panels reinforced by stiffeners and geometric parameters as shown

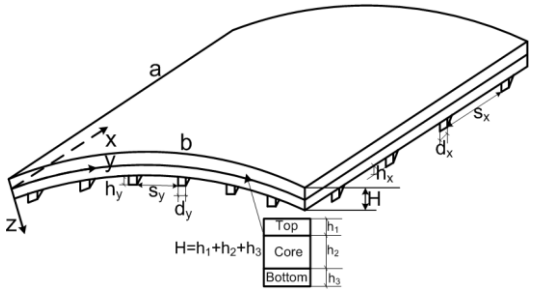

Figure 2. Model of auxetic honeycomb cylindrical panels reinforced by stiffeners.

2.2. Honeycomb core materials

The plate with the auxetic honeycomb core with negative Poisson's ratio is introduced in this paper. Unit cells of core material discussed in the paper are shown in Figure 2.

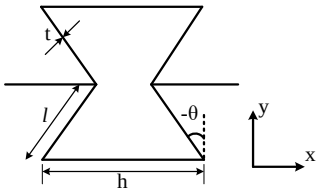

Figure 3. Geometric of the cell of honeycomb core.

Formulas in reference (Deng and Yang, 2010) are adopted for calculation of honeycomb core material property

$$
\begin{aligned}
&E_1^C = E\left(\frac{t}{l}\right)^3 \frac{\cos\theta}{\left(\frac{h}{l}+\sin\theta\right)\sin^2\theta},\\
&E_2^C = E\left(\frac{t}{l}\right)^3 \frac{\left(\frac{h}{l}+\sin\theta\right)}{\cos^3\theta}, \upsilon_{12}^C = \frac{\cos^2\theta}{\left(\frac{h}{l}+\sin\theta\right)\sin\theta},\\
&G_{12}^C = E\left(\frac{t}{l}\right)^3 \frac{\left(\frac{h}{l}+\sin\theta\right)}{\left(\frac{h}{l}\right)^2\left(1+2\frac{h}{l}\right)\cos\theta}\\
&G_{13}^C = G\frac{t}{l}\frac{\cos\theta}{\frac{h}{l}+\sin\theta}, G_{23}^C = G\frac{t}{l}\frac{1+2\sin^2\theta}{2\cos\theta\left(\frac{h}{l}+\sin\theta\right)},\\
&\rho^C = \rho\frac{t/l\left(h/l+2\right)}{2\cos\theta\left(h/l+\sin\theta\right)}
\end{aligned}
\tag{1}
$$

where symbol "c" represents core material, E, G and ρ are Young's moduli, shear moduli and mass density of the origin material.

3. Theoretical formulations

The strain-displacement relations taking into account the von Karman nonlinear terms are expressed as

$$
\begin{aligned}
&\varepsilon_x = \varepsilon_x^0 + z\varepsilon_x^1, \varepsilon_y = \varepsilon_y^0 + z\varepsilon_y^1\\
&\gamma_{yz} = \gamma_{yz}^0, \gamma_{xz} = \gamma_{xz}^0, \gamma_{xy} = \gamma_{xy}^0 + z\gamma_{xy}^1
\end{aligned}
\tag{2}
$$

where

$$\begin{aligned}
&\varepsilon_x^0 = u_{,x} + \left(w_{,x}\right)^2/2,\\
&\varepsilon_y^0 = v_{,y} - w/R + \left(w_{,y}\right)^2/2\\
&\gamma_{xy}^0 = u_{,y} + v_{,x} + w_{,x}w_{,y}, \gamma_{xz}^0 = w_{,y} + \phi_y,\\
&\gamma_{yz}^0 = w_{,x} + \phi_x, \varepsilon_x^1 = \phi_{x,x}, \varepsilon_y^1 = \phi_{y,y},\\
&\gamma_{xy}^1 = \phi_{x,y} + \phi_{y,x}
\end{aligned} \tag{3}$$

in the above equations, u,v,w are displacement components corresponding to the coordinates (x,y,z), and ϕ_x,ϕ_y are the rotations of normals to the mid-surface with respect to the x and y axes, respectively.

The forces and moments of the auxetic honeycomb cylindrical panels reinforced by orthogonal stiffeners can be expressed

$$\begin{aligned}
&\begin{Bmatrix} N_x \\ N_y \\ M_x \\ M_y \end{Bmatrix} = \begin{bmatrix} A_1 & A_2 & A_3 & A_4 \\ A_2 & A_5 & A_4 & A_6 \\ A_3 & A_4 & A_9 & A_{10} \\ A_4 & A_6 & A_{10} & A_{11} \end{bmatrix} \begin{Bmatrix} \varepsilon_x^0 \\ \varepsilon_y^0 \\ \varepsilon_x^1 \\ \varepsilon_y^1 \end{Bmatrix},\\
&\begin{Bmatrix} N_{xy} \\ M_{xy} \end{Bmatrix} = \begin{bmatrix} A_7 & A_8 \\ A_8 & A_{12} \end{bmatrix} \begin{Bmatrix} \gamma_{xy}^0 \\ \gamma_{xy}^1 \end{Bmatrix},\\
&\begin{Bmatrix} Q_x \\ Q_y \end{Bmatrix} = \begin{bmatrix} KA_{13} & 0 \\ 0 & KA_{14} \end{bmatrix} \begin{Bmatrix} \gamma_{xz}^0 \\ \gamma_{yz}^0 \end{Bmatrix}
\end{aligned} \tag{4}$$

where $K = 4/5$ and the coefficients are given in Appendix.

According to FSDT, the motion equations of the auxetic honeycomb cylindrical panels reinforced by orthogonal stiffeners are

$$N_{x,x} + N_{xy,y} = I_0 u_{,tt} + I_1 \phi_{x,tt} \tag{5}$$

$$N_{xy,x} + N_{y,y} = I_0 v_{,tt} + I_1 \phi_{y,tt} \tag{6}$$

$$\begin{aligned}
&Q_{x,x} + Q_{y,y} + N_x w_{,xx} + 2N_{xy} w_{,xy}\\
&+ N_y w_{,yy} + p - k_1 w + k_2\left(w_{,xx} + w_{,yy}\right)\\
&+ N_y / R = I_0 w_{,tt} + 2\varepsilon I_0 w_{,t}
\end{aligned} \tag{7}$$

$$M_{x,x} + M_{xy,y} - Q_x = I_1 u_{,tt} + I_2 \phi_{x,tt} \tag{8}$$

$$M_{xy,x} + M_{y,y} - Q_y = I_1 v_{,tt} + I_2 \phi_{y,tt} \tag{9}$$

Introduce the Airy stress function $F(\mathrm{X},\mathrm{Y},t)$ satisfying

$$N_X = F_{,yy}, N_Y = F_{,xx}, N_{XY} = -F_{,xy} \tag{10}$$

Replacing Eqs. (10) and (4) into (7-9), yields

$$\begin{aligned}
&H_{11}(w) + H_{12}(\phi_x) + H_{13}(\phi_y) + S(w,f) + q\\
&= I_0 w_{,tt} + 2\varepsilon I_0 w_{,t}
\end{aligned} \tag{11}$$

$$\begin{aligned}
&H_{21}(w) + H_{22}(\phi_x) + H_{23}(\phi_y) + H_{24}(f)\\
&= \left(I_2 - I_1^2/I_0\right)\phi_{x,tt}
\end{aligned} \tag{12}$$

$$\begin{aligned}
&H_{31}(w) + H_{32}(\phi_x) + H_{33}(\phi_y) + H_{34}(f)\\
&= \left(I_2 - I_1^2/I_0\right)\phi_{y,tt}
\end{aligned} \tag{13}$$

the linear operators and nonlinear operators are given in Appendix.

In Eqs. (11-13), there are three equations and four unknown variables, so one more equation is needed to solve this problem. As is known to us, the compatibility equation of auxetic honeycomb cylindrical panels reinforced by stiffeners can be derived as

$$\begin{aligned}
&-A_1/\left(A_2^2 - A_1A_5\right)F_{,xxxx} - A_5/\begin{pmatrix} A_2^2 \\ -A_1A_5 \end{pmatrix}F_{,yyyy}\\
&+\left(2A_2/\left(A_2^2 - A_1A_5\right) + 1/A_7\right)F_{,xxyy}\\
&+\left(\left(A_3A_5 - A_2A_4\right)/\left(A_2^2 - A_1A_5\right) + A_8/A_7\right)\phi_{x,xyy}\\
&+\left(A_1A_4 - A_2A_3\right)/\left(A_2^2 - A_1A_5\right)\phi_{x,xxx}\\
&+\left(A_4A_5 - A_2A_6\right)/\left(A_2^2 - A_1A_5\right)\phi_{y,yyy}\\
&+\left(\left(A_1A_6 - A_2A_4\right)/\left(A_2^2 - A_1A_5\right) + A_8/A_7\right)\phi_{y,xxy}\\
&= \left(w_{,xy}\right)^2 - w_{,xx}w_{,yy} - w_{,xx}/R
\end{aligned} \tag{14}$$

Eqs. (11-13) and (14) are the basic nonlinear governing equations regarding to four variables w,ϕ_X,ϕ_Y,F and can be solved to investigate the nonlinear dynamic response of auxetic honeycomb cylindrical panels reinforced by orthogonal stiffeners subject to blast load.

4. Solution methodology

Considering the following boundary condition, four edges of the cylindrical panels are simply supported and freely movable. And the corresponding boundary conditions are defined as

$$\begin{aligned}
&w = N_{xy} = \phi_y = M_x = 0, N_x = -P_x h\\
&w = N_{xy} = \phi_x = M_y = 0, N_y = -P_y h
\end{aligned} \tag{15}$$

The approximate solutions of the system of Eqs. (11-13) and (14) satisfying the boundary condition (15) can be written as

$$\begin{aligned}
&w(x,y,t)=W(t)\sin(\lambda_m x)\sin(\delta_n y),\\
&w^*(x,y,t)=\mu h\sin(\lambda_m x)\sin(\delta_n y),\\
&\phi_x(x,y,t)=\Phi_x(t)\cos(\lambda_m x)\sin(\delta_n y),\\
&\phi_y(x,y,t)=\Phi_y(t)\sin(\lambda_m x)\cos(\delta_n y),\\
&f(x,y,t)=B_1\cos(2\lambda_m x)+B_2\cos(2\delta_n y)+\\
&B_3\sin(\lambda_m x)\sin(\delta_n y)-\frac{1}{2}P_x hy^2-\frac{1}{2}P_y hx^2
\end{aligned} \tag{16}$$

Then, substituting Eqs. (16) into Eq. (11-13) and applying Galerkin method, the nonlinear dynamic response governing equations of auxetic honeycomb cylindrical panels reinforced by orthogonal stiffeners becomes

$$\begin{aligned}
&h_{11}W(t)+h_{12}\Phi_x(t)+h_{13}\Phi_y(t)+\\
&h_{14}\Phi_x(t)W(t)+h_{15}\Phi_y(t)W(t)+h_{16}W^2(t)\\
&+h_{17}W^3(t)+h_{18}+4ab/\pi^2 q\\
&=ab/4\left(I_0 w_{,tt}+2\varepsilon I_0 w_{,t}\right)
\end{aligned} \tag{17}$$

$$\begin{aligned}
&h_{21}W(t)+h_{22}\Phi_x+h_{23}\Phi_y+h_{24}W^2\\
&=ab/4\left(I_2-I_1^2/I_0\right)\phi_{x,tt}
\end{aligned} \tag{18}$$

$$\begin{aligned}
&h_{31}W(t)+h_{32}\Phi_x+h_{33}\Phi_y+h_{34}W^2\\
&=ab/4\left(I_2-I_1^2/I_0\right)\phi_{y,tt},
\end{aligned} \tag{19}$$

Taking linear parts of the set of Eqs. (17-19) and putting $q(t)=0$, the natural frequencies of the plate can be determined directly by solving determinant

$$\begin{vmatrix}
h_{11}+\dfrac{ab}{4}I_0\omega^2 & h_{12} & h_{13}\\
h_{21} & h_{22}+\rho_1\omega^2 & h_{23}\\
h_{31} & h_{32} & h_{33}+\rho_1\omega^2
\end{vmatrix}=0 \tag{20}$$

Solving Eqs. (20) yields three angular frequencies, the smallest one is being considered.

4. Numerical results

The material and load parameters using in this section are as follows:

$$q(t)=1.8Ps_{\max}\left(1-t/T_s\right)\exp^{-b_s t/T}$$

where the "1.8" factor accounts for the effects of a hemispherical blast, $Ps_{\max}$ is the maximum (or peak) static over-pressure, b_s is the parameter controlling the rate of wave amplitude decay and T_s is the parameter characterizing the duration of the blast pulse.

$$\begin{aligned}
&h_1=h_3=0.008m, h_2=0.02m, a/b=1, h/l=2,\\
&a/H=30, T/l=0.0138571, \theta=-55^o, \upsilon=0.33,\\
&b/R=1/2, h_x=h_y=H, s_x=s_y=0.12m\\
&\rho=2700kg/m^3, E=69GPa, G=26GPa
\end{aligned}$$

4.1. Validation

Table 1 shows the comparison between calculation results of the natural frequency parameter $\bar{\omega}=\dfrac{\omega a^2}{h}\sqrt{\dfrac{12\rho\left(1-\nu^2\right)}{E}}$ of aluminum honeycomb sandwich plate with negative Poisson's ratio for different unit cell angle θ and h_2/h with the results in the article of Di and Mao (2016).

Table 1. Comparison study of natural frequency parameter $\bar{\omega}$ of aluminum honeycomb sandwich plate with negative Poisson's ratio for different unit cell angle θ and h_2/h.

θ	h_2/h	Present	Di and Mao (2016)
0	0.3	22.786	22.499
	0.5	24.892	24.621
	0.7	26.3	26.310
	0.9	23.598	24.725
-30	0.3	22.533	22.456
	0.5	24.304	24.292
	0.7	25.058	25.481
	0.9	21.049	22.593

Notes: $T/l=0.1, h/l=2, a/b=1.$

According to Table 1, the errors of natural frequency parameter with Di and Mao (2016) are very small, indicating that the approach of this study is highly reliable.

4.2. Analysis of auxetic materials

Figure 4 presents the effect of different Poisson's ratio on the nonlinear dynamic response of cylindrical panels reinforced by

orthogonal stiffeners. Two Poisson' ratio are considered in this case $v_{12} = (-0.4371, 0.3054)$. From figure 4, it can be seen that the deflection-time curve in the case $v_{12} = -0.4371$ is lower than that in the case $v_{12} = 0.3054$.

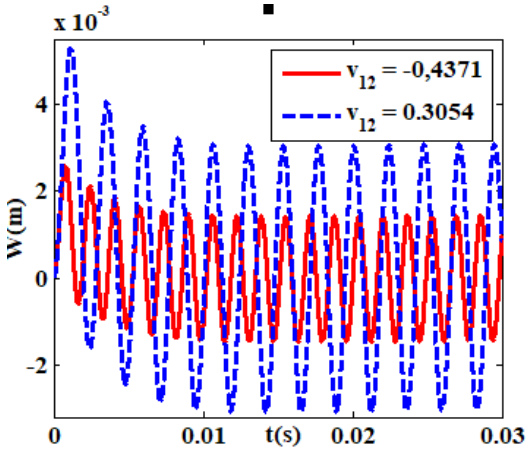

Figure 4. The effect of Poisson's ratios on the nonlinear dynamic response curve of cylindrical panels reinforced by stiffeners under blast load.

The influence of cell inclined angle θ on the deflection-time curve is shown in Figure 5. Clearly, the deflection-time curve is significantly changed by θ angle and the load capacity of auxetic honeycomb cylindrical panels reinforced by stiffeners is the best in the case $\theta = -70$.

4.3. Effect of stiffeners and elastic foundation

Effect of various types of stiffeners and elastic foundations on the natural frequencies of auxetic honeycomb cylindrical panels are shown in Tables 2 and 3.

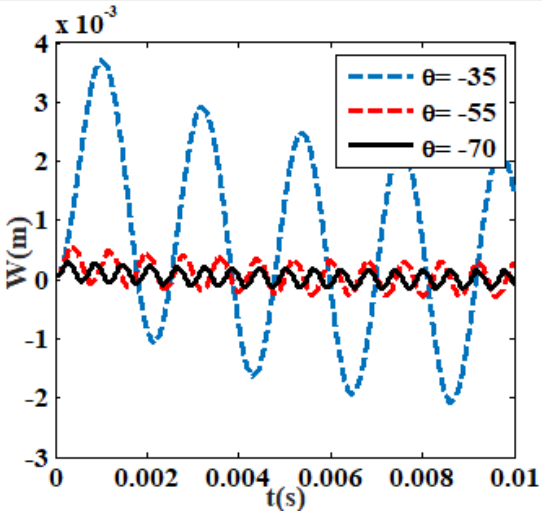

Figure 5. The effect of cell inclined angle θ on the nonlinear dynamic response curve of auxetic honeycomb cylindrical panels reinforced by stiffeners.

It is clear that the value of the natural frequencies are affected by different types of elastic foundations and stiffeners. The value of the fundamental frequency is the lowest in the case un-stiffened cylindrical panels without elastic foundation ($K_1 = K_2 = 0$) and the value of the fundamental frequency is highest when cylindrical panels resting on Pasternak' elastic foundation ($K_1 = 0.1GPa/m$, $K_2 = 0.04GPa.m$). From tables 2 and 3, the natural frequencies of the orthogonal stiffened auxetic honeycomb cylindrical panels higher than that of cylindrical panels reinforced by stiffeners in the x or y direction.

Table 2. Effect of type of stiffeners and elastic foundations on natural frequencies $\omega(1/s)$ of auxetic honeycomb cylindrical panels reinforced by stiffeners.

(K_1, K_2)	Un-Stiffened	Orthogonal Stiffeners	Stiffeners in the x direction	Stiffeners in the y direction
$K_1 = 0, K_2 = 0$	5216	7853	5470	7331
$K_1 = 0.3GPa/m, K_2 = 0$	5813	8262	6043	7767
$K_1 = 0.3GPa/m, K_2 = 0.02GPa.m$	6421	8701	6630	8231
$K_1 = 0.1GPa/m, K_2 = 0.04GPa.m$	6653	8874	6855	8414

Table 3. Effect of distances between stiffeners and type of stiffeners on natural frequencies ω($\omega(1/s)$ of auxetic honeycomb cylindrical panels reinforced by stiffeners.

Type of stiffeners	$s_1 = 0.05m$, $s_2 = 0.05m$	$s_1 = 0.1m$, $s_2 = 0.1m$	$s_1 = 0.2m$, $s_2 = 0.2m$	$s_1 = 0.5m$, $s_2 = 0.5m$
Orthogonal Stiffeners	10422	7853	6933	5971
Stiffeners in the x direction	5587	5470	5407	5316
Stiffeners in the y direction	9061	7331	6625	5847

Figure 6 shows the influence of the stiffeners (orthogonal, x-stiffeners and y-stiffeners) and un-stiffened on the nonlinear dynamic response of auxetic honeycomb cylindrical panels. The deflection-time curve of auxetic honeycomb cylindrical panels reinforced by orthogonal stiffeners is the lowest among four cases.

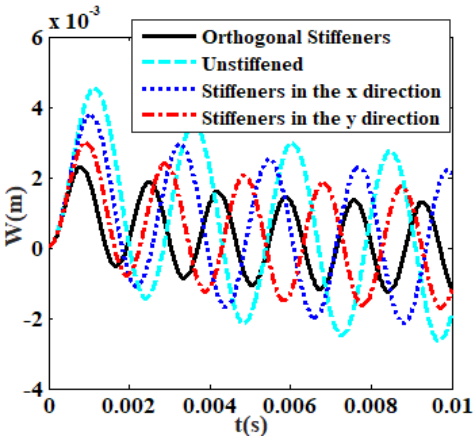

Figure 6. Comparison the effect of the different stiffeners

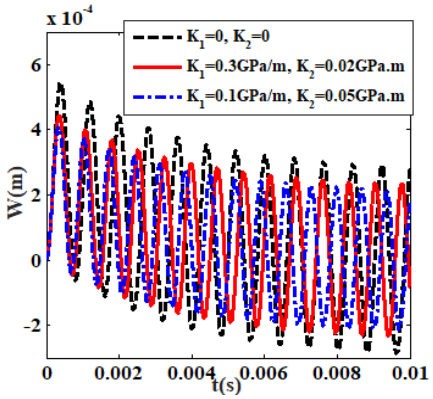

Figure 7. Effect of the elastic foundations on the nonlinear dynamic response of auxetic honeycomb cylindrical panels

Figure 7 shows the effect of different elastic foundations on the deflection-time curve of auxetic honeycomb cylindrical panels reinforced by orthogonal stiffeners. It is observed that the value of amplitude of cylindrical panels without elastic foundations ($K_1 = K_2 = 0$) is the highest while this figure for cylindrical panels resting on Pasternak's elastic foundation ($K_1 = 0.1GPa/m, K_2 = 0.05GPa.m$) is the lowest.

4.4. Effect of load and geometric parameter

Figure 8 shows the effect of pre-loaded axial compression (P_x) on the deflection-time curve of auxetic honeycomb cylindrical panels reinforced by orthogonal stiffeners. It is clear that the pre-loaded axial compression has an considerable effect to change the value of the amplitude of cylindrical panels. For instance, the value of amplitude of auxetic honeycomb cylindrical panels in the case $P_x = 300MPa$ is seven times higher than that in the case $P_x = 0$.

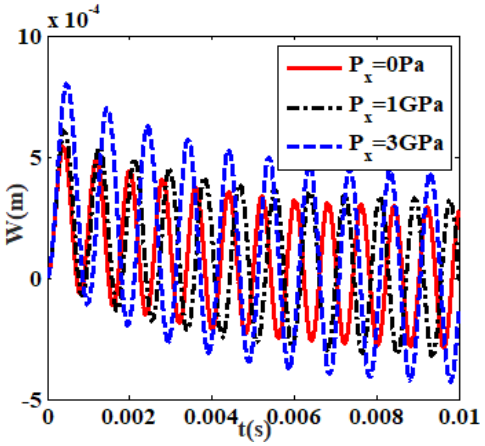

Figure 8. Effect of pre-loaded axial compression (P_x) on the nonlinear dynamic response of auxetic honeycomb cylindrical panels reinforced by orthogonal stiffeners

Figure 9 describes the effect of a/h ratio on the deflection-time curve of auxetic honeycomb cylindrical panels reinforced by orthogonal stiffeners. As can be seen, a/h increase leads

to the increase of the amplitude of cylindrical panels.

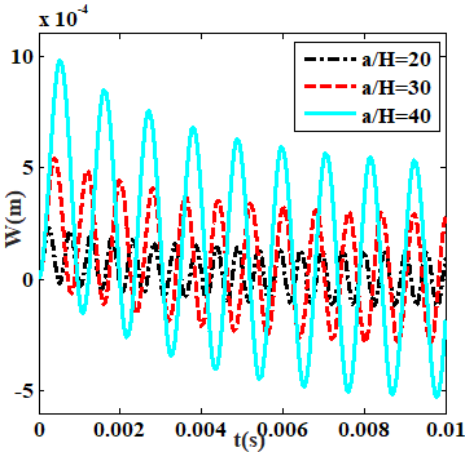

Figure 9. Effect of a/h ratio on the nonlinear dynamic response of auxetic honeycomb cylindrical panels reinforced by orthogonal stiffeners

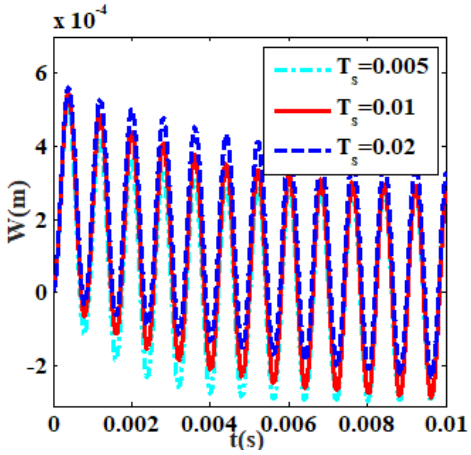

Figure 10. Effect of the parameter characterizing the duration of the blast pulse (T_s) on nonlinear dynamic response of the auxetic honeycomb cylindrical panels

Figure 10 shows the effect of $T_s = (0.005, 0.01, 0.02)$ on nonlinear dynamic response of auxetic honeycomb cylindrical panels. As can be seen, the value of amplitude of cylindrical panels reinforced by orthogonal stiffeners increases when T_s parameter increases

5. Conclusion

- The stiffeners increase strongly the load capacity of auxetic honeycomb cylindrical panels. The orthogonal stiffeners are the best among three type of stiffeners.
- The pre-loaded axial and blast loads are considered to study the nonlinear dynamic response.
- The detailed analysis of material and geometric parameters is shown.

Acknowledgements

This research is funded by Vietnam National Foundation for Science and Technology Development (NAFOSTED) under grant number 107.02-2019.04.

References

Cong, P. H., N.D. Khanh, N.D. Khoa, N.D. Duc (2018), New approach to investigate nonlinear dynamic response of sandwich auxetic double curves shallow shells using TSDT, *Composite Structures* 185, pp. 455-465.

Cong, P. H., P. T. Long, N. V. Nhat, N. D. Duc (2019). Geometrically nonlinear dynamic response of eccentrically stiffened circular cylindrical shells with negative Poisson's ratio in auxetic honeycombs core layer, *International journal of Mechanical Sciences*, 152, pp. 443-453.

Deng, Q. T., Y. C. Yang (2010), Wave Propagation in Sandwich Panel with Auxetic Core. *Journal of Solid Mechanics*, 2(4), pp. 393-402.

Di, K., X. B. Mao (2016), Free lexural vibration of honeycomb sandwich plate with negative Poisson's ratio simple supported on opposite edges, *Acta Materiae Compositae Sinica* 33, pp. 910–920.

Duc, N. D. and P. H. Cong (2018). Nonlinear dynamic response and vibration of sandwich composite plates with negative Poisson's ratio in auxetic honeycombs, *Journal of Sandwich Structures and Materials*, 20 (6), pp. 692-717.

Duc, N. D., Eock, K. S., Tuan, N. D., P. Tran, N. D. Khoa (2017), New approach to study nonlinear dynamic response and vibration of sandwich composite cylindrical panels with auxetic honeycomb core layer, *Journal Aerospace Science and Technology*, 70, pp. 396-404.

Duc, N. D., K. S. Eock, P. H. Cong, N. T. Anh, N. D. Khoa (2017), Dynamic response and vibration of composite double curved shallow shells with negative Poisson's ratio in auxetic honeycombs core layer on elastic foundations subjected to blast and

damping loads, *International Journal of Mechanical of Sciences*, 133, pp. 504-512.

Huang, C. and L. Chen (2016). Negative Poisson's Ratio in Modern Functional Materials. *Advanced Materials*; 8079-8096.

Zhu, X., J. Zhang, W. Zhang, J. Chen (2018), Vibration frequencies and energies of an auxetic honeycomb sandwich plate, Mechanics of Advanced *Materials and Structures*, DOI: 10.1080/15376494.2018.1455933.

Appendix

$$A_1 = Q_{11}^T\left(h_1+h_3\right)+Q_{11}^C h_2+\frac{d_1E_0h_{s1}}{s_1},$$

$$A_2 = Q_{12}^C h_2+Q_{12}^T\left(h_1+h_3\right),$$

$$A_3 = \frac{1}{2}Q_{11}^T\left[-h_2h_3-h_3^2+h_1h_2+h_1^2\right]+\frac{1}{2}\frac{d_1E_0\left(h.h_{s1}+h_{s1}^2\right)}{s_1},$$

$$A_4 = \frac{1}{2}Q_{12}^T\left[\left(-h_2h_3-h_3^2+h_1h_2+h_1^2\right)\right],$$

$$A_5 = Q_{22}^T\left(h_1+h_3\right)+Q_{22}^C h_2+\frac{d_2E_0h_{s2}}{s_2},$$

$$A_6 = \frac{1}{2}Q_{22}^T\left[-h_2h_3-h_3^2+h_1h_2+h_1^2\right]+\frac{1}{2}\frac{d_2E_0\left(h.h_{s2}+h_{s2}^2\right)}{s_2},$$

$$A_7 = Q_{66}^C h_2+Q_{66}^T\left(h_1+h_3\right),$$

$$A_8 = \frac{1}{2}Q_{66}^T\left[\left(\frac{1}{2}h_2+h_1\right)^2-\left(\frac{1}{2}h_2+h_3\right)^2\right],$$

$$A_9 = \frac{1}{3}\frac{d_1E_0\left(\frac{-1}{8}h^3+\left(\frac{1}{2}h+h_{s1}\right)^3\right)}{s_1}+\frac{1}{12}Q_{11}^C h_2^3+\frac{1}{3}Q_{11}^T\left(\left(\frac{1}{2}h_2+h_1\right)^3+\left(\frac{1}{2}h_2+h_3\right)^3-\frac{1}{4}h_2^3\right),$$

$$A_{10} = \frac{1}{3}Q_{12}^T\left(\left(\frac{1}{2}h_2+h_1\right)^3+\left(\frac{1}{2}h_2+h_3\right)^3-\frac{1}{4}h_2^3\right)+\frac{1}{12}Q_{12}^C h_2^3,$$

$$A_{11} = \frac{1}{3}\frac{d_2E_0\left(\frac{-1}{8}h^3+\left(\frac{1}{2}h+h_{s2}\right)^3\right)}{s_2}+\frac{1}{12}Q_{22}^C h_2^3+\frac{1}{3}Q_{22}^T\left(\left(\frac{1}{2}h_2+h_1\right)^3+\left(\frac{1}{2}h_2+h_3\right)^3-\frac{1}{4}h_2^3\right),$$

$$A_{12} = \frac{1}{3}Q_{66}^T\left(\left(\frac{1}{2}h_2+h_3\right)^3+\left(\frac{1}{2}h_2+h_1\right)^3-\frac{1}{4}h_2^3\right)+\frac{1}{12}Q_{66}^C h_2^3,$$

$$A_{13} = \left(Q_{55}^C h_2+Q_{55}^T\left(h_1+h_3\right)+\frac{d_1G_{sx}h_{s1}}{s_1}\right),$$

$$A_{14} = \left(Q_{44}^C h_2+Q_{44}^T\left(h_1+h_3\right)+\frac{d_2G_{sy}h_{s2}}{s_2}\right).$$

$$H_{11} = KA_{13}\frac{\partial^2 w}{\partial x^2}+KA_{14}\frac{\partial^2 w}{\partial y^2}-k_1 w+k_2\left(\frac{\partial^2 w}{\partial x^2}+\frac{\partial^2 w}{\partial y^2}\right),H_{12}\left(\phi_x\right) = KA_{13}\frac{\partial\phi_x}{\partial x},$$

$$H_{13}\left(\phi_x\right) = KA_{14}\frac{\partial\phi_y}{\partial y},$$

$$\mathrm{S}\left(w,f\right) = \frac{\partial^2 f}{\partial y^2}\frac{\partial^2 w}{\partial x^2}-2\frac{\partial^2 f}{\partial x\partial y}\frac{\partial^2 w}{\partial x\partial y}+\frac{\partial^2 f}{\partial x^2}\frac{\partial^2 w}{\partial y^2}+\frac{1}{R}\frac{\partial^2 f}{\partial x^2},H_{21}\left(w\right) = -KA_{13}\frac{\partial w}{\partial x},$$

$$H_{22}\left(\phi_x\right) = D_{11}\frac{\partial^2\phi_x}{\partial x^2}+D_{66}\frac{\partial^2\phi_x}{\partial y^2}-KA_{13}.\phi_x,$$

$$H_{23}(\phi_y) = \left(D_{12}+D_{66}\right)\frac{\partial^2\phi_y}{\partial x\partial y},$$

$$H_{24}\left(f\right) = \left(\frac{A_2A_4-A_3A_5}{A_2^2-A_1A_5}-\frac{A_8}{A_7}\right)\frac{\partial^3 f}{\partial x\partial y^2}+\frac{A_2A_3-A_1A_4}{A_2^2-A_1A_5}\frac{\partial^3 f}{\partial x^3},$$

$$H_{31}\left(w\right) = -KA_{14}\frac{\partial w}{\partial y},$$

$$H_{32}(\phi_x) = \left(D_{21}+D_{66}\right)\frac{\partial^2\phi_x}{\partial x\partial y},$$

$$H_{33}\left(\phi_y\right) = D_{22}\frac{\partial^2\phi_y}{\partial y^2}+D_{66}\frac{\partial^2\phi_y}{\partial y^2}-KA_4\phi_x,$$

$$H_{34}\left(f\right) = \left(\frac{A_2A_4-A_1A_6}{A_2^2-A_1A_5}-\frac{A_8}{A_7}\right)\frac{\partial^3 f}{\partial y\partial x^2}+\frac{A_2A_6-A_5A_4}{A_2^2-A_1A_5}\frac{\partial^3 f}{\partial y^3},$$

$$D_{11} = \frac{A_3^2A_5-2A_2A_3A_4+A_1A_4^2}{A_2^2-A_1A_5}+A_9,$$

$$D_{12} = \frac{A_3\left(A_4A_5-A_2A_6\right)+A_4\left(A_1A_6-A_2A_4\right)}{A_2^2-A_1A_5}+A_{10},$$

$$\mathrm{D}_{21} = \frac{A_4\left(A_3A_5-A_2A_4\right)+A_6\left(A_1A_4-A_2A_3\right)}{A_2^2-A_1A_5}+A_{10},$$

$$\mathrm{D}_{22} = \frac{A_4^2A_5-2A_2A_4A_6+A_1A_6^2}{A_2^2-A_1A_5}+A_{11},$$

$$D_{66} = A_{12}-\frac{A_8^2}{A_7}.$$

$$h_{11}=\frac{ab}{4}\begin{pmatrix}-KA_4\delta_n^2+h\left(\lambda_m^2P_x+\delta_n^2P_2\right)-KA_{13}\lambda_m^2-\dfrac{a_1\lambda_m^2}{R}\\-k_1-k_2\left(\lambda_m^2+\delta_n^2\right)\end{pmatrix}$$

$$+\frac{ab}{3R}\frac{h\mu\delta_n^2\left(A_1A_5-A_2^2\right)}{A_1\pi^2}$$

$$-\frac{ab}{32}h^2\mu^2\left(A_1A_5-A_2^2\right)\left(\frac{\delta_n^2}{\lambda_m^2A_1}+\frac{\lambda_m^2}{\delta_n^2A_5}\right)\lambda_m^2\delta_n^2,$$

$$h_{12}=\frac{8}{3}\frac{ab\lambda_m^2\delta_n^2a_2h\mu}{\pi^2}-\frac{ab}{4}\left(\frac{\lambda_m^2a_2}{R}+KA_{13}\lambda_m\right),$$

$$h_{13}=\frac{8}{3}\frac{ab\lambda_m^2\delta_n^2a_3h\mu}{\pi^2}-\frac{ab}{4}\left(\frac{\lambda_m^2a_3}{R}+KA_{14}\delta_n\right),$$

$$h_{14}=\frac{8}{3}\frac{aba_2\lambda_m^2\delta_n^2}{\pi^2},h_{15}=\frac{8}{3}\frac{ab\lambda_m^2\delta_n^2a_3}{\pi^2},$$

$$h_{16}=\frac{8}{3}\frac{\lambda_m^2\delta_n^2a_1ab}{\pi^2}+\frac{1}{6}\frac{\delta_n^2}{A_1R\pi^2}\left(A_1A_5-A_2^2\right)$$

$$-\frac{3ab}{64}\lambda_m^2\delta_n^2h\mu\left(A_1A_5-A_2^2\right)\left(\frac{\lambda_m^2}{\delta_n^2A_5}+\frac{\delta_n^2}{\lambda_m^2A_1}\right),$$

$$h_{17}=-\frac{\lambda_m^2\delta_n^2}{64}ab\left(A_1A_5-A_2^2\right)\left(\frac{\lambda_m^2}{\delta_n^2A_5}+\frac{\delta_n^2}{\lambda_m^2A_1}\right),$$

$$h_{18}=\frac{ab}{4}\left(h^2\mu\left(\lambda_m^2P_x+\delta_n^2P_y\right)\right)+4ab/\pi^2\left(-P_yh/R\right)$$

$$h_{21}=\frac{ab}{4}\begin{pmatrix}\left(\dfrac{\left(A_4A_1-A_2A_3\right)\lambda_m^3a_1-\left(A_4A_2-A_5A_3\right)a_1\lambda_m\delta_n^2}{A_2^2-A_1A_5}\right)\\+\dfrac{A_8\lambda_m\delta_n^2}{A_7}a_1-KA_{13}\lambda_m\end{pmatrix}$$

$$+\frac{4}{3}\frac{ab}{\pi^2}h\mu\delta_n^2\lambda_m\left(A_4-\frac{A_2A_3}{A_1}\right),$$

$$h_{22}=\frac{ab}{4}\begin{pmatrix}\left(\dfrac{\left(A_4A_1-A_2A_3\right)\lambda_m^3a_2-\left(A_4A_2-A_5A_3\right)a_2\lambda_m\delta_n^2}{A_2^2-A_1A_5}\right)\\+\dfrac{a_2A_8\lambda_m\delta_n^2}{A_7}-D_{11}\lambda_m^2-KA_{13}-\delta_n^2D_{66}\end{pmatrix},$$

$$h_{23}=\frac{ab}{4}\begin{pmatrix}\left(\dfrac{\left(A_4A_1-A_2A_3\right)\lambda_m^3a_3-\left(A_4A_2-A_5A_3\right)a_3\lambda_m\delta_n^2}{A_2^2-A_1A_5}\right)\\+\dfrac{a_3A_8\lambda_m\delta_n^2}{A_7}-\lambda_m\delta_n\left(D_{12}+D_{66}\right)\end{pmatrix},$$

$$h_{24}=\frac{2}{3}\frac{ab\lambda_m\delta_n^2}{\pi^2}\left(A_4-\frac{A_2A_3}{A_1}\right),$$

$$h_{31}=\frac{ab}{4}\begin{pmatrix}\left(\dfrac{\left(A_1A_6-A_4A_2\right)a_1\lambda_m^2\delta_n+\left(A_2A_6-A_4A_5\right)\delta_n^3a_1}{-A_1A_5+A_2^2}\right)\\+\dfrac{A_8\lambda_m^2\delta_n}{A_7}a_1-KA_{14}\delta_n\end{pmatrix}$$

$$+\frac{4}{3}\frac{ab}{\pi^2}h\mu\delta_n\lambda_m^2\left(A_4+\frac{A_2A_6}{A_1}\right),$$

$$h_{32}=\frac{ab}{4}\begin{pmatrix}\left(\dfrac{\left(A_1A_6-A_4A_2\right)a_2\lambda_m^2\delta_n+\left(A_2A_6-A_4A_5\right)\delta_n^3a_2}{-A_1A_5+A_2^2}\right)\\-\left(D_{66}+D_{21}\right)\lambda_m\delta_n+\dfrac{a_2A_8\lambda_m^2\delta_n}{A_7}\end{pmatrix},$$

$$h_{33}=\frac{ab}{4}\begin{pmatrix}-D_{22}\delta_n^2\\+\left(\dfrac{\left(A_1A_6-A_4A_2\right)a_3\lambda_m^2\delta_n+\left(A_2A_6-A_4A_5\right)\delta_n^3a_3}{-A_1A_5+A_2^2}\right)\\-\lambda_m^2D_{66}+\dfrac{a_3A_8\lambda_m^2\delta_n}{A_7}-KA_{14}\end{pmatrix},$$

$$h_{34}=\frac{2}{3}\frac{ab\lambda_m^2\delta_n}{\pi^2}\left(\frac{A_2A_6}{A_1}+A_4\right).$$

The 5th International Conference on Engineering Mechanics and Automation (ICEMA 5)
Hanoi, October 11÷12, 2019

Buckling and post-buckling of FGM toroidal shell segments loaded by axial compression using Reddy's third-order shear deformation theory

Pham Minh Vuong[a,b] and Nguyen Dinh Duc [c,d]

[a] *Faculty of Civil and Industrial, National University of Civil Engineering, 55 Giai Phong Street, Hai Ba Trung District, Hanoi, Vietnam, vuongpm@nuce.edu.vn*
[b]*VNU Hanoi – University of Science, 334 Nguyen Trai – Thanh Xuan – Hanoi – Vietnam*
[c] *Advanced Materials and Structures Laboratory, VNU-Hanoi, University of Engineering and Technology (UET), 144 – Xuan Thuy – Cau Giay – Hanoi – Vietnam, ducnd@vnu.edu.vn*
[d] *Infrastructure Engineering Program -VNU-Hanoi, Vietnam-Japan University (VJU), My Dinh 1 – Tu Liem – Hanoi – Vietnam, ducnd@vnu.edu.vn*

Abstract

An analytical investigation on nonlinear buckling and post-buckling of FGM toroidal shell segments subjected to axial compression are presented in this study. Formulations are established in framework of Reddy third-order shear deformation theory. By applying Galerkin method, the closed-form expressions for determining critical buckling load and post-buckling relation curve are obtained. Effects of geometrical and material properties on stability of shells are examined in detail

Key Words: FGM toroidal shell segments, Reddy's third-order shear deformation, axial compressive load.

1. Introduction

The buckling and post-buckling of shells under compressive load is one of the basic problems on stability of structures. Hence, there are many investigations carried out into this subject. Brush and Almroth (1975) based on classical shell theory and adjacent equilibrium criterion to study buckling of isotropic cylindrical shell under external pressure and compressive load. Also based on classical shell theory, Dung et al. (2017) presented an investigation on buckling and post-buckling of FGM cylindrical shell using Galerkin method; Huang and Han (2009) studied buckling and post-buckling of FGM cylindrical shell using the Ritz energy method; Shen (2002) used a boundary layer theory of shell buckling and a singular perturbation technique to study post-buckling of FGM cylindrical shell. Higher order shear shell theories also are used to study stability of cylindrical shell. Dung and Vuong (2017) investigated buckling and post-buckling of FGM cylindrical shell using Reddy third order shear deformation shell theory and Galerkin method. Sun et al. (2015) used Reddy third order shear deformation shell theory, adjacent equilibrium criterion and Galerkin method to study buckling of FGM cylindrical shell loaded by axial compression.

Buckling and post-buckling of isotropic truncated conical shells are studied by Tani and Yamaky (1970) using classical shell theory. Sofiyev (2010) used the modified Donnell type stability and compatibility equations and Galerkin's method to study buckling of FGM

truncated conical shells under axial compressive load. Chan et al. (2018) based on the first-order shear deformation shell theory, adjacent equilibrium criterion and Galerkin method to investigate buckling of FGM truncated conical shell.

Static and dynamic stability problems of toroidal shell segments under axial compressive load have been studied by scientists. McElman (1965), Hutchinson (1967) based on classical shell theory to study buckling of homogenous and isotropic toroidal shell segments under external pressure and axial compressive load. Thang and Thoi (2016) presented an investigation on dynamic buckling of FGM toroidal shell segment loaded by axial compression linearly increasing on time.

To the best of author's knowledge, there is no investigation on buckling and post-buckling of FGM toroidal shell segment subjected to axial compressive load using higher order-shear deformation theory. In the present study, an investigation on nonlinear buckling and post-buckling of FGM toroidal shell segments subjected to axial compression by analytical approach are performed. The governing equations are established in the framework of Reddy third-order shear deformation theory. Then, Galerkin method are used to obtain the closed-form expressions of buckling axial compressive load and post-buckling load-deflection curves. The effects of geometric and material parameters on stability of shells are considered in detail.

2. Governing equations

Consider a toroidal shell segment with radius of equator R, longitudinal curvature radius a, thickness h and length L as shown in Fig. 1. The shell is defined in a coordinate system (x, y, z) whose origin is located at the end on the middle surface of shell, x and y are in the axial and circumferential directions, respectively, z is perpendicular to surface and pointed inwards.

The shell is made of functionally graded material (FGM) which composed of ceramic and metal components. Assume that the Young modulus E varying continuously through the thickness direction according to a simple power law distribution in term of the volume fractions of the constituents as

$$E(z) = E_m + (E_c - E_m)\left(\frac{2z+h}{2h}\right)^k \tag{1}$$

where E_m and E_c are Young modulus of metal and ceramic constituent, respectively, k is the volume fraction index. The Poisson's ratio ν is assumed to be constant.

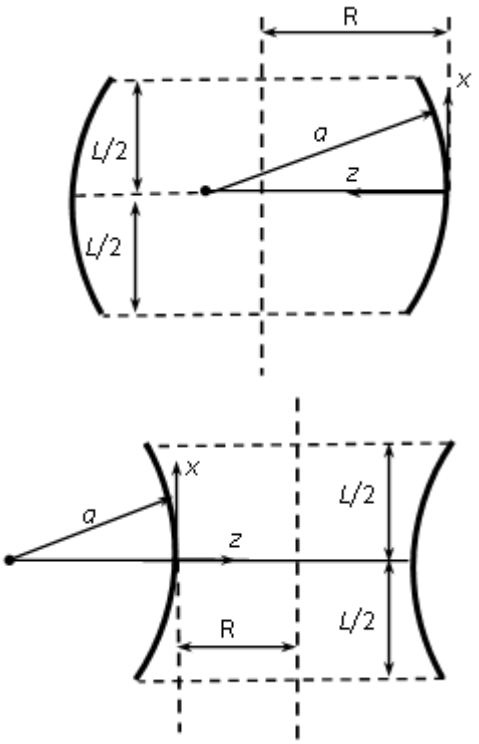

Figure 1. Configuration of convex and concave toroidal shell segments

In the present study, governing equations are established based on the Reddy third-order shear deformation theory (Reddy and Liu 1985). According to this theory strain components at a distance z from the middle surface are

$$\begin{bmatrix} \varepsilon_x \\ \varepsilon_y \\ \gamma_{xy} \end{bmatrix} = \begin{bmatrix} \varepsilon_x^0 \\ \varepsilon_y^0 \\ \gamma_{xy}^0 \end{bmatrix} + z\begin{bmatrix} \kappa_x^{(1)} \\ \kappa_y^{(1)} \\ \kappa_{xy}^{(1)} \end{bmatrix} + z^3\begin{bmatrix} \kappa_x^{(3)} \\ \kappa_y^{(3)} \\ \kappa_{xy}^{(3)} \end{bmatrix}, \tag{2}$$

$$\begin{bmatrix}\gamma_{xz}\\ \gamma_{yz}\end{bmatrix}=\begin{bmatrix}\gamma_{xz}^{0}\\ \gamma_{yz}^{0}\end{bmatrix}+z^{2}\begin{bmatrix}\kappa_{xz}^{(2)}\\ \kappa_{yz}^{(2)}\end{bmatrix}$$

where

$$\begin{bmatrix}\varepsilon_{x}^{0}\\ \varepsilon_{y}^{0}\\ \gamma_{xy}^{0}\end{bmatrix}=\begin{bmatrix}\dfrac{\partial u}{\partial x}-\dfrac{w}{a}+\dfrac{1}{2}\left(\dfrac{\partial w}{\partial x}\right)^{2}\\ \dfrac{\partial v}{\partial}-\dfrac{w}{R}+\dfrac{1}{2}\left(\dfrac{\partial w}{\partial y}\right)^{2}\\ \dfrac{\partial u}{\partial y}+\dfrac{\partial v}{\partial x}+\dfrac{\partial w}{\partial x}\dfrac{\partial w}{\partial y}\end{bmatrix},$$

$$\begin{bmatrix}\kappa_{x}^{(1)}\\ \kappa_{y}^{(1)}\\ \kappa_{xy}^{(1)}\end{bmatrix}=\begin{bmatrix}\dfrac{\partial\phi_{x}}{\partial x}\\ \dfrac{\partial\phi_{y}}{\partial y}\\ \dfrac{\partial\phi_{x}}{\partial y}+\dfrac{\partial\phi_{y}}{\partial x}\end{bmatrix}$$

$$\begin{bmatrix}\kappa_{x}^{(3)}\\ \kappa_{y}^{(3)}\\ \kappa_{xy}^{(3)}\end{bmatrix}=-\lambda\begin{bmatrix}\dfrac{\partial\phi_{x}}{\partial x}+\dfrac{\partial^{2}w}{\partial x^{2}}\\ \dfrac{\partial\phi_{y}}{\partial y}+\dfrac{\partial^{2}w}{\partial y^{2}}\\ \dfrac{\partial\phi_{x}}{\partial y}+\dfrac{\partial\phi_{y}}{\partial x}+2\dfrac{\partial^{2}w}{\partial x\partial y}\end{bmatrix},$$

$$\begin{bmatrix}\gamma_{xz}^{0}\\ \gamma_{yz}^{0}\end{bmatrix}=\begin{bmatrix}\phi_{x}+\dfrac{\partial w}{\partial x}\\ \phi_{y}+\dfrac{\partial w}{\partial y}\end{bmatrix}$$

$$\begin{bmatrix}\kappa_{xz}^{(2)}\\ \kappa_{yz}^{(2)}\end{bmatrix}=-3\lambda\begin{bmatrix}\phi_{x}+\dfrac{\partial w}{\partial x}\\ \phi_{y}+\dfrac{\partial w}{\partial y}\end{bmatrix},\ \lambda=\frac{4}{3h^{2}} \tag{3}$$

where u,v and w are the displacement components at the middle surface and ϕ_x,ϕ_y are the slope rotations of normal to middle surface in the (x,z) and (y,z) planes.

From the equations (3), the compatibility equation is given by

$$\frac{\partial^{2}\left(\varepsilon_{x}^{0}\right)}{\partial y^{2}}+\frac{\partial^{2}\left(\varepsilon_{y}^{0}\right)}{\partial x^{2}}-\frac{\partial^{2}\left(\gamma_{xy}^{0}\right)}{\partial x\partial y}=$$
$$-\frac{1}{R}\frac{\partial^{2}w}{\partial x^{2}}-\frac{1}{a}\frac{\partial^{2}w}{\partial y^{2}}+\left(\frac{\partial^{2}w}{\partial x\partial y}\right)^{2}-\frac{\partial^{2}w}{\partial x^{2}}\frac{\partial^{2}w}{\partial y^{2}}. \tag{4}$$

Applying Hooke's law, the constitutive stress-strain equations are obtained as

$$\begin{bmatrix}\sigma_{x}\\ \sigma_{y}\end{bmatrix}=\frac{E(z)}{1-\nu^{2}}\begin{bmatrix}\varepsilon_{x}+\nu\varepsilon_{y}\\ \varepsilon_{y}+\nu\varepsilon_{x}\end{bmatrix},\begin{bmatrix}\sigma_{xy}\\ \sigma_{xz}\\ \sigma_{yz}\end{bmatrix}=\frac{E(z)}{2(1+\nu)}\begin{bmatrix}\gamma_{xy}\\ \gamma_{xz}\\ \gamma_{yz}\end{bmatrix} \tag{5}$$

The nonlinear equilibrium equations of toroidal shell segment based on the Reddy third-order shear deformation shell theory are given by

$$\frac{\partial N_{x}}{\partial x}+\frac{\partial N_{xy}}{\partial y}=0,\frac{\partial N_{y}}{\partial y}+\frac{\partial N_{xy}}{\partial x}=0 \tag{6}$$

$$\frac{\partial Q_{x}}{\partial x}+\frac{\partial Q_{y}}{\partial y}-3\lambda\left(\frac{\partial R_{x}}{\partial x}+\frac{\partial R_{y}}{\partial y}\right)$$
$$+\lambda\left(\frac{\partial^{2}P_{x}}{\partial x^{2}}+2\frac{\partial^{2}P_{xy}}{\partial x\partial y}+\frac{\partial^{2}P_{y}}{\partial y^{2}}\right)+\frac{1}{R}N_{y}+\frac{1}{a}N_{x}$$
$$+N_{x}\frac{\partial^{2}w}{\partial x^{2}}+2N_{xy}\frac{\partial^{2}w}{\partial x\partial y}+N_{y}\frac{\partial^{2}w}{\partial y^{2}}=0 \tag{7}$$

$$\frac{\partial M_{x}}{\partial x}+\frac{\partial M_{xy}}{\partial y}-Q_{x}+3\lambda R_{x}-\lambda\left(\frac{\partial P_{x}}{\partial x}+\frac{\partial P_{xy}}{\partial y}\right)=0 \tag{8}$$

$$\frac{\partial M_{y}}{\partial y}+\frac{\partial M_{xy}}{\partial x}-Q_{y}+3\lambda R_{y}-\lambda\left(\frac{\partial P_{y}}{\partial y}+\frac{\partial P_{xy}}{\partial x}\right)=0 \tag{9}$$

where

$$\left(N_{i},M_{i},P_{i}\right)=\int_{-h/2}^{h/2}\sigma_{i}\left(1,z,z^{3}\right)dz,$$
$$\left(Q_{i},R_{i}\right)=\int_{-h/2}^{h/2}\sigma_{iz}\left(1,z^{2}\right)dz,\ i=x,y,$$
$$\left(N_{xy},M_{xy},P_{xy}\right)=\int_{-h/2}^{h/2}\sigma_{xy}\left(1,z,z^{3}\right)dz. \tag{10}$$

Substituting Eqs. (1) – (3) into Eq. (5) and the results into Eq. (10) and then introduce results into Eq. (4) and Eqs. (7) – (9) yields

$$\frac{\partial^4 F}{\partial x^4}+2\frac{\partial^4 F}{\partial x^2\partial y^2}+\frac{\partial^4 F}{\partial y^4}=-\frac{E_1}{R}\frac{\partial^2 w}{\partial x^2}$$
$$-\frac{E_1}{a}\frac{\partial^2 w}{\partial y^2}+E_1\left(\frac{\partial^2 w}{\partial x\partial y}\right)^2-E_1\frac{\partial^2 w}{\partial x^2}\frac{\partial^2 w}{\partial y^2}, \quad (11)$$

$$A_1\frac{\partial^2\phi_x}{\partial x^2}+A_2\frac{\partial^2\phi_x}{\partial y^2}+A_3\phi_x+A_4\frac{\partial^2\phi_y}{\partial x\partial y}$$
$$+A_5\frac{\partial^3 w}{\partial x^3}+A_6\frac{\partial^3 w}{\partial x\partial y^2}+A_7\frac{\partial w}{\partial x}=0, \quad (12)$$

$$A_1\frac{\partial^2\phi_y}{\partial y^2}+A_2\frac{\partial^2\phi_y}{\partial x^2}+A_3\phi_y+A_4\frac{\partial^2\phi_x}{\partial x\partial y}$$
$$+A_5\frac{\partial^3 w}{\partial y^3}+A_6\frac{\partial^3 w}{\partial y\partial x^2}+A_7\frac{\partial w}{\partial y}=0, \quad (13)$$

$$A_8\left(\frac{\partial^4 w}{\partial x^4}+2\frac{\partial^4 w}{\partial x^2\partial y^2}+\frac{\partial^4 w}{\partial y^4}\right)+\frac{1}{R}\frac{\partial^2 F}{\partial x^2}+\frac{1}{a}\frac{\partial^2 F}{\partial y^2}$$
$$+A_9\left(\frac{\partial^3\phi_x}{\partial x^3}+\frac{\partial^3\phi_x}{\partial x\partial y^2}+\frac{\partial^3\phi_y}{\partial y\partial x^2}+\frac{\partial^3\phi_y}{\partial y^3}\right)$$
$$+\frac{\partial^2 F}{\partial y^2}\frac{\partial^2 w}{\partial x^2}-2\frac{\partial^2 F}{\partial x\partial y}\frac{\partial^2 w}{\partial x\partial y}+\frac{\partial^2 F}{\partial x^2}\frac{\partial^2 w}{\partial y^2}=0, \quad (14)$$

where $F(x,y)$ is stress function defined as

$$N_x=\frac{\partial^2 F}{\partial y^2}, N_y=\frac{\partial^2 F}{\partial x^2}, N_{xy}=-\frac{\partial^2 F}{\partial x\partial y} \quad (15)$$

and

$$A_1=\frac{E_1E_3-E_2^2+2\lambda\left(E_2E_4-E_1E_5\right)+\lambda^2\left(E_1E_7-E_4^2\right)}{E_1\left(1-\nu^2\right)},$$
$$A_2=\frac{A_1\left(1-\nu\right)}{2},\ A_3=\frac{-E_1+6\lambda E_3-9\lambda^2E_5}{2\left(1+\nu\right)},$$
$$A_4=\frac{A_1\left(1+\nu\right)}{2},$$
$$A_5=\frac{\lambda\left(E_2E_4-E_1E_5\right)+\lambda^2\left(E_1E_7-E_4^2\right)}{E_1\left(1-\nu^2\right)},$$
$$A_6=A_5, A_7=A_3,\ A_8=\frac{\lambda\left(E_2E_4-E_1E_5\right)}{E_1\left(1-\nu^2\right)},$$
$$A_9=\frac{E_1E_3-E_2^2+\lambda\left(E_2E_4-E_1E_5\right)}{E_1\left(1-\nu^2\right)}.$$

3. Solution of basic equations

In the present study, FGM toroidal shell segments are assumed to be simply supported at two edges and subjected to axial compressive load $N_{0x}=-P.h$. Therefore, the boundary conditions are

$$w=0,\ M_x=0,\ N_x=-Ph,\ N_{xy}=0,\ \phi_y=0$$

at $x=0$ and $x=L$. (16)

The solutions of governing equations, satisfying simply supported boundary condition in average sense are chosen as

$$w=f\sin Mx\sin Ny,$$
$$F=B_1f\sin Mx\sin Ny+B_2f^2\cos 2Mx$$
$$+B_3f^2\cos 2Ny+\frac{1}{2}N_{y0}x^2-\frac{1}{2}Phy^2, \quad (17)$$
$$\phi_x=C_1f\cos Mx\sin Ny,$$
$$\phi_y=C_2f\sin Mx\cos Ny.$$

where $M=\frac{m\pi}{L}, N=\frac{n}{R}$. f is the amplitude of deflection, m and n are the numbers of half waves in x and y directions, respectively. N_{y0} is average circumferential force resultant.

Subtitling the first equation of Eqs. (17) into Eqs. (11) – (13), coefficients B_1, B_2, B_3, C_1 and C_2 can be determined as

$$B_1=\frac{E_1}{\left(M^2+N^2\right)^2}\left(\frac{M^2}{R}+\frac{N^2}{a}\right),$$
$$B_2=\frac{E_1N^2}{32M^2}, B_3=\frac{E_1M^2}{32N^2},$$
$$C_1=\frac{A_3-A_5\left(M^2+N^2\right)}{A_1\left(M^2+N^2\right)-A_3}M, \quad (18)$$

$$C_2 = \frac{A_3 - A_5\left(M^2 + N^2\right)}{A_1\left(M^2 + N^2\right) - A_3} N$$

Putting Eq. (17) into Eq. (14) then applying Galerkin procedure for resulting equation yields

$$\frac{-Ph}{a} + \frac{N_{y0}}{R} = 0 \tag{19}$$

$$D_1 + M^2 Ph - N^2 N_{y0} + D_2 f^2 = 0 \tag{20}$$

where

$$D_1 = A_8\left(M^2 + N^2\right)^2 - A_9 C_1\left(M^2 + N^2\right) - \left(\frac{M^2}{R} + \frac{N^2}{a}\right) B_1,$$

$$D_2 = -2M^2 N^2\left(B_3 + B_4\right).$$

Solving Eqs. (19) and (20) yields

$$P = \frac{D_1 + D_2 f^2}{\left(\frac{R}{a} N^2 - M^2\right) h} \tag{21}$$

It is evident that the toroidal shell segments exhibit a bifurcation buckling response. The buckling axial compressive loads can be presented as

$$P_b = \frac{aD_1}{\left(RN^2 - aM^2\right) h} \tag{22}$$

The critical buckling axial compression P_{cr} is the smallest value among values of P_b.

4. Numerical results and discussions

4.1. Validation of the present study

In this section, isotropic toroidal shell segments is considered with geometric and material properties are chosen as: $h = 0.01\text{m}$, $R/h = (30;50;100;300)$, $L/R = 1$, $a/R = 5$, $E = 10\times10^9\,\text{Pa}$, $\nu = 0.3$. The critical axial compressive buckling loads are calculated by using Eq. (22) and compared with results reported by Hutchinson (1967) and listed in Table 1. As can be seen, this comparison shows a very good agreement.

Table 1. Comparison of critical axial buckling load for isotropic toroidal shell segments

R/h	P_{cr} (**MPa**)		
	Hutchinson (1967)	Present study	Error (%)
30	1424.28(3,1)[a]	1406.31(3,1)	1.3
50	849.96(4,1)	842.64(4,1)	0.86
100	425.41(6,1)	423.10(6,1)	0.54
300	141.28(10,1)	141.06(10,1)	0.16

4.2. Results of buckling and post-buckling analysis of FGM toroidal shell segments

Effect of a/R and L/R ratios

In this section, material and geometric properties of FGM toroidal shell segments are chosen as: $E_m = 70\times10^9\,\text{Pa}$, $E_c = 380\times10^9\,\text{Pa}$, $k = 3$, $\nu = 0.3$, $h = 0.01\text{m}$, $R/h = 80$, $a/R = (\pm5;\pm10;\infty)$, $L/R = (0.5;1;1.5)$. Effects of a/R and L/R ratios on buckling and post-buckling of FGM toroidal shell segments are illustrated in Table 2, Figure 2, Figure 3 and Figure 4. It can be seen that, both the critical buckling load and the post-buckling capacity of shell increases as a/R ratio and/or L/R ratio decreases. The more convex and/or shorter shell is, the better carrying capacity is it. Moreover, information in Table 2, Fig. 2 and Fig. 3 also show that convex shells are better carrying capacity than concave shells.

Table 2. Effects of a/R and L/R on buckling and post-buckling behavior of FGM toroidal shell segments.

a/R	$L/R = 0.5$	$L/R = 1$	$L/R = 1.5$
∞	1061.0(2,7)[a]	1059.3(5,4)	1059.0(8,1)
10	1090.1(3,1)	1067.3(5,1)	1059.7(8,1)
5	1090.6(3,1)	1068.2(5,1)	1060.5(8,1)
-10	775.7(1,8)	504.6(1,6)	329.3(1,5)
-5	579.9(1,8)	266.0(1,6)	171.2(1,4)

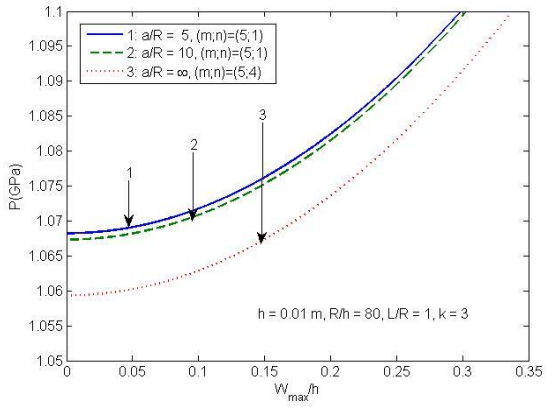

Figure 2. Effect of a/R ratio on post-buckling of convex shells.

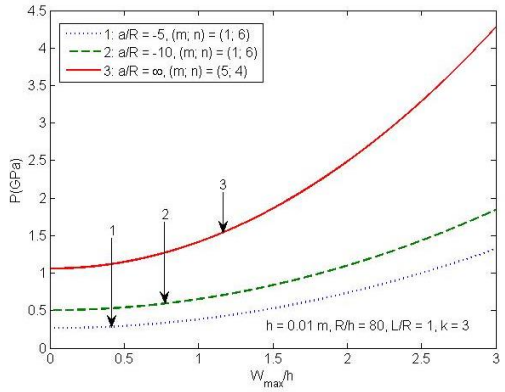

Figure 3. Effect of a/R ratio on post-buckling of concave shells.

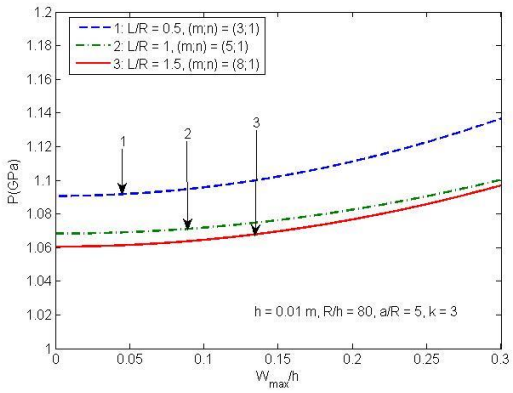

Figure 4. Effect of L/R ratio on post-buckling of FGM toroidal shell segments.

Effects of R/h ratio and the volume fraction index k

Table 3 Figure 5 and Figure 6 demonstrate the effects of R/h ratio and volume fraction index k on buckling and post-buckling of FGM toroidal shell segments. Parameters of FGM shells are chosen as: $E_m = 70\times10^9\,\text{Pa}$, $E_c = 380\times10^9\,\text{Pa}$, $k = (0.2;0.5;1;10;\infty)$, $\nu = 0.3$, $h = 0.01\text{m}$, $R/h = (50;100;150)$, $L/R = 1$, $a/R = 10$,. The volume fraction index (k) defines contribution of material constituents. Eq. 1 shows that, when the value k increases the volume fraction of metal constituent in FGM increases and effective elastic modulus of FGM decreases – FGM becomes softer. This characteristic of FGM is also shown in Table 3 and Fig. 5 when both critical buckling load and pots-buckling carrying capacity of shells decline as the volume fraction index increases. Information in Table 3 and Fig. 6 also reveals that the buckling resistance and post-buckling carrying capacity of FGM toroidal shell segments become greater as R/h ratio become less.

Table 3. Effects of R/h ratio and volume fraction index k on buckling of FGM toroidal shell segments.

k	$R/h = 50$	$R/h = 100$	$R/h = 150$
∞	841.6(4,1)	422.9(6,1)	281.8(7,1)
10	1266(4,1)	642.4(6,1)	425.5(7,1)
1	2502.7(4,2)	1244.9(6,1)	836.1(7,1)
0.5	3154.6(4,1)	1574.1(6,1)	1054.4(7,1)
0.2	3852.6(4,1)	1929.8(6,1)	1288.9(7,1)
0	4568.4(4,1)	2295.6(6,1)	1529.6(7,1)

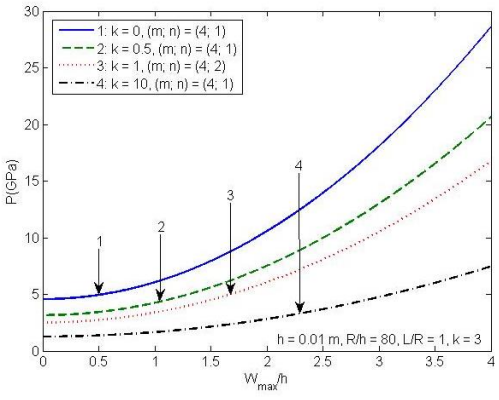

Figure 5. Effect of volume fraction index on post-buckling of FGM toroidal shell segment

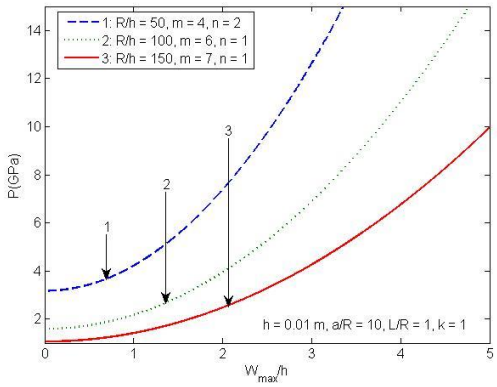

Figure 6. Effect of R/h ratio on post-buckling of FGM toroidal shell segment.

5. Conclusions

This study presents an analytical approach to investigate buckling and post-buckling behavior of simply supported FGM toroidal shell segments subjected to axial compressive load based on the Reddy third-order shear deformation theory. By applying Galerkin method, the closed-form expressions of buckling load and post-buckling load-deflection relation are obtained. Numerical examples illustrate the effects of material and geometric properties on stability of shells. Some conclusions are drawn from study:

- Both the buckling resistance and the post-buckling carrying capacity of shell increases as a/R ratio and/or L/R ratio and/or R/h decreases.
- Convex shells and richer ceramic shells are axial loaded resistance stronger than concave shells and less ceramic shells.

Acknowledgements: This research is funded by the National Science and Technology Program of Vietnam for the period of 2016-2020 "Research and development of science education to meet the requirements of fundamental and comprehensive reform education of Vietnam" under Grant number KHGD/16-20.ĐT.032. The authors are grateful for this support.

References

Brush, D.O. and B.O. Almroth (1975). *Buckling of Bars, Plates and Shells*, Mc Graw-Hill.

Chan, D. Q., D. Van Dung, and L. K. Hoa (2018). Thermal buckling analysis of stiffened FGM truncated conical shells resting on elastic foundations using FSDT. *Acta Mechanica*, 229(5), pp. 2221–2249.

Dung, D. V., N. T Nga, and L. K. Hoa (2017). Nonlinear stability of functionally graded material (FGM) sandwich cylindrical shells reinforced by FGM stiffeners in thermal environment. *Applied Mathematics and Mechanics*, 38(5), pp. 647–670.

Huang, H. and Q. Han (2009). Nonlinear elastic buckling and postbuckling of axially compressed functionally graded cylindrical shells. *International Journal of Mechanical Sciences*, 51(7), pp. 500–507.

Hutchinson, J. W. (1967). *Initial post-buckling behavior of toroidal shell segments*. International Journal of Solids and Structures, 3(1), pp. 97–115.

McElman, J. (1965). Buckling of segments of toroidal shells. *2nd Aerospace Sciences Meeting*.

Reddy, J. N., and C. F. Liu (1985). A higher-order shear deformation theory of laminated elastic shells. *International Journal of Engineering Science*, 23(3), pp. 319–330.

Shen, H. S 2002. Postbuckling analysis of axially loaded functionally graded cylindrical shells in thermal environments. *Composites Science and Technology*, 62(7-8), pp. 977–987.

Sofiyev, A. H. (2010). The buckling of FGM truncated conical shells subjected to axial compressive load and resting on Winkler–Pasternak foundations. *International Journal of Pressure Vessels and Piping*, 87(12), pp. 753–761.

Sun, J., X. Xu, C. W. Lim, and W. Qiao (2015). Accurate buckling analysis for shear deformable FGM cylindrical shells under axial compression and thermal loads. *Composite Structures*, 123. pp, 246–256.

Tani, J., and N. Yamaki (1970). Buckling of truncated conical shells under axial compression. *AIAA Journal*, 8(3), pp. 568–571.

Thang, P.T., and T. Nguyen-Thoi (2016). A new approach for nonlinear dynamic buckling of S-FGM toroidal shell segments with axial and circumferential stiffeners. *Aerospace Science and Technology*, 53, pp. 1–9.

Vuong, P. M. and D. V. Dung (2017). Nonlinear Analysis on Buckling and Postbuckling of Stiffened FGM Imperfect Cylindrical Shells Filled Inside by Elastic Foundations in Thermal Environment Using TSDT. *Latin American Journal of Solids and Structures*, 14(5), pp. 950–977

The 5th International Conference on Engineering Mechanics and Automation (ICEMA-5)
Hanoi, October 11÷12, 2019

Effect of pre-existing cracks on the behavior of steel girder

Tran The Truyen[a], Nguyen Duc Hieu[b], Bui Thanh Tung[c], and Doan Bao Quoc[d], Tu Sy Quan[e]

[a] *University of Transport and Communications, Viet Nam and tranthetruyen@utc.edu.vn*
[b] *University of Transport and Communications Campus in Ho Chi Minh City, Viet Nam*
[c,d,e] *University of Transport and Communications, Viet Nam*

Abstract

The crack failure of the steel diaphragm of Vam Cong Bridge during construction stage in Viet Nam has raised issues that it is necessary to control the behavior of steel bridge structures with considering the pre-defects of steel materials such as pre-existing cracks due to welding process. This type of crack can be caused by many factors depending on the materials used, welding process, environment the weld is being exposed to, etc.

This study analyses the effect of pre-existing cracks on the behavior of steel girders in laboratory scale. The results will clarify the damage mechanism of steel girder with considering the influence of both the number of pre-cracks and pre-cracks angles to crack growth.

Key Words: pre-existing cracks, crack propagation, failure mechanism, and steel girder.

1. Introduction

Recently, the crack failure on the diaphragm of Vam Cong Bridge has raised an issue that is necessary consideration of damage on steel structures according to brittle damage instead of plastic damage like conventional standpoint [1], [2]. Applying fracture mechanics into analyzing fatigue damage mechanism in steel members would partially contribute to answers of brittle damage mechanism of steel structures in general and steel bridges in particular [3].

Likewise, necessity is to have to have investigations about damage features of steel material and structure in bridges due to propagation of cracks according to brittle damage mechanism which particularly, is investigations of applying theories of fracture mechanics and cracking-plasticity [4].

This study would clarify influence of pre-crack to behavior of steel beam by investigating numerical and experimental models. On the steel beam, pre-cracks are created by mechanics method.

Equivalent calculation results in case of integrity steel beam without pre-crack would be used to be referent results.

In this paper, ANSYS software Mechanical/Workbench 2019R1 was used to model calculation [5]. This is specialized

software for structure analysis models with high reliability.

2. The study model in laboratory

2.1. Samples and arrangement of experiment

Samples are steel beams with the same geometries and dimensions but structural conditions are different.

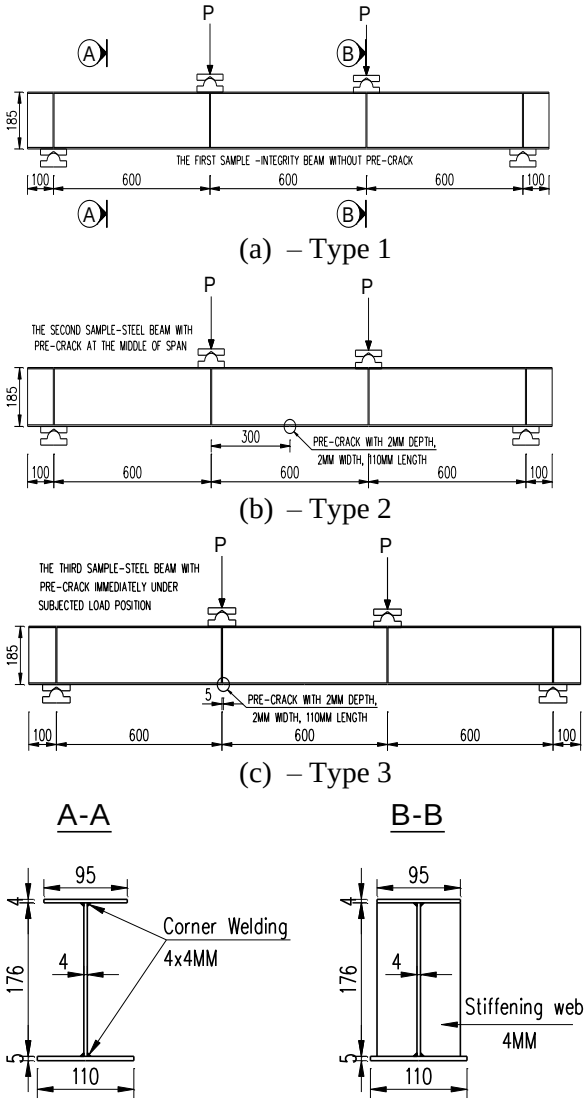

Figure 1. Dimension of samples.

- The 1st ample (Type 1): Integrity beam without defect being created. Figure 1(a).

- The 2nd sample (Type 2): Steel beam has pre-crack with 2mm depth, 2mm width and 110mm length. Pre-crack is on the bottom side and at the middle of beam. Pre-crack is lengthened according to transverse direction. Figure 1(b).

- The 3rd sample (Type 3): Steel beam has pre-crack with 2mm depth, 2mm width and 110mm length. Pre-crack is on the bottom side and the one third position of beam span length where stiffening rids are laid immediately under subjected load position. Pre-crack is lengthened according to transverse direction. Figure 1(c).

Dimension of samples and pre-cracks is in Figure 1 (Dimensions are according to millimeter).

Arrangement of experiments is performed in Figure 2. Load-cells which record subjected load and deflection values, equivalent deformation are laid at positions as being performed in Figure 2.

Figure 2. Bending test of steel beams

2.2. The experimental procedure

Loads subjeted on the steel beams are gradually increased from zero to value which at that moment, large crack would appear on beam and loading capacity of beam would not remain yet. In the period of increased loads, datum of

deflection, deformation are updated with corresponding load grades.

3. Numerical model

ANSYS software Mechanical/Workbench 2019R1 was used to make virtual models of steel beams with pre-cracks and their behavior according to the theory of linear elastic fracture mechanics. Three samples of steel beam are modeled with dimensions and pre-cracks likes experimental beam samples. The properties of steel material are taken from experiments in laboratory.

Physio-mechanical properties of steel material are performed in Table 1.

Table 1. Physio-mechanical properties of steel material

Label	*Description*	*Value*
E	Young modulus	2000Mpa
υ	Poisson's ratio	0.3
α	Thermal expansion coefficient	0.0000117 $1/^{c}o.$
γ	Specific density	7850 kg/m^3
f_y	Yield strength	345 MPa
f_u	Ultimate strength	450 MPa
K_C	Stress intensity	54 MPa m$^{1/2}$

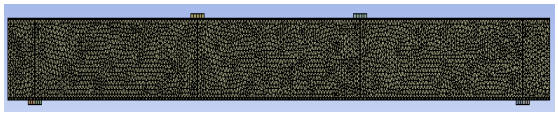

(a) – Type 1

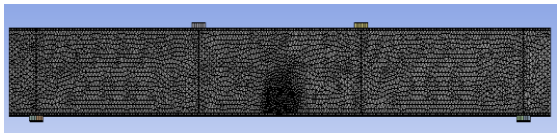

(b) – Type 2

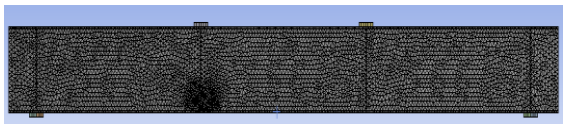

(c) – Type 3

Figure 3. Element meshs of three beam samples are modeled in ANSYS software.

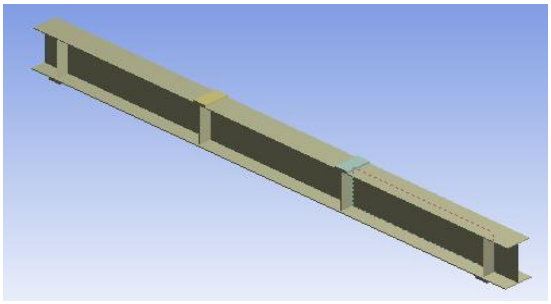

Figure 4. 3D model of steel beam in ANSYS software.

3. Result and Comment

3.1. Result of deflection and stress

Models of three beam samples are non-linearly analysed in ANSYS software.

Analysis result of deflection is performed in detail in Figure 5.

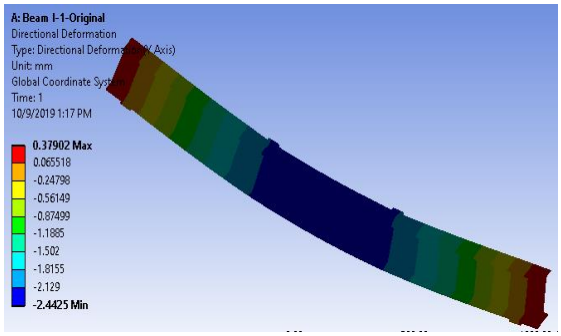

Figure 5.Direction deformation (mm) – beam Type 1

Analysis result of stress is performed in detail in Figure 6.

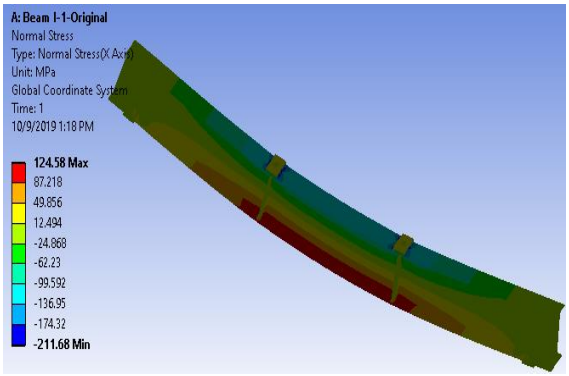

Figure 6. Normal stress (MPa) –beam Type 1

Figure 5 and Figure 6 show deflection and stress on beam sample Type 1. The things can

be seen that max deflection and max normal stress are at the middle of beam span, in which the max deflection value is 2.4425mm and the max normal tensile stress value is 124.58 Mpa on the bottom of beam.

Diagram of load and stress of beam sample Type 1 is performed in Figure 7.

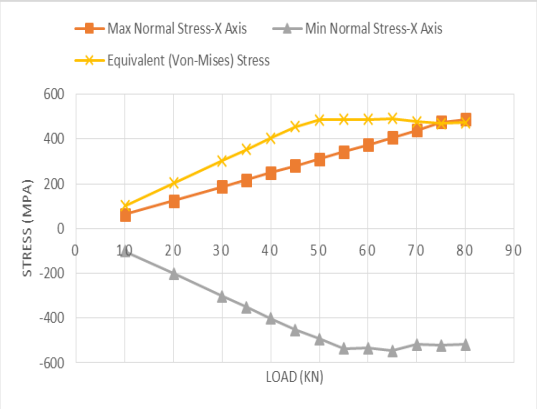

Figure 7. Diagram of load and stress of beam sample Type 1

Comparison diagram of analysis results of deflection for three types of beam is performed in Figure 8.

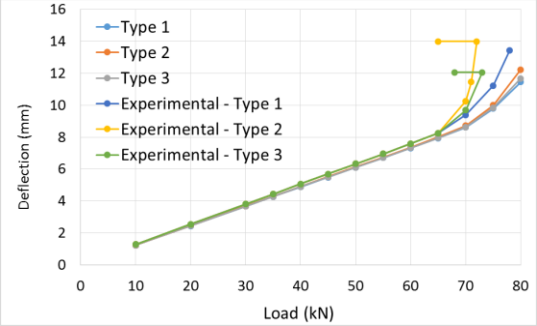

Figure 8. "Deflection – load" relations of beams.

Comment:

- Deflection: Relations between deflection and load of three types of beam are approximately linear with increase of load from 10kN to 65kN for both experimental and numerical results. The relations in experimental results become non-linear earlier than in the numerical ones.

- Stress: Relations between tensile stress and load is linear with load under 70kN while relations between compressive stresses is linear with load under 50kN. This reason is because of relating to stable issue of compressive flange in steel beam.

- In comparison with numerical model result, experimental results show landmarks of behavior stage of steel beams under increasing load grade. Particularly, from the experiment, beam samples being Type 1, Type 2 and Type 3 were damaged (break and crack) at load grade of 78kN, 70kN and 73kN, respectively. Meanwhile, at numerical model samples, with these corresponding loads, samples nearly begin to have behaviors out of plastic area. This can be explained by more ideal boundary conditions of numerical model steel beam than experimental steel beam.

- In both of experimental and numerical model results, steel beam sample with pre-crack at the middle of span showed the soonest degradation of load capacity.

3.2. Damage analysis

Analysis results of Stress Intensity Factor for two beam samples with pre-cracks are performed in Table 2.

Table 2. Result of Stress Intensity Factor.

P	*K_I - Type 2*	*K_I-Type 3*
kN	*MPa $m^{1/2}$*	*MPa $m^{1/2}$*
10	1.34	2.03
20	2.67	4.26
30	4.05	6.86
35	4.91	8.21
40	5.91	9.51
45	7.05	10.85
50	8.29	12.90
55	9.74	15.18
60	11.29	17.81
65	13.20	20.83
70	15.52	25.23
75	23.01	35.41
80	53.83	63.47

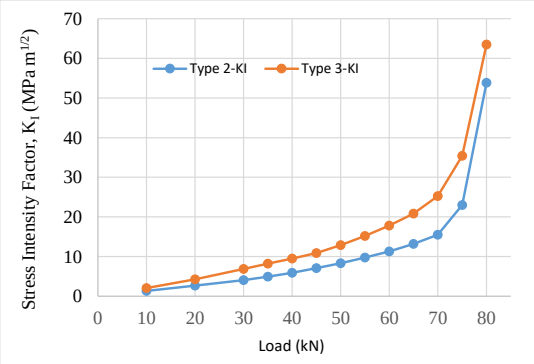

Figure 9. Diagram of relation between Stress Intensity Factor and Load.

Comment: Stress Intensity Factor (SIF) in case of steel beam with pre-crack immediately under subjected load position (the 3rd sample) is greater than that of case of steel beam with pre-crack at the middle of span (the 2nd sample). When Load P = 70kN, at the 3rd sample, SIF K_I = 63.47MPa $m^{1/2}$ > K_{IC} = 54MPa $m^{1/2}$, crack is propagated up to web of steel beam. When load is small, relation between SIF and load is approximately linear; when load is more than 70kN, SIF increases rapidly, raise speed of SIF is faster than that of deflection.

3.3. Result of crack propagation from experiment in laboratory

Figure 10 – Crack image of the steel beam sample with pre-crack on the bottom side of beam at the middle of span – Type 2.

Achieved crack images from experimental steel beam samples of Type 2 and Type 3, all showed propagations of cracks from pre-cracks positions . These cracks appeared from the bottom flange of beams and propagated gradually to the web and top flange of beams according to a straight line which is parallel with the axis of subjected load. Achieved crack images are shown in Figure 10.

4. Conclusion

Deflection of steel beams with pre-crack was smaller than that of integrity steel beam. When load was great (>70kN), relation between deflection and SIF along with load become linear while raised speed of SIF is faster than that of deflection. When SIF approaches to ultimate SIF, cracks would be propagated which make dangerous for structure. Therefore, beams which have defects work out of elastic limit, are absolutely dangerous.

Pre-cracks effect significantly to behaviors of steel beam. Beam was failed although deflection was low, when pre-cracks at the position where both tensile normal and principal stress appeared corresponding with case of beam sample Type 3. Appearance of pre-crack at the middle of span made steel beam be failed at the lowest load grade along with the greatest deflection.

The difference of results from numerical model and experiment showed necessity of having to consider completely boundary condition as well as material parameters of model beam in order to guarantee similarity between experimental and numerical model findings.

References

[1] https://thanhnien.vn/thoi-su/nut-dam-thep-tru-cau-vam-cong-bac-qua-song-hau-900770.html

[2] https://baotintuc.vn/thoi-su/da-xac-dinh nguyen-nhan-gay-nut-cau-vam-cong-20180606173407714.htm

[3] Mustafa Aygül, Mohammad Al-Emrani , Zuheir Barsoum , John Leander (2014). An investigation of distortion-induced fatigue cracking under variable amplitude loading using 3D crack propagation analysis, *Engineering Failure Analysis*, 45 (2014) 151-163.

[4] Ronald B. Madison (June 1969). Application of fracture mechanics to bridges. *Fritz Engineering Laboratory Report No. 335.2*, Lehigh University.

[5] Ansys Inc. headquarters building in Canonsburg, Pennsylvania.

The 5th International Conference on Engineering Mechanics and Automation (ICEMA 5)
Hanoi, October 11÷12, 2019

Analytical solutions for bending of FGM cylindrical shells using higher order shear and normal deformation theory

Tran Van Hung[a], Tran Ngoc Doan[a], Nguyen Truong Thanh[b], Nguyen Ngoc Hoa[a]

[a] *Le Quy Don Technical University, hungsr79@gmail.com*
[b] *Academy of Military Science and Technical*

Abstract

The purpose of this paper is to investigate an analytical solutions for the bending behavior of functionally graded (FG) cylindrical shells under static loading. The material properties of FG are assumed to vary continuously through the thickness of the shells, according to the simple power-law distribution. Derivations of equations are based on higher-order shear and normal deformation theory. The displacement field accounts for a cubic variation of the in-plane displacements and a quadratic variation of the transverse displacement through the thickness. Numerical results for FG shells with a variety of boundary conditions are presented and compared with those available in the literature.

Key Words: Higher-order Shear and Normal Deformation Theory, Functionally graded materials, Analytical Solution, Bending, Cylindrical Shells.

1. Introduction

The laminated composite has the disadvantage of concentrating stress at the surface divided between material layers. This leads to structural failure in the form of layering, fracturing and separation of substrates (Reddy, 2004). Therefore functionally graded materials (FGM) were created to overcome this problem. FGM is an advanced composite material made of two or more constituent phases with a smooth, continuous change of properties from one surface to another, thus eliminating stress concentration in composite layer materials. With outstanding properties, FGM materials are widely applied, especially in aerospace nuclear power (due to very high thermal resistance) in medicine etc.

Due to the outstanding advantages, FGM materials are interested by many domestic and international scientists. The computational models used in plate and shell analysis made from FGM materials have been formulated as: Classical plate theory (CPT), also known as Kirchoff theory (Kirchhoff, 1850), first-order shear deformation theory (FSDT) developed by Mindlin (Mindlin, 1951), Reddy's (Reddy, 1984) third-order shear deformation theory (TSDT), higher-order shear deformation theories (HSDT), quasi-3D shear deformation high theory, three-dimensional elastic theory, etc. In the calculation of composite shells, high quasi-3D shear strain theory is rarely used by researchers because of the complexity and cumbersome of calculation models. This paper uses high quasi-3D shear strain theory in studying static behavior of FGM cylinder shell by analytical approach.

2. Theoretical basis

When works at high temperatures, often found in in refractory structures, the mechanical properties

of the material will change with temperature. In the general case, the change of material parameter P_i according to temperature $T(K)$ is determined by the formula (1) (Kadoli, 2006; Shen, 2009):

$$P_i = P_0(P_{-1}T^{-1} + 1 + P_1T + P_2T^2 + P_3T^3) \quad (1)$$

Where, P_i is the mechanical and physical properties of materials such as Young's modulus (E), density (ρ), Poisson' ratio (μ), thermal expansion coefficient (α), thermal conductivity (κ), specific heat (C_v). In the case stainless steel (SUS304) and zirconia oxide (ZrO_2), the P_i coefficients are used to determine the modulus of elasticity E, Poisson's ratio μ of the material as in (Brischetto, 2017).

The material parameter variation according to thickness is determined by the formula (2) (Shen, 2009):

$$P(z) = P_c + (P_m - P_c)V_m \quad (2)$$

where, index *m*, *c* denote metals and ceramics. Voigt's power-volume ratio distribution according to the thickness of the shell of FGM used, with $V_c = \left(\frac{1}{2} + \frac{z}{2h}\right)^{\eta}$, $V_m = 1 - V_c$, η - power factor. Inside is metal, outside is ceramic.

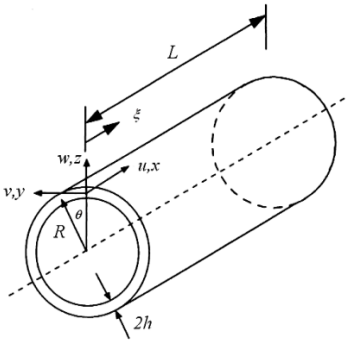

Figure 1. Geometric parameter of FGM cylinder and coordinate system.

Consider FGM cylinder shell thickness $2h$ with the geometric parameters show in Figure 1 (2019). Assume that the FGM cylindrical shell is subjected to radial pressure load $q(\xi,\theta)$ on the outer surface.

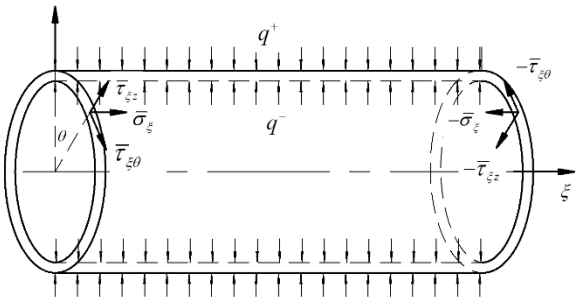

Figure 2. Schematic calculation of closed cylinders under the influence of radial load with boundary conditions at $\xi = 0$ and $\xi = L/R$.

The displacement of cylinder shell is analyzed as the following sum (3) (2019; Firsanov, 2015; Firsanov, 2014).

$$\begin{aligned} u(\xi,\theta,z) &= \sum_{i=0}^{3} u_i(\xi,\theta)\frac{z^i}{i!}, \\ v(\xi,\theta,z) &= \sum_{i=0}^{3} v_i(\xi,\theta)\frac{z^i}{i!}, \\ w(\xi,\theta,z) &= \sum_{i=0}^{2} w_i(\xi,\theta)\frac{z^i}{i!}, \ \xi = \frac{x}{R}. \end{aligned} \quad (3)$$

Where, u_0, v_0, w_0 is the linear displacement in the mean surface, respectively; u_1, v_1, w_1 - the midplane rotations of the normal; u_2, v_2, w_2 - high order straight displacements; u_3, v_3 - high order angle displacement component. Analysis of displacement field as a total (2) allows studying stress–strain state of cylindrical shell taking into account the effect of high order shear deformation and transverse-normal stress.

Strain of cylindrical shell FGM is determined by the following formulas (4) (Reddy, 2004):

$$\begin{aligned} \varepsilon_\xi &= \frac{1}{R}\left(\frac{\partial u}{\partial \xi}\right), \ \varepsilon_\theta = \frac{1}{R+z}\left(\frac{\partial u}{\partial \theta} + w\right) \\ \gamma_{\xi\theta} &= \frac{1}{R+z}\left(\frac{\partial u}{\partial \theta}\right) + \frac{1}{R}\left(\frac{\partial v}{\partial \xi}\right), \\ \gamma_{\xi z} &= \frac{1}{R}\left(\frac{\partial w}{\partial \xi}\right) + \left(\frac{\partial u}{\partial z}\right), \\ \gamma_{\theta z} &= \frac{1}{R+z}\left(\frac{\partial w}{\partial \theta}\right) + \frac{\partial v}{\partial z} + \frac{v}{R+z}, \ \varepsilon_z = \frac{\partial w}{\partial z}. \end{aligned} \quad (4)$$

Shell stress is determined from the formula of Hooke's law (5) (Reddy, 2004):

$$\begin{aligned}
&\sigma_{\xi} = A_{11}\varepsilon_{\xi} + A_{12}\varepsilon_{\theta} + A_{13}\varepsilon_{z},\\
&\sigma_{\theta} = A_{21}\varepsilon_{\xi} + A_{22}\varepsilon_{\theta} + A_{23}\varepsilon_{z},\\
&\sigma_{z} = A_{31}\varepsilon_{\xi} + A_{32}\varepsilon_{\theta} + A_{33}\varepsilon_{z},\\
&\tau_{\xi\theta} = A_{44}\gamma_{\xi\theta},\ \tau_{\xi z} = A_{55}\gamma_{\xi z},\ \tau_{\theta z} = A_{66}\gamma_{\theta z}.
\end{aligned} \tag{5}$$

Where, $A_{ij}(i=1,2,3,\ j=1,2,3)$, A_{44}, A_{55}, A_{66} are the conversion constants of the shell material and are determined as follows (Santos, 2009):

$$\begin{aligned}
&A_{11} = A_{22} = A_{33} = \frac{E(z)\left[1-\mu(z)\right]}{\left[1+\mu(z)\right]\left[1-2\mu(z)\right]},\\
&A_{44} = A_{55} = A_{66} = \frac{E(z)}{2\left[1+\mu(z)\right]},\\
&A_{12} = A_{21} = A_{13} = A_{31} = A_{23} = A_{32} =\\
&= \frac{E(z)\mu(z)}{\left[1+\mu(z)\right]\left[1-2\mu(z)\right]}.
\end{aligned} \tag{6}$$

Building system of equations of equilibrium, we apply the Lagrange variational principle (Reddy, 2004):

$$\begin{aligned}
&\iiint\left(\sigma_{\xi}\delta\varepsilon_{\xi} + \sigma_{\theta}\delta\varepsilon_{\theta} + \sigma_{z}\delta\varepsilon_{z} + \tau_{\xi\theta}\delta\gamma_{\xi\theta} +\right.\\
&\left.+\tau_{\xi z}\delta\gamma_{\xi z} + \tau_{\theta z}\delta\gamma_{\theta z}\right)R(R+z)d\xi d\theta dz -\\
&-\iint\left(q(\xi,\theta)\right)\left(\delta \mathrm{w}(\xi,\theta,h)\right)\left(R(R+z)\right)d\xi d\theta =\\
&=0.
\end{aligned} \tag{7}$$

Substituting (3), (4) and (5) into (7), performing simple transformations yields a system of equilibrium equations:

$$\begin{aligned}
&\frac{\partial N_{\xi}}{\partial\xi} + \frac{\partial N_{\theta\xi}}{\partial\theta} = 0,\\
&\frac{\partial N_{\theta}}{\partial\theta} + \frac{\partial N_{\xi\theta}}{\partial\xi} + Q_{\theta} = 0,\\
&\frac{\partial Q_{\xi}}{\partial\xi} + \frac{\partial Q_{\theta}}{\partial\theta} - N_{\theta} + \left(R+h\right)q = 0,\\
&\frac{\partial M_{\xi}}{\partial\xi} + \frac{\partial M_{\theta\xi}}{\partial\theta} - RQ_{\xi} = 0,\\
&\frac{\partial M_{\xi\theta}}{\partial\xi} + \frac{\partial M_{\theta}}{\partial\theta} - Q_{\theta} = 0,\\
&\frac{\partial S_{\xi}}{\partial\xi} + \frac{\partial S_{\theta}}{\partial\theta} - M_{\theta} - RQ_{z} + \left(R+h\right)hq = 0,\\
&\frac{\partial N^{*}_{\xi}}{\partial\xi} + \frac{\partial N^{*}_{\theta\xi}}{\partial\theta} - S_{\xi}R = 0,\\
&\frac{\partial N^{*}_{\xi\theta}}{\partial\xi} + \frac{\partial N^{*}_{\theta}}{\partial\theta} - RS_{\theta} - Q^{*}_{\theta} = 0\\
&\frac{\partial Q^{*}_{\xi}}{\partial\xi} + \frac{\partial Q^{*}_{\theta}}{\partial\theta} - N^{*}_{\theta} - RS_{z} + \left(R+h\right)\frac{h^{2}}{2}q = 0\\
&\frac{\partial M^{*}_{\xi}}{\partial\xi} + \frac{\partial M^{*}_{\theta\xi}}{\partial\theta} - RQ^{*}_{\xi} = 0\\
&\frac{\partial M^{*}_{\xi\theta}}{\partial\xi} + \frac{\partial M^{*}_{\theta}}{\partial\theta} - RQ^{*}_{\theta} - 2S^{*}_{\theta} = 0.
\end{aligned} \tag{8}$$

In equation system (8), we use the following extrapolation symbols:

$$\begin{aligned}
&\left(N_{\xi}, N_{\xi\theta}, Q_{\xi}, Q_{z}\right) = \int_{-h}^{+h}\left(\sigma_{\xi}, \tau_{\xi\theta}, \tau_{\xi z}, \sigma_{z}\right)\left(1+\frac{z}{R}\right)dz,\\
&\left(M_{\xi}, M_{\xi\theta}, S_{\xi}, S_{z}\right) = \int_{-h}^{+h}\left(\sigma_{\xi}, \tau_{\xi\theta}, \tau_{\xi z}, \sigma_{z}\right)\left(1+\frac{z}{R}\right)zdz,\\
&\left(N^{*}_{\xi}, N^{*}_{\xi\theta}, Q^{*}_{\xi}\right) = \int_{-h}^{+h}\left(\sigma_{\xi}, \tau_{\xi\theta}, \tau_{\xi z}\right)\left(1+\frac{z}{R}\right)\frac{z^{2}}{2}dz,\\
&\left(M^{*}_{\xi}, M^{*}_{\xi\theta}\right) = \int_{-h}^{+h}\left(\sigma_{\xi}, \tau_{\xi\theta}\right)\left(1+\frac{z}{R}\right)\frac{z^{3}}{3!}dz,\\
&\left(N_{\theta\xi}, N_{\theta}, Q_{\theta}\right) = \int_{-h}^{+h}\left(\tau_{\xi\theta}, \sigma_{\theta}, \tau_{\theta z}\right)dz,\\
&\left(M_{\theta\xi}, M_{\theta}, S_{\theta}\right) = \int_{-h}^{+h}\left(\tau_{\xi\theta}, \sigma_{\theta}, \tau_{\theta z}\right)zdz,\\
&\left(N^{*}_{\theta\xi}, N^{*}_{\theta}, Q^{*}_{\theta}\right) = \int_{-h}^{+h}\left(\tau_{\xi\theta}, \sigma_{\theta}, \tau_{\theta z}\right)\frac{z^{2}}{2}dz,\\
&\left(M^{*}_{\theta\xi}, M^{*}_{\theta}, S^{*}_{\theta}\right) = \int_{-h}^{+h}\left(\tau_{\xi\theta}, \sigma_{\theta}, \tau_{\theta z}\right)\frac{z^{3}}{3!}dz.
\end{aligned}$$

Equation system of equations (8) is rewritten in terms of displacement (9):

$$\begin{aligned}
&\sum_{n=0}^{3}\left(K_{1n}^{m}u_n+K_{1n,11}^{m}\frac{\partial^2 u_n}{\partial\xi^2}+K_{1n,22}^{m}\frac{\partial^2 u_n}{\partial\theta^2}\right)+\\
&+\sum_{n=0}^{3}K_{2n,12}^{m}\frac{\partial^2 v_n}{\partial\xi\partial\theta}+\sum_{n=0}^{2}K_{3n,1}^{m}\frac{\partial w_n}{\partial\xi}=0,\\
&\sum_{n=0}^{3}K_{1n,12}^{i}\frac{\partial^2 u_n}{\partial\xi\partial\theta}+\sum_{n=0}^{3}\left(K_{2n}^{i}v_n+K_{2n,11}^{i}\frac{\partial^2 v_n}{\partial\xi^2}+\right.\\
&\left.+K_{2n,22}^{i}\frac{\partial^2 v_n}{\partial\theta^2}\right)+\sum_{n=0}^{2}K_{3n,2}^{i}\frac{\partial w_n}{\partial\theta}=0,\\
&\sum_{n=0}^{3}K_{1n,1}^{j}\frac{\partial}{\partial\xi}u_n+\sum_{n=0}^{2}\left(K_{3n}^{j}+K_{3n,11}^{j}\frac{\partial^2}{\partial\xi^2}+\right.\\
&\left.+K_{3n,22}^{j}\frac{\partial^2}{\partial\theta^2}\right)w_n+\sum_{n=0}^{3}K_{2n,2}^{j}\frac{\partial}{\partial\theta}v_n=K_{43}^{j}q,
\end{aligned}\tag{9}$$

$m=1,\,2,\,3,\,4;\;\; i=5,\,6,\,7,\,8;\;\; j=9\,,10,11.$

Where, the K coefficients depend on the material and geometry parameters of the cylindrical shell FGM. Due to the cumbersome nature of the expressions defining K coefficients, this paper does not present the framework for determining these coefficients.

3. The Navier Solution

In this section, we study analytic solutions for the case of a simply supported cylindrical shell using Navier technique. The displacement components u_0, u_1, u_2, u_3, v_0, v_1, v_2, v_3, w_0, w_1, w_2 and external forces q are analysed in series of trigonometric series. The selected trigonometric functions are those that satisfy the simply supported boundary condition. In order to obtain the algebraic expressions that relate between displacement components and give coefficients, we replace the equations of analysis of displacement and external forces according to double trigonometric series into equations (9).

The simply supported boundary conditions for cylinder shells is written in the following form:

$$\begin{aligned}
&N_{\xi}(0,\theta)=N_{\xi}(L/R,\theta)=0,\\
&M_{\xi}(0,\theta)=M_{\xi}(L/R,\theta)=0,\\
&N_{\xi}^{*}(0,\theta)=N_{\xi}^{*}(L/R,\theta)=0,\\
&M_{\xi}^{*}(0,\theta)=M_{\xi}^{*}(L/R,\theta)=0,\\
&v_i(0,\theta)=v_i(L/R,\theta)=0,\;\; i=0,1,2,3,\\
&w_j(0,\theta)=w_j(L/R,\theta)=0,\;\; j=0,1,2,\\
&N_{\theta}(\xi,0)=N_{\theta}(\xi,b/R)=0,\\
&M_{\theta}(\xi,0)=M_{\theta}(\xi,b/R)=0,\\
&N_{\theta}^{*}(\xi,0)=N_{\theta}^{*}(\xi,b/R)=0,\\
&M_{\theta}^{*}(\xi,0)=M_{\theta}^{*}(\xi,b/R)=0,\\
&u_i(\xi,0)=u_i(\xi,b/R)=0,\;\; i=0,1,2,3,\\
&w_j(\xi,0)=w_j(\xi,b/R)=0,\;\; j=0,1,2.
\end{aligned}\tag{10}$$

Analysis of load, displacement by dual trigonometric series:

$$\begin{aligned}
u_i&=\sum_{r=1}^{\infty}\sum_{s=1}^{\infty}U_{rs}^{i}\sin\beta\theta\cos\alpha\xi,\\
v_i&=\sum_{r=1}^{\infty}\sum_{s=1}^{\infty}V_{rs}^{i}\cos\beta\theta\sin\alpha\xi,\\
w_j&=\sum_{r=1}^{\infty}\sum_{s=1}^{\infty}W_{rs}^{j}\sin\beta\theta\sin\alpha\xi,\\
q&=\sum_{r=1}^{\infty}\sum_{s=1}^{\infty}Q_{rs}\sin\beta\theta\sin\alpha\xi,\\
\alpha&=\frac{r\pi}{L/R},\;\; s=\frac{m\pi}{b/R}.
\end{aligned}\tag{11}$$

Obviously, the expansion (11) perfectly satisfies the boundary conditions (10).

Substituting (10) into (9) and performing some basic transformations gives us a system of algebraic equations for U_{rs}^{i}, V_{rs}^{i}, W_{rs}^{j} coefficients:

$$\begin{aligned}
&\sum_{n=0}^{3}\left(K_{1n}^{m}U_{rs}^{n}-\alpha^2K_{1n,11}^{m}U_{rs}^{n}-\beta^2K_{1n,22}^{m}U_{rs}^{n}\right)+\\
&-\alpha\beta\sum_{n=0}^{3}K_{2n,12}^{m}V_{rs}^{n}+\alpha\sum_{n=0}^{2}K_{3n,1}^{m}W_{rs}^{n}=0,\\
&-\alpha\beta\sum_{n=0}^{3}K_{1n,12}^{i}U_{rs}^{n}+\sum_{n=0}^{3}\left(K_{2n}^{i}V_{rs}^{n}-\alpha^2K_{2n,11}^{i}V_{rs}^{n}+\right.\\
&\left.-\beta^2K_{2n,22}^{i}V_{rs}^{n}\right)+\beta\sum_{n=0}^{2}K_{3n,2}^{i}W_{rs}^{n}=0,\\
&-\alpha\sum_{n=0}^{3}K_{1n,1}^{j}U_{rs}^{n}+\sum_{n=0}^{2}\left(K_{3n}^{j}W_{rs}^{n}-\alpha^2K_{3n,11}^{j}W_{rs}^{n}+\right.
\end{aligned}\tag{12}$$

$$-\beta^2 K^j_{3n,22} W^n_{rs}\Big) - \beta \sum_{n=0}^{3} K^j_{2n,2} V^n_{rs} = K^j_{43} Q_{rs},$$

$m = 1, 2, 3, 4;\ \ i = 5, 6, 7, 8;\ \ j = 9, 10, 11.$

Solving the system of equations (12), we get the coefficients U^i_{rs}, V^i_{rs}, W^j_{rs}, continue to change these factors into (11) to determine the displacements u_i, v_i $(i = 0, 1, 2, 3)$, w_j $(j = 0, 1, 2)$. From the geometric equations (4), we find the strains ε_ξ, ε_θ, ε_z, $\gamma_{\xi\theta}$, $\gamma_{\xi z}$ and $\gamma_{\theta z}$. Next, use the three expressions σ_ξ, σ_θ and $\tau_{\xi\theta}$ of (5) to determine the membrane stresses σ_ξ, σ_θ and $\tau_{\xi\theta}$. The stress components are determined, when using the equilibrium equations of spatial elasticity theory:

$$\sigma_{\xi z} = -\frac{1}{R+z}\int_{-h}^{z}\left[\left(1+\frac{z}{R}\right)\frac{\partial \sigma_\xi}{\partial \xi} + \frac{\partial \tau_{\xi\theta}}{\partial \theta}\right]dz$$

$$\sigma_{\theta z} = -\frac{R}{(R+z)^2}\int_{-h}^{z}\left[\left(1+\frac{z}{R}\right)\frac{\partial \sigma_\theta}{\partial \theta} + \left(1+\frac{z}{R}\right)^2\frac{\partial \tau_{\xi\theta}}{\partial \xi}\right]dz$$

$$\sigma_z = -\frac{1}{R+z}\int_{-h}^{z}\left[\left(1+\frac{z}{R}\right)\frac{\partial \sigma_{\xi z}}{\partial \xi} + \frac{\partial \sigma_{\theta z}}{\partial \theta} - \sigma_\theta\right]dz$$

4. Results and discussion

4.1. Validation of the model

For verification calculations, we choose the input parameters according to document (Brischetto, 2017), specifically as follows: the inner surface of the shell is metal with $\mu_m = 0.3$, $E_m = 70\ (GPa)$, and the outer surface is ceramic with $\mu_c = 0.3$, $E_c = 380\ (GPa)$. The shell has a radius $R = 10\ (m)$ (m), length $L = \pi R/3$ (m), width $b = 1\ (m)$. Shell is affected by the harmonic load $q = \sin\beta\theta \sin\alpha\xi$, $m = 1$, $n = 1$. Result of comparative calculations between quasi-3D theory used in this work with the exact solution using elastic theory 3D (Brischetto, 2017) is presented in Table 1. Calculation results are performed with shells with different h/R relative thickness and different η material distribution coefficients. The relative deflection value $\bar{w} = w \times 10^{10}$ is calculated in the middle position of the shell at $z = 0$.

Table 1. the deflection $\bar{w} = w \times 10^{10}$ of the cylindrical shell FGM at the middle position.

$2h/R$	Exact solution 3D (Brischetto, 2017)	Present	Error
	$\eta = 1$		
1/100	5,2783	5,9959	13,60%
1/10	0,017	0,0181	6,47%
	$\eta = 4$		
1/100	7,9738	8,9171	11,83%
1/10	0,0314	0,0343	9,24%
	$\eta = 10$		
1/100	9,2029	10,1298	10,07%
1/10	0,0404	0,0447	10,64%

Analyzing the data in Table 1, it can be concluded that the calculation model used in this work gives the calculation results quite consistent with the exact solution according to the 3D elastic theory.

4.2. Investigate the effect of shell thickness

The displacements and stresses are given in the following no-dimensional forms (Brischetto, 2017):

$$\bar{w} = \frac{10^4 E_m w}{Q_{rs} h S^4};\ \{\bar{\sigma}_\xi, \bar{\sigma}_\theta\} = \frac{10^2\{\sigma_\xi, \sigma_\theta\}}{Q_{rs} S^2};$$

$$\bar{\sigma}_z = \sigma_z;\ \bar{\tau}_{\xi z} = \frac{10^2 \tau_{\xi z}}{Q_{rs} S};$$

First, with the data as given in Section 4.1, survey the graph of deflection in shell length (Figure 3), at $\theta = b/(2R)$. Stress state ($\bar{\sigma}_\xi$, $\bar{\sigma}_\theta$, $\bar{\sigma}_z$, $\bar{\tau}_{\xi z}$) in shell thickness at $\xi = L/(2R)$, $\theta = b/(2R)$ (Figure 4).

When surveying with the change of the shell thickness we get the maximum value of the stress at $\xi = L/(2R)$, $\theta = b/(2R)$ and the deflection ($\bar{w} = w \times 10^{10}$) of the shell at $\theta = b/(2R)$ (Table 2).

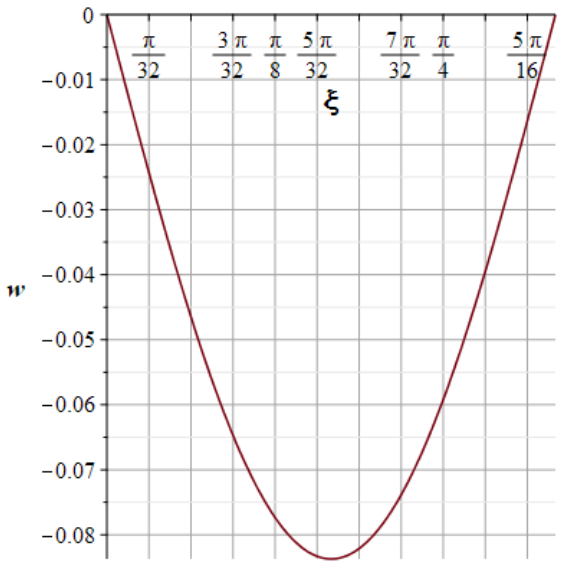

Figure 3. The deflection $\bar{w}$ of cylindrical shell with length.

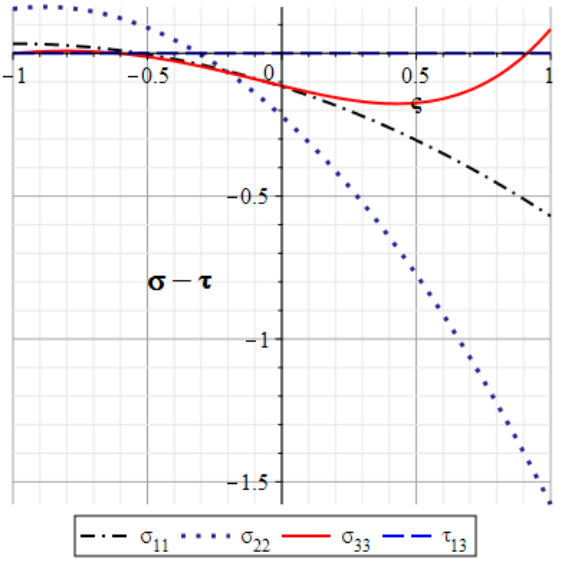

Figure 4. Stress state according to shell thickness at $\xi = L/(2R)$, $\theta = b/(2R)$.

Table 2. Maximum stress and deflection at $\xi = L/(2R)$, $\theta = b/(2R)$ when thickness changes.

$2h/R$	$-\bar{\sigma}_\xi$	$-\bar{\sigma}_\theta$	$-\bar{\sigma}_z$	$-\bar{w}$
1/20	0.6826	1.6501	0.2000	0.0743
1/50	0.5315	1.4674	0.2451	0.8043
1/100	0.5700	1.5785	0.1762	5.9959
1/200	0.6931	1.8665	0.1664	47.0114
1/400	0.9510	2.4603	1.1565	373.8264

Comment: When the thickness of cylindrical shell changes, the stress state and deflection both change and increase with decreasing thickness. In which stress $\bar{\sigma}_z$ and deflection $\bar{w}$ have rapid changes, especially deflection.

4.3. Investigate the effect of shell length

Surveying with the change of the shell length we get the maximum value of the stress at $\xi = L/(2R)$, $\theta = b/(2R)$ and the deflection ($\bar{w} = w \times 10^{10}$) of the shell at $\theta = b/(2R)$ (Table 3).

Table 3. Maximum stress and deflection at $\xi = L/(2R)$, $\theta = b/(2R)$ when length varies.

L/R	$-\bar{\sigma}_\xi$	$-\bar{\sigma}_\theta$	$-\bar{\sigma}_z$	$-\bar{w}$
1/2	0.5710	1.4969	0.1684	5.6474
1	0.5701	1.5761	0.1759	5.9855
4	0.5693	1.6021	0.1786	6.0972
10	0.5692	1.6036	0.1788	6.1035
20	0.5692	1.6038	0.1788	6.1044

Comment: When the cylindrical shell length changes, the stress and deflection status both change and increase as the length increases. However, the change of the values is not much.

4.4. Investigate the effect of material volume distribution coefficient

Surveying with the change of material distribution coefficient η, we get the maximum value of stress at $\xi = L/(2R)$, $\theta = b/(2R)$ and deflection ($\bar{w} = w \times 10^{10}$) of shell at $\theta = b/(2R)$ (Table 4).

Table 4. Maximum stress and deflection at $\xi = L/(2R)$, $\theta = b/(2R)$ when η varies.

η	$-\bar{\sigma}_\xi$	$-\bar{\sigma}_\theta$	$-\bar{\sigma}_z$	$-\bar{w}$
0,02	0.2621	0.7732	0.3867	3.0552
0,1	0.2885	0.8434	0.3490	3.3150

0,2	0.3221	0.9325	0.3098	3.6429
0,5	0.4225	1.1962	0.2315	4.6078
1	0.5700	1.5785	0.1762	5.9959
2	0.7544	2.0503	0.1618	7.7058
5	0.8983	2.4351	0.1873	9.1962
10	0.9591	2.6435	0.2161	10.1299
50	1.1792	3.4058	0.3288	13.3707

Comment: The material coefficient (η) changes, the stress state and deflection both change and increase with increasing η and its values increase steadily. This is appropriate, because as η increases, the metal component increases, the hardness of FGM cylindrical shell will decrease.

5. Conclude

Based on theoretical research and numerical simulations, some major conclusions can be drawn:

- The paper presented theoretical basis and numerical analysis in calculating FGM cylindrical shell based on the theory of quasi-3D high shear strain theory. The Navier solution is used to analyze the problem with simply supported boundary conditions. The authenticity of the method when comparing results with the exact solution of Brischetto 3D elastic theory.

- Results of survey with changes in thickness, length and distribution of materials show that the stress and deflection status of the FGM cylindrical shell also varies. Especially when changing the thickness of the shell leads to a very rapid change with deflection and a large change of the horizontal stress $\bar{\sigma}_z$. This gives recommendations for structures use thin case.

References

Trần Văn Hùng, Trần Ngọc Đoàn, et al. (2019). Phân tích trạng thái ứng suất của vỏ trụ FGM với các điều kiện biên khác nhau trên cơ sở lý thuyết biến dạng trượt bậc cao kiểu quasi - 3D. *Hội nghị Cơ học kỹ thuật toàn quốc, Kỷ niệm 40 năm thành lập Việc Cơ học*, Tr.167-174.

Brischetto, Salvatore. (2017). A general exact elastic shell solution for bending analysis of functionally graded structures. *Composite Structures, 175*, 70-85. doi:10.1016/j.compstruct.2017.04.002

Firsanov VV, & TN Doan. (2015). Investigation of the statics and free vibrations of cylindrical shells on the basis of a nonclassical theory. *Composites: Mechanics, Computations, Applications: An International Journal, 6*(2), 135-166.

Firsanov VV, & TN Doan. (2014). Natural oscillations of general shells based on nonclassical theory. *Journal of Machinery Manufacture and Reliability, 43*(5), 349-357.

Kadoli, Ravikiran, & Ganesan, N. (2006). Buckling and free vibration analysis of functionally graded cylindrical shells subjected to a temperature-specified boundary condition. *Journal of Sound and Vibration, 289*(3), 450-480. doi:10.1016/j.jsv.2005.02.034

Kirchhoff, VG. (1850). Uber das gleichgewicht und die bewegung einer elastischen scheibe. *Journal für die reine und angewandte Mathematik, 1850*(40), 51–88. doi:https://doi.org/10.1515/crll.1850.40.51.

Mindlin, RD. (1951). Influence of rotatory inertia and shear on flexural motions of isotropic, elastic plates. *Journal of Applied Mechanics, 1*(18), 31-38.

Reddy, JN. (2004). *Mechanics of laminated composite plates and shells: theory and analysis* (2 Ed.): CRC press.

Reddy, JN. (1984). A simple higher-order theory for laminated composite plates. *Journal of Applied Mechanics, 51*(4), 745-752.

H, Santos, Mota Soares, Cristóvão M, et al. (2009). A semi-analytical finite element model for the analysis of cylindrical shells made of functionally graded materials. *Composite Structures, 91*(4), 427-432. doi:10.1016/j.compstruct.2009.04.008

Shen, Hui-Shen. (2009). *Functionally Graded Materials. Nonlinear Analysis of Plates and Shells*: CRC Press.

The 5th International Conference on Engineering Mechanics and Automation (ICEMA 5)
Hanoi, October 11÷12, 2019

Nonlinear dynamic response analysis of porous graphene platelet-reinforced composite sandwich shallow spherical shells

Vu Thi Huong[a], Pham Dinh Nguyen[a], Vu Thi Thuy Anh[a] and Nguyen Dinh Duc[a,b]

[a] *Advanced Materials and Structures Laboratory, VNU-Hanoi - University of Engineering and Technology (UET), 144 - Xuan Thuy - Cau Giay - Hanoi - Vietnam. nguyenpd@vnu.edu.vn*

[b] *Infrastructure Engineering Program - VNU-Hanoi, Vietnam Japan University (VJU),*

My Dinh 1 - Tu Liem - Hanoi - Vietnam. ducnd@vnu.edu.vn

Abstract

This paper presents the results of the nonlinear dynamic behavior and natural frequencies of porous graphene platelet-reinforced composite (P-GPL-RC) sandwich shallow spherical shells supported by elastic foundations. The composite shallow spherical shell is considered with three layers: isotropic layer – P-GPL-RC layer – isotropic layer. The formulations of the shallow spherical shell are derived according to the first-order shear deformation shell theory in conjunction with von Kármán geometrical nonlinearity. The nonlinear equations are solved by Galerkin method and Runge-Kutta method. The material properties are determined by the modified Halpin-Tsai model and rule of mixtures. The porosity distributions and graphene platelet patterns are presented. In numerical results, the influences of geometrical parameters, elastic foundations and weight fractions on the nonlinear dynamic response of porous graphene platelet-reinforced composite sandwich shallow spherical shells are investigated.

Key Words: Dynamic response analysis, shallow spherical shell, graphene platelet-reinforced composite.

1. Introduction

Porosity is one of the problems in composite manufacturing which appears due to the difference of component materials. The presence of porosity decreases the stiffness of composite materials leads to the load capacity of composite structures to become lower. There are some studies that analyze the effect of porosity on the static and dynamic response of various structures made of functionally graded materials, such as beams (Tuyen, 2001; Liu et al., 2019), plates (Saidi et al., 2019; Cong et al., 2018; Xue et al., 2019; Chen et al., 2019), shells (Nam et al., 2019; Li et al., 2019).

Sandwich structures are light materials that composed of two thin facesheets and one moderately thick core layer. In these structures, reinforcing phases always have the high strength and stiffness, especially, carbon fiber, carbon nanotubes (CNTs), graphene platelets (GPLs), and so on. Thanks to precious mechanical properties, these structures are applied in aeronautics, road vehicles, ships, and civil engineering. In recent years, many researchers propose to analyze the effect of CNTs and GPLs reinforcements on the porous sandwich plates and shells. The results of thermoelastic

behavior, vibration, and dynamic response of porous sandwich plates were reported in (Safaei et al., 2019; Gao et al., 2018; Li et al., 2018). In (Setoodeh et al., 2019; Karimiasl et al., 2019) investigated the free and forced vibration of sandwich doubly curved shells.

This paper aims to study the nonlinear dynamic response and free vibraion of P-GPL-RC sandwich shallow spherical shells based on FSDT with the results of the natural frequencies and the deflection-time curve of P-GPL-RC sandwich shallow spherical shells are considered in a narrow examination.

2. Graphene platelet-reinforced sandwich-structured composite shallow spherical shells

Consider the graphene-reinforced sandwich-structured composite shallow spherical shell consists of three layers, in which two isotropic homogeneous facesheets which have the thickness presented as h_f, a P-GPL-RC core layer with the thickness h_c. The total thickness of the shell is $h = h_c + 2h_f$.

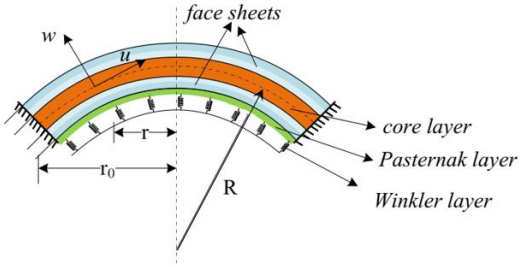

Figue 1. Cross-sectional model and coordinate system of the shallow spherical shell.

The elastic modulus of the core layer are estimated through the Halpin-Tsai model follows as (Villoria and Miravete, 2007):

$$E_1 = \frac{3}{8}\left(\frac{1+\xi_L\eta_L V_G}{1-\eta_L V_G}\right)E_m + \frac{5}{8}\left(\frac{1+\xi_T\eta_T V_G}{1-\eta_T V_G}\right)E_m,$$
$$\eta_L = \frac{E_G/E_m - 1}{E_G/E_m + \xi_L}, \quad \eta_T = \frac{E_G/E_m - 1}{E_G/E_m + \xi_T}, \tag{1}$$
$$\xi_L = 2\left(a_G/h_G\right), \quad \xi_T = 2\left(b_G/h_G\right).$$

where, the subscript "$_G$" and "$_m$" represent GPLs and matrix, respectively. a_G, b_G, h_G represent the length, width, and thickness of GPs, respectively.

The mass density, Poisson's ratio of the core layer are calculated by applying the rule of mixture:

$$\rho_1 = \rho_G V_G + \rho_m V_m,$$
$$\nu_1 = \nu_G V_G + \nu_m V_m. \tag{2}$$

The material properties of the porous core layer are shown as (Li et al., 2018):

$$E(z) = E_1\left[1 - e_0\lambda(z)\right],$$
$$\rho(z) = \rho_1\left[1 - e_m\lambda(z)\right]. \tag{3}$$

where e_0 denotes the cofficient of porosity, $e_m = 1 - \sqrt{1-e_0}$ is the mass density cofficient.

The porous distribution function $\lambda(z)$ can be determined as:

$$\lambda(z) = \begin{cases} \cos\left(\dfrac{\pi z}{h}\right) & \text{Type 1} \\ \cos\left(\dfrac{\pi z}{2h} + \dfrac{\pi}{4}\right) & \text{Type 2} \\ \lambda & \text{Type 3} \end{cases} \tag{4}$$

in which, Type 1: non-uniform symmetric porosity distribution, Type 2: Non-uniform asymmetric porosity distribution, Type 3: uniform distribution,

$$\lambda = \frac{1}{e_0} - \frac{1}{e_0}\left(\frac{2}{\pi}\sqrt{1-e_0} - \frac{2}{\pi} + 1\right)^2.$$

The relationship between V_G and Λ_{GPL} is determined as:

$$V_G^* \int_{-h/2}^{h/2}\left[1 - e_m\lambda(z)\right]dz = \int_{-h/2}^{h/2} V_G\left[1 - e_m\lambda(z)\right]dz,$$
$$V_G^* = \frac{\Lambda_{GPL}}{\Lambda_{GPL} + \left(\rho_G/\rho_m\right) - \left(\rho_G/\rho_m\right)\Lambda_{GPL}} \tag{5}$$

with V_G, Λ_{GPL} are the volume and weight fractions of GPLs, respectively.

3. Theoretical formulations

Based on the geometric nonlinear assumption of Von Kármán and FSDT, the strain components are taken as (Xu, 1991):

$$\varepsilon_r = \varepsilon_r^0 + z\chi_r, \varepsilon_\theta = \varepsilon_\theta^0 + z\chi_\theta, \varepsilon_{rz} = \psi + \frac{\partial w}{\partial r}. \quad (6)$$

where

$$\varepsilon_r^0 = \frac{\partial u}{\partial r} - \frac{w}{R} + \frac{1}{2}\frac{\partial^2 w}{\partial r^2}, \varepsilon_\theta^0 = \frac{u}{r} - \frac{w}{R},$$
$$\chi_r = \frac{\partial \psi}{\partial r}, \chi_\theta = \frac{\psi}{r}.$$

in which ε_r^0 and ε_θ^0 are normal strains components, $\gamma_{r\theta}^0$ is the shear strain in the middle surface of the shell and $\chi_r, \chi_\theta, \chi_{r\theta}$ are curved and twisted ingredients.

Hooke's law for P-GPL-RC sandwich shallow spherical shells:

$$\begin{Bmatrix} \sigma_r \\ \sigma_\theta \\ \sigma_{rz} \end{Bmatrix}^{(k)} = \begin{bmatrix} Q_{11} & Q_{12} & 0 \\ Q_{12} & Q_{22} & 0 \\ 0 & 0 & Q_{66} \end{bmatrix}^{(k)} \begin{Bmatrix} \varepsilon_r \\ \varepsilon_\theta \\ \varepsilon_{rz} \end{Bmatrix}^{(k)} \quad (7)$$

where the superscript $k(k = f, c)$ represents the face and core layers,

$$Q_{11}^{(k)} = \frac{E(z)^{(k)}}{1 - \nu^{(k)}\nu^{(k)}} = Q_{22}^{(k)}, Q_{12}^{(k)} = \frac{\nu^{(k)} E(z)^{(k)}}{1 - \nu^{(k)}\nu^{(k)}},$$

$$Q_{66}^{(k)} = G_{12}^{(k)} = \frac{E(z)^{(k)}}{2\left(1 + \nu^{(k)}\right)}.$$

The force and moment fields of the shell can be defined as:

$$(N_i, M_i) = \int_{-\frac{h_c}{2} - h_f}^{-\frac{h_c}{2}} \sigma_i^f(1, z)dz + \int_{-\frac{h_c}{2}}^{\frac{h_c}{2}} \sigma_i^c(1, z)dz + \int_{\frac{h_c}{2}}^{\frac{h_c}{2} + h_f} \sigma_i^f(1, z)dz \ \{i = r, \theta, rz\} \quad (8)$$

$$Q_r = K\left(\int_{-\frac{h_c}{2} - h_f}^{-\frac{h_c}{2}} \sigma_{rz}^f dz + \int_{-\frac{h_c}{2}}^{\frac{h_c}{2}} \sigma_{rz}^c dz + \int_{\frac{h_c}{2}}^{\frac{h_c}{2} + h_f} \sigma_{rz}^f dz \right)$$

Substituting Eqs. (7) into Eqs. (8), the forces and moments of P-GPL-RC sandwich shallow spherical shells can be expressed:

$$\begin{Bmatrix} N_r \\ N_\theta \\ M_r \\ M_\theta \end{Bmatrix} = \begin{bmatrix} A_{11} & A_{12} & B_{11} & B_{12} \\ A_{12} & A_{11} & B_{12} & B_{11} \\ B_{11} & B_{12} & D_{11} & D_{12} \\ B_{12} & B_{11} & D_{12} & D_{11} \end{bmatrix} \begin{Bmatrix} \varepsilon_r^0 \\ \varepsilon_\theta^0 \\ \chi_r \\ \chi_\theta \end{Bmatrix}, \quad (9)$$

$$Q_r = KA_{66}\left(\psi + \frac{\partial w}{\partial r}\right)$$

with

$$\left(A_{ij}, B_{ij}, D_{ij}\right) = \int_{-h_c/2 - h_f}^{-h_c/2} Q_{ij}^f(1, z, z^2)dz +$$

$$\int_{-h_c/2}^{h_c/2} Q_{ij}^c(1, z, z^2)dz + \int_{h_c/2}^{h_c/2 + h_f} Q_{ij}^f(1, z, z^2)dz, i, j = 1, 2, 6.$$

According to FSDT, the motion equations of P-GPL-RC sandwich shallow spherical shells as (Li et al., 2003):

$$\frac{\partial(rN_r)}{r\partial r} - \frac{N_\theta}{r} = I_0\frac{\partial^2 u}{\partial t^2} + I_1\frac{\partial^2 \psi}{\partial t^2}, \quad (10a)$$

$$\frac{\partial(rM_r)}{r\partial r} - \frac{M_\theta}{r} - Q_r = I_2\frac{\partial^2 \psi}{\partial t^2} + I_1\frac{\partial^2 u}{\partial t^2}, \quad (10b)$$

$$\frac{\partial(rQ_r)}{r\partial r} + \frac{1}{R}\left(N_r + N_\theta\right) + \frac{\partial(rN_r\frac{\partial w}{\partial r})}{r\partial r} + q - k_1 w + k_2\Delta w = I_0\frac{\partial^2 w}{\partial t^2}. \quad (10c)$$

Airy's stress function $f(\mathrm{r}, \theta, t)$ can be defined by:

$$N_r = \frac{1}{r}\frac{\partial f}{\partial r}, \quad N_\theta = \frac{\partial^2 f}{\partial r^2} \quad (11)$$

The compatibility equation is represented in the form:

$$C_{10}\left(-\frac{\partial^4 f}{\partial r^4}-2\frac{\partial^3 f}{\partial r^3}+\frac{1}{r^2}\frac{\partial^2 f}{\partial r^2}-\frac{1}{r^3}\frac{\partial f}{\partial r}\right)$$
$$-C_{13}\frac{\partial^3 \psi}{\partial r^3}+\left(\frac{1}{r}C_{12}-C_{12}-\frac{2}{r}C_{13}\right)\frac{\partial^2 \psi}{\partial r^2} \quad (12)$$
$$+\left(C_{13}-2C_{12}\right)\frac{1}{r}\frac{\partial \psi}{\partial r}=\frac{1}{R}\Delta w+\frac{1}{r}\frac{\partial w}{\partial r}\frac{\partial^2 w}{\partial r^2}.$$
$$C_{10}=\frac{-A_{11}}{A_{12}^2-A_{11}^2},C_{11}=\frac{A_{12}}{A_{12}^2-A_{11}^2},C_{12}=\frac{A_{11}B_{11}-A_{12}B_{12}}{A_{12}^2+A_{11}^2},$$
$$C_{13}=\frac{A_{11}B_{12}-A_{12}B_{11}}{A_{12}^2+A_{11}^2},C_{14}=\frac{A_{12}-A_{11}}{A_{12}^2+A_{11}^2}.$$

4. Analytical Solution

The boundary condition and symmetrical condition of the shallow spherical shell are (Liu, 1991):

$$\begin{aligned} &r=0, \quad \psi=0 \\ &r=r_0, \quad \psi=0, w=0 \end{aligned} \quad (13)$$

The solutions of the shallow spherical shell, satisfying the boundary condition, is assumed to be:

$$w=W\frac{\left(r_0^2-r^2\right)^2}{r_0^4},\psi=\Phi\frac{r\left(r_0^2-r^2\right)}{r_0^3}, \quad (14)$$
$$f=F\frac{r\left(r_0-r\right)}{r_0^2}.$$

where $F=F_1W^2+F_2W+F_3\Phi$,

$$F_1=\left(-\frac{48r^7}{r_0^7C_{10}}+\frac{64r^5}{r_0^5C_{10}}-\frac{16r^3}{r_0^3C_{10}}\right),$$
$$\mathrm{F}_2=\left(-\frac{16r^5}{r_0^3RC_{10}}+\frac{8r^3}{r_0RC_{10}}\right),$$
$$F_3=\frac{\left(12C_{12}-3C_{13}\right)r^4}{r_0^2C_{10}}+\frac{\left(-6C_{12}+18C_{13}\right)r^3}{r_0^2C_{10}}+$$
$$\frac{\left(C_{13}-12C_{12}\right)r^2}{C_{10}}.$$

Substituting Eqs. (14), (9) into Eqs. (10) and applying Galerkin method, the nonlinear dynamic response governing equations of P-GPL-RC sandwich shallow spherical shells are obtained:

$$I_0\frac{\partial^2 W}{\partial t^2}=l_1W^3+l_2W^2+l_3W+l_4q \quad (15)$$

where $I_0,l_i\left(i=1-3\right)$ are given in the Appendix.

The natural frequencies of P-GPL-RC sandwich shallow spherical shells can be obtained from Eq. (15) without q:

$$\omega_{mn}=-l_3/I_0 \quad (16)$$

5. Numerical results

5.1. Comparison

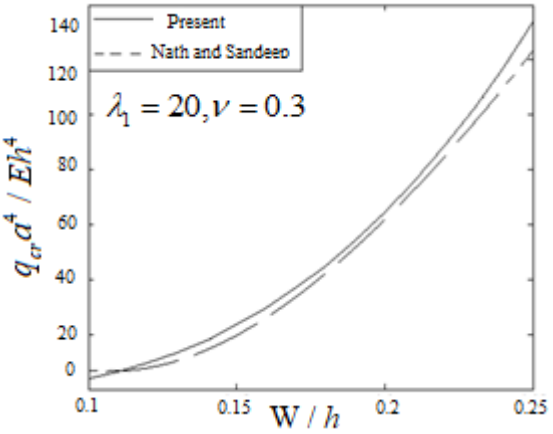

Figure 2. The comparison with results of Nath and Sandeep

To validate the present formulation, the relation of quantity $q_{cr}a^4/Eh^4$ in this study are considered with the results in Nath and Sandeep in the same conditions boundary and material. It is clear that there is no significant difference between two studies.

5.2. Natural frequency

Table 1 shows influences of elastic foundations, R/h ratio, and three types of porosity distribution on the natural frequencies of sandwich shallow spherical shells. It is clear that the value of the natural frequencies is significantly affected by these factors. The value of the natural frequencies increases when the stiffness of elastic foundations increases. In contrast, this figures decreases when R/h ratio increases. Furthermore, the value of the natural frequencies in the case Type 1 (non-uniform

symmetric porosity distribution) is the highest among three types.

Table 2 presents the results of the natural frequencies of P-GPL-RC sandwich shallow spherical shells. Overall, the natural friquencies are affected by the cofficient of porosity and r_0 / R ratio. The value of the natural friquencies descrease when the cofficient of porosity and r_0 / R ratio increase which means that the natural friquencies of P-GPL-RC sandwich shallow spherical shells is lower than that of the sandwich shallow spherical shell without porosity ($e_0 = 0$).

Table 1. Effect of the elastic foundations, R / h ratio, and porosity distribution on the natural frequencies $h_c / h = 0.8, r_0 / R = 0.3, e_0 = 0.3, \Lambda_{GPL} = 1\%$

(k_1, k_2)	R / h	**Type 1**	**Type 2**	**Type 3**
(0,0)	60	6726.6	6504.3	6647.0
	70	5379.7	5215.6	5324.4
	80	4473.0	4348.4	4432.9
(20,2)	60	8051.9	7867.2	7989.2
	70	6598.9	6465.9	6557.3
	80	5601.8	5502.8	5572.8
(40,4)	60	9188.0	9026.6	9136.2
	70	7625.7	7510.8	7592.5
	80	6538.5	6453.9	6516.3

Table 2. Effect of the cofficient of porosity and r_0 / R ratio on the free vibration of sandwich shallow spherical shells ($h_c / h = 0.8, R / h = 80, \Lambda_{GPL} = 1\%, \text{Type1}, k_1 = k_2 = 0$)

r_0 / R	$e_0 = 0$	$e_0 = 0.3$	$e_0 = 0.5$
0.3	4568.7	4473.0	4424.6
0.4	4020.9	3894.4	3817.1
0.5	3857.1	3720.0	3632.6

5.3. Dynamic response

Figure 3 presents the influence of r_0 / R ratio on the deflection-time curve of P-GPL-RC sandwich shallow spherical shells. Clearly, the amplitude of sandwich shallow spherical shells is considerably changed with three case of $r_0 / R = (0.3, 0.4, 0.5)$ ratio. The load capacity of sandwich shallow spherical shells decreases when r_0 / R ratio increases.

Figure 4 shows the cofficient of porosity on the deflection-time curve of P-GPL-RC sandwich shallow spherical shells. Clearly, the value of the amplitude of P-GPL-RC sandwich shallow spherical shells increases when the cofficient of porosity increases. Furthermore, the stiffness of P-GPL-RC sandwich shallow spherical shells ($e_0 = (0.3, 0.5)$) is lower than that of the sandwich shallow spherical shell without porosity ($e_0 = 0$).

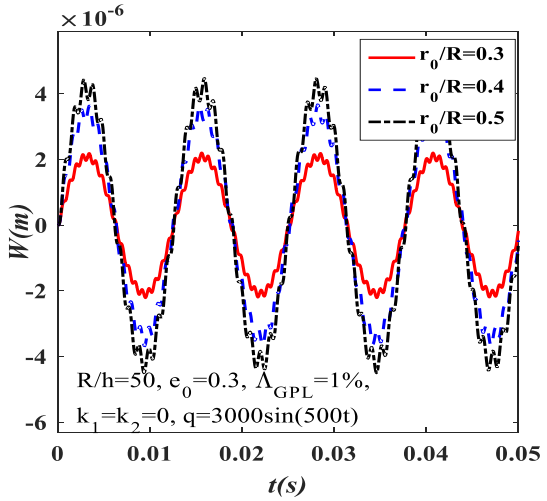

Figure 3. Effect of r_0 / R on the nonlinear dynamic response of P-GPL-RC sandwich shallow spherical shells.

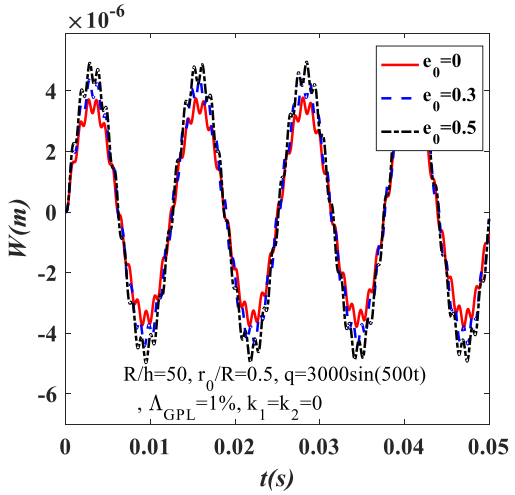

Figure 4. Effect of the cofficient of porosity on the nonlinear dynamic response of P-GPL-RC sandwich shallow spherical shells.

Figures 5 and 6 illustrate the effect of GPL's weight fractions on the nonlinear dynamic response of P-GPL-RC sandwich shallow spherical shells. Three various GPL weight fractions, which are $\Lambda_{GPL} = (0.3, 0.5, 1)\%$, are considered. The zoomed-in view of Figure 5 is shown in Figure 6. As can be seen, the deflection-time curve of P-GPL-RC sandwich shallow spherical shells is the highest in the case $\Lambda_{GPL} = 0.3\%$ and lowest in the case $\Lambda_{GPL} = 1\%$, that can understand that the load capacity of sandwich shallow spherical shells is improved by GPLs' reinforcement.

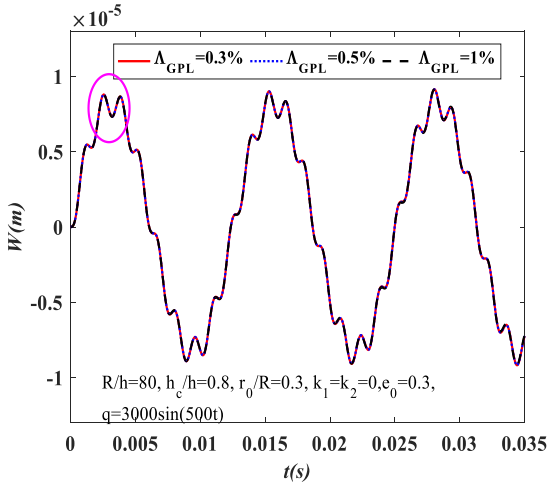

Figure 5. Effect of GPL's weight faction on the nonlinear dynamic response of P-GPL-RC sandwich shallow spherical shells.

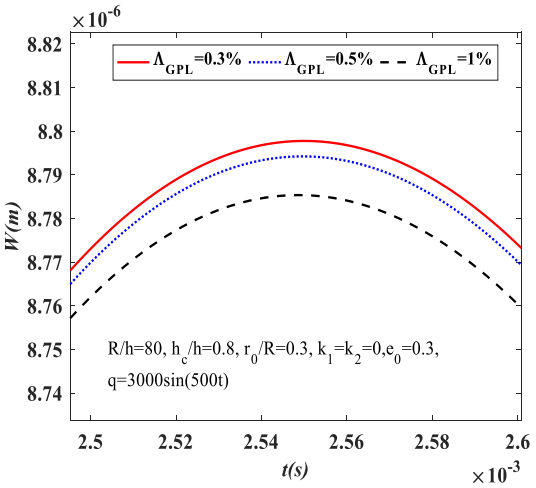

Figure 6. Zoomed-in view of Figure 5

Figure 7 describes the influence of various types of porosity distribution on the deflection-time curve of GPL-RC sandwich shallow spherical shells. The zoomed-in view of this figure is presented in Figure 7. In these figures, three types of porosity distribution are considered with non-uniform porosity distribution (Types 1 and 2) and uniform distribution (Type 3). The deflection-time curve is changed by different types of porosity distribution.

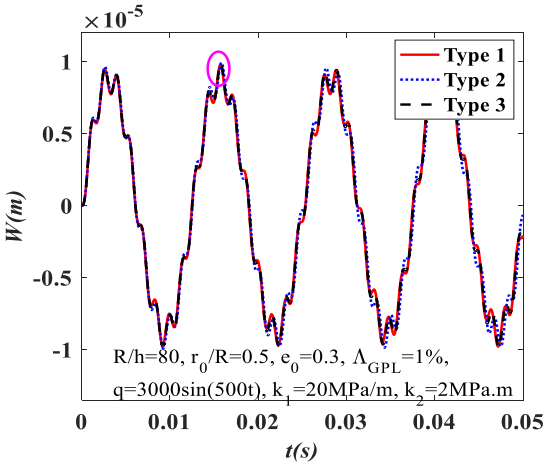

Figure 7. Comparison of three type of porosity distribution on the nonlinear dynamic response of sandwich shallow spherical shells.

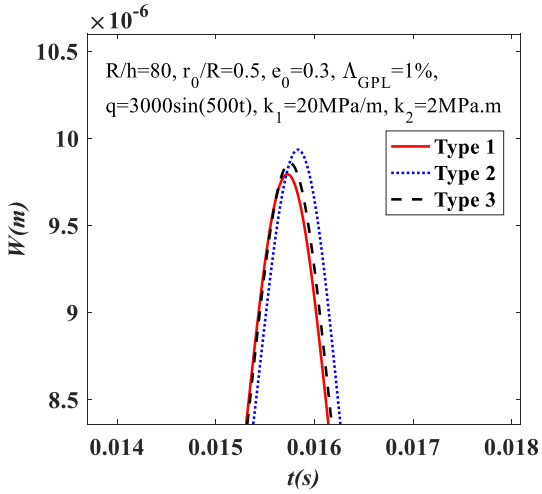

Figure 8. Zoomed-in view of Figure 6

6. Conclusion

This paper investigates the nonlinear dynamic response and natural frequencies of P-GPL-RC sandwich shallow spherical shells:

- The GPLs improve significantly the load capacity of sandwich shallow spherical shells. GPL's weight faction increase leads to reducing the amplitude-time curve of the sandwich shallow spherical shells.
- The load capacity of sandwich shallow spherical shells decreases when the shell consists of porosity and three type of porosity distribution are examined.
- The geometrical and material parameters affect strongly on the results of analyzing the nonlinear dynamic response of P-GPL-RC sandwich shallow spherical shells.

Acknowledgements

This research is funded by Vietnam National Foundation for Science and Technology Development (NAFOSTED) under grant number 107.02-2018.314. The authors are grateful for this support.

References

Tuyen, B.V (2018). Dao động của dầm fgm có lỗ rỗng vi mô trong môi trường nhiệt độ chịu tải trọng di động. Luận án tiến sỹ.

Liu, Y., S. Su, H. Huang, and Y. Liang (2019). Thermal-mechanical coupling buckling analysis of porous functionally graded sandwich beams based on physical neutral plane. *Composites Part B: Engineering*, 168, pp. 236-242.

Saidi, A.R., R. Bahaadini, and K. M. Mozafari (2019). On vibration and stability analysis of porous plates reinforced by graphene platelets under aerodynamical loading. *Composites Part B: Engineering*, 164, pp. 778-799.

Cong, P.H., T.M. Chien, N.D. Khoa, and N.D. Duc (2018). Nonlinear thermomechanical buckling and post-buckling response of porous FGM plates using Reddy's HSDT. *Aerospace Science and Technology*, 77, pp. 419-428.

Xue, Y., G. Jin, X. Ma, H. Chen, T. Ye, M. Chen, and Y. Zhang (2019). Free vibration analysis of porous plates with porosity distributions in the thickness and in-plane directions using isogeometric approach. *International Journal of Mechanical Sciences*, 152, pp. 346-362.

Chen, D., J. Yang, and S. Kitipornchai (2019). Buckling and bending analyses of a novel functionally graded porous plate using Chebyshev-Ritz method. *Archives of Civil and Mechanical Engineering*, 19(1), pp. 157-170.

Nam, H.V., N.T. Trung, L.K. Hoa (2019). Buckling and postbuckling of porous cylindrical shells with functionally graded composite coating under torsion in thermal environment. *Thin-Walled Structures*, 144, pp. 106253.

Li, H., F. Pang, Y. Ren, X. Miao, K. Ye (2019). Free vibration characteristics of functionally graded porous spherical shell with general boundary conditions by using first-order shear deformation theory. *Thin-Walled Structures*, 144, pp. 106331.

Safaei, B., M. D. Rasool, K. Behdinan, Z. Qin, and F. Chu (2019). Thermoelastic behavior of sandwich plates with porous polymeric core and CNT clusters/polymer nanocomposite layers. *Composite Structures*, 226, pp. 111209.

Gao, K., W. Gao, D. Chen, and J. Yang (2018). Nonlinear free vibration of functionally graded graphene platelets reinforced porous nanocomposite plates resting on elastic foundation. *Composite Structures*, 204, pp. 831-846.

Li, Q., D. Wu, X. Chen, L. Liu, Y. Yu, W. Gao (2018). Nonlinear vibration and dynamic buckling analyses of sandwich functionally graded porous plate with graphene platelet reinforcement resting on Winkler–Pasternak elastic foundation. *International Journal of Mechanical Sciences*, 148, pp. 596-610.

Setoodeh, A.R., M. Shojaee, and P. Malekzadeh (2019). Vibrational behavior of doubly curved smart sandwich shells with FG-CNTRC face sheets and FG porous core. *Composites Part B: Engineering*, 165, pp. 798-822.

Karimiasl, M., F. Ebrahimi, and V. Mahesh (2019). Nonlinear forced vibration of smart multiscale sandwich composite doubly curved porous shell. *Thin-Walled Structures*, 143, pp. 106152

Xu, C. S. (1991). Buckling and post-buckling of symmetrically laminated moderately thick spherical caps. *International Journal of Solids and Structures*, 28 (9), pp. 1171-1184.

Villoria, R.G. and A. Miravete (2007). Mechanical model to evaluate the effect of the dispersion in nanocomposites. *Acta Materialia*, 55(9), pp. 3025-3031.

Li, Q. S., J. Liu, and J. Tang (2003). Buckling of shallow spherical shells including the effects of transverse shear deformation. *International Journal of Mechanical Sciences*, 45(9), pp. 1519-1529.

Liu R. H., D. Li, G.H. Nie, and Z.Q. Cheng (1991). Nonlinear buckling of squarely-latticed shallow spherical-shells. *International Journal of Non-linear Mechanics*, 26, pp. 547-65.

Nath Y. and Sandeep K. (1993). Postbuckling of symmetrically laminated, moderately thick, axisymmetric shallow spherical shells. International Journal of Mechanical Sciences. 35(11), pp. 965-975.

Appendix

$$l_1 = m_1 - \frac{n_1 m_3}{n_3}, l_2 = m_2 - \frac{n_2 m_3}{n_3} - \frac{n_1 m_5}{n_3},$$

$$l_3 = m_4 - \frac{n_2 m_5}{n_3}, l_4 = \frac{21}{16}, n_1 = \frac{15}{4}\frac{C_{20}}{r_0^3 C_{10}},$$

$$n_2 = \frac{\left(8KA_{66} + 415\right)C_{10}R - 2C_{20}}{2C_{10}Rr_0},$$

$$n_3 = -KA_{66} + \frac{-4139C_{12}C_{20} + 823C_{13}C_{20}}{16C_{10}r_0}$$

$$+ \frac{12495C_{12}C_{20} - 1785C_{13}C_{20} - 1140C_{10}C_{22} + 600C_{10}C_{23}}{80C_{10}r_0^2},$$

$$m_1 = -\frac{1611}{1144}\frac{1}{r_0^4 C_{10}}, \quad m_2 = -\frac{93}{352}\frac{1}{r_0^2 RC_{10}},$$

$$m_3 = \frac{315}{128}\frac{-\frac{427}{165}C_{12} + \frac{134}{1155}C_{13}}{r_0^2 C_{10}} + \frac{315}{128}\frac{\frac{127}{35}C_{12} - \frac{381}{35}C_{13}}{r_0^3 C_{10}},$$

$$m_4 = -k_1 - \frac{45}{128R^2 C_{10}} + 15\frac{-C_{10}\mathrm{KA}_{66} - C_{10}k_2}{2r_0^2 C_{10}},$$

$$m_5 = \frac{315}{128}\frac{\frac{29}{30}C_{12} - \frac{17}{168}C_{13}}{RC_{10}}$$

$$+ \frac{2100C_{10}R\mathrm{KA}_{66} + 315\left(-149C_{12} + 447C_{13}\right)}{1120r_0 C_{10}R}.$$

The 5th International Conference on Engineering Mechanics and Automation (ICEMA 5)
Hanoi, October 11÷12, 2019

Design and manufacturing of a micro Penton turbine

Vu Lam Dong[a], Vu Duc Thanh[b] and Nguyen Tuan Trung[c]

[a] *Institute of Mechanics, VAST, vldong@imech.vast.vn*
[b] *Institute of Mechanics, VAST, thanhvuduc@hotmail.com*
[c] *University of Engineering and Technology, VNU, tuantrung2201@gmail.com*

Abstract

Penton turbine is a component of wave energy converter (WEC) system, the device types that represent current wave energy converter technology. Design process require to optimize parameters of equipment.

The aim of present paper to create a prototype micro Penton turbine from calculation, design and manufacturing by 3D printer. Testing and modification of parameters are available in process.

Key Words: wave energy converter, Penton turbine, Pelton turbine runner, 3D printer

1. Introduction

Lately wave energy converter (WEC) technology is researched and developed to generate renewable electricity which changing traditional energy as hydraulic power, thermal power or nuclear power. WECs can be classified into three predominant types (B Drew. at al, 2009).

This paper introduces a process to create a micro Penton turbine with 300 W power output. It is a component of Oyster Wave Energy Converter System (Oscillating wave surge converter type) (Christopher Cargo, 2012).

We use 3D printer to make parts of micro Penton turbine. It is reasonable for prototype in experimental conditions.

2. Design micro Pelton turbine

On the Pelton turbine the torque is generated by deflection of the free jet in the double buckets of the runner. That is why the Pelton turbine is also called free jet turbine.

The free jet turbine was invented around 1880 by the American Pelton, after whom it got its name. The greatest improvement that Pelton made was to introduce symmetrical double buckets. This shape is basically still valid today. The splitter ridge separates the jet into two equal halves, which are diverted sideways. Since then the turbine has been considerably improved in all respects and the output of power has increased.

2.1. Calculation

Dimensioning of Pelton Turbines

Following are the necessary formulas for the design and the layout of micro Pelton turbines (Markus Eisenring, 1991):

$$c_1 = k_c\sqrt{2gH_n} \tag{1}$$

$$d = \sqrt{\frac{4Q}{\pi c_1}} \tag{2}$$

$$u_1 = k_u\sqrt{2gH_n} \tag{3}$$

$$b = (2.5,\ldots,3.2)\,d \tag{4}$$

$$h = (2.1,\ldots,2.8)\,d \tag{5}$$

$$t \approx 0.9d \tag{6}$$

$$D = \frac{60u_1 i}{\pi n_G} \tag{7}$$

$$a \approx 1.2d \tag{8}$$

$$z \approx \frac{D\pi}{2d} \tag{9}$$

$$P = QH_n g\rho\eta\frac{1}{1000} \tag{10}$$

where:

c_1 : absolute velocity of water jet [ms^{-1}]

k_c : nozzle coefficient (k_c = 0.96...0.98)

g : gravitational constant = 9.81 [ms^{-2}]

H_n : net head [m]

d : optimal jet diameter [m]

Q : water discharge [m^{3}s^{-1}]

u_1 : optimal peripheral velocity [ms^{-1}] (at the pitch circle diameter)

k_u : coefficient (k_u = 0.45...0.49)

h : bucket height [m]

t : bucket depth [m]

D : pitch circle diameter (PCD) [m]

n_G : rotational speed of driven machine (RPM) [min^{-1}]

i : transmission ratio (RPM of driven machine/RPM of turbine) (i=l if a generator is coupled directly)

a : width of bucket opening [m]

z : approximate number of buckets

P : power output [kW]

η : efficiency

ρ : density of water = 1000 [kgm^{-3}]

The main parameters of Pelton Turbine are illustrated in fig.1 to fig.3.

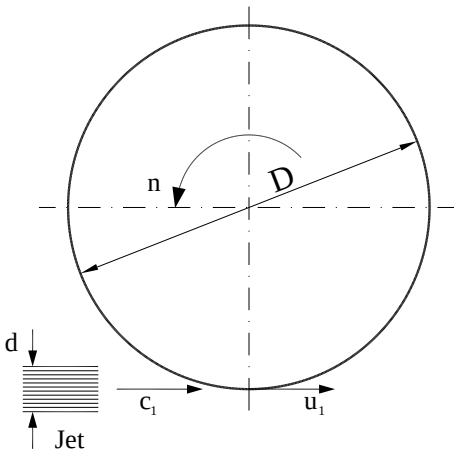

Figure 1. Fundamentals of the Free Jet Turbine

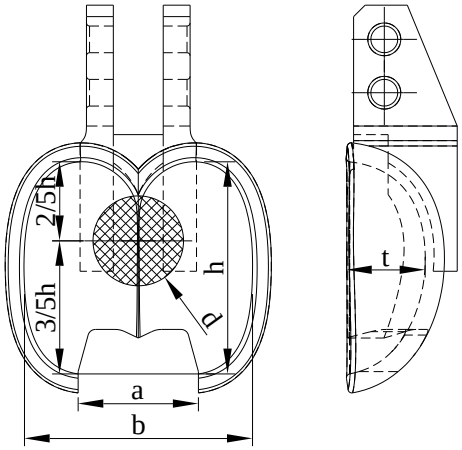

Figure 2. Main dimensions of Pelton buckets

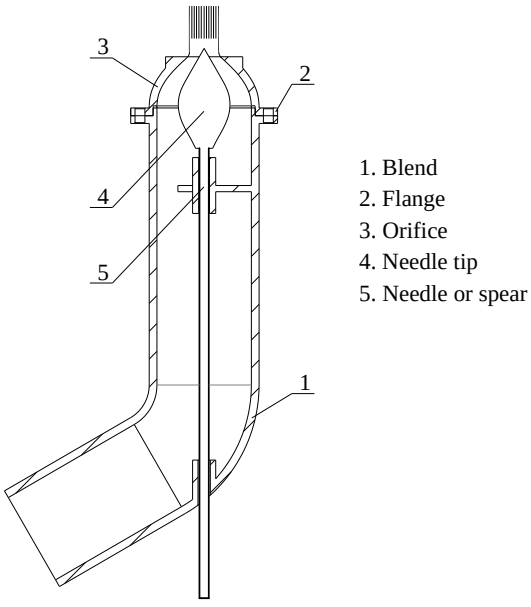

Figure 3. Example of Nozzle

In this case we intend to install a generator with 300W power output, turning at as peed of 1500 RPM.

An overall efficiency of 60 % of the machinery is assumed. Oyster System includes 2 piston pumps, the discharge of the piston pump (Henry Liu, 2003) is:

$$Q = 2A_pL_pN \quad (11)$$

where:

A_p: is the piston cross-sectional area, A_p = 0.005 [m^2].

L_p: is piston stroke length, L_p =0.5 [m].

N: is reciprocating speed, N = 1/3 [s^{-1}].

Using formulas (1) to (11) we calculate parameters of micro Pelton turbine as:

Q = 0.00167 m^3/s = 1.67 lt/s;

H_n = 30.4380 m;

c_1 = 23.460 m/s; u_1 = 10.997 m/s;

d = 0.00954 m = 9.54 mm;

D = 0.140 m = 140 mm;

z = 23.0652.

Considering with suitable parameter for design parts of turbine, we define:

D = 140 mm; d = 10 mm; b = 30 mm; a = 12 mm; h = 28 mm; t = 9 mm and z =24.

If different sizes of Pelton turbines have to be manufactured frequently, it is recommended to use a series of standardized bucket sizes which work with the following jet diameters:

Table 1. Jet diameter and bucket width (Markus Eisenring, 1991)

Jet diameter d	Bucket width b
3 to 6 mm	19 mm
6 to 10 mm	30 mm
10 to 15 mm	45 mm
15 to 20 mm	60 mm
20 to 25 mm	75 mm
25 to 30 mm	90 mm

2.2. Modelling

We use SOLIDWORKS software to design parts, from the initial sketch to the final result, we create a 3D mode. From this model, we can create 2D drawings or mate components consisting of parts or subassemblies to create 3D assemblies.

Bucket:

Generally each cutting of the water jet by the buckets means a disturbance of the jet. Part of the water gets an abrupt and unwanted diversion. This explains why the number of buckets should not be chosen too large. On the other hand not all the water of the jet may hit a bucket if the number of buckets is too small.

From calculated results in 2.1, we construct bucket which illustrate in Fig.4, Fig.5.

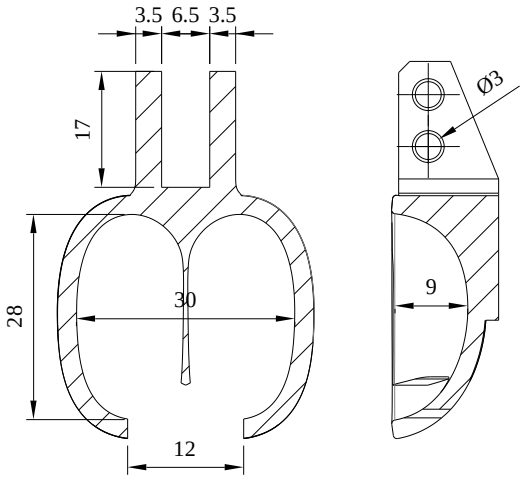

Figure 4. 2D sketch of cross sections of Pelton bucket

Figure 5. 3D layout of Pelton bucket

Rotor:

The rotor, wheel or runner of a Pelton turbine basically consists of a disk with a number of buckets fixed at its circumference. The disk is mounted on a shaft by means of a hub.

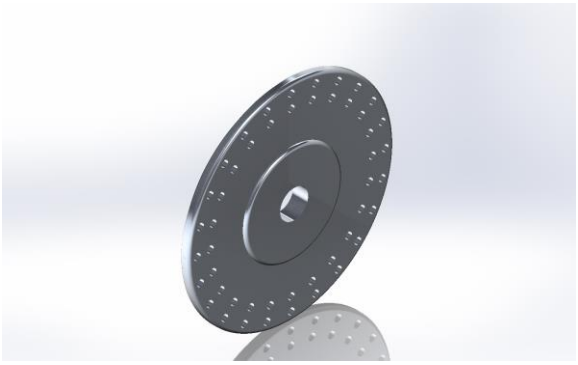

Figure 6. 3D layout of disk

Figure 7. Pelton turbine runner with 24 buckets

Nozzle and needle:

The manifold with its needles and spear valves is a costly component of the Pelton turbines. Such devices are used to regulate the speed or the discharge of the turbine. Generally the valve is regulated by a governor.

The manifold should have as few bends as possible, with a radius as large as possible to avoid losses and turbulence of the jet.

The water from the penstock is distributed to the nozzles by the manifold. Towards the last jet the diameters of the distribution pipes are gradually reduced.

The nozzle must be designed in such a way that the pressure loss is as small as possible and that thus the nozzle coefficient is increased.

An increased velocity of the water means higher losses. That is why the part of the nozzle, in which the water has a high speed, has to be as short as possible.

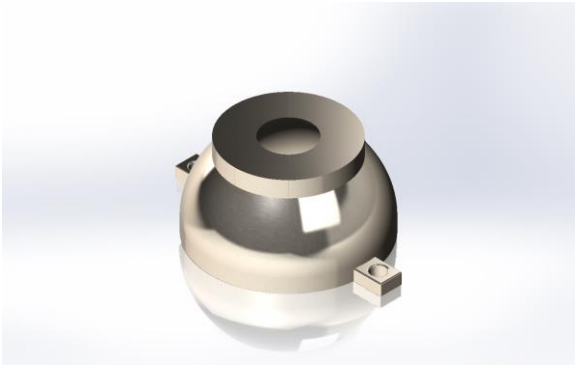

Figure 8. Nozzle up

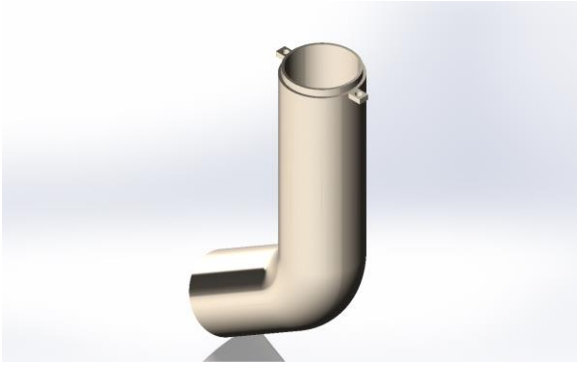

Figure 9. Nozzle down

Figure 10. Needle of Pelton turbine nozzle

Figure 11. Nozzle assembly

Assembly:

After building all parts, we continue to mate components for full turbine.

The water jet impinges on one bucket at a time as the wheel turns, to generate a more-or-less continuous torque on the wheel as it rotates (Fig 12).

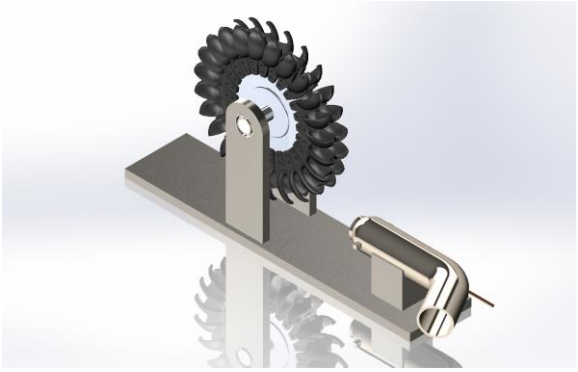

Figure 12. Principle of Pelton turbine

3. Finite Element Analysis (FEA) using ANSYS Workbench

All numerical simulation and analysis are carried out using FEM software with static structural analysis.

The simulation and analysis list are as follows:

- Engineering data
- Geometry
- Model/mesh
- Setup
- Solution
- Results

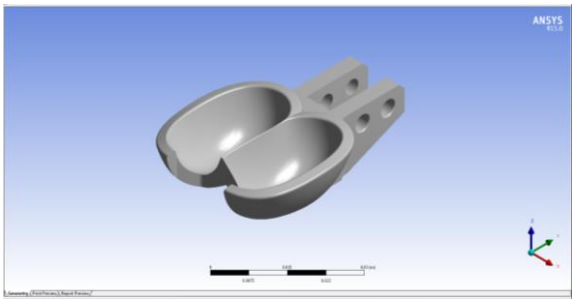

Figure 13. Bucket ANSYS model

Table 2. Statistics of bucket

Statistics	Quantity
Bodies	1
Activities	1
Nodes	9880
Element	5195

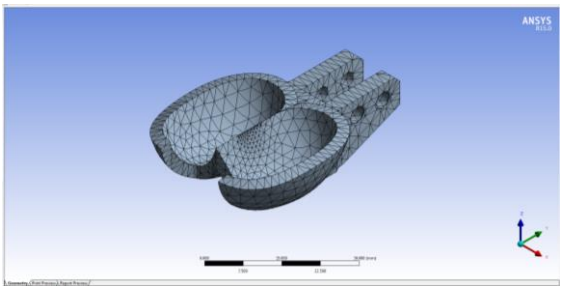

Figure 14. Meshing of bucket

Using PLA (Polylactic Acid) plastic to make a bucket of turbine. PLA is a polymer made from renewable resources.

Table 3. Properties of PLA (X. Li, 2014)

No	Properties	Values
1	Density	1240
2	Tensile Ultimate Strength (MPa)	46
3	Young's Modulus (MPa)	4000
4	Poisson's Ratio	0.36

Table 4. Model Static Structural Loads

Type	Pressure
Normal	0.011 MPa

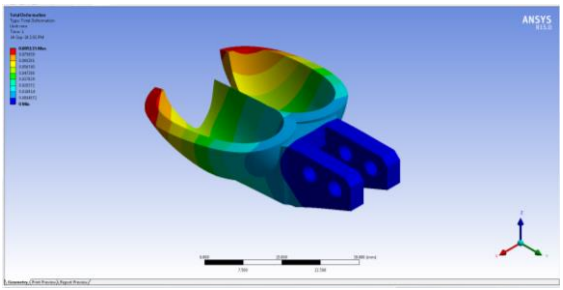

Figure 15. Total deformation of bucket

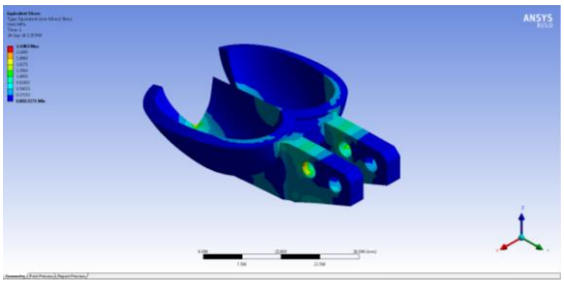

Figure 16. Equivalent stress of bucket

Table 5. Deformation and stress analysis

Type	Equivalent (von-Mises) Stress	Total Deformation
Minimum	0.0013 MPa	0.0 mm
Maximum	2.4403 MPa	0.0085 mm

In this case the results satisfy strength of materials of bucket from then to make products.

4. Prototype manufacturing by 3D printer

3D printing refers to a manufacturing process that builds layers of material to create a three-dimensional solid object from a digital model. There are several different techniques to 3D Print an object.

3D Printing brings two fundamental innovations: the manipulation of objects in their digital format and the manufacturing of new shapes by addition of material.

We use 3D printer which names ANYWELL – Prusa i3 mk2 (made in Vietnam) to print all parts as bucket, nozzle, needle…It is driven by Ultimaker Cura 4.0 sotfware.

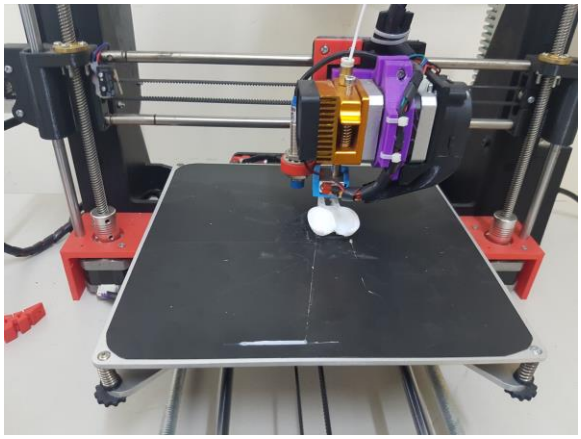

Figure 17. Printing process of a bucket

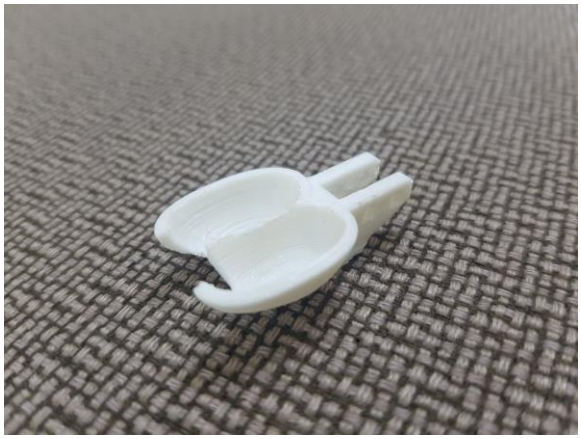

Figure 18. A completed bucket

Figure 19. Photograph of Pelton turbine runner

Figure 20. Photograph of needle

Depending on types of different parts, we need to modify suitable parameters in Ultimaker Cura 4.0.

Note: if we setup wrong parameters, the products will be failure.

Table 6. Parameters in Ultimaker Cura 4.0

Parameters	Bucket	Needle
Layer height (mm)	0.1	0.05
Infill (%)	20	60
Printing Temperature (^{0}C)	200	200
Build plate Temperature (^{0}C)	60	60
Print speed (mm/s)	50	20

All parameters effect to time print process of prototype.

Fig. 17 to Fig. 20 show parts of turbine runner after complete. The next step we assemble parts and carry out experiments.

5. Conclusion

The paper outlines the process of designing and manufacturing a micro Pelton turbine in form of a prototype. The supported tools include software for design, simulation and 3D printer.

Given parameters are discharge Q, efficiency η and install a generator with 300 W power output P. The main dimensions of Pelton turbine are defined and can be adjusted to take the optimal model. This turbine is a part of wave energy converter system (not available in Vietnam yet)

Using 3D printer makes parts of turbine more effective, especially in case we research and manufacture prototypes. It helps to reduce cost of products and creates complex shapes. In future 3D printing would replace more traditional manufacturing techniques.

Acknowledgment

The work presented in this article has been support by Vietnam Academy of Science and Technology, grant No. VAST06.05/18-19.

References

B Drew, A R Plummer, and M N Sahinkaya (2009). A review of wave energy converter technology. *Proc. IMechE Vol. 223 Part A: J. Power and Energy*, pp. 887-902.

Christopher Cargo (2012). *Design and Control of Hydraulic Power Take-Offs for Wave Energy Converters.* Doctor of Philosophy, University of Bath.

Markus Eisenring (1991). *Micro Pelton Turbines*. MHPG Series, Volume 9, Switzerland.

Henry Liu (2003). *Pipeline engineering*. Lewis Publishers, A CRC Press Company, Florida.

Xuan Li, Chao Guo, Xiaokai Liu, Lei Liu, Jing Bai, Feng Xue, Pinghua Lin, Chenglin Chu (2014). Impact behaviors of poly-lactic acid based biocomposite reinforced with unidirectional high-strength magnesium alloy wires. *Progress in Natural Science: Materials International,* 24, pp. 472-478.

Mechatronics and Automation

The 5th International Conference on Engineering Mechanics and Automation (ICEMA 5)
Hanoi, October 11÷12, 2019

A Research on Conveyor Belt 3D Printer in Industrial Applications

Dam Dinh Hiep[a], Le Hoai Nam[a] , Bui Duy Toan[a] and Nguyen Ngoc Linh[a]

[a] *Faculty of Engineering Mechanics and Automation, University of Engineering and Technology*

Abstract

A 3d printing technique is an additive manufacturing technique where 3D objects and parts are made by the addition of multiple layers of material.[1] It is a type of rapid prototyping. The layers are stacked up in a variety of ways depending on the technology being used. It can use a wide range of materials such as ABS, PLA, and composites as well. This technology allows the design of complex components, therefore, avoiding assembly requirements at no additional cost.

This paper presents research on 3D printer design with a conveyor belt, which can be applied in industrial applications. Firstly, a CAD model of a 3d printer has been created using SolidWorks. In this step, all the parts of the model are designed and then are assembled in the SolidWorks workbench to create the 3D printer assembly. Then, the electronics board which controls the entire printing process is studied and integrated into the mechanical structure. The electronics board compiles the STL file to a suitable form to carry out the printing process and is connected to the PC using a USB-to-serial converter. Finally, a portable 3D printer is built and tested with various types of models.

Key Words

1. Introduction

3D printing is a method of manufacturing known as 'Additive manufacturing', due to the fact that instead of removing material to create a part, the process adds material in successive patterns to create the desired shape. The designs for printing come from computer-aided design (CAD) software, such as SolidWorks or Inventor. The first working 3D printer was created by Charles W. Hull in 1984 and the technique was named Stereolithography(SLA).[2] In 1992, S. Scott Crump and his company. Stratasys marketed the first fused deposition modeling (FDM) machine.[2] FDM is a 3D printing process that uses a continuous filament of a thermoplastic material. Our printer is a variant of an FDM cartesian 3d printer.

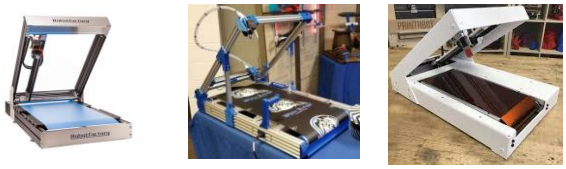

Figure 1. 3D Printers with Conveyor

In this study, we developed a 3D printer that prints at a 45-degree angle onto a moving conveyor belt. By printing onto a conveyor belt and provided enough print material, there are no longer any limitations on the length of the prints along the axis parallel to the belt. This can be applied to prototypes for airplane wings,

prosthetics and other parts that are longer than a typical 3D printer. And because the printer is equipped with a moving conveyor belt so it can print continuously. The printer can keep printing parts and they will move down the conveyor belt once they are completed. By printing layers at 45 degrees, we could be able to reduce the need for support material for overhangs compared to ground up layering. During the modeling process, our team took some inspiration from the BlackBelt 3d printer.[3]

2. Mechanical Design and Calculations

In this paper, we use Inventor to design the model (Figure 2 and 3).

The overall size of our machine is 600 mm x 420 mm x 350 mm. We separate this model in three main parts:

- The frame
- The conveyor belt
- The transmission

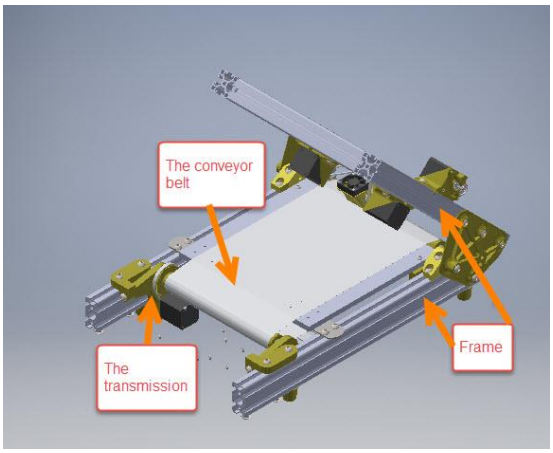

Figure 2. The model of printer in Inventor

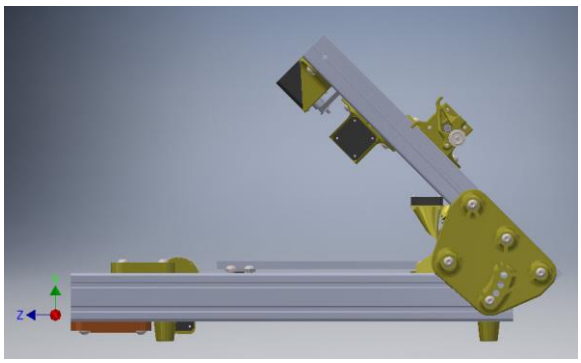

Figure 3. The model from the side

The upper frame is connected to the lower frame by an aluminum plate. The angle of two frames is kept at 45-degree.The Z-axis that aligned with the conveyor belt could have more freedom in length. As you can see in figure 3.

There were multiple approaches the team determined to be viable for the print angle of the printer, 30 degrees, 45 degrees, and 60 degrees. This allowed us to analyze the advantages and disadvantages of a lower angle, higher angle or something in between. The decision matrix we generated to compare these components is shown in Table 1.(3 – Great, 2 – Good, 1 – Normal, 0 – Bad)

Table 1. Decision Matrix for Print Angle

Print Angle	Software Compatibility	Build Height	Support Material	Sum
60	0	3	3	6
45	3	2	2	7
30	3	1	1	5

With a higher angle, less support material is needed, and a higher build height can be achieved. If we were to create the same build height for each angle, the 30-degree angle would cost the most as the top frame would have to extend much further to reach the same build height as the 45 degrees or 60 degrees. Based on these specifications, the 60-degree angle would be the most effective choice, however, open-source software is not readily available for 60-degree angled printing, limiting our choice to 45 degrees.

2.1. The frame of 3D printer

Many 3D printers can be constructed out of 3D printed materials. There are also possibilities in producing the frame through machined metals, such as aluminum profile, which is particularly useful for components of 3D printers as the aluminum profile allows for simple connections between the bars. Our machine is mainly conducted by 30×60 T-Slot Aluminium Extrusion Profile. The frame measurement is 600 mm x 420 mm.

Figure 4. 30×60 T-Slot Aluminium Extrusion Profile

2.1.1 Beam calculation

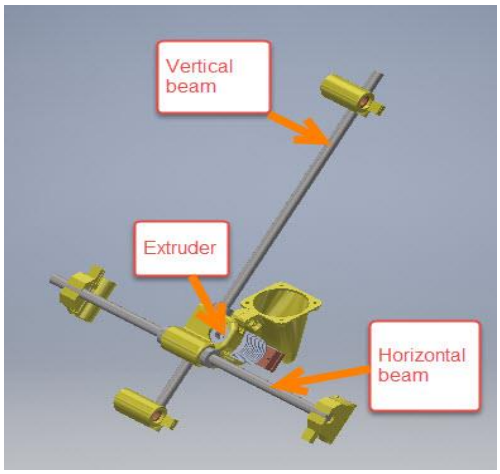

Figure 5. Extruder holder

We need to calculate the diameter of both beams to handle a 5-kilogram load from the extruder. Both of them are carbon fiber tube with a ultimate tensile strength of 350 MPa[4] . The factor of safety is 10.

The vertical beam length is 310 mm. It is subjected to an external force of 18 N and a bending force of 18 N. The horizontal beam length is 260 mm. It is subjected to a bending force of 25 N. The maximum bending moment is found by drawing the Sheer-Moment diagram[5] (figure 6 and 7)

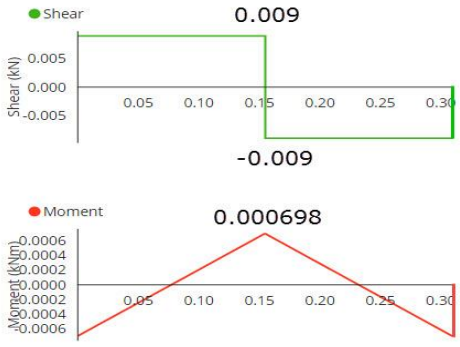

Figure 6. The vertical beam diagram

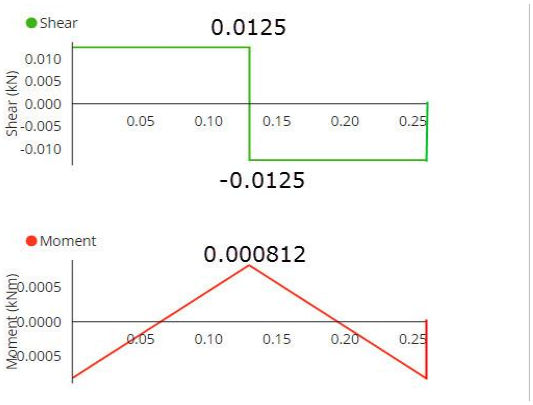

Figure 7. The horizontal beam diagram

The calculated vertical beam diameter is shown in equation (1)..

$$\frac{M_b \times y}{I} + \frac{P}{A} = \frac{S_{ut}}{f_s} \; with \; I = \frac{\pi d^4}{64}; y = \frac{d}{2}; A = \frac{\pi d^2}{4}$$

$$\Rightarrow \frac{32 \times 698}{\pi d^3} + \frac{72}{\pi d^2} = \frac{350}{10} \Rightarrow 35\pi d^3 - 72d - 2236 = 0$$

$$\Rightarrow d \approx 6(mm) \quad (1)$$[6]

The calculated horizontal beam diameter is shown in equation (2).

$$\frac{M_b \times y}{I} = \frac{S_{ut}}{f_s} \; with \; I = \frac{\pi d^4}{64}; y = \frac{d}{2}$$

$$\Rightarrow \frac{32 \times 812}{\pi d^3} = \frac{350}{10} \Rightarrow d = 6.2 \; (mm) \quad (2)$$[6]

We chose d = 8 mm because 8 mm carbon fiber tube was more easy to purchase.

2.2. The conveyor belt

With the conveyor belt, the problem that we look into is the heat resistance and adhesion. Our machine now uses a 250 mm x 1000 mm green PVC conveyor belt. For a normal PVC conveyor belt, testing shows that the PLA was able to adequately stick to it. And the main problem left is heat resistance. So to see what happened during the contact of the extruder tip and the belt, we conduct a thermal study in SolidWork and the result is shown below.

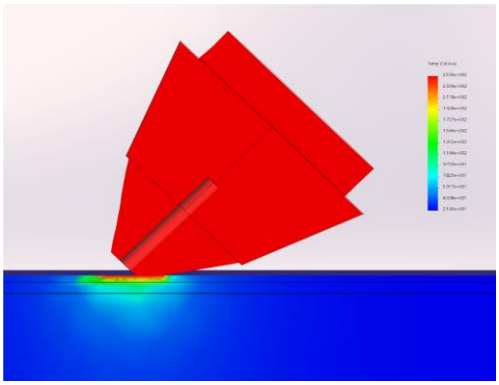

Figure 8. Thermal Study

Table 2. Maximum Belt Temperatures

Location	Value, **°C**	x, **mm**	y, **mm**	z, **mm**
14954	110.60	-1.587	3.048	3.968
118549	98.750	-1.587	3.048	4.365
134934	97.070	-1.190	3.048	3.968
134933	91.080	-1.984	3.048	3.968

From the result of table 2, the PVC belt will melt if the contact occurs. The ideal solution would be to use a carbon fiber belt. This would be a surface that PLA can easily adhere to and typical carbon fiber can withstand 3652° C, so the belt can easily withstand the roughly 250°C max temperature of our extruder. But for now, we secure the bell with a heat resistance tape.

2.3. The transmission

The transmission system that we use is a V-belt system. By calculating the torque required, we could choose the motor for the job. In equation (3), the torque required is calculated with the following parameter.

The total mass of load test is 1 kilogram, the gear ratio is 5:1. The Friction coefficient of the sliding surface is 0.05. The tilt angle is 0-degrees and the pulley diameter is 31mm with the efficiency of the system is set at 90 percent

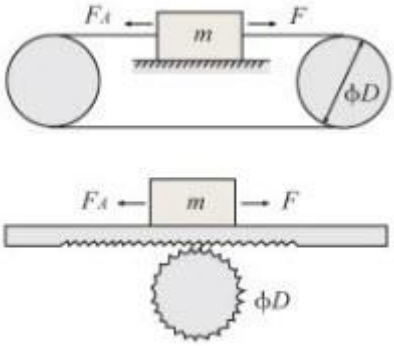

Figure 9. Torque calculation

F: Force of moving direction

μ_0: Internal friction coefficient of preload nut

η: Efficiency

i: Gear ratio

F_A: External force

m: Total mass of the table and load

μ: Friction coefficient of sliding surface

θ: Tilt angle

D: Final pulley diameter

g: Gravitational acceleration

$$T_L = \frac{F}{2\pi\eta} \times \frac{\pi D}{i} = \frac{FD}{2\eta i} \quad (3)^{[7]}$$

$$F = F_A + mg(\sin\theta + \mu\cos\theta)$$

$$\Rightarrow T_L = \frac{0.05 \times 1 \times 9.8 \times 0.031}{2 \times 0.9 \times 0.2} = 0.042\,(Nm)$$

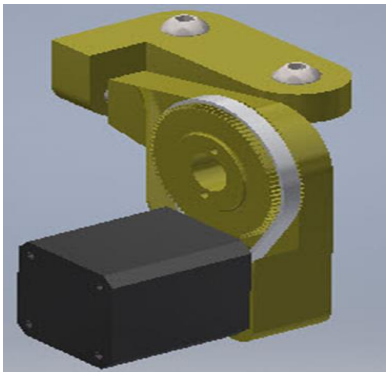

Figure 10. V-belt system in Inventor

2.4. Other parts

Some other parts are designed and machined to assembly the main parts together.

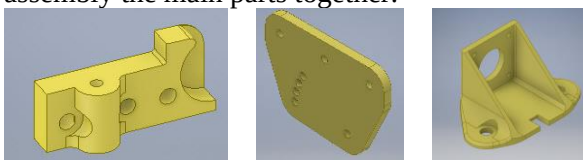

Figure 11. Roller mount, frame connect and stepper motor mount

3. Electronic Parts and Control

In order to operate the 3D printer smoothly and flexibly, we need to integrate electronic part and controller into the 3D printer mechanical design.

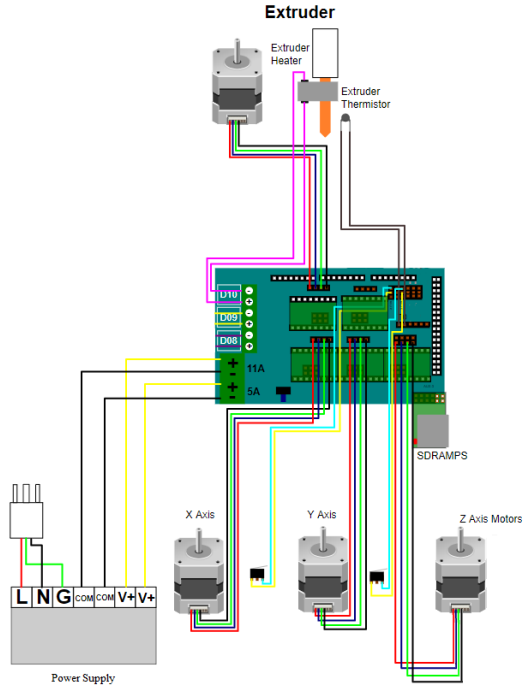

Figure 12. Connection diagram

3.1. Main controller part

In this project, we used board Arduino Mega 2560 – a type of Single-board microcontroller. Because of its high efficiency, easy to work with and is commonly used in many 3D printers.

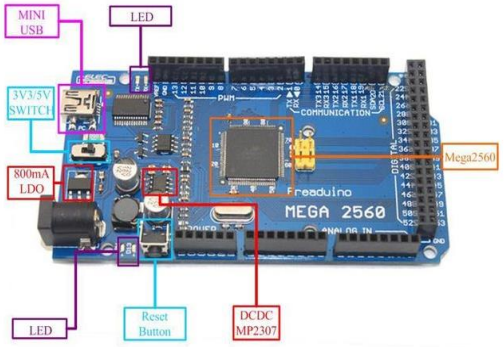

Figure 13. Arduino Mega 2560

Along with board Arduino Mega 2560, we used RAMPS 1.4 motherboard. RAMPS 1.4 is a board that serves as the interface between the Arduino Mega — the controller computer — and the electronic devices in the printer. The board is accessible, reliable, easy to replaced and it comes with all the necessary components to run most 3D printers.[8]

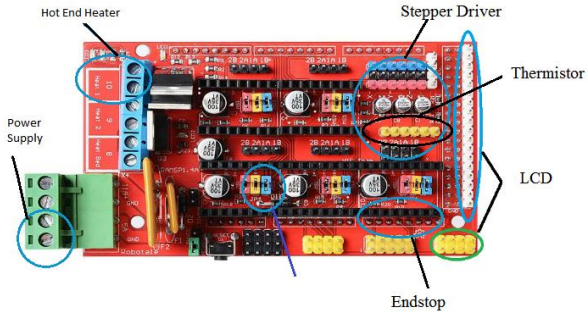

Figure 14. RAMPS 1.4

3.2. Stepper driver

A stepper drive is the driver circuit that controls how the stepper motor operates. Stepper drives work by sending current through various phases in pulses to the stepper motor. The driver has only two primary functions: sequencing the phases and controlling the phase current. The two most commonly used driver is driver A4988 and DRV8825. We used A4988 in this project

Figure 15. Driver A4988

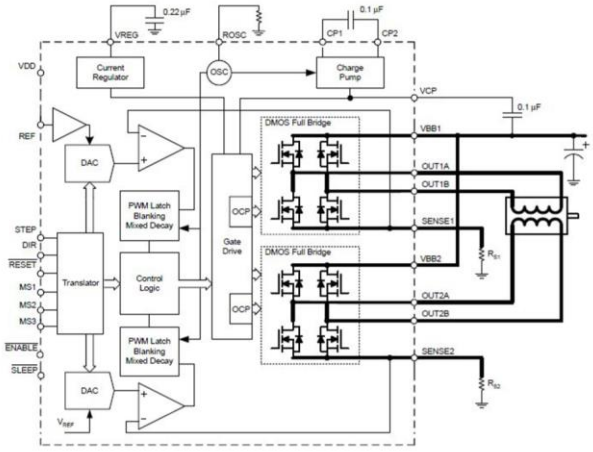

Figure 16. A4988 blocks diagram

3.3. Thermal monitor and control

The thermistor allows us to monitor the temperature in the nozzle and the heat bed (optional) before and during printing. With that information from the thermistor, we control the output of another thermistor to heat the nozzle. Both thermistor and heater are controlled by Arduino Mega. The heater can be set to a specific temperature.

Figure 17. Thermistor NTC 3950 100K

Figure 18. Cartridge Heater 12V 40W

3.4. Program and control

G-code is a language in which people tell computerized machine tools on how to make something. The "how" is defined by g-code instructions provided to a machine controller (industrial computer) that tells the motors where to move, how fast to move, and what path to follow.[9] And slicer, also called slicing software, is computer software used in the majority of 3D printing processes for the conversion of a 3D object model to specific instructions for the printer. In particular, the conversion from a model in STL(Standard Tessellation Language) format to printer commands in g-code format. [10]

Our team's plan for software is to use the open-source BlackBelt Cura Slicing software that has compatibility with Blackbelt's printer and printer with similar design like our printer[11]

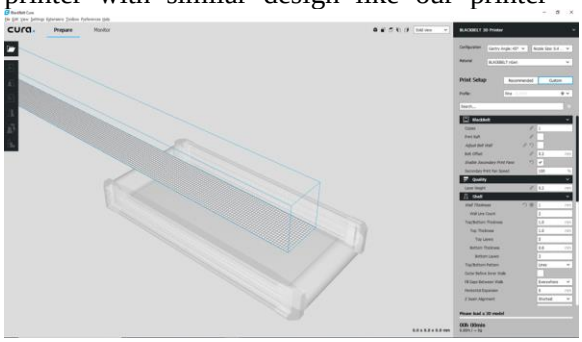

Figure 19. BlackBelt Cura

Arduino IDE is an open-source software that is mainly used for writing and compiling the code into the Arduino Module. It is available for operating systems like MAC, Windows, Linux. It comes with inbuilt functions and commands that play a vital role in debugging, editing and compiling the code in the environment.

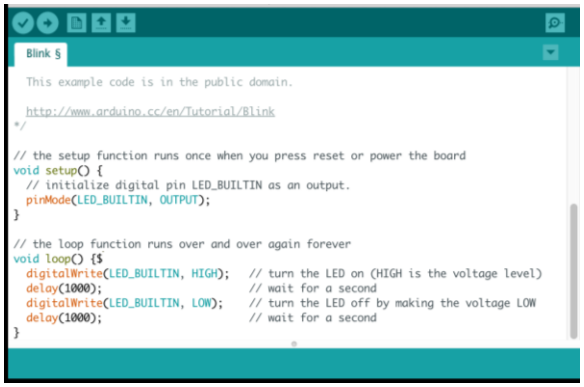

Figure 20. Arduino IDE

Marlin is the software that is embedded in the 3D printers control board. It controls everything from heaters, motors,.. and abstract concepts such as exploration, speed limits, thermal regulation, and safety. To adapt marlin to our printer, we change the setting to fit our needs. We calculate the XYZ steps-per-mm by using the motor, pulley, and belt characteristics, limit the nozzle temperature, test and tune the extruder steps

4. Assembly and Testing

Figure 21. Final product

The size of the final product is 600 mm x 420 mm x 400 mm. The weight is 12 kg. With its large size and heavyweight. The machine can be quite cumbersome and it is not mobile. It is quite a disadvantage in assemble and transport

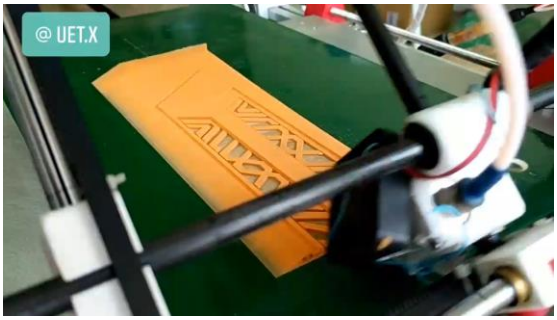

Figure 22. During operation

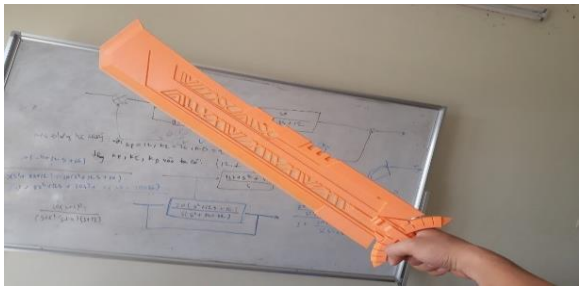

Figure 23. Printed sample

The sample size is 101 mm x 803 mm x 6 mm. It proved the ability to print object which its length is longer than the machine. And we also test with multiple objects printing function.

Figure 24. Multiple objects print test

We also print the 20mm Calibration Cube to check the precision of our printer.

The printed result parameter is Z = 20.25 mm, Y = 19.7 mm, X = 19.7 mm. The percent error of Z is 1.25%, Y is 1.5% and X is 1.5 %.By visually, the surface texture is not smooth. But we could not determine the actual average roughness of the surface texture because of our lack of precise tools.

Figure 25. 20 mm Calibration Cube

5. Conclusions

At the end of this project, we were able to construct a working prototype of the conveyor 3d printer. We had grasped the technology of designing and printing 3d objects. The printer has shown the potential in multiple objects printing and printing long objects. It opens a new way to create faster and easier prototype. And with some improvement, it could become a a semi-mass-producing tool.

References

[1] *"https://en.wikipedia.org/wiki/3D_printing_processes"*.

[2] *"https://en.wikipedia.org/wiki/3D_printing"*

[3] *" https://blackbelt-3d.com "*

[4] *"http://www.performance-composites.com/carbonfibre/mechanicalproperties_2.asp"*

[5] R. K. Bansal (2006). *A Textbook of Strength of Materials*. Laxmi Publications

[6] V. B. Bhandari (2010). *Design of Machine Elements*. Mcgraw Hill, third edition, pp 76-81

[7] *"https://klinikrobot.com/mobile-articles/47-motor-speed-and-torque-ratio.html"*

[8] *"https://reprap.org/wiki/RAMPS_1.4*".

[9] *"https://en.wikipedia.org/wiki/G-code"*

[10] *"https://en.wikipedia.org/wiki/Slicer_(3D_printing)"*

[11] *"https://blackbelt-3d.com/software"*.

The 5th International Conference on Engineering Mechanics and Automation (ICEMA 5)
Hanoi, October 11÷12, 2019

Design and Implement Low-cost UAV for Agriculture Monitoring

Giang Thi-Huong Dang[a], Minh-Trung Vu[b], Quang-Huy Vuong[b], Viet-Thang Nguyen[b], Cong-Hoang Quach[b], Ninh-Thuan Truong[b] and Minh-Trien Pham[b]

[a]University of Economic and Technical Industries;
[b] VNU University of Engineering and Technology, 144 Xuan Thuy, Cau Giay, Hanoi, Vietnam

Abstract

In the recent years, appling Unmanned Aerial Vehicles (UAVs) on agriculture have become more common with many applications such as: crop monitoring, irrigation, crop protection, etc. However, UAV's cost is too expensive for agriculture application. The research aims to develop a compact and cost-effective drone for agriculture monitoring. There are many difficult problems for farmers to check crop health in the large-scale field. The drone mobility helps to solve large area monitoring problem and minimizes crop care cost. The quadcopter was intergrated by following components: Pixhawk 4 flight controller, SunnySky brushless motor, Electronic Speed Controller (ESC), Lipo Battery, Skydroid Radio Control and an RGB camera. During flight under preset path, the images are captured continuously. An aerial stitching image from taken images can be used for determining land distribution, current crop life cycle, vegetables heath. Therefore, farmers can promptly adjust factors which affecting plant health to improve the productivity. The implemented drone had a stable and handy quadcopter with the payload approximately 1.50 kg and 15 minutes flight time. The system has been tested under different scenarios. The 2D map is built with the clear image and the accuracy up to 99%. It is suitable for agriculture monitoring with reasonable price.

Key Words: Unmanned aerial vehicles, agriculture, large-scale field, Pixhawk 4, 2D map.

1. Introduction

In recent years, the development of flying vehicles was driven by advances in aeronautics, engineering and embedded processing. UAVs are used in various fields, especially for inspection and monitoring applications such as environmental, agricultural and natural resources monitoring.

Over the last few decades, UAVs have been widely used for non-military purposes such as forest and agriculture applications [1], surveillance in complex environment [2], traffic monitoring [3]. The uses of drone in these applications is mainly due to the fast speed, high maneuverability, low-cost and safety.

With the advantages of UAVs, many different research groups have begun to develop photogrammetric application for mapping and modelling application such as [4], [5], [6]. UAVs are used as a platform for images collecting missions autonomously without the need for human control.

In forestry and agriculture domains, drones are a vital tool used for highly accurate and detailed observation data. Orthomosaic map can present

the health of plants in terms of chlorophyll levels and leaf thickness, get quick and accurate record of damages or identify potential problems in the field. This information can allow producers to adjust the necessary parameters of their agricultural process so as addressing the problems before they become more widespread. Producers can take reliable decision to save money and time.

In this paper, we propose a low-cost UAV system for agricultural mapping and modeling. The main contribution is a cost-efficiency UAV which able to perform autonomous surveillance mission for mapping application. The paper is organized as follows: Section 2 describes the design of the UAV platform and the approach that was developed, Section 3 verifies the effectiveness of proposed UAV by presenting the experimental results and we conclude the paper in section 4.

2. Design

The working principle of the quadcopter is simple. But complete the implementation requires quite a bit of attention to detail. This section focuses on design method and details of each subsystem. The first phase considered the quadcopter design while second phase involved agriculture monitoring applications. Design components have been tested to ensure safety and have the lowest price. It is suitable for crop monitoring.

2.1. Design Specification

The specification for the quadcopter is listed on table 1 below.

Table 1. Specification

Parameter	Value
Weight	1.5 kg
Power supply	a. Type of cells – Lithium Polymer (3S) b. Flight time – 15 mins
Visibility	Suitable in clear weather only
Range control	10 kilometers
Camera	Camera can trigger in flight and has GPS information

2.2. Hardware Design

The following factors are put into consideration during design the quadcopter. The list of the components with respective weights shown in Table 2.

Table 2. List of the components

Components	Estimated weight	Number of units	Total weight
Brushless Motor	60g	4	240g
Propellers	15g	4	60g
Li-po battery	415g	1	415g
Frame	282g	1	282g
Skywalker ESC 30A	37g	4	148g
Pixhawk 4	15.6g	1	15.6g
Power board	36g	1	36g
RC receiver	26g	1	26g
Camera	14g	1	14g
		Total	1236.6g

The block diagram in Figure 1 below shows the input/output relationship of all other components to the micro-controller.

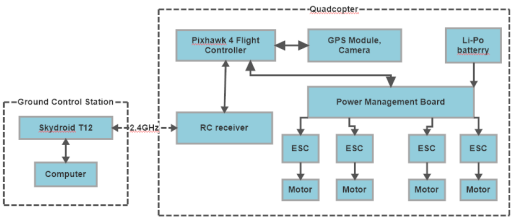

Figure 1. The hardware diagram

2.2.1. The Quadcopter Frame

The frame of the quadcopter was made of very strong materials. The arms are made from ultra strong PA66+30GF material, which provides better resistance to dame on hard landings. The frame plate uses a high strength compound PCB material. The overall frame design provides enough space when assembled to fit an autopilot system. The body frame made slim with holes drilled to it to maintain stability while flying and

to reduce the weight. The width of the frame was 450 mm and the height was 55 mm.

2.2.2. Motors and Electronic Speed Controllers

From the above weight estimate, SunnySky 2212-13 980Kv provides enough power to lift. Using 3 cells battery and a 10x47 propeller, each motor generates lift up to 8.5 N [7]. The total load of the quadcopter is 3 kg but the weight for stable flight is about 1.5 kg. And ESC Skywalker 30A was used for speed control.

2.2.3. Flight Controller and Sensor System

Pixhawk 4 flight controller is an advanced autopilot designed and developed in collaboration between Holybro and PX4 team. It's optimized to run Dronecode stack, and comes preinstalled with newest PX4 firmware. With the newest advanced processor technology from STMicroelectronics, sensor technology from Bosch and InvenSense, and Nuttx real-time operating system, Pixhawk 4 provides incredible performance, flexibility, and reliability for controlling any autonomous vehicle.

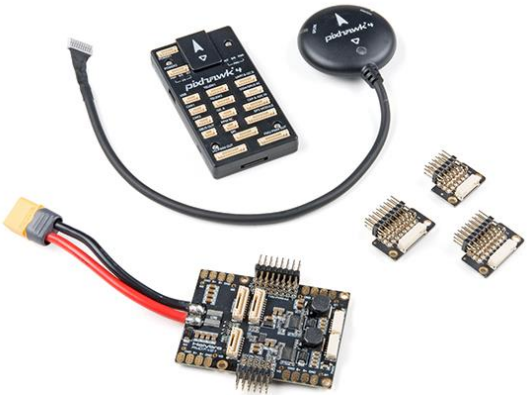

Figure 2. Pixhawk 4 controller, GPS and PM board

2.2.4. Image capture device

For image capturing, the quadcopter is equipped an RGB Camera. The Skydroid camera provides image with a resolution of 720p. It controlled by the trigger pin directly from the drone.

2.2.5. Communication system

An important part of the drone's design is the communication system. It plays a decisive role in the operation range of the drone and the mode control. For a safety flight, the quadcopter uses a Radio Controller to switch safety modes on the flight and use telemetry to observe quadcopter's flight. Because of the range flight and cost, Skydroid T12 RC (Figure 2) allows to control in 5km range without too much trouble. LORA technology and redundancy algorithms allow long distances control and save energy. Skydroid T12 provides a stable connection for control [8].

Figure 3. Skydroid RC and Camera

2.3. Software

2.3.1. PX4 Architecture

PX4 is an open-source flight control software for drones and other unmanned vehicles. It provides a standard to deliver drone hardware support and software stack and allows an ecosystem to build and maintain hardware and software in a scalable way. PX4 consists of two main layers: the flight stack is an estimation and flight control system, and the middleware is a general robotics layer that can support any type of autonomous robot, providing internal/external communications and hardware integration.[9]

2.3.2. QGroundControl

The ground control station that called QGroundControl provides full flight control and mission planning for any MAVLink enabled drone. Its primary goal is ease of use for professional users and developers. All the code is open-source source. For survey mission in this

research, we use the Survey plan pattern. A survey allows user to create a grid flight pattern over a polygonal area. QGroundControl can specify an arbitrary polygon, the angle and other properties of the grid, and camera settings appropriate for creating geotagged images[10].

3. Results

As a result, the figure below shows the complete quadcopter ready for agriculture monitoring. The system stability has been tested successfully before monitoring mission. Through many experiments and many changes in hardware, quadcopter was ready to fly.

Figure 4. Quadcopter's Flight

With survey mission in football field, the quadcopter was set up a flight with 22 set-points. During mission, the camera capture image each 4.29 meter. The Figure 4 shows the survey mission and Figure 5 shows the flight trajectory in reality (the violet path is survey mission).

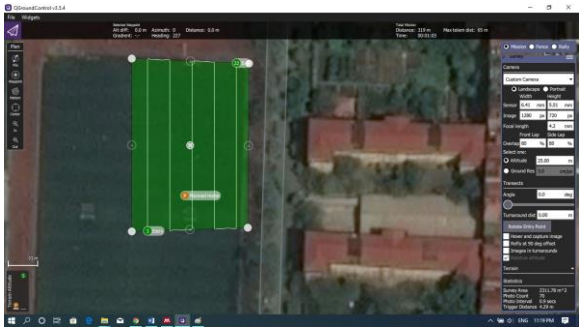

Figure 5. Survey mission in QGroundControl

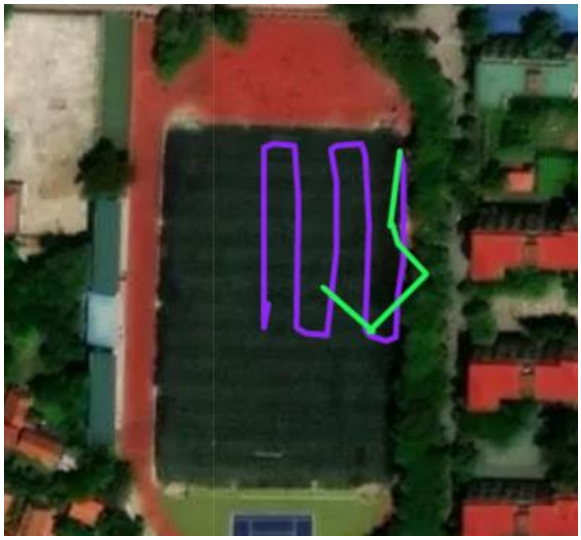

Figure 6. Quadcopter's flight trajectory

The graph below shows the set-point and reality trajectory. This result represents a stable system. The error between system estimation and actual GPS data is negligible. This design is perfectly suitable for automate flying missions especially in surveillance.

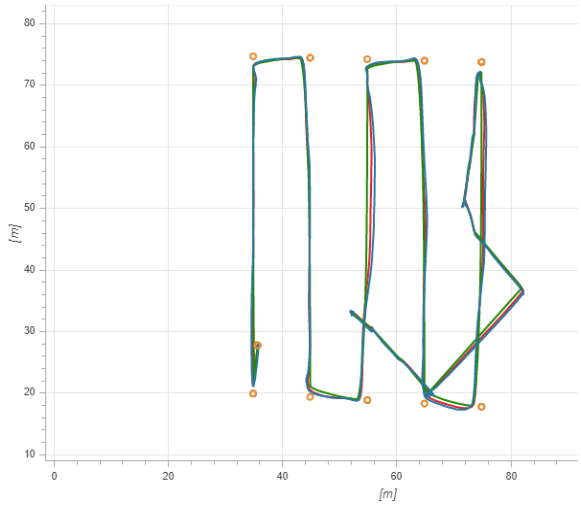

Figure 7. Trajectory of autonomous mission

The survey mission collects 70 pictures with GPS information and 80% overlap. All data processed by Pix4d mapper software. The figure 8 shows the large-scale map after processing. From stitching image, the size of football field is calculated. The dimension of a mini football yard is 48.31 meters long and 31.27 meters wide. The actual measurement results are 48.2 meters long and 31 meters wide. The calculation

shows the difference less than 1%. The results prove the feasibility of the project. Large-scale map with detailed length information is an effective tool for monitoring density.

Figure 8. Large-scale map building

4. Conclusion

In this paper, we introduce a low-cost UAV design and mapping method for observing crops and estimating their current production and environmental states. This open source system greatly reduces the monitoring costs compared to other flying systems. Hardware equipment optimized to increase flight time and minimized errors to improve the image quality obtained. The initial results show the effectiveness of UAV system for mapping application. On the other hand, the low-cost hardware system in the paper is suitable for academic and commercial. In the future, an embedded computer will be integrated in quadcopter for more complex survey mission.

References

[1] H. Saari *et al.*, "Unmanned Aerial Vehicle (UAV) operated spectral camera system for forest and agriculture applications," *Remote Sens. Agric. Ecosyst. Hydrol. XIII*, vol. 8174, p. 81740H, 2011.

[2] E. Semsch, M. Jakob, D. Pavlíček, and M. Pěchouček, "Autonomous UAV surveillance in complex urban environments," *Proc. - 2009 IEEE/WIC/ACM Int. Conf. Intell. Agent Technol. IAT 2009*, vol. 2, pp. 82–85, 2009.

[3] M. M. B. Coifman, "Roadway traffic monitoring from an unmanned aerial vehicle," *IEE Proc. - Intell. Transp. Syst.*, vol. 153, no. 4, pp. 276–291, 2006.

[4] F. Remondino, L. Barazzetti, F. Nex, M. Scaioni, and D. Sarazzi, "UAV PHOTOGRAMMETRY FOR MAPPING AND 3D MODELING," vol. XXXVIII, no. September, pp. 14–16, 2011.

[5] F. Neitzel and J. Klonowski, "3D mobile mapping with a low cost UAV system," *Int. Arch. Photogramm. Remote Sens. Spat. Inf. Sci. - ISPRS Arch.*, vol. 42, no. 2W8, pp. 127–132, 2011.

[6] H. Eisenbeiss, "UAV photogrammetry," 2009.

[7] "Sunnysky 2212-13 kv980." [Online]. Available: https://www.foxtechfpv.com/sunnysky-221213-kv980-p-384.html. [Accessed: 10-Oct-2019].

[8] "T12 12-Channel Radio Controller User Manual."

[9] "Documentation - PX4 Open Source Autopilot." [Online]. Available: https://px4.io/documentation/. [Accessed: 11-Oct-2019].

[10] "Overview · QGroundControl User Guide." [Online]. Available: https://docs.qgroundcontrol.com/en/. [Accessed: 11-Oct-2019].

The 5th International Conference on Engineering Mechanics and Automation (ICEMA 5)
Hanoi, October 11÷12, 2019

A Research on Sensorless Control of Brushless DC Motor using Inductance Variation Technique

Dang Hai Ninh[a], Nguyen Quang Tan[a] and Nguyen Ngoc Linh[a]

[a] *Faculty of Engineering Mechanics and Automation, University of Engineering and Technology*

Abstract

Today, brushless DC motors (BLDCM) have been used in many applications replacing to brushed DC motors. Compared to brushed DC motors, BLDCM offer improved reliability, longer life, smaller size, and lower weight. Besides, BLDCM have become more popular in applications where efficiency is a critical concern and, generally speaking, a BLDCM is considered to be a high-performance motor capable of providing large amounts of torque over a wide speed range.

In this paper, a research on sensorless control method which can drive a BLDCM smoothly from standstill to high speeds without position or speed sensors is carried out. Initial rotor position as well as speed of motor at a low speed range is estimated based on the inductance variation principle while at higher speed, the back EMF technique is applied. This sensorless control algorithm is modeled and simulated with MATLAB/SIMULINK software to verify the abilities of the method. The drive control scheme has been implemented on a single-chip controller (STM32F103) and experimental results reveal that the control procedure can work smoothly.

Key Words: Sensorless Control, BLDCM, Inductance Variation, back EMF technique, Matlab/Simulink

1. Introduction

The BLDCM is used in various applications of electromechanical systems because of its high efficiency and good controllability over a wide range of speeds. The drive for the brushless DC motor requires an inverter and a position sensor for providing proper commutation sequence to turn on the power devices in the inverter bridge. However, the position sensor not only increases the cost and encumbrance of the overall drive system but also reduces its control robustness and reliability. Furthermore, it might be difficult to install and maintain a position sensor due to the limited assembly space and rigid working environment with severe vibration and/or high temperature. As a result, many researches have been carried out for sensorless control of BLDCM that can control position, speed and/or torque without shaft-mounted position sensors, which can be categorized into the following:

Back-EMF Sensing Techniques [1]:

These methods include terminal voltage sensing of the motor; detection of the conducting state of freewheeling diode in the unexcited phase; back-EMF integration method; Stator third harmonic voltage components. These methods have been shown to be successful only at medium and high rotor speeds.

Flux Linkage-Based Technique [1]:

In these methods, the flux linkage is calculated using measured voltages and currents. The fundamental idea is to take the voltage equation of the machine and by integrating the applied voltage and current, flux can be estimated. From the initial position, machine parameters, and the flux linkages' relationship to rotor position, the rotor position can be estimated. This method also has significant estimation error in low speeds.

Extended Kalman filters [1]:

The Extended Kalman Filter (EKF) is able to provide optimum filtering of the noises in measurement and inside the system if the covariances of these noises are known. It is an optimal stochastic observer in the least-square sense for estimating the states of dynamic non-linear systems. Hence it is a viable candidate for the on-line determination of the rotor position and speed [22-24]. However, none of the practical industry applications of EKF-based sensorless PMSM control has been reported due to the technical difficulties.

Estimators based on inductance variation due to geometrical and saturation effects [1]:

The rotor position can be estimated by using inductance variations due to magnetic saturation and/or geometrical effects of BLDCM. This method was proposed by Schroedl, which was based on real-time inductance measurements using saliency and saturation effects. During a short time interval, the "complex INFORM reactance" was calculated for estimating flux angle [9]. Corley and Lorenz [10] investigated a high frequency signal injection method in such a way that carrier-frequency voltages were applied to the stator windings of PMSM, producing high-frequency currents of which the magnitude varies with rotor position.

2. BLDCM Drive [3]

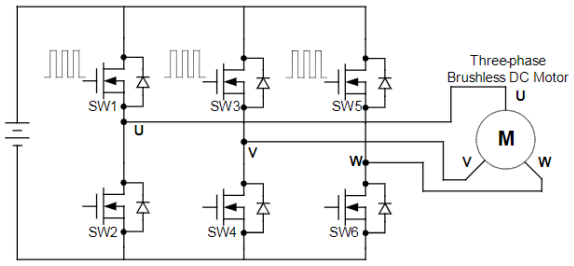

Figure 1. BLDCM Driver

A typical Brushless DC motor is driven by voltage pulses to specific phase of the stator in accordance to the position of the rotor. To generate the maximum torque in the brushless DC motor, these voltage pulses should be applied properly to the active phases of the three-phase winding system so that the angle between the rotor flux and the stator flux is kept close to 90 degrees. Therefore, special controllers are required which control the voltage on the basis of rotor position detected. Once the rotor position is detected, the controller works appropriately to generate a proper commutation sequence of the voltage strokes so that the BLDC motor keeps rotating. The BLDC motor is supplied with the three-phase inverter and the commutation sequence can be simply used to trigger the switching actions of the inverter. There are different control techniques available in the industry for brushless DC motors and are explained below:

- Six step Commutation
- Sinusoidal Commutation
- Field Oriented Control
- Direct Torque Control

3. Sensorless Control Method

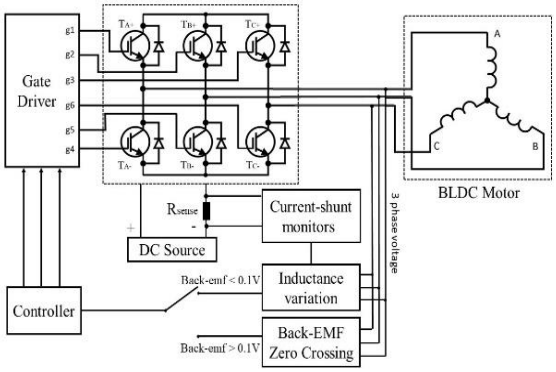

Figure 2. System architecture

The measurement/estimation of rotor position is the most critical step in controlling the BLDC motors. A small error in position estimation for BLDC motor can result in very poor performance and in some cases it may result in a complete motor failure. The estimation of the rotor position can be done by sensored and sensorless approaches. In sensored approach, some types of external sensor are attached with the motor, while

for sensorless there are no sensors attached to the motor itself.

The problems associated with the cost and reliability of sensors used to detect the rotor position have motivated research in the area of sensorless position detection for BLDC motor drives. In the last decade, many sensorless drive solution has been offered to eliminate the costly and fragile position sensors for BLDC motor. Below are the main sensorless approaches for controlling the BLDC motors.

3.1. Back-EMF technique [2]

When a brushless DC motor starts rotating, the electromotive force (back-EMF) is generated by each winding which opposes the supplied voltage to the windings in accordance with Lenz's law. Back-EMF is directly proportional to the speed of the motor.

The shape of this back-EMF in brushless DC motor is trapezoidal. The direction of the back-EMF is opposite to the applied voltage, so it is harmful in the normal DC motor. But we can use back-EMF in BLDC to detect the information of rotor position by using "the zero crossing". R is the phase resistance. i_a, i_b, i_c are three-phase current. E_a, E_b, E_c are the back-EMF of three-phases. V_n is the motor neutral voltage, V_a, V_b, V_c are the motor terminal voltage.

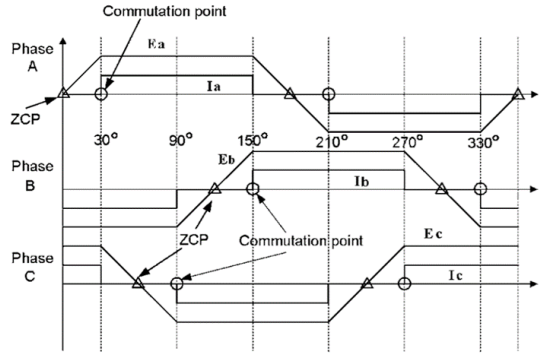

Figure 3. Ideal back-EMF waveforms.

The voltage equations can be written as follows:

$$V_a = Ri_a + L\frac{di_a}{dt} + E_a + V_n \quad (1)$$

$$V_b = Ri_b + L\frac{di_b}{dt} + E_b + V_n \quad (2)$$

$$V_c = Ri_c + L\frac{di_c}{dt} + E_c + V_n \quad (3)$$

Since all three resistors are symmetrical, we have:

$$E_a + E_b + E_c = 0 \quad (4)$$

And it is obvious that:

$$i_a + i_b + i_c = 0 \quad (5)$$

At the zero-crossing point of the Back–EMF phase C we have:

$$E_c = \frac{1}{2}V_{dc} \quad (6)$$

Similarly:

$E_a = \frac{1}{2}V_{dc}$ (at the zero crossing of phase A). (7)

$E_b = \frac{1}{2}V_{dc}$ (at the zero crossing of phase B). (8)

So we can find the zero crossing by feeding the voltage of the un-powered winding with the virtual ground and half the DC bus voltage to comparator.

The Back – EMF sensing is not suitable at the very low speed and at stationary state. So we need a sensorless technique which can control the BLDCM

3.2. Inductance Variation Technique [7]

Three voltage pulses are applied in the rotor position estimation. Voltage pulse injection consists of two intervals: pulse injecting interval and freewheeling interval.

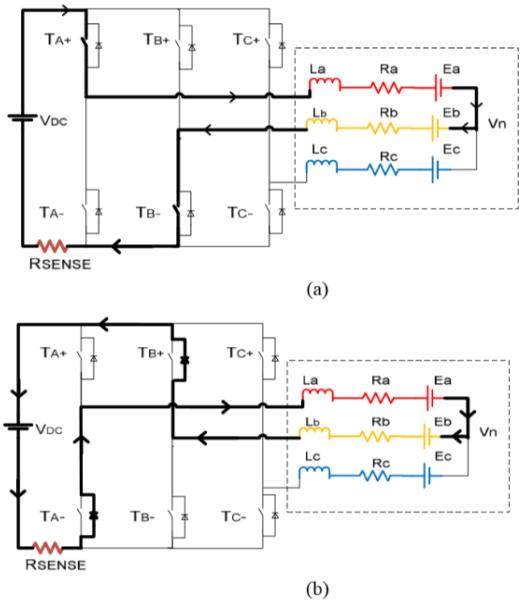

Figure 4. Pulse injecting interval (a) and freewheeling interval (b).

This technique consists of two process:

Inductance comparison process:

Two voltage pulses are injected to phases A, B and phases A, C. Based on the mathematical model of BLDCM:

$$V = Ri + L\frac{di}{dt} + e \quad (9)$$

And $e = 0$ when motor standstill or rotating in low speed, we have:

$$V = Ri + L\frac{di}{dt} \quad (10)$$

$$V \sim L \text{ or } V \sim f(\theta) \quad (11)$$

With θ is the initial rotor position.

Because R is constant and i in each phase is same so the:

Polarity determination process [5]:

The third voltage pulse is injected, the direction is based on the initial rotor position (look up column 4 on the Table 1).

The north and south poles of the rotor magnet can be determined from the idea that the winding currents from the injected pulse voltages can further increase or decrease the stator saturation. With this ideal, the sector where the north pole locates can be discriminated.

Phase voltage comparison	Inductance comparison	Possible initial position	3^{th} injection	Peak Current	Initial position
$V_{NB1} > V_{NA1}$ $V_{NC2} \geq V_{NA2}$ $V_{NB1} > V_{NC2}$	$L_B > L_C \geq L_A$	$0^0 < \theta_0 < 30^0$ $180^0 < \theta_0 < 210^0$	$T_{C+}\ T_{A-}$	$I_2 > I_3$ $I_3 > I_2$	$0^0 < \theta_0 < 30^0$ $180^0 < \theta_0 < 210^0$
$V_{NB1} \geq V_{NA1}$ $V_{NC2} < V_{NA2}$ $V_{NB1} > V_{NC2}$	$L_B > L_A \geq L_C$	$30^0 < \theta_0 < 60^0$ $210^0 < \theta_0 < 240^0$	$T_{C+}\ T_{A-}$	$I_2 > I_3$ $I_3 > I_2$	$30^0 < \theta_0 < 60^0$ $210^0 < \theta_0 < 240^0$
$V_{NB1} < V_{NA1}$ $V_{NC2} < V_{NA2}$ $V_{NB1} \geq V_{NC2}$	$L_A > L_B \geq L_C$	$60^0 < \theta_0 < 90^0$ $240^0 < \theta_0 < 270^0$	$T_{C+}\ T_{A-}$	$I_2 > I_3$ $I_3 > I_2$	$60^0 < \theta_0 < 90^0$ $240^0 < \theta_0 < 270^0$
$V_{NB1} < V_{NA1}$ $V_{NC2} \leq V_{NA2}$ $V_{NB1} < V_{NC2}$	$L_A > L_C \geq L_B$	$90^0 < \theta_0 < 120^0$ $270^0 < \theta_0 < 300^0$	$T_{B+}\ T_{A-}$	$I_3 > I_1$ $I_1 > I_3$	$90^0 < \theta_0 < 120^0$ $270^0 < \theta_0 < 300^0$
$V_{NB1} \leq V_{NA1}$ $V_{NC2} > V_{NA2}$ $V_{NB1} < V_{NC2}$	$L_C > L_A \geq L_B$	$120^0 < \theta_0 < 150^0$ $300^0 < \theta_0 < 330^0$	$T_{B+}\ T_{A-}$	$I_3 > I_1$ $I_1 > I_3$	$120^0 < \theta_0 < 150^0$ $300^0 < \theta_0 < 330^0$
$V_{NB1} > V_{NA1}$ $V_{NC2} > V_{NA2}$ $V_{NB1} \leq V_{NC2}$	$L_A > L_B \geq L_C$	$150^0 < \theta_0 < 180^0$ $330^0 < \theta_0 < 360^0$	$T_{B+}\ T_{A-}$	$I_3 > I_1$ $I_1 > I_3$	$150^0 < \theta_0 < 180^0$ $330^0 < \theta_0 < 360^0$

Table 1. Comparison table of position determination

4. Simulation and Experiment Results

4.1. Simulation results

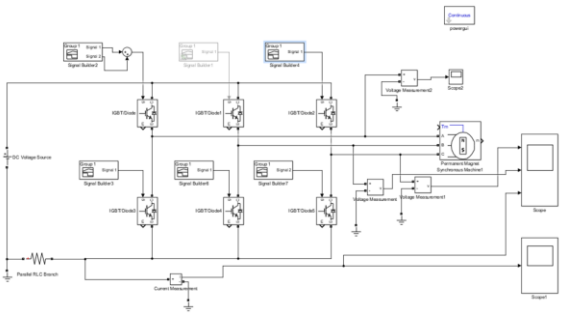

Figure 5. BLDCM Driver in Matlab/Simulink

In order to verify the proposed methods, a simulation is carried out by using Matlab/Simulink software. The parameter of simulation is synthesized in Table 1. The Simulink model is described in Figure 5.

Parameters	**Value**
Polarity poles	4
DC source	25V
Inductance of stator (L)	0.2H
Reluctance of stator (R)	2.8Ω

Table 2. Parameters of BLDCM in simulation

The shape of Back-EMF in the motor is trapezoidal as shown in Figure 6. The Back-EMF detection is made in the floating phase, and the power of detecting circuit is directly supplied by the power unit of driver system.

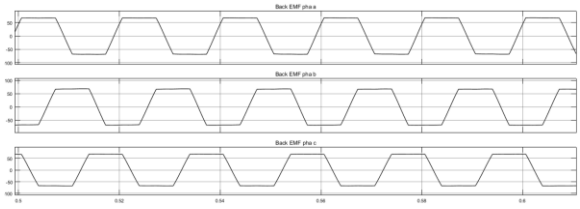

Figure 6. Simulation Back EMF in three-phase

Effectiveness of the method is validated from simulation results. The simulation had been done in Matlab/Simulink platform. The validity of this method is verified by conducting the simulation for $\theta = 35^0$ and $\theta = 280^0$ by adjusting the motor model in simulink. In case of $\theta = 35^0$ after two pulses voltage are injected, we have $V_{NA2} < V_{NC2}$ and $V_{NB1} > V_{NC2}$.

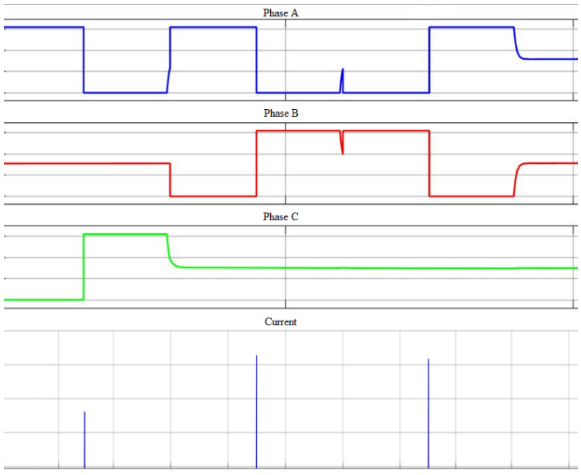

Figure 7. Phase voltage and DC-link current at 35^0

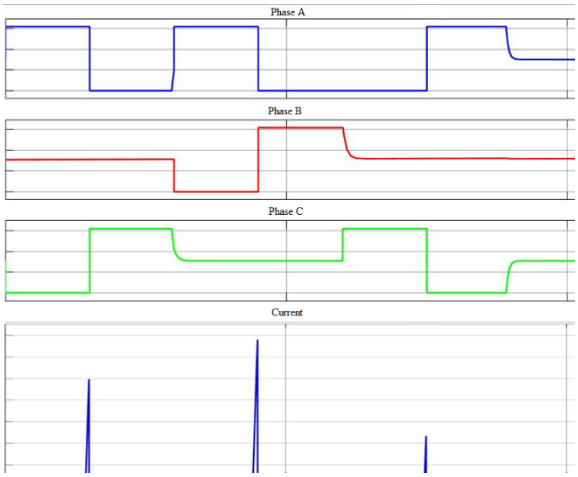

Figure 8. Phase voltage and DC-link current at 280^0

From Table 1, it is clear that the direction of the third pulse voltage is turn on switches T_{C+} and T_{A-} and also the current comparison is between I_2 and I_3. Because $I_2 > I_3$ so the estimated initial rotor position is $30^0 < \theta < 60^0$. Similarly, we also have $V_{NA2} > V_{NC2}$; $V_{NB1} < V_{NC2}$ so the estimated initial rotor position can be between $90^0 < \theta < 120^0$ or between $270^0 < \theta < 300^0$. But the DC- link current, which is measured for the rotor position $\theta = 280^0$, shown that $I_3 < I_1$. Hence from the table 1, it is clear that the rotor position is at sector $270^0 < \theta < 300^0$.

4.2. Experiment results

In order to validate the claims made in the proposed approach, the targeted experimental setup was used to implement the proposed method.

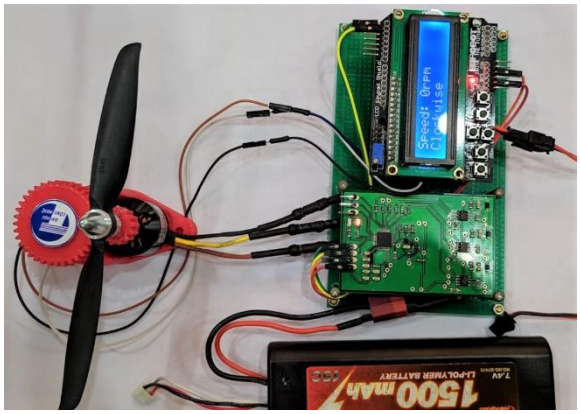

Figure 9. BLDCM Control scheme

BLDCM drive control board includes:
- 6 step control.
- Four-layer PCB.
- IPC-2221 Generic Standard on Printed Board Design.
- STM32F103 microcontroller with RTOS.
- INA214 current-sense amplifiers.
- The phase voltage is measured using ADC pin of the microcontroller.
- 6x IRF7828 power MOSFET.
- UART and CAN communication bus

The proposed method is verified with several tested speed ranging from low to medium (20rpm, 60rpm and 200rpm). Phase voltage, DC-link current and back-EMF waveforms of BLDCM in experiment is same as these in the simulation. The results show that the proposed method can be applied in the real application.

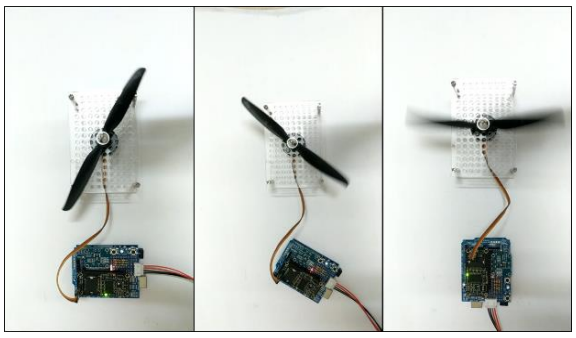

Figure 10. Test at three speed 20rpm, 60rpm and 200rpm.

5. Conclusion

The research studies how to drive a BLDCM smoothly from standstill to high speeds without position or speed sensors is carried out, using one and the only current sensor. Its applications is decreasing the cost of a BLDCM attached system.

This study mainly focuses on rotor position of the BLDCM without controlling the motor moment which might be discussed in another study in the future.

References

[1] Wang Hua-bin, Liu He-ping. "*Novel Driving Method For BLDCM From Standstill To High Speeds*". WSEAS Transactions on Systems, Volume 7, Issue 11, November 2008, pp.1269-1279.

[2] P.Damodaran, Krishna Vasudevan, "*Sensorless Brushless DC Motor Drive Based on the Zero Crossing Detection of Back Electromotive Force (EMF) from the Line Voltage Difference*", IEEE Trans on Energy conservation, Vol.25, No.3, Sept 10.

[3] Zezhong Xia, Wen Li, Wenjuan Sheng, Youxin Yuan, *"Design of a control system for sensorless brushless DC motor using dsPIC*", IEEE Conf. Ind. Appl, 2008, pp. 551-556.

[4] S.Ogaswara and H.Agaki "*An approach to position sensorless drives for brushless DC motors*" IEEE Trans.Ind.Appl, vol.27, no.5, Sep/Oct.1991, pp.928-933.

[5] Prasit Champa, Pakasit Somsiri, Pongpit Wipasuramonton, Paiboon Nakmahachalasint, "*Initial rotor position estimation for sensorless brushless DC drives*," IEEE Trans.Ind. Appl, vol.45, no.4, Jul/Aug.2009, pp.1318-1324.

[6] P.B Schmidt, M .L Gasperi, G.Ray and A.H Wijenayke, "*Initial rotor angle detection of non salient pole permanent magnet synchronous machine*", in Conf.Rec.IEEE IAS Annu. Meeting. NewOrleans, LA,1997, pp459-463.

[7] G.H.Jang, J.H Park and J.H Chang "*Position detection and start up algorithm of a rotor in a sensorless BLDC Motor utilizing inductance variation*", Proc.Inst.Elect.Eng-Elect Power Appl, vol.149, no.2, pp.137-142, Mar.2002.

[8] Y.S. Lai, F.s Shyu and S.S.Tseng, "*New initial position detection for three phase brushless DC motor without position and current sensor*" IEEE Trans. Ind.Appl, vol.39, no.2, Mar/Apr.2003, pp.485-491.

The 5th International Conference on Engineering Mechanics and Automation (ICEMA-5)
Hanoi, October 11÷12, 2019

Automated the QRS complex detection for monitoring the electrical activity of the heart

Manh Hoang Van[a], Viet Dang Anh[a], Quan Dang Hong[b] and Thang Pham Manh[a]

[a] *Lecturer, University of Engineering and Technology, Vietnam National University, Ha Noi*
[b] *Master student, University of Engineering and Technology, Vietnam National University, Ha Noi*

Abstract

In this work, we present a novel QRS complex detection approach in noisy exercise ECG signals based on a continuous wavelet transform (CWT) for a single-lead ECG signal. First, the adaptive filtering algorithm is employed to remove the additive artifacts from the signals. The ECG signals are then transformed by a CWT at a suitable scale. Finally, the QRS complex is detected in processed signals. The performance of the proposed algorithm is evaluated on the MIT-BIH Noise Stress Test Database. The recordings in this dataset are specially selected and characterized by baseline wander, muscle artifacts, and electrode motion artifacts as noise sources. Obtained results show that the proposed method reached the most satisfactory performance compared with several other QRS complex detection algorithms.

Key Words: ECG, continuous wavelet transform, stress ECG test, RLS filter.

I. Introduction

The Electrocardiogram (ECG) is simply a recording of the electrical activity of the heart by electrodes placed on the surface of the body. Changes in the voltage measured by the electrodes are due to the action potentials of irritating heart cells that cause cell contractions. The resulting ECG heart cycle is represented by a series of waves whose morphology and occurrence time contain information utilized to diagnose cardiovascular diseases. However, the challenge when diagnosing heart diseases with ECG signals is that these signals vary considerably between different people. Besides, different patients might have various morphologies for the same condition. Also, two different diseases may have similarities in the properties of an ECG signal. These issues cause several difficulties for heart disease diagnosis [1][2]. To determine the abnormalities of the heartbeat, each beat of the ECG signal must be analyzed. The QRS complex is the essential waveform within the ECG signal since its shape provides much information about the current condition of the heart.

Within the last decade, many new approaches have been proposed to improve the accuracy of the QRS complex detector. The well-known Pan and Tompkins approach, which is based on the slope, amplitude, and width of the ECG signal [3]. After filtering the signal, smoothing the waveform, and

emphasizing the QRS complex slope and width, the two threshold sets are applied to locate the true positive R peaks. An improved version of the Pan and Tompkins method is introduced in [4], where the process of calculating the threshold is optimized through analyzing three estimators (mean, median, and an iterative peak level). In [5], the authors proposed the real-time QRS complex detection approach consisting of four phases. First, the unwanted noises are removed from the ECG signals by using a band-pass filter. A five-point first-order differentiation, absolute and backward searching operation, was then utilized to improve the QRS complex. For an accurate determination of local maxima with different shapes, a K-nearest neighbor-based peak-finding and particle swarm optimization algorithm was implemented.

This paper aims to develop an algorithm to detect and localize QRS complexes in ECG signals during exercise by analyzing a wide range of other morphologies. The performance of the method is evaluated on reputable standard manually annotated MIT-BIH Noise Stress Test Database [6].

The remainder of this work is organized as follows: the proposed approach is introduced in Section II. Experimental results and performance are presented in Section III. The novelty and findings of this work are summarized in Section IV.

II. Description of the proposed approach

The proposed wavelet-based algorithm for the detection of the QRS complex is presented in Figure 1. This method includes the signal preprocessing, the continuous wavelet transform, the thresholding and determination of candidate extremum pairs, and the identification of QRS complexes. The detail of each stage is described in the following sections.

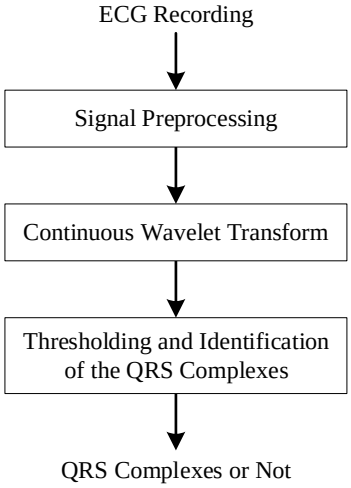

Figure 1. Block diagram of the proposed wavelet-based algorithm for the detection of the QRS complex.

1. Signal preprocessing

Each ECG signal was first segmented by a sliding window of 4096 samples with an overlap of 150 samples between two adjacent windows, as shown in Figure 2. The design of the 150-sample overlap aims to avoid the incomplete QRS complexes located at the end of the 4096-sample segments, which could be misidentified as Not QRS complexes. Each section was then filtered by the adaptive filter algorithm to remove the Powerline Interference (PLI) and Baseline Wander (BW) noise from the ECG signals.

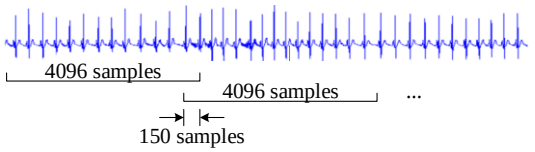

Figure 2. Illustration of segmentation of the ECG signal

2. Continuous wavelet transform

In this work, the numerical realization of the CWT has been chosen because the execution speed of the algorithm will be faster. The wavelet transform (WT) describes a signal from a time-frequency perspective on different scales, with a different frequency band corresponding to each scale. While the dyadic form of discrete-time wavelet transform (DyDTWT) is limited to scales that are powers of two [9][10], the CWT can be calculated for any scale. Thus, a CWT-based

approach is offered as an alternative tool to detect the QRS complexes in ECG signals. The use of the appropriate scales, the effects of interference, and signal fluctuations caused by breathing and patient movements during recording can be significantly reduced.

The CWT of the continuous signal $x(t)$ at the scale $a \in R^+$ and translational value $b \in R^+$ is expressed by the integral [10]

$$CWT(b,a) = \frac{1}{\sqrt{a}} \int_{-\infty}^{+\infty} x(t) \psi^* \left(\frac{t-b}{a}\right) dt \quad (1)$$

where $\psi(t)$ is a continuous function called the mother wavelet, and the asterisk denotes the operation of the complex conjugate.

The most commonly used types of mother wavelet for detecting the QRS complexes are the quadratic spline function [9][10] and the first derivative of the Gaussian function [11]. However, by experimenting with several other mother wavelets, especially from the biorthogonal family, we achieved the best results with *bior*1.5. In [9][10], the authors found the similarities across the other DyDTWT scales; our approach is based on finding and using an appropriate scale. The best results were achieved with the scale 15. The wavelet *bior*1.5 is an odd symmetry wavelet that transforms the extremes of the original signal into zero-level passages and transforms the inflection points into extremes. Thus, by transform, the signal is altered in a similar way to the derivative.

3. The thresholding and identification of the QRS complexes

After the filtered signal is transformed by the CWT at the scale 15, the algorithm will search in the transformed signal of pairs of near opposite sign extremes, whose absolute values are greater than the threshold ξ_{QRS}. If such pairs of extremes are found, and if these extremes are spaced less than $120\ ms$, then the positions of these extremes correspond to the ascending and descending edges of several of the QRS complexes. The wave position is then determined by the zero-crossing position between the two adjacent extremes. In this way, one or more waves of the QRS complex can be detected. Because the detector indicates the location of the complex as a whole, it is necessary to select a single position representing the QRS complex. For this purpose, there is a refractory period $120\ ms$ before the next one can be detected since the QRS complexes cannot occur more closely than this physiologically. The positions preceded by another location in an interval shorter than the refractory period are removed from the detected positions. Therefore, the location of the QRS complex is the position of the first detected wave within the complex. The threshold level ξ_{QRS} is given by the equation,

$$\xi_{QRS} = 1{,}6. \sqrt{\frac{1}{n} \sum_{i=1}^{n} (x_i - \bar{x})^2} \quad (2)$$

And thus, we can see that the threshold value corresponds to 1.6 times the standard deviation calculated from all the values of the transformed signal segment analyzed. The constant of 1.6 was determined as a suitable factor of the standard deviation based on the analysis of the complete ECG signal database (highest detection rate). Deriving a threshold level from a standard deviation is a more robust approach than a threshold derived from the maximum value or the difference between the maximum and the minimum that can easily be affected by the artifact or extrasystoles. The threshold is fixed, and its value is the same for the entire segment of the analyzed signal.

III. Results and Discussion

1. The ECG database

The proposed algorithm is evaluated using the MIT-BIH Noise Stress Test Database [6], which includes twelve half-hour ECG records and three half-hour records of noise typical in ambulatory ECG records. The ECG records were created by adding calibrated amounts of noise (baseline wander, electrode motion artifact, or muscle noise) to clean ECG recordings from the MIT-BIH Arrhythmia Database [12]. To evaluate the performance of

this work, only the files provided from the database (files 118 and 119) are used in the test. They are only affected by the artifact of EM type (electrode motion artifact noise).

The noise was added beginning after the first five minutes of each record, during two-minute segments, alternating with two-minute clean sections. The three noise signal records were assembled from the signal files by selecting parts that contained an electrode motion artifact. Since the original ECG recordings are clean, the correct beat annotations are known even when the noise makes the records visually unreadable. The reference annotations for these records are simply copies of those for the original clean ECG signals. The signal-to-noise ratios (SNRs) during the noisy segments of these records are listed in the flowing Table 1.

Table 1. The records in the MIT-BIH Noise Stress Test Database [13].

Record	SNR (dB)	Record	SNR (dB)
118e24	24	119e24	24
118e18	18	119e18	18
118e12	12	119e12	12
118e06	6	119e06	6
118e00	0	119e00	0
118e_6	-6	119e_6	-6

To compare the performance of our proposed algorithm with several other prominent QRS complex detectors specified in the literature, only the first channel of each ECG record is used.

2. *Performance evaluation and comparisons*

For the performance evaluation of the proposed method, the parameters such as sensitivity, positive prediction, and detection error rate are taken into account. The sensitivity (Se) is defined as the probability of detecting a QRS complex when a QRS exists; the positive prediction (P^+) represents the probability of detecting the QRS complex among the detected ECG peaks. They are calculated by using the following equations:

$$\text{Sensitivity: } Se = \frac{TP}{TP+FN} \quad (3)$$

$$\text{Positive Prediction: } P^+ = \frac{TP}{TP+FN} \quad (4)$$

$$\text{Detection Error Rate: } DER = \frac{FP+FN}{TP+FN} \quad (5)$$

where, TP (the number of true positive detections) is the number of correct identified QRS complexes present in the signal under test; FN (stands for the amount of false-negative detections) is the number of QRS complexes present in the signal that the algorithm is not able to detect; FP (stands for the amount of false-positive misdetections) is the number of QRS complexes detected by the algorithm that are not actually in the signal.

To evaluate the accuracy of the detected QRS complex, a tolerance window of $150\ ms$, centered at the reference annotation, has been used. Different signal to noise ratio (SNR) levels for the same ECG record is analyzed; in particular, values ranging from $24\ dB$ to $0\ dB$ are tested. The performance of the proposed method related to different SNR levels of the same ECG signal is shown in Figures 3 and 4.

From the analytical figures, we can see that the sensitivity parameter is almost constant. Therefore, it is rather unaffected by artifact corrupting the ECG signal. The obtained results show that the algorithm is almost immune to noise up to SNR levels equal to 6 dB. Specifically, for SNR = 6 dB, the obtained Se and P^+ values are 99.51% and 96.63%, respectively. For SNR levels lower than 6 dB, the parameters Se and P^+ are dependent on the amount of noise. In particular, an assessment of the results achieved for SNR values equal to 0 dB, Se and P^+ reach values of 95.97% and 88.61%, respectively.

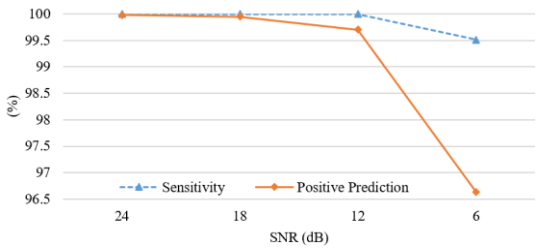

Figure 3. Algorithm behavior as a function of different SNR levels.

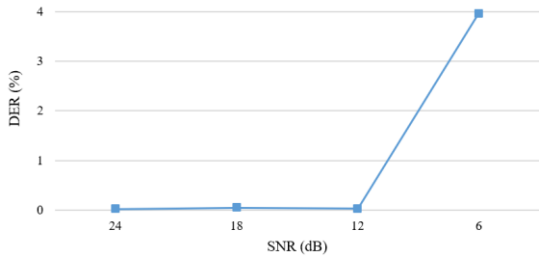

Figure 4. Detection error rate achieved as a function of different SNR levels.

To compare the performance of the proposed algorithm with several available works, the same test procedure indicated in the article [14] has been implemented. In [14], the authors have analyzed the algorithms in [15][16][17][11] for the assessment of their robustness against artifact using the MIT-BIH Noise Stress Test Database as a test bench. Table 2 shows a comparative study among the performance of the proposed method in this paper and the results of the algorithms, as reported in [13][14].

Table 2. The Se and P^+ values obtained using the MIT BIH Noise Stress Test Database, with an SNR = 6 dB and 0 dB.

	SNR = 6 dB		SNR = 0 dB	
Method	**Se**	**P^+**	**Se**	**P^+**
This work	99.51	96.63	95.97	88.61
Pangerc U. et al.	99.91	95.91	83.97	68.92
De Cooman T. et al.	99.47	73.30	96.51	59.36
Vollmer M.	98.50	96.73	77.10	74.91
Matteo D'Aloia et al.	98.13	96.91	78.98	75.25
Antink C.H. et al.	84.89	76.40	72.20	66.37

The data table indicates that our proposed algorithm has good results compared to other algorithms shown in the literature. More specifically, it achieves the most effective P^+ value compared to all the analyzed methods for SNR value equal to 0 dB.

IV. Conclusion

This paper introduces an innovative approach to the detection of QRS complexes in noisy exercise ECG signals. The method is based on the numerical implementation of the continuous wavelet transform, an appropriate choice of mother wavelet and scale used, thresholding with a fixed threshold.

The MIT-BIH Noise Stress Database was employed to evaluate the noise robustness of the proposed algorithm. Experimental results indicate that the algorithm can still obtain good results when the SNR level is up to 6 dB. For SNR levels lower than 6 dB, the achieved results get worse, since an increase of the FP and FN is observed.

V. Acknowledgment

This work is supported by the research project N0. 01C02/01-2016-2 granted by the Department of Science and Technology Hanoi.

VI. References

[1] J. Mateo, A. M. Torres, A. Aparicio, and J. L. Santos, "An efficient method for ECG beat classification and correction of ectopic beats," *Comput. Electr. Eng.*, vol. 53, pp. 219–229, 2016.

[2] S. Shadmand and B. Mashoufi, "A new personalized ECG signal classification algorithm using Block-based Neural Network and Particle Swarm Optimization," *Biomed. Signal Process. Control*, vol. 25, pp. 12–23, 2016.

[3] J. Pan and W. J. Tompkins, "A Real-time {QRS} Detection Algorithm," *IEEE Trans. Biomed. Eng.*, vol. 32, no. 3, pp. 230–236, 1985.

[4] P. S. Hamilton and W. J. Tompkins, "Quantitative Investigation of QRS Detection Rules Using the MIT/BIH Arrhythmia Database," *IEEE Trans. Biomed. Eng.*, vol. BME-33, no. 12, pp. 1157–1165, Dec. 1986.

[5] R. He *et al.*, "A novel method for the detection of R-peaks in ECG based on K-Nearest Neighbors and Particle Swarm Optimization," *EURASIP J. Adv. Signal Process.*, vol. 2017, no. 1, 2017.

[6] G. B. Moody, W. K. Muldrow, and R. G. Mark, "Noise Stress Test for Arrhythmia Detectors.," *Computers in Cardiology*. pp. 381–384, 1984.

[7] G. D. Clifford, F. Azuaje, and P. E. McSharry, "Advanced Methods and Tools for ECG Data Analysis," *Adv. Methods Tools ECG Data Anal.*, pp. 1–400, 2006.

[8] P. L. and T. Hill, "Statistics : Methods and Applications By Pawel Lewicki and Thomas Hill," *Statistics (Ber).*, vol. 1st, pp. 1–719, 2006.

[9] C. Li, C. Zheng, and C. Tai, "Detection of ECG characteristic points using wavelet transforms," *IEEE Trans Biomed Eng*, vol. 42, no. Bmei, pp. 21–28, 1995.

[10] J. P. Martínez, R. Almeida, S. Olmos, A. P. Rocha, and P. Laguna, "A Wavelet-Based ECG Delineator Evaluation on Standard Databases," *IEEE Trans. Biomed. Eng.*, vol. 51, no. 4, pp. 570–581, 2004.

[11] M. Vollmer, "Robust detection of heart beats using dynamic thresholds and moving windows," *Comput. Cardiol. (2010).*, vol. 41, no. January, pp. 569–572, 2014.

[12] G. B. Moody and R. G. Mark, "The impact of the MIT-BIH arrhythmia database," *IEEE Eng. Med. Biol. Mag.*, vol. 20, no. 3, pp. 45–50, 2001.

[13] M. D'Aloia, A. Longo, and M. Rizzi, "Noisy ECG signal analysis for automatic peak detection," *Inf.*, vol. 10, no. 2, pp. 1–12, 2019.

[14] M. Vollmer, "Noise resistance of several top-scored heart beat detectors," *Comput. Cardiol. (2010).*, vol. 44, no. April, pp. 1–4, 2017.

[15] C. H. Antink, C. Brüser, and S. Leonhardt, "Detection of heart beats in multimodal data: A robust beat-to-beat interval estimation approach," *Physiol. Meas.*, vol. 36, no. 8, pp. 1679–1690, 2015.

[16] T. De Cooman, G. Goovaerts, C. Varon, D. Widjaja, T. Willemen, and S. Van Huffel, "Heart beat detection in multimodal data using automatic relevant signal detection," *Physiol. Meas.*, vol. 36, no. 8, pp. 1691–1704, 2015.

[17] U. Pangerc and F. Jager, "Robust detection of heart beats in multimodal records using slope- and peak-sensitive band-pass filters," *Physiol. Meas.*, vol. 36, no. 8, pp. 1645–1664, 2015.

The 5th International Conference on Engineering Mechanics and Automation (ICEMA-5)
Hanoi, October 11÷12, 2019

Automatic detection of QRS complex based on wavelet transform and cluster analysis

Manh Hoang Van[a], Viet Dang Anh[a], Tuan Ngo Anh[a], and Thang Pham Manh[a]

[a] *Lecturer, University of Engineering and Technology, Vietnam National University, Ha Noi*

Abstract

The paper briefly presents the idea of designing an algorithm for automatically locating the QRS complexes in the single-lead ECG signal based on continuous wavelet transform (CWT) and cluster analysis. The local QRS complexes are first detected in the transformed signals at three different scales. The global QRS complexes were then determined from separate locations in the transformed signals by using a cluster analysis method. The proposed algorithm was evaluated on the two-lead ECG database (MIT-BIH Arrhythmia Database), which contains global reference positions common for all lead.

Key Words: ECG, continuous wavelet transform, cluster analysis, MIT-BIH ST Change Database.

I. Introduction

Electrocardiogram (ECG) is a nearly periodic signal that reflects the activity of the heart. Much information on the normal and pathological physiology of heart can be obtained from ECG. Therefore, the features extracted from the ECG signal are significant for the doctors as a guide to correct clinical diagnosis [1].

Many studies have been done in the field of ECG signal analysis using various approaches and methods for the past three decades. The basic principle of all the methods involves the transform of ECG signal using different transform techniques including Fourier Transform, Hilbert Transform, Wavelet Transform, etc. Pan and Tompkins [2] proposed an algorithm (the so-called PT method) to recognize the QRS complexes. In [3], the authors have been implemented as a method to detect the ECG beat using Geometrical Matching Approach algorithm. Based on the estimation of the first-order derivative, the slope vector form algorithm has also been proposed in [4]. However, the ECG signals are considered to be a quasi-period that is of finite duration and non-stationary; it is challenging to analyze them visually. Hence, a technique like Fourier series (based on sinusoids of infinite duration) is inefficient for ECG.

On the other hand, wavelet transform (WT), which is a very recent addition in this field of research, provides a powerful tool for extracting information from such signals. There has been the use of both continuous wavelet transform (CWT) as well as discrete wavelet transform (DWT). However, CWT has some inherent advantages over DWT. Unlike DWT, there is no dyadic frequency jump in CWT. Moreover, the high resolution in the time-frequency domain is achieved in CWT [5].

The paper is organized as follows: in Section II, we present the materials and the QRS complex detection method. The results of the validation on

the MIT-BIH Arrhythmia Database in Section III. Finally, the conclusions are presented in Section IV.

II. Materials and Methods

The proposed algorithm for the detection of the QRS complex is presented in Figure 1. This method includes signal preprocessing, continuous wavelet transforms, thresholding and identification of local QRS complexes, and determination of global QRS complexes using cluster analysis. The detail of each phase is described in the following sections.

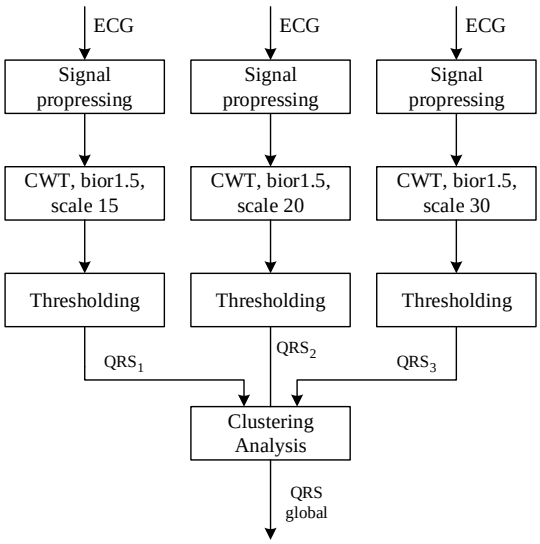

Figure 1. Block diagram of the proposed method for the detection of the QRS complexes.

1. *Signal preprocessing*

In this phase, the ECG signal was divided into the 4096-sample segments by a sliding window. The incomplete QRS complexes located at the end of the 4096-sample segments can be misidentified as Not QRS peaks, so an overlap of 150 samples has been designed to overcome this problem. Thanks to the 150-sample overlap, these unfinished QRS complexes can be included entirely at the beginning of the next segment. We used then two median filters to remove the low-frequency baseline drift [6]. Each segment was first filtered by a median filter with a width of $200\,ms$ to remove the QRS complexes and P waves, the resulting signal was then filtered again by a median filter with a width of $600\,ms$ to eliminate the T waves. Therefore, the baseline drift noise can be extracted by the output of the second median filter, and the baseline drift eliminated ECG signal can be obtained by subtracting the estimated baseline drift signal from the original ECG signal.

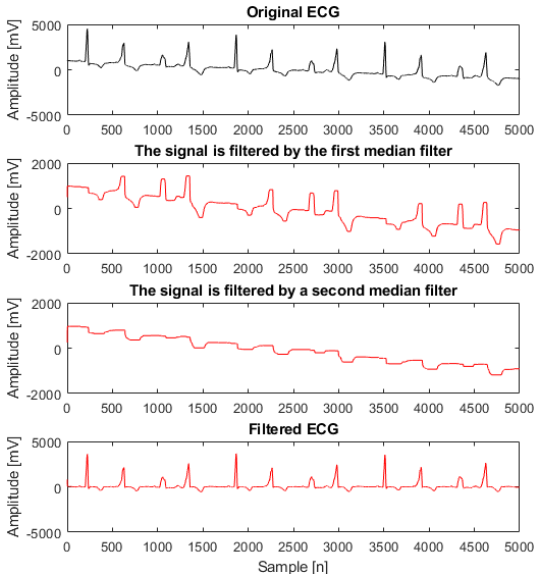

Figure 2. Illustration of removing the low-frequency baseline drift noise.

2. *Continuous wavelet transforms*

Wavelets are a powerful tool for the representation and analysis of physiological waveforms like ECG, etc. [5], [7]. They provide both time and frequency view. Unlike the Fourier transform, the WTs are very efficient for non-stationary signals like ECG. In WT, a fully scalable modulated window is used to solve the signal-cutting problem. The window is shifted along with the signal. Spectrum is calculated for every position. This process is repeated by varying the length of the window. The result is that we have a collection of representations, hence the name multi-resolution analysis.

In this work, the CWT is applied to decompose the ECG signal into a set of coefficients that describe the signal frequency content at given times. The CWT of the continuous signal, $x(t)$, is defined as

$$CWT(b,a) = \frac{1}{\sqrt{a}} \int_{-\infty}^{+\infty} x(t) \psi^* \left(\frac{t-b}{a} \right) dt \qquad (1)$$

where $\psi(t)$ is a continuous function called the mother wavelet, and the asterisk denotes the operation of the complex conjugate.

To implement the proposed algorithm, each filtered signal segment is transformed into the wavelet domain by CWT at an appropriate mother wavelet and scales. The most commonly used types of mother wavelet for detecting the QRS complexes are the quadratic spline function [8], [9] and the first derivative of the Gaussian function [10]. However, the mother wavelet used in this work is the biorthogonal family, namely *bior*1.5. The wavelet *bior*1.5 is an odd-symmetry wavelet that transforms the extremes of the original signal into zero-level passages and transforms the inflection points into extremes. Moreover, instead of finding for similarities across the other dyadic form of discrete-time wavelet transforms (DyDTWT) scales as in [8], [9], the proposed algorithm used appropriate scales. The best results were achieved with scales such as 15, 20, and 30.

3. Thresholding and identification of the local QRS complexes

The output from the CWT phase is signals transformed at three different scales 15, 20, and 30. For each of these transformed signals, the algorithm will then find pairs of near opposite sign extremes, whose absolute values are higher than the threshold ξ_{QRS}. If such pairs of extremes are found, and if these extremes are spaced less than the refractory period, $120\,ms$, then the positions of these extremes correspond to the ascending and descending edges of several of the QRS complexes. The position of the waves is then determined by the zero-crossing position between the two adjacent extremes. In this way, one or more candidates of the QRS complex can be detected. Because the detection indicates the position of the complex as a whole, it is necessary to identify a unique exact position representing the QRS complex. Therefore, there is a refractory period, $120\,ms$, before the next one can be detected since the QRS complexes cannot occur more closely than this physiologically. The positions preceded by another position in an interval shorter than this refractory period are removed from the detected positions. Therefore, the position of the QRS complex is the position of the first detected wave within candidates of the complex. The threshold level, ξ_{QRS}, is given by the equation,

$$\xi_{QRS} = K.\sqrt{\frac{1}{n}\sum_{i=1}^{n}(x_i - \bar{x})^2} \qquad (2)$$

and thus, the threshold level corresponds to *K* times the standard deviation calculated from all the values of the transformed signal. In this work, the constant *K* was determined as a suitable factor of the standard deviation based on the analysis of the complete ECG signal database (highest detection rate) and is 1.3. Deriving a threshold level from a standard deviation is a more robust approach than once derived from the maximum value or the difference between the maximum and the minimum values that can easily be affected by the artifact or extrasystoles. The threshold level is fixed and is the same for the entire segment of the analyzed signal.

From the position of the detected QRS complexes in the signal segments, the local QRS complexes of the whole signal transformed at a specific scale will again be reconnected by the location of the segments.

4. Determination the global QRS complexes

The reliability of detection will increase significantly if we can combine the complex locations across the individual transformed signals. The result of such a combination is the global position of QRS complexes that are the QRS complexes to the original signal. This algorithm used to combine the local QRS complexes here is cluster analysis.

The term cluster analysis refers to a variety of algorithms and methods for grouping similar objects into clusters. The similarity between the objects of one cluster should be as large as possible, and the similarity between objects belonging to different clusters is as small as possible. The clustering method used by us is one of the so-called hierarchical agglomerative methods that are based on individual objects, and their sequential clustering creates a hierarchical tree structure ending with a single cluster of all

objects. The clustering of objects in more massive clusters is based on the measurement of similarities or distances between objects.

In this study, we used the clustering-based method taken from [11], [12], and [13]. The input of the used method is the position of all detected QRS complexes in the individual transformed signals. A matrix of Euclidean distances is first calculated between all possible pairs of QRS complex positions. Besides, a hierarchical tree structure is created, and for the clustering itself, the nearest distance method is used. The cluster parameter of this method is the smallest distance between two objects of different clusters. The set of clusters is then selected from the tree structure that meets the specified criterion. The criterion used here was the minimum distance of adjacent clusters of $100\ ms$.

The obtained clusters represent candidates for global QRS positions. Clusters containing fewer objects than half the number of scales is excluded from the set of clusters. These clusters are considered to be false detection. From the remaining clusters, global QRS complex positions are determined based on median positions within each cluster.

III. Results and Discussions

This section will present the results of the QRS complexes detection on several signal segments from the MIT-BIH Arrhythmia Database. At the top of each figure, short red lines are used to denote the detected QRS peaks. FP denotes a false positive peak. Figure 3 shows the QRS complex detection results for a high-noise ECG signal from recording 104. From the figure, we can see that if the detection of QRS peaks is based on CWT at scale 15, several peaks are misidentified as QRS peaks, as shown in the top figure of Figure 3. If the detection of QRS peaks is based on CWT at scale 20 or 30, all QRS peaks are identified accurately, as shown in the middle two images of Figure 3. These local QRS complexes achieved at each scale were then used as the input to the cluster analysis algorithm. As a result, the global QRS complexes have been correctly identified despite the high-noise in the signal.

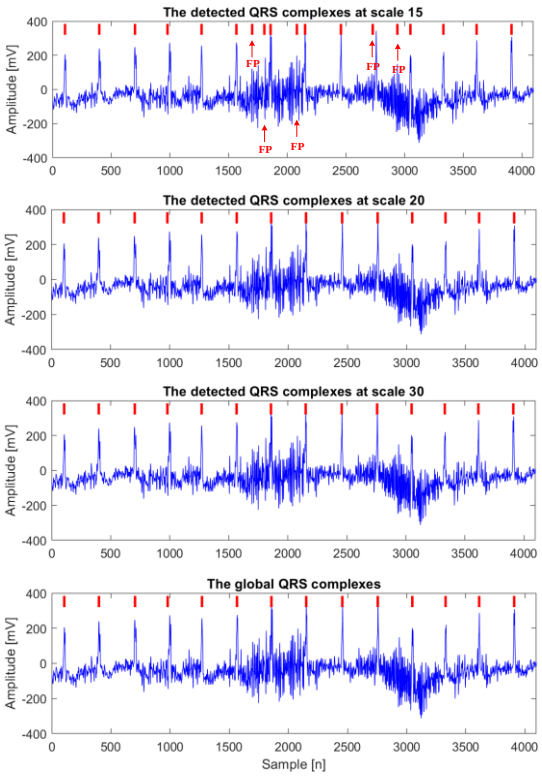

Figure 3. Illustration of the QRS detection results for a noisy ECG signal (take from recording 104).

From Figure 4, the results indicate that the proposed algorithm succeeded in finding a QRS peak with a significantly reduced amplitude compared to the two adjacent QRS peaks (6^{th} peak). This beat is the peak of a Ventricular Premature Contraction (VPC) beat.

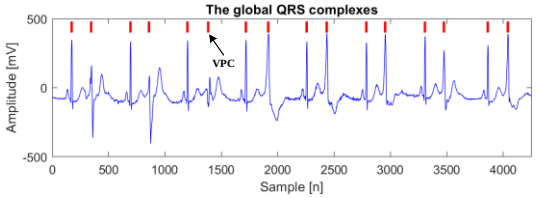

Figure 4. Illustration of the detection failures caused by significantly reduced amplitudes of QRS peaks compared to the adjacent QRS peak (take from recording 106).

Besides the above results, the proposed algorithm still has some limitations. Figure 5 shows the detection failures caused by large-amplitude artifacts. It is evident that the three peaks of large-amplitude noises are very similar to QRS peaks and are misidentified as QRS

complexes. Figure 6 illustrates the detection failures caused by a P-peak sharper than the QRS peak. When a P- or T-peak is sharper than a QRS peak, it can cause detection failures.

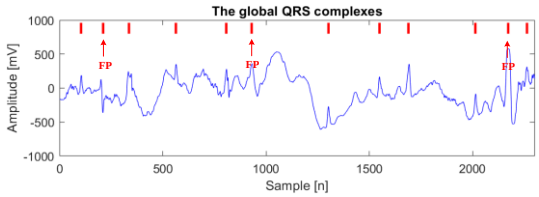

Figure 5. Illustration of the detection failures caused by large-amplitude artifacts (take from recording 105).

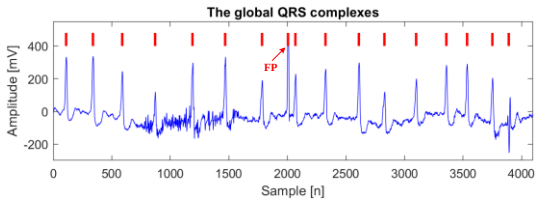

Figure 6. Illustration of the detection failures caused by the P-peak being sharper than the QRS peak (take from recording 203).

IV. Conclusion

This paper proposes a QRS complex detection algorithm based on a continuous wavelet transform. The identification of QRS complexes was based on the extremum pairs in the wavelet coefficients and the proposed decision rules (cluster analysis). The performance of the proposed algorithm has been tested on several pieces of data in the MIT-BIH arrhythmia database and yielded good results despite some limitations.

V. Acknowledgment

This work is supported by the research project N0. 01C02/01-2016-2 granted by the Department of Science and Technology Hanoi.

VI. References

[1] B. U. Köhler, C. Hennig, and R. Orglmeister, "The principles of software QRS detection," *IEEE Engineering in Medicine and Biology Magazine*, vol. 21, no. 1. pp. 42–57, 2002.

[2] J. Pan and W. J. Tompkins, "A Real-time {QRS} Detection Algorithm," *IEEE Trans. Biomed. Eng.*, vol. 32, no. 3, pp. 230–236, 1985.

[3] K. V. Suárez, J. C. Silva, Y. Berthoumieu, P. Gomis, and M. Najim, "ECG beat detection using a geometrical matching approach," *IEEE Trans. Biomed. Eng.*, vol. 54, no. 4, pp. 641–650, 2007.

[4] X. Xu and Y. Liu, "ECG QRS complex detection using slope vector waveform (SVW) algorithm.," *Conference proceedings : ... Annual International Conference of the IEEE Engineering in Medicine and Biology Society. IEEE Engineering in Medicine and Biology Society. Conference*, vol. 5. pp. 3597–3600, 2004.

[5] A. Ghaffari, H. Golbayani, and M. Ghasemi, "A new mathematical based QRS detector using continuous wavelet transform," *Comput. Electr. Eng.*, vol. 34, no. 2, pp. 81–91, 2008.

[6] P. De Chazal, M. O'Dwyer, and R. B. Reilly, "Automatic classification of heartbeats using ECG morphology and heartbeat interval features," *IEEE Trans. Biomed. Eng.*, vol. 51, no. 7, pp. 1196–1206, 2004.

[7] S. W. Chen, H. C. Chen, and H. L. Chan, "A real-time QRS detection method based on moving-averaging incorporating with wavelet denoising," *Comput. Methods Programs Biomed.*, vol. 82, no. 3, pp. 187–195, 2006.

[8] C. Li, C. Zheng, and C. Tai, "Detection of ECG characteristic points using wavelet transforms," *IEEE Trans Biomed Eng*, vol. 42, no. Bmei, pp. 21–28, 1995.

[9] J. P. Martínez, R. Almeida, S. Olmos, A. P. Rocha, and P. Laguna, "A Wavelet-Based ECG Delineator Evaluation on Standard Databases," *IEEE Trans. Biomed. Eng.*, vol. 51, no. 4, pp. 570–581, 2004.

[10] M. Vollmer, "Robust detection of heart beats using dynamic thresholds and moving windows," *Comput. Cardiol. (2010).*, vol. 41, no. January, pp. 569–572, 2014.

[11] G. D. Clifford, F. Azuaje, and P. E. McSharry, "Advanced Methods and Tools for ECG Data Analysis," *Adv. Methods Tools ECG Data Anal.*, pp. 1–400, 2006.

[12] P. L. and T. Hill, "Statistics : Methods and Applications By Pawel Lewicki and Thomas Hill," *Statistics (Ber).*, vol. 1st, pp. 1–719, 2006.

[13] R. M. Rangayyan, "Biomedical Signal Analysis: A Case-Study Approach," *Wiley IEEE Press*, p. 552 pp, 2001.

The 5th International Conference on Engineering Mechanics and Automation (ICEMA-5)
Hanoi, October 11÷12, 2019

Monitoring system of special-purposed power conversion module for Compact and Robust Medium Wind Turbine (CART)

Anh Tuan Ngo[a], Manh Thang Pham[b], Anh Viet Dang[a], Van Manh Hoang[a]

[a] Lectures, Faculty of Engineering Mechanics and Automation
University of Engineering and Technology, Vietnam National University
144 Xuan-Thuy, Cau-Giay, Hanoi, Vietnam. Email: natuan0502@vnu.edu.vn
[b] Assoc. Professor, Faculty of Engineering Mechanics and Automation
University of Engineering and Technology, Vietnam National University
144 Xuan-Thuy, Cau-Giay, Hanoi, Vietnam; Email: thangpm@vnu.edu.vn

Abstract

This paper introduces a monitoring system containing hardware parts and software applications to supervise the state of operation of a CART power conversion system. The software is developed to coordinate with embedded web server inside the power system to get and store data in local as well as online database. Those pieces of software run on several platforms such as Window computers, Android phones and Raspberry Pi mini boards and allow users to analyze data, diagnose and remotely monitor the CART power conversion system.

Key Words: CART, Power Conversion System, Monitoring Software, Embedded, Raspberry Pi.

1. Introduction

Using renewable energy is currently one of the most the prevailing trends of the world, and wind energy makes up a considerable proportion in this field. To generate electricity from the wind, large static-scale turbines (up to a few MW rated power) are commonly used. These turbines have the advantage of generating a great deal of power and are ideal for building large power farms. However, the disadvantages of these turbines are that they are too bulky and lack of portability, along with the need of immense cost when building ones. To address the disadvantages mentioned above, as well as to build a more suitable power supply solution

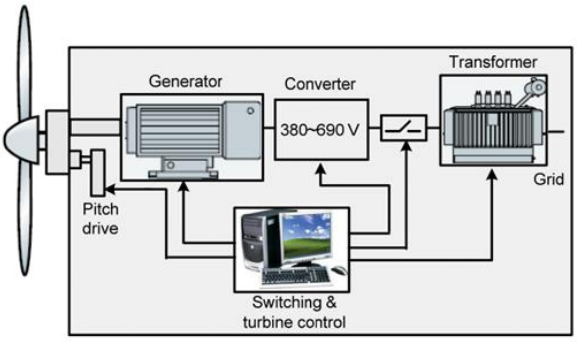

Figure1. Inside a wind energy conversion system in (Islam, 2013).

for remote places and off-grid regions such as islands and mountains, small and medium-sized wind turbine with 10-250kW rated power (known as CART) was first introduced in 1990s

(Adam & Schroeter, 2018). A complete CART system included generator, converter, transformer and turbine controller, as demonstrated in figure 1 (Islam, Guo, Zhu, & Zhu, 2013).

In particular, the electrical system including power converters and controllers has the highest failure rate. (see figure 2) (Bala, Pan, Das, Apeldoorn, & Ebner, 2012).

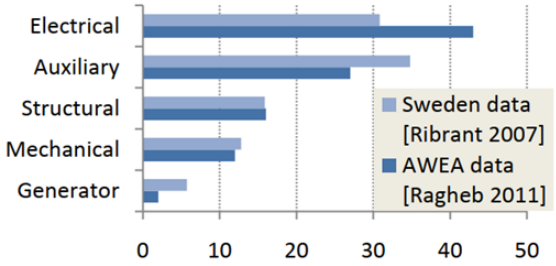

Figure 2. Distribution % of type of failure (Bala, 2012).

Therefore, the creation of a real-time data monitoring system to analyze the operational condition of the converters is really necessary. This will help the operator quickly diagnose if the system has a problem, thereby giving appropriate solutions. As the result, not only can enormous maintenance cost be saved but also the possibility of failure be significantly reduced.

This paper is organized as follows: In chapter 2, an overview of a particular structure of the special-purposed power conversion system for CART is reviewed. In chapter 3, the monitoring system's architecture is outlined. Also, the architecture and functions of the software applications making up the monitoring system will be thoroughly reviewed. All in all, chapter 4, 5, 6 present achieved results, conclusions and acknowledgement of this project.

2. CART power conversion system

Power converters are one of the most important parts of the CART system. In wind power systems, some functions of power converters are reducing mechanical stress, tracking maximum power from the wind and generating the smooth AC voltage output (Wu, Yongqiang, Navid, & Samir, 1965).

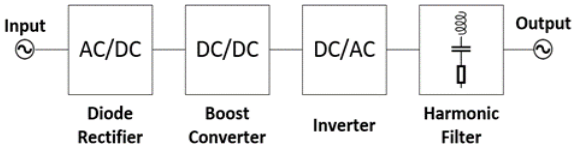

Figure 3. Block diagram of CART power conversion system.

In this paper, CART power conversion system using DC/DC boost converter is introduced. In this topology, the converter consists of diode rectifier, boost converter, inverter and harmonic filter (figure 3), which will be explored in detail in the below sections.

2.1. Single-phase bridge rectifiers

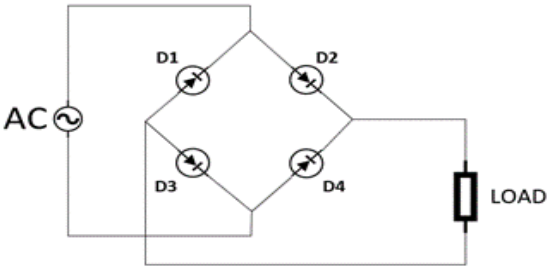

Figure 4. Full-bridge diode rectifier.

In this topology, a low-cost full bridge diode rectifier is used to convert AC voltage into DC voltage. During the positive half-cycle, D2 and D3 open, which allow current to flow through. Whereas during the negative half-cycle, D1 and D4 conduct and let the current flows through. In term of performance, the following parameters can be considered.

The average value of load voltage:

$$V_{dc} = \frac{1}{\pi}\int_0^{\pi} V_m sin\omega t \; d(\omega t) \qquad (1)$$

The root means square voltage of the resistive load:

$$V_{rms} = \sqrt{\frac{1}{\pi}\int_0^{\pi} (V_m sin\omega t)^2 \; d(\omega t)} \qquad (2)$$

Others are given as follow: the rectification ratio σ = 81%, the form factor FF = 1.11, the ripple factor: RF = 0.482, Transformer Utilization Factor TUF = 0.81 (Rashid, 2011).

2.2. DC/DC boost converter

Figure 5 illustrates a DC/DC boost converter. It contains a DC input source, a controlled switch, an inductor, a filter capacitor, and a resistive load. In CART power conversion system, boost converter's functions are tracking maximum power from the wind and boosting DC voltage to an appropriate value for the inverter (Wu et al., 1965).

Boost converter operates in continuous conduction mode, which divided into 2 stages depending on the status of the controlled switch. When the switch is on, the inductor stores energy, the capacitor is discharged. When the switch is off, the diode is on, inductor is dissipated, releasing the stored energy to the load.

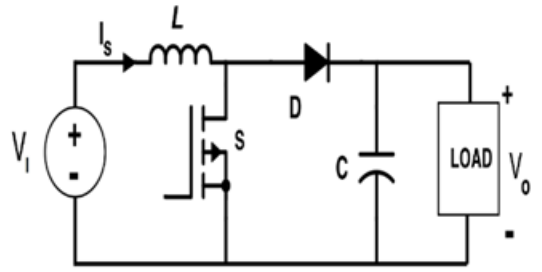

Figure 5. Boost converter.

Equations (3) gives the relation between the input and output voltage, while equations (4) and (5) shows how to design boost converter.

$$\frac{V_I}{V_O} = \frac{1}{1-D} \quad (3)$$

$$L = \frac{(1-D)^2 DR}{2f} \quad (4)$$

$$C = \frac{DV_O}{V_r Rf} \quad (5)$$

Where: D is the duty cycle of PWM signal sent to the switch, V_r is the voltage ripple.

2.3. Inverter

Inverters are used in most wind energy power conversion systems. Their functions are to generate AC voltage output from DC voltage input. The generated AC voltage can then be used to connect to the grid or AC loads. There are many different types of inverters, each type has its own advantages and disadvantages. In this section, Cascaded H-Bridge (CHB) multilevel inverter is briefly studied. This inverter has several great advantages such as high voltage capability, good power quality, easy to package and scale. The CHB multilevel inverter uses a series of H-bridge cells, each cell contains 4 IGBT switches, capacitors and requires separate input DC voltage. Figure 6 depicts the CHB multilevel inverter topology.

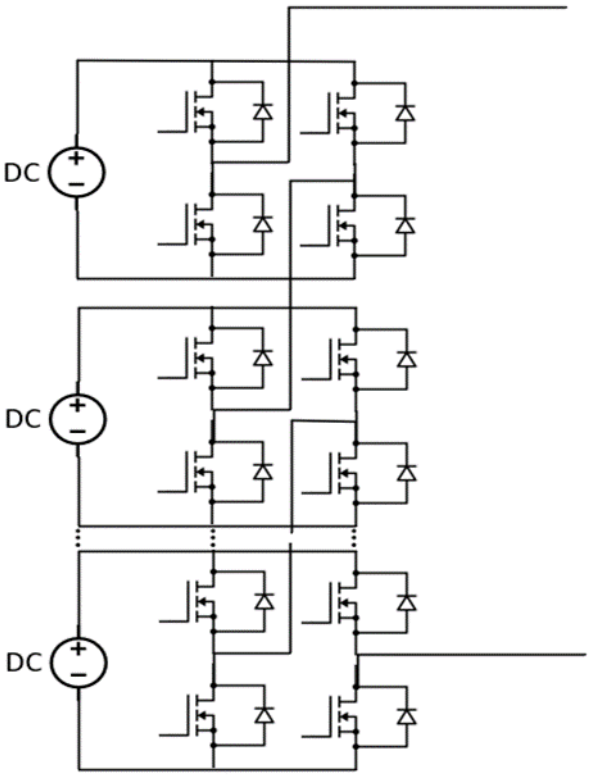

Figure 6. CHB multilevel converter

Equations (6) (7) (10) elaborately demonstrate the performance of CHB multilevel inverter (Aborisade, Adeyemo, & Akinwale, 2013; Porselvi & Muthu, 2014).

Output voltage waveform in three-phase power system of the CHB multilevel inverter givens by:

$$V(\omega t) = \sum_{n=1,3,5}^{\infty} \frac{4V_{DC}}{n\pi}\left(\cos(n\theta_1) + \cos(n\theta_2) + \cdots + \cos(n\theta_k)\right)\sin(n\omega t)) \quad (6)$$

Where $0 < \theta_1, \theta_2, \ldots \theta_k < \frac{\pi}{2}$ are the switching angles.

Fundamental voltage is derived from switching angles and equation (6) as follow:

$$V_1 = \frac{4V_{DC}}{\pi}(\cos(\theta_1) + \cos(\theta_2) + \cdots + \cos(\theta_k)) \quad (7)$$

The third harmonic can be eliminated by using the switching angles derived by solving equations (8) and (9) using Newton-Raphson method (Porselvi & Muthu, 2014).

$$\cos(\theta_1) + \cos(\theta_2) + \cdots + \cos(\theta_k) = \frac{\pi V_1}{4V_{DC}} \quad (8)$$

$$\cos(3\theta_1) + \cos(3\theta_2) + \cdots + \cos(3\theta_n) = 0 \quad (9)$$

The Total Harmonic Distortion (THD) is provided as:

$$\text{THD} = \frac{\sqrt{\sum_{i=5,7,11,13}^{49} {V_i}^2}}{V_1} \quad (10)$$

2.4. Harmonic filter

Due to the high frequency PWM switching of the inverter, a level of harmonics is generated. This causes current and voltage distortions, thus damages electronic components inside the adapter. In the system need the durability and precision as CART power conversion system, harmonic filters should be applied. Harmonic filters are resonant circuits which block harmonic current as well as reduce the harmonic voltage distortion in the system. The applications of harmonic filters vary among different systems. Here the single tune shunt filter is examined. To design the series filter for a specific application, some input parameters need to be considered (Bayliss & Hardy, 2012). Firstly, selectivity response or quality factor:

$$Q = \frac{\omega L}{R} \quad (11)$$

High quality factor gives narrow frequency response.

Second is the tuned resonance frequency:

$$f = \frac{1}{2}\sqrt{\frac{1}{LC}} \quad (12)$$

Thirdly, the detuning of filters for changes in harmonic frequency can be expressed as:

$$\delta = \frac{\Delta f}{f_n} + \frac{1}{2}\left(\frac{\Delta L}{L_n} + \frac{\Delta C}{C_n}\right) \quad (13)$$

3. Monitoring system for CART power conversion module

The structure of monitoring system for CART power conversion module is designed in figure 7. The focus is as follow:

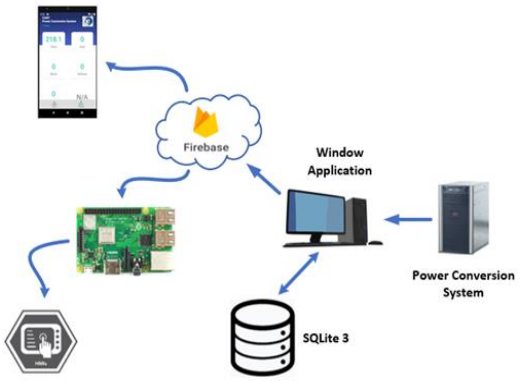

Figure 7. Structure of the monitoring system

3.1. Firebase real-time database

Firebase is a cloud-based platform run by Google which contains great tools for users to create mobile and web applications. It provides a real-time NoSQL database which enable quick queries executions (Alhomsi et al., 2018; Li, Yen, Lin, Tung, & Huang, 2018; Rahmi, Piarsa, & Wira Buana, 2017). Firebase real-time database is a backend service which allows developers to build applications without the need of the servers, hence makes develops app more quickly. To use Firebase real-time database, users must create a new project to get database token, then set up the access rule of the database.

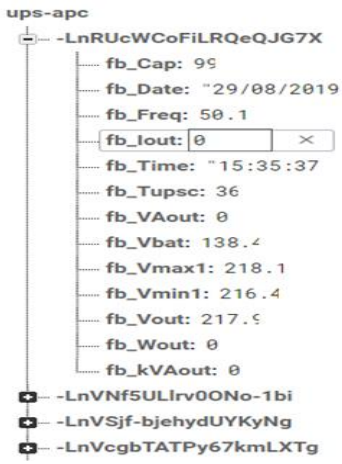

Figure 8. Firebase database structure

3.2. Window Application

Window application is written in C# using Visual Studio IDE. There are two main part of this application:

The back-end part gets data from an embedded web server inside the power conversion system for CART using http web client request. The embedded server is provided by APC network management card which has some feature such as generating data and even log, using DHCP server to provide network values (TCP/IP) (APC™ Corporation, 2002). Additionally, in the back-end side, the program stores data in local SQLite3 database and Firebase online database.

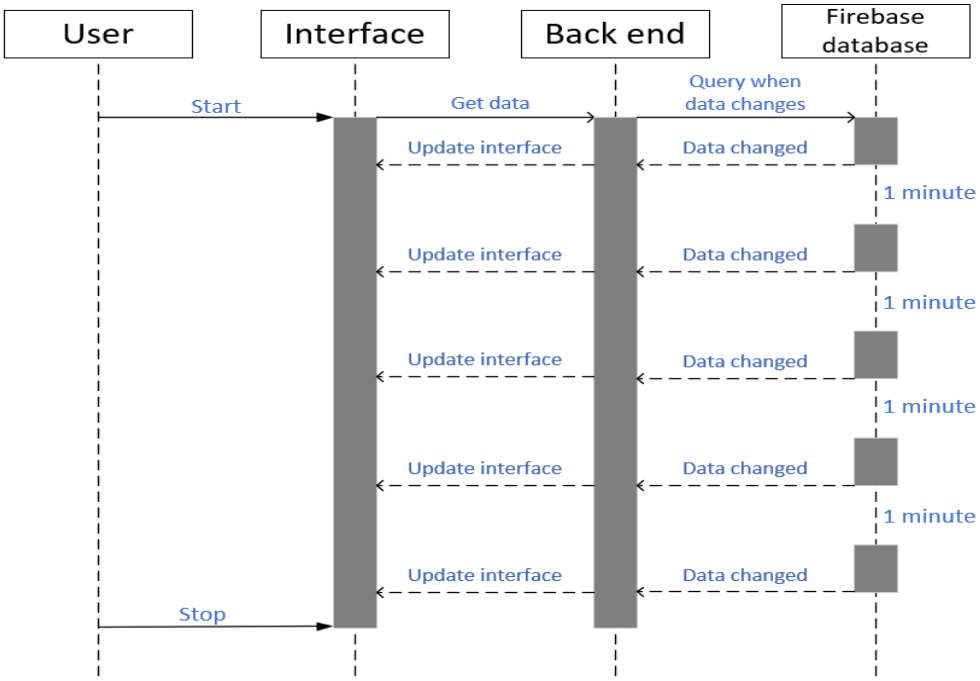

Figure 9. Android application sequence diagram

In this monitoring system, the database is designed as flat as possible allowing applications to quickly fetch data. The "Post" query is used by the Window app and the "Get" query is used by HMI app running Raspberry Pi board and the Android app in term of communicating with Firebase database. Data structure of this database is shown in figure 8.

Data from the embedded web updates every 60 seconds, so does the database.

The frond-end part has an interface containing 3 windows. The Dashboard window shows important parameters of the power conversion system, which is updated every minute. The Realtime window has real-time charts which constantly changes. The Graph window draws accumulated data of a specific date chosen by users. To draw charts and graphs, LiveCharts library is used. This library provides simple way

to create attractive, flexible and interactive visualization plot. Thanks to LiveCharts, users can easily manipulate how data is shown, thus analyze the system more effectively.

3.3. Android Application

Android is an open source operating system produced by Google. It is now running on 2.5 billion devices all around the world (Google Inc. Android. android.com). The android SDKs provides libraries which help developers easily make use of the hardware. Android operating system is chosen for this project because of its widespread popularity and the excellent compatibility with Google's services, one of which is Firebase platform.

The Android program in this project is designed for the purpose of simple use and interacting with the app. It has a bright user interface, and a bottom navigation bar allowing users to easily navigate through the app. This application queries data from Firebase database, listens to OnDataChange() event, and updates the interface when the event triggered. Figure 9 demonstrates the sequence diagram of the Android app.

3.4. Human-Machine Interface (HMI) software running on Raspberry Pi

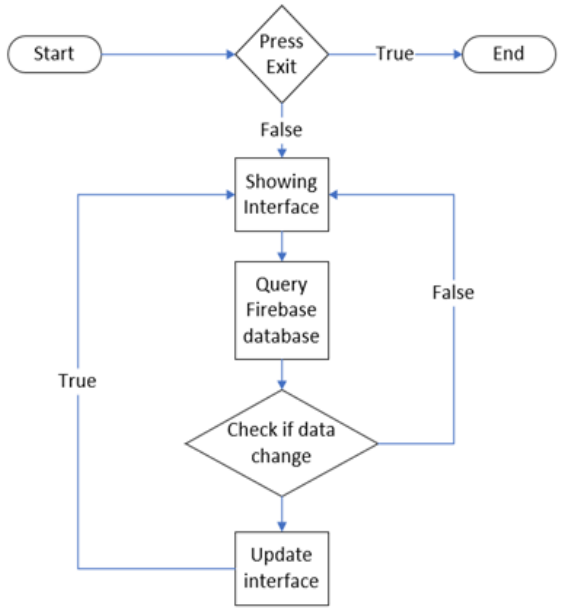

Figure 10. HMI software's flow chart

Raspberry Pi is a minicomputer with the size is just equal a credit card. It has an ability to run operating systems such as Linux, Raspbian, Window IoT from a micro SD card attached inside. Raspberry Pi is used in many applications both in laboratory and real-world projects because of its small size, low cost but powerful processing capability.

The HMI software is attached on the surface of CART power conversion system. It runs on a Raspberry Pi Model B+ and is written in Python script. To build the HMI software, GUIzero library is used. This library has the advantage of helping developers quickly and easily create GUI for Raspberry Pi, but it still has powerful features which inherited from Tkinter library. Below is the flow diagram of the HMI software:

4. Results

After the procedure of installation and testing, the first prototype of the monitoring system has run stably and gives fairly accurate results. Below are the result figures of the applications.

4.1. Window Application

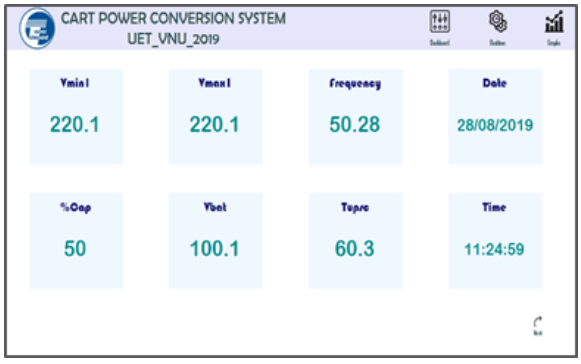

(a)

(b)

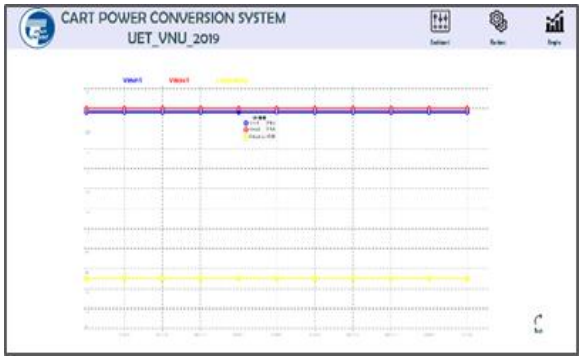

(c)

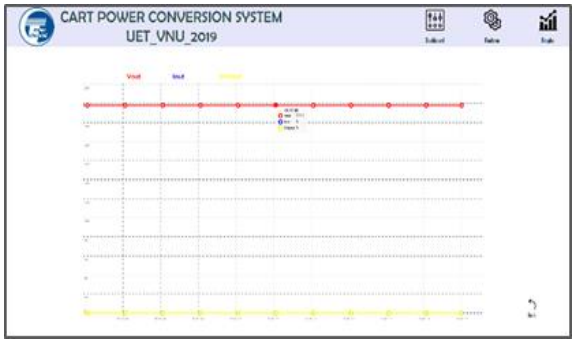

(d)

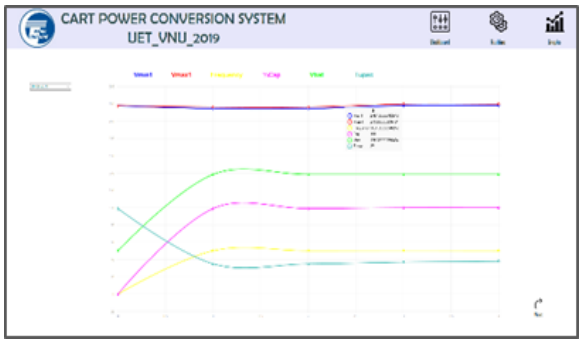

(e)

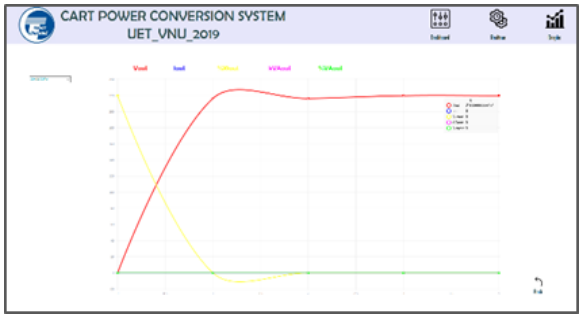

(f)

Figure 11. The user interface of Window application

Figure 11 (a) (b) shows Dashboard containing some parameters of the power conversion system.

Figure 11 (c) (d) shows Real-time charts of Vmin1, Vmax1, Freq, and Vout, Iout, AVout.

Figure 11 (e) (f) shows Graphs drawing data of specific date chosen by users.

4.2. Android Application

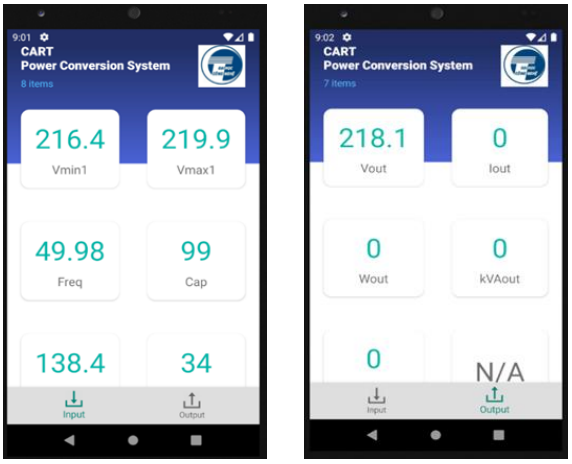

(a) (b)

Figure 12. User interface of Android application

Figure 12 (a) shows input parameters of the power conversion system.

Figure 12 (b) shows output parameters of the power conversion system.

4.3. HMI software running on Raspberry Pi

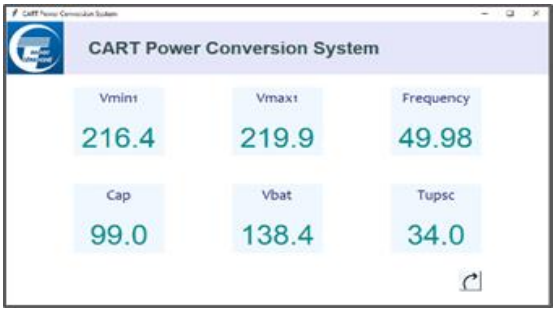

(a)

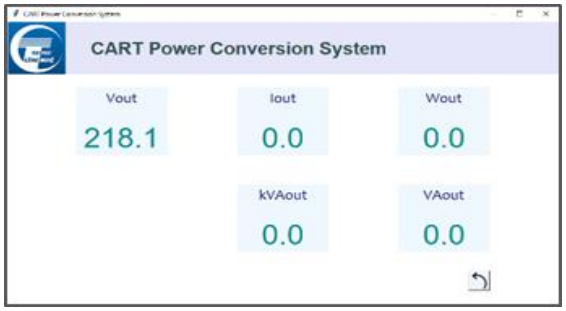

(b)

Figure 13. The HMI software running on Raspberry Pi

Figure 13 (a) shows input parameters of the power conversion system.

Figure 13 (b) shows output parameters of the power conversion system.

5. Conclusion

This paper presents in detail about the monitoring system for a CART power conversion system, including hardware components and software applications.

The result of this work shows that data collected from the power conversion module has been stably stored in both SQLite local database and Firebase Realtime database. Aside from that, Realtime charts and Graphs by date provide great tools for users to analyze and diagnose the operating status of the power conversion module.

6. Acknowledgement

This work is supported by the research project No. QG17.68 granted by Vietnam National University, Hanoi.

References

Aborisade, D. O., Adeyemo, I. A., & Akinwale, O. C. (2013). Harmonics Optimization in Multilevel Inverter Using Real Coded Genetic Algorithm. *International Journal of Electrical Engineering Research & Applications (IJEERA)*, *1*(November 2015), 20–26.

Adam, F., & Schroeter, M. (2018). *CART - A compact and robust wind turbine design for south Asia*. (October).

Alhomsi, Y., Alsalemi, A., Aldisi, M., Ahmed, I., Bensaali, F., Amira, A., & Alinier, G. (2018). Real-Time Communication Network Using Firebase Cloud IoT Platform for ECMO Simulation. *Proceedings - 2017 IEEE International Conference on Internet of Things, IEEE Green Computing and Communications, IEEE Cyber, Physical and Social Computing, IEEE Smart Data, IThings-GreenCom-CPSCom-SmartData 2017*, *2018-Janua*, 178–182. https://doi.org/10.1109/iThings-GreenCom-CPSCom-SmartData.2017.31

APC™ Corporation. (2002). *Network Management Card USER ' S GUIDE USER ' S GUIDE*.

Bala, S., Pan, J., Das, D., Apeldoorn, O., & Ebner, S. (2012). Lowering failure rates and improving serviceability in offshore wind conversion-collection systems. *PEMWA 2012 - 2012 IEEE Power Electronics and Machines in Wind Applications*, *1*, 1–7. https://doi.org/10.1109/PEMWA.2012.6316362

Bayliss, C. R., & Hardy, B. J. (2012). Chapter 24 - Power Quality – Harmonics in Power Systems. In *Transmission and Distribution Electrical Engineering (Fourth Edition)* (pp. 987–1012).

Islam, R., Guo, Y., Zhu, J. G., & Zhu, J. (2013). *Power converters for wind turbines: Current and future development*. Retrieved from https://www.researchgate.net/publication/262974138

Li, W. J., Yen, C., Lin, Y. S., Tung, S. C., & Huang, S. M. (2018). JustIoT Internet of Things based on the Firebase real-time database. *Proceedings - 2018 IEEE International Conference on Smart Manufacturing, Industrial and Logistics Engineering, SMILE 2018*, *2018-Janua*, 43–47.

Porselvi, T., & Muthu, R. (2014). Wind Energy Conversion System with Boost Converter and CHB MLI with single DC input. *International Energy Journal*, *14*(1), 43–56.

Rahmi, A., Piarsa, N., & Wira Buana, P. (2017). FinDoctor-Interactive Android Clinic Geographical Information System Using Firebase and Google Maps API. *International Journal of New Technology and Research*, (3), 8–12.

Rashid, M. H. (2011). *Power electronics handbooks - Third Edition*.

Wu, B., Yongqiang, L., Navid, Z., & Samir, K. (1965). Power Conversion and Control of Wind Energy Systems. In *The British Journal of Psychiatry* (Vol. 111).

Google Inc. Android. android.com.

The 5th International Conference on Engineering Mechanics and Automation (ICEMA 5)
Hanoi, October 11÷12, 2019

A remote monitoring system design based on MEMS sensor and GPRS technology for vibration measurement

Nguyen Thi Van Anh[1], Hoang Van Manh[1], Nguyen Ngoc Viet[1], and Pham Manh Thang[1]

[1]Faculty of Engineering Mechanics and Automation,
University of Engineering and Technology, Vietnam National University, Hanoi, Vietnam.
144 Xuan Thuy, Cau Giay, Hanoi, Vietnam
manhhv@vnu.edu.vn

Abstract

Vibration measurement plays a vital role in structural health monitoring and testing bridges, train rail systems, dams, high and broad buildings, and other civil structures. Besides, remote sensing has become an attractive area in various engineering applications. This paper presents a remote monitoring approach for vibration-related responses using MEMS sensors, a microcontroller board, and GPRS technology. An MPU-6050 sensor with 6-DOF utilizes a standard I^2C bus for data transmission in real-time through the microcontroller circuit board. A SIM800A module is used to transfer data to the cloud server via the GPRS wave. Subsequently, the data can be downloaded by the user to analyze the required mechanical signals. The values obtained by the sensor, including a 3-axis gyroscope and 3-axis accelerometer, are recorded and stored on the server in this work. The system is found to be useful, reliable and cost-effective for construction vibration investigation.

Key Words: MPU6050 MEMS sensor, SIM800A modem, GPRS technology, vibration measurement, remote monitoring

1. Introduction

The safety of the infrastructure is tightly related to the protection of humans and properties. For example, the monitoring of vibration in real-time is essential to understand the maintenance operations of bridge/railway, and prevent potential risks for people and vehicles (R et al., 2017; Tong et al., 2019). However, the existing structural vibration monitoring systems often use complicated, inflexibility, and expensive devices, which increases the overall cost of the installation and repair process. Various other sources of vibrations can affect human activities such as road traffic, high-speed trains, and large machinery, etc. (Nguyen et al., 2018). In Vietnam, the critical requirement for vibration monitoring of structures and load testing approaches is rapidly increasing. The specific objectives of the study are efficient, fast, accurate, and low-cost devices.

In recent years, advancements in MEMS and wireless sensor technology have brought the automated real-time, remote health monitoring system (Tegtmeier, 2008; Uchimura et al., 2010; Zhou and Yi, 2013). Thus, structural health monitoring has an excellent opportunity for technological improvements. This paper proposed a remote measurement module for sensing the mechanical vibrations by MEMS-based sensors and GPRS technology (Fu and Han, 2017). The system automatically detects the

acceleration and gyroscope values by the MPU6050 sensor, which immediately transfers to the cloud server and hosts a computer through the SIM800A modem. The module can help end-users to control and analyze the sensing signals from a remote location.

2. Hardware system design and components

2.1. System block diagram

Fig.1 shows the hardware design block diagram of the vibration monitoring and measuring system. The measurement module is comprised of four main components: an MPU6050 sensor, a SIM800A modem, an STM32F407VGT6 microcontroller, and a memory microSD card. The microcontroller plays the central processing role in the whole system. The MPU6050 sensor is used to measure the acceleration and gyroscope parameters in the different axes. The SIM800A element is utilized to transfer data to the server via GPRS. The data can also be stored on the module by the microSD card. A source circuit is built and integrated into the module to supply power to all the components. The power consumption of the sensor, as well as the module, is very low. The whole system can use renewable energy sources such as solar power at stations where the electricity is not available. The specifications of the elements are described in detail in the following subsections.

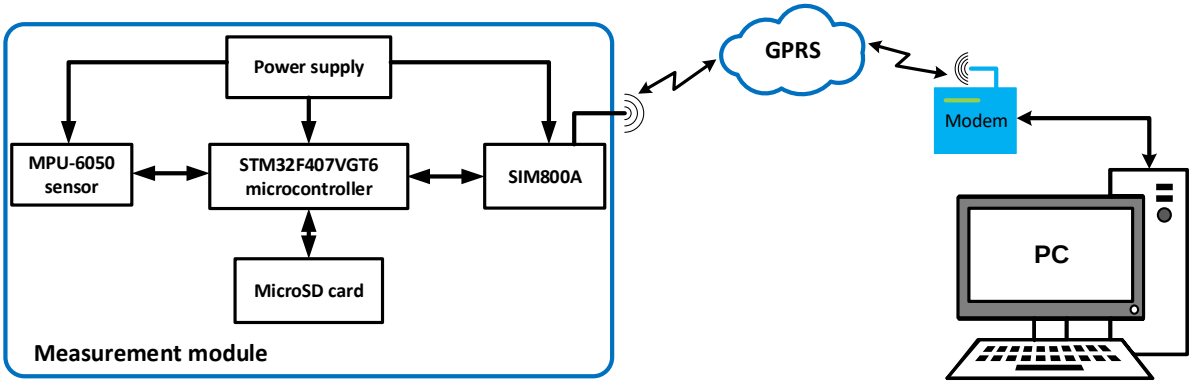

Figure 1. Block diagram of the vibration monitoring system.

2.2. STM32F407VGT6 microcontroller

The STM32F407VGT6 is used that is a general high-performance ARM microcontroller purchased from STMicroelectronics. The ARM Cortex-M4 processor with a floating-point unit (FPU) single precision is one of the latest 32-bit processors for embedded systems. It could provide a low-cost platform, with a reduced pin count, an advanced real-time response, and low-power consumption. This microcontroller family is suitable for a wide range of civil and industrial applications. Its main features:

- Core: operating at a frequency of up to 168 MHz, memory protection unit, 210 DMIPS/1.25 DMIPS/MHz (Dhrystone 2.1);
- Memories: Up to 1 Mbyte of flash memory, up to 192 Kbytes of SRAM, and up to 4 Kbytes of backup SRAM;
- Supply power: 1.8 V to 3.6 V in the temperature ranging from –40 to +105 °C;
- Clock: 4 to 26 MHz crystal oscillator, internal 16 MHz factory-trimmed RC (1% accuracy), 32 kHz oscillator for RTC, and internal 32 kHz RC with calibration;
- Low-power operation: Sleep, Stop and Standby modes;
- Additional others: 3×12-bit A/D converters, 2×12-bit D/A converters, up to 17 timers, 140 I/O ports with interrupt capability, 15 communication interfaces (4×USARTs/UARTs, 3×SPIs, 3×I2Cs, 2×CAN, and SDIO interface), advanced connectivity (USB 2.0 full-speed/high-speed/device/host/OTG controller with on-chip PHY, ULPI and dedicated DMA, 10/100 Ethernet MAC with dedicated DMA).

2.3. MPU-6050 sensor

The InvenSense MPU-6050 module is a Micro-Electro-Mechanical Systems (MEMS) sensor that combines both a 3-axis accelerometer and a 3-axis gyroscope within a single chip. It can be used to measure orientation, displacement, velocity, acceleration, and other motion-related parameters in applications ranging from health and fitness monitoring to location-based services. The device is offered in a small package size of 4×4×0.9 mm (QFN). It contains six 16-bit A/D converters for digitizing the motion sensor output channels. This type of piezoelectric accelerometer covers a wide frequency range to more than to about 30 kHz and is known as high accuracy, repeatability, and low-price device for shock and vibration measurement (Babakhani et al., 2018).

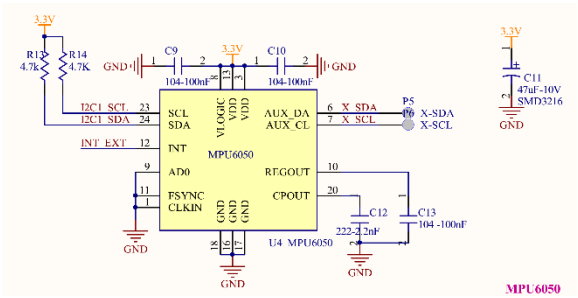

Figure 2. Principle circuit for connecting the MPU-6050 sensor to the microcontroller.

The MPU-6050 sensor operates from a VDD power supply voltage range of 2.375-3.46V. It has a 6-16V input voltage, a low-pass filter response between 5-260 Hz, and has an output data rate between 4-1000 Hz. For precision tracking of both fast and slow motions, the parts feature a user-programmable accelerometer full-scale range of ±2g, ±4g, ±8g, and ±16g, and a user-programmable gyroscope full-scale range of ±250, ±500, ±1000, and ±2000 degrees per second (DPS). In this study, the sensor uses the I2C bus to interface with the microcontroller at different bus speeds of 100kHz (Standard Mode), 400kHz (Fast Mode), 1 MHz (Fast-Mode Plus), 3.4MHz (High-Speed Mode), and 5MHz (Ultra-Fast Mode). A 1024 Byte FIFO register helps lower system power consumption due to the sensor data read in bursts of the processor (InvenSense Inc., 2013). Fig. 2 shows the MPU-6050 module and its primary connections to the microcontroller. A working voltage of 3.3 V is used. The I2C lines are pulled high using a 4.7k resistor, and the interrupt pin is pulled down using another 4.7k resistor. We use the ARM microcontroller to read the data from this FIFO buffer through I^2C communication. Any change in motion will be reflected in the mechanical system which will, in turn, vary the voltage.

2.4. SIM800A modem

The SIM800A modem is a quad-band GSM/GPRS interface designed by SIMCom, which can be embedded in the customer applications. It works on four frequency bands: GSM 850MHz, EGSM 900MHz, DCS 1800MHz, and PCS 1900MHz. It also supports GPRS multi-slot classes 1~12, and GPRS coding schemes CS-1, CS-2, CS-3, and CS-4. GPRS data downlink and uploading transfers are up to 85.6 kbps. The supply voltage range for SIM800A is from 3.4V to 4.4V, with the operating temperature ranging from -40 to +85 ℃. The typical power consumption in sleep mode is 1.2mA. The SIM800A has 68 SMT pads and provides all hardware interfaces between the module and electronic boards. With a small size of 24×24×3 mm and a weight of 3.14 g, it can be applied in many applications, such as a smartphone, M2M, PDA, and other mobile devices. In this study, the SIM800A modem communicates with the microcontroller STM using the UART communication standard through AT commands.

2.5. Memory microSD card

The memory MicroSD Card is used to store data with a capacity of 16 Gigabyte. Communication between the card and the microcontroller is the SDIO standard with a 4-bit data bus. Data is transmitted on all 4 data pins (DAT [3:0]) at speeds up to 100 Megabyte/second.

3. Software architecture description

The system software mainly involves the sensor, data communication, collection, and storage with the GPRS module. Fig. 3 shows the process flow of the monitoring system. When the system is started up, the variables are initialized. After each period of 50 ms, the program tests the value of the Status_MPU:

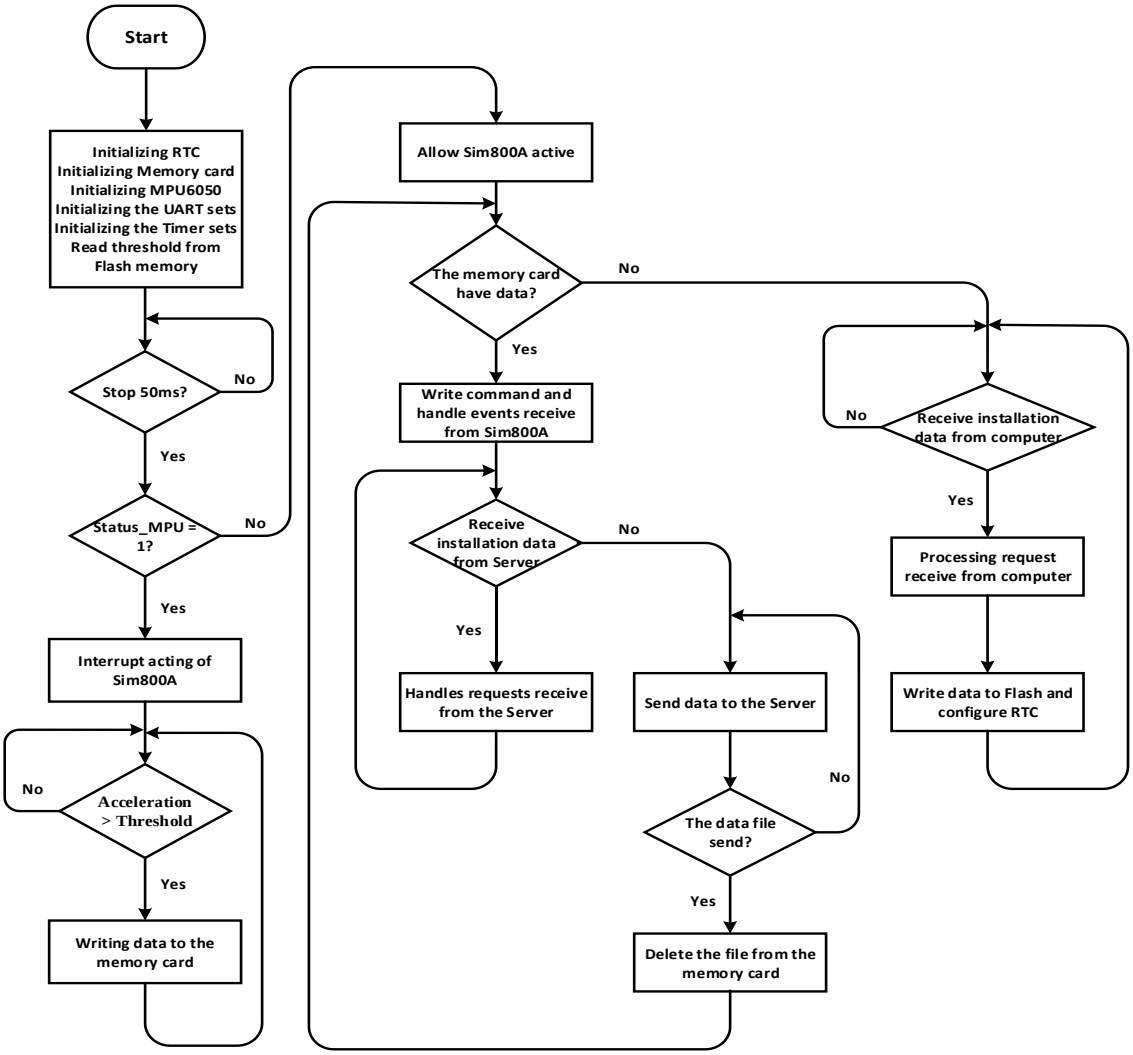

Figure 3. Operation flow chart of the controller program.

- If the Status_MPU = 1 (occurred vibration): The SIM800A is disconnected the communication with the microcontroller. The sensing signals are read and compared with the threshold values (stored in the Flash memory).

  - ✓ When the recorded values are less than the threshold values, the program continuously checks the status of the Status-MPU.
  - ✓ While any value exceeds the allowed level, data are written to the memory MicroSD card. The files are stored in a folder named corresponding to the recorded date and time of data.

- If the Status_MPU = 0 (no vibration): The program allows the SIM800A to operate and check the data in the memory card.

  - ✓ When the card has data, the microcontroller sends the control command to connect the SIM800A to GPRS, and response to the related events. The installation parameters are downloaded from the Server, and compared with the current values in the microcontroller memory, to update the new setting values, including acceleration, gyroscope, date and time, threshold values. In the case of no change, the data are herein transferred from the memory card to the Server using

the GET and POST methods. After sending the data, the program deletes the sent files in the memory card and continues checking the next data.

- ✓ If the card has no data, the program checks the process of receiving the installation parameters from the computer. Upon receiving the setting commands, the program writes the setting values to the Flash and RTC memories of the microcontroller. Upon receiving the current status commands, the program sends the data to the computer. Several command structures:

+ *Setting date and time: ST 19 03 19 09 03 00*
+ *Setting thresholds: A 0.2 0.2 1.25*
+ *Reading the current setting parameters: L*

4. Measurement module and results

A circuit board was designed and manufactured using cheap and small electronic components. The measurement module with the sizes of 10×15×8 cm was built. DC supply sources from 3.3 to 5 V were used for all elements on the module. The block diagram and layout of the PCB module are illustrated in Fig.4(a and b). A fabricated module is shown in Fig.4(c).

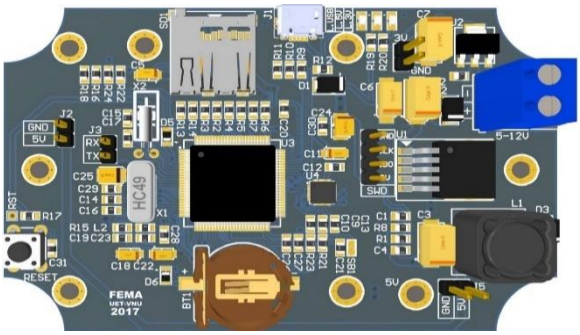

(a)

(b)

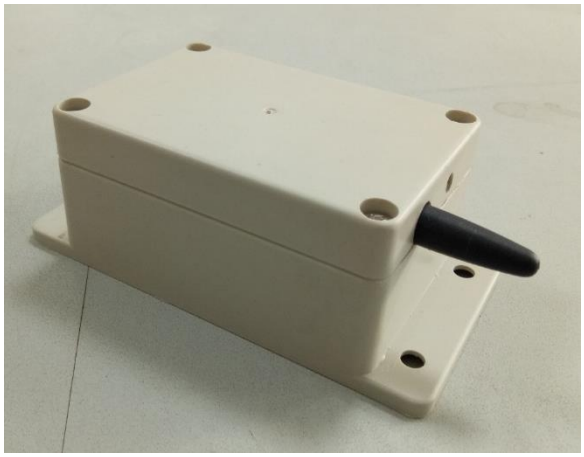

(c)

Figure 4. Photos of the measurement module: (a) Layout the components on the printed circuit board; (b) A fabricated circuit board; (c) A device module after packing.

The module includes four main parts: the MPU6050 sensor, a SIM800A modem, an STM32F407VGT6 microcontroller, and a memory microSD card. With its compact design, the module could measure six parameters by the sensor, including 3-axes acceleration values (Ax, Ay, Az) and 3-axes gyroscope values (Gx, Gy, Gz). The sensing data were written to the memory MicroSD card and then transferred to the cloud server using GPRS technology by the SIM800A modem and the microcontroller. The maximum number of samples is 2048 samples, with sampling time between 1 and 20 ms. The interval between two times of data collection can be set via USART communication standard, or from the Server.

The module can be mounted on the surface of the monitoring structure. Due to using the GPRS wave, the module can be placed at the stations where have had mobile phone signals. When there are vibrations, the acceleration and gyroscope signals change. If a value is higher than a preset level, the microcontroller starts reading the values from the sensor and writing to the memory card. The data are then sent to the Server via GPRS waves using the SIM800A modem for the storage and proceeding analysis.

Fig. 5 shows the results of installing, collecting, and storing the sensing data. The Server link that is registered at https://www.hostinger.vn/, is

https://sg-files.hostinger.vn/. The Server is used to save the data received from the module as the text files. The data can be downloaded to a computer for processing as needed. The possible loss of data is small because the parameters are written to the memory card before sending them. If any data is not sent due to a GPRS network error, the device can read back the data from the memory card and then send it again. In this work, the experiments were conducted in a small confined area in the radius of a few kilometers. The optimal transmission distance will be investigated in subsequent studies.

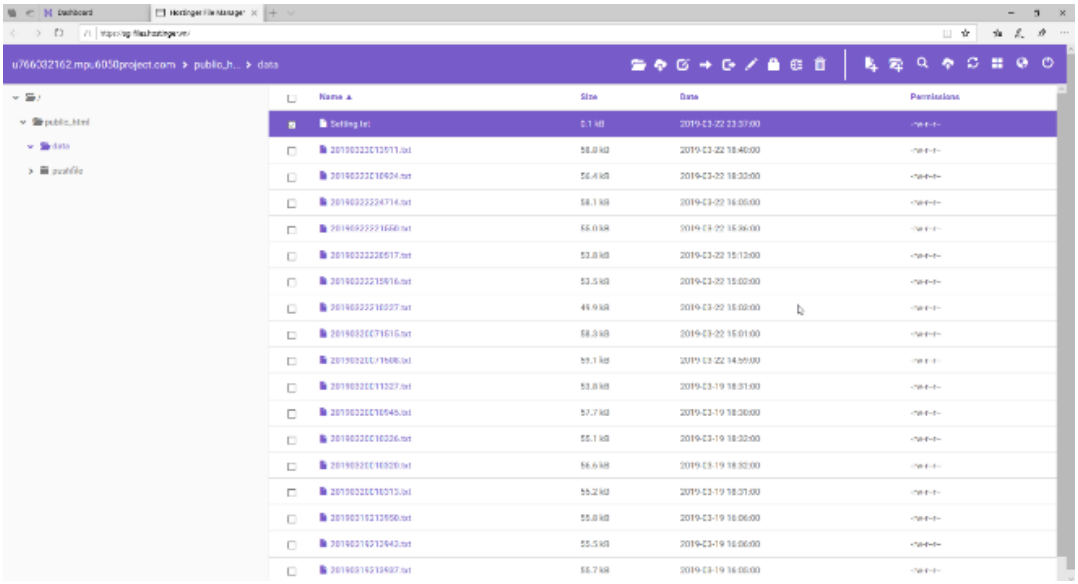

(a)

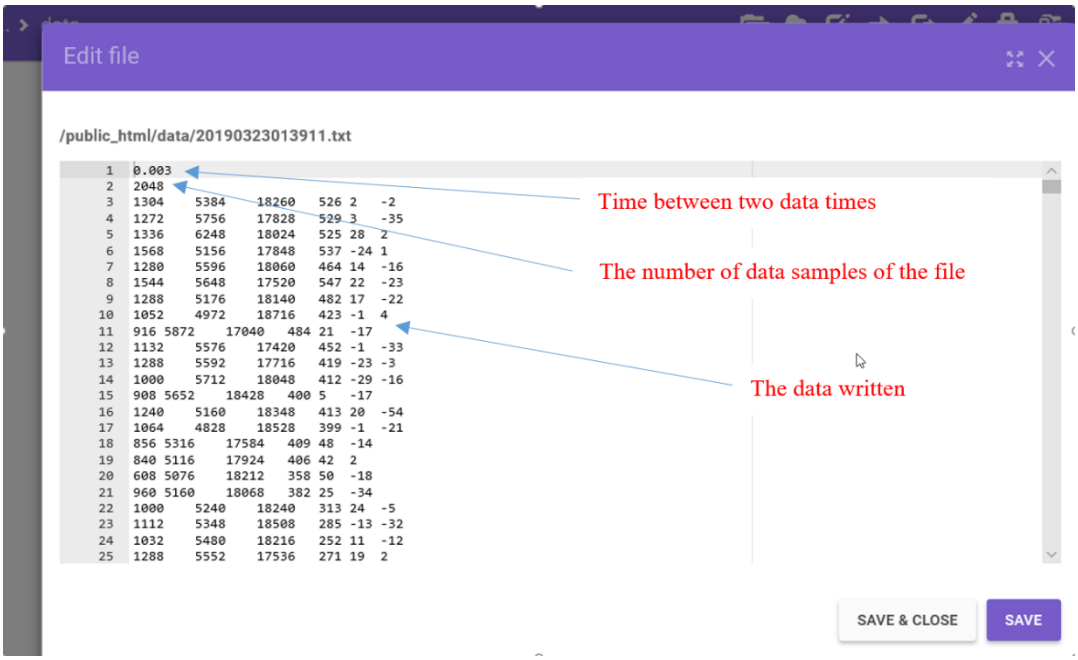

(b)

Figure 5. Data collection and storage on the server: (a) Server link; (b) Stored parameters structure.

5. Conclusion

A wireless low-cost monitoring system for vibration monitoring of structures is potential for data acquisition, analysis, and interpretation. In this study, a measurement module was built for remote sensing of the vibration parameters of the mechanical structures. The acceleration and gyroscope responses could be monitored and recorded via the use of a MEMS sensor and GPRS technology. The data were also stored on the memory MicroSD card or transferred to the cloud server. Although there are still some limitations, the product can be improved for practical application in proceeding works.

Acknowledgments

This work is supported by the research group of Mechatronics of the University of Engineering and Technology, Vietnam National University, Hanoi.

References

Babakhani B, Rahami H, Karami Mohammadi R. 2018. Determining Structural Resonance Frequency via Low-Cost Micro-Electromechanical Systems. *Iranian Journal of Science and Technology, Transactions of Civil Engineering* **10**:1–8.

Fu Q, Han B. 2017. Bridge vibration monitoring system based on vibrating-wire sensor and ZigBee technologies. In: *2017 9th IEEE International Conference on Communication Software and Networks*, Vol. 978, pp. 338–343.

Nguyen CD, Huynh QH, Phan CB, Tran VM, Nguyen CM, Pham BT, Ngo KN. 2018. Low-Cost Vibration Measurement for Behavior of Small-Scale Steel Modeling Low-Cost Vibration Measurement for Behavior of Small-Scale Steel Modeling using MEMS, Raspberry Pi-3 and Arduino Mega 2560. In: *Hội nghị Khoa học toàn quốc Cơ học Vật răn lần thứ XIV*, pp. 0–7.

R A, Mesta SS, A U V, G R, Sivaranan HK. 2017. Bridge monitoring system using wireless networks. *IJARIIE* **2**:107–111.

Tegtmeier FL. 2008. Strain gauge based microsensor for stress analysis in building structures. *Measurement* **41**:1144–1151.

Tong X-L, Yang H-L, Wang L-B, Miao Y-H. 2019. The Development and Field Evaluation of an IoT System of Low-Power Vibration for Bridge. *Sensors* **19**:1222.

Uchimura Y, Nasu T, Takahashi M. 2010. IEEE 802.11-Based Wireless Sensor System for Vibration Measurement. *Advances in Civil Engineering* **2010**:1–9.

Zhou G-D, Yi T-H. 2013. Recent Developments on Wireless Sensor Networks Technology for Bridge Health Monitoring. *Mathematical Problems in Engineering* **2013**:1–33.

The 5th International Conference on Engineering Mechanics and Automation (ICEMA 5)
Hanoi, October 11÷12, 2019

Design and manufacture of a tensile and bending fatigue testing machine for steel specimens in experimental method with gradually increasing stress amplitude

Nguyen Dinh Dung[a], Vu Le Huy[b] and Hoang Van Bao[c]

[a] *Phenikaa University, Hanoi, Vietnam, dung.nguyendinh@phenikaa-uni.edu.vn*
[b] *Phenikaa University, Hanoi, Vietnam, huy.vule@phenikaa-uni.edu.vn*
[c] *Hanoi University of Science and Technology, Hanoi, Vietnam, bao.hoangvan@hust.edu.vn*

Abstract

Fatigue curve presents a relation between stress and lifetime of a machine element, which is used in calculation and design for the machine element in mechanical engineering field. This curve has been being created traditionally from fatigue experimental data, where the applied stress amplitude is constant. Besides, creating the fatigue curve was shown to be performable by using fatigue test with gradually increasing amplitude. This is the new method and therefore there is no testing machine to perform this kind of experiments for steel machine elements. This paper presents the results in design, manufacture of a tensile and bending fatigue testing machine in experimental method with gradually increasing stress amplitude for steel specimens.

Key Words: Testing machine, Fatigue test, Stress, Lifetime, Gradually increasing amplitude

1. Introduction

Static strength is the stress level, where a machine element would be immediately broken if it is applied by a stress larger than that level. But fatigue fracture is a phenomenon that a machine element is broken under applied cyclic stress after a number of cycles (Broek, 1986; Perez, 2004) even it is much smaller than static strength level. It was found in 19th century and becomes a main criterion in machine design to determine the size of elements. The design formula for this criterion are usually based on fatigue curves, which presents the relation between the applied stress and number of cycles, also called as S-N curve. Fatigue lifetime of each element depends on crack growth rate in a cycle of applied stress. This leads to the difference of fatigue curves for different materials. Therefore, it is necessary to build the fatigue curves, which are only done by fatigue experiments.

A fatigue curve is created traditionally by using fatigue test data, which is performed under cyclic stress with constant stress amplitude until failure occurs. This test method is called here as normal fatigue test. The information of the cyclic stress with constant stress amplitude is presented in Figure 1. However, by applying this type of stress in experiments, there are inconvenient matters. The experiment may have to be stopped before failure occurs, because it exceeds an allowed time limit when applied stress level is too small in comparison with the static strength level of the testing specimen. Otherwise, if the applied stress is higher than the

static strength level of the specimen, the specimen will be broken before reaching the expected stress amplitude. It means that the specimen was not broken by fatigue test, and therefore it could not be taken into account.

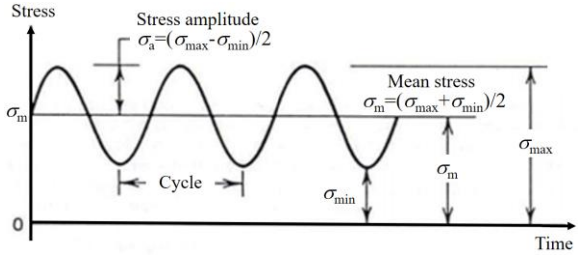

Figure 1. Information of cyclic stress

In order to overcome those matters of the normal fatigue test, Huy et. al. (2010) proposed a fatigue test method with gradually increasing stress amplitude as shown in Figure 2 applied on silicon specimens at micro-scale. This test method is here called as ramping fatigue test. Since the stress amplitude at the beginning is small, it does not make the specimen to be broken but gradually decreasing the strength. When the stress amplitude is higher than the static strength, the specimen will be completely broken. By controlling the ramping increment per cycle $\Delta\sigma$, the consumed time for each experiment will be estimated.

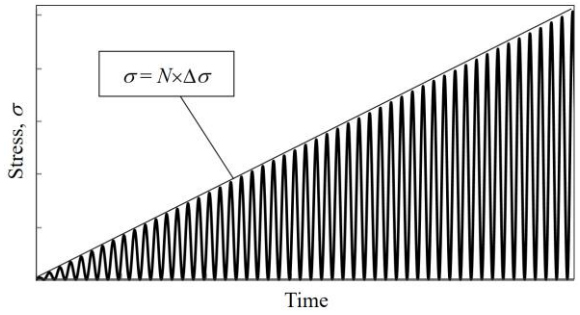

Figure 2. History of stress with gradually increasing amplitude, where N is the number of cycles and $\Delta\sigma$ is the ramping increment per cycle

The theory used for the ramping fatigue test method presented by Huy et. al. (2010) is based on Paris' law (Paris and Erdogan, 1963), which describes fatigue crack growth happened by dislocation of the crystal lattice. This is also the fatigue mechanism of metal materials such as steel. Therefore, the ramping fatigue test is applicable for steel specimens. For the case of the normal fatigue test, it is easy to perform the tests by using the testing machine on the market. However, for the case of the ramping fatigue test with steel specimens especially at large-scale, there is not any machine to perform this test. Therefore, this paper presents the results of designing and manufacturing a fatigue testing machine for steel specimens. This machine could perform both the normal and ramping fatigue tests with tensile and bending specimens.

2. Proposal of machine diagram

In order to perform both the normal and ramping fatigue tests with tensile and bending specimens, a fatigue test machine is prosed with the diagram shown in Figure 3. This machine has 3 main complexes as follow:

- Controller complex consists of a personal computer (1) running the experimental program and a control box (2) with a source, control circuits, etc.
- Holder table complex consists of a specimen holder (15) moved in horizontal screw shaft (13) by the stepper motor (3) through the spur gears and the ball-screw (13). The specimen holder (15) is supported by two guideways parallel to the screw shaft (13). The specimen holder (15) allows setting up the specimens in vertical direction for tensile test and in horizontal direction for bending test.

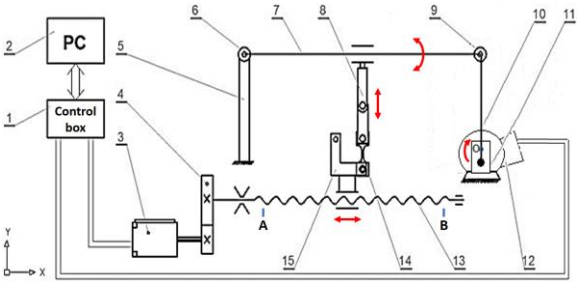

1. Control Box
2. Personal computer
3. Stepper motor
4. Spur gears
5. Static frame
6. Bearings (rotation joint)
7. Shaking rod
8. Vertical rod + Loadcell
9. Bearings (rotation joint)
10. Connecting rod
11. Eccentric
12. AC motor
13. Ball screw
14. Specimen
15. Specimen-holder table

Figure 3. Machine diagram

- Crank-and-rocker mechanism complex consists of the static frame (5), a guideway on the shaking rod (7), the connecting rod (10) and the eccentric (11) receiving the transmission from the AC motor (12).

All the three complexes are set on the ground frame made of shaped steel bars by welding. At the start position, the specimen-holder table (15) is at the left limit (presented as A in Figure 3), both the motors (3,12) are on the stop state. By pressing the start button in the software on the computer (2), the computer sends a command to the control box (1) to control the operation of the two motors (3,12). The stepper motor (15) makes the movement of the specimen-holder table (15) to the intended position on the right side along the screw shaft (13), which helps increasing the deformation of the specimen and therefore increases the applied stress on the specimen. When the AC motor (12) rotates, the crank-and-rocker mechanism creates the shake of the shaking rod (7), which pulls the vertical rod and the loadcell (8) moving up and down cyclically. Therefore, the specimens will be applied by a tensile cyclic load (Figure 4.a) or bending cyclic load (Figure 4.b) depending on the setup of the experiment as shown in Figure 4. The loadcell will measure the load applied to the specimen and send it to the computer.

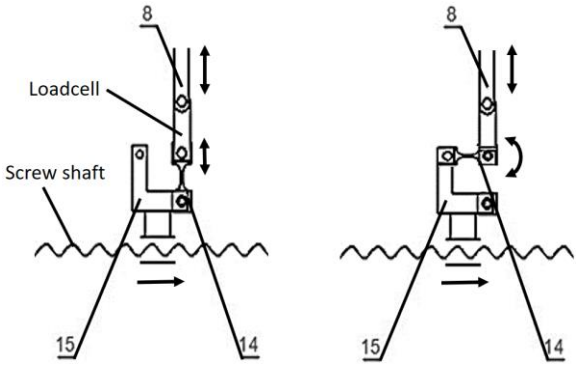

(a) (b)

Figure 4. Setting up the specimen in tensile (a) and bending (b) tests

3. Design of specimen

To get the input parameters to calculate and design the fatigue test machine, the specimens should be designed first. The material of the specimens is here selected as the steel 40CrNi, which is a good material used for machine elements such as gears (Perez, 2004). This steel has the properties (Chat, 2006)) as annealing to have hardness of 48~54HRC, ultimate strength σ_u of 1600 MPa, Yield strength of σ_y of 1400 MPa, density of 7850 kg/m^3, Young's modulus E of 2.1x10^{11} Pa, Poison factor of 0.3.

In order to limit the size of the fatigue test machine, the cross section of the specimen has the maximum as 5x5 mm^2. The shape of the specimen was designed as shown in Figure 5, where the total length is 130 mm. The two end parts with the holes of 20 mm in diameter are used to fit up the specimen onto the test machine. The testing part has the length of 50 mm and was designed with the flares to avoid stress concentration.

The stress concentration factor of this design was investigated with the stress distribution on the specimen obtained by finite element method (FEM). The 3D model of the specimen was built on SolidWorks software and then input it in Ansys Workbench software to perform FEM calculation. The 3D model in the Ansys Workbench software is shown in Figure 6, where the elements were set to be quadrangular mesh with the size of 1 mm. By applying a tensile load as F = 35000 N, the stress distribution on the specimen was obtained as shown in Figure 7, where the maximum stress is

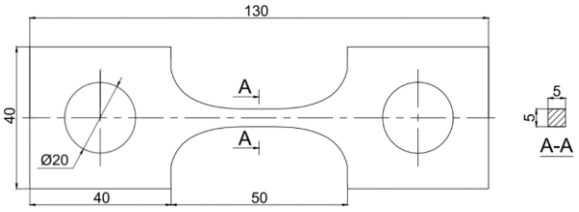

Figure 5. Specimen design

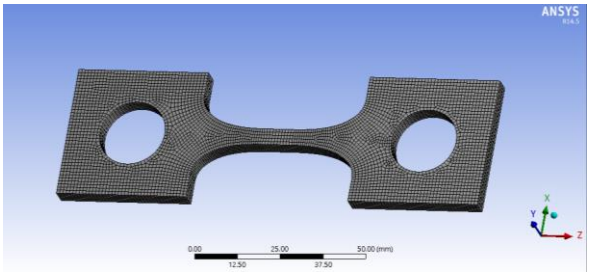

Figure 6. Mesh model of FEM

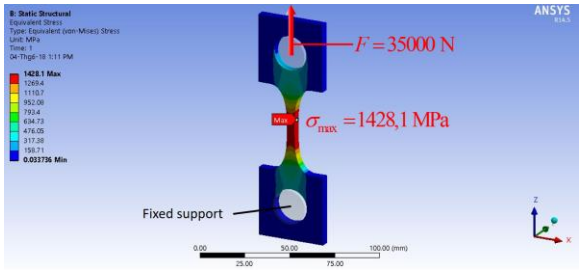

Figure 7. Stress distribution on the tensile specimen

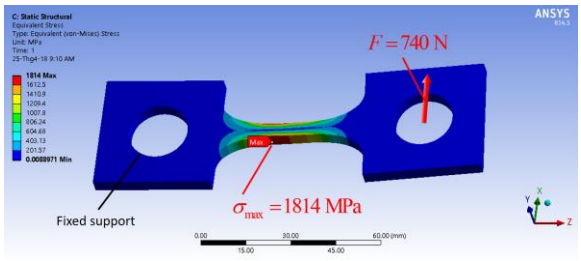

Figure 8. Stress distribution on the bending specimen

σ_{max} = 1428.1 MPa. In comparison with the norminal stress as σ = 1400 MPa, the stress concentration factor is calculated as $k = \sigma_{max} / \sigma$ = 1.02. With the bending specimen, the maximum stress is σ_{max} = 1814 MPa under the applied load of F = 740 N. For this case, the norminal stress is σ = 1791.6 MPa, and therefore the stress concentration factor is k = 1.01. These result shows that the stress concentration is negligible and therefore can be ignored.

By using FEM calculation, from the ultimate strength σ_u, the maximum force and the maximum deformation of the specimens are also estimated. For the case of tensile test, the maximum force, which should break the specimen, could be applied on the specimen to be F = 40000 N, then the maximum deformation of the specimen is obtained as Δx_{max} = 0,317 mm. For the case of bending test, the maximum force is F = 740 N, then the maximum deformation is Δx_{max} = 4 mm. These maximum deformations were measured at the center of the hole on the end part anchored to the loadcell. Summarizing both the cases, the maximum force F = 40000 N and the maximum deformation Δx_{max} = 4 mm are the input parameters to calculate and design the fatigue test machine.

4. Calculation and design of the machine

From the machine diagram shown in Figure 3 and the two input parameters (the maximum force and the maximum deformation) estimated in the previous section, the elements in the machine were calculated and designed by using the formulae in Chat (2006). The following are the calculation of some primary elements in the machine.

4.1. Main power motor

The main power motor is the AC motor numbered as 12 in Figure 3. The mission of this motor is to create the motion of the shaking rod (numbered as 7 in Figure 3). They are connected by the crank-and-rocker mechanism as shown in Figure 9. With the maximum force F = 40000 N and the maximum displacement corresponding to the maximum deformation Δx_{max} = 4 mm, the length of the links was selected as shown in Figure 9 in order to satisfy the movement and the size limitation of the machine.

The torque applied on the motor is calculated as

$$M_O = F_C l_{OC} \approx 160 \text{ Nm} \quad (1)$$

where l_{OC} is the length of the crank OC, F_C is the load along the connecting rod BC (numbered as 10 in Figure 3) which is calculated from force and moment balance equations of the crank-and-rocker mechanism. Since frequency f of the cyclic load applied on the specimen is selected to be 1 Hz, the angular velocity of the motor is

$$\omega = 2\pi f = 2\pi \text{ rad/s} \quad (2)$$

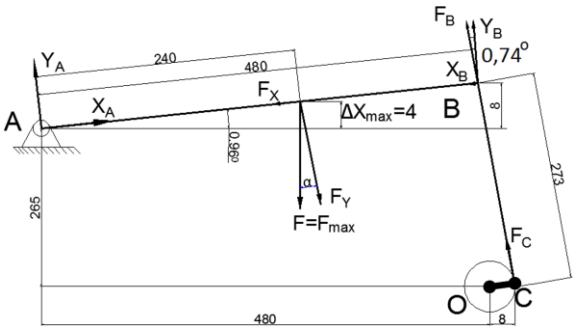

Figure 9. Crank-and-rocker mechanism for calculation to select the AC motor

Therefore, the power on the output shaft of the motor should be larger than the estimated power P_e as

$$P_e = M_O \omega = 1005 \text{ W} \quad (3)$$

The motor was then selected as a 3-phase motor including a reducer box with the output shaft's power and speed as

$$\begin{cases} P = 1.5 \text{ kW} \\ n = 60 \text{ rpm} \end{cases} \quad (4)$$

4.2. Ball-screw

Ball-screw shaft (13) is used to move the specimen holder table (15) in horizontal direction. This complex is illustrated in Figure 10. The screw shaft will be applied by an axial load F_a induced from friction loads. Since the maximum force F = 40000 N will be transferred onto the guideways and lead to the appearance of the friction loads, where the friction load on the guideways for specimen holder table (Figure 10) is notated as F_{f1} and the friction load on the guideway of the shaking rod (7) is notated as F_{f2}. The friction loads F_{f1} and F_{f2} are calculated as

$$F_{f1} = F\mu = 6800 \text{ N} \quad (5)$$

$$F_{f2} = F\mu \cos\alpha = 6796 \text{ N} \quad (6)$$

where μ is the friction factor in the guideways with the value as 0.17, α is the maximum angle of the shaking rod in comparison with the horizontal. The axial load F_a is then evaluated as

$$F_a = F_{f1} + F_{f2} \cos\alpha = 13592 \text{ N} \quad (7)$$

Diameter of the screw shaft is calculated from the tensile strength criterion as

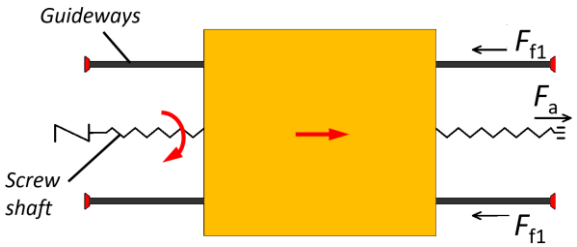

Figure 10. Stress distribution on the bending specimen

$$d_1 \geq 2\sqrt{\frac{1.3F_a}{\pi[\sigma_t]}} \quad (8)$$

where $[\sigma_t]$ is the allowed tensile strength and has the value determined from Yield strength as

$$[\sigma_t] = \frac{\sigma_y}{3} = \frac{360}{3} = 120 \text{ MPa} \quad (9)$$

with Yield strength of the steel material C45 of the screw shaft as σ_y = 360 MPa. By substituting $[\sigma_t]$ into Equation (8), the diameter of the screw shaft is obtained as $d_1 \geq 13.7$ mm. Based on this value, ball-screw is selected with following parameters:

- Root diameter of screw shaft d_1 = 14 mm.
- Ball diameter d_b = 4 mm.
- Lead $p = d_b + (1 \ldots 5)$ mm = 6 mm.
- Ball groove radius r_l = 2.04 mm.
- Pitch circle diameter of balls D_m = 18 mm
- Lead angle $\gamma = 6^o$
- Equivalent friction angle $\varphi_e = 0.057^o$

The torque applied on the screw shaft is

$$T = \frac{F_a D_m \tan(\gamma + \varphi_e)}{2} = 12980.2 \text{ MPa} \quad (10)$$

On the other hand, the ramping increment per cycle is here selected to be maximum as $\Delta\sigma$ = $5\text{x}10^6$ Pa/cycle. With the cross section of the specimen as A = 5x5 mm^2, the load increment in each cycle is calculated as

$$\Delta F = A\Delta\sigma = 125 \text{ N/cycle} \quad (11)$$

By using FEM calculation with Ansys software for tensile specimen with the applied load of ΔF = 125 N, the deformation increase of the specimen after each cycle is $\Delta x = 1.25\text{x}10^{-3}$ mm. Therefore, the specimen-holder table needs to move amount of $\Delta x/\tan\alpha$ = 0.037 mm after each cycle. With the frequency of the applied cyclic load as f = 1 Hz and the lead of screw shaft p = 6 mm, the speed of the screw shaft is estimated as n_s = 0.37 rpm.

4.3. Stepper motor

From the required torque and the speed of the

screw shaft are T = 12980.2 Nmm and n_s = 0.37 rpm, respectively, the required power of the stepper motor (numbered as 3 in Figure 3) is calculated as $P = Tn_s/9.55$ = 0.5 kW. It means that the selected stepper motor should have torque and power to be $T \geq 13$ Nm and $P \geq 0.5$ kW. By using the spur gear transmission with transmission ratio u of 3.3, the required torque of the stepper motor might be reduced to $T \geq 13/u$ = 3.94 Nm. Therefore, the stepper motor is here selected as Model 86J18118-842 with the maximum torque and power on the output shaft to be T = 8.5 Nm and P = 0.714 kW, respectively.

4.4. Loadcell

Loadcell is used to measure the load applied on the specimen in the tests. The selected loadcell should have rated capacity to be higher than the maximum load applied on the specimen as F_{max} = 40000 N. Therefore, the loadcell is selected as PST-KELI loadcell with the rated load of 1.2ton, sensitivity of 2.0±0.003 mV/V, accuracy class of 0.03, operating temperature range: -30 to +70°C, etc.

The other elements of this machine were calculated and selected by using the formulas and guides in Chat (2006) and Norton (2006) to satisfy their strength and have reasonable dimensions. The 3D assembly model was built in SolidWorks software as shown in Figure 11. It was then converted into 2D assembly drawing as shown in Figure 12 for manufacturing purpose.

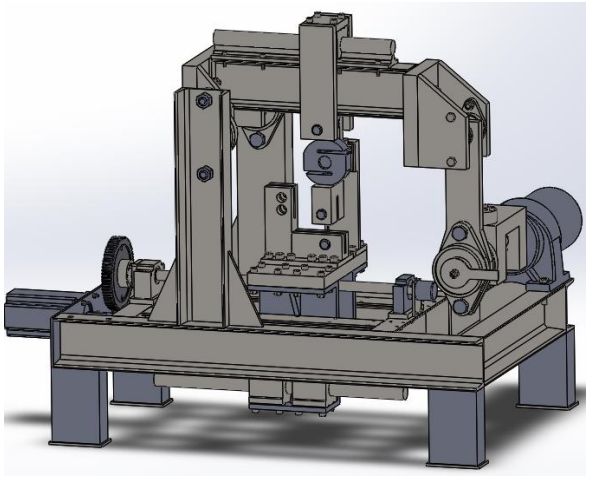

Figure 11. 3D model of the fatigue test machine

5. Control system

From the operation mechanism of the fatigue test machine designed above and the require of collecting data, there are electronic elements on the machine as shown in Figure 13. These elements are controlled by a control system as illustrated in Figure 14. This system has the main missions as follows:

- Turning on/off the AC motor and stopping it at required position to set up the specimen by using the infrared sensor.

- Controlling the stepper motor to move the specimen-holder table and determining the position of the specimen-holder table by using the limit switches and encoder.

- Recording the load applied on the specimen by using the loadcell.

The electronic elements are connected by the wires as shown in Figure 14 to the main controller which is used here to be Arduino Uno circuit board. The Arduino Uno board connects with the computer by USB cable to receive the commands and return the measured data.

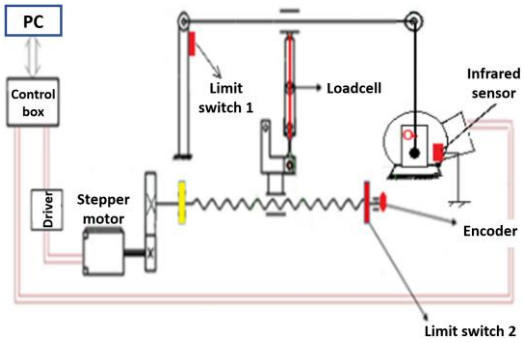

Figure 13. Electronic elements on the machine

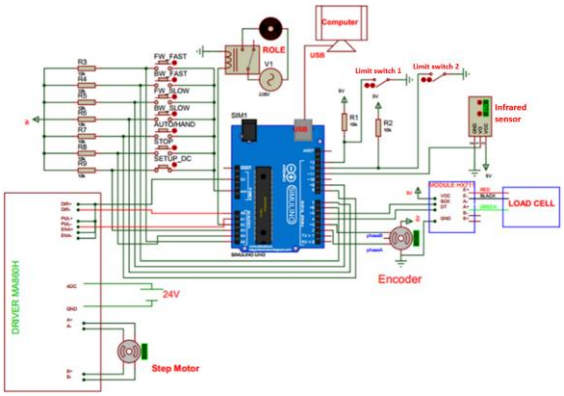

Figure 14. Control system diagram

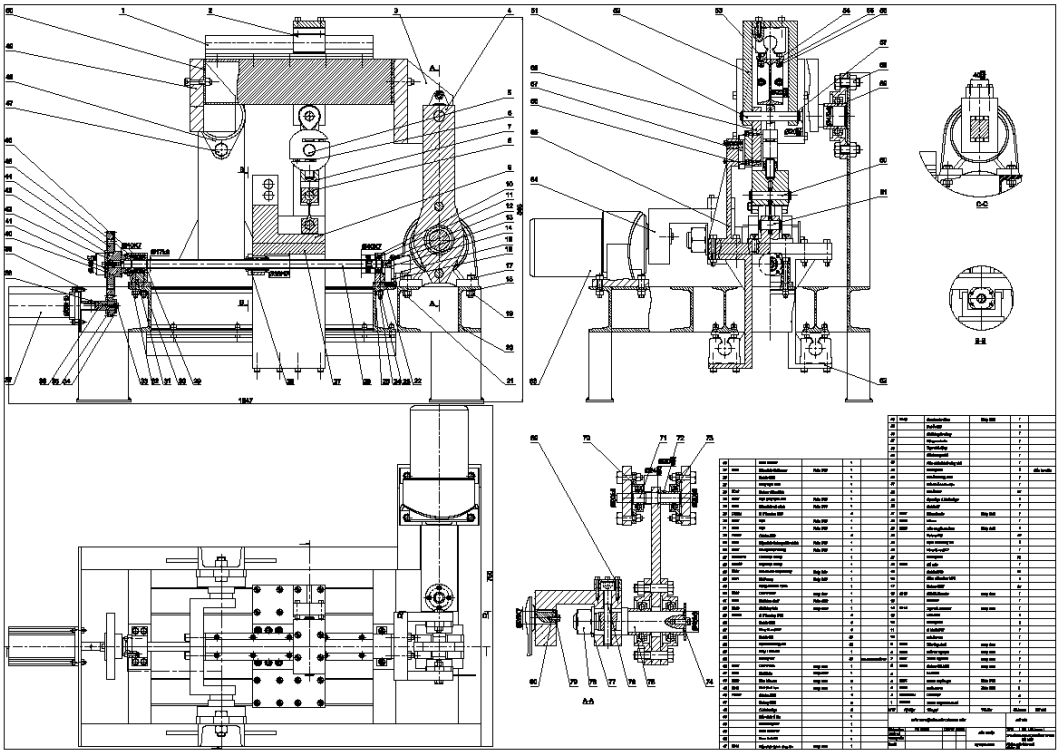

Figure 12. Assembly drawing of the fatigue test machine

6. Result and discussion

With the design presented above, the fatigue test machine was manufactured completely as shown in Figure 15. To perform the test with this machine, a software was programmed by C++ language and has the interface as shown in Figure 16. The machine was then tested with the tensile specimens made of steel C45 as shown in Figure 17, where the cross section of these specimens is 2.5x2.5mm^2. Figure 17(a) shows that the broken region of the specimen in static test was tighten showing plastic deformation. However, the plastic deformation was not seen in the specimens tested with normal and ramping fatigue tests (Figures 17(b) and 17(c)), i.e., fatigue cracks extend in the region of elastic deformation. Fatigue crack propagation was clearly seen as the beach marks on the crack surface shown in Figure 18.

From the applied load on the specimens recorded by the loadcell, stress on the specimens was calculated by FEM. The experimental data of the static and fatigue tests are shown in Figure 19 as the symbols, where the abscissa is the number of stress cycles in the fatigue tests and the ordinate is the applied stress at the moment that specimens broken. A specimen was tested with the static test is shown by the circle symbol and its strength is measured as 0.452 GPa. A specimen was tested with the normal fatigue test at the stress amplitude of 0.239 GPa and was broken after 38214 cycles. The data of this test is shown by the square symbol Figure 19. An other specimen was tested with the ramping fatigue test and its experimental data is shown by the lozenge symbol. This test was performed at the intended ramping increment per cycle $\Delta\sigma$ = 15000 Pa/cycle. The specimen was broken at the stress amplitude of 0.355 GPa and the number of cycles as 24582 cycles. It means that the ramping increment per cycle in the reality of this test is $\Delta\sigma$ = 14435.6 Pa/cycle and it is different from the intended value about 3.7%. The stress amplitudes in these fatigues tests are smaller than static strength and did not induce the plastic deformation on the specimens. Therefore, the theory to create fatigue curve on the basis of Paris' law in Huy et. al. (2010) could be applied to these experimetal data.

Figure 15. Completely manufactured machine

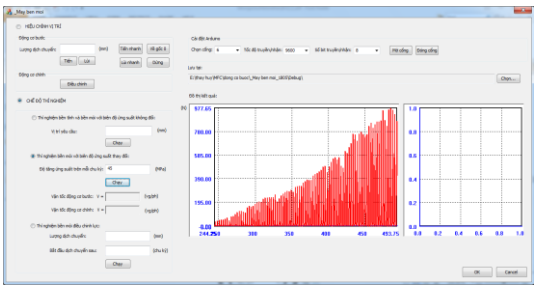

Figure 16. Interface of the control software

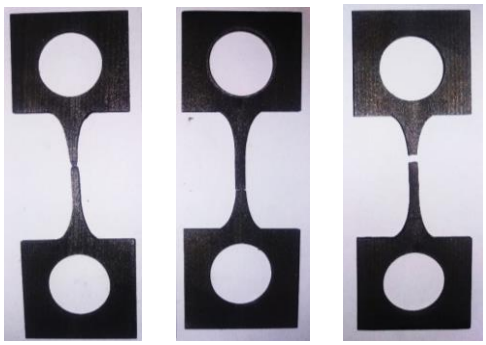

(a) (b) (c)

Figure 17. Specimens with (a) static test, (b) normal fatigue test and (c) ramping fatigue test

Figure 18. Close view of fatigue crack

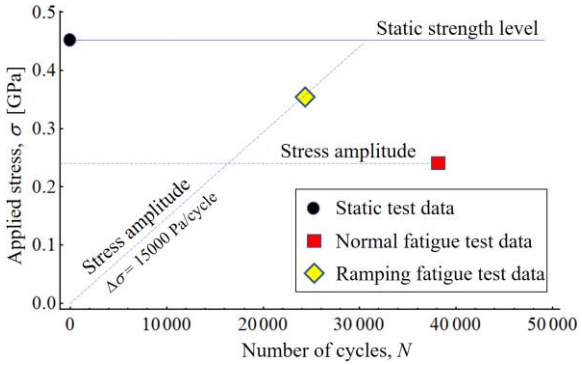

Figure 19. Experimental data

7. Conclusion

In this paper, the design and manufacture of a fatigue testing machine for steel specimens is presented. This machine could perform the static test, the fatigue tests with constant and gradually increasing stress amplitudes on the tensile and bending specimens. Specimens for this machine were also designed, producted to perform the tests. The results showed the posibility of using this machine in the fatigue tests with gradually increasing stress amplitude to create fatigue curve of the steel specimens.

Acknowledgement

This research is funded by PHENIKAA University under grant number 04.2019.02.

References

Broek D. (1986). *Elementary Engineering Fracture Mechanics*, Dordrecht: Kluwer.

Chat T., Uyen L.V. (2006). *Calculation and design of mechanical transmission systems*, Vietnamese Education Publishing House.

Huy V.L., Gaspar J., Paul O., Kamiya S. (2010). A novel fatigue test with ramping stress amplitude to evaluate fatigue behavior of polysilicon thin films, *2010 IEEE 23rd International Conference on Micro Electro Mechanical Systems*, pp.220-33.

Norton R.L. (2006) *Machine Design, An Integrated Approach*, Pearson Education Inc.

Paris P., Erdogan F. (1963). A critical analysis of crack propagation laws, Journal of Basic Engineering, *Transactions of the American Society of Mechanical Engineers*, pp.528-534

Perez N. (2004). *Fracture Mechanics*, Kluwer Academic Publishers.

The 5th International Conference on Engineering Mechanics and Automation (ICEMA-5)
Hanoi, October 11÷12, 2019

Enhancing the stress test ECG signal for real-time QRS detector

Thang Pham Manh[a], Manh Hoang Van[a] and Viet Dang Anh[a]

a Lecturer, University of Engineering and Technology, Vietnam National University, Ha Noi

Abstract

The Electrocardiogram (ECG) signal, which is a record of the electrical activity of the heart, can be treated as a combination of a free-noise signal and noises. The primary source of interference in the ECG recording during exercise is broadband myopotentials (EMG), contained in a full frequency band. Because the frequency ranges of both signals (ECG and EMG) overlap, band-stop filters distort the ECG signal, especially of QRS complexes. An alternative method of removing interference may be using Adaptive Wavelet Wiener Filter (AWWF) with noise-free signal estimation. As a result of a straightforward wavelet transform, it is possible to extract noise with some components of the QRS complex in the highest frequency bands. The central part of the QRS components is in the lower frequency bands. The resulting signal can be filtered by matching the transform coefficients. Testing was performed on muscle (EMG) artifact noised signals from the MIT-BIH Noise Stress Test Database at 360 Hz sampling frequency.

Key Words: EMG, Wavelet Wiener Filtering, Stress ECG Test, MIT-BIH Database.

I. Introduction

Exercise testing can be an inexpensive and non-invasive standard diagnostic procedure performed by physicians to assess cardiovascular diseases, and the prescription of exercise and training. When performing the test, the patient's ECG signal will be monitored while their exercise level is increased gradually. There are several different methods and modes available that can provide vital information to the clinician to help patients and athletes improve their fitness or cardiovascular status. This method is based on the increase in the organism's need for oxygen and glucose exchange during physical exercise, and consequent heart beating capacity raise. As a result, it is possible to uncover potential cardiovascular problems that may not manifest at rest.

Since this testing procedure involves significant physical movement and breathing activities, multiple sources of additive noises affect the ECG analysis, and they make the cardiac monitoring difficult in practice. These sources of interference mainly include baseline wander, electrode motion artifact, and electromyogram-induced (EMG) noise. EMG is considered as the significant artifact source and is difficult to separate because its frequency spectrum overlaps the frequency spectrum of the ECG signal.

Wavelet transform (WT) based denoising methods can increase the efficiency of suppression of wide-band EMG artifact compared to linear filtering. The WT will decompose the signal into different bands so that the highest bands contain EMG artifact and several components of QRS complexes, while QRS complex components are mainly located in the lower frequency bands. Then, the resulting signal can be filtered by appropriately adjusting

the transform coefficients depending on the estimated noise level. In this way, the selection of parameters such as decomposition and reconstruction filter banks, level of decomposition, and the strategy of wavelet transform coefficient adjustment will play an important role.

In [1], the authors proposed an optimal denoising approach for ECG using stationary wavelet transform (SWT). This method includes the choice of optimal mother wavelet, appropriate thresholding method, and level of decomposition. The authors in [2] presented the use of wiener filtering in the shift-invariant wavelet domain with the pilot estimation of the signal to eliminate EMG noise. This method utilizes the shift-invariant dyadic discrete-time wavelet transform (DyDWT) with four-levels of decomposition for the pilot estimation and wiener filtering blocks. In [3], the authors presented an algorithm for ECG denoising using discrete wavelet transform (DWT). This proposed method is implemented through three main steps that are forward DWT, thresholding, and inverse DWT. The ECG signal denoising algorithm including two-stage which combines wavelet shrinkage with wiener filtering in the translation-invariant wavelet domain, was presented in [4].

In this work, we focused on the wavelet Wiener filtering to eliminate EMG artifact in the ECG signal. We utilized DyDWT for both the Wiener filter and in the estimation of a noise-free signal. The goal of this work was to find the most suitable parameters for the Wiener filter based on the signal-to-noise ratio.

The remainder of this paper is organized as follows: we present the materials and proposed method in Section II. The results are presented and discussed in section III. Finally, the conclusions are presented.

II. Materials and Methods

1. Stationary Wavelet Transform

Nowadays, the wavelet transform has been a popular and useful computational tool for signal and image processing applications, because it provides signal characteristics in both the time domain and frequency domain. While analyzing non-stationary signals had been a significant challenge for various transform techniques such as Fourier Transform (FT), short-time Fourier Transform (STFT), wavelet transform techniques can effectively analyze both non-stationary and stationary signals. With the wavelet decomposition, the signal is decomposed in like-tree structure using filter banks of low-pass and high-pass filters with down-sampling of their outputs. The dyadic transform, where only decomposed outputs of the low-pass filter, is the most commonly used decomposition tree structure. In this work, we used the Stationary Wavelet Transform when it gives better filtration results [4].

2. Wavelet Filtering (WF) Method

When using the wavelet transform to remove the artifact from ECG signals, the parameters used are decomposition depth of input signal, thresholding method, threshold level, and filter banks. The selection of appropriate parameters is an essential task because the signal will be separated from interference by thresholding of wavelet coefficients.

We assume that the corrupted signal denoted $x(t)$ is an additive mixture of the noise-free signal $s(n)$ and the noise $w(n)$, both uncorrelated.

$$x(n) = s(n) + w(n) \tag{1}$$

where n represents the discrete-time ($n = 0, 1, \ldots, N-1$), and N is the length of the signal.

If the noisy signal $x(n)$ is transformed into the wavelet domain using the dyadic SWT, we can obtain wavelet coefficients.

$$y_m(n) = u_m(n) + v_m(n) \tag{2}$$

where $u_m(n)$ are coefficients of the noise-free signal and $v_m(n)$ denote the coefficients of the noise, m is the level of decomposition and denotes m-th frequency band. We need to recover coefficients of the noise-free signal $u_m(n)$ from $y_m(n)$. The idea of Wiener filtering of each wavelet coefficient can solve it.

To the modification of the wavelet coefficients to be more efficient, the threshold sizes should be set separately for each decomposition level m. For the calculation of the

threshold value, the standard deviation of the noise is multiplied by an empirical constant *K* and described by the equation.

$$\lambda_m = K.\sigma_{vm} \quad (3)$$

where σ_{vm} is the standard deviation of noise in the *m*-th frequency band, and it can be estimated using the median [5], [6].

$$\sigma_{vm} = \frac{median(y_m)}{0.6745} \quad (4)$$

If the standard deviation of the noise is estimated using a sliding window, we can obtain the time-dependent $\sigma_{vm}(n)$, and the threshold value becomes,

$$\lambda_m(n) = K.\sigma_{vm}(n) \quad (5)$$

3. Wavelet Wiener Filtering (WWF) Method

By input signal preprocessing using wavelet transform and thresholding we obtain an estimation of coefficients $u_m(n)$. This strategy is showed in Figure 1.

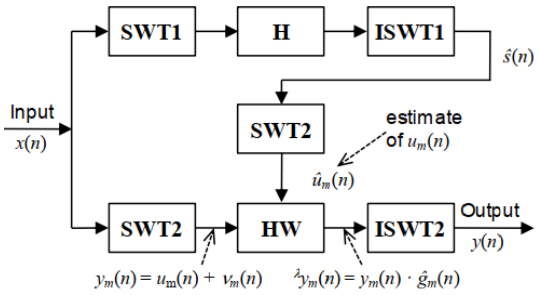

Figure 1. The block diagram of the Wavelet Wiener Filtering method.

The upper path of the scheme consists of four blocks: the wavelet transforms SWT1, modification of coefficients in the block H, the inverse wavelet transforms ISWT1, and the wavelet transform SWT2. The lower path of the scheme consists of three blocks: the wavelet transforms SWT2, the Wiener filter in the wavelet domain HW, and the inverse wavelet transforms ISWT2.

Because the signal can be easily separated from noise in the wavelet domain, the noisy signal, $x(n)$, will first be transformed into the wavelet domain by the SWT1 block. Threshold level, $\lambda_m(n)$, will then be estimated for thresholding to separate the free-noise signal and noise. The estimation $\hat{s}(n)$, which approximate noise-free signal $s(n)$ is obtained by using the ISWT1 block. This estimate is used to design the Wiener filter (HW), which is applied to the original corrupted signal $x(n)$ in SWT2 transformed domain (lower path) via Wiener correction factor [1], [7].

$$\hat{g}_m(n) = \frac{\hat{u}_m^2(n)}{\hat{u}_m^2(n)+\sigma_{vm}^2(n)} \quad (6)$$

where $\hat{u}_m^2(n)$ are the squared wavelet coefficients obtained from the pilot estimation $\hat{s}(n)$, and $\sigma_{vm}^2(n)$ is the variance of the noise coefficients $v_m(n)$ in the *m*-th frequency band. We get final signal $y(n)$ by inverse transform IWT2 of modified coefficients ${}^{\lambda}y_m(n)$.

$${}^{\lambda}y_m(n) = y_m(n).\hat{g}_m(n) \quad (7)$$

4. Adaptive Wavelet Wiener Filtering (AWWF) Method

In order to use the wavelet Wiener filter effectively, it is necessary to choose the exact parameters of the filter. The most important ones are the decomposition depth, the thresholding method, the empirical constant *K*, and the wavelet filter banks used in the SWT3 and SWT4 blocks. It is evident that if the noise levels in the input signal changes, the parameters need to change accordingly to get the best results.

To adapt to the change of noise, the input signal is divided into segments with an approximately constant level of noise. Besides, the WWF is also improved by adding the block for noise estimate (NE). This block has two inputs: the first input is the noisy signal $x(n)$, and the other is the estimate of the free-noise signal $y(n)$ obtained by the WWF method. The estimate of the input noise is the difference between these two signals, and the signal-to-noise ratio (SNR) can thus be calculated. The NE block is responsible for monitoring SNR changes at the beginning of each segment to choose the appropriate parameters for the filter at each segment. The filtered segments will then be reconnected.

The parameters in blocks SWT3, H3, ISWT3, SWT4, and ISWT4 are set up using an estimated SNR_{est} value.

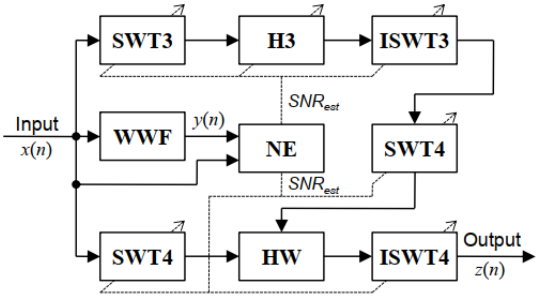

Fig. 2. The block diagram of the Adaptive Wavelet Wiener Filtering Method.

5. *Rules for evaluating results*

The results were assessed according to achieved signal to noise ratio SNR_{out} [dB] of the output signal $z(n)$ by the following equation,

$$SNR_{out} = 10log_{10}\left(\frac{\sum_{n=0}^{N-1}[s(n)]^2}{\sum_{n=0}^{N-1}[z(n)-s(n)]^2}\right) \quad (8)$$

where $s(n)$ is the free-noise signal.

From Eq. (8) it is apparent that we need to know the free-noise signal $s(n)$ to calculate the SNR_{out}, which is not possible in real situations. Because free-noise signals are not available, we selected several segments of signals of the MIT-BIH Noise Stress Test Database [8]. These signals were corrupted by a noise, which calibrated amounts of noise from record 'em'. The signal-to-noise ratios (SNRs) during the noisy segments of these records are listed in the flowing Table 1.

Table 1. The records in the MIT-BIH Noise Stress Test Database [8].

Record	SNR (dB)	Record	SNR (dB)
118e24	24	119e24	24
118e18	18	119e18	18
118e12	12	119e12	12
118e06	6	119e06	6
118e00	0	119e00	0
118e_6	-6	119e_6	-6

III. Simulation results

1. *Thresholding of pilot estimation*

The choice of thresholding in block H has an essential influence on the result. It is vital to remove the maximum of the noise. We tested three different methods for pilot estimation: hard, soft and hybrid. Table 2 summarizes the achieved results.

Table 2. Influence of different thresholding methods on results

Filters: SWT3/SWT4: db4/bior1.3

SNR_{in} [dB]	SNR_{out} [dB]		
	Pilot estimation thresholding		
	Hard	**Soft**	**Hybrid**
-6	34.3933	33.3418	33.3377
0	34.3492	33.3670	33.3012
6	34.6166	33.6817	31.3878
12	36.2835	35.4364	34.1689
18	37.6831	37.0186	35.2549
24	38.2241	37.5143	35.9313

We can see from SNR_{out}, that better results are achieved using hard or soft thresholding. Results are worse when we apply hybrid thresholding.

2. *Choice of filters for SWT3 and SWT4*

Our next investigation will be focused on the choice of the filters for SWT3, and SWT4 transforms. We have experimented with wavelet families in the library of Matlab 2017b. The best results are received as described in Table 3.

Table 3. Influence of different filters SWT3/SWT4 on results.

Hard thresholding in the pilot estimation

SWT3/SWT4	SNR_{in}	
	24 dB	**18 dB**
haar/boir1.3	37.4013	36.5682
db4/sym2	37.4619	36.9358
db4/bior1.3	38.2241	37.6831
db4/coif1	37.4740	36.9106
sym2/bior1.3	38.1714	37.6207
sym2/coif1	37.3964	36.7957
rbio1.3/coif1	37.5431	36.9949

According to SNR_{out}, we can say that the combination of filters used for SWT3 and SWT4 transforms yields the best result, db4/bior1.3. So, we have chosen db4/bior1.3 for STW3/SWT4 transforms and the hard thresholding approach to design filter.

The filtered results for the segments taken from [8] are summarized in Table 4. Where SNR_{in} is the signal-to-noise ratio of the input signal, SNR_{out} denotes signal-to-noise ratio of the filtered signal, and SNR_z denotes improvement

signal-to-noise ratio, $SNR_z = SNR_{out} - SNR_{in}$. Our effort is to make the SNR_z the highest possible.

Table 4. The result achieved with the filter AWWF

SNR_{in} [dB]	SNR_{out} [dB]	SNR_z [dB]
-6	32.9	38.9
0	32.8	32.8
6	31.1	25.1
12	33.8	21.8
18	34.9	16.9
24	35.6	11.6

Besides, we also compared the results achieved when using the AWWF filter with other filters like WWF and WF. The comparison results are given in Table 5.

Table 5. Comparison results between filters AWWF, WWF and WF

Filter	SNR_{avg} [dB]
AWWF	24.51
WWF	20.73
WF	18.72

From the data table, we can see that the AWWF filtering method gives the best results, followed by WWF and WF with improved SNR of 24.51 dB, 20.73 dB, and 18.72 dB, respectively.

IV. Conclusion

In this study, we used the Adaptive Wavelet Wiener Filter for improving stress test ECG signals. From the obtained results, we can see that the proposed algorithm provides better filtering results than several other tested algorithms. The setting of suitable parameter values to the estimated noise level has a positive effect on the performance of the filtering algorithm.

V. Acknowledgment

This work is supported by the research project N0. 01C02/01-2016-2 granted by the Department of Science and Technology Hanoi.

References

[1] L. Suyi and L. Jun, "The optimal de-noising algorithm for ECG using stationary wavelet transform," *2009 WRI World Congr. Comput. Sci. Inf. Eng. CSIE 2009*, vol. 6, no. 2007, pp. 469–473, 2009.

[2] L. Chmelka and J. Kozumplík, "Wavelet-based Wiener filter for electrocardiogram signal denoising," *Comput. Cardiol.*, vol. 32, pp. 771–774, 2005.

[3] G. Garg, V. Singh, J. R. P. Gupta, and A. P. Mittal, "Optimal algorithm for ECG denoising using Discrete Wavelet Transforms," *2010 IEEE Int. Conf. Comput. Intell. Comput. Res. ICCIC 2010*, no. 2, pp. 577–580, 2010.

[4] N. Nikolaev, Z. Nikolov, A. Gotchev, and K. Egiazarian, "Wavelet domain Wiener filtering for ECG denoising using improved signal estimate," *ICASSP, IEEE Int. Conf. Acoust. Speech Signal Process. - Proc.*, vol. 6, pp. 3578–3581, 2000.

[5] L. N. Sharma, S. Dandapat, and A. Mahanta, "Multiscale wavelet energies and relative energy based denoising of ECG signal," *2010 IEEE Int. Conf. Commun. Control Comput. Technol. ICCCCT 2010*, no. 1, pp. 491–495, 2010.

[6] A. Phinyomark, C. Limsakul, and P. Phukpattaranont, "EMG denoising estimation based on adaptive wavelet thresholding for multifunction myoelectric control," *2009 Innov. Technol. Intell. Syst. Ind. Appl. CITISIA 2009*, no. July, pp. 171–176, 2009.

[7] P. Lander and E. J. Berbari, "Time-frequency plane Wiener filtering of the high-resolution ECG: Development and application," *IEEE Trans. Biomed. Eng.*, vol. 44, no. 4, pp. 256–265, 1997.

[8] G. B. Moody, W. K. Muldrow, and R. G. Mark, "Noise Stress Test for Arrhythmia Detectors.," *Computers in Cardiology*. pp. 381–384, 1984.

The 5th International Conference on Engineering Mechanics and Automation (ICEMA 5)
Hanoi, October 11÷12, 2019

An automatic air pollution measurement system

Thang Pham Manh[a], Seung Chul Jung[a], Kim Hee Joong[b], Son Thai Tran[c], Tuan Ngo Anh[a]

[a] Faculty of Engineering Mechanics and Automation
University of Engineering and Technology, Vietnam National University
G2 Building, 144 Xuan-Thuy, Cau-Giay, Hanoi, Vietnam
Email: thangpm@vnu.edu.vn
[b] Kentek Enviroment Technology - Korea
Rm 526, Hansin S-MECA 65, Techno 3-ro, Yuseong-gu, Daejeong 34016, Korea
[c]Faculty of Information Technology
University of Engineering and Technology, Vietnam National University
E3 Building, 144 Xuan-Thuy, Cau-Giay, Hanoi, Vietnam

Abstract

Air pollution is becoming a serious problem in Vietnam as well as in the world. Some natural activities have a negative impact on the environment, but the main cause of this problem is also the result of human activity. Some major cities in Vietnam have been equipped with a number of imported air quality monitoring stations (Horiba - Japan, Environment SA - France), but these systems are very expensive and equipped only in capital Hanoi and Ho Chi Minh city. This paper presents some of the results of research and design the automatic air pollution measurement system, that's based on modern microcontrollers and IoT technology. The designed system can monitor automatically air pollution via data from sensors and send it to a computer with the database in the real time. The monitoring parameters are: PM_{10}, $PM_{2.5}$ and concentration of SO_2, NO_2, CO_2 in the air. Laboratories results and industrial application were implemented in Hoa Binh province.

Key Words: Air pollution, Embedded, PM_{10}, $PM_{2.5}$, Monitoring Software, AQI

I. Introduction

Air pollution is an excessive increase of harmful substances in the atmosphere. These may be solid particles, liquid droplets or gases. The sources of these substances may be natural or artificial. This abnormal increase creates adverse effects on people and the ecosystem. In the current context with the sudden increase of air pollutants, monitoring and monitoring of air pollutant concentrations is becoming essential for each country. Scientists from the Shanghai Institute of Applied Physics Research have done researches on the unique toxic mechanism of $PM_{2.5}$ fine dust, which shows the unique toxic mechanism of $PM_{2.5}$ particles are completely different from PM_{10} and other types of pollution. Because $PM_{2.5}$ is smaller in size and has a large total surface area, they easily absorb air pollutants, therefore, their toxicity

is stronger and more harmful than PM_{10}. The toxin in the dust enters the human body will cause lung diseases, damage to the alveolar walls, causing stagnant lungs. In addition, $PM_{2.5}$ in the blood can cause heart attack.

According to Professor Pham Ngoc Dang, Vice President of Vietnam Association of Nature and Environment Protection, $PM_{2.5}$ fine dust can penetrate deep into the lungs, causing shortness of breath, especially dangerous for people with lung diseases, asthma, respiratory infections. Exposure to fine particles can cause short-term effects on health such as eyes, nose, throat and lungs, coughing, sneezing, runny nose and difficulty breathing. Ultra-fine dust on prolonged contact increases the incidence of chronic bronchitis, decreases lung function and increases mortality from lung cancer and heart disease. It is estimated that if $PM_{2.5}$ increase by 10 µg/m3, the number of emergency patients for hypertension will increase by 8%, cardiovascular diseases will incline as well. Therefore, people with respiratory and heart problems, children and the elderly who are sensitive to dust, need special care to prevent complications.

In cities like Hanoi, Ho Chi Minh City and industrial cities in our country, the pollution level in recent years has sometimes reached an alarming threshold. The number of patients having air-related diseases such as respiratory diseases, ear, nose and throat diseases is increasing. Among the pollution measurements, fine dust is the most dangerous and influential agent. However, the monitoring of air quality has not really met the current situation due to the lack of the number of industrial standard monitoring systems as well as the degradation of the quality of the aided system.

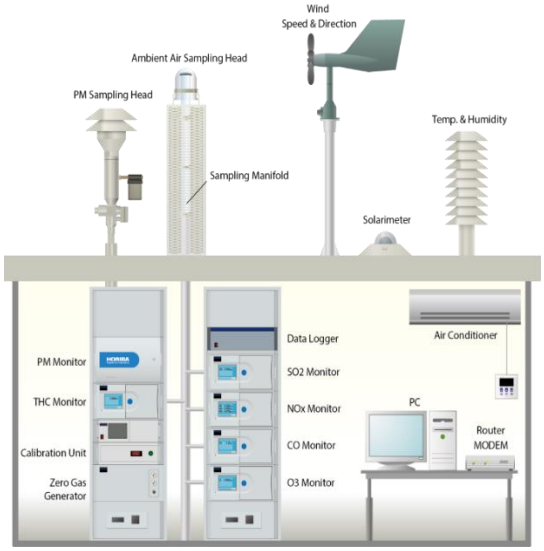

Figure 01: Example of station for measuring air pollution

In this paper, we formulate a solution to measure air quality for the continuous monitoring of concentrations of pollutants in the air. The device is designed with small size, high mobility, can be quickly installed to monitor air quality in a new area. Sensors used on the device are integrated such as CO, NO_x, PM_{10}, $PM_{2.5}$, SO_2.[1], [2] [8]. The device allows communication with sensors and can calculate the air quality index AQI according to current standards.

II. System design

The proposed solution of this project is to master the technology (hardware and software) in designing and manufacturing automation systems to monitor air pollution with the outputs as follows: 01 station for measurement of fine dust and toxic gases automatically installed and tested in Vietnam. This system is modularized for a mass production after product calibration and testing.

In order to carry out the mastering the technology [4], [5] [10],[12], the specific tasks were been done, including:

- Design schematic, layout circuitry and design, assembly PCB for hardware system boards (HW).

- Embedded programming for hardware boards.
- Programming SCADA (Supervisory Control And Data Acquisition) software system.
- Programming to connect an online database.
- Programming application for monitoring parameters on tablets, smart phones.

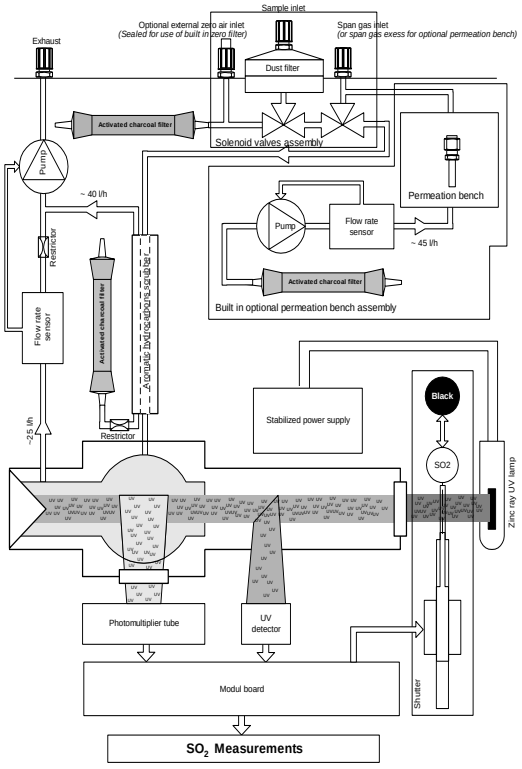

Figure 2: Diagram of the module for measuring SO_2 in the project

The designed hardware and software are compatible with the common electronic design process, but the development integrates new generation of components and modern technology. Compared to the imported stations that only monitors data on the spot and transfer offline data to a PC, the project's product is capable of measuring dust and gas parameters in real time, sending data to online database, read data on devices such as tablets, smart phones remotely. The system can also alert users when parameters exceed the Vietnamese Standards (QCVN) threshold for air. Mastering technology also has a great meaning in terms of national security.

Due to the technological mastery in the research and design, there are several advantages results which this project brings compared to similar products on the market, in particular:

a) The project product is designed and integrated with IoT technology (Internet of Things) with new-generation, high-performance electronic components, real-time data is transmitted and monitored on Firebase (Google's Online database), thus this product is able to monitor data about fine dust pollution in place as well as remote monitoring on mobile devices.

b) Because it is researched, designed in domestic technology, the product is easy to use, the interface can be selected in Vietnamese (or English). Products are also modularized according to customer needs.

c) Warranty work and fast maintenance (after 24h) do not depend on foreign experts.

d) The mastery of technology ensures security and defense. (There are no security holes about transmitting data abroad or hardware that performs other functions we cannot control).

e) The added value of the system is largely in embedded control and communication software. These pieces software will be programmed by Vietnamese scientists, from which the product cost will be significantly reduced (up to 70% of the cost of imported products), saving for the state budget.

III. Practical Applications

According to Document No. 5417/ BTNMT-TCMT dated November 18, 2016 of the Ministry of Natural Resources and Environment in Vietnam on real time

monitoring and transmission of monitoring data automatically, the fixed measurement stations for fine dust and toxic air pollution are needed for Departments of Natural Resources and Environment in 62 provinces in Vietnam.

Our product of this project is the system of measuring fine dust automatically (PM_{10}, $PM_{2.5}$, $PM_{1.0}$) and toxic gases: NOx; CO; SO_2 [21], [22] [23],[24] was tested in Hoa Binh and the results showed that the system worked stably and good connectivity and data transmission.

Figure 3: Assembling and testing of pollution measurement stations in Hoa Binh

IV. Acknowledgements

This work was supported by research project No. NDT.04.GER/15 granted by the Ministry of Science and Technology (Vietnam) as well as by the KENTEK Co.Ltd. (Korea).

V. References

[1]. http://aqicn.org/sensor/pms5003-7003/

[2]. https://community.particle.io/t/dust-sensor-pms-5003-6003-7003/24221

[3]. Dan Stefan Tudose, Traian Alexandru Patrascu, Andrei Voinescu, Razvan Tataroiu, Nicolae Tapus¸ Mobile Sensors in Air Pollution Measurement‖, 2011 8th Workshop on Positioning Navigation and Comm., pp. 166- 170, Apr. 2011.

[4]. Amnesh Goel, Sukanya Ray, Prateek Agrawal, Nidhi Chandra, - Air Pollution Detection Based On Head Selection Clustering and Average Method from Wireless Sensor Network‖, 2012 Second International Conference on Advanced Computing & Communication Technologies, pp. 434-438, Jan. 2012.

[5]. Ajay,V.D. (2005). Microcontrollers -Theory and Applications, Tata McGraw - Hill Publishing company Limited, ISBN 0- 07-058595 - 4, New Delhi. Atmel Corporation. (2006). Atmega8 Datasheet, [Online], Available from: http://atmel.com

[6]. C1101EM 315 - 433 MHz Reference Design (swrr046.zip), http://ti.com

[7]. R. Al-Ali, Imran Zualkernan, and Fadi Aloul: A Mobile GPRS-Sensors Array for Air Pollution Monitoring. IEEE Sensor Journal, Vol. 10, No. 10, October 2010

[8]. N. Kularatna and B. H. Sudantha, "An environmental air pollution monitoring system based on the IEEE 1451 standard for low cost requirements," IEEE Sensors J., vol. 8, pp. 415–422, Apr. 2008.

[9]. F. Tsow, E Forzani, A. Rai, R. Wang, R. Tsui, S. Mastroianni, C. Knobbe, A. J. Gandolfi, and N. J. Tao, "A wearable and wireless sensor system for real-time monitoring of toxic environmental volatile organic compounds," IEEE Sensors J., vol. 9, pp. 1734–1740, Dec.2009.

[10]. Y. J. Jung, Y. K. Lee, D. G. Lee, K. H. Ryu, and S. Nittel, "Air pollution monitoring system based on geosensor network," in Proc. IEEE Int. Geoscience Remote Sensing Symp., 2008, vol. 3, pp. 1370–1373.

[11]. C. J. Wong, M. Z. MatJafri, K. Abdullah, H. S. Lim, and K. L. Low, "Temporal air quality monitoring using surveillance camera," in Proc. IEEE Int. Geoscience and Remote Sensing Symp., 2007, pp. 2864–2868.

[12]. M. Gao, F. Zhang, and J. Tian, "Environmental monitoring system with wireless mesh network based on embedded system," in Proc. 5th IEEE Int. Symp. Embedded Computing, 2008, pp. 174–179.

[13]. W. Chung and C. H. Yang, "Remote monitoring system with wireless sensors module for room environment," Sens. Actuators B, vol. 113, no. 1, pp. 35–42, 2009.

[14]. J. W. Kwon, Y. M. Park, S. J. Koo, and H. Kim, "Design of air pollution monitoring system using ZigBee networks for ubiquitous-city," in Proc. Int. Conf. Convergence Information Technology, 2007, pp.

[15]. CC1100/CC1150DK, CC1101DK, Examples and Libraries User Manual (swru109.pdf), http://ti.com

[16]. Vasek, V., Pham Manh, T. : HC11 Control Unit Applications IFAC Workshop on Programmable Devices and Systems PDS 2001, Gliwice, Poland.

[17]. Sabillaa, Shoffi Izza, Sarnoa, Riyanarto và Siswantorob, Joko. Estimating Gas Concentration using Artificial Neural Network for Electronic Nose. Bali : 4th Information Systems International Conference 2017, 2017.

[18]. Navreetinder, Kaur, Mahajan, Rita và Deepak, Bagai. Air Quality Monitoring System based on Arduino Microcontroller. Chandigarh : International Journal of Innovative Research in Science, Engineering and Technology- Vol. 5, 2016.

[19]. Nayak, Riteeka, và những tác giả khác. IoT Based Air Pollution Monitoring System.: Imperial Journal of Interdisciplinary Research (IJIR) - Vol-3, Issue-4, 2017.

[20]. Instruments, Texas. Micropower Electrochemical Gas Sensor Amplifier Reference Design. 2017.

[21]. Arduino-CO-Monitor-Using-MQ-7-Sensor. instructables.com. https://www.instructables.com/id/Arduino-CO-Monitor-Using-MQ-7-Sensor/.

[22]. Electronic Circuits for Use in Electrochemical Gas Sensors. azosensors.com. 2015. https://www.azosensors.com/article.aspx?ArticleID=583.

[23]. Detect-co-with-mq-7-sensor-module. areresearch.net. 2017. http://www.areresearch.net/2017/03/detect-co-with-mq-7-sensor-module.html.

[24]. principle/electrochemical-type. figaro.co.jp. https://www.figaro.co.jp/en/technicalinfo/principle/electrochemical-type.html.

[25]. https://www.figaro.co.jp/en/technicalinfo/principle/catalytic-type.html.

The 5th International Conference on Engineering Mechanics and Automation (ICEMA 5)
Hanoi, October 11÷12, 2019

Feedforward Control of Piezo-electric Actuator Using Prandlt-Ishlinskii Model

Tran Vu Minh[*,a], Tran Thanh Tung[b]

[a] *1Department of Machinery Engineering, Hanoi University of Science and Technology, Hanoi, Vietnam*
email: minh.tranvu@hust.edu.vn, corresponding author
[b] *Faculty of Mechanics and Automation Engineering ,VNU University of Engineering and Technology,*
email: tranthanhtung@vnu.edu.vn

Abstract

Piezoelectric actuators (PEAs) are finding broad acceptance in applications where precision motion (sub-nanometer level), large actuated force and/or high frequency operation is required. However, PEA also exhibits an undesired hysteresis phenomenon which is nonsmooth nonlinearity. Because of the unknown hysteresis, the performance of PEA is limited especially in speed and accurateness. Therefore, there is a need for an approach to model and control in order to eliminate the hysteresis effects. In this paper, an identified Prandlt-Ishlinskii (PI) model is proposed to describe the hysteresis. Then, a feedforward controller is design using the inverse of PI model to control the piezoelectric actuators. Finally, the experimental results demonstrate the effectiveness of proposal method.*Key Words: Piezoelectric actuator, hysteresis, Prandlt-Ishlinskii model, feedforward control*

1. Introduction

Piezoelectric actuators (PEA) with their advantages in nano resolution in positioning, large actuating force and rapid respond, are becoming more popular for micro/nano positioning applications such as ultrafine-movement stage of semiconductor exposure systems, precision positioning probes and probes for scanning tunnel microscopy (STM) and atomic force microscopy (AFM). However, PEA also exhibits an undesired hysteresis phenomenon which is nonsmooth nonlinearity, between electric strength and displacement. Because of the unknown hysteresis, the performance of PEA is limited especially in speed and accurateness. The development of control techniques to overcome the hysteretic effects is attracted a lot recently.

Several mathematical models have been proposed to describe hysteresis nonlinearities. Prandlt-Ishlinskii model is a superposition of elementary stop or play operators that are parameterized by a threshold variable as in A. Visintin. Presach model and Krasnosel'skii-Pokrovskii model are parameterize by a pair of threshold variable as in I. Mayergoyz and M. A. Kranosklskii et al. Bouc-Wen model consists of a first-order nonlinear differential equation as in YK. Wen, M. Ismail et al, and R. Bouc. Among these models, Bouc-Wen model has received an increasing interest due to the capability to describe a wide class of hysteresis system such as piezoelectric actuators ad in C. Lin et al,

magnetorheological dampers, forced vibration of mechanical systems.

The basic idea of feedforward control is the inverse compensation. The approximate inverse hysteresis model is used to cancel the effects of hysteresis. Assume an actuator with an approximate mathematical model. The inverse model is calculated based on identified model . In no load condition the open-loop feedforward compensation has been shown effective in, S. Bashash et al, U.-X. Tan et al, C. Ru et al, and W. T. Ang et al. In this paper, the Prandlt-Ishlinskii model and its inverse are adopted. After that, a direct feedforward control is used to control the piezo electric actuator. Finally, the experimental results demonstrate the effectiveness of proposal method.

2. The Prandlt-Ishlinskii model and its inverse

2.1 The Prandlt-Ishlinskii model, play operator

One of the well-known operator-based models, which is used to characterize the hysteresis in PEAs and other types of smart materials, is the classical PI model that utilizes a hysteresis operator, the play operator.

The rate-independent play operator is demonstrated in Figure 1. This operator implies the reciprocating motion of a piston inside a cylinder with length $2r$, where the instantaneous position of center of piston is defined by u and w as input and output subsequently. In analytical form, for any input $u(k) \in C_m[0, K]$ and $r \geq 0$, the play operator is inductively defined by

$$F_r[u; w_{-1}](0) = f_r(u(0) - w_{-1}) \quad (1)$$

$$F_r[u; w_{-1}](k) = f_r(u(k), F[u](k_i))$$

$$f_r(u, w_{-1}) = \max(u - r, \min(u + r, w)) \quad (2)$$

where w_{-1} defines the initial state.

Then the output of the Prandlt-Ishlinskii hysteresis model using play operator is defined by

$$y(k) = Au(k) + \int_0^R p(r) F_r[u](k) dr \quad (3)$$

where A is a constant, $p(r)$ is the density function, satisfying $p(r) \geq 0$, and R is a positive constant.

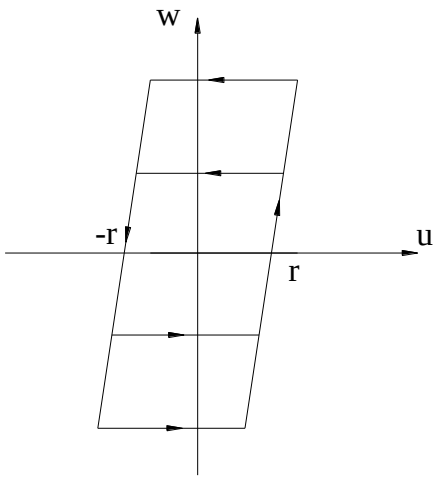

Figure 1 Play operator

The discrete form of classical PI model using play operator can be written as follows:

$$y(k) = Au(k) + \sum_{i=1}^{N} \mu(r_i) F_{r_i}[u](k) \quad (4)$$

Where N is the number of the adopted play operators, and $\mu(r_i)$ are the weighted coefficients for the threshold r_i .

It should be note that the classical PI model can only describe the symmetric hysteresis. To be able to describe the asymmetric hysteresis curve, the classical PI model has to be modified.

2.2 Identifying PI model parameters

The number of thresholds in play operator (1) (2) is chosen as 16. The constant and the weighted coefficients are identified off-line by curve fitting toolbox in MATLAB using experimental data. This tool box uses Levenberh-Marquardt algorithm to identify model parameters. The input $u(k) = 20*(-0.06*k*0.001 + 1.1)$ $\sin(2*\pi*k*0.001 + 3*\pi/2)$ $+1.1$ is applied to the PEA for identification, the sampling time

period is chosen as 0.001 s. Table 1 shows the identified parameters.

Table 1 Identified parameters of Prandlt Ishlinskii model

Number	Threshold r_i	Parameter $\mu(r_i)$	A
1	1	0.3209	0.5
2	2	0.0011	
3	3	0.0172	
4	4	0.0205	
5	5	0.0173	
6	6	0.0158	
7	7	0.0158	
8	8	0.0188	
9	9	0.0111	
10	10	0.0010	
11	11	0.1161	
12	12	0.5591	
13	13	0.0010	
14	14	0.0010	
15	15	0.0010	
16	16	0.0010	

Figure 2 shows comparison of the experimental and simulation results. The difference between measure output and calculated output is shown in Figure 3.

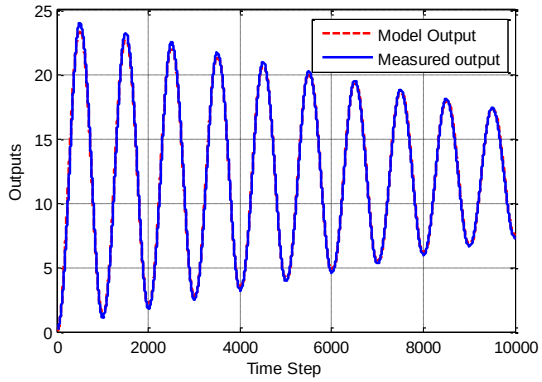

Figure 2 Comparison of measured output and model output

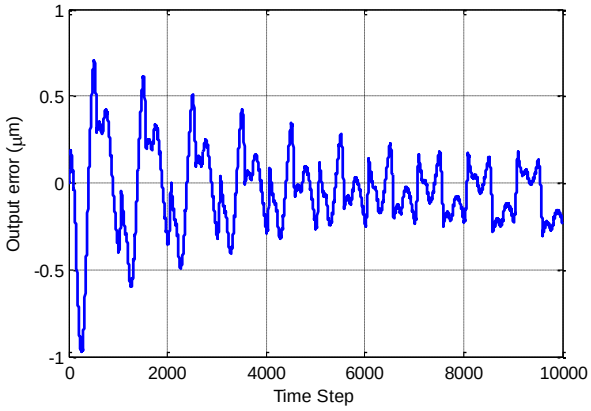

Fig. 3 Difference between measured output and calculated PI model output

It should be mentioned that the identified parameters are not unique; they depend upon the nature of hysteresis of PEAs. Furthermore, the relationship between input and modelling error is still some kinds of hysteresis (as in Figure 4). Thus, the compensation is difficult.

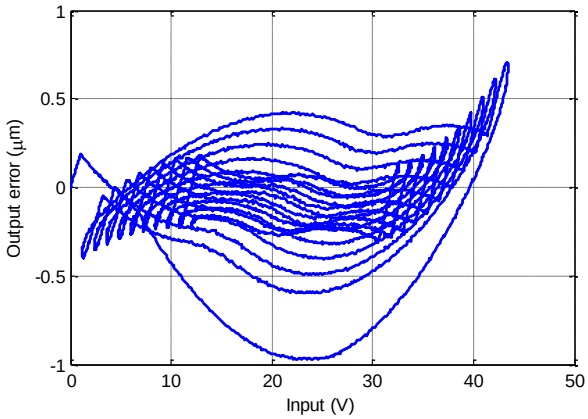

Figure 4 Input and output error

The validity of the Prandlt-Ishlinskii model employing play operators are examined by comparing the model output with the measured data, as shown in Figure 5. The results clearly suggest that the model can describe the hysteresis properties of PEAs.

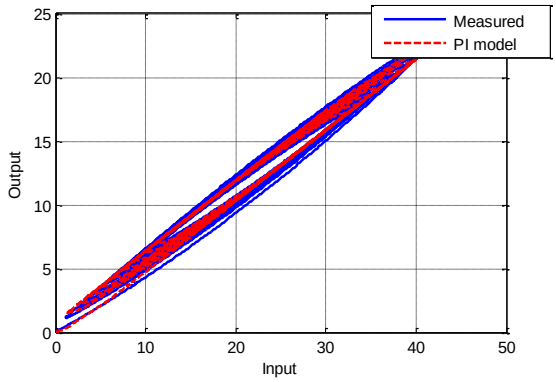

Figure 5 Comparison of hysteresis loop

2.3 PI model inverse

Open-loop control schemes are a conventional control for PEA. Figure 6 depicts block diagram of open-loop controller. The object here is to find an appropriate inversion from the identified model.

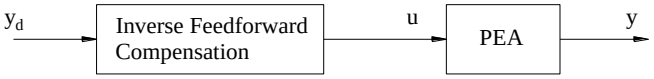

Figure 6 Block diagram of open-loop control schemes

In this section, the inverse Prandlt-Ishlinskii model is introduced as a feed forward compensator for purpose of control PEA.

From the identified data in Table 2, an explicit inverse of the Prandlt-Ishlinskii can be formulated analytically.

According to P. Krejci et al, the control input is calculated as follow

$$u(k) = \hat{A} y_d(k) + \sum_{i=1}^{N} \hat{\mu}(\hat{r}_i) F_{\hat{r}_i}[y_d](k) \qquad (5)$$

where $u(k)$ is the control input, $y_d(k)$ is the reference signal, $\hat{A}$ is a constant; $\hat{\mu}(\hat{r}_i)$ are the coefficients of the inverse operator; N is the number of operators, $\hat{r}_i$ are the thresholds of inverse operators. All these parameters will be calculated based on identified parameters from Prandlt-Ishlinskii hysteresis model as follows

$$\hat{r}_j = A r_j + \sum_{i=1}^{j} \mu(r_i)(r_j - r_i) \qquad (6)$$

$$\hat{A} = \frac{1}{A} \qquad (7)$$

$$\hat{\mu}(\hat{r}_j) = -\frac{\mu(r_j)}{\left(A + \sum_{i=1}^{j} \mu(r_i)\right)\left(A + \sum_{i=1}^{j-1} \mu(r_i)\right)} \qquad (8)$$

Table 2 shows the calculated results.

Table2 Inverse Prandlt-Ishlinskii model parameters

Number	Threshold $\hat{r}_i$	Parameter $\hat{\mu}(\hat{r}_i)$	$\hat{A}$
1	0.5	0.4762	2
2	1.0011	0.0016	
3	1.5183	0.0395	
4	2.0388	0.0443	
5	2.5561	0.0355	
6	3.0719	0.0309	
7	3.5877	0.0296	
8	4.1065	0.0334	
9	4.6176	0.0192	
10	5.1186	0.0017	
11	5.7347	0.1497	
12	6.7938	0.2676	
13	7.2948	0.0005	
14	7.7958	0.0005	
15	8.2968	0.0005	
16	8.7978	0.0005	

3. Experimental results

The experimental setup on piezoelectric actuator is shown in Figure 7. The PEA is PFT-1110

(Nihon Ceratec Corporation). The displacement is measured by the noncontact capacitive displacement sensor (PS-1A Nanotex Corporation) which has 2-nm resolution.

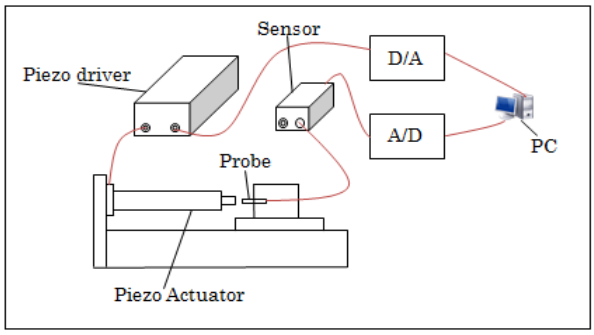

Fig. 7 Experimental scheme

The experiments are conducted with one reference outputs which is $y_d(k) = 10\sin(2\pi * k * 0.0005)\mu m$. The sampling period is chosen as 0.0005s. The offset voltage of the driver is set to 30V.

Figure 8 shows the control input for the first experiment which is 1Hz. The tracking result is shown in Figure 9. The maximum tracking error is about 1.2 μm.

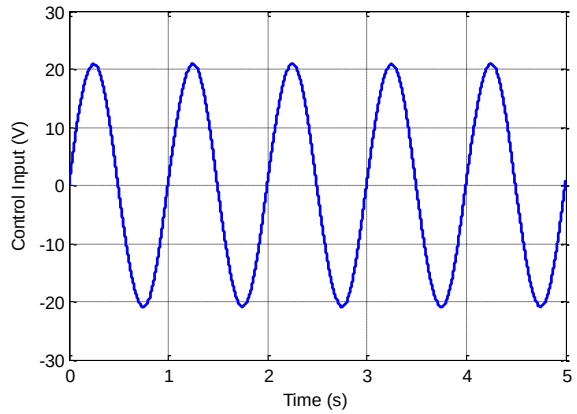

Figure 8 Control input of feedforward compensation

The result is expected since the control is an open-loop system. In order to improve the tracking performance, it is necessary to combine the PI model with a closed-loop control technique.

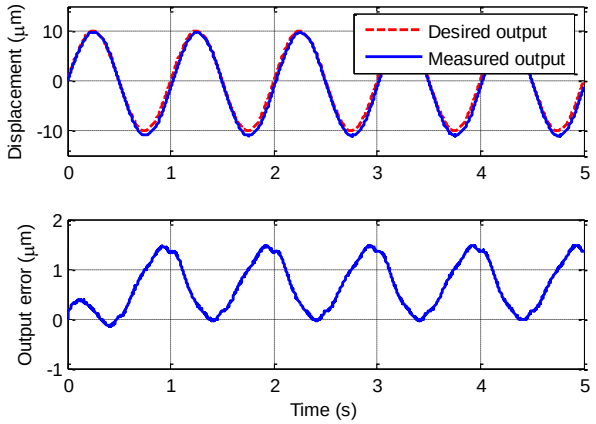

Figure 9 Tracking error of feedforward compensation

4. Conclusion

This paper has discussed the feedforward control for piezoelectric actuators, where a PI model of hysteresis is used to describe the nonlinear relation existing in the input and the output. The unknown parameters in the model are identified using Levenberh-Marquardt algorithm. The proposed method shows a better result in tracking performance with low frequency input. It is also expected to be applied to other types of smart material-based actuators. In the future, in order to improve the performance of PEAs, a combination of feedback control and feedforward compensation is desired.

References

A. Visintin (1994), Differential Models of Hysteresis, Berlin, Germany: Springer-Verlag.

C. Lin and S. Yang (2006), Precise positioning of piezo-actuated stages using hysteresis-observer based control, Mechatronics, vol 16, pp. 417-426.

C. Ru and L. Sun (2005), Hysteresis and Creep Compensation for Piezoelectric Actuator in Open-loop Operation, Sensors and Actuators A: Physical, Vol.122, No. 1, pp. 124-130.

I. Mayergoyz (2003), Mathematical Models of Hysteresis and their applications, Netherlands: Elsevier.

M. A. Kranosklskii and A. V. Poorovskii (1989), System with Hysteresis. Berlin, German: Springer-Verlag.

M. Ismail, F. Ikhouane, J. Rodellar (2009), The Hysteresis Bouc-Wen Model, a survey, Arch Comput Methods Eng 16, Barcelona, Spain, pp. 161-188.

P. Krejci and K. Kuhnen (2001), Inverse Control of Systems with Hysteresis and Creep, IEEE Proceedings of Control Theory and Applications, Vol. 148, No. 3, pp. 185-192.

R. Bouc (1967), Forced vibration of mechanical system with hysteresis, in Fourth Conference on Nonlinear Oscilltion, Prague, Czechoslovakia, pp. 315.

S. Bashash and N. Jalili (2008), A Polunomial-Based Linear Mapping Strategy for Feedforward Compensation of Hysteresis in Piezoelectric Actuators, Journal of Dynamic Systems, Measurement, and Control, Vol. 130, No. 3, pp 1-10.

U.-X. Tan, W. T. Latt, C. Y. Shee (2009), C. N. Riviere and W. T. Ang, Feedforward Controller of Ill-Conditioned Hysteresis Using Singularity-Free Prandlt-Ishlinskii Model, IEEE/ASME Transactions on Mechatronics, Vol 14, No 5, pp. 398-605

W. T. Ang, F. A. Garmón, P. Khosla and C. N. Riviere (2003), Modelling Rate-Dependent Hysteresis in Piezoelectric Actuators, 2003 IEEE/RSJ International Conference on Intelligent Robots and Systems, Las Vegas, USA, pp 1975-1980.

W. T. Ang, P. Khosla, C. N. Riviere (2007), Feedforward Controller with Inverse Rate-Dependent Model for Piezoelectric Actuators in Trajectory-Tracking Applications, IEEE/ASME Transactions on Mechatronics, Vol. 12, No. 2, pp 134-142.

YK. Wen (1976), Method for random vibration of hysteresis system, Journal of Engineering Mechanics. ASCE, vol 102, pp. 249-263.

The 5th International Conference on Engineering Mechanics and Automation (ICEMA 5)
Hanoi, October 11÷12, 2019

Comparative study of three MPPT methods for Photovoltaic systems

Cuong Hung Tran

Faculty of Engineering Mechanics and Automation, University of Engineering and Technology
Email: tchung@vnu.edu.vn

Abstract

In order to ensure that the photovoltaic (PV) module always operates at the maximum power point for any weather conditions, a maximum power point tracking (MPPT) system is indispensable. This paper presents a comparative analysis of three methods MPPT: Perturb and observe (P&O), Fuzzy Logic Controller (FLC) and Backstepping Controller. The parameters considered for the comparison are the performance of these MPPTs such as the extracted power from the PV system, steady and dynamic response of the system under various conditions like changing solar irradiance or temperature. Simulations results, obtained by using MATLAB/Simulink, shown that the MPPT controller based on the Backstepping technique is the most robust controller under changing conditions.

Key Words: Maximum Power Point Tracking (MPPT), Backsteping, P&O, FLC, Photovoltaic (PV) System, Boost Converter

1. Introduction

In Vietnam, more than half a million people do not have access to electricity. They are mainly in mountainous regions or on islands. Moreover, our country has great potential for renewable energy such as solar, wind, hydroelectric, biomass power (Dang, 2014). In this context, these sources of energy can be regarded as promising solution that are both economically and environmentally sustainable for supplying electrical power. Solar energy is the most suitable source to supply villages with electricity because of the plentiful solar radiation and relatively easy maintenances of the structures.

Maximum power point tracking (MPPT) plays an important role in PV power systems because it maximizes the power output from a PV system, thus an MPPT can minimize the overall system cost. Over the years, many MPPT algorithms have been developed and implemented, ranging from simple to more complex methods depending on the weather conditions and the application (Al Nabulsi and Dhaouadi, 2012; Alik and Jusoh, 2017; Karami et al., 2017; Salas et al., 2006; Subudhi and Pradhan, 2013).

Numerous MPPT methods have been discussed in the literature; the Perturb and Observe (P&O) Methods (Karami et al., 2017) (Femia et al., 2005) , the Incremental Conductance (IncCond) Methods (Safari and Mekhilef, 2011) and the Fuzzy Logic Controller (FLC) Method (Tran et al., 2017) (Huynh, 2012) (Al Nabulsi and Dhaouadi, 2012)

In this study, a Backsteping controller is proposed and designed to implement the MPPT algorithm. A comparative study with P&O, FLC was conducted and show the effectiveness of the approach proposed. The parameters considered for the comparison are the performance of these MPPTs such as the extracted power from the PV system, steady and dynamic response of the

system under changeable conditions like the temperature and the irradiation.

This paper is structured as follows. Section 2 explains the mathematical modelling of PV system and DC-DC Boost converter. Section 3 describes the different MPPT techniques in this work. The simulation results and conclusion are presented in Section 4 and 5, respectively.

2. Mathematical modelling of PV system

2.1. Solar cell model

A solar PV system configuration can be very simple, which have only two components (PV panel and load), or it can be complex, containing several components such as power source, controllers, energy storage units. In this work, the PV system consists of a solar module, a DC/DC converter, in this case a Boost converter, connected to a resistive load, and a MPPT algorithm.

In this study, a PV cell is represented by a current source. The photocurrent I_{ph} depends on the irradiation G and the cell temperature T_c (Figure 1).

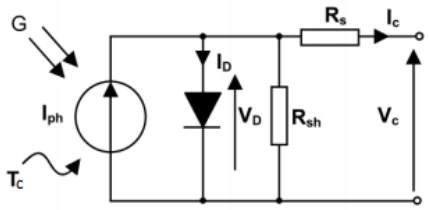

Figure 1 PV Module equivalent circuit.

The characteristic equation is:

$$I_c = I_{ph} - I_0\left(\exp\frac{e(V_c + R_s I_c)}{nkT_c} - 1\right) - \frac{V_c + R_s I_c}{R_{sh}} \quad (1)$$

Where:

I_0 is the saturation current;
e is the charge of an electron;
k is Boltzmann's gas constant;
n is the idealizing factor of the diode.
R_s represents the losses due to the contacts as well as the connection
R_{sh} represents the leakage currents in the diode

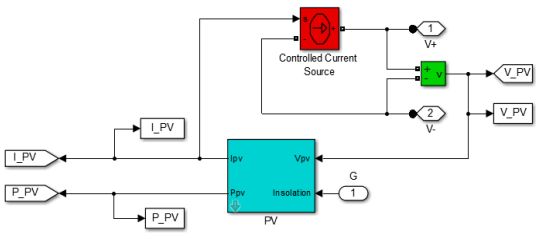

Figure 2 Implemented MATLAB Simulink.

Based on the mathematical equation (1), a dynamic model for a PV module has been developed by using MATLAB/Simulink as shown in Figure 2.

2.2. DC-DC Boost converter

The MPPT is achieved by adding a power converter between the PV generator and the load. In order to track MPP, the converter must be operated with duty cycle corresponding to it. A Boost converter is a DC to DC converter with an output voltage greater than the source voltage, as shown in Figure 3

$$V_{out} = \frac{V_{in}}{1 - D} \quad (2)$$

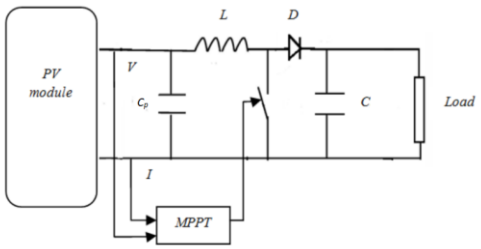

Figure 3 PV system with DC-DC Boost converter

3. MPPT algorithms for PV generator

The PV systems operation depends strongly on temperature, irradiation and the load characteristics. When a direct connection is carried out between the source and the load, the output of the PV module is not optimal. To overcome this problem, it is necessary to add an adaptation device. MPPT controller with a Boost DC-DC converter is presented in this section.

3.1. Perturbe and Observe (P&O)

This is one of the simplest and most popular methods of MPPT because it does not require any prior knowledge of the system or any additional sensor except the measurement of the power. The principle of algorithm is keep perturbing the control variable in the same direction until the power is decrease as shown in Table 1.

Table 1 Summary of P&O algorithm

Perturbation	Change in power	Next perturbation
Positive	Positive	Positive
Positive	Negative	Negative
Negative	Positive	Negative
Negative	Negative	Positive

Choosing a step size is a very important task in this method. A larger step size leads to a faster response but more oscillations around the MPPT point. On the other hand, a smaller step-size improves efficiency but reduces the convergence speed.

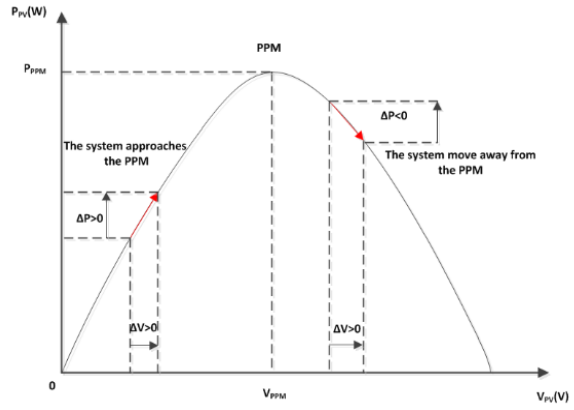

Figure 4 Principle of P&O method.

The principle of P&O method is presented by the flow chart in Figure 5.

3.2. Fuzzy control

The advantages of fuzzy logic controller (FLC) over the conventional methods are: (a) it does not need an accurate mathematical model; (b) it can work with imprecise inputs; (c) it can handle nonlinearity; and (d) it is more robust than conventional nonlinear controllers (Raviraj and Sen, 1997).

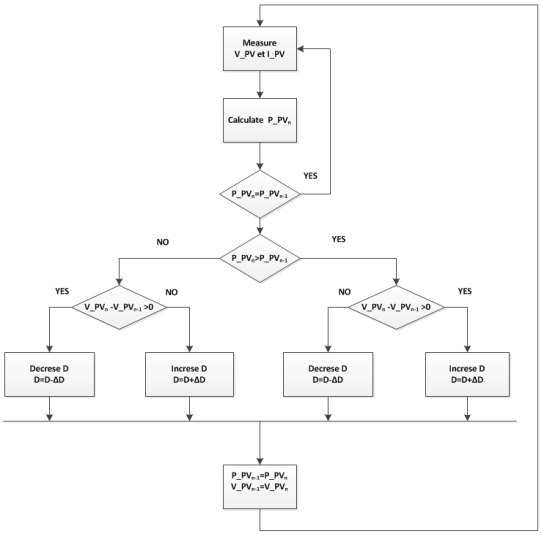

Figure 5 Flowchart of the P&O algorithm

FLC consists of four major elements: fuzzification, rules, interference engine and defuzzification as shown in Figure 6.

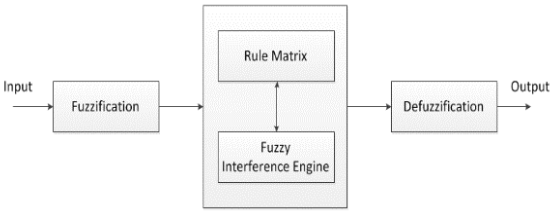

Figure 6 Principle of Fuzzy logic controller.

To implement the FLC for MPPT algorithm, the input and output variables should be determined. In this study, two inputs are considered: change in PV power (dP/dV) and its derivative. The output is duty cycle D of the Boost converter.

The output given as:

$$D(n) = D(n-1) + \Delta D(n) \quad (3)$$

Membership Functions: The input and output variables are expressed by linguistic variables. The linguistic terms used are:

• dP/dV [VeryNegative, Negative, Zero, Positive, VeryPositive] (Figure 7)

• (dP/dV)' [Negative, Zero, Positive] (Figure 8)

The five various terms of (dP/dV) and three terms of its derivative (dP/dV)' are shown in the Table 2.

Table 2 Rules of ΔD.

ΔD		(dP$_{PV}$/dV$_{PV}$)'		
		Negative	Zero	Positive
dP$_{PV}$/dV$_{PV}$	NB	3%	3%	3%
	NS	3%	1%	1%
	ZE	0%	0%	0%
	PS	-1%	-1%	-3%
	PB	-3%	-3%	-3%

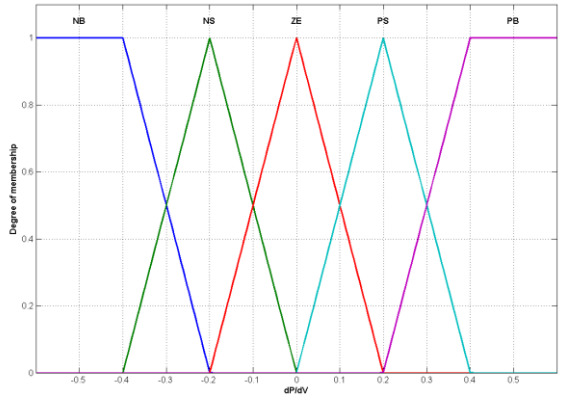

Figure 7 Membership Function (dP/dV)

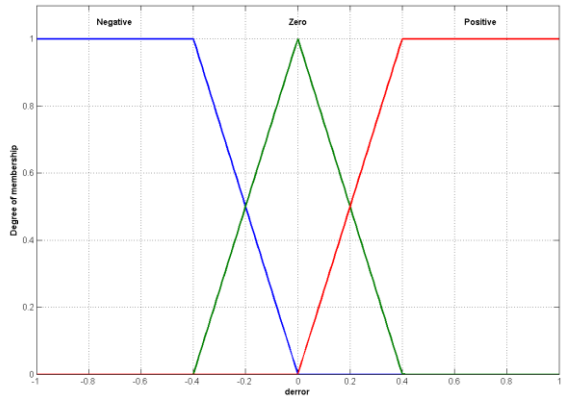

Figure 8 Membership Function (dP/dV)'

The Control Rules: The fuzzy rules are defined as follows:

IF (dP/dV) is A$_i$ **AND** (dP/dV)' is B$_i$, **THEN** ΔD(n+1) is C$_i$

There are several known methods in order to get the output of inference. This paper used the min-max inference and Takagi-Sugeno system. They are designed to achieve zero error at the state of the Maximum Point Puissance (MPP). The idea is to bring operating point to MPP by increasing or decreasing the duty ratio D. If the operating point is distant from the MPP, the duty ratio D will increase or decrease largely.

Defuzzification: After the fuzzification, the defuzzification is performed which converts the fuzzied value into defuzzied value. This study used the centre gravity defuzzification method. The weighting factor is obtained by minimum operation, which is given by:

$$w_i = \min\left\{\mu_{dP/dV}, \mu_{(dP/dV)^*}\right\} \tag{4}$$

The final output of the system is the weighted average of all rules output:

$$\Delta D(k) = \frac{\sum_{i=1}^{N} \omega_i C_i}{\sum_{i=1}^{N} w_i} \tag{5}$$

3.3. Backstepping MPPT control

The Backstepping method is based on the statement of errors in function of the system parameters and instructions. The main objective is to reset these errors to zero by applying the control law respecting the *Lyapunov* stability conditions (Hassan, 2001).

In this work, the objective of Backstepping controller is to keep the ration $\partial P / \partial V = 0$. The development of the control law imposes a general knowledge of the model of the system. The equations of the system in the Figure 3 defined are:

$$\begin{cases} C_p \dfrac{dV_{PV}}{dt} = i_{PV} - i_L \\ L\dfrac{di_L}{dt} = V_{PV} - (1-\alpha)V_{DC} \\ C\dfrac{dV_{DC}}{dt} = (1-\alpha)i_L - i_{DC} \end{cases} \tag{6}$$

The variable of our control is:

$$y = \frac{\partial P_{PV}}{\partial V_{PV}} = i_{PV} + V_{PV}\frac{\partial i_{PV}}{\partial V_{PV}} \quad (7)$$

The purpose of the Backstepping command is to assume a variable y, whose value is equal $\frac{\partial P_{PV}}{\partial V_{PV}}$,then make this variable move towards a reference $y_{ref} = 0$.

The control is based on two main steps.

Step 1 : The first error considered in designing the Backstepping controller is : $z_1 = y - y_{ref}$ with $y_{ref} = 0$.

The tracking error derivative is written as follows:

$$\dot{z}_1 = \frac{1}{C_P}(i_{PV} - i_L)(2\frac{\partial i_{PV}}{\partial V_{PV}} + V_{PV}\frac{\partial^2 i_{PV}}{\partial V^2_{PV}}) \quad (8)$$

To study the stability of the system, we introduce the 1st function of Lyapunov: $V_1 = \frac{1}{2}z_1^2$

Deriving it we obtain the equation:

$$\dot{V}_1 = z_1(\frac{1}{C_P}(i_{PV} - i_L)(2\frac{\partial i_{PV}}{\partial V_{PV}} + V_{PV}\frac{\partial^2 i_{PV}}{\partial V^2_{PV}})) \quad (9)$$

The stability condition of the Lyapunov function requires that its derivative be strictly negative. The choice of $\dot{V}_1 = -k_1 z_1$ lead us $\dot{V}_1 < 0$

$$\frac{1}{C_P}(i_{PV} - i_L)(2\frac{\partial i_{PV}}{\partial V_{PV}} + V_{PV}\frac{\partial^2 i_{PV}}{\partial V^2_{PV}}) = -K_1 z_1 \quad (10)$$

Where K_1 is the positive coefficient representing design constant.

As i_L is not the effective command of the system, it behaves as a virtual control input, we pose γ_1 whose is considered as the desired value for i_L and called the first stabilization function. We can obtain the equation:

$$\gamma_1 = i_{PV} + \frac{K_1 C_p}{2\frac{\partial i_{PV}}{\partial V_{PV}} + V_{PV}\frac{\partial^2 i_{PV}}{\partial V^2_{PV}}} z_1 \quad (11)$$

Step 2 : We consider the second errors as z_2 :

$$z_2 = i_L - \gamma_1 \quad (12)$$

Its derivate is:

$$\dot{z}_2 = \frac{1}{L}\left[V_{PV} - (1-\alpha)V_{DC}\right] - \dot{\gamma}_1 \quad (13)$$

Substituting (13) into (8) and (9), gives that

$$\dot{z}_1 = \frac{1}{C_P}(2\frac{\partial i_{PV}}{\partial V_{PV}} + V_{PV}\frac{\partial^2 i_{PV}}{\partial V^2_{PV}})(i_{PV} - z_2 - \gamma_1) \quad (14)$$

$$\dot{V}_1 = -K_1 z^2_1 - \frac{1}{C_P}(2\frac{\partial i_{PV}}{\partial V_{PV}} + V_{PV}\frac{\partial^2 i_{PV}}{\partial V^2_{PV}})z_1 z_2 \quad (15)$$

Introduce the 2nd candidate function of Lyapunov: $V_2 = \frac{1}{2}z_1^2 + \frac{1}{2}z_2^2$

Its derivate is:

$$\dot{V}_2 = -K_1 z^2_1 - \frac{1}{C_P}(2\frac{\partial i_{PV}}{\partial V_{PV}} + V_{PV}\frac{\partial^2 i_{PV}}{\partial V^2_{PV}})z_1 z_2 + \frac{1}{L}\left[V_{PV} - (1-\alpha)V_{DC}) - \dot{\gamma}_1\right]z_2 \quad (16)$$

The stability condition of Lyapunov's 2nd candidate function imposes $\dot{V}_2 < 0$ so:

$$-\frac{1}{C_P}(2\frac{\partial i_{PV}}{\partial V_{PV}} + V_{PV}\frac{\partial^2 i_{PV}}{\partial V^2_{PV}})z_1 + \frac{1}{L}\left[V_{PV} - (1-\alpha)V_{DC}\right] - \dot{\gamma}_1 = -K_2 z_2 \quad (17)$$

Where K_2 is the positive coefficient representing design constant.

Finally, we obtain the control law of DC-DC Boost converter for maximum power tracking given by equation

$$\alpha = \frac{L}{V_{DC}}\left[\begin{array}{l} -K_2 z_2 + \frac{1}{C_P}(2\frac{\partial i_{PV}}{\partial V_{PV}} + \\ V_{PV}\frac{\partial^2 i_{PV}}{\partial V_{PV}^2})z_1 + \frac{1}{L}(V_{DC} - V_{PV}) + \dot{\gamma}_1 \end{array}\right] \quad (18)$$

4. Simulation results

The system is implemented in MATLAB Simulink as show in Figure 9.

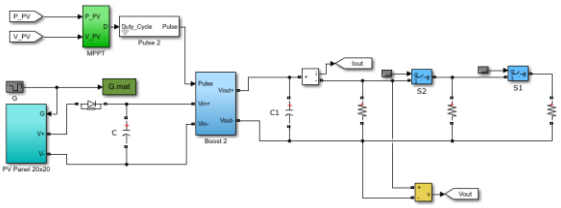

Figure 9 Implemented MATLAB Simulink.

The model parameters used in the simulation are given in Table 3. The PV array is made of 20 strings of 20 series connected modules each other, connected in parallel. All modules are considered to be identical, and to work in the same conditions of temperature and irradiance.

Table 3 The PV model parameters at G=1000W/m^2

I_{sc}	1 A
V_{oc}	19,34 V
I_{mpp}	0.904 A
V_{mpp}	15.138 V
P_{mpp}	13.69 W

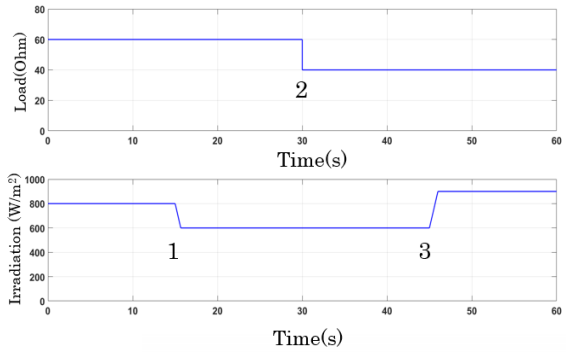

Figure 10 Various climatic and operating conditions

Irradiation and load demand are varied within 60 seconds to test the controllers in various climatic and operating conditions.

In the first 15 seconds, the system operates in G=800 w/m^2 and T=25 °C. Our controller has chosen the good value of D to make power generated around 4.56 kW. From 15th seconds to 45th seconds, when the irradiation decreases from 800 w/m^2 to 600 w/m^2, the PV system moves toward to the new MPP. The controller adjusts the duty cycle which make power around 3.9 kW. Other tests are also applied when irradiation increases from 600 w/m^2 to 900 w/m^2. From the simulation results, when irradiation changes, P&O, FLC and Backstepping controller work well to track the MPP of the PV array (at the 15th second, 45th second) to produce the maximum power output. Besides, the Figure 11 show that the controller also works well to track the maximum power point when load demand change at 30th second.

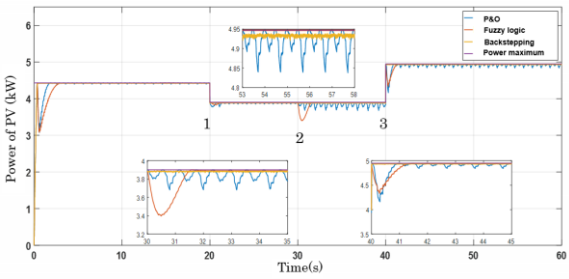

Figure 11 Power output under varying irradiation and load

Table 4 Tracking efficiency of MPPT

	Method		
	Back-stepping	Fuzzy Logic	P&O
Response time (variation of irradiation)	0.022 0.05	1.2 1.4	1.5 1.5
Response time (variation of load)	0.02	1.5	0.5
Convergence speed	Very fast	Average	Average

However, these results still have some oscillations in P&O method because of non-linear voltage-current characteristic in the PV systems, but it does not affect the result. Compared with P&O method and FLC, a

Backstepping controller not only get a quick response under various conditions but also had small oscillation at the maximum power point and small transient response time as shown in Table 4.

5. Conclusion

This paper presents simulation of three MPPT algorithms based respectively on the P&O, the fuzzy logic and the sliding mode for Photovoltaic Energy Conversion System. Based on the simulation results it can be concluded that with both P&O, FLC and Backstepping controller can track the maximum power. However, the MPPT controller based on the Backstepping approach is the most robust controller under changing conditions, the transient response time is very small.

References

Al Nabulsi, A., Dhaouadi, R., 2012. Fuzzy logic controller based perturb and observe maximum power point tracking, in: Proceedings of International Conference on Renewable Energies and Power Quality. Spain.

Alik, R., Jusoh, A., 2017. Modified Perturb and Observe (P&O) with checking algorithm under various solar irradiation. Sol. Energy 148, 128–139. https://doi.org/10.1016/j.solener.2017.03.064

Dang, X.-L., 2014. Contribution à l'étude des systèmes Photovoltaïque/Stockage distribués. Impact de leur intégration à un réseau fragile. (Thèse de doctorat). Ecole Doctorale Sciences Pratiques de Cachan.

Femia, N., Petrone, G., Spagnuolo, G., Vitelli, M., 2005. Optimization of Perturb and Observe Maximum Power Point Tracking Method. IEEE Trans. Power Electron. 20, 963–973. https://doi.org/10.1109/TPEL.2005.850975

Hassan, E.F., 2001. Commande non-linéaire des convertisseurs de puissance DC-DC Approches de passivité et de Backstepping.

Huynh, Q.M., 2012. Optimisation de la production de l'électricité renouvelable pour un site isolé (Thèse de doctorat). Université de Reims Champagne-Ardenne.

Karami, N., Moubayed, N., Outbib, R., 2017. General review and classification of different MPPT Techniques. Renew. Sustain. Energy Rev. 68, 1–18. https://doi.org/10.1016/j.rser.2016.09.132

Raviraj, V.S.C., Sen, P.C., 1997. Comparative study of proportional-integral, sliding mode, and fuzzy logic controllers for power converters. IEEE Trans. Ind. Appl. 33, 518–524.

Safari, A., Mekhilef, S., 2011. Incremental conductance MPPT method for PV systems, in: 2011 24th Canadian Conference on Electrical and Computer Engineering(CCECE). Presented at the 2011 24th IEEE Canadian Conference on Electrical and Computer Engineering (CCECE), IEEE, Niagara Falls, ON, Canada, pp. 000345–000347. https://doi.org/10.1109/CCECE.2011.6030470

Salas, V., Olías, E., Barrado, A., Lázaro, A., 2006. Review of the maximum power point tracking algorithms for stand-alone photovoltaic systems. Sol. Energy Mater. Sol. Cells 90, 1555–1578. https://doi.org/10.1016/j.solmat.2005.10.023

Subudhi, B., Pradhan, R., 2013. A Comparative Study on Maximum Power Point Tracking Techniques for Photovoltaic Power Systems. IEEE Trans. Sustain. Energy 4, 89–98. https://doi.org/10.1109/TSTE.2012.2202294

Tran, C.H., Nollet, F., Essounbouli, N., Hamzaoui, A., 2017. Modeling And Simulation Of Stand Alone Photovoltaic System Using Three Level Boost Converter. Presented at the 2017 International Renewable and Sustainable Energy Conference (IRSEC), IEE, Tangier, Morocco, Morocco, p. 6. https://doi.org/10.1109/IRSEC.2017.8477246

The 5th International Conference on Engineering Mechanics and Automation (ICEMA 5)
Hanoi, October 11÷12, 2019

Development and Validation of Finite Element Model for Metal cutting test

Tran Thanh Tung[a], Nguyen Thi Anh[a]

[a] *Faculty of Engineering Mechanics and Automation Engineering ,VNU University of Engineering and Technology, email : tranthanhtung@vnu.edu.vn*

[a] *Faculty of Engineering Mechanics and Automation Engineering ,VNU University of Engineering and Technology, email : nguyenthianh850@gmail.com*

Abstract

Recently, the computer simulation method is usually used by researchers to examine the performance of metal cutting phenomenon. With advance in computer technology, the finite element method could become a good solution instead of expensive experimental tests. This paper presents an approach method to construct of finite element model of metal cutting on CNC machine. The purpose of this study was to investigate and evaluate a finite element simulation of metal cutting using LS-DYNA software. Excellent agreement of real test and simulation results was performed for both term behavior and impact severities value. The result of the model assures the exactly of proposed method and proved that numerical method is a practical approach to metal cutting problems. Furthermore, the presented model was able to replace experimental in the development of metal cutting to reduce time and money.

Key Words: Metal cutting, Computer simulation, Experimental test, LS-DYNA

1. Introduction

Metal cutting is becoming important problem in mechanical manufacturing field. In the cutting processes, material is removed from surface of the work- part by the cutting tool to achieve the desire product. Metal cutting was the complex process due to large deformation, high strain- rate and the frictional contact between the tool and work-part along the shear zone.

Until now, there was a lot of research on the metal cutting impact tests. There are two methods to investigate and evaluated: experimental test and numerical simulation. The experimental method is an ideal approach and achieve results close to the real world. In this way, in order to evaluate metal cutting, the researchers must did an iterative process: fabricated, test, and repeat until achieve desired results. For example, A.Kuebler (1965) presented chip formation during metal machining is accomplished by converting a standard horizontal milling machine into a planer, providing an auxiliary light source and photographing the cutting action through a microscope. C.J.Rao et al (2014) proposed an alternative approach to determine the optimal process parameters used to predict cutting forces, tool life and surface finish. Sachin M. Agrawal et al (2014) determine the influence of lubricant on wear and frictional force by using

pin on disc machine with M2 HSS tool through experimental.

However, the experimental implementation is extremely costly, complex and time-consuming, and the researchers couldn't examined all cases, the different tests conditions. Therefore the numerical method was the choice of many researchers when evaluate and enhance the road safety barrier. Many various research were presented to prove the capability of computer to simulate full-scale crash tests on metal cutting in recent years. Eyup Bagci (2011) present the application of mesh-free SPH (Smoothed Particle Hydrodynamic) methodology to the simulation and analysis of 3-D hard machining. Yangcheng Zhang et al (2015) used Johnson-Cook parameters for Ti-6Al-4V using three types of numerical model of orthogonal cutting. J. Rodriguez et al (2013,2017) using finite element [FE] to build the computational model of metal cutting to prove the effective of numerical simulation in the process of metal cutting. Mathias Agmell et al (2017) present a numerical model that is able to determine the effect that the uncut chip thickness has on the stagnation zone and the connection between the stagnation zone and the deformation layer in the machined subsurface. A. Attanasio et al (2017) simulate tool wear in drilling of nickel-based alloys, in particular Inconel 718 to predict and measured tool wear data. Quing Zhang et al (2017) built three dimensional (3D) finite element (FE) simulation model to investigate the Temperature in Hard Milling of AISI H13 Steel.

Nowadays computers have become more powerful and popular. As a result, computer simulation has become a reliable tool for many mechanical engineers in the investigate performance of metal cutting. The numerical tests not only save time and money but also help researchers could predict behavior of metal cutting in many difference conditions (different materials, cutting tool, cutting parameters…). In fact to examine all tests with multiple conditions with experimental is very difficult and costly. This study performs FE analysis of metal cutting base on an existing full-scale crash testing by using LS-DYNA software. This paper presented an approach to build a metal cutting simulation model. The results of the present model fit the experimental results well, confirmed that the numerical method is a reasonable approach to metal cutting examine problems. Moreover, the introduced model here would be the basis foundation for the development of metal cutting process in the future.

2. The finite element modeling of metal cutting model

The study chose experimental base on research of H.Jamshidi et al (2013) to development a standard simulation. The model consists of two mains: Workpiece and cutting tool. The Workpiece made from Al 6061. A CNC- TME40 lathe was used for the experiments. Figure 1 depict metal cutting experimental before test.

Figure 1. Turning experimental test

[H.Jamshidi et al]

2.1. LS DYNA Introduction

LS-DYNA is among the best finite element application software invented by Livermore Software Technology Corporation (LSTC) which is adopted to forecast the effect of dynamic scenarios. Time step size, which determines the amount of time elapsing during each time integration loop, as shown in Figure 2, is an important concept in LS-DYNA code. In order to ensure the stability of time integration, the time step size is the minimum of the Δt_{max}

values calculated for all the elements in the models. When the simulation is set to run, program automatically processed all the elements and calculated the minimum time step size based on element in the finite element meshes used in the analysis. Throughout the analysis, the program loops through elements in the analysis so as to update the stress and force vectors, check for contacts, determination of the displacements, and updating time step size based on new element dimensions.

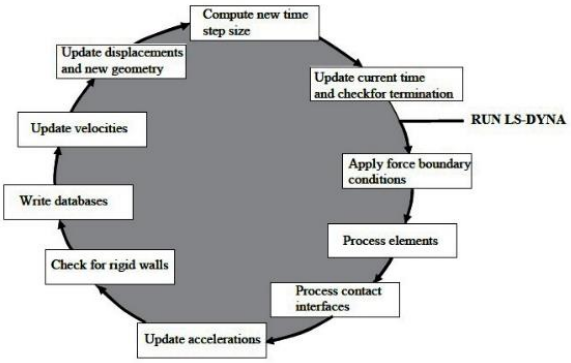

Figure 2. The time integration loop in LS-DYNA

Contact modelling is a way of treating interaction between different parts. Generally in contact problem, each of the two contacting interfaces is discretized into group of segments, with one interface denoted as the slave and the other as the master, as shown in Figure 3

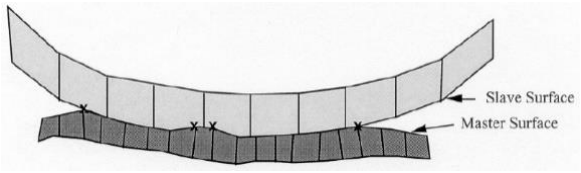

Figure 3. Typical contact types used in LS-DYNA

2.2. Workpiece model

The work piece model was modelled according to actual dimension workpiece which used in experimental.

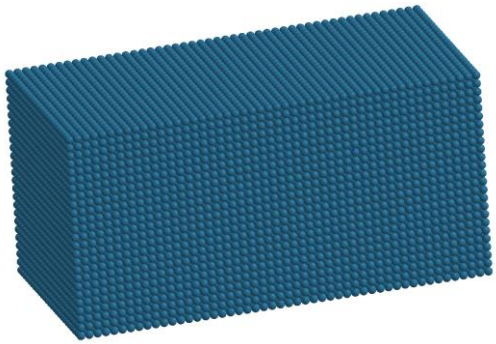

Figure 4. Work piece model.

All parts of safety barrier were modelled with SPH (Smooth Particle Hydrodynamics) method [13, 14] as shown in Figure 4. In this study the Aluminum material model of workpiece was defined by Johnson-Cook in LS-DYNA Manual (2006, 2007), as shown in Table 1, 2.

Table 1. Mechanical properties of Al 6061

Density (kg/m^3)	Elastic modulus (MPa)	Poisson's ration
2700	73000	0.33

Table 2. J – C Plastic and failure parameters of Al6061

A (MPa)	B (MPa)	N	D1	D2	D3
352	440	0.42	0.13	0.13	-1.5

2.3. The cutting tool model

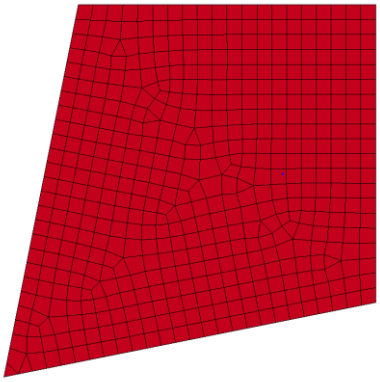

Figure 5. Finite cutting tool model

The cutting tool model was mesh by Solid mesh method consist of 115 solids elements and 13026 nodes as shown in Figure 5. Table 3 presented the material's properties of cutting tool was defined by Mat 02 Rigid in LS-Dyna.

Table 3. Parameters of tool material model

Density (kg/m^3)	Young's modulus (GPa)	Poisson's ration
15250	600	0.21

2.4. Simulation of model

Figure 6 present initial condition the cutting model simulation test based on the experimental. . The tool had the contact length measured 1.43 mm (right side), depth of cut 2.25 mm, feed rate 10 mm/ min, cutting speed 15.198 m/ min, the contact length measured 1.33 mm (left side) and cutting speed 21.277 m/min.

The *AUTOMATIC_SURFACE_TO_SURFACE* card was specified contact between the work piece and the cutting tool [14].

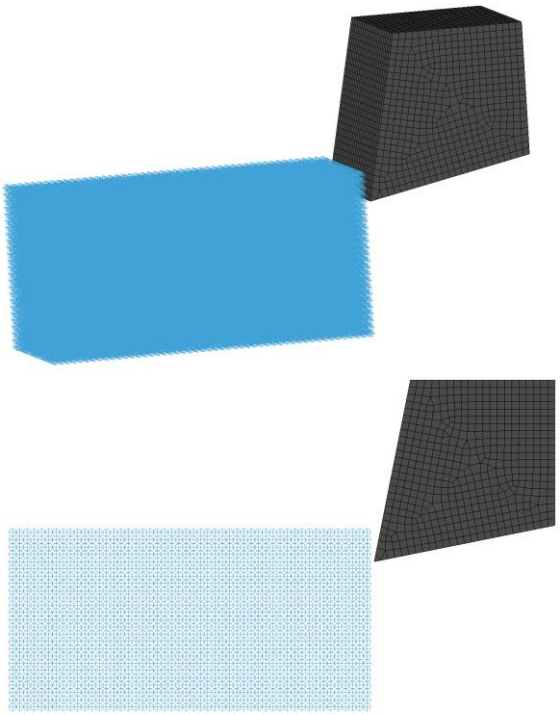

Figure 6. The model test simulation

3.Analysis of simulation model results

Figure 7 and 8 presents the finite element model of metal cutting results on isometric and top view, respectively

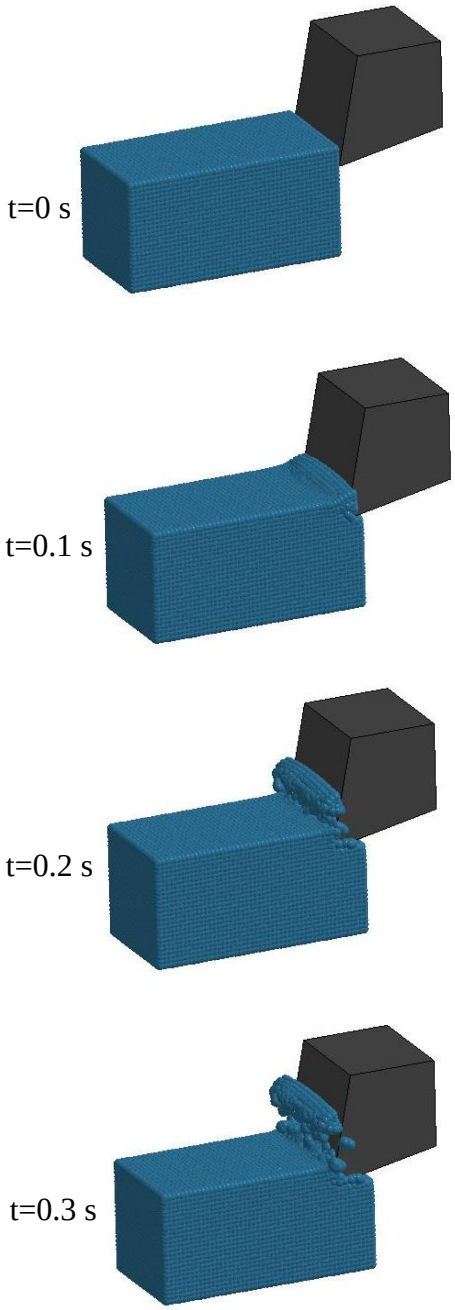

Figure 7. Results of simulation on isometric view

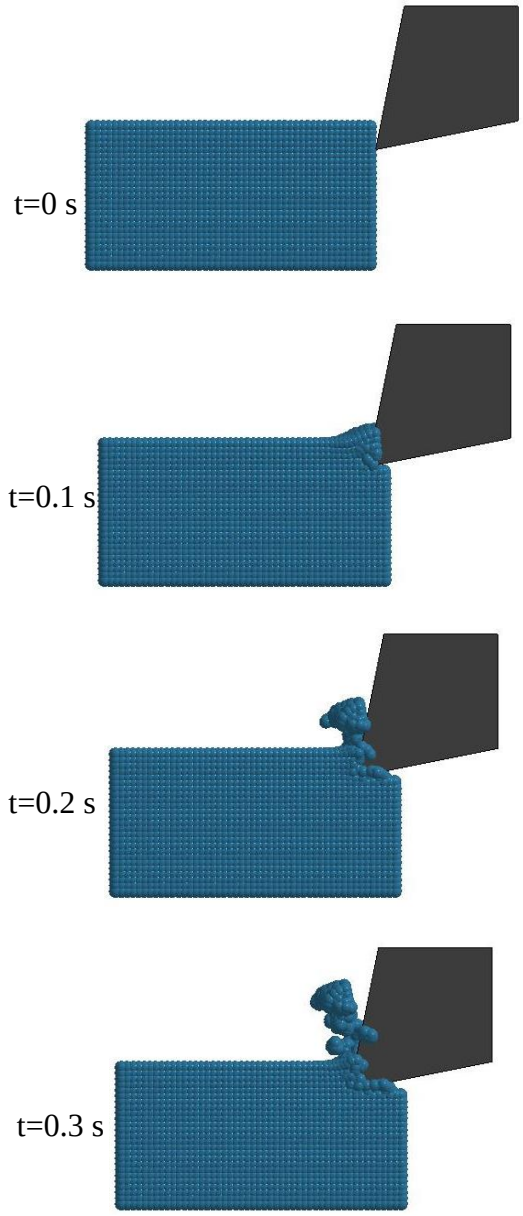

Figure 8. Results of simulation on front view

The data output in the NODOUT ASCII file and were used to compute cutting parameters (velocity, acceleration, normal force, friction force…). .There was a very good agreement both of behavior and severity parameters (normal force and friction) while comparing experimental and simulation.

Table 4. Comparison between experimental and simulation in depth of cut 2.25 mm, feed rate 10 mm/ min, rake angle = 0^0

Evaluation Criteria	Experimental Result [H.Jamshidi et al]	Simulation Result
Cutting speed Vc (m/min)	15.198	15.198
Tool-chip contact length (mm)	1.43	1.4
Normal force (N)	515	502
Friction force (N)	112	121
Cutting speed Vc (m/min)	21.277	21.277
Tool-chip contact length (mm)	1.33	1.2
Normal force (N)	385	376
Friction force (N)	100	115
Cutting speed Vc (m/min)	27.356	27.356
Tool-chip contact length (mm)	1.132	1.4
Normal force (N)	375	368
Friction force (N)	109	112

The Table 4 show a very closely tool-chip contact length, normal force and friction force value between experimental and simulation. There was a very good agreement both of behavior and cutting parameters while comparing experimental and simulation. The simulation model of metal cutting corresponds to reality.

4. Conclusion

This paper presents the approach method to construct of finite element model of metal

cutting according to lathe process on CNC machine. Simulations were performed with LS-DYNA code base on experimental test. There was very good agreement in comparison results between experimental test and simulation on both behavior and cutting parameters value. The results also proved the capacity of computer in researching metal cutting model instead of expensive experimental. Moreover, the proposed model could be used as a reliable tool to assist the future in the investigation of metal cutting process.

References

A.Attanasio , F.Faini , J.C.Outeiro (2017). FEM Simulation of Tool Wear in Drilling. Procedia CIRP. Volume 58, Pages 440-444'

Alfred A.Kuebler (1965). SMPTE Periodical-Study of Chip formation in Metal Cutting, Journal of the SMPTE .Volume: 74, Issue: 10 .

C.J.Raoa, D.SreeamuluaArun, TomMathew (2014). Analysis of Tool Life during Turning Operation by Determining Optimal Process Parameters. Procedia Engineering Volume 97, 2014, Pages 241-250.

Eyup Bagci (2011). 3-D numerical analysis of orthogonal cutting process via mesh-free method. International Journal of the Physical Sciences. Vol.6(6), pp. 1267-1282.

H. Jamshidi, M.J. Nategh (2013). Theoretical and experimental investigation of the friction behavior of the tool-chip interface in ultrasonic- vibration assisted turning. International Journal of Machine Tool & Manufacture 65 1-7

J.M.Rodriguez, J.M.Carbonell, J.C. Cante, J. Oliver (2017). Continuous chip formation in metal cutting processes using the Particle Finite Element Method (PFEM). International Journal of Solids and Structures. Volume 120, Page 81-102.

J.Rodriguez, P. Arrazola, J. Cante, A. Kortabarria, J. Oliver (2013). A Sensibility Analysis to Geometric and Cutting Conditions Using the Particle Finite Element Method (PFEM). Procedia CIRP 8, 105 – 110.

LS-DYNA Keyword user's manual (2007). Livermore Software Technology Corporation.

LS-DYNA Theoretical Manual (2006). Livermore Software Technology Corporation, Livermore.

Mathias Agmell, Daniel Johansson, Sampsa VA Laakso, Aylin Ahadi, Jan-Eric Stahl (2017). The influence the uncut chip thickness has on the stagnation point in orthogonal cutting. Procedia CIRP 58.

QingZhangSong, ZhangJianfengLi (2017). Three Dimensional Finite Element Simulation of Cutting Forces and Cutting Temperature in Hard Milling of AISI H13 Steel. Procedia Manufacturing. Volume 10, Pages 37-47

Rodriguez, J.M. Jonsen, P. Svoboda, A. Dislocation (2017) Density Based Material Model Applied in PFEM-simulation of Metal Cutting. Procedia CIRP 58 193 – 197.

Sachin M.Agrawal, Subhash Lahane, N.G Patil (2014). Experimental Investigations into Wear Characteristics of M2 Steel Using Cotton Seed Oil. Procedia Engineering Volume 97, Pages 4-14.

Yancheng Zhang, J.C. Outeiro, Tarek Mabrouki (2015). On the selection of Johnson-Cook constitutive model parameters for Ti-6AL-4V using three types of numerical models of orthogonal cutting. Procedia CIRP 31, 112 – 117.

The 5th International Conference on Engineering Mechanics and Automation (ICEMA 5)
Hanoi, October 11÷12, 2019

Employing Extended Kalman Filter with Indoor Positioning System for Robot Localization Application

Dong Tran Huu Quoc[a], Anh Phan Hoang[a], Tuan Nguyen Dinh[a], Nam Bui Duy[a], Van Nguyen Thi Thanh[a], Tung Bui Thanh[a], Trinh Chu Duc[a]

[a] *VNU - University of Engineering and Technology, Hanoi, 123106, Vietnam*
trinhcd@vnu.edu.vn

Abstract

IPS (Indoor Positioning System) is used to localize the robot position in a narrow environment. However, IPS signal is not accurate in some cases, the IPS signal transmission will be obstructed by people the public museums, for example. The combination with other sensors will reduce the poor signal from IPS and noise in the environment with many obstacles. The Extended Kalman Filter (EKF) have been widely used for mobile robot localization system and gained certain results. In this paper, EKF is embedded to Central Processing Unit with Robot Operating System on "UET-FuSo" robot to fuse IPS signal with encoder and IMU sensor for the determination of position and orientation robot. The obtained results show the effect of the proposed method when the robot localization is more stable and accurate than using only IPS signal. This localization will be applied for mapping and navigation of mobile robot in exhibition guidance robot.

Key Words: Extended Kalman Filters, IPS, Localization, ROS

1. Introduction

In progress working with Robot on real environment and real situation, it's positions are required conditions, without them Robot can't locate and move. IPS is used to get Robot coordinates for localization on small or medium places that GPS and other satellite technologies lack of precision or fail entirely, such as inside multistory buildings, airports, alleys, parking garages, and underground locations. However, IPS doesn't always give accurate signal, especially if so many people obstructing the transmission. Moreover, not only IPS but also sometimes sensor data isn't accurate and have so much noise. To make Robot more smart and doesn't do anything jerkily, stable messages and trustful data is needed. Therefore, the most reasonable way is combine all sensors and make each sensor support another. To solve these problems, Kalman Filters is considered. On the other hand, if the robot has enough sensors fuse with IPS for Kalman Filters, it feel everything around very quickly and accurately. Filtering is a very common method in engineering and embedded system, especially in Robot.[1] A good filtering algorithm can reduce the noise from signals while retaining the useful data.[3] Kalman Filters is one of the common filters use for Signal Processing.[6][10]

2. Indoor Positioning System

Indoor Positioning System is an off-the-shelf indoor navigation system, designed to provide

precise location data to autonomous robots, vehicles (AGV), and copters. It can also be used to track moving objects via mobile beacons attached to them. The navigation system consists of a network of stationary ultrasonic beacons interconnected via radio interface in a license-free band, one or more mobile beacons installed on objects to be tracked and modem providing gateway to the system from a PC or other computers. Mobile beacon's location is calculated based on a propagation delay of an ultrasonic pulses (Time-Of-Flight or TOF) between stationary and mobile beacons using trilateration algorithm. The system can build the map of stationary beacons automatically (For Non-Inverse Architecture).

Minimum configuration requirements (Non-Inverse Architecture) to ensure optimal performance of the Indoor Positioning System:

- For 3D (X, Y, Z) tracking: an unobstructed line of sight (hearing) between a mobile beacon and 3 or more stationary beacons within 30 meters

- For 2D (X, Y) tracking: an unobstructed line of sight (hearing) between a mobile beacon and 2 or more stationary beacons within 30 meters

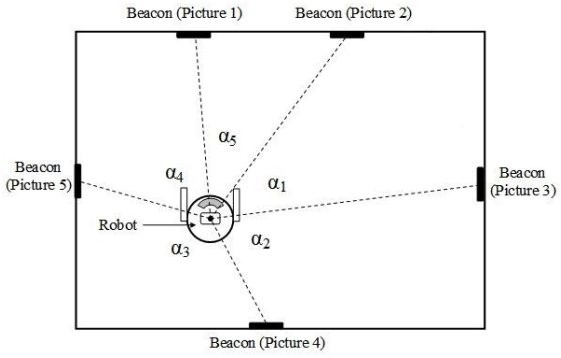

Figure 1. Robot Get Positions with IPS Beacons

We built a program to get 2D coordinates (X, Y) from IPS. After that, 2D coordinates is used for localization, used for Robot navigation. If the goals to Robot are sent, system calculated a path

to go to goals for a Robot and send velocities to motors. Robot stopped when it reached the goals, coincides with robot coordinates get from IPS. But these are requirements for optimal performance. In real situation, data isn't accurate if a line of sight from beacon to beacon and from beacon to robot is obstructed. People walking through the lines make coordinates got from IPS is jerky.

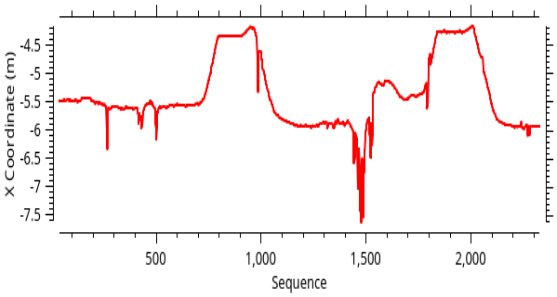

Figure 2. Raw X Coordinate/Sampling Times from IPS

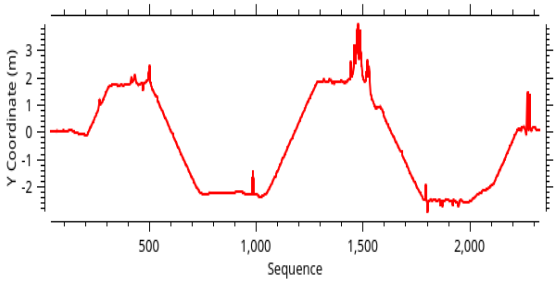

Figure 3. Raw Y Coordinate/Sampling Times from IPS

Figure 2 and 3 above represent X and Y coordinates on the domain of the sampling times.

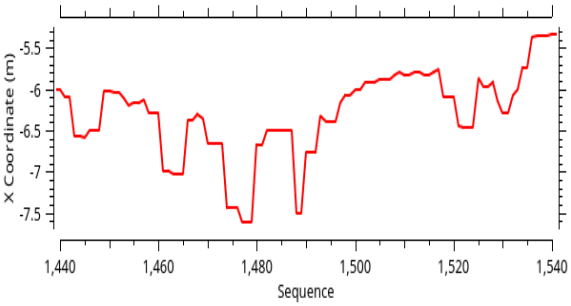

Figure 4. Raw X Coordinate with low accuracy

It can be seen in figures 4 and 5 that the coordinates fluctuate sharply, from about 1440th to 1540th sampling. So robot wasn't stable and moved jerkily. Signals are raw and didn't go through any signal processing system. These noises appeared because so many people walking around our robot and they obstructed the radio line.

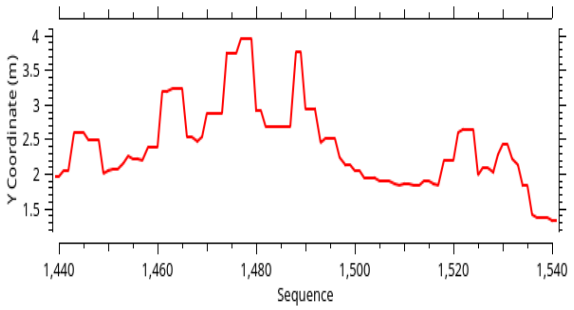

Figure 5. Raw Y Coordinate with low accuracy

Extended Kalman filters (EKF) can decrease them. So we embed EKF to system, combined with Encoder and Imu, to make signals great again.

It can be seen in figures 4 and 5 that the coordinates fluctuate sharply, from about 1440th to 1540th sampling. So robot wasn't stable and moved jerkily. Signals are raw and didn't go through any signal processing system. These noises appeared because so many people walking around our robot and they obstructed the radio line.

Extended Kalman filters (EKF) can decrease them. So we embed EKF to system, combined with Encoder and Imu, to make signals great again.

3. Extended Kalman Filter Implementation

The Extended Kalman filter (EKF) is a mathematical tool that can estimate the variables of a wide range of process to nonlinear systems. It works by linearizing the nonlinear state dynamics and measurement models. It is widely used in robot engineering, popular in navigation, positioning and control applications.[12][13]

This type of filter works very well in practice and that is why it is often implemented in embedded control system and because robot needs an accurate estimate of the process variables. The Extended Kalman filter is a smarter way to integrate measurement data into an estimate by recognising that measurements are noisy and that sometimes they should be ignored or have only a small effect on the state estimate. It smooths out the effects of noise in the state variable being estimated by incorporating more information from reliable data than from unreliable data. The user can tell the Extended Kalman filter how much noise there is in the system and it calculates an estimate of the position taking the noise into account[5][14] Extended Kalman Filter algorithm is still the most basic and common solution for discrete and low accurate signals such as GPS, IPS,...[7]

In our robot - "UET-FuSo", IPS, Wheel Encoders and IMU are fused into EKF and embed to Central Processing Unit for localization part. The input is 2D data format includes: Coordinates from IPS (MarvelMind Beacon Indoor Position System), Velocities from Wheel Encoders, Rotations and Angular Velocities measured by Gyroscope sensor, Accelerations measured by Accelerometer sensor, 2 sensors are integrated into a 6DOF - Sensor called IMU-MPU6050.

The EKF algorithm is divided into three parts: Initialization and Linearization, Prediction and Update. Assume that robot had x y coordinate from IPS, v_x v_y linear velocity from Wheel Encoders, a_x a_y yaw v_{yaw} linear acceleration, orientation and angular velocity from IMU. Our goal is to predict, update and process 2D coordinates for robots. so the kinematic and kinetic equations for the mobile robot:

$$\widehat{x_k} = \begin{bmatrix} x_k \\ v_{x_k} \\ a_{x_k} \end{bmatrix} = \begin{bmatrix} x_{k-1} + \Delta t \cdot v_{x_{k-1}} + \frac{1}{2} \cdot \Delta t^2 \cdot a_{x_{k-1}} + w_{1_{k-1}} \\ v_{x_{k-1}} + \Delta t . a_{x_{k-1}} + w_{2_{k-1}} \\ a_{x_{k-1}} + w_{3_{k-1}} \end{bmatrix} \quad (1)$$

$$\widehat{x_k'} = \begin{bmatrix} x_k' \\ v_{x_k}' \\ a_{x_k}' \end{bmatrix} = \begin{bmatrix} x_k + u_{1_k} \\ v_{x_k} + u_{2_k} \\ a_{x_k} + u_{3_k} \end{bmatrix} \quad (2)$$

All equations are implemented to get updated x_k, calculate y_k is similar.

The relationship of each state to the previous state is shown as follows:

$$x_k = f(x_{k-1}) + w_{k-1} \quad (3)$$

Where x_k is the state parameter of signal at time k, f is a nonlinear function representing x_k from x_{k-1}.

In addition, eight parameters including coordinates, linear velocities, linear accelerations, rotation angles and angular velocities are represented by 3 vectors. Because the units and scale of sensor data might not be the same as the units and scale of the measurement. So the state to measurement systems transform function is represented:

$$x_k^{'} = h(x_k) + u_k \quad (4)$$

Where x_k is the status parameter of signal at time k, h is a function mapping signal into the measurement space containing x_k signal.

- w_{k-1} and u_k respectively are process and observation noises. These two types of noise have multivariate Gaussian form with covariances, Q and R respectively.

- f and h can be used to calculate and predict the state of a signal. However, if using these two functions, the robot will not be able to use the covariances to estimate. Jacobi matrices is used instead with partial derivative to calculate. Let F and H respectively be the Jacobi matrices of partial derivatives of f and h, with respect to x_k, F and H have the form:

$$F = \left.\frac{\partial f}{\partial x}\right|_{\widehat{x_{k-1}}, w_{k-1}} \quad (5)$$

$$H = \left.\frac{\partial h}{\partial x}\right|_{\widehat{x_k}} \quad (6)$$

$$\widehat{x_k} = F.\widehat{x_{k-1}} + w_{k-1} \quad (7)$$

$$\widehat{x_k^{'}} = H.\widehat{x_k} + u_k \quad (8)$$

With $w_{k-1} = 0$, $u_k = 0$, the Jacobian Matrices F, H are:

$$F = \begin{bmatrix} 1 & \Delta t & \Delta t^2 \\ 0 & 1 & \Delta t \\ 0 & 0 & 1 \end{bmatrix} \quad (9)$$

$$H = \begin{bmatrix} 1 & 0 & 0 \\ 0 & 1 & 0 \\ 0 & 0 & 1 \end{bmatrix} \quad (10)$$

This is an estimation of the current covariance over time, represented by equation, Predicted Covariance Estimate:

$$P_k^{'} = F.P_{k-1}.F^T + Q \quad (11)$$

P_{k-1} is the covariance matrix of signals at time k - 1, F^T is the transposed matrix of F, Q is the matrix representing the noise during the estimation process, set by hand.

Particularly for the first signal received, since there is no previous signals to calculate the state, the matrix P_0 will be set manually. This is also the first initialization step.

$$P_1^{'} = F.P_0.F^T + Q \quad (12)$$

Matrix $P^{'}_k$ will be included to update the new status for the signal, we employ the Joseph form covariance update equation to promote filter stability by ensuring that P_k remains positive semi-definite[2]. Specific steps are as follows:

First, compute the Kalman Gain:

$$K = P_k^{'}.H^T\left(H.P_k^{'}.H^T + R\right)^{-1} \quad (13)$$

Second, update new state estimate:

$$x_k = \widehat{x_k} + K\left(\widehat{x_k^{'}} - H.\widehat{x_k}\right) \quad (14)$$

Last, update new covariance estimate:

$$P_k = (I - K.H)P_k^{'}(I - K.H)^T + K.R.K^T \quad (15)$$

In particular, H^T is the transposed matrix of H, R is covariance matrix representing signal noises of data from the sensors. We also write a program to calculate R with equation (16):

$$R = \begin{bmatrix} \sum_x & 0 & 0 \\ 0 & \sum_{v_x} & 0 \\ 0 & 0 & \sum_{a_x} \end{bmatrix} \quad (16)$$

$$\sum_x = \frac{1}{k-1}.\sum_{i=1}^{k}(x_i - \bar{x})^2 \quad (17)$$

Set the process noise covariance Q by hand is difficult. A problem is that u_k and w_{k-1} are uncorrelated zero-mean Gaussian noise sequences with covariance matrix Q and R[8]. So that EKF doesn't do the best work in theory.

Final, get and use x, y coordinates after update step instead of raw data from IPS.

4. Program Algorithm Implementation

- First sampling:

- Input:

1.1. The first signal received gives coordinate x_0 y_0, velocity v_{x0} v_{y0}, acceleration a_{x0} a_{y0}, Q and P_0 set by hand

1.2. Coordinate x_1 y_1 is the x y coordinate at time of first sampling (k = 1)

1.3. Velocity v_{x1} v_{y1} is the x y velocity at time of first sampling (k = 1)

1.4. Acceleration a_{x1} a_{y1} is the x y acceleration at time of first sampling (k = 1)

- Calculate:

1.5. Calculate F and H using the formula (7) (8)

1.6. The filter will calculate covariance P'_1 from P_0 and Q using the formula (12)

1.7. Calculate Kalman Gain (K) using the formula (13)

- Output:

1.8. Update x_1 y_1, using the formula (14)

1.9. Update Covariance P_1, using the formula (15)

- Second sampling:

- Input:

2.1. The EKF gives coordinate x_1 y_1, velocity v_{x1} v_{y1}, acceleration a_{x1} a_{y1}, Q and P_1

2.2. Coordinate x_2 y_2 is the x y coordinate at time of second sampling (k = 2)

2.3. Velocity v_{x2} v_{y2} is the x y velocity at time of first sampling (k = 2)

2.4. Acceleration a_{x2} a_{y2} is the x y acceleration at time of first sampling (k = 2)

- Calculate:

2.5. Calculate F and H using the formula (7) (8)

2.6. The filter will calculate covariance P'_2 from P_1 and Q using the formula (11)

2.7. Calculate Kalman Gain (K) using the formula (13)

- Output:

2.8. Update x_2 y_2, using the formula (14)

2.9. Update Covariance P_2, using the formula (15)

- Third sampling and more: Same as Second sampling

5. Experimentations and Results

In this section, x, y coordinates provided by raw data obtained from IPS will be compared with x, y coordinates after using EKF. For this purpose both signals were implemented in rqt_multiplot setup on ROS (Robot Operating System)[9], a tool help us to plot all messages got in embedded system into coordinate systems. We control a Robot to goal points with a very simple case: the robot that follows a path obtained from the system model. In the figures it is presented the estimated path of the robot compared to the real path.

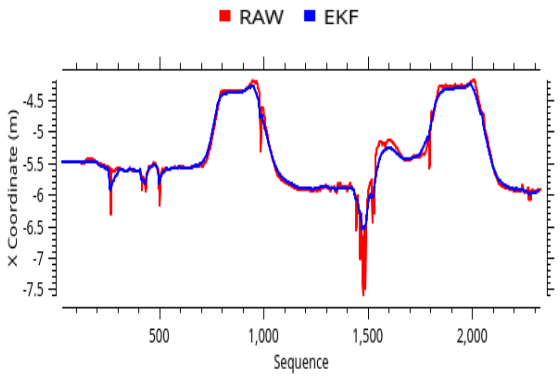

Figure 6. Illustration of using the EKF to estimate the position on the X axis

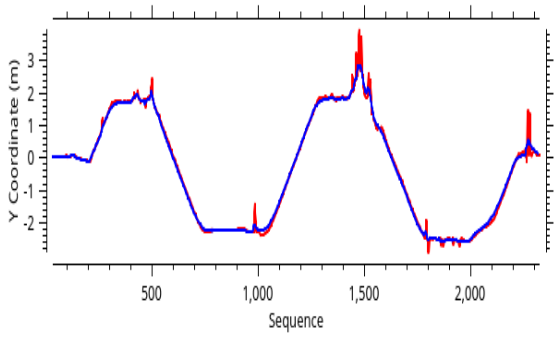

Figure 7. Illustration of using the EKF to estimate the position on the Y axis

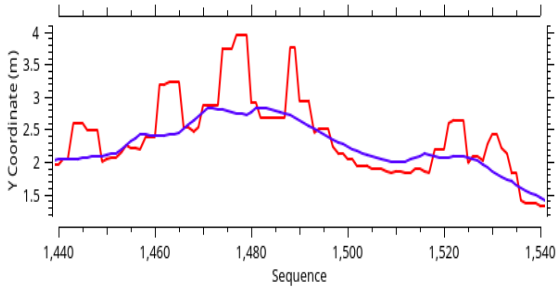

Figure 8. Using the EKF to estimate position on the X axis with low accuracy

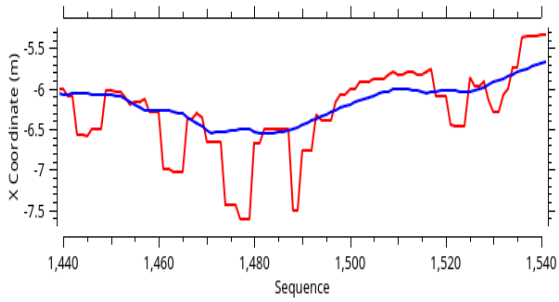

Figure 9. Using the EKF to estimate position on the Y axis with low accuracy

In figure 6, it is shown the path estimated with the help of the EKF and the raw path get from IPS on X axis. The same plot shows estimated data for Y axis shown in figure 7. In both plots it can be seen clearly that the EKF (blue line) predicted path is closer to the real path (red line). But at about 1440th to 1540th sampling or other sampling, IPS send us very poor data but EKF filter data is better (Figure 8 and 9). The difference between the performance of the filter and raw can be seen above.

6. Conclusions And Future Works

In this paper, the Indoor Positioning System with Extended Kalman filters is embedded into a real robot system to localize robot in special environment. The results show that the fusion between IPS and other sensors in EKF makes the robot localization more stable and accurate than the only IPS usage.

In order to implement the simultaneous localization and mapping (SLAM)[11] next time, the camera data such as visual coordinates, velocities, and orientations will be fused into the EKF. This will make the estimation of robot state more accurate.

7. Acknowledgement

This work has been supported by Vietnam National University, Hanoi (VNU), under Project No. QG.17.69.

8. References

[1] Aguirre, E., González, A., Muñoz, R. (2004), *Mobile Robot Map-Based Localization using approximate locations and the Extended Kalman Filter*, Proceedings of the 10th International Conference on Information Processing and Management of Uncertainty in Knowledge-Based Systems, Perugia, Italy, pp. 191-198.

[2] Bierman, G. J. and Thornton, C. L. (1977), *Numerical comparison of Kalman filter algorithms: Orbit determination case study*, Automatica vol. 13, no. 1, pp. 23-35.

[3] Casanova, O. L., Alfissima, F., Machaca, F. Y. (2008), *Robot Position Tracking Using Kalman Filter*, Proceedings of the World Congress on Engineering, London, UK, pp. 1604-1608.

[4] Choomuang, R., Afzulpurkar, N. (2005), *Hybrid Kalman Filter/Fuzzy Logic based Position Control of Autonomous Mobile Robot*, International Journal of Advanced Robotic Systems, IN-TECH, Vol. 2, No. 3, pp. 197-208.

[5] Kalman, R. E. (1960), *A New Approach to Linear Filtering and Prediction Problems*. Transactions of the ASME pp. 35-45, 1960.

[6] Kim, S. G., Crassidis, J. L., Cheng, Y., Fosbury, A. M., Junkins, J. L. (2007), *Kalman filtering for relative spacecraft attitude and position estimation*, Journal of Guidance Control and Dynamics, American Institute Of Aeronautics and Astronautics, Vol. 30, No. 1 pp. 133-143.

[7] Leonard, J. J. and Durrant-Whyte, H. F. (1991), *Mobile robot localization by tracking geometric beacons*, Robotics and Automation, IEEE Transactions on vol. 7, no. 3, pp. 376-382.

[8] Odelson, B. J., Rajamani, M. R., Rawlings J. B. (1997), *A new autocovariance least-squares method for estimating noise covariances*, Automatica vol. 13, no. 1, pp. 23-35.

[9] Quigley, M., Conley, K., Gerkey, B., Faust, J., Foote, T., Leibs, J., Wheeler, R. and Ng, A.Y. (2009), *ROS: an open-source robot operating system*, ICRA workshop on open source software vol. 3, no. 3.2.

[10] Santana, A. M., Sousa, A. S. S., Britto, R. S., Alsina, P. J., Medeiros, A. A. D. (2008), *Localization Of A Mobile Robot Based In Odometry And Natural Landmarks Using Extended Kalman Filter*, Proceedings of the 5th International Conference on Informatics in Control, Automation & Robotics, Funchal-Madeira, Portugal.

[11] Sasiadek, J.Z. Monjazeb, A. Necsulescu, D. (2008), *Navigation of an autonomous mobile robot using EKF-SLAM and FastSLAM*, Proceedings of the 16th Mediterranean Conference on Control and Automation, Ajjacio, France, pp. 517-522.

[12] Thomas, M., Daniel, S. (2015), *A Generalized Extended Kalman Filter Implementation for the Robot Operating System*, Intelligent Autonomous Systems 13 Proceedings of the 13th International Conference IAS-13.

[13] Wang, L. C., Yong, L. S., Ang, M. H. (2002), *Mobile Robot Localisation for Indoor Environment*, Technical Report, Singapore Institute of Manufacturing Technology, Singapore.

[14] Welch, G., Bishop, G. (2006), *An Introduction to the Kalman Filter*, Technical Report, University of North Carolina, Chapel Hill, USA.

The 5th International Conference on Engineering Mechanics and Automation (ICEMA-5)
Hanoi, October 11÷12, 2019

Forward Dynamics of a 3RUS Delta Parallel Robot

Vu Le Huy[a], Nguyen Dinh Dung[b*]

[a] *Phenikaa University, Hanoi, Vietnam, huy.vule@phenikaa-uni.edu.vn*
[b] *Phenikaa University, Hanoi, Vietnam, dung.nguyendinh@phenikaa-uni.edu.vn*

Abstract

The robot dynamics problem consists of two problems: inverse dynamics and forward dynamics. Forward dynamic of parallel robots is a quite complex problem but it is necessary for simulation in the robot control methods. Motion of a parallel robot is usually formulated by a system of the differential-algebraic equations (DAEs). In this paper, DAEs of parallel robots were transformed into the system of ordinary differential equations (ODEs) with redundant coordinates. On the basis of ODEs, the forward dynamics problem of the 3-RUS Delta parallel robot with specific parameters is simulated numerically. The simulation results are then compared by the error of the constrained equation with and without of using the Baumgarte stabilization method.

Keywords: Forward dynamics, Paralell robot, differential-algebraic equations, Baumgarte stabilization.

1. Introduction

Nowadays, parallel robots have been being used widely in industrial applications owing to their light compact structure, high stiffness and accuracy, where delta robot is one of the most successful parallel robots with thousands of versions created around the world. Delta robot was invented by Reymond Clavel in the early '80s (Merlet 2006), which consists of three arms connected to universal joints at the base. This robot uses the parallelogram structure to create three translational degrees of freedom by three revolute actuators.

The main research areas on Delta robots are kinetic, dynamic, control, singular configurations, work space, mechanical design, etc., which are carried out continuously in recent decades (Staicu and Carp-Ciocardia 2003, López, Castillo et al. 2006, Staicu 2009, Mohsen, Mahdi et al. 2013, Park, Kim et al. 2013, Uzunovic, Golubovic et al. 2013, Brinker, Corvers et al. 2015, Brinker and Corves 2015, Hoang, Khang et al. 2015, Zhang, Li et al. 2015, Harada 2016). Especially, the issues of improving the control quality of Delta robot are being studied a lot in recent years (Zhao-Hui and Taiki 2008, Müller and Hufnagel 2012, Zubizarreta, I et al. 2012, Castañeda, Luviano-Juárez et al. 2015, Huang and Huang 2015, Khang, Hoang et al. 2015, Ramirez-Neria, Sira-Ramirez et al. 2015, Du and Lou 2016, Dung, Khang et al. 2016, Fabian, Monterrey et al. 2016, Khang, Hoang et al. 2016, Lu and Liu 2016, Lu, Zhao et al. 2017, Angel and Viola

2018, Escorcia, Aguilar-Sierra et al. 2019). One problem should be considered in the numerical simulation diagram of robotic control methods that forward dynamics problems. It is used to calculate the actual position and velocity of the robot (Taghirad 2013). However, there are rarely documents mentioning this problem. In the viewpoint of mechanism, since parallel robots are the closed-loop multibody systems, Lagrange equations with multipliers, virtual work principle, Newton-Euler equations, subsystem, etc. are used to establish their movement equations. These equations are usually the differential-algebraic systems of equations, where the methods to solve them are often divided into two groups (Khang 2017). The first group is that the methods of transforming the systems to ordinary differential equations, and then using the numerical algorithm to solve them. The second group is that using the numerical methods to solve directly the algebraic differential systems. In this paper, a method in the first group is applied to calculate the forward dynamics of the Delta 3-RUS parallel robot.

2. Forward dynamics problem of parallel robot

The forward dynamics problem of the parallel robot is expressed as: The equations of motion of the robot, the driving moment / force $\boldsymbol{\tau}_a \in \mathbb{R}^f$ are known, the requirement is that finding the law of manipulator motion $\mathbf{x} = \mathbf{x}(t) \in \mathbb{R}^m$.

By using the Lagrange equations with multipliers, the differential-algebraic system of equations is obtained to describe the motion of multibody system with holonomic constraints of hold, stop and ideal (Khang 2017):

$$\boldsymbol{M}\ \boldsymbol{s}\ \ddot{\boldsymbol{s}} + \boldsymbol{C}\ \boldsymbol{s},\dot{\boldsymbol{s}}\ \dot{\boldsymbol{s}} + \boldsymbol{g}\ \boldsymbol{s}\ = \boldsymbol{\tau}\ t\ - \boldsymbol{\Phi}_s^T\ \boldsymbol{s}\ \boldsymbol{\lambda} \tag{1}$$

$$\boldsymbol{f}(\boldsymbol{s},t) = \boldsymbol{0} \tag{2}$$

where $\boldsymbol{s} = \left[s_1, s_2, ..., s_n\right]^T$ is the vector of redundant coordinates, $\boldsymbol{M}\ \boldsymbol{s}$ is then mass matrix with the size of $n \times n$ elements, $\boldsymbol{C}\ \boldsymbol{s},\dot{\boldsymbol{s}}$ is the $n \times n$ Coriolis/Centripetal matrix, $\boldsymbol{f}$ is a $r \times 1$ vector of the constraint equations, $\boldsymbol{\Phi}_S(\boldsymbol{s})$ is the $r \times n$ Jacobian matrix of the vector $\boldsymbol{f}$, $\boldsymbol{\tau}$ is a $n \times 1$ vector of the generalized non-conservative external forces, $\boldsymbol{\lambda}$ is a $r \times 1$ vector of Lagrangian multipliers. The Coriolis/Centripetal matrix $\boldsymbol{C}(\boldsymbol{s},\dot{\boldsymbol{s}})$ is determined from the mass matrix according the following formula (Khang 2011, Khang 2017):

$$\boldsymbol{C}\ \boldsymbol{s},\dot{\boldsymbol{s}}\ = \frac{\partial \boldsymbol{M}}{\partial \boldsymbol{s}}\ \boldsymbol{E}_n \otimes \dot{\boldsymbol{s}}\ - \frac{1}{2}\left(\frac{\partial \boldsymbol{M}}{\partial \boldsymbol{s}}\ \dot{\boldsymbol{s}} \otimes \boldsymbol{E}_n\ \right)^T \tag{3}$$

Vector $\boldsymbol{g}\ \boldsymbol{s}$ is determined by the potential energy of the system

$$\boldsymbol{g}\ \boldsymbol{s}\ = \left(\frac{\partial \Pi}{\partial \boldsymbol{s}}\right)^T \tag{4}$$

For the convenience of writing, the following symbol is used

$$\boldsymbol{p}_1(\boldsymbol{s},\dot{\boldsymbol{s}},t) = \boldsymbol{\tau}(\mathrm{t}) - \boldsymbol{C}(\boldsymbol{s},\dot{\boldsymbol{s}})\dot{\boldsymbol{s}} - \boldsymbol{g}(\boldsymbol{s}) \tag{5}$$

Then equations (1) and (2) are written as

$$\boldsymbol{M}\ \boldsymbol{s}\ \ddot{\boldsymbol{s}} + \boldsymbol{\Phi}_s^T\ \boldsymbol{s}\ \boldsymbol{\lambda} = \boldsymbol{p}_1\ \boldsymbol{s},\dot{\boldsymbol{s}},t \tag{6}$$

$$\boldsymbol{f}(\boldsymbol{s},t) = \boldsymbol{0} \tag{7}$$

As used in the literatures on multibody dynamics, the constrained equations are differentiated two times and obtained as

$$\dot{\boldsymbol{f}} = \frac{\partial \boldsymbol{f}}{\partial \boldsymbol{s}}\dot{\boldsymbol{s}} + \frac{\partial \boldsymbol{f}}{\partial t} = \boldsymbol{\Phi}_s\dot{\boldsymbol{s}} + \boldsymbol{f}_t = \boldsymbol{0} \tag{8}$$

$$\ddot{\boldsymbol{f}} = \boldsymbol{\Phi}_s\ddot{\boldsymbol{s}} + \dot{\boldsymbol{\Phi}}_s\dot{\boldsymbol{s}} + \dot{\boldsymbol{f}}_t = \boldsymbol{0} \quad \Rightarrow$$

$$\boldsymbol{\Phi}_s\ddot{\boldsymbol{s}} = -(\dot{\boldsymbol{\Phi}}_s\dot{\boldsymbol{s}} + \dot{\boldsymbol{f}}_t) = \boldsymbol{p}_2 \tag{9}$$

The equations (6), (7) and (9) can be rewritten in the form of matrix, where the equivalence was proved in the literature of (Khang 2017), as follows

$$\begin{bmatrix} \boldsymbol{M} & \boldsymbol{\Phi}_s^T \\ \boldsymbol{\Phi}_s & \boldsymbol{0} \end{bmatrix} \begin{bmatrix} \ddot{\boldsymbol{s}} \\ \boldsymbol{\lambda} \end{bmatrix} = \begin{bmatrix} \boldsymbol{p}_1 \\ \boldsymbol{p}_2 \end{bmatrix} \tag{10}$$

In this paper, an algorithm to transform the differential-algebraic system of equations (10) into the system of ordinary differential equations by removing Lagrangian multipliers is used. The physical coordinates $s_1,\ldots,s_n$ are divided into a set of the independent coordinates $q_1,\ldots,q_f$ and a set of the dependent coordinates $z_1,\ldots,z_r$. It is noticed that $f+r=n$ and the number of coordinates is equal to the number of additional constrained equations. Matrix $\boldsymbol{\Phi}_s$ has the form as

$$\Phi_s = \begin{bmatrix} \frac{\partial f_1}{\partial s_1} & \ldots\ldots & \frac{\partial f_1}{\partial s_n} \\ \ldots & \ldots\ldots & \ldots \\ \frac{\partial f_r}{\partial s_1} & \ldots\ldots & \frac{\partial f_r}{\partial s_n} \end{bmatrix} = \begin{bmatrix} \frac{\partial f_1}{\partial q_1} & \ldots & \frac{\partial f_1}{\partial q_f} & \frac{\partial f_1}{\partial z_1} & \ldots & \frac{\partial f_1}{\partial z_r} \\ \ldots & \ldots & \ldots & \ldots & \ldots & \ldots \\ \frac{\partial f_r}{\partial q_1} & \ldots & \frac{\partial f_r}{\partial q_f} & \frac{\partial f_r}{\partial z_1} & \ldots & \frac{\partial f_r}{\partial z_r} \end{bmatrix} \tag{11}$$

In order to perform the transformation, the following symbols are used

$$\boldsymbol{\Phi}_z = \begin{bmatrix} \frac{\partial f_1}{\partial z_1} & \ldots\ldots & \frac{\partial f_1}{\partial z_r} \\ \ldots & \ldots\ldots & \ldots \\ \frac{\partial f_r}{\partial z_1} & \ldots\ldots & \frac{\partial f_r}{\partial z_r} \end{bmatrix},$$

$$\boldsymbol{\Phi}_q = \begin{bmatrix} \frac{\partial f_1}{\partial q_1} & \ldots\ldots & \frac{\partial f_1}{\partial q_f} \\ \ldots & \ldots\ldots & \ldots \\ \frac{\partial f_r}{\partial q_1} & \ldots\ldots & \frac{\partial f_r}{\partial q_f} \end{bmatrix} \tag{12}$$

Here, the symbol $R(q,z)$ is additionally taken as

$$\boldsymbol{R}(\boldsymbol{q},\boldsymbol{z}) = \begin{bmatrix} \boldsymbol{E} \\ -\boldsymbol{\Phi}_z^{-1}\boldsymbol{\Phi}_q \end{bmatrix}, \tag{13}$$

where $\boldsymbol{E}$ is the unit matrix with the size of $f \times f$. The relation between the matrix $\boldsymbol{R}$ and matrix $\boldsymbol{\Phi}_z$ is formulated by (Khang 2017)

$$\boldsymbol{R}^T\boldsymbol{\Phi}_s^T = \boldsymbol{0} \tag{14}$$

From the equations (6) and (14), an equation is obtained as

$$\boldsymbol{R}^T\boldsymbol{M}\ddot{\boldsymbol{s}} = \boldsymbol{R}^T\boldsymbol{p}_1 \tag{15}$$

Then the two equations (15) and (9) can be rewritten in the form of matrix as follows

$$\begin{bmatrix} \boldsymbol{R}^T\boldsymbol{M} \\ \boldsymbol{\Phi}_s \end{bmatrix} \ddot{\boldsymbol{s}} = \begin{bmatrix} \boldsymbol{R}^T\boldsymbol{p}_1 \\ \boldsymbol{p}_3 \end{bmatrix} \tag{16}$$

By calling the symbol *D* as

$$\boldsymbol{D} = \begin{bmatrix} \boldsymbol{R}^T\boldsymbol{M} \\ \boldsymbol{\Phi}_s \end{bmatrix}, \tag{17}$$

then a system of differential equations is deduced from the equation (16) as

$$\ddot{\boldsymbol{s}} = \boldsymbol{D}^{-1} \begin{bmatrix} \boldsymbol{R}^T\boldsymbol{p}_1 \\ \boldsymbol{p}_3 \end{bmatrix} = \boldsymbol{h}(\boldsymbol{s},\dot{\boldsymbol{s}}) \tag{18}$$

This is the differential equation system of motion for the closed-loop multibody system in the redundant coordinates.

Note that the method of numerical integral applied on the equation (18) often encounters integral errors. After each step of integration, due to calculation errors, the values of $\boldsymbol{s}_i, \dot{\boldsymbol{s}}_i$ no longer satisfy the constrained equations of position and velocity, which lead to deviations

$$\boldsymbol{f}(\boldsymbol{s}_k) \neq \boldsymbol{0}, k = 1,2,\ldots,\ \dot{\boldsymbol{f}}(\boldsymbol{s}_k,\dot{\boldsymbol{s}}_k) \neq \boldsymbol{0}, k = 1,2,\ldots \tag{19}$$

According to Baumgarte method (Baumgarte 1972, Khang 2017), instead of solving equations $\ddot{\boldsymbol{f}}(\boldsymbol{s},\dot{\boldsymbol{s}}) = \boldsymbol{0}$, the following equation will be solved

$$\ddot{\boldsymbol{f}}(\boldsymbol{s},\dot{\boldsymbol{s}}) + 2\alpha\dot{\boldsymbol{f}}(\boldsymbol{s},\dot{\boldsymbol{s}}) + \beta^2\boldsymbol{f}(\boldsymbol{s}) = \boldsymbol{0} \tag{20}$$

where the coefficients are chosen to satisfy the condition $0 < \alpha \leq \beta$, the components $2\alpha\dot{\boldsymbol{f}}$ and $\beta^2\boldsymbol{f}$ act as control terms.

By using equation (20), the cumulative error should be gradually or completely eliminated in the integration process. Therefore, the system of the following equations is going to be solved

$$\begin{aligned} &\boldsymbol{M}\ \boldsymbol{s}\ \ddot{\boldsymbol{s}} + \boldsymbol{\Phi}_s^T\ \boldsymbol{s}\ \boldsymbol{\lambda} - \boldsymbol{p}_1\ \boldsymbol{s}, \dot{\boldsymbol{s}}, t\ = \boldsymbol{0} \\ &\ddot{\boldsymbol{f}}(\boldsymbol{s}, \dot{\boldsymbol{s}}, t) + 2\alpha\dot{\boldsymbol{f}}(\boldsymbol{s}, \dot{\boldsymbol{s}}, t) + \beta^2\boldsymbol{f}(\boldsymbol{s}, t) = \boldsymbol{0} \end{aligned} \tag{21}$$

The above equations (21) can be rewritten in matrix form as

$$\begin{bmatrix} \boldsymbol{M}\ \boldsymbol{s} & \boldsymbol{\Phi}^T\ \boldsymbol{s} \\ \boldsymbol{\Phi}\ \boldsymbol{s} & \boldsymbol{0}_{r\times r} \end{bmatrix} \begin{bmatrix} \ddot{\boldsymbol{s}} \\ \boldsymbol{\lambda} \end{bmatrix} = \begin{bmatrix} \boldsymbol{p}_1(\boldsymbol{s}, \dot{\boldsymbol{s}}, t) \\ \hat{\boldsymbol{p}}_2(\boldsymbol{s}, \dot{\boldsymbol{s}}, t) \end{bmatrix} \tag{22}$$

where

$$\hat{\boldsymbol{p}}_2(\boldsymbol{s}, \dot{\boldsymbol{s}}, t) = \boldsymbol{p}_2\ \boldsymbol{s}, \dot{\boldsymbol{s}}, t\ - 2\alpha\left[\boldsymbol{\Phi}\ \boldsymbol{s}, \mathrm{t}\ \dot{\boldsymbol{s}} + \boldsymbol{f}_t\right] - \beta^2\boldsymbol{f}(\boldsymbol{s}, t)$$

$$= -\left[\frac{\partial\boldsymbol{\Phi}}{\partial\boldsymbol{s}}\ \boldsymbol{E}_n \otimes \dot{\boldsymbol{s}}\ + \frac{\partial\boldsymbol{\Phi}}{\partial t} + 2\alpha\boldsymbol{\Phi}\ \boldsymbol{s}, \mathrm{t}\ \right]\dot{\boldsymbol{s}} - 2\alpha\boldsymbol{f}_t - \boldsymbol{f}_{tt} \tag{23}$$

The values of the constants α, β are usually selected between 1 and 20. According to (Baumgarte 1972, Khang 2017), it is recommended to select their values by $\alpha = \frac{1}{h}, \beta = \frac{\sqrt{2}}{h}$, where h is the integral step.

3. Simulation of dynamics problem for the 3RUS Delta parallel robot

The model of 3RUS Delta parallel robot used for simulation is shown in Figure 1. It consists of a fixed frame, a manipulator, three active bars and three passive bars. In particular, shown in Figure 2, the three active bars A_iB_i, $i = 1, 2, 3$ connect to the fixed frame by rotary joints and are driven by three motors. The three passive bars B_iD_i are parallelogram structures, therefore the manipulator will move translationally in space. Therefore, the Delta robots have three degrees of freedom translating in space. The parallelograms could be considered in calculation as the bars which are equal to their length, mass and inertia (Hoang, Khang et al. 2015, Dung, Khang et al. 2016). Thus the dynamic model of the robot consists of 7 rigid bodies moving in space, in which 3 active links A_iB_i $i = 1, 2, 3$, 3 passive bars B_iD_i $i = 1, 2, 3$ and the manipulator. The 3 active links A_iB_i $i = 1, 2, 3$ rotate around their rotation axes and are positioned by the angles θ_i. The 3 passive bars B_iD_i $i = 1, 2, 3$ move in space and are positioned by the angles ψ_i, γ_i as illustrated in Figure 3. The manipulator is a solid moving object in space and is positioned by a point P with the coordinates x_P, y_P, z_P.

The redundant coordinates are chosen as follows to set up the motion equation of the robot:

$$\mathbf{s} = \left[\theta_1\ \ \theta_2\ \ \theta_3\ \ \psi_1\ \ \psi_2\ \ \psi_3\ \ \gamma_1\ \ \gamma_2\ \ \gamma_3\ \ x_P\ \ y_P\ \ z_P\right]^T \tag{24}$$

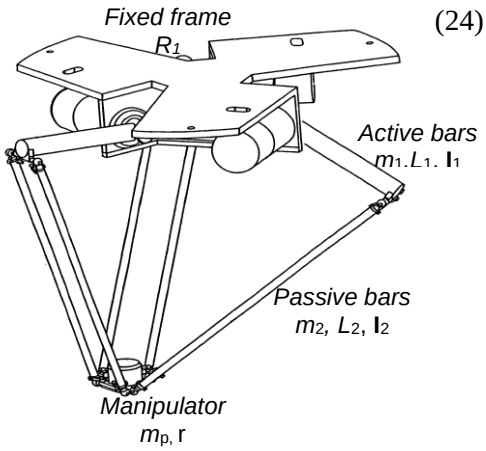

Figure 1. Delta robot with three parallelogram mechanisms

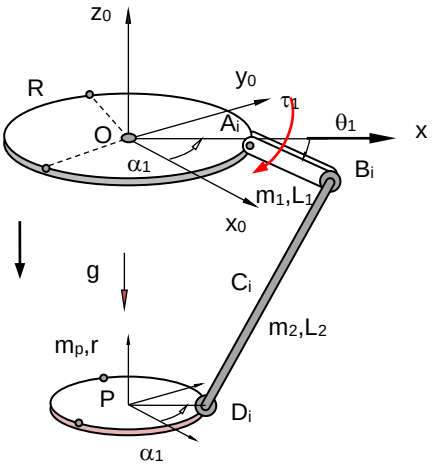

Figure 2. The dynamic model of the Delta robot

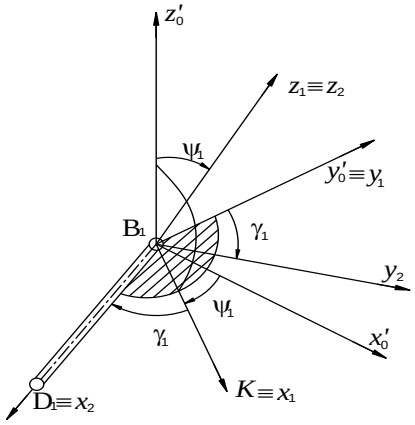

Figure 3. Position of the B_iD_i *rod in the space*

Using the Lagrange matrix form equation (Khang 2017), the robot's equation of motion is set in matrix form with the form as equation (1), (2) with 12 differential equations and 9 algebraic equations (Hoang, Khang et al. 2015) (specific equations seen in Appendix A). Applying the algorithm presented above, the numerical simulation of the forward dynamics problem is performed with a specific robot, where its parameters are given in Table 1. The driving moments are given as figure 4, the first condition is given as follows:

$$\theta_1 = -0.2348; \theta_2 = 0.8105; \theta_3 = 0.8105;$$
$$\psi_1 = 1.8465; \psi_2 = 2.4499; \psi_3 = 2.4499;$$
$$\gamma_1 = 0; \gamma_2 = -0.3308; \gamma_2 = 0.3308(rad);$$
$$x_P = 0.3;\ y_P = 0.0;\ z_P = -0.7(m),$$

They were obtained by selecting the position of the manipulator at the center of the machine table. The parameters of 3RUS Delta robot are given as follows:

$$L_1 = 0.3; L_2 = 0.8; R = 0.266; r = 0.04; \ \text{[m]}$$
$$\alpha_A = 0; \alpha_B = 2\pi/3; \alpha_C = 4\pi/3, \ \text{[rad]}$$
$$m_1 = 0.416; m_2 = 2 \times 0.195; m_P = 0.3, \ \text{[kg]}$$
$$\mathbf{I}_1 = 0.0125\,\mathrm{diag}(0,1,1) \ \text{[kg.m}^2\text{]}$$
$$\mathbf{I}_2 = 0.0208\,\mathrm{diag}(0,1,1) \ \text{[kg.m}^2\text{]}.$$

The results of calculation and simulation are presented by the graphs shown in the figures from Figure 5 to Figure 8. The driving torque is periodic with cycle time to be 1 (s) (Figure 4), the movement of the manipulator and the active bars are also periodic with the cycle time of 1 (s) (Figures 5, 6). Figure 7 shows that when using the stabilization technique of Baumgarte constrained equations, the error of the equations approximates to 10^{-12} (m). Otherwise, Figure 8 presents the errors without using the Baumgarte stabilization technique. It shows that the errors of the equation are larger than the case of using the stabilization technique and the errors tend to increase.

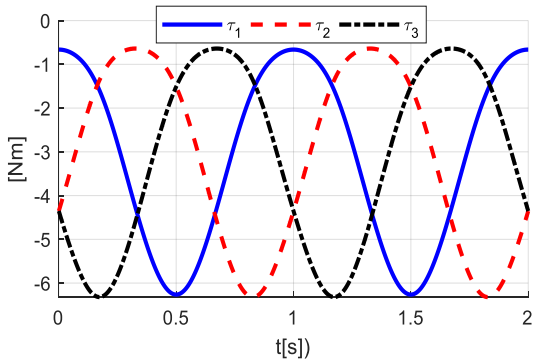

Figure 4. Graph of driving torques

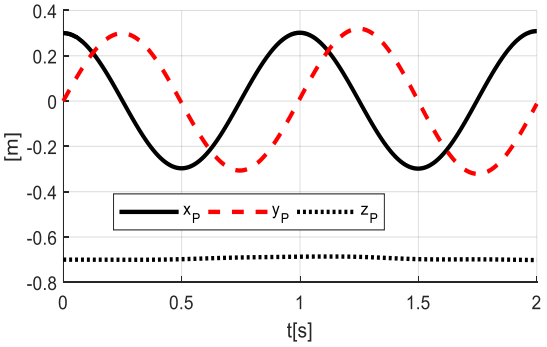

Figure 5. Graph of the coordinates x_P, y_P, z_P

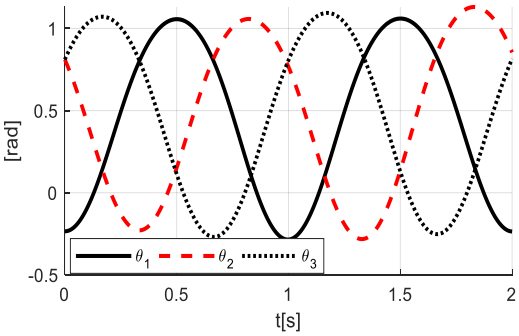

Figure 6. Graph of the active joint coordinates θ_1, θ_2, θ_3

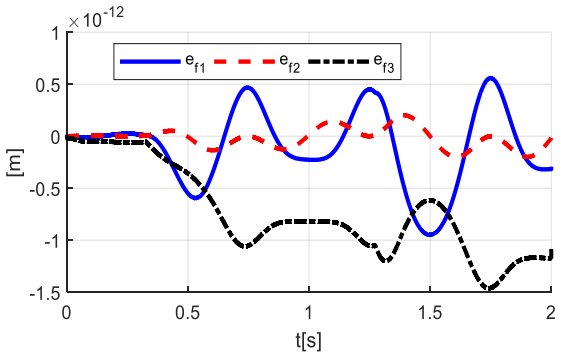

Figure 7. Errors of the constrained equations with Baumgarte stabilization technique

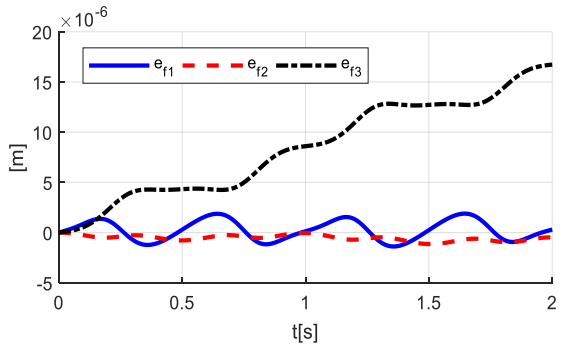

Figure 8. Errors of the constrained equations without Baumgarte stabilization technique

4. Conclusion

In this paper, the method of transforming the system of differential – algebraic equations into systems of ordinary differential equations was implemented. Additionally, the method of Baumgarte to stabilize the equations after each step of calculation for the system of differential equations was also applied. The forward dynamics problem was then simulated numerically with a specific case of the 3RUS Delta robot. The results showed that the method implemented in this study gave the error about 10^{-12} (m) which is small enough for control problem of Delta robot. This is a significant problem in simulating the control methods for parallel robots.

Acknowledgement

This research is funded by PHENIKAA University under grant number 04-2019.03.

References

Angel, L. and J. Viola (2018). Fractional order PID for tracking control of a parallel robotic manipulator type delta. *ISA Transactions* **79**: 172-188.

Baumgarte, J. (1972). Stabilization of constraints and integrals of motion in dynamic systems. *Computer Methods in Applied Mechanics and Engineering* **1**: 1-16.

Brinker, J., B. Corvers and M. Wahle (2015). *A comparative study of inverse dynamics based on Clavel's Delta robot* The 14th IFToMM World Congress, Taipei, Taiwan.

Brinker, J. and B. Corves (2015). *A Survey on Parallel Robots with Delta-like Architecture*. Proceedings of the 14th IFToMM World Congress, Taipei, Taiwan.

Castañeda, L., A. Luviano-Juárez and I. Chairez (2015). Robust Trajectory Tracking of a Delta Robot Through Adaptive Active Disturbance Rejection Control. *Control Systems Technology, IEEE Transactions on* **23**: 1387-1398.

Du, J. and Y. Lou (2016). Simplified dynamic model for real-time control of the delta parallel robot. *Proceedings of the IEEE International Conference on Information and Automation (ICIA)*. Ningbo, China**:** 1647-1652.

Dung, N. D., N. V. Khang and N. Q. Hoang (2016). *Modelling and sliding mode control based models of a 3RUS spatial parallel*. Proceedings of the 4th International Conference on Engineering Mechanics and Automation (ICEMA4), Hanoi, Vietnam.

Escorcia, J., H. Aguilar-Sierra, O. Aguilar-Mejia, A. Chemori and J. Arroyo-Nunez (2019). An Intelligent Compensation Through B-Spline Neural Network for a Delta Parallel Robot. *Proceedings of the International Conference on Control, Decision and Information Technologies (CoDIT 2019).* Paris, France**:** 235-240.

Fabian, J., C. Monterrey and R. Canahuire (2016). Trajectory tracking control of a 3 DOF delta robot: a PD and LQR comparison. *Proceedings of the 23rd IEEE International Congress on Electronics,*

Electrical Engineering and Computing (INTERCON). Piura, Peru**:** 1-5.

Harada, T. (2016). *Design and Control of a Parallel Robot for Mold Polishing*. Proceedings of the 3rd International Conference on Control, Mechatronics and Automation (ICCMA).

Hoang, N. Q., N. V. Khang and N. D. Dung (2015). *Influence of models on computed torque of delta spatial parallel robot.* Proceedings of the 16th Asia Pacific Vibration Conference, Hanoi, Vietnam.

Huang, Y. and Z. Huang (2015). Neural Network based dynamic trajectory tracking of Delta parallel robot. *Proceeding of the IEEE International Conference on Mechatronics and Automation (ICMA).* Beijing, China**:** 1938-1943.

Khang, N. V. (2011). "Kronecker Product and a new Matrix Form of Lagrange Equations with Multipliers for Constrained Multibody Systems." *Mechanics Research Communications, Elsevier* **38**: 294-299.

Khang, N. V. (2017). *Dynamics of Multibody Systems*, Scientific and Technical Publishing, (in Vietnamese).

Khang, N. V., N. Q. Hoang, N. D. Dung and N. V. Quyen (2016). "Model-based Control of a 3-PRS Spatial Parallel Robot in The Space of Redundant Coordinates." *Journal of Science and Technology Technical Universities* **112**: 49-53.

Khang, N. V., N. Q. Hoang, N. D. Sang and N. D. Dung (2015). "A comparison study of some control methods for Delta spatial parallel robot." *Journal of computer science and cybernetics, VAST* **31**: 71-81.

López, M., E. Castillo, G. García and A. Bashir (2006). Delta robot: inverse, direct, and intermediate Jacobians. *Proceedings IMechE, **220**, Part C: Journal Mechanical Engineering Science:* 103-109.

Lu, X. and M. Liu (2016). Optimal Design and Tuning of PID-Type Interval Type-2 Fuzzy Logic Controllers for Delta Parallel Robots. *International Journal of Advanced Robotic Systems* **13**: 1-12.

Lu, X., Y. Zhao and M. Liu (2017). Self-Learning Interval Type-2 Fuzzy Neural Network Controllers for Trajectory Control of a Delta Parallel Robot. *Neurocomputing* **283**: 107-119.

Merlet, J. P. (2006). *Parallel Robots*. Berlin, Springer Verlag.

Mohsen, A., A. A. Mahdi and A. Mersad (2013). Dynamics and Control of a Novel 3-DoF Spatial parallel Robot. *Proceedings of the RSI/ISM International Conference on Robotics and Mechatronics*: 183-188.

Müller, A. and T. Hufnagel (2012). Model-based control of redundantly actuated parallel manipulators in redundant coordinates. *Robotics and Autonomous Systems* **60**: 563-571.

Park, S. B., H. S. Kim, C. Song and K. Kim (2013). *Dynamics modeling of a Delta-type parallel robot (ISR 2013)*. Proceedings of the 44th IEEE International Symposium on Robotics.

Ramirez-Neria, M., H. Sira-Ramirez, A. Luviano-Juárez and A. Rodrguez-Ángeles (2015). Active Disturbance Rejection Control Applied To A Delta Parallel Robot In Trajectory Tracking Tasks. *Asian Journal of Control* **17**: 636-647.

Staicu, S. (2009). Recursive modelling in dynamics of agile wrist spherical parallel robot. *Robotics and Computer-Intergrated Manufacturing* **25**: 409-416.

Staicu, S. and D. C. Carp-Ciocardia (2003). *Dynamic analysis of Clavel's Delta parallel Robot*. Proceeding of the IEEE International Conference on Robotics and Automation (ICRA), Taipei, Taiwan.

Taghirad, H. D. (2013). *Parallel Robots: Mechanics and Control*, CRC Press.

Uzunovic, T., E. Golubovic, E. A. Baran and A. Sabanovic (2013). *Configuration space control of a parallel Delta robot with a neural network based inverse kinematics.* Proceedings of the 8th International Conference on Electrical and Electronics Engineering (ELECO), Bursa, Turkey.

Zhang, Q., R. Li and Y. Tian (2015). *Dynamic Performance Analysis of 3-Delta Type Parallel Robot.* Proceedings of the 14th IFToMM World Congress, Taipei, Taiwan.

Zhao-Hui, J. and I. Taiki (2008). A Neural Network Controller for Trajectory Control of Industrial Robot Manipulators. *Journal of Computers* **3**.

Zubizarreta, A., C. I, M. Marcos and C. Pinto (2012). A Redundant Dynamic Model of Parallel Robots for Model-Based Control. Robotica **31**: 203-216.

Appendix A: Establishing the differential equations of robot's movement

$$\tau_1 = \frac{1}{2}m_2L_1L_2\ddot{\psi}_1\cos\gamma_1\cos(\theta_1-\psi_1)+\frac{1}{2}m_2L_1L_2\ddot{\gamma}_1\sin\gamma_1\sin(\theta_1-\psi_1)+\frac{1}{2}m_2L_1L_2\dot{\psi}_1^2\cos\gamma_1\sin(\theta_1-\psi_1)$$
$$+\frac{1}{2}m_2L_1L_2\dot{\gamma}_1^2\cos\gamma_1\sin(\theta_1-\psi_1)-m_2L_1L_2\dot{\gamma}_1\dot{\psi}_1\sin\gamma_1\cos(\theta_1-\psi_1)+\left[\left(\frac{1}{4}m_1+m_2\right)L_1^2+I_{y11}^{(11)}\right]\ddot{\theta}_1$$
$$-\left(\frac{1}{2}m_1+m_2\right)gL_1\cos\theta_1+\lambda_1L_1\cos\alpha_1\sin\theta_1+\lambda_2L_1\sin\alpha_1\sin\theta_1+\lambda_3L_1\cos\theta_1$$

$$\tau_2 = \frac{1}{2}m_2L_1L_2\ddot{\psi}_2\cos\gamma_2\cos(\theta_2-\psi_2)+\frac{1}{2}m_2L_1L_2\ddot{\gamma}_2\sin\gamma_2\sin(\theta_2-\psi_2)+\frac{1}{2}m_2L_1L_2\dot{\psi}_2^2\cos\gamma_2\sin(\theta_2-\psi_2)$$
$$+\frac{1}{2}m_2L_1L_2\dot{\gamma}_2^2\cos\gamma_2\sin(\theta_2-\psi_2)-m_2L_1L_2\dot{\gamma}_2\dot{\psi}_2\sin\gamma_2\cos(\theta_2-\psi_2)+\left[\left(\frac{1}{4}m_1+m_2\right)L_1^2+I_{y12}^{(12)}\right]\ddot{\theta}_2$$
$$-\left(\frac{1}{2}m_1+m_2\right)gL_1\cos\theta_2+\lambda_4L_1\cos\alpha_2\sin\theta_2+\lambda_5L_1\sin\alpha_2\sin\theta_2+\lambda_6L_1\cos\theta_2$$

$$\tau_3 = \frac{1}{2}m_2L_1L_2\ddot{\psi}_3\cos\gamma_3\cos(\theta_3-\psi_3)+\frac{1}{2}m_2L_1L_2\ddot{\gamma}_3\sin\gamma_3\sin(\theta_3-\psi_3)+\frac{1}{2}m_2L_1L_2\dot{\psi}_3^2\cos\gamma_3\sin(\theta_3-\psi_3)$$
$$+\frac{1}{2}m_2L_1L_2\dot{\gamma}_3^2\cos\gamma_3\sin(\theta_3-\psi_3)-m_2L_1L_2\dot{\gamma}_3\dot{\psi}_3\sin\gamma_3\cos(\theta_3-\psi_3)+\left[\left(\frac{1}{4}m_1+m_2\right)L_1^2+I_{y13}^{(13)}\right]\ddot{\theta}_3$$
$$-\left(\frac{1}{2}m_1+m_2\right)gL_1\cos\theta_3+\lambda_7L_1\cos\alpha_3\sin\theta_3+\lambda_8L_1\sin\alpha_3\sin\theta_3+\lambda_9L_1\cos\theta_3$$

$$0 = \frac{1}{2}m_2L_1L_2\ddot{\theta}_1\cos\gamma_1\cos(\theta_1-\psi_1)-\frac{1}{2}m_2L_1L_2\dot{\theta}_1^2\cos\gamma_1\sin(\theta_1-\psi_1)$$
$$-\left(\frac{1}{2}m_2L_2^2-2I_{x21}^{(21)}+2I_{y21}^{(21)}\right)\dot{\psi}_1\dot{\gamma}_1\sin\gamma_1\cos\gamma_1+\left[\cos^2\gamma_1\left(\frac{1}{4}m_2L_2^2-I_{x21}^{(21)}+I_{y21}^{(21)}\right)+I_{x21}^{(21)}\right]\ddot{\psi}_1$$
$$-\frac{1}{2}m_2gL_2\cos\psi_1\cos\gamma_1+\left(\lambda_1\cos\alpha_1+\lambda_2\sin\alpha_1\right)L_2\sin\psi_1\cos\gamma_1+\lambda_3L_2\cos\psi_1\cos\gamma_1$$

$$0 = \frac{1}{2}m_2L_1L_2\ddot{\theta}_2\cos\gamma_2\cos(\theta_2-\psi_2)-\frac{1}{2}m_2L_1L_2\dot{\theta}_2^2\cos\gamma_2\sin(\theta_2-\psi_2)$$
$$-\left(\frac{1}{2}m_2L_2^2-2I_{x22}^{(22)}+2I_{y22}^{(22)}\right)\dot{\psi}_2\dot{\gamma}_2\sin\gamma_2\cos\gamma_2+\left[\cos^2\gamma_2\left(\frac{1}{4}m_2L_2^2-I_{x22}^{(22)}+I_{y22}^{(22)}\right)+I_{x22}^{(22)}\right]\ddot{\psi}_2$$
$$-\frac{1}{2}m_2gL_2\cos\psi_2\cos\gamma_2+\left(\lambda_4\cos\alpha_2+\lambda_5\sin\alpha_2\right)L_2\sin\psi_2\cos\gamma_2+\lambda_6L_2\cos\psi_2\cos\gamma_2$$

$$0=\frac{1}{2}m_2L_1L_2\ddot{\theta}_3\cos\gamma_3\cos(\theta_3-\psi_3)-\frac{1}{2}m_2L_1L_2\dot{\theta}_3^2\cos\gamma_3\sin(\theta_3-\psi_3)$$
$$-\left(\frac{1}{2}m_2L_2^2-2I_{x23}^{(23)}+2I_{y23}^{(23)}\right)\dot{\psi}_3\dot{\gamma}_3\sin\gamma_3\cos\gamma_3+\left[\cos^2\gamma_3\left(\frac{1}{4}m_2L_2^2-I_{x23}^{(23)}+I_{y23}^{(23)}\right)+I_{x23}^{(23)}\right]\ddot{\psi}_3$$
$$-\frac{1}{2}m_2gL_2\cos\psi_3\cos\gamma_3+\left(\lambda_7\cos\alpha_3+\lambda_8\sin\alpha_3\right)L_2\sin\psi_3\cos\gamma_3+\lambda_9L_2\cos\psi_3\cos\gamma_3$$

$$0=\frac{1}{2}m_2L_1L_2\ddot{\theta}_1\sin\gamma_1\sin(\theta_1-\psi_1)+\frac{1}{2}m_2L_1L_2\dot{\theta}_1^2\sin\gamma_1\cos(\theta_1-\psi_1)$$
$$+\dot{\psi}_1^2\sin\gamma_1\cos\gamma_1\left(\frac{1}{4}m_2L_2^2-I_{x21}^{(21)}+I_{y21}^{(21)}\right)+\left(\frac{1}{4}m_2L_2^2+I_{z21}^{(21)}\right)\ddot{\gamma}_1+\frac{1}{2}m_2gL_2\sin\psi_1\sin\gamma_1$$
$$+\left(\lambda_1\cos\alpha_1+\lambda_2\sin\alpha_1\right)L_2\cos\psi_1\sin\gamma_1+\left(\lambda_1\sin\alpha_1-\lambda_2\cos\alpha_1\right)L_2\cos\gamma_1-\lambda_3L_2\sin\psi_1\sin\gamma_1$$

$$0=\frac{1}{2}m_2L_1L_2\ddot{\theta}_2\sin\gamma_2\sin(\theta_2-\psi_2)+\frac{1}{2}m_2L_1L_2\dot{\theta}_2^2\sin\gamma_2\cos(\theta_2-\psi_2)$$
$$+\dot{\psi}_2^2\sin\gamma_2\cos\gamma_2\left(\frac{1}{4}m_2L_2^2-I_{x22}^{(22)}+I_{y22}^{(22)}\right)+\left(\frac{1}{4}m_2L_2^2+I_{z22}^{(22)}\right)\ddot{\gamma}_2+\frac{1}{2}m_2gL_2\sin\psi_2\sin\gamma_2$$
$$+\left(\lambda_4\cos\alpha_2+\lambda_5\sin\alpha_2\right)L_2\cos\psi_2\sin\gamma_2+\left(\lambda_4\sin\alpha_2-\lambda_5\cos\alpha_2\right)L_2\cos\gamma_2-\lambda_6L_2\sin\psi_2\sin\gamma_2$$

$$0=\frac{1}{2}m_2L_1L_2\ddot{\theta}_3\sin\gamma_3\sin(\theta_3-\psi_3)+\frac{1}{2}m_2L_1L_2\dot{\theta}_3^2\sin\gamma_3\cos(\theta_3-\psi_3)$$
$$+\dot{\psi}_3^2\sin\gamma_3\cos\gamma_3\left(\frac{1}{4}m_2L_2^2-I_{x23}^{(23)}+I_{y23}^{(23)}\right)+\left(\frac{1}{4}m_{23}L_2^2+I_{z23}^{(23)}\right)\ddot{\gamma}_3+\frac{1}{2}m_2gL_2\sin\psi_3\sin\gamma_3$$
$$+\left(\lambda_7\cos\alpha_3+\lambda_8\sin\alpha_3\right)L_2\cos\psi_3\sin\gamma_3+\left(\lambda_7\sin\alpha_3-\lambda_8\cos\alpha_3\right)L_2\cos\gamma_3-\lambda_9L_2\sin\psi_3\sin\gamma_3$$

$$0=m_3\ddot{x}_P+\lambda_1+\lambda_4+\lambda_7;\quad 0=m_3\ddot{y}_P+\lambda_2+\lambda_5+\lambda_8;\quad 0=m_3\ddot{z}_P+m_3g+\lambda_3+\lambda_6+\lambda_9$$

$$f_1=x_P-\left(R-r+L_1\cos\theta_1+L_2\cos\psi_1\cos\gamma_1\right)\cos\alpha_1+L_2\sin\gamma_1\sin\alpha_1=0$$
$$f_2=y_P-\left(R-r+L_1\cos\theta_1+L_2\cos\psi_1\cos\gamma_1\right)\sin\alpha_1-L_2\sin\gamma_1\cos\alpha_1=0$$
$$f_3=z_P+L_1\sin\theta_1+L_2\sin\psi_1\cos\gamma_1=0$$
$$f_4=x_P-\left(R-r+L_1\cos\theta_2+L_2\cos\psi_2\cos\gamma_2\right)\cos\alpha_2+L_2\sin\gamma_2\sin\alpha_2=0$$
$$f_5=y_P-\left(R-r+L_1\cos\theta_2+L_2\cos\psi_2\cos\gamma_2\right)\sin\alpha_2-L_2\sin\gamma_2\cos\alpha_2=0$$
$$f_6=z_P+L_1\sin\theta_2+L_2\sin\psi_2\cos\gamma_2=0$$
$$f_7=x_P-\left(R-r+L_1\cos\theta_3+L_2\cos\psi_3\cos\gamma_3\right)\cos\alpha_3+L_2\sin\gamma_3\sin\alpha_3=0$$
$$f_8=y_P-\left(R-r+L_1\cos\theta_3+L_2\cos\psi_3\cos\gamma_3\right)\sin\alpha_3-L_2\sin\gamma_3\cos\alpha_3=0$$
$$f_9=z_P+L_1\sin\theta_3+L_2\sin\psi_3\cos\gamma_3=0$$

Nonlinear Dynamics

The 5th International Conference on Engineering Mechanics and Automation (ICEMA 5)
Hanoi, October 11÷12, 2019

Optimal design of fuzzy controller for active control of structure using scaling factors of variables

Hai-Le Bui[a]

[a] *School of Mechanical Engineering - Hanoi University of Science and Technology, No. 1 Dai Co Viet Street – Hanoi – Vietnam, le.buihai@hust.edu.vn*

Abstract

In this paper, the problem of optimal design of hedge-algebras based fuzzy controller (HAC) for structural vibration control with actuator saturation is presented. The main advantages of HAC are: (i) inherent order relationships among linguistic values of each linguistic variable are always ensured; (ii) instead of using any fuzzy sets, linguistic values of linguistic variables are determined by an isomorphism mapping called semantically quantifying mapping (SQM) based on a few fuzziness parameters of each linguistic variable and hence, the process of fuzzy inference is very simple due to SQM values occurring in the fuzzy rule base. In numerical simulations, the optimal HAC based on tuned scaling factors of state variables have been designed to active control of a 3-DOF structure subjected to earthquake excitation. Control results of HACs are also compared with those of the other methods to show advantages of the proposed controllers.

Key Words: active control, hedge-algebras based fuzzy controller, optimal design, scaling factor.

1. Introduction

Protection of civil structures and human from natural hazards as strong earthquakes and winds is very important and challenging problem in practice as well as in research. Structural vibration control can be considered as a modern solution to reduce dynamic responses in order to protect structures (Thenozhi and Yu, 2013).

Based on the fuzzy set theory introduced by Zadeh in 1965, fuzzy controllers is very flexible and easy to use and they have been successfully applied in many theoretical as well as practical problems in general and in vibration control of civil structures in practical (Bui et al., 2018). Several optimal algorithms, such as genetic algorithms (GA) or particle swarm optimization (PSO) and so on, were utilized for designing optimal fuzzy controllers based on objective functions of minimizing control energy or structural responses in order to enhance their control performance in vibration control of structures (Bui et al., 2018; Kim and Kang, 2012; Marinaki et al., 2010; Pourzeynali et al., 2007; Rao and Sivasubramanian, 2008; Uz and Hadi, 2014).

However, some disadvantages of fuzzy controllers can be found as follows: (1) Inherent semantic order of linguistic values of a linguistic variable is not closely guaranteed and the methods of fuzzification, inference and defuzzification are quite complicated (Anh et al., 2013); (2) When optimizing fuzzy controllers, a large number of overlap parameters of membership functions was used as design variables. It results in increasing

volume of calculation, especially in global and random optimal algorithms such as GA or PSO.

Hedge algebras (HA) theory, first introduced in 1990, showed that linguistic values can formulate an algebraic structure (Ho and Wechler, 1990; Ho and Wechler, 1992). It is a complete and rich enough algebra structure, and therefore, it can describe completely reasoning processes (Ho and Nam, 2002). HA gives an algebraic foundation to study a kind of fuzzy logic, called linguistic-valued logic, and provide a good mathematical tool to define and investigate the concept of fuzziness of vague terms and quantification problem and some approximate reasoning methods. Therefore, HA can be applied in many different fields of fuzzy theory such as fuzzy control, fuzzy database, fuzzy logic programming and linguistic truth value, fuzzy classification and regression problem, forecasting enrollments with fuzzy time series, fuzzy data mining, fuzzy linguistic database summarization, and so on. Applications of HA in fuzzy vibration control of mechanical structures were implemented recently (Anh et al., 2013; Bui et al., 2017a; Bui et al., 2017b; Bui et al., 2015; Bui et al., 2012; Bui et al., 2018; Duc et al., 2012; Tran et al., 2019).

Therefore, the approach of HA in fuzzy control is further extended in the present work by proposing the problem of optimal design of HAC which is based on scaling factors of variables for vibration control of a benchmark structure subjected to earthquake excitations.

2. Problem under consideration

As presented in Fig. 1, a three-storey building model with active bracing system (ABS), installed on the first floor, subjected to seismic excitation $\ddot{x}_0$ is considered (Du et al., 2011; Lim et al., 2006). The structural parameters are given as m_i =1000 kg, c_i = 1.407 kNs/m, and k_i = 980 kN/m, where i = 1 ÷ 3, respectively (Du et al., 2011; Lim et al., 2006). The motion equations of the structure system with actuator saturation can be condensed into the matrix form as:

$$[M]\{\ddot{x}\}+[C]\{\dot{x}\}+[K]\{x\}=\{B\}\text{sat}(u)-\{\delta\}\ddot{x}_0 \quad (1)$$

where $\{x\}=\left[x_1\ x_2\ x_3\right]^{\mathrm{T}}$, $\{\delta\}=\left[m_1\ m_2\ m_3\right]^{\mathrm{T}}$ and $\{B\}=\left[1\ 0\ 0\right]^{\mathrm{T}}$.

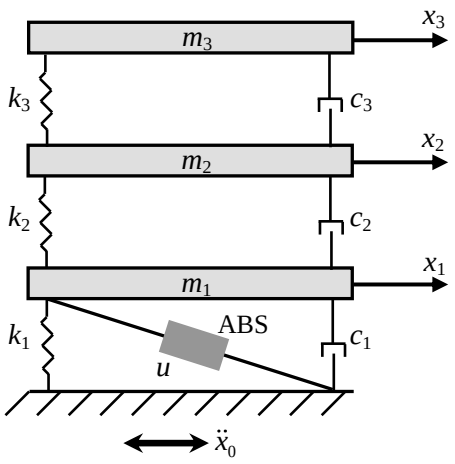

Figure 1. The structural system.

Saturation of the control force u is expressed as follows:

$$\text{sat}(u)=\begin{cases} u_{\max} & \text{if} \quad u \geq u_{\max} \\ u & \text{if} \quad -u_{\max} \leq u \leq u_{\max} \\ -u_{\max} & \text{if} \quad u \leq -u_{\max} \end{cases} \quad (2)$$

The $n \times n$ (n = 3) mass matrix $[M]$, damping matrix $[C]$ and stiffness matrix $[K]$ are expressed as below:

$$[M]=\begin{bmatrix} m_1 & 0 & ... & 0 & 0 \\ 0 & m_2 & ... & 0 & 0 \\ ... & ... & ... & ... & ... \\ 0 & 0 & ... & m_{n-1} & 0 \\ 0 & 0 & ... & 0 & m_n \end{bmatrix}$$

$$C_{ij}=\begin{cases} c_i+c_{i+1} & i=j\neq n \\ c_n & i=j=n \\ -c_i & i-j=1 \\ -c_{i+1} & j-i=1 \\ 0 & \text{Else.} \end{cases} \quad (3)$$

$$K_{ij} = \begin{cases} k_i + k_{i+1} & i = j \neq n \\ k_n & i = j = n \\ -k_i & i - j = 1 \\ -k_{i+1} & j - i = 1 \\ 0 & \text{Else.} \end{cases}$$

where m_i, c_i and k_i ($i = 1 \div n$) is the i^{th} storey mass, damping and stiffness, respectively.

3. Designing of the controllers

In this section, SQM values of a HA structure are presented in subsection 3.1, subsection 3.2 shows control diagram and components of the hedge-algebras-based fuzzy controllers containing two-input state variables x_1 and $\dot{x}_1$ and one-output control variable u in vibration control of the structure mentioned in section 2, parameters of the controllers HAC and *op*HACs are given in subsections 3.3 and 3.4, respectively while discussions are presented in subsection 3.5.

3.1. SQM values of a HA structure

The idea and basic formulas of HA theory based on definitions, theorems, and propositions in Ho and Long (2007) and Ho et al. (2008) are recalled, summarized and presented in Bui et al. (2015). Specific semantically quantifying mapping (SQM) values of a HA structure will be illustrated through as bellow. Consider a HA structure *AX* of a linguistic variable with its term-set *X* as follows:

$$AX = (X, G, C, H, \leq) \quad (4)$$

where $G = (Small, Big) = (c^-, c^+)$ is the set of primary terms; $C = (\mathbf{0}, \mathbf{W}, \mathbf{1})$ where $\mathbf{0}$, $\mathbf{W}$ and $\mathbf{1}$ are specific constants called *absolutely Small*, *neutral* and *absolutely Big*, respectively; $H = (Very, Little) = H^+ \cup H^-$ is the set of hedges; and $\leq$ is a partially ordering relation on X. It is assumed that $H^- = (h_{-1}, ..., h_{-q})$, where $h_{-1} < h_{-2} < ... < h_{-q}$, $H^+ = (h_1, ..., h_p)$, where $h_1 < h_2 < ... < h_p$. In this case, $p = q = 1$, and as a result, SQM values φ for all linguistic values of a linguistic variable with its term-set X are determined through only two independent fuzziness parameters, which are $0 < fm(c^-)$ and $\mu(h^-) < 1$, where $fm(c^-)$ is fuzziness measure of c^- and $\mu(h^-)$ is fuzziness measure of h^-. Some typical linguistic values with SQM of the term-set X are presented in Table 1, in which, $\mu(h^-) = fm(c^-) = 0.5$. It is found from Table 1 that, by utilizing HA theory to describe term-set of a linguistic variable, inherent order relationships among vague terms (linguistic values) existing in the term-set are completely guaranteed without any purposeful interventions.

Table 1. SQM φ of linguistic values of *AX*

V Sm	*Sm*	*L Sm*	***W***	*L Bi*	*Bi*	*V Bi*
0.125	0.25	0.375	0.5	0.625	0.75	0.875

3.2. Hedge-algebras-based fuzzy controller

A proportional-derivative hedge-algebras-based controller for the system, including two state variables (x_1 and $\dot{x}_1$) and one control variable (u), is introduced. Its control diagram is shown in Figure 2.

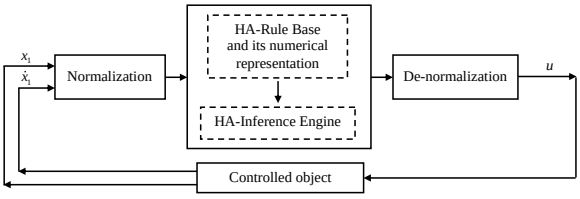

Figure 2. Control diagram for the system.

It is assumed that the scaling factors of the state variables x_1 and $\dot{x}_1$ and the control variable u are given by a (m), b (m/s) and c (N), respectively.

Normalization: In order to convert the reference domain of the linguistic variables into their SQM domain, linear normalization schemes of the state variables are used as shown in Figure 3, where x_{1s} and $\dot{x}_{1s}$ are the SQM values of x_1 and $\dot{x}_1$, respectively.

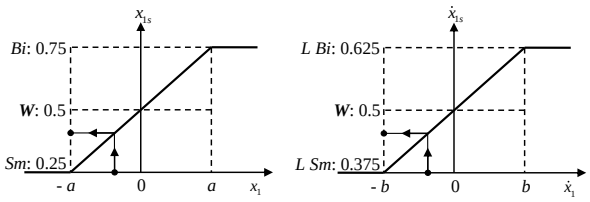

Figure 3. Normalization of the state variables.

HA-Rule Base and its numerical representation: The HA-Rule Base containing fifteen rules is

presented in Table 2. Based on SQM φ of the linguistic values of the variables (Table 1), the numerical representation of the HA-Rule Base is tabulated in Table 3. Hence, the numerical representation of the HA-Rule Base can be described in term of a grid of nodes, each node presents one fuzzy rule in Table 2, as shown in Figure 4, where u_s is the SQM value of u. This grid is hereafter called the HA-numerical grid.

Table 2. HA-Rule Base

x_1 \ $\dot{x}_1$	*L Sm*	***W***	*L Bi*
Sm	*V Sm*	*Sm*	*L Sm*
L Sm	*Sm*	*L Sm*	***W***
W	*L Sm*	***W***	*L Bi*
L Bi	***W***	*L Bi*	*Bi*
Bi	*L Bi*	*Bi*	*V Bi*

Table 3. Numerical representation of HA-Rule Base

x_{1s} \ $\dot{x}_{1s}$	0.375	0.5	0.625
0.25	0.125	0.25	0.375
0.375	0.25	0.375	0.5
0.5	0.375	0.5	0.625
0.625	0.5	0.625	0.75
0.75	0.625	0.75	0.875

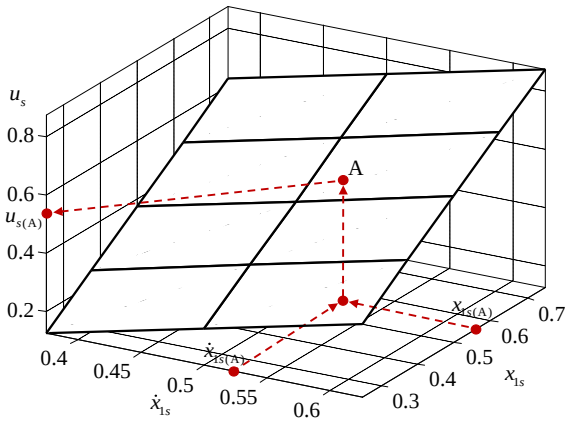

Figure 4. HA-numerical grid (planar grid).

The HA inference engine: The HA inference engine to calculate the SQM value u_s of the control variable from given SQM values x_{1s} and $\dot{x}_{1s}$ of the state variables is also illustrated in Figure 4. For example, if $x_{1s} = x_{1s(A)}$ and $\dot{x}_{1s} = \dot{x}_{1s(A)}$ then $u_s = u_{s(A)}$. Hence, the SQM value u_s of the control variable is the height of point A in the $(x_{1s}, \dot{x}_{1s}, u_s)$ coordinate system.

De-normalization: The obtained SQM value u_s must be converted to the real value of the control variable. This step can be re-used the normalization process, called de-normalization step. Figure 5 shows linear de-normalization scheme of the control variable.

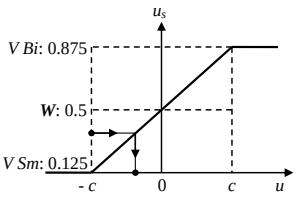

Figure 5. De-normalization of control variable.

3.3. Optimal design of HAC

The controller HAC presented in subsection 3.3 is designed by the predetermined values of the scaling factors of the variables. In this subsection, the optimal hedge-algebras-based fuzzy controllers (*op*HACs) are now constructed based on an optimal problem as follows:

* Objective function: it is decided by designers. In this study, objective functions used to design the *op*HACs are described as follows:

i) Minimise the peak storey drift, which is related to structural safety:

$$J_1 = \max_{t,i}\left(\frac{|d_i(t)|}{d_{\max}}\right) \to \min \qquad (5)$$

ii) Minimise the peak absolute acceleration, which is related to human tolerance:

$$J_2 = \max_{t,i}\left(\frac{|\ddot{x}_{ai}(t)|}{\ddot{x}_{a\max}}\right) \to \min \qquad (6)$$

where, $d_i(t)$ and $d_{\max}$ respectively are storey drift of the i^{th} floor and peak storey drift in the

controlled and uncontrolled responses, $\ddot{x}_{ai}(t)$ and $\ddot{x}_{a\max}$ respectively are absolute acceleration of the i^{th} floor and peak absolute acceleration in the controlled and uncontrolled responses, $u(t)$ is the control force vector, T = 15 s is the total time of simulation, Δt = 0.001 s is the time step size.

* Design variables: the scaling factors of the state variables, a and b, are here considered as design variables with following conditions:

$$a \in [0.001 \quad 0.01]; b \in [0.01 \quad 0.1] \tag{7}$$

* Constraints: the optimal problem will be solved without any "boundary (overlap) conditions" of the linguistic values of the variables because their inherent semantic order is completely guaranteed.

Therefore, components and operation principle of the controllers *op*HACs are similar to those of the controller HAC. The difference among them is the values of the scaling factors of the state variables, a and b.

The optimal HACs using objective functions J_1 and J_2 are denoted by *op*HAC1 and *op*HAC2, respectively.

4. Numerical results

The 1940 El Centro earthquake is used as excitation load $\ddot{x}_0$ of the structure, where the peak ground acceleration is scaled to 0.112 g.

By using the module GA of Matlab software to optimize the system, the obtained results are presented as below. The scaling factors of the state variables, a and b, are arranged in Table 4. The values of J_1 and J_2 are presented in Table 5, where the results obtained by different methods are also involved for comparison.

Table 4. Scaling factor of state variables

Scaling factor	HAC	*op*HAC1	*op*HAC2
a	0.0046	0.0038	0.0062
b	0.0500	0.0564	0.0464

Table 5. The values of J_1 and J_2

Controllers	J_1	J_2
LQR (Lim et al., 2006)	0.657	0.584
MBBC (Lim et al., 2006)	0.381	0.548
SSMC (Lim et al., 2006)	0.388	0.560
Lim et al. (2006)	0.396	0.543
Du et al. (2011)	0.41	0.53
HAC	0.432	0.523
*op*HAC1	0.428	0.556
*op*HAC2	0.450	0.484

It is found that the proposed controllers provide good results in term of reduction of the peak storey drift J_1 as well as the peak absolute acceleration J_2. The criterion J_2 has higher reduction ratios for the *op*HAC2 in comparison with remaining controllers.

Time responses of the storey drift of the first floor, the absolute acceleration of the top floor, and the control force are shown in Figure 5 and the maximum storey drift and absolute acceleration of the floors are plotted in Figure 6.

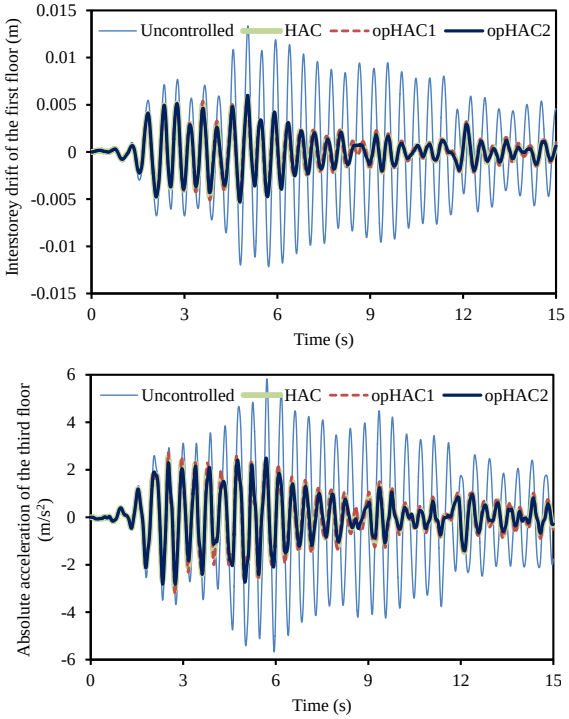

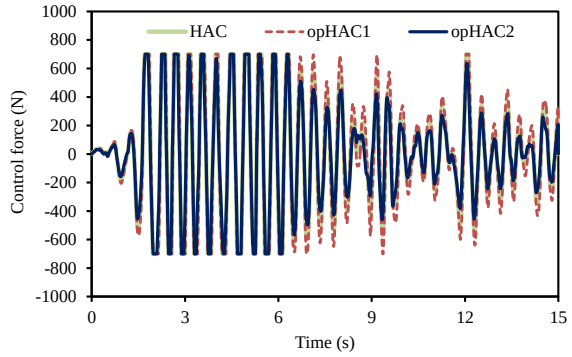

Figure 5. Time responses of the structure.

From the multi-objective optimization view point, Pareto front which describe trade-off level among the objective functions J_1 and J_2 is shown in Figure 7.

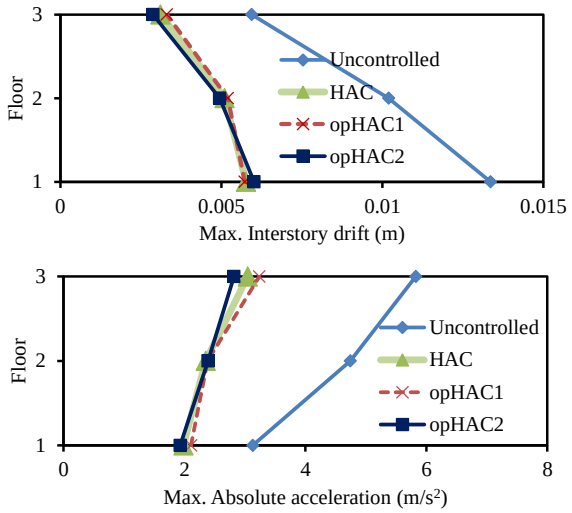

Figure 6. Maximum storey drift and absolute acceleration of the floors.

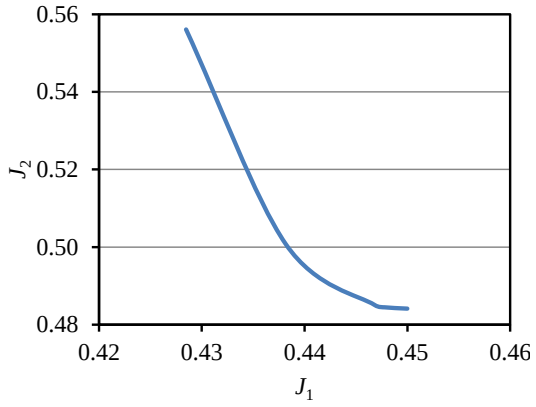

Figure 7. Pareto front of J_1 and J_2.

For example, if the peak storey drift expressed by the criterion J_1 is decreased in order to ensure the structural safety, the peak absolute acceleration expressed by the criterion J_2 is increased. It is emphasized that Pareto front shown in Figure 7 provide many trade-off solutions to make appropriate choices based on practical requirements that have to be carefully considered.

5. Conclusions

In this paper, the optimal hedge-algebras-based fuzzy controllers based on tuned scaling factors of state variables have been designed to active control of a 3-DOF structure subjected to earthquake excitation. Main results are summarized as follows:

- The hedge-algebras-based fuzzy controller has high performance in reducing dynamic response of the structure.

- The tuned scaling factors of state variables are more appropriate for the system instead of using factors determined by experience.

- From the multi-objective optimization view point, the Pareto fronts provide many trade-off solutions to make appropriate choices based on practical requirements.

Considering structural parameter uncertainties or input time delay in the proposed controllers and analyzing influence of locations of actuators as well as influence of interactions among actuators in the same time but at different stories on the control performance will be further developed in vibration control of civil structures subjected to natural hazards as strong earthquakes and winds.

Acknowledgements

This research is funded by Vietnam National Foundation for Science and Technology Development (NAFOSTED) under grant number “107.01-2017.306”.

References

Anh N. D., H. L. Bui, N. L. Vu and D. T. Tran (2013). Application of hedge algebra-based fuzzy controller to active control of a structure against

earthquake. *Structural Control and Health Monitoring*, 20, pp. 483-495.

Bui H.-L., T.-A. Le and V.-B. Bui (2017a). Explicit formula of hedge-algebras-based fuzzy controller and applications in structural vibration control. *Applied Soft Computing*, 60, pp. 150-166.

Bui H.-L., C.-H. Nguyen, V.-B. Bui, K.-N. Le and H.-Q. Tran (2017b). Vibration control of uncertain structures with actuator saturation using hedge-algebras-based fuzzy controller. *Journal of Vibration and Control*, 23, pp. 1984-2002.

Bui H.-L., C.-H. Nguyen, N.-L. Vu and C.-H. Nguyen (2015). General design method of hedge-algebras-based fuzzy controllers and an application for structural active control. *Applied Intelligence*, 43, pp. 251-275.

Bui H.-L., D.-T. Tran and N.-L. Vu (2012). Optimal fuzzy control of an inverted pendulum. *Journal of vibration and control*, 18, pp. 2097-2110.

Bui V.-B., Q.-C. Tran and H.-L. Bui (2018). Multi-objective optimal design of fuzzy controller for structural vibration control using Hedge-algebras approach. *Artificial Intelligence Review*, 50, pp. 569-595.

Du H., N. Zhang and F. Naghdy (2011). Actuator saturation control of uncertain structures with input time delay. *Journal of Sound and Vibration*, 330, pp. 4399-4412.

Duc N. D., N.-L. Vu, D.-T. Tran and H.-L. Bui (2012). A study on the application of hedge algebras to active fuzzy control of a seism-excited structure. *Journal of Vibration and Control*, 18, pp. 2186-2200.

Ho N. C., V. N. Lan and L. X. Viet (2008). Optimal hedge-algebras-based controller: Design and application. *Fuzzy Sets and Systems*, 159, pp. 968-989.

Ho N. C. and N. V. Long (2007). Fuzziness measure on complete hedge algebras and quantifying semantics of terms in linear hedge algebras. *Fuzzy Sets and Systems*, 158, pp. 452-471.

Ho N. C. and H. V. Nam (2002). An algebraic approach to linguistic hedges in Zadeh's fuzzy logic. *Fuzzy Sets and Systems*, 129, pp. 229-254.

Ho N. C. and W. Wechler (1990). Hedge algebras: an algebraic approach to structure of sets of linguistic truth values. *Fuzzy sets and systems*, 35, pp. 281-293.

Ho N. C. and W. Wechler (1992). Extended hedge algebras and their application to fuzzy logic. *Fuzzy sets and systems*, 52, pp. 259-281.

Kim H.-S. and J.-W. Kang (2012). Semi-active fuzzy control of a wind-excited tall building using multi-objective genetic algorithm. *Engineering Structures*, 41, pp. 242-257.

Lim C., Y. Park and S. Moon (2006). Robust saturation controller for linear time-invariant system with structured real parameter uncertainties. *Journal of Sound and Vibration*, 294, pp. 1-14.

Marinaki M., Y. Marinakis and G. E. Stavroulakis (2010). Fuzzy control optimized by PSO for vibration suppression of beams. *Control Engineering Practice*, 18, pp. 618-629.

Pourzeynali S., H. Lavasani and A. Modarayi (2007). Active control of high rise building structures using fuzzy logic and genetic algorithms. *Engineering Structures*, 29, pp. 346-357.

Rao A. R. M. and K. Sivasubramanian (2008). Multi-objective optimal design of fuzzy logic controller using a self configurable swarm intelligence algorithm. *Computers & Structures*, 86, pp. 2141-2154.

Thenozhi S. and W. Yu (2013). Advances in modeling and vibration control of building structures. *Annual Reviews in Control*, 37, pp. 346-364.

Tran D.-T., V.-B. Bui, T.-A. Le and H.-L. Bui (2019). Vibration control of a structure using sliding-mode hedge-algebras-based controller. *Soft Computing*, 23, pp. 2047-2059.

Uz M. E. and M. N. Hadi (2014). Optimal design of semi active control for adjacent buildings connected by MR damper based on integrated fuzzy logic and multi-objective genetic algorithm. *Engineering Structures*, 69, pp. 135-148.

The 5th International Conference on Engineering Mechanics and Automation (ICEMA 5)
Hanoi, October 11÷12, 2019

Optimal positions of TMDs for the transverse vibration control of beams using Taguchi method

Nguyen Van Khang, Nguyen Phong Dien, Hoang Trung Nghia, Nguyen Thi Van Huong

Dept. Applied Mechanics, School of Mechanical Engineering, Hanoi University of Science and Technology

Abstract

Tuned mass dampers are frequently used to suppress the undesired vibrations in structural systems. In this paper, the mode technique and Taguchi method are applied for transverse vibration suppression of Euler-Bernoulli beams subjected to forced harmonic excitations by means of multiple dynamic vibration absorbers (DVAs). The aim of the present study is to examine the influence of positions of the dynamic absorbers on the beam vibration suppression in the global control problem. Numerical tests are performed to show the effectiveness of the optimal positions.

Key Words: Dynamic vibration absorber, Taguchi method, harmonic excitations, optimal positions, passive vibration control

1. Introduction

Beams are conventional constructions such as house beams, suspended cables in suspension structures, air traffic control towers, wind turbine columns, etc. In the course of the work, these structures are exposed to the effects of wind exploitation and operation. Under the influence of changing external frequencies, beam structures appear to be subjected to forced vibration. Since the frequency of the external force changes over a wide band, there is the possibility of a resonance which can cause structural damage. Therefore, the reduction of the amplitude range of the structure at resonant frequencies is a necessary task. In order to determine the resonance frequencies and to investigate the behavior of the system under the action of external forces, the natural frequencies of the structure must first be evaluated [1-4]. Vibration amplitudes at different points in the structure excited by the external force in a wide frequency band are then calculated. The Tuned Mass Dampers (TMDs) are usually used to reduce the vibrations of the beams.

Optimal parameter design for dynamic vibration absorber installed in beam structures becomes an interesting problem in recent years. It is well known that Taguchi method for the product design process may be divided into three stages: system design, parameter design, and tolerance design. Taguchi method of parameter design is successfully applied to many mechanical systems: an acoustic muffler, a gear/pinion system, a spring, an electro-hydraulic servo system, a dynamic vibration absorber. In each system, the design parameters to be optimized are identified, along with the desired response [5-7]. The problem of optimal installation positions of TMDs has not been studied much [8-9].

In this paper, a model of the beam subjected to harmonic forces is presented, in which a system

of translational dynamic vibration absorbers is attached.The effectiveness of vibration reduction by TMDs is then investigated. The optimization procedure for position parameters of the attached absorbers in a beam subjected to an uniform harmonic force is also presented.

2. Transverse vibration equations of a beam with TMDs

Let us consider the model of a Euler-Bernoulli beam of length L and the flexural rigidity EI, which is attached with a number of multiple Tuned Mass Dampers (TMDs) at positions $x = \eta_j$ ($j = 1,\ldots, n_a$) as shown in Fig. 1. For simplicity, it is assumed that the considered beam is homogeneous with an uniform cross section, where w is the dynamic deflection, u_j is vertical coordinate of j-absorber, k_j, d_j, m_j are stiffness, damping coefficients and mass of

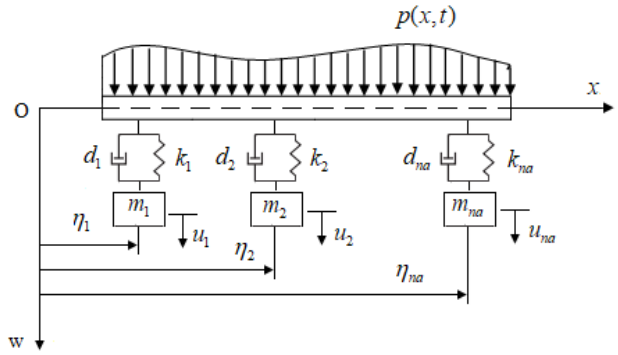

Fig. 1 Modelling of a beam with TMDs

j-absorber, respectively, and $p(x,t)$ is the distributed force.

Using the method of substructures, the system is now divided into $n_a + 1$ substructures, namely, the beam structure and n_a absorbers (Fig. 2).

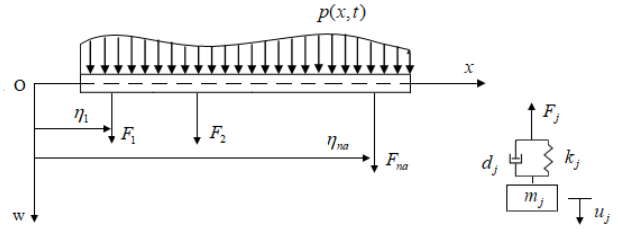

(a) (b)

Fig. 2 Substructures, (a) beam, (b) absorber

Reaction forces have the following form

$$F_j(t) = k_j(u_j - \mathrm{w}_{\eta j}) + d_j(\dot{u}_j - \dot{\mathrm{w}}_{\eta j}) \quad (1)$$

(j = 1, 2,…, n_a)

where

$$\mathrm{w}_{\eta j} = \mathrm{w}(\eta_j, t), \quad \dot{\mathrm{w}}_{\eta j} = \frac{\partial \mathrm{w}(\eta_j, t)}{\partial t}$$

Using Newton's second law, the equation describing the vibration of j-absorber can be expressed in the form

$$m_j \ddot{u}_j = -F_j \quad (2)$$

Substitution of Eq. (2) into Eq. (1) yields the vibration equation of j-absorber

$$m_j\ddot{u}_j + d_j\dot{u}_j + k_j u_j = k_j w_{hj} + d_j \dot{w}_{hj} \quad (j = 1,2,...,n_a) \quad (3)$$

Applying the basic principles of dynamics, the equation that describes transverse vibration of beam including internal friction is [1, 2]

$$\mu\left(\frac{\partial^2 w}{\partial t^2} + c^{(e)}\frac{\partial w}{\partial t}\right) + EI\left[\frac{\partial^4 \mathrm{w}}{\partial x^4} + c^{(i)}\frac{\partial^5 w}{\partial x^4 \partial t}\right] = p(x,t) + \sum_{j=1}^{n_a} F_j \delta(x - \eta_j) \quad (4)$$

In Eq. (4), μ denotes mass per length unit, $c^{(e)}$, $c^{(i)}$ are damping coefficient and internal friction coefficient per length unit of the beam, respectively, and Delta-Dirac function $\delta(x-\eta_j)$ is defined by

$$\delta(x-\eta_j) = \begin{cases} 1 & when \quad x = \eta_j \\ 0 & when \ x \neq \eta_j \end{cases} \quad (5)$$

The vibration equations according to Eqs. (3) and (4) are a mixed set of ordinary and partial differential equations. Four boundary conditions, two at x = 0 and two at x = L, and the initial conditions must be specified to find the solution of this set.

Using Ritz-Galerkin method, the solution of Eqs. (3) and (4) can be found in the form

$$w(x,t) = \sum_{r=1}^{n_b} X_r(x) q_r(t) \quad (6)$$

where $X_r(x)$ denotes the mode shape of the beam and $q_r(t)$ is the generalized displacement to be determined. Substituting Eq. (6) into Eqs. (4) and (3), we find

$$\ddot{q}_k(t)+(c^{(e)}+c^{(i)}\omega_k^2)\dot{q}_k(t)+\omega_k^2 q_k(t)= \frac{\int_0^l p(x,t)X_k(x)dx}{\mu\int_0^l X_k^2(x)dx}+\frac{\sum_{j=1}^{n_a}\int_0^l F_j(t)X_k(x)\delta(x-\eta_j)dx}{\mu\int_0^l X_k^2(x)dx} \quad (k=1,...,n_b) \tag{7}$$

and

$$m_j\ddot{u}_j(t)+d_j\dot{u}_j(t)+k_j u_j(t)-d_j\sum_{r=1}^{n_b}X_r(\eta_j)\dot{q}_r(t) -k_j\sum_{r=1}^{n_b}X_r(\eta_j)q_r(t)=\mathrm{m}_j g\ (j=1,2,...,n_a) \tag{8}$$

where ω_k is eigenfrequency of the beam [1-4]. Using the notations

$$2\delta_k=(c^{(e)}+c^{(i)}\omega_k^2),\quad D_k=\mu\int_0^l X_k^2(x)dx=const,, \quad \alpha_k(t)=\int_0^l p(x,t)X_k(x)dx, \tag{9}$$

$$h_k(t)=\frac{\alpha_k(t)}{D_k}, \tag{10}$$

it follows from Eq. (7) that

$$\ddot{q}_k(t)+2\delta_k\dot{q}_k(t)+\omega_k^2 q_k(t)= h_k(t)+\frac{1}{D_k}\sum_{j=1}^{n_a}\int_0^l F_j(t)X_k(x)\delta(x-\eta_j)dx \tag{11}$$

Substitution of Eq. (6) into Eq.(1) yields

$$F_j(t)=d_j\left[\dot{u}_j(t)-\dot{\mathrm{w}}_{\eta j}\right]+k_j\left[u_j(t)-w_{\eta j}\right] \quad F_j(t)=d_j\dot{u}_j(t)+k_j u_j(t) -d_j\sum_{r=1}^{n_b}X_r(\eta_j)\dot{q}_r(t)-k_j\sum_{r=1}^{n_b}X_r(\eta_j)q_r(t) \tag{12}$$

in which $d_j,k_j,X_r(\eta_j)$ $(j=1,2,...,n_a)$ are the known constants. According to the property of the Delta-Dirac function we have

$$\sum_{j=1}^{n_a}\int_0^l F_j(t)X_k(x)\delta(x-\eta_j)dx=\sum_{j=1}^{n_a}F_j(t)X_k(\eta_j) \tag{13}$$

Substitution of Eq. (12) into Eq. (13) one obtains

$$\begin{aligned}\sum_{j=1}^{n_a}F_j(t)X_k(\eta_j)&=\sum_{j=1}^{n_a}d_j\dot{u}_j(t)X_k(\eta_j)+\sum_{j=1}^{n_a}k_j u_j(t)X_k(\eta_j)\\ &-\sum_{j=1}^{n_a}\sum_{r=1}^{n_b}d_j X_r(\eta_j)X_k(\eta_j)\dot{q}_r(t)\\ &-\sum_{j=1}^{n_a}\sum_{r=1}^{n_b}k_j X_r(\eta_j)X_k(\eta_j)q_r(t)\\ &=\sum_{j=1}^{n_a}X_k(\eta_j)\left[d_j\dot{u}_j(t)+k_j u_j(t)\right]\\ &-\sum_{j=1}^{n_a}X_k(\eta_j)\left\{\sum_{r=1}^{n_b}\left[d_j\dot{q}_r(t)+k_j q_r(t)\right]X_r(\eta_j)\right\}\end{aligned} \tag{14}$$

Substitution of Eq. (14) into Eq. (11) yields

$$\begin{aligned}&\ddot{q}_k(t)+2\delta_k\dot{q}_k(t)+\omega_k^2 q_k(t)\\ &=h_k(t)+\frac{1}{D_k}\sum_{j=1}^{n_a}X_k(\eta_j)\left[d_j\dot{u}_j(t)+k_j u_j(t)\right]\\ &-\frac{1}{D_k}\sum_{j=1}^{n_a}X_k(\eta_j)\left\{\sum_{r=1}^{n_b}\left[d_j\dot{q}_r(t)+k_j q_r(t)\right]X_r(\eta_j)\right\}\\ &(k=1,2,...,n_b)\end{aligned} \tag{15}$$

It follows from Eq. (8) that

$$\begin{aligned}&\sum_{r=1}^{n_b}\left[d_j\dot{q}_r(t)+k_j q_r(t)\right]X_r(\eta_j)\\ &=m_j\ddot{u}_j(t)+d_j\dot{u}_j(t)+k_j u_j(t)\end{aligned} \tag{16}$$

By substituting Eq. (16) into Eq.(15) leads to

$$\begin{aligned}&\ddot{q}_k(t)+2\delta_k\dot{q}_k(t)+\omega_k^2 q_k(t)\\ &=h_k(t)+\frac{1}{D_k}\sum_{j=1}^{n_a}X_k(\eta_j)\left[d_j\dot{u}_j(t)+k_j u_j(t)\right]\\ &-\frac{1}{D_k}\sum_{j=1}^{n_a}X_k(\eta_j)\left[m_j\ddot{u}_j(t)+d_j\dot{\mathrm{u}}_j(t)+k_j u_j(t)\right]\\ &(k=1,2,...,n_b).\end{aligned} \tag{17}$$

Eqs. (17) and (8) consist of a system of $n=n_a+n_b$ ordinary differential equations that

describes the vibration of the beam with dynamic vibration absorbers.

We consider now the vibration of the beam under harmonic excitation $p(t) = p_0 \sin \Omega t$. According to Eqs. (9) and (10) we have

$$\alpha_k(t) = [p_0 \int_0^l X_k(x)dx] \sin \Omega t,$$

$$h_k(t) = \frac{p_0 \int_0^l X_k(x)dx}{D_k} \sin \Omega t$$

It follows that

$$h_k(t) = \hat{h}_k \sin \Omega t; \quad \hat{h}_k = \frac{p_0 \int_0^l X_k(x)dx}{D_k} \qquad (18)$$

In this case, Eq. (17) has the following form

$$\ddot{q}_k(t) + 2\delta_k \dot{q}_k(t) + \omega_k^2 q_k(t) = \hat{h}_k \sin \Omega t - \frac{1}{D_k} \sum_{j=1}^{n_a} m_j X_k(\eta_j) \ddot{u}_j \quad (k = 1,2...,n_b) \qquad (19)$$

Using the notations $\frac{d_j}{m_j} = 2\delta_{jc}$; $\frac{k_j}{m_j} = \omega_{jc}^2$,

it follows from Eq. (8) that

$$\ddot{u}_j(t) + 2\delta_{jc} \dot{u}_j(t) + \omega_{jc}^2 u_j(t) = 2\delta_{jc} \sum_{r=1}^{n_b} X_r(\eta_j) \dot{q}_r(t) + \omega_{jc}^2 \sum_{r=1}^{n_b} X_r(\eta_j) q_r(t) \qquad (20)$$
$$(j = 1,2,...,n_a)$$

Eqs. (19) and (20) are a system of $n = n_a + n_b$ differential equations describing the transverse vibration of the beam with a number of dynamic vibration absorbers under the action of harmonic distributed forces, where $X_k(x)$ denotes the eigenfunction. The particular form of $X_k(x)$ depends on the boundary conditions of the beam.

3. The complex frequency response function

In this section, we consider cases that often occur in structural, when the excitation frequency Ω is approximately equal to the fundamental frequency ω_1 of the beam ($\Omega \approx \omega_1$). It follows from Eq. (19) and Eq.(20) that

$$\ddot{q}_1(t) + 2\delta_1 \dot{q}_1(t) + \omega_1^2 q_1(t) = \hat{h}_1 \sin \Omega t - \frac{1}{D_1} \sum_{j=1}^{n_a} m_j X_k(\eta_j) \ddot{u}_j \qquad (21)$$

$$\ddot{u}_j(t) + 2\delta_{jc} \dot{u}_j(t) + \omega_{jc}^2 u_j(t) = 2\delta_{jc} X_1(\eta_j) \dot{q}_1(t) + \omega_{jc}^2 X_1(\eta_j) q_1(t) \qquad (22)$$
$$(j = 1,2,...,n_a)$$

We use the following notations

$$x_s = q_1, \ \omega_s = \omega_1, \ \delta_s = \delta_1, \ \hat{h}_s = \hat{h}_1 \qquad (23)$$

Eq. (21) can be written in the following form

$$\ddot{x}_s(t) + 2\delta_s \dot{x}_s(t) + \omega_s^2 x_s(t) = \hat{h}_1 \sin \Omega t - \frac{1}{D_1} \sum_{j=1}^{n_a} m_j X_1(\eta_j) \ddot{u}_j \qquad (24)$$

The solution of Eqs. (22) and (24) can now be found using the method of frequency response function.

We note that $\cos \Omega t = \mathrm{Re} e^{i\Omega t}$, $\sin \Omega t = \mathrm{Im} e^{i\Omega t}$, Eq. (24) can thus be written as follows

$$\ddot{x}_s(t) + 2\delta_s \dot{x}_s(t) + \omega_s^2 x_s(t) = \hat{h}_s e^{i\Omega t} - \frac{1}{D_1} \sum_{j=1}^{n_a} m_j X_1(\eta_j) \ddot{u}_j \qquad (25)$$

We find the solutions of Eqs. (22) and (25) in the form

$$x_s(t) = H_s e^{i\Omega t}, \ u_j(t) = H_{jc} e^{i\Omega t} \qquad (26)$$

Substitution of Eq. (26) into Eqs. (25) and (22) leads to the system of linear algebraic equations

$$\left[\omega_s^2 - \Omega^2 + i2\delta_s \Omega\right] H_s = \hat{h}_s + \frac{\Omega^2}{D_1} \sum_{j=1}^{n_a} m_j X_1(\eta_j) H_{jc} \qquad (27)$$

$$\left[\omega_{jc}^2 - \Omega^2 + 2i\delta_{jc}\Omega\right] H_{jc} = \left[\omega_{jc}^2 + 2i\delta_{jc}\Omega\right] X_1(\eta_j) H_s \qquad (28)$$
$$(j = 1,2,...,n_a)$$

From Eq. (28) one has

$$H_{jc} = \frac{\left[\omega_{jc}^2 + i2\delta_{jc}\Omega\right]}{\left[\omega_{jc}^2 - \Omega^2 + i2\delta_{jc}\Omega\right]} X_1(\eta_j) H_s \quad (j = 1,2,...,n_a) \tag{29}$$

Substitution of Eq. (29) into Eq. (27) yields

$$\left[\omega_s^2 - \Omega^2 + i2\delta_s\Omega\right] H_s = \hat{h}_s + H_s \frac{\Omega^2}{D_1} \sum_{j=1}^{n_a} \left(m_j X_1^2(\eta_j) \frac{\left[\omega_{jc}^2 + i2\delta_{jc}\Omega\right]}{\left[\omega_{jc}^2 - \Omega^2 + i2\delta_{jc}\Omega\right]} \right) \tag{30}$$

By introducing

$$a_{11} = \sum_{j=1}^{n_a} m_j X_1^2(\eta_j) \frac{\left[\omega_{jc}^2 + i2\delta_{jc}\Omega\right]}{\left[\omega_{jc}^2 - \Omega^2 + i2\delta_{jc}\Omega\right]} \tag{31}$$

Eq. (30) can be written in the following form

$$\left(\left[\omega_s^2 - \Omega^2 + i2\delta_s\Omega\right] - \frac{\Omega^2}{D_k} a_{11} \right) H_s = \hat{h}_s \tag{32}$$

From Eq. (32) one obtains

$$H_s = \frac{\hat{h}_s}{\left[\omega_s^2 - \Omega^2 + i2\delta_s\Omega\right] - \dfrac{\Omega^2}{D_1} a_{11}} \tag{33}$$

in which

$$\begin{aligned} a_{11} &= \sum_{j=1}^{n_a} m_j X_1^2(\eta_j) \frac{\left[\omega_{jc}^2 + i2\delta_{jc}\Omega\right]}{\left[\omega_{jc}^2 - \Omega^2 + i2\delta_{jc}\Omega\right]} \\ &= \sum_{j=1}^{n_a} m_j X_1^2(\eta_j) \frac{\left[\omega_{jc}^2 + i2\delta_{jc}\Omega\right]\left[\omega_{jc}^2 - \Omega^2 - i2\delta_{jc}\Omega\right]}{\left[\left(\omega_{jc}^2 - \Omega^2\right)^2 + 4\delta_{jc}^2\Omega^2\right]} \\ &= \sum_{j=1}^{n_a} m_j X_1^2(\eta_j) \frac{\left[\omega_{jc}^2\left(\omega_{jc}^2 - \Omega^2\right) + 4\delta_{jc}^2\Omega^2 - 2i\delta_{jc}\Omega^3\right]}{\left[\left(\omega_{jc}^2 - \Omega^2\right)^2 + 4\delta_{jc}^2\Omega^2\right]} \end{aligned} \tag{34}$$

The denominator in Eq. (33) takes the form

$$\begin{aligned} \left[\omega_s^2 - \Omega^2 + i2\delta_1\Omega\right] + \frac{\Omega^2}{D_1} a_{11} &= \left[\omega_s^2 - \Omega^2 + i2\delta_s\Omega\right] \\ &+ \frac{\Omega^2}{D_1} \sum_{j=1}^{n_a} m_j X_1^2(\eta_j) \frac{\left[\omega_{jc}^2\left(\omega_{jc}^2 - \Omega^2\right) + 4\delta_{jc}^2\Omega^2\right]}{\left[\left(\omega_{jc}^2 - \Omega^2\right)^2 + 4\delta_{jc}^2\Omega^2\right]} \\ &- i \sum_{j=1}^{n_a} m_j X_1^2(\eta_j) \frac{2\Omega^3\delta_{jc}}{\left[\left(\omega_{jc}^2 - \Omega^2\right)^2 + 4\delta_{jc}^2\Omega^2\right]}. \end{aligned}$$

By introducing the following notations

$$\begin{aligned} a &= \left[\omega_s^2 - \Omega^2\right] \\ &- \frac{\Omega^2}{D_1} \sum_{j=1}^{n_a} m_j X_1^2(\eta_j) \frac{\left[\omega_{jc}^2\left(\omega_{jc}^2 - \Omega^2\right) + 4\delta_{jc}^2\Omega^2\right]}{\left[\left(\omega_{jc}^2 - \Omega^2\right)^2 + 4\delta_{jc}^2\Omega^2\right]} \end{aligned} \tag{35}$$

$$b = 2\delta_s\Omega + \frac{\Omega^2}{D_1} \sum_{j=1}^{n_a} m_j X_1^2(\eta_j) \frac{2\Omega^3\delta_{jc}}{\left[\left(\omega_{jc}^2 - \Omega^2\right)^2 + 4\delta_{jc}^2\Omega^2\right]} \tag{36}$$

function H_s can be written in the form

$$H_s = \frac{\hat{h}_s}{a + ib} = \frac{\hat{h}_s(a - ib)}{a^2 + b^2} \tag{37}$$

The modulus of the complex frequency response function H_s can now be calculated by the following formula

$$H = \left|\tilde{H}_s\right| = \frac{\hat{h}_s}{\sqrt{a^2 + b^2}} \tag{38}$$

The optimum problem is stated as follows: Find the parameters of dynamic vibration absorbers m_j, c_j, k_j (j = 1, 2,... n_a) which minimize the objective function according to Eq. (38).

4. Select the mass parameters of vibration absorbers

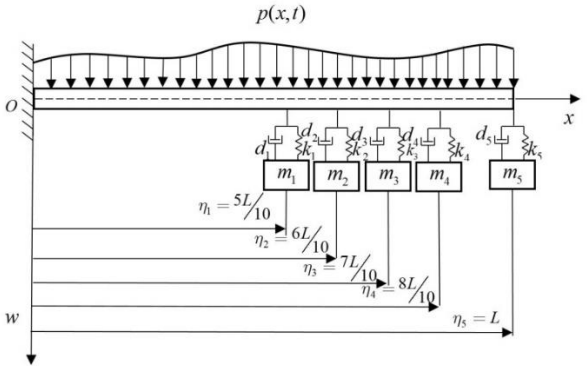

Fig. 3 A clamped -free Beam with five TMDs

To determine the mass of vibration absorbers on the beam, we consider the bending vibration of a clamped-free beam with five TMDs at the installation positions η_i ($i = 1,...,5$) as shown in Fig. 3. The parameters of the beam are listed in Tab. 1. From the given parameters, it results $\omega_1 = 110.3005\ s^{-1}$. We consider the case

of the distributed load $p = p_0 \sin \Omega t$, where $p_0 = 15$ N/m and $\Omega = \omega_1$.

Table 1. Beam parameters

Parameters	Value	Unit
EI	3.06×10^7	Nm^2
L	10	m
μ	24.5	kg/m
$c^{(e)}$	0.4	1/s
$c^{(i)}$	0.0001	s/m

In order to optimize the parameters of the TMDs, a procedure is proposed here to determine the masses of TMDs based on the mode shapes of the beam. The mode shape of the beam and the mode function values at the installation positions are shown in Fig. 4 [3, 4].

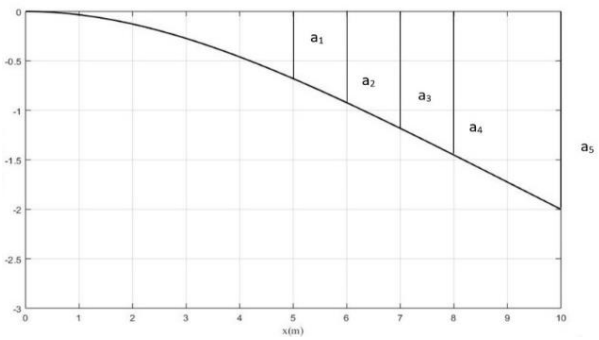

Fig. 4 First mode shapes of the beam and the positions of the TMDs

The masses of TMDs are calculated as follows

$$m_j = \alpha a_j, \quad j = 1,2...,5.$$

where α is scaling factor, a_j denotes the value of the first mode shape at position η_j. According to [4] we get

$$a_1 = \|X_1 \ \eta_1\| = 0.6790, \ a_2 = \|X_1 \ \eta_2\| = 0.9223$$
$$a_3 = \|X_1 \ \eta_3\| = 1.1818, \ a_4 = \|X_1 \ \eta_4\| = 1.4510$$
$$a_5 = \|X_1 \ \eta_5\| = 2.0000$$

From the designers' experience, Suppose that the total mass of the TMDs is approximately 1% of the mass of the beam. This yields

$$m_1 + m_2 + m_3 + m_4 + m_5 =$$
$$\alpha \ a_1 + a_2 + a_3 + a_4 + a_5 \ = \frac{m_b}{100}$$

It follows that

$$\alpha = \frac{m_b}{100 \ a_1 + a_2 + a_3 + a_4 + a_5} = 0.393$$

Hence, the masses of TMDs can then be determined as

$$m_1 = 0.2669, \ m_2 = 0.3625, \ m_3 = 0.4644,$$
$$m_4 = 0.5702, \ m_5 = 0.7860 \ \ kg \ .$$

5. Using the Taguchi method to determine optimal parameters of the TMDs

In [10-14], Nguyen Van Khang and his colleagues have proposed a convenient algorithm to determine the optimal parameters of vibration dampers installed on the main system based on Taguchi's methodology. Based on this, the optimal parameters d and k of 5 different TMDs at $\Omega = \omega_1$ as mentioned above can be determined and given in Table 2.

Table 2. The optimal parameters of the TMDs

	m (kg)	d (Ns/m)	k (N/m)
TMD1	0.2669	0.625	414.5
TMD2	0.3625	1.000	536.6
TMD3	0.4644	1.500	723.0
TMD4	0.5702	2.500	900.0
TMD5	0.7860	3.000	1225.4

When the excitation frequency Ω changes in a neighborhood with the first-order specific frequency ω_1, the optimum parameters of TMDs with weighting factors are given in Tab.3

and the corresponding frequency response functions shown in Fig. 5. From fig 5, it can be seen that the vibration of the beam at position $x = L$ using 5 TMDs mounted at L/2, 6L/10, 7L/10, 8L/10 and 10L/10 is 2.665 (mm), compared to before damper mounting is 44.01 (mm). Thus beam fluctuations are significantly reduced by about 94%.

Table 3. The optimal parameters of the TMDs using the weighting factors

	m (kg)	*d* (Ns/m)	*k* (N/m)
TMD1	0.2669	1.6257	386.6
TMD2	0.3625	1.7942	523.2
TMD3	0.4644	3.2942	670.1
TMD4	0.5702	2.5696	793.5
TMD5	0.7860	4.6654	1165.4

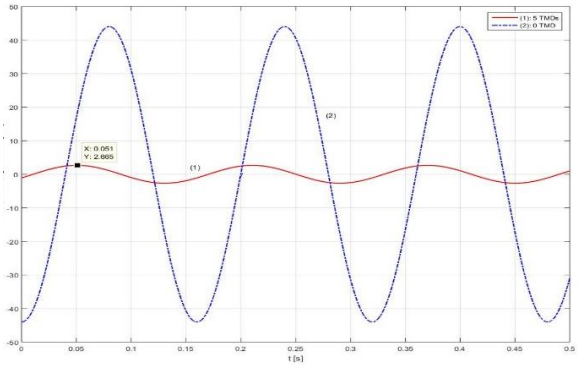

Fig. 5 The time response of a beam at x=L with 5 TMDs and without TMD

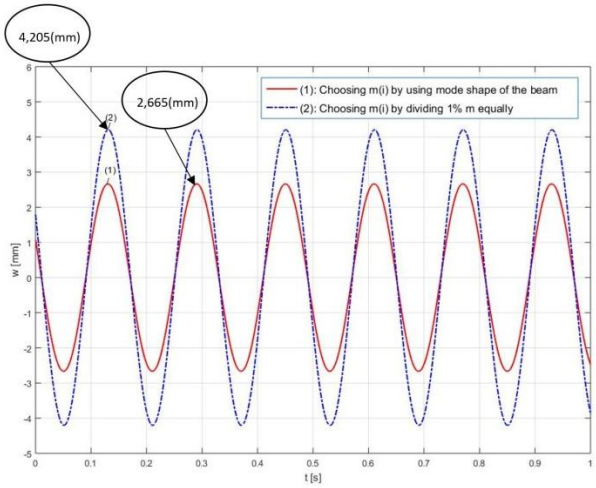

Fig. 6 Time response of beam at position $x = L$

The above results are based on the selection parameters using vibration modes. Now we choose the masses of TMDs so that the total mass is equal to 1% of the mass of the beam, and divide them evenly into the mass of the 5 TMDs. Then, Taguchi method is applied to determine the parameters for hardness and viscosity resistance. The calculation results are shown in Fig. 6.

6. Optimal installation positions of dynamic vibration absorbers

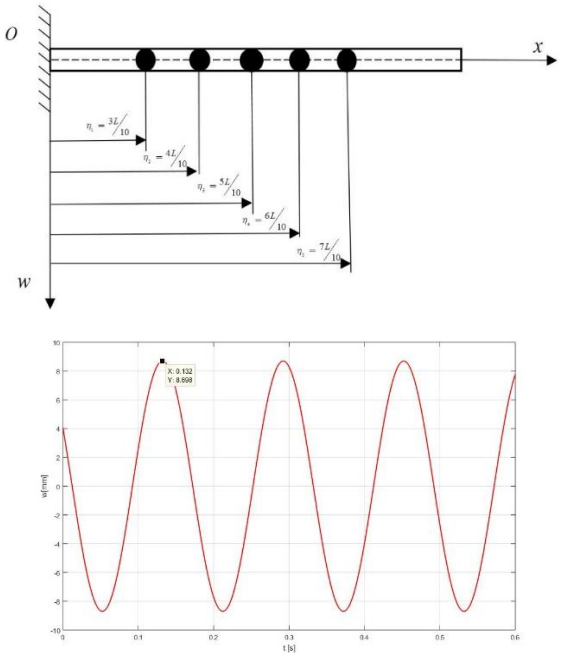

Fig. 7 Installation positions of TMDs at *3L/10, 4L /10, 5L /10, 6L/10, 7L /10*

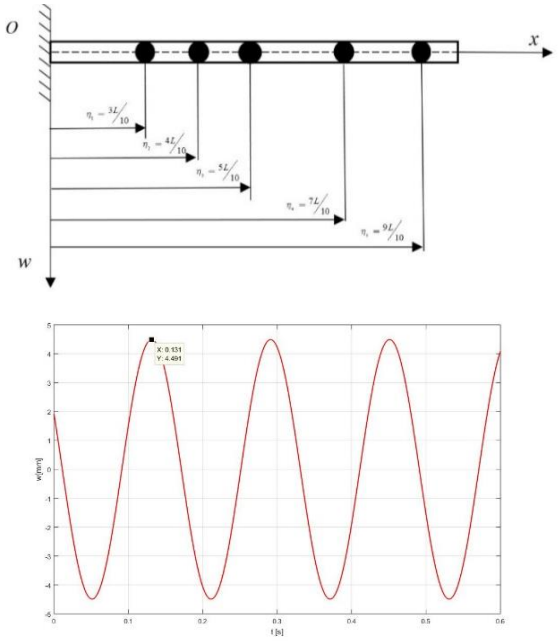

Fig. 8 Installation positions of TMDs at 3/*10, 4L/10, 5L/10, 7L/10, 9L/10*

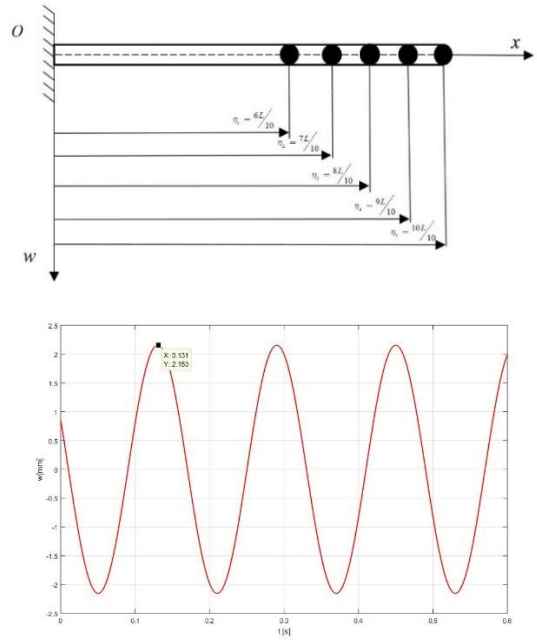

Fig. 9 Installation positions of TMDs at *6L/10, 7L/10, 8L/10, 9L/10, 10L/10*

Using the optimal parameters of TMDs in Tab.3, the vibration efficiency of installation positions of the TMDs is now investigated. Three options for installing the TMDs are shown in Figs 7, 8 and 9.

From the above calculation results, the results of vibration reduction according to the positions of TMDs are summarized in Tab. 4.

Table 4. Vibration amplitude and vibration reduction effect by various installation locations

Installation positions of TMDs	5L/10	5L/10	3L/10
	6L/10	6L/10	4L/10
	7L/10	7L/10	5L/10
	8L/10	9L/10	6L/10
	10L/10	10L/10	7L/10
w (mm)	2.665	2.46	8.698
Effect (%)	93.94	94.41	80.24
Installation positions of TMDs	3L/10	6L/10	3L/10
	4L/10	7L/10	5L/10
	5L/10	8L/10	7L/10
	7L/10	9L/10	9L/10
	9L/10	10L/10	10L/10
w (mm)	4.491	2.153	2.622
Effect (%)	89.80	95.11	94.04

From these numerical simulation results, it can be seen that: if the positions of the TMDs are installed in the area of large mode amplitudes, the effect of vibration reduction is great, and the amplitude of vibration of the beam becomes small.

7. Conclusion

Determination of the optimal locations of TMDs for the vibration control of beams is an important problem in practical application, but there is little research concerning this problem. In this paper, we propose an approach to determine the optimal mass parameters of TMDs using the mode of beam transverse vibration. The determination of the optimal parameters of viscous elements and spring elements based on an algorithm derived from the

experimental method by Taguchi. If the TMDs is installed closer to the position at large amplitudes in vibration mode, the vibration reduction effect is greater and the amplitude of the bending vibrations becomes smaller. The numerical simulation results show the optimal results of the proposed method. It can be shown that the vibration damping effect is approx. 90%.

Acknowledgements

This paper was completed with the financial support of the Vietnam National Foundation for Science and Technology Development (NAFOSTED).

References

[1] L. Meirovitch, *Dynamics and Control of Structures*, John Wiley & Sons, New York 1990.

[2] D.J. Inman, *Vibration with Control*, John Wiley & Sons, Chichester 2006.

[3] S.G. Kelly, *Fundamentals of Mechanical Vibrations*, McGraw-Hill, Singapore 1993.

[4] S.S. Rao, *Vibration of Continuous Systems*, John Wiley & Sons, New Jersey 2007.

[5] Roy R.K, *A Primer on the Taguchi Method*, Society of Manufacturing Engineers, USA,2010.

[6] Taguchi G, Chowdhury S, Wu Y, *Taguchi's Quality Engineering Handbook''*, John Wiley & Sons, New Jersey, 2005.

[7] Zambanini. R.A, *The application of Taguchi's method of parameter design to the design of mechanical systems*, Master Thesis, Lehigh University,1992.

[8] W.Latas, Optimal positions of tunable translational and rotational dynamic absorbers in global vibration control in beams, *Journal of Theoretical and Applied Mechanics*, 53(2), pp. 467-476, Warsawa 2015.

[9] S.S. Patil, P.J. Awasare, Vibration suppression along the segment of beams by imposing nodes using multiple vibrations absorbers, Journal of Vibration Analysis, Measurement, and Control,Vol.4(1), pp.29-39, ColumbiaInternational Publishing 2016.

[10] Nguyen Van Khang, Vu Duc Phuc, Nguyen Thi Van Huong, Do The Duong, Optimal control of transverse vibration of Euler-Bernoulli beam with multiple dynamic vibration absorbers using Taguchi's method, *Vietnam Journal of Mechanics*, VAST, Vol.40, No.3, pp.1-19, Hanoi 2018.

[11] Nguyen Van Khang, Vu Duc Phuc, Do The Duong, Nguyen Thi Van Huong, A procedure for optimal design of a dynamic vibration absorber installed in the damped primary system based on Taguchi's method. *Vietnam Journal of Science and Technology*, VAST, Vol. 55, No.5, pp. 649-661, Hanoi 2018.

[12] Nguyen Van Khang, Do The Duong, Nguyen Thi Van Huong, Nguyen Duc Thi Thu Dinh, Vu Duc Phuc , Optimal control of vibration by multiple tuned liquid dampers using Taguchi method, *Journal of Mechanical Science and Technology* 33(4), pp.1563-1572, 2019.

[13] Vu Duc Phuc, *Optimal control of vibration by combining many dynamic vibration absorbers* (in Vietnamese), PhD thesis, Hanoi University of Science and Technology, 2019.

[14] Nguyen Van Khang,Nguyen Phong Dien, Vu Duc Phuc, Do The Duong, Nguyen Thi Van Huong, Optimal positions of dynamic absorbers in transverse vibration control of beams, *Proc. of the National Conference on Dynamics and Control*, Danang 2019.

The 5th International Conference on Engineering Mechanics and Automation (ICEMA 5)
Hanoi, October 11÷12, 2019

Force Control of an Upper limb Exoskeleton for Perceiving Reality using Force Feed Forward Model.

Nguyen Cao Thang[a], Manukid Parnichkun[b], Phan Thi Tra My[a], Nguyen Nhu Hieu[a], Le Thi Hong Gam[c], and Pham Ngoc Chung[d].

[a] Institute of Mechanics, 264 DoiCan street, BaDinh district, Hanoi, Vietnam, email: caothang2002us@yahoo.com, nhuhieu1412@gmail.com, tramypt86@gmail.com
[b] Asian Institute of Technology, Bangkok, Thailand,email: manukid@ait.ac.th
[c] Thai Nguyen University of Education
[d] Hanoi University of Mining and Geology, email: chunghumg86@gmail.com

Abstract

This paper presents the development of a 3 DOF upper limb exoskeleton having force sensing ability. The device can sense the force feedback of real object, and can produce necessary forces through joints at wrist, elbow and shoulder. When the user exerts force at handle, the force is measured by a force sensor placed at the handle. A force feed forward control is used to compensate the force generated by user to perform some tasks: moving freely and lifting some objects vertically and horizontally. Simulation result shows the force control for a desired loading motion.

Key Words: upper limb exoskeleton, perceiving reality, force feedback, sensing and actuation, feed forward control.

1. Introduction

Arm exoskeleton have a force feedback system for perceiving reality that has been studied and developed worldwide from the US (O'Malley M. K. et. al. (2011), Perry C. et. al. (2007)), UK, France, Italy (Frisoli A. et al. (2007), Vertechy et. al., 2009) to Japan, South Korea, Thailand (Chaiyaporn S., Manukid P., (2019)), and Vietnam. An arm exoskeleton designed with a force feedback system is an electromechanical system of sensors and actuators. The device is designed to measure angle of rotation of the joints on the arm of the wearer and can generate control forces when interacting with other objects. It can move according to the wearer's instructions. It also has a force feedback system that is capable of transmitting feedback force to controller to help the robot perceiving reality. Virtual Reality technology (Perceiving Reality) includes real-time simulation and creating realistic sensations related to multiple senses. The senses for sensing as see, hear, touch, smell, taste. Between these five senses, force feedback can be applied to the sense of touch for a realistic feel.

Recently, detailed reviews of force feedback arm exoskeleton studies were given by Lo H. and Xie S. (2012), and in Proietti T. et al. (2016). Force feedback control has many advantages. For example, when working with micro objects, the dexterity, precision, and speed are significantly improved when the force acting on the object can be felt and controlled in real

time. The development of such miniature manipulations has a great interest in surgery and microrobotics and was reported by Carrozza M. C., et. al. (2003). Manipulating micro objects with a traditional micro gripper without the usual built-in force sensor requires a camera to get visual feedback. This approach results in a simple 2D image and a lack of sense of contact between the manipulator and the object in contact, making it difficult to locate the tool (Carrozza M. C., et. al. (2003)). A micro gripper with built-in load cell can solve this, therefore, is suitable for holding objects firmly, while avoiding any excessive pressure on the object. The application of force feedback control helps to recreate, according to human activity, the forces sensing ability for robot during the controlled process in a remote or virtual environment (O'Malley M. K. et. al. (2011), Chaiyaporn S. et al. (2019)).

Am arm exoskeleton can be used for one of the four main applications depending on its control algorithm (Perry C. et al. (2007)): a) Rehabilitation - human interaction with robot in two ways active and passive, b) Haptic device, human interacting with the virtual environment, while arm exoskeleton respond to human a force to perceive reality, c) Master device, master-slave control, interaction force appear in the master sent by the robot - slave, d) Assisted human device - when worn on the wearer can feel the lighter load with the help of the arm exoskeleton.

For example, the L-EXO (Light Exoskeleton - Frisoli (2007), Vertechy (2009)), is a force-feedback arm designed for the human arm that can generate control force in the right hand, the end point can be held by the wearer (Figure 1). The control force responds from the end of the arm exoskeleton in the direction along the moving trajectory or in the direction perpendicular to the trajectory. Due to the design towards weight reduction, L-EXO developed by Frisoli, (2007) used a motor system connected to cables and reduction gears to increase the control torque at the joints. The limitation of L-EXO (2007) is the quality of controlling the feedback force due to the use of cables. As a result, a new design for L-EXO design (Vertechy et. al., 2009), was developed. The control algorithm in (Vertechy et. al., 2009) is proposed so that the arm exoskeleton can operate in two modes: passive and active and have been applied in habilitation for patients.

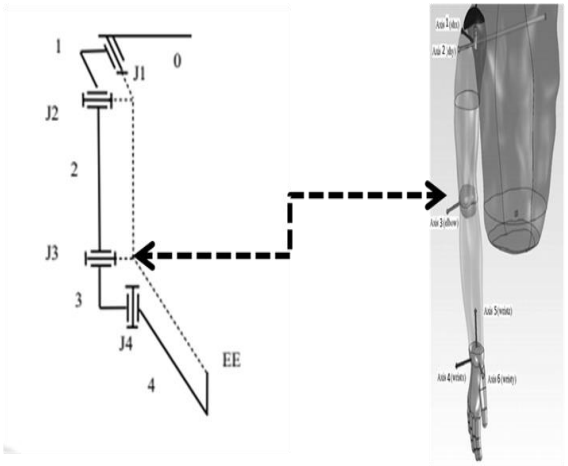

Figure 1. Model of arm exoskeleton structure with force feedback (4 degrees of freedom) including 2 joints in the shoulder, 2 joints in the elbow (J1-J4), 5 links (0-4), and a place to hold the hand (EE) (Dimitar Chakarov et. al. (2017)).

The application of engines in the joints will increase the quality of the feedback force, but the engines also need to generate more torque to offset the engine's weight. Due to the increased torque, the engines also need to increase both in volume to ensure sufficient power and can cause the quality of the feedback force to degradation. In recent, Chaiyaporn S., Manukid P., (2019) have designed, built a control model using a Particle Swarm Optimization (PSO) control algorithm for upper limb exoskeleton. Sensors measuring the rotation angle of joints are incremental encoder (1024 pulses/ cycle). The 6 DOF device has load cells measuring the force exerted by the user, actuators (for shoulder elbow, and wrist), specialized DAQ card connected to a PC, PC as a controller and display force feedback to user. Figure 2 will show its subsystems. To enhance the control quality of the arm exoskeleton, the AIT upper limb exoskeleton system has control system using PSO algorithm.

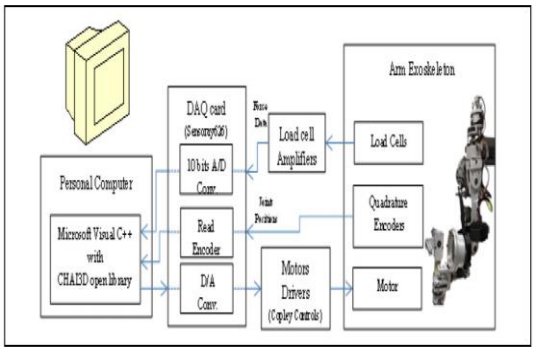

Figure 2: Architecture of AIT upper limb exoskeleton (Chaiyaporn S., Manukid P., (2019)).

The importance as well as practical significance of force control for the robot is increasing with the development of robotics. There are some projects in Institute of Mechanics (VAST) in this interesting field. We focus on an arm exoskeleton and a leg exoskeleton with force feedback using force control. These devices contain both hardware and software and are designed and built for rehabilitation purpose. Besides, control algorithm design is a very important part of this research. As the result, the available controls such as Proportional Integral Derivative (PID) control (Nguyen Q. Hoang et al. (2016)), position/force control (Pham Van Bach Ngoc et al., (2008)), adaptive control (Vu Minh Hung et al., (2014)) will be implemented for force control of the device.

This paper presents the development of a 3 DOF upper limb exoskeleton having force sensing ability. The device can track the position and magnitude of the contact force between the user's hand and the robot. Furthermore, it can produce necessary forces through joints at wrist, elbow and shoulder. One scenario is considered in which there are two steps. Step 1 starts when the user exerts force at handle, the force is measured by a force sensor placed at the handle. The position of the force is tracked by angular sensors located at joints. In Step 2, a force feed forward control is used to control motors located at joints to compensate the force generated by the user to perform some tasks: moving freely and lifting some objects vertically and horizontally. Simulation result shows the performance of force control for a desired loading motion.

2. Model of a 3DOF upper limb exoskeleton

In this section, model of a 3DOF upper limb exoskeleton is explained as shown in figure 3. The arm exoskeleton system is a robotic chain including a joint at the shoulder (J1), a joint at the elbow (J2), and a joint at the wrist (J3), with 3 links (1-3): upper link (connecting shoulder and elbow), lower link (connecting elbow and wrist), and the last link for hand holding called handle (or end effector). Three geared DC motors are installed at these joints with sensors used to measure rotation angle. A force sensor is used to measure force exerted by the user's hand. Its D-H table is shown in table 1. Where, a_i = 0.32, 0.25, 0.1 (m) (i=1,2,3) are length of links i, respectively, set in table 1. The masses of links are set as $m_1 = m_2 = m_3 = 1$ (kg).

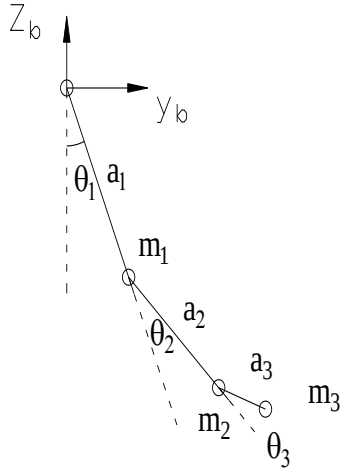

Figure 3: Structure of a 3 DOF upper limb exoskeleton

Table 1: Denavite - Hartenberge (D-H) table

Joint	A	d	α	θ
0	0	0	π/2	π/2
1	a_1 = 0.32	0	0	θ_1-π/2
2	a_2 = 0.25	0	0	θ_2
3	a_3 = 0.10	0	0	θ_3

In Table 1, the parameters a_i are constant. Only the variables θ_i (i=1..3) vary by rotation around

z_i axis. From D-H table, we can get the homogeneous transformation matrix using equation (1), (Chaiyaporn S., Manukid P., 2019).

$$A_n^{n-1} = Rot(z,\theta)Trans(0,0,d)Trans(l,0,0)Rot(x,\alpha) = \begin{bmatrix} \cos(\theta) & -\sin(\theta)\cos(\alpha) & \sin(\theta)\sin(\alpha) & l\cos(\theta) \\ \sin(\theta) & \cos(\theta)\cos(\alpha) & -\cos(\theta)\sin(\alpha) & l\cos(\theta) \\ 0 & \sin(\alpha) & \cos(\alpha) & d \\ 0 & 0 & 0 & 1 \end{bmatrix}; \quad (1)$$

The homogeneous transformation matrix that transform the reference coordinate {3}, which is at the end – effector to reference coordinate {0}, can be calculated by mutiplying individual transformation matrices as follows.

$$A_3^0 = A_1^0 A_2^1 A_3^2 \quad (2)$$

3. Force feed forward control

In this section, dynamics equation of motion is presented as the following.

$$M(\theta)\ddot{\theta}+C(\theta,\dot{\theta})\dot{\theta}+G(\theta)=u_r+J(\theta)^T F_h \quad (3)$$

Where,

u_r - Vector of control torques

F_h - Vector of forces exerted by user

$M(\theta)\ddot{\theta}$, $C(\theta,\dot{\theta})\dot{\theta}$, $G(\theta)$ - Vectors of inertia force, centrifugal force and gravity force, respectively, which are derived using Lagrange equation (Chaiyaporn S., Manukid P., 2019)

In this paper, we consider a scenario:

Step 1: At the beginning (t=0, $u_r=0$), a user move the robot by rotating its joints following a desired loading motion. The force of the user (F_h) is generated to compensate the weight of exoskeleton and the force of loading. The joints angles and the forces exerted by the user can be measured by the angular sensors and the force sensors which are installed in the robot.

Step 2: At the other time, the robot becomes active ($t=t_1, u_r \neq 0$), it uses the force exerted by the user as the input of feed forward control to compensate the user's force.

In Step 2, a force control is utilized to compensate the force exerted by the user. The force exerted by the user is desired to decrease to zero; or the force exerted by the user is considered as an error (or a disturbance); and the target of the control is to cancel the error.

In order to deal with this scenario, we use a feed forward control approach with formula (4).

$$u_{r(i+1)} = w_P.\left[J(\theta_{(i)})^T F_{h(i)} \right] + w_I.\left[\sum_{j=1}^{i-1} J(\theta_{(j)})^T F_{h(j)} \right] \quad (4)$$

Where:

- $\theta_{(i)}, F_{h(i)}$ are joints angles and force of the user which are sensed by encoders and force sensors at time t_i.
- w_P, w_I are constant gains.

In this scenario, firstly, the user applies some force to control the exoskeleton by moving in a desired loading motion using his own hand. By using a mechanical device as the exoskeleton, the burden in his hand will be compensated by the robot. Control block diagram of the upper limb exoskeleton is shown in figure 4.

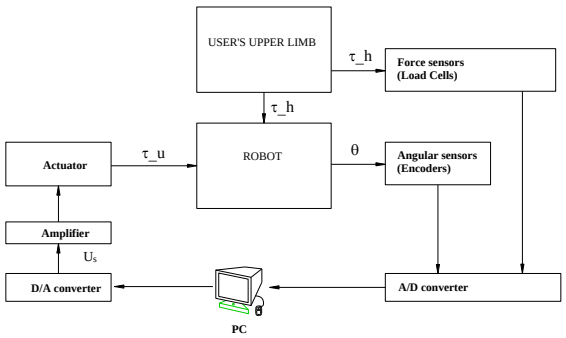

Figure 4. Control block diagram of upper limb exoskeleton

3. Simulation of force control

- Step 1: In this step, based on the desired

loading motion, the variables θ, w_P, w_I are given as follows.

$$\theta_{1(i)} = \omega_1 * t_i$$
$$\theta_{2(i)} = \omega_2 * t_i$$
$$\theta_{3(i)} = \omega_3 * t_i$$
$$\omega_1 = \omega_2 = \omega_3 = 0.025\pi \ (rad/s);$$
$$w_P = 1; \quad w_I = 1$$

The force exerted by the user F_h is an unknown parameter and measured by force sensor. In this paper, F_h is desired to decrease with time as expressed by formula (5). We move slowly so that the force F_h decreases moderately and the force control can have enough time to bear the load and the gravity force. For example, the total gravity force and load is set equal 50 (N).

$$F_{h(i)} = [F_{h(i)X}; F_{h(i)Y}; F_{h(i)Z}]^T = \\ = 50 * e^{(-0.1*t_i)} * [0;1;1]^T \ (N) \quad (5)$$

Using Matlab, the corresponding motion of the end effector and the force exerted by the user are shown in figures 5, 6, 7, 8, 9, respectively.

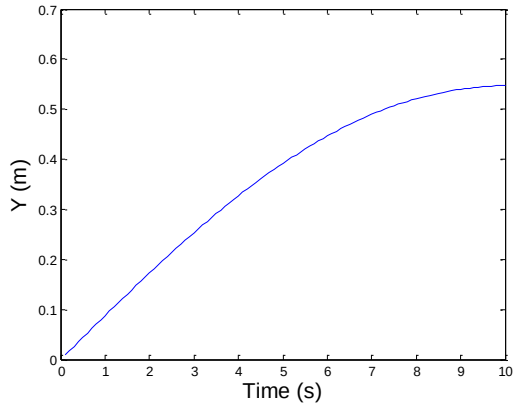

Figure 5. Motion of end effector in Y axis

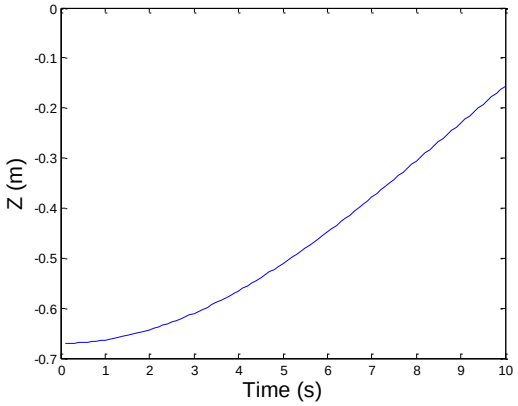

Figure 6. Motion of end effector in Z axis

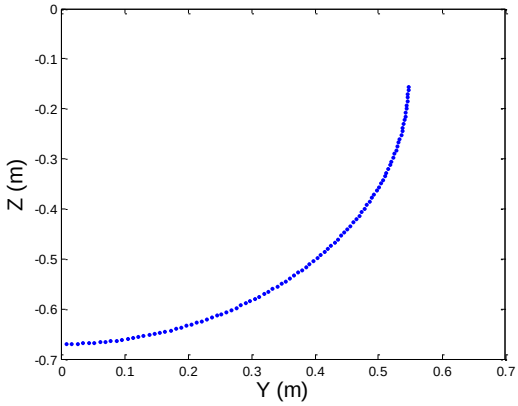

Figure 7. Workspace of end effector in YZ plane

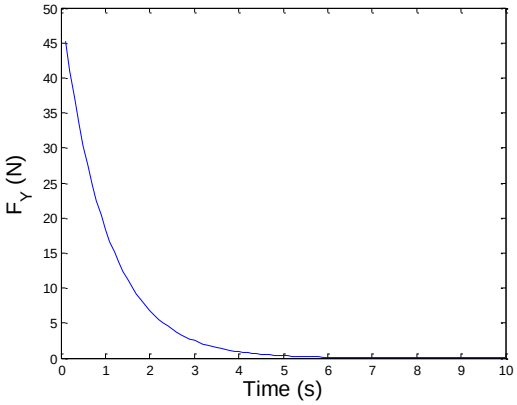

Figure 8. Force exert by user in Y direction

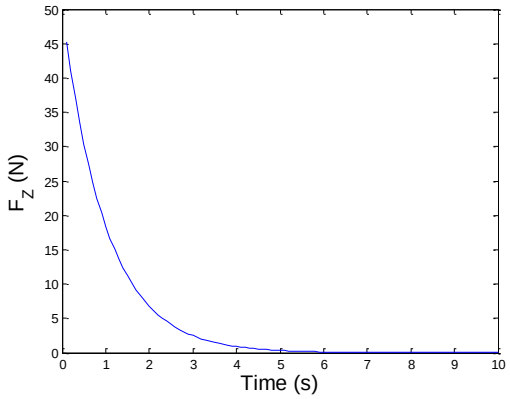

Figure 9. Force exert by user in Z direction

- Step 2: According to feed forward control as explained in section 3, the control torques are computed to compensate force exerted by hand of the user. By substituting the formula (5) into equation (4), the control torques at joint 1, 2, 3 are computed and shown in figures 10, 11, and 12, respectively.

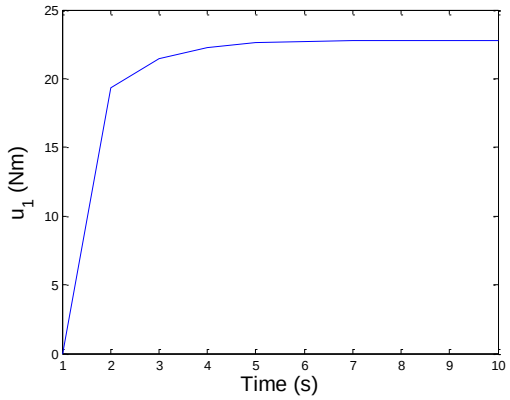

Figure 10. Torque u_1

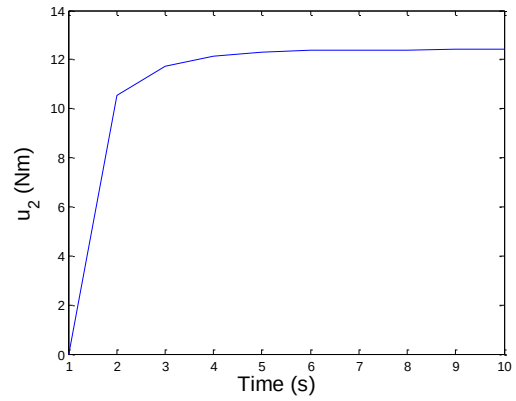

Figure 11. Torque u_2

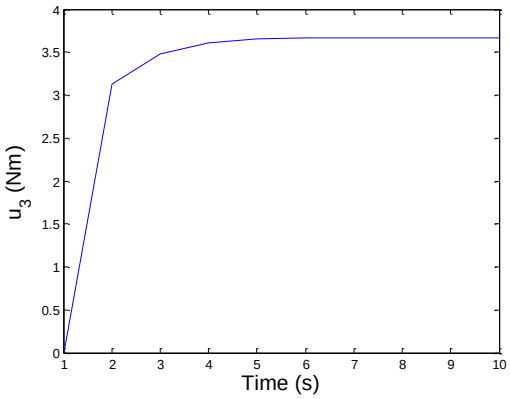

Figure 12. Torque u_3

However, this feed forward control still has some disadvantages and needs to be evaluated in a real model to adjust the parameters towards a more realistic control.

4. Conclusions

In the paper, the kinematic and dynamic analysis of a force feedback arm exoskeleton for sensing reality was presented. The device can sense the force feedback from reality and apply torque through joints at wrist, elbow and shoulder. When human exerts force at the handle, the exerted force is measured by a force sensor placed at the handle and used for computing torques generated at the joints based on configuration of the robot. The feed forward (FF) control was used to compensate the force exerted by the user. In this paper the force exerted by the user is desired to become zero value. Moreover, torques at joints generated by FF control could perform some tasks: moving freely and moving with loading. Simulation results showed the computed force control and the corresponding loading motions. The results could be used to estimate the maximum moment of DC motors for the design steps of the robot. In the future work, we plan to present some experiment test results to compare with the simulation results.

Acknowledgments

This research is supported by Vietnam Academy of Science and Technology (VAST), project VAST01.09/20-21 in which Nguyen Cao Thang is co-ordinator.

References

Carrozza M. C., Dario P., and Jay L. P. S. (2003), *Micromechanics in surgery*, Trans. Inst. Meas. Control, vol. 25, no. 4, pp. 309–327, 2003.

Chaiyaporn Silawatchananai, Manukid Parnichkun, *Haptic control of an arm exoskeleton for virtual reality using PSO based fixed structure H∞ control*, Journal of advance robotic systems, DOI: 10.1177/1729881419849198, May, 2019.

Dimitar Charakov, Ivanka Veneva, Mihail Tsveov, Dimitar Trifonov, *Design and control of a force reflecting Arm exoskeleton for Virtual reality Applications*, Proceedings of the 14th International Conference on Informatics in Control, Automation and Robotics, Vol. 2, pp. 335-342, 2017.

Frisoli A., Borelli L., Montagner A., Marcheschi S., Procopio C., Salsedo F., Bergamasco M., M. Carboncini, M. Tolaini, and B. Rossi (2007), *Arm rehabilitation with a robotic exoskeleleton in virtual reality*, in ICORR, pp. 631–642, IEEE, 2007.

Lo H. and Xie S. (2012), *Exoskeleton robots for upper-limb rehabilitation: State of the art and future prospects*, MED ENG PHYS, vol. 34, pp. 261–268, Apr. 2012.

Nguyen Q. Hoang, Nguyen V. Hoi, Nguyen T. Doan, Pham V. B. Ngoc, "*Automatic PD Controller Tuning Based on Genetic Algorithm for 3RRR Planar Parallel Robots"*, the 4th international conference on engineering mechanics and automation (ICEMA-4), August 25 ÷ 26, 2016, Hanoi, Vietnam

O'Malley M. K. (2011), *Mechanical design of distal arm exoskeleton for rehabilitation*, IEEE Int Conf Rehabil Robot. 2011: 5975428. doi: 10.1109/ICORR.2011.5975428.

Perry C. et. al. (2007), *Upper arm power exoskeleton design*, IEEE/ASME Transactions on Mechatronics, Volume 12, Issue 4 , 2007, pp. 408 - 417.

Pham Van Bach Ngoc, Han Sung Kim, *"Position/Force Control with a 6-DOF Compliance Device"*, International symposium on Robotics, Seoul Korea 2008.

Proietti T. et. al. (2016), *Upper-limb robotic exoskeletons for neurorehabilitation: a Review on control strategies*. IEEE Reviews in Biomedical Engineering, 2016, PP (99), pp.1-12.

Vertechy R., Frisoli A., Dettori A., Solazzi M., and Bergamasco M. (2009), *Development of a new exoskeleton for upper limb rehabilitation*, in ICORR, pp. 188–193, IEEE, 2009.

Vu Minh Hung, Trinh Quang Trung (2014), *Model reference adaptive control of a haptic feedback device for improving force performance*, Journal of SCIENCE & TECHNOLOGY DEVELOPMENT, Vol 17, No.K1- 2014, tr. 102-114.

The 5th International Conference on Engineering Mechanics and Automation (ICEMA-5)
Hanoi, October 11÷12, 2019

Application of TQWT denoising and spectral envelope in early fault detection of rolling element bearings

Nguyen Trong Du, Nguyen Phong Dien, Phung Minh Ngoc

School of Mechanical Engineering, Hanoi University of Science and Technology.
Email: du.nguyentrong@hust.edu.vn

Abstract

Bearings are always working under harsh environment, which makes them easily to failure. Condition monitoring of rolling element bearing is a key issue for maintaining the whole machinery system. Rolling element bearing faults in rotating systems are observed as impulses in the vibration signals, which are usually buried in noise. Many methods of vibration signal analysis based on fourier and wavelet tranform has been proposed to reduce noise. These methods have advantages and disadvantages. In this paper, a novel method based on wavelet tranform is proposed to detect the fault of bearings. Tunable Q-factor wavelet transform (TQWT) is used to decompose the original vibration bearing signal to several levels, the Hilbert envelope analysis method is applied to each wavelet decomposed signal. The fault feature of the bearing can be detected from the envelope spectrum. Both the simulation study and the application demonstrate the effectiveness of the proposed method.

Key Words: Gear fault, diagnosis, Neural network, wavelet packet, vibration signal.

1. Introduction

The rolling element bearing is one of the most important elements in the tranmission system, it is a component used between two parts that allows rotational or liner movement, reducing friction and enhancing performance to save energy. The working efficiency of rolling element bearing will be reduced when it is damaged, and generates abnormal transient signals during the operation conditions. Earlier research on bearing fault diagnosis was focused on the use of time domain or frequency domain to detect different types of defect. In the recent years, many different methods have been widely developed to detect bearing failure such as Fourier transform (Mallat, S., 1999), short-time Fourier transform (Heneghan et al., 1994), wavelet trasform (Peng, Z.K. & F.L. Chu, 2004), etc. A new wavelet transform called tunable Q-factor wavelet transform (TQWT) is proposed by Selesnick (Selesnick, I.W., 2011a) in recent years. Application of TQWT in machinery fault detection has proven its effectiveness (Cai, G. et al., 2013). However, when the background noise is strong, TQWT cannot precisely extract the fault features. Hilbert envelope spectrum (Huang, N.E. et al., 1998) is another classical method which has been widely used in fault detection of bearing. By incorporating the TQWT and Hilbert envelope spectrum, a novel method is proposed in this paper. Firstly, TQWT is applied to reduce a noise of original vibration signal and then decompose it into small components. The analytical method of Hilbert energy spectrum is used to analyze each decomposed signal. The fault feature of the bearing can be found in the Hilbert energy spectrum. The remaining parts are

organized as follows. Firstly, the theoretical basis of the method is introduced, which includes the TQWT and Hilbert energy spectrum analysis method. Then the proposed early fault detection method is applied to bearing fault feature extraction. Finally, conclusions are drawn in the last section.

2. Theoretical background

2.1 Denosing by Tunable Q-factor wavelet transform

Tunable Q-factor Wavelet Transform. The Q factor, which is used as a quantification of the oscillatory nature of a signal transient, affects the oscillatory behavior of the wavelet basis function. TQWT, whose *Q* factor can be tuned, is proposed to analyze the discrete time signal. There are two important factors in TQWT, one is the *Q* factor, another is the redundancy. *Q* measures the number of oscillations in the wavelet basis function, higher *Q* factor means more oscillatory cycles. *r* is the redundancy of the TQWT when it is computed using infinitely many levels. Suppose the TQWT decompose the original signal into *J* levels, the relations between the parameters are (Selesnick, I.W., 2011a):

$$Q=\frac{2}{\beta}-1,\ r=\frac{\beta}{1-\alpha},\ J=\frac{\log(\beta N/8)}{\log(1/\alpha)}$$

The characteristic parameters of the TQWT are given in Table 1.

Table 1: Component health by case

Components	Parameters
Q-factor	Q
Redundancy	r
Decomposition level	J
Low pass scaling parameter	α
High pass scaling parameter	β

As we all know, the measured sensor acceleration signal is affected by the ambient noise. So the *x* signal is rewritten as follows:

$$x(t)=y(t)+n \tag{1}$$

where *x* is the original signal, *n* is the noise, *y* is the return signal after noise cancellation.

To obtain a pure *y(t)* signal we have to go through a noise filter. The method used in this paper is *Basis pursuit denoising* (BPD) which is part of the TQWT algorithm(Selesnick, I.W., 2011b). BPD is essentially the optimal problem, we find the parameter **w** so that $\mathbf{A}=\left\|\mathbf{x}-TQWT^{-1}(\mathbf{w})\right\|_2^2+\sum_{i=1}^{J+1}\lambda_i\left\|\mathbf{w}_i\right\|_1$ reaches a minimum. Or rewrite:

$$\mathbf{w}=\arg\min_{\mathbf{w}}\left\|\mathbf{x}-TQWT^{-1}(\mathbf{w})\right\|_2^2+\sum_{i=1}^{J+1}\lambda_i\left\|\mathbf{w}_i\right\|_1 \tag{2}$$

With λ is the parameter of *TQWT*.

After finding **w**, which is shown in the figure 1 below, the denoised signal **y**(t) is estimated by taking the inverse *TQWT* tranform of **w**.

$$\mathbf{y}=TQWT^{-1}(\mathbf{w}) \tag{3}$$

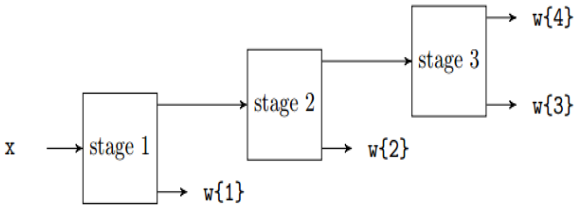

Figure 1: Flowt chart of BPD transform with three stages

2.2 Hilbert energy spectrum

During the period between 1996 and 1998, NE Huang et al (Huang, N.E. et al., 1998) proposed a method of empirical mode decomposition (EMD) and introduced concept and analysis method of the Huang spectrum based on the Hilbert transform named HHT by NASA, denoted as HHT. EMD has many excellent properties including the adaptability, orthogonality and completeness, and it has been widely used in many areas. By adopting EMD, the vibration signal is decomposed into a number of intrinsic mode function (IMF) components. If the functions are IMF components, the following two criteria must be satisfied:

1. *The number of zero points and extreme points, in the continuance of the signals, must be equal or no more than one point difference.*

2. *The mean of the upper envelope composed by the local maximum and lower envelope composed by the local minimum is zero at any time.*

EMD method has four procedures as follows (Dien, N.P. & N.T. Du, 2018):

1. *Search all local extreme points of the signal, and fit all local maximum by cubic spline to form upper envelope.*
2. *Fit all local minimum by cubic spline to form lower envelope. All data points are contained between upper and lower envelopes.*

3. The average of upper and lower envelope is denoted as m_1. And h_1 is calculated as follows

$$x(t) - m_1(t) = h_1(t) \quad (4)$$

If h_1 meets the principle of IMF, it will be the first IMF of decomposed signal.

4. Conversely, if h_1 does not meet the principle of IMF, it should be decomposed by above steps continually until we get h_{1k} (k is the times that h_1 is decomposed) that satisfies the regulations. The first IMF $c_1(t)$ is described as:

$$c_1(t) = h_{1k}(t) \quad (5)$$

As mentioned above, EMD can be used in describing how frequency components change with time and in generating the time–frequency distribution of signals. For the signal *x(t)*, we define *H(ω,t)* as the result of hilbert transform. Furthermore, $H^2(\omega,t)$ is Hilbert transform of $\left|x(t)^2\right|$, which is the energy density of signal *x(t)*. Accordingly, Hilbert energy spectrum is described as follows (Cheng, J. et al., 2007):

$$E(\omega) = \int_0^T H^2(\omega,t)\,dt \quad (6)$$

where *T* is the time range of sampling. Hilbert energy spectrum demonstrates how the energy of signal *x(t)* varies with frequency. And it can be used in analyzing amplitude and energy of each frequency of nonlinear and non-stationary signals with high resolution, while there is not information of time domain in results of Fourier transform.

After the original signal is decomposed by the *TQWT* into several levels, the hilbert energy spectrum method is applied for new signal to detect failure.

2.3. Proposed method to detect bearing fault

By using a combination of TQWT and Hilbert envelope analysis method, the authors propose the following model to detect rolling element bearing fault as shown figure 2.

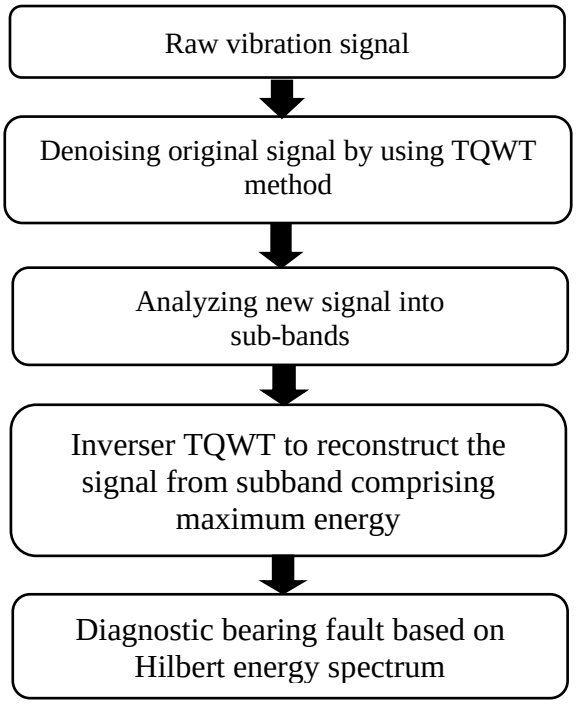

Figure 2: Flowt chart of proposed approach

3. Experimental result

An experimental model to test the ability to detect and assess local damage to the drive was built at CAE Western Reserve University (USA) as part of a research project on oscilloscope diagnostics ("Case Western Reserve University Bearing Data Center Website,") .

The experimental model is a simple transmission system consisting of an electric motor that can change the rotation speed with a frequency converter, a drive shaft, a coupling and a load-generating device (Figure 3). The motor shaft is supported on a SKF 6205-2RS JEM type bearing.

These bearings are subject to experimental research.

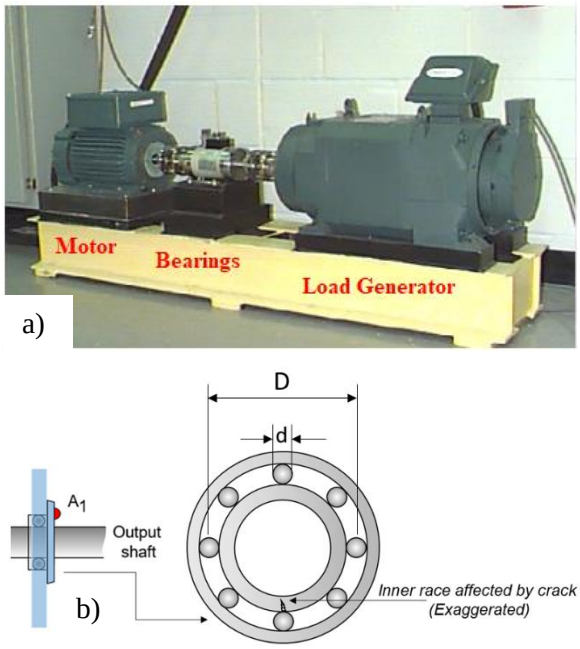

Figure 3: (a) Actual test model for measuring the failure signal of bearings; (b) Detailed model of damaged bearings (inner race fault)

The oscillometric system used on the experimental model consists of two accelerometers to measure system oscillations in the vertical direction and a reference pulse signal probe. The first accelerometer is mounted at the bearing housing. The returned results are the measured acceleration values of the bearing with a sampling frequency of 48000 samples/second. The following figure shows the Amplitude-Time spectrum of the bearing signal.

As shown figure 4 we have 2 time-domain signal of 2 cases of normal bearings and inner race fault bearings. Looking at the normal time-domain signal, it is not possible to determine the characteristic failure frequency. The main reason is due to non-stationary signal as folowing below:

$$x(t) = \cos(at) + \sin(bt)$$

At the same time, the signal is also affected by ambient noise, making it difficult to diagnose damage. So we have to remove the noise for the original signal. Additionally, if applying the hilbert transform for this signal will estimate an average instantaneous frequency of *x(t)* (instead of frequencies *a* or *b*). Thus, using hilbert tranform for original signal will made it more or less be skewed.

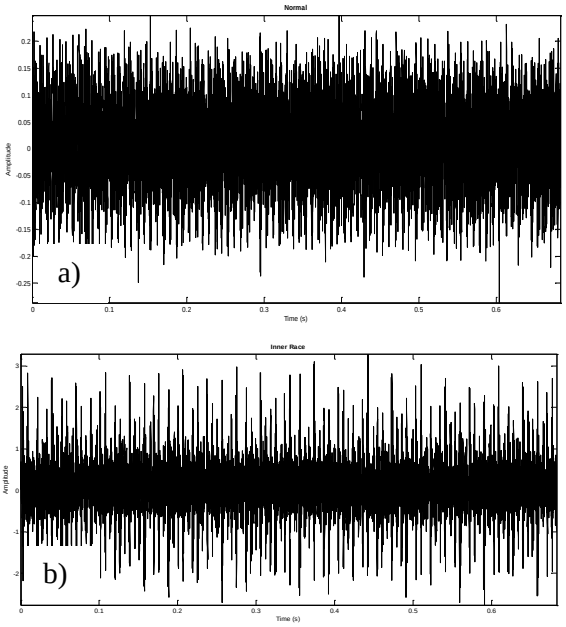

Figure 4: Time-domain signal of the normal bearing (a) and fault bearing (b)

To overcome this problem, we use the previously mentioned TQWT algorithm to eliminate noise as shown in figure 5 and analyze the signal after filtering the noise into small components. Then, instead of using the hilbert transform for original signals, we use the hilbert transform for each of its small components. Signal reconstruction from the small component signals, which have a higher energy level, will get into hilbert tranform to obtain the hilbert energy spectrum.

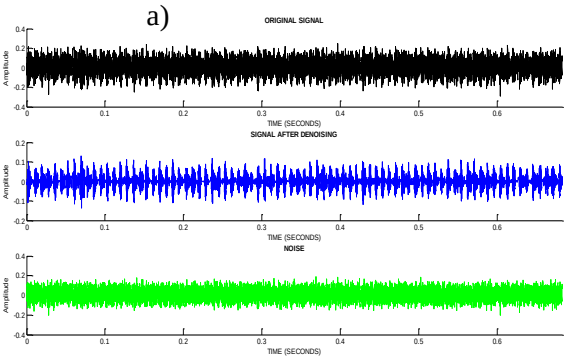

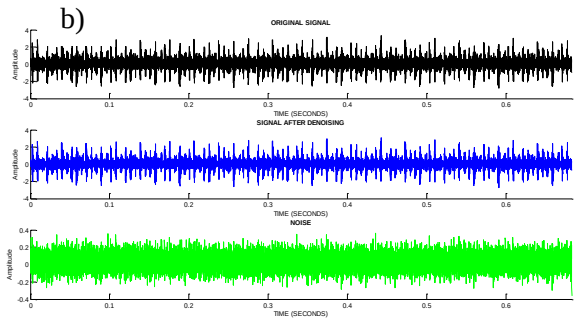

Figure 5: Using BPD method to reduce noise with normal bearing (a) and fault bearing (b)

The signal after reducing noise has become more noticeable. However, when comparing the normal bearings and the inner race fault bearings, we still cannot realize the characteristic difference to identify which one is a damaged bearing. Thus, applying TQWT for denoised signal. In this paper we initialize the input parameters for the TQWT algorithm as follows:

$$Q = 3.5; r = 3; J = 14$$

The subbands are created by dividing the new signal into small components, a total of $J + 1 = 15$ subbands are created. The subbands are shown through the figure 6 below

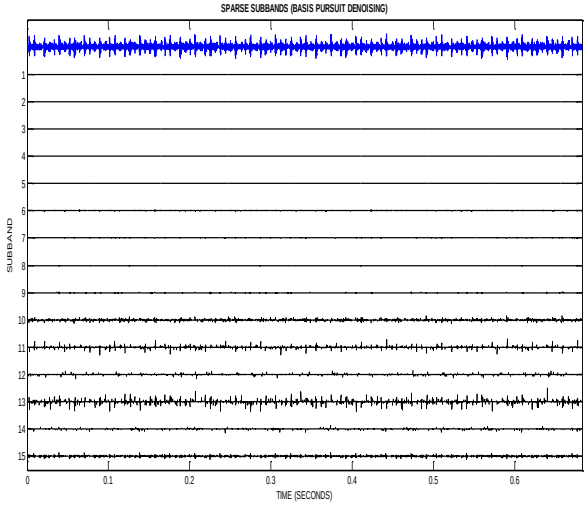

Figure 6: The subbands obtained from the new signal of fault bearings.

To see the contribution of the subbands, we have a figure of the energy distribution of the subbands for the new signal. From the figure 7 we see, subbands 11 and 13 are the ones with the highest energy level throughout the range. This subbands will be used to resconstuction the signal.

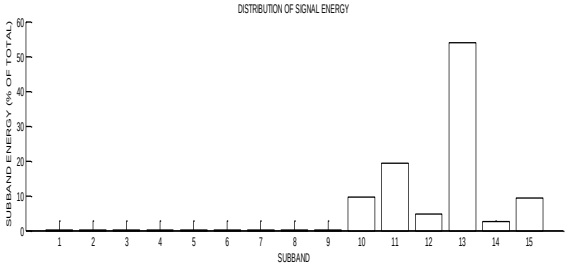

Figure 7: Subbands energy of inner race fault bearings

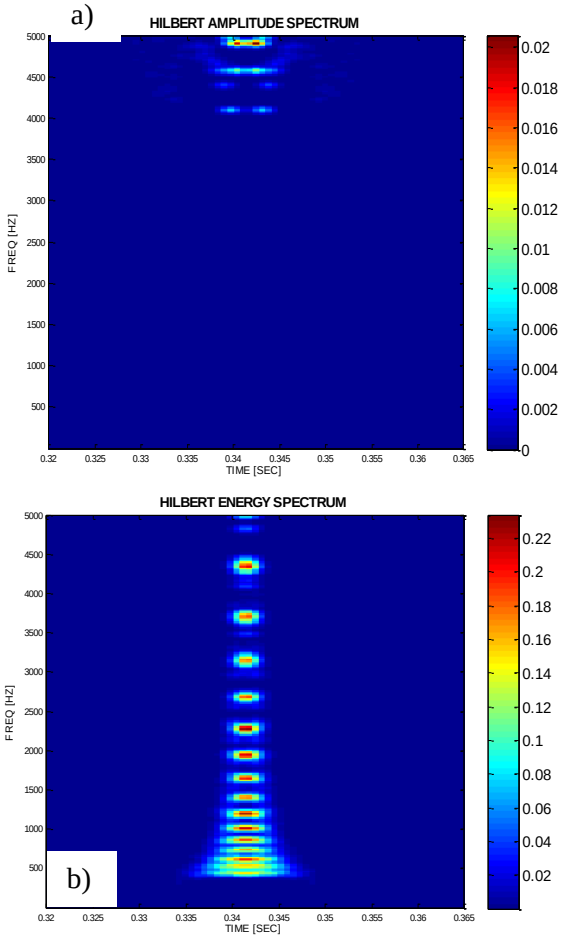

Figure 8: Hilbert energy spectrum of normal bearing (a) and inner race fault bearing (b)

The above Hilbert energy spectrum represents the change of vibrating energy of bearings in 2 cases: normal and inner race fault. The common point is that there is a change in energy from low to high, the red areas are where the energy is highest.

However, the difference is that, in the Hilbert energy spectrum of damaged bearings, the number of red areas appears much and much darker than normal bearings as shown in figure 8. While in normal bearings, these areas of energy change are very faint. This proves that bearings appear to be damaged. Because at the points of failure, large vibrations created a sudden change in the energy level on the Hilbert energy spectrum.

This is one of the signs that helps us diagnose a damaged bearings. If the Hilbert spectrum appears dense in red areas at a given time, it is likely that this bearings has appeared damaged.

On the other hand, we see the maximum energy at the time of 0.33 to 0.36s. This is the moment that the sensor is damaged, from which we can determine the exact location of the bearing failure.

4. Conclusion

In this study, the method of TQWT is used to denoise the raw vibration signals measured at a bearing test-rig. The TQWT is applied to decompose the denoised signals to level 15. The small component signals corresponding to higher energy level are choosen then reconstruct to obtain a new signal without noise. An hilbert transform-based procedure is proposed to identify bearing fault conditions using this new signal.

The results obtained from experiments show that the proposed approach can be used to detect and identify rolling element bearing faults in transmission systems.

References

Cai, G., X. Chen, & Z. He (2013). *Sparsity-enabled signal decomposition using tunable Q-factor wavelet transform for fault feature extraction of gearbox*. Mechanical System and Signal Processing, vol 41, pp. 34–53.

Case Western Reserve University Bearing Data Center Website. Retrieved from https://csegroups.case.edu/bearingdatacenter/home

Cheng, J., D. Yu, J. Tang, et al. (2007). *Application of frequency family separation method based upon EMD and local Hilbert energy spectrum method to gear fault diagnosis*. Paper presented at the Mechanism and Machine Theory 43

Dien, N.P., & N.T. Du (2018). *On a Diagnostic Procedure to Automatically Classify Gear Faults Using the Vibration Signal Decomposition and Support Vector Machine*. Lecture Notes in Networks and Systems, vol 63, pp. 425-432. doi: https://doi.org/10.1007/978-3-030-04792-4_55

Heneghan, C. Khanna, S.M. Flock, et al. (1994). *Investigating the nonlinear dynamics of cellular motion in the inner ear using the short-time Fourier and continuous wavelet transforms*. IEEE Transactions on Signal Processing, vol 42(12), pp. 3335-3352.

Huang, N.E., Z. Shen, S.R. Long, et al. (1998). *The empirical mode decomposition and the Hilbert spectrum for nonlinear and non-stationary time series analysis.* Proceeding of Proceedings of The Royal Society A, 454 (1971), pp. 903-995

Mallat, S. (1999). *A Wavelet Tour of Signal Processing*: Academic Press, New York.

Peng, Z.K., & F.L. Chu (2004). *Application of the wavelet transform in machine condition monitoring and fault diagnostics: a review with bibliography*. Mechanical Systems and Signal Processing, vol 18, pp. 199-221.

Selesnick, I.W. (2011a). *Wavelet transform with tunable Q-factor*. IEEE Transactions on Signal Processing, vol 59.8, pp. 3560-3575.

Selesnick, I.W. (2011b). *Sparse signal representations using the tunable Q-factor wavelet transform*. Paper presented at the Proceedings of SPIE - The International Society for Optical Engineering.

The 5th International Conference on Engineering Mechanics and Automation (ICEMA 5)
Hanoi, October 11÷12, 2019

Dynamics Equation and Design of Fuzzy Controller for a 4-DOF Car Motion Simulator

Pham Van Bach Ngoc[a], Bui Quoc Khanh[a], Bui Trung Thanh[b]

[a]Institute of Mechnics, VietNam Academy Of Science And Technology
pbngoc@imech.vast.vn; phamvanbachngoc@gmail.com
[b]Hung Yen University of Technology and Education, Khoai Chau, Hung Yen

Abstract

In recent years, parallel mechanisms have been researched and applied in many areas such as motion simulators, which simulate the experience of being in a car, plane, tank, and in a virtual reality environment or create motions to serve different goals. In this study, the authors focus on four degrees of freedom (4-DOF) car motion simulators. The 4-DOF car motion simulator consists of one serial structure and one parallel mechanism. The actual model of the simulator is often deficient in the system's parameters and has the nonlinear disturbance. Therefore, a fuzzy control method is proposed to approximate the uncertain elements and to ensure the stability of the system at the same time. This paper, the authors present a fuzzy control system of 4-DOF car motion simulators. Firstly, the kinematics and dynamics modeling of 4-DOF car motion simulators are presented. Secondly, based on the dynamics model, the Fuzzy control technique for 4-DOF car motion simulator is designed. Finally, the simulation results are shown for the demonstration of the control system and comparison with the PID control to verify the accuracy of the control technique.

Keywords: Car motion simulator, fuzzy control, dynamics and kinematics of parallel robot, 4-DOF mechanism

1. Introduction

In the blasting of cutting edge technology, the demand for developing an appropriate structure model assisting in practicing driving in virtual reality environment for trainees plays an imperative role in many industrial fields. Previously, a portion of the recreation models was utilized in the number of various fields, for example, airplane driving practice, vehicles driving practice, car tires checking, and virtual reality environments. The greatest part of these models has been fabricated dependent on a couple of points of interest of parallel mechanism such as low inertia moment, high load capacity, and great transmission in D. Stewart (1965). One of the simulations model including 6 degrees of freedom based on the structure of Stewart-Gough which is written in L. W. Tsai (1999). However, the fact that it is unnecessary to build 6-DOF in the mechanical system which leads to complexity in control and an increasing cost as well.

In the attempt of reducing motion time and costs of the whole model system, the authors have constructed the four degrees of freedom (4-DOF) car motion simulators, comprising of the movements of rotating and translating along the vertical OZ axis, revolving around the OX axis and OY axis. Until present, the control of the nonlinear system with nonlinear parameters is still a dilemma, so feedback control

methodologies accompanied by the Lyapunov stability approach in N.D. Phuoc (2008) were a great deal of consideration. One of these planned schemes for non-linear control systems getting intrigued by numerous researchers is Backstepping control technique in M. Zhang (2012) to achieve the necessity of movement. In any case, the calculation of the Backstepping controller becomes more complex when the model has more parameters and degrees of freedom.

In this paper, the authors focus on constructing an intelligent control algorithm for the 4-DOF car motion simulator which is affected by unknown external force and the uncertain components in the mathematical model. This paper is organized like this: Firstly, the 4-DOF car motion simulator is briefly introduced, the kinematic and constraints equations are derived by using the geometric method; secondly, Lagrange's formulation is used to design differential equations of motion; finally, the research could be used for dynamic simulation and conducting experiments on real models in the near future. To verify the correctness of the proposed control algorithm technique, the system was simulated with the external disturbance, along with the techniques to minimize the "chattering" phenomenal due to sliding mode control design process.

2. Kinematics and Dynamics of 4-DOF Car motion simulator

Let's consider a 4-DOF car motion simulator shown in **Fig. 1**, this car motion simulator model has 3 linear actuator free-standing mechanisms mounted vertically on a platform by 3 rotary joints; the upper plate is connected with 3 actuators by 3 universal joints. Each limb consists of an upper plate and lower plate connected by a prismatic joint. This entire motion is attached to a platform fixed by a rotating joint around the OZ-axis. With links like this, the upper plate will have 04 movements. The upper plate can spin around the OZ axis, OY axis, and OX axis and move forward in OZ axis. So this model parallel Car motion simulator ensures 4 degrees of freedom.

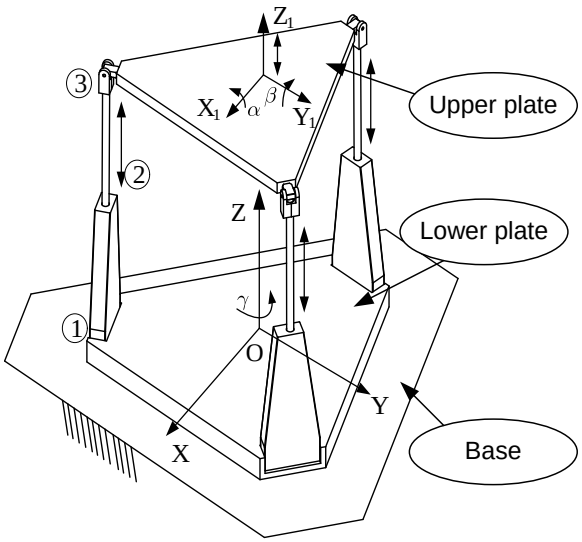

Fig 1. Mechanical model of 4-DOF car motion simulators

2.1 Inverse kinematics

In this situation, the position of vector **P** of the moving plate is given, and the problem is to find the length of limb l_i with $i = 1, 2, 3$, and the angle of rotation about Z-axis γ required to bring the moving plate to the desired position.

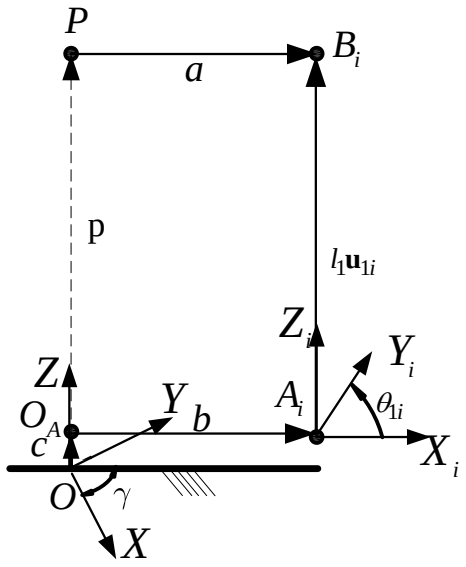

Fig 2. Vector diagram of 4-DOF car motion simulators

The 4-DOF car motion simulator vector diagram is expressed as in Fig 2, in which the parameters with u_i with $i=1,2,3$ is directional vectors, l_i with $i=1,2,3$ is length of limbs, a is the upper plate radius, b is the lower plate radius (in this model assumption that $a=b$), c is the distance OO_A. Fig.2 also shows the car driving simulator's mechanism model in which the global axis is chosen.

As shown fig 2, a loop-closure equation can be written for each limb as:

$$\overline{A_iB_i} = \overline{OP} + \overline{PB_i} - \overline{O_AA_i} - \overline{OO_A} \quad (1)$$

or rewritten in the vector equation as

$$l_i\mathbf{u_{1i}} = \mathbf{c} + \mathbf{p} + \mathbf{b} - \mathbf{a} \quad (2)$$

The lengths of each limb can be obtained as:

$$l_i = \sqrt{A_iB_i^T * A_iB_i} \text{ with } i=1,2,3 \quad (3)$$

2.2 Dynamics equations

In the paper, we use Euler - Lagrange equations to build a dynamics equations. The dynamics equations of 4-DOF car motion simulators have been written as:

$$\frac{d}{dt}\left(\frac{\partial L}{\partial \dot{q}_i}\right) - \frac{\partial L}{\partial q_i} = Q_i \text{ with } i=1,2,3 \quad (4)$$

where Q_i is the actuator force of torque with $i=1,2,3$ and $q = \begin{bmatrix} l_1 & l_2 & l_3 & \gamma \end{bmatrix}^T$

The total kinetic energy of the 4DOF car motion simulator can be written as:

$$K = K_p + K_{piston} + K_\gamma \quad (5)$$

where

$$K_p = \frac{1}{2}m_p\dot{p}_z^2 + \frac{1}{2}I_{px}\dot{\alpha}^2 + \frac{1}{2}I_{py}\dot{\beta}^2;$$

$$K_{piston} = \frac{1}{2}m_2\left(\dot{l}_1^2 + \dot{l}_2^2 + \dot{l}_3^2\right);\ K_\gamma = \frac{1}{2}I_\gamma\dot{\gamma}^2$$

The rotation about OX and OY can be obtained as:

$$\alpha = \arcsin\left(\sqrt{3}\frac{p_z - l_2}{a}\right);\ \beta = \arcsin\left(\frac{p_z - l_1}{a}\right);$$

and $p_z = \frac{1}{3}\left(l_1 + l_2 + l_3\right)$; m_p is the mass of the moving platform, m_1 is the mass of moving base, the total mass of piston cover and motors is $\left(m_2 + m_{dc}\right)$.

The inertial momentum of each part can be written as:

$$I_\gamma = \frac{1}{2}\left(m_p + m_1\right)a^2\left(1 - \frac{2}{3}\sin^2\left(\frac{\pi}{3}\right)\right) + 3\left(m_2 + m_{dc}\right)a^2$$

and $I_{px} = \frac{3a^2}{24}m_p$; $I_{py} = \frac{3\sqrt{3}a^4}{32}$

The total potential energy of the 4-DOF car motion simulator can be obtained as:

$$U = U_p + U_{piston} + U_\gamma \quad (6)$$

where

$$U_p = m_p g p_z;\ U_{piston} = m_2 g\left(l_1 + l_2 + l_3 - 3c\right)$$

$$U_\gamma = \left(m_1 + 3m_2 + 3m_{dc} + m_p\right)gc$$

Therefore, the Lagrangian function is

$$\begin{aligned} L = {} & \frac{1}{2}m_p\dot{p}_z^2 + \frac{1}{2}I_{px}\dot{\alpha}^2 + \frac{1}{2}I_{py}\dot{\beta}^2 \\ & + \frac{1}{2}m_2\left(\dot{l}_1^2 + \dot{l}_2^2 + \dot{l}_3^2\right) + \frac{1}{2}I_\gamma\dot{\gamma}^2 \\ & - \frac{1}{3}m_p g\left(l_1 + l_2 + l_3\right) - m_2 g\left(l_1 + l_2 + l_3 - 3c\right) \\ & - \left(m_1 + 3m_2 + 3m_{dc} + m_p\right)gc \end{aligned} \quad (7)$$

Taking the derivatives of the Lagrangian function with respect to the generalized coordination, the dynamics equation of 4-DOF car motion simulators can be written as follows:

$$M\ddot{q} + C(\dot{q}, q) + G = F \quad (8)$$

where

$$M = \begin{vmatrix} \left(m_2 + \frac{m_p}{9} + 4I_{py}\right) & \frac{m_p}{9} & \frac{m_p}{9} & 0 \\ \frac{m_p}{9} & m_2 + \frac{m_p}{9} + 4I_{px} & \frac{m_p}{9} & 0 \\ \frac{m_p}{9} & \frac{m_p}{9} & m_2 + \frac{m_p}{9} & 0 \\ 0 & 0 & 0 & I_\gamma \end{vmatrix}$$

$$C(\dot{q}, q) = \begin{bmatrix} \frac{60 l_1 \dot{l}_1^2}{\left(4a^2 - l_1^2\right)^2} & \frac{60 l_2 \dot{l}_2^2}{\left(12a^2 - l_2^2\right)^2} & 0 & 0 \end{bmatrix}^T$$

$$G = g\left[\left(m_1 + \frac{m_p}{3}\right) \quad \left(m_1 + \frac{m_p}{3}\right) \quad \left(m_1 + \frac{m_p}{3}\right) \quad 0\right]^T$$

and $g = 9.8(m/s^2)$ is the gravity coefficient.

$F = \begin{bmatrix} F_1 & F_2 & F_3 & \tau_\gamma \end{bmatrix}^T$ is force and moment vector.

Solving the equation (8) the forces and moment of each motor can be obtained as:

$$F_1 = \left(m_2 + \frac{m_p}{9} + 4I_{py}\right)\ddot{l}_1 + \frac{m_p}{9}\ddot{l}_2 + \frac{m_p}{9}\ddot{l}_3 + \frac{60 l_1 \dot{l}_1^2}{\left(4a^2 - l_1^2\right)^2} + \left(m_1 + \frac{m_p}{3}\right)g$$

$$F_2 = \frac{m_p}{9}\ddot{l}_1 + \left(m_2 + \frac{m_p}{9} + 4I_{px}\right)\ddot{l}_2 + \frac{m_p}{9}\ddot{l}_3 + \frac{60 l_2 \dot{l}_2^2}{\left(12a^2 - l_2^2\right)^2} + \left(m_1 + \frac{m_p}{3}\right)g \qquad (9)$$

$$F_3 = \frac{m_p}{9}\ddot{l}_1 + \frac{m_p}{9}\ddot{l}_2 + \left(m_2 + \frac{m_p}{9}\right)\ddot{l}_3 + \left(m_1 + \frac{m_p}{3}\right)g$$

$$\tau_\gamma = I_\gamma \ddot{\gamma}$$

3. Design controller for 4-DOF car motion simulators

3.1 Design a PID controller for 4-DOF car motion simulators

The objective of control design is to find the law of applied moments to force the upper plate to track the given trajectory $q = q_d$. The trajectory deviation is defined by $e = q - q_d$. From eq.8 the PID control law can be applied as

$$F = K_p e + K_D \dot{e} + K_I \int_0^t e(t) d(t) \qquad (10)$$

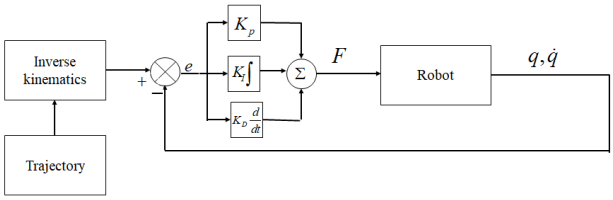

Fig 3: The PID control block diagram for 4-DOF car motion simulators

We have control gains:

$$K_P = 245.6;\ K_I = 190.2;\ K_D = 16.2$$

3.2 Design a Fuzzy controller for 4-DOF car motion simulators

The input of the fuzzy controller will be the error value e and change-in-error de. The output of the fuzzy controller will be the force of piston (F_i) with $i = 1,2,3$. While car motion simulators move the elements such as noise, friction and external forces are ignored.

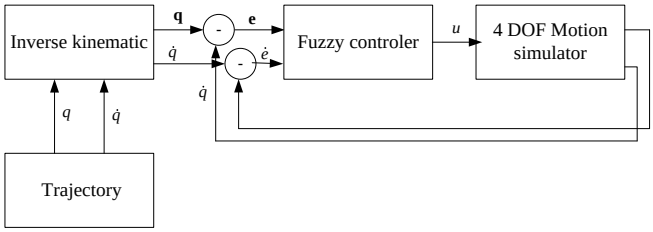

Fig 4: The Fuzzy control block diagram for 4-DOF car motion simulators

Robot is modeled based on the dynamic equation in Matlab simulink as follows:

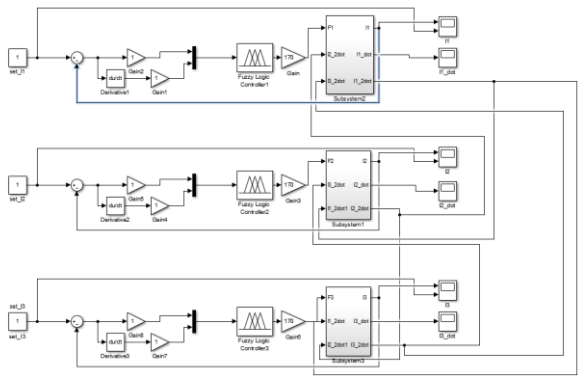

Fig 5: Block diagram of the 4-DOF car motion simulators

A fuzzy controller law is built as follows:

First: The linguistic description provided by the expert can generally be broken into several parts. There will be "linguistic variables" that describe each of the time-varying fuzzy controller inputs and outputs. For the inverted pendulum:

"error" describes $e\ t$

"change-in-error" describes $de\ t$

"force" describes $u\ t$

There are many possible choices for the linguistic descriptions for variables. Some designers like to choose them as they are quite descriptive for documentation purposes. However, this can sometimes lead to long descriptions. Others seek to keep the linguistic descriptions as short as possible in this situation; the authors choose the following linguistic variables:

error =(NB,NM,NS,NT,ZE,PT,PS,PM,PB)

change-in-error=(NB,NM,NS,NT,ZE,PT,PS, PM,PB)

Force = (F1,F2,F3,F4,F5,F6,F7,F8,F9)

Second: Membership function

Table 1: Variable parameters error

Name	Value domain
NB	[-30 -20 -1 -0.75]
NM	[-1 -0.75 -0.5]
NS	[-0.75 -0.5 -0.25]
NT	[-0.5 -0.25 0]
ZE	[-0.25 0 25]
PT	[0 0.25 0.5]
PS	[0.25 0.5 0.75]
PM	[0.5 0.75 1]
PB	[0.75 1 10]

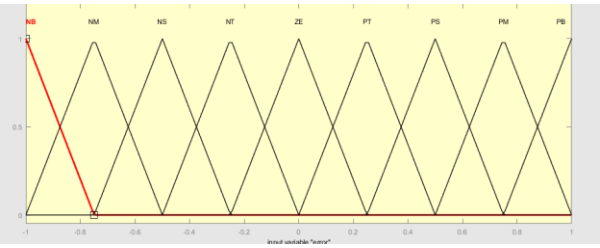

Table 2: Variable parameters change-in-error

Name	Value domain
NB	[-30 -20 -1 -0.75]
NM	[-1 -0.75 -0.35]
NS	[-0.75 -0.35 0]
ZE	[-0.35 0 35]
PS	[0 0.35 0.65]
PM	[0.35 0.65 1]
PB	[0.65 1 10]

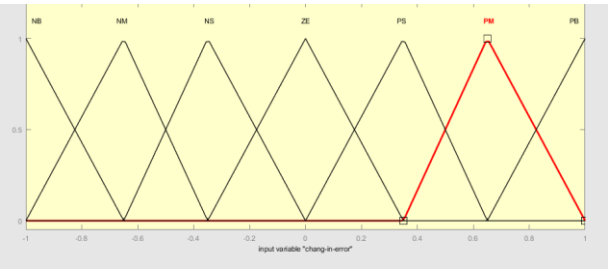

Table 3: Variable parameters force

Name	Value domain
F1	[-30 -20 -1 -0.75]
F2	[-1 -0.75 -0.5]
F3	[-0.75 -0.5 -0.25]
F4	[-0.5 -0.25 0]
F5	[-0.25 0 25]
F6	[0 0.25 0.5]
F7	[0.25 0.5 0.75]
F8	[0.5 0.75 1]
F9	[0.75 1 10]

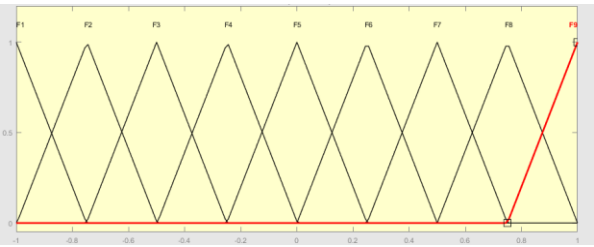

The third: Rule of the Fuzzy control system

e / de	NB	NM	NS	NT	ZE	PT	PS	PM	PB
NB	F1	F1	F1	F1	F2	F3	F4	F5	F6
NM	F1	F1	F1	F2	F3	F4	F5	F6	F7
NS	F1	F1	F2	F3	F4	F5	F6	F7	F8
ZE	F1	F2	F3	F4	F5	F6	F7	F8	F9
PS	F2	F3	F4	F5	F6	F7	F8	F9	F9
PM	F3	F4	F5	F6	F7	F8	F9	F9	F9
PB	F4	F5	F6	F7	F8	F9	F9	F9	F9

4 Simulation results and discussion

The fuzzy controller is designed for the generalized case of the 4-DOF car motion simulator. The 4-DOF car motion simulator kinematics and dynamics parameters are shown in **table 4.** In the simulation results, the quality of the fuzzy control method in comparison with the PID control law to verify the accuracy of the control algorithm is shown in **Fig.6** and **Fig.7**.

Table 4. 4-DOF **c**ar motion simulator kinematics and dynamics parameters

Items	Value
Upper plate radius (a)	300 [mm]
Lower plate radius (b)	300[mm]
Leg struts	300[mm]
c	50[mm]
m_p	15(kg)
m_1	0.5(kg)
m_2	10(kg)
m_{dc}	3(kg)

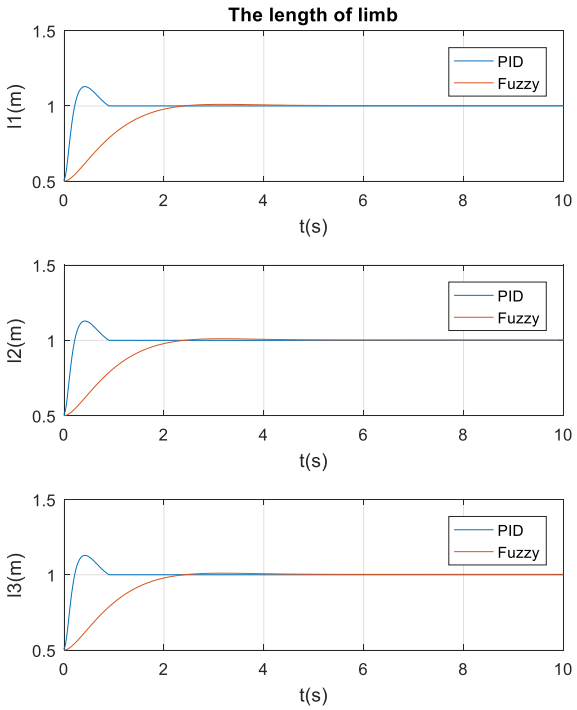

Fig 6. The length of limbs

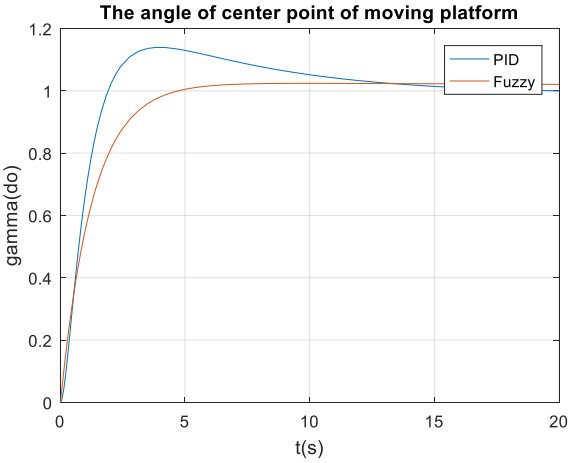

Fig 7. The angle of center point of moving plate

Based on the above results, both fuzzy and PID controller provide good grip quality. Both fuzzy controller and PID controller laws ensure that the motion of the system can track the desired trajectory with the small oscillation despite the influence of external disturbance. From the simulation results shown in **fig. 5** and **fig. 6**, we see the deviation when using the PID controller with much variation and larger deviation than the Fuzzy controller. The error of the Fuzzy controller ≈ 0.5%, compared to the set value and the trajectory, we can consider this deviation ≈ 0.

5. Conclusions

This paper presents the dynamics equation and a fuzzy control scheme for the 4-DOF Car motion simulator. We have proposed a fuzzy controller for mechanism based on the dynamic equation. Through the simulation results, we can see that the fuzzy method is able to ensure the stability and the effectiveness of the 4-DOF car motion simulator; the 4-DOF car motion simulator omits well the unknown disturbance with the proposed controller. Therefore, the fuzzy can be recommended for nonlinear systems requiring high accuracy and safe transportation.

Acknowledgement: This work is funded by VAST project under grant number VAST01.06/19-20.

References

D. Stewart (1965), "A Platform with Six Degrees of Freedom" Proc. Inst. Mech. Eng., 180 Part, Vol. 1, No. 15, pp. 371-386.

L. W. Tsai (1999.), Robot Analysis: The Mechanics of Serial and Parallel Manipulators, Wiley.

Nguyễn Doãn Phước, Phan Xuân Minh, Hán Thành Trung (2008), Lý thuyết điều khiển phi tuyến, Nhà xuất bản Khoa học và Kỹ thuật.

Q. Z. Cui, X. Li, X. K. Wang, and M. Zhang, (2012) "Backstepping Control Design on the Dynamics of the Omni-Directional Mobile Robot," Appl. Mech. Mater., vol. 203, pp. 51–56.

D. Swaroop, J. C. Gerdes, P. P. Yip, and J. K. Hedrick (2002), "Dynamic surface control of nonlinear systems," pp. 3028–3034 vol.5.

G. Sun, D. Wang, X. Li, and Z. Peng, (2013) "A DSC approach to adaptive neural network tracking control for pure-feedback nonlinear systems," Appl. Math. Comput., vol. 219, no. 11, pp. 6224–6235.

Authour Index